

Applicable Solutions in Non-Linear Dynamical Systems

Editors

JAN AWREJCEWICZ, MAREK KAŻMIERCZAK, PAWEŁ OLEJNIK

© Copyright by Politechnika Łódzka 2019

ISBN 978-83-66287-30-3

Cover design: Marek Kaźmierczak
Technical editor: Marek Kaźmierczak

Wydawnictwo Politechniki Łódzkiej
ul. Wólczańska 223, 90-924 Łódź
tel. 42 631 20 87, fax. 42 631 25 38
e-mail: wydawnictwo@lib.p.lodz.pl

Printed by:
ARSA Druk i Reklama
90-270 Łódź, ul. Piotrkowska 4
tel./fax (042) 633 02 52
marta@arsa.net.pl
www.arsa.net.pl

PREFACE

The 15th International Conference “Dynamical Systems - Theory and Applications” (DSTA 2019, 2-5 December, 2019, Lodz, Poland) gathered a numerous group of outstanding scientists and engineers who deal with widely understood problems of theoretical and applied dynamics.

Organization of the conference would not have been possible without great effort of the staff of the Department of Automation, Biomechanics and Mechatronics of the Lodz University of Technology. The patronage over the conference has been taken by the Committee of Mechanics of the Polish Academy of Sciences and Ministry of Science and Higher Education of Poland.

It is a great pleasure that our event was attended by over **180** researchers from **35** countries all over the world, who decided to share the results of their research and experience in different fields related to dynamical systems.

This year, the DSTA Conference Proceedings were split into two volumes entitled “*Theoretical Approaches in Non-Linear Dynamical Systems*” and “*Applicable Solutions in Non-Linear Dynamical Systems*”. In addition, DSTA 2019 resulted in three volumes of Springer Proceedings in Mathematics and Statistics entitled “*Control and Stability of Dynamical Systems*”, “*Mathematical and Numerical Approaches in Dynamical Systems*” and “*Dynamical Systems in Mechatronics and Life Sciences*”. Also, many outstanding papers will be recommended to special issues of renowned scientific journals.

The DSTA Conference Proceedings include papers covering the following topics:

- asymptotic methods in non-linear dynamics,
- bifurcation and chaos in dynamical systems,
- control in dynamical systems,
- dynamics in life sciences and bioengineering,
- engineering systems and differential equations,
- non-smooth systems
- mathematical approaches to dynamical systems
- original numerical methods of vibration analysis,
- stability of dynamical systems,
- vibrations of lumped and continuous systems,
- other problems.

Proceedings of the 15th Conference „Dynamical Systems - Theory and Applications” summarize **106** papers of university teachers and students, researchers and engineers from all over the world. The papers were selected by the Scientific Committee of DSTA 2019 from **360** papers submitted to the conference. Therefore, the reader is provided with an overview of recent developments in dynamical systems and can study the most progressive tendencies in this field of science.

Our experience shows that a broad thematic scope comprising dynamical systems encourages researchers to exchange their opinions on different branches of dynamics. We think that the vivid discussion will influence positively creativity and will result in effective solutions of many problems of dynamical systems in mechanics and physics, both in terms of theory and applications.

We do hope that DSTA 2019 will contribute to establishing new and tightening the already existing relations and scientific and technological cooperation between Polish and foreign institutions.

On behalf of both
Scientific and Organizing Committees

A handwritten signature in black ink, appearing to read 'Awrejcewicz', with a stylized flourish at the end.

Chairman
Professor Jan Awrejcewicz

CONTENTS

Nurtay Albanbay , Bekbolat Medetov , Michael Zaks <i>Distribution of lifetimes for transient bursting states in coupled noisy excitable systems</i>	11
Tariq Alzarooni , Mohammad AL-Shudeifat , Oleg Shiryayev , C. Nataraj <i>On backward whirl excitation in linear time-variant intact and cracked rotor systems</i>	25
Jan Awrejcewicz , Dmytro Bilichenko , Akram Khalil Cheib , Nataliya Losyeva , Volodymyr Puzyrov <i>Estimation of the domain of attraction for a nonlinear mechanical system</i>	37
Jan Awrejcewicz , Olga Saltykova , Vadim Krysko , Anton Krysko <i>Nonlinear dynamics of flexible nanobeams taking into account the Casimir, van der Waals and Coulomb forces</i>	47
Jan Awrejcewicz , Roman Starosta , Grażyna Sypniewska-Kamińska <i>Vibration of nonlinear lumped systems with serially connected elastic elements</i>	55
Jan Awrejcewicz , Maxim Zhigalov , Sergey Pavlov , Vadim Krysko <i>Nonlinear dynamics of thermoelastic Sheremetiev-Pelekh nanobeams with topologically optimal microstructure</i>	65
Włodzimierz Bielski , Ryszard Wojnar <i>Gravity waves in channels with corrugated bottom: asymptotic approaches</i>	75
Ivan Bizyaev , Alexey Borisov , Alexander Kilin , Ivan Mamaev , Elena Pivovarova <i>Nonholonomic acceleration and chaotic dynamics of locomotion</i>	87
Vasily Buyadzhi , Anna Buyadzhi , Alexey Chernyshev , Evgeniya Plisetskaya , Eugeny Pavlov , Sergey Kir'yanov <i>Nonlinear dynamics of laser systems: Chaos, bifurcations and strange attractors</i>	99
Jarosław Chruściel , Anna Frątczak , Angelika Puchalska , Siam Streibl , Bartłomiej Zagrodny <i>Thermographic analysis of the additional load influence on the muscle activation during gait</i>	107
Stefan Chwastek <i>Finding globally optimal combinations of cranes drive mechanisms by the method of exhausting alternative design structures of mechanisms</i>	117

Eva-H. Dulf , Cristina-I. Muresan , Daniel D. Timis	
<i>Adaptive fractional order control of a quadrotor</i>	129
Wiesław Fiebig	
<i>The use of mechanical resonance for the reduction of torque pulsation and energy demand in machines with crankshaft systems</i>	139
Gustavo de Freitas Fonseca , Airton Nabbarrete	
<i>Finite element analysis of magneto-rheological fluid embedded on journal bearings</i>	151
Miroslaw Gidlewski , Leszek Jemioł , Dariusz Żardecki	
<i>Influence of control system parameters and it's disturbances on lane change process</i>	163
Aurélien Grolet , Zein Shami , Sadaf Arabi , Olivier Thomas	
<i>Experimental nonlinear localisation in a system of two coupled beams</i>	171
Dariusz Grzelczyk , Jan Awrejcewicz	
<i>Stability and control of a hybrid walking robot on planar, unstable and vibrating terrain</i>	183
Ben Gunn , Stephanos Theodossiades , Steve Rothberg	
<i>A rotational energy harvester for propulsion systems: design and experimental validation</i>	193
Nicolae Herisanu , Vasile Marinca	
<i>A new analytical approach to nonlinear free vibration of microtubes</i>	205
Elżbieta Jarzębowska , Krzysztof Augustynek , Andrzej Urbaś	
<i>Dynamics and vibration analysis of a spatial linkage model with flexible links and joint friction subjected to position and velocity motion constraints</i>	215
Olga Jarzyna , Dariusz Grzelczyk , Jan Awrejcewicz	
<i>A simple pattern generator for biped walking</i>	227
Kalkunte R. Jayaprakash , Yuli Starosvetsky	
<i>Analytical and numerical study of piecewise linear Mathieu equation with non-zero offset</i>	237
Krzysztof Kaliński , Marek Galewski , Michał Mazur , Natalia Morawska	
<i>Optimization of the spindle speed during milling of large-sized structures with the use of technique of Experiment-Aided Virtual Prototyping</i>	249

Olga Yu. Khetselius , Andrey A. Svinarenko , Yuliya Ya. Bunyakova , Alexander V. Glushkov	
<i>Chaos-geometric approach to analysis and forecasting evolutionary dynamics of complex systems: Atmospheric pollutants dynamics</i>	259
Olga Yu. Khetselius , Andrey A. Svinarenko , Anna V. Ignatenko , Anna A. Buyadzh	
<i>New generalized chaos-geometric and neural networks approach to nonlinear modeling of complex chaotic dynamical systems</i>	267
Anton Krysko , Jan Awrejcewicz , Ilya Kutepov , Vadim Krysko	
<i>Nonlinear dynamics of NEMS resonators in temperature field</i>	277
Vadim A. Krysko-jr , Jan Awrejcewicz , Maxim V. Zhigalov , Vadim. A. Krysko	
<i>Dimension reduction method in nonlinear equations of mathematical physics (MEMS/NEMS problems)</i>	289
Vadim A. Krysko-jr , Jan Awrejcewicz , Ekaterina Yu. Krylova , Irina V. Papkova	
<i>Nonlinear dynamics of flexible nanoplates resting on an elastic foundation in a stationary temperature field</i>	301
Izabela Krzysztofik , Zbigniew Koruba	
<i>An optimal control of the gyroscope system in the process of homing an air-to-air missile</i>	313
Paweł Latosiński , Andrzej Bartoszewicz	
<i>Discrete-time model reference sliding mode control using an exponential reaching law</i>	323
Enrique Roberto Carrillo Li , Philipp Schorr , Tobias Kaufhold , Jorge Antonio Rodríguez Hernández , Lena Zentner , Klaus Zimmermann , Valter Böhm	
<i>Kinematic analysis of the rolling locomotion of mobile robots based on tensegrity structures with spatially curved compressed components</i>	335
António M. Lopes , J.A. Tenreiro Machado	
<i>Fractional dynamics and power law behavior in soccer leagues</i>	345
Alexey Lukin , Popov Ivan , Udalov Pavel	
<i>Nonlinear dynamics of the sensory element of the atomic force microcopy</i>	355
Olga Mazur , Jan Awrejcewicz	
<i>Size-dependent nonlinear vibrations of micro-plates subjected to in-plane magnetic field</i>	365
Ewelina Ogińska , Krystian Polczyński , Dariusz Grzelczyk , Jan Awrejcewicz	
<i>Numerical and experimental investigations of dynamics of magnetic pendulum with an aerostatic bearing</i>	375

Alexey Papirovskiy , Alexey Lukin , Ivan Popov <i>Analytical and numerical modelling of surface acoustic waves in rotating media</i>	387
Wojciech Paszkowiak , Tomasz Bartkowiak <i>Dynamics of logistic train</i>	397
Leon Prochowski , Mateusz Ziubiński , Patryk Szwajkowski , Tomasz Pusty , Mirosław Gidlewski <i>Experimental and simulation examination of the impact of the control model on the motion of a motorcar with a trailer in a critical situation</i>	409
Andrzej Rysak , Magdalena Gregorczyk <i>Study of the Duffing van der Pol system dynamics using RQA measures</i>	423
Alireza Ture Savadkoohi , Claude-Henri Lamarque , Célien Goossaert <i>Control of tremors of human's arm by a passive nonlinear absorber</i>	431
Yury Selyutskiy <i>Alternation of stability character in systems with positional non-conservative forces</i>	439
Aleksander Skurjat <i>The influence of lateral swaying on the trajectory of articulated rigid body vehicles</i>	449
Valeri Smirnov , Leonid Manevitch <i>Strong mode coupling in vibrations of single-walled carbon nanotubes</i>	457
Anna Šmeringaiová , Imrich Vojtko <i>Experimental assessment of the test station support structure rigidity by the vibration diagnostics method</i>	469
Rafael Teloli , Samuel da Silva , Gaël Chevallier <i>Parameters estimation by harmonic probing of hysteresis models of bolted jointed</i>	479
Valentin Ternovsky , Alexander Glushkov , Eugeny Ternovsky , Andrey Tsudik <i>Dynamics of non-linear processes in a backward-wave tubes chain: Chaos and strange attractors</i>	491
Hans True <i>Bifurcations and transitions in railway vehicle dynamics</i>	499
Ferdinand Verhulst <i>Systems with fast limit cycles and slow interaction</i>	511

Wiktorja Wojnicz , Bartłomiej Zagrodny , Michał Ludwicki , Jerzy Mrozowski , Jan Awrejcewicz , Edmund Wittbrodt <i>Multibody models for gait analysis</i>	523
Kiyotaka Yamashita , Naoto Nishiyama , Kohsuke Katsura , Hiroshi Yabuno <i>Nonlinear stability of a spring-supported pipe conveying fluid</i>	539
Azhar Ali Zafar , Jan Awrejcewicz <i>On the dynamics of blood through the circular tube along with magnetic properties</i>	547
Klaus Zimmermann , Igor Zeidis , Victor Lysenko , Simon Gast , Lars Günther , Florian Schale , Michel Rohn <i>Mathematical model and a prototype of a linear motor controlled by a periodic magnetic field</i>	559
Ádám Zsiros , János Lelkes , Tamás Kalmár-Nagy <i>Energy spectrum of inhomogeneous rods with elastic and viscous boundary conditions</i>	567

Distribution of lifetimes for transient bursting states in coupled noisy excitable systems

Nurtay Albanbay, Bekbolat Medetov, Michael A. Zaks

Abstract: In ensembles of coupled oscillators, intrinsic fluctuations often enable nontrivial dynamics in seemingly simple situations. We investigate one of such effects on the example of two coupled FitzHugh-Nagumo oscillators subjected to external noise. At the considered parameter values, the unique global attractor of the deterministic system is the state of rest. Additive white noise of low or moderate intensity leads to the onset of transient bursting regime: series of intermittent bursts (patches of spikes), followed by the abrupt decay to the state of rest. Depending on the noise strength and the initial conditions, the number of bursts before the ultimate decay displays strong variations. Our numerical studies disclose that in the sufficiently large ensembles of realizations, the statistics of lifetimes for the transient bursting states follows the exponential distribution. The distribution slope (i.e. the mean duration of the bursting regime) depends on the noise intensity, being small for very weak noise and asymptotically diverging when the noise becomes stronger. Observations on the statistics of transient bursting regimes have been qualitatively and quantitatively confirmed by our experiments with the coupled analog electronic circuits, modeling the FitzHugh-Nagumo dynamics. We relate the exponential character of the distribution to the probability that the trajectory of the system, under the action of noise, escapes the local attraction basin of the state of rest.

1. Introduction

One of the characteristic properties of the cerebral cortex is its ability to display neural activity even in the absence of external stimuli. This effect can be traced from large populations of neural cells down to small ensembles of electrically or chemically coupled neurons. Different mechanisms of this self-sustained activity are related to excitability: the property of a neuron whose membrane potential is contained at the state of rest, to react with the large-scale action potential (spike) to the sufficient, but nevertheless relatively weak, perturbations [1]. Collective properties of the neuronal ensembles are largely defined by the spiking patterns: the temporal arrangement of action potentials. One of the prominent patterns is bursting: alteration of relatively long intervals of quiescence with periodically or irregularly occurring groups (bursts) of densely packed spikes. Experimentally, bursting is well documented; its adequate mathematical modeling goes back to the formalism suggested by Rinzel [2]. In particular, it was shown that for the correct reproduction of bursting, the modeling dynamical

system should involve the timescale separation and be of the slow-fast type: the phase space should include subsets corresponding, respectively, to slow and fast evolution.

Recently, it turned out that dynamics of the bursting type, a bit surprisingly, can be observed in the setups that, strictly speaking, preclude the existence of bursting [3]. The set of two linearly coupled FitzHugh-Nagumo neuronal oscillators was numerically simulated in the parameter region where the only attractors were verified to be the stable states of rest or the limit cycles. It turned out that these simple attracting states could be reproduced only if the precision of the integrating routine was sufficiently high: at the default accuracy of the standard Runge-Kutta integrator, the numerical solutions, instead of converging to the equilibrium or mild oscillations, demonstrated non-abating large-scale bursting. Inaccuracies of integration played the role of numerical noise; a similar effect was observed, when additive white noise was explicitly included into the system.

Below, we return to the setup with additive noise where, in the absence of random terms, the only global attractor is the state of rest. If the noise intensity is sufficiently weak, only mild fluctuations around the equilibrium are observed. If, on the contrary, the noise is strong, the (deterministically non-existent) bursting is established which does not cease as long as the simulation goes on. There exists, however, a remarkable intermediate range of moderate noise intensities, where the system finally settles in the neighborhood of equilibrium, but this relaxation is preceded by a bursting transient: a number (from a few to thousands) of bursting episodes. A repetition of the process with the same starting conditions but under the different noise realization results, as a rule, in the transient with the different number of bursting epochs. By repeating this procedure sufficiently many times, we obtain the large ensemble of transients, and estimated the probability to observe the transient with the given number of bursts (“lifetime”). The distribution of lifetimes in the large ensemble of realizations turns out to be exponential; this qualitative result is robust against variation of parameter values in the original deterministic system. Furthermore, we model this system of two coupled neurons with the help of coupled analog electronic circuits, modeling the FitzHugh-Nagumo neurons. There, the noise does not need to be added explicitly: random fluctuations are inherently present in the voltage dynamics. Processing the experimental data from the series of experiments, we again recover the exponential distribution of lifetimes.

The layout is as follows. Sect.2 contains formulation of the problem and description of general properties of the dynamical system. In Sect.3 we show how the exponential distribution of bursting lifetimes manifests itself in numerical simulations, whereas in Sect.4 we describe the analog electronic circuit and present results of the experimental measurements. Results are summarized in Sect.5; there, we briefly discuss the reasons that stand behind the onset of exponential distributions in the lifetime of the bursting transients.

2. Model equations and their properties

The dynamical system consists of two coupled FitzHugh-Nagumo oscillators [4, 5]. Within the FitzHugh-Nagumo formalism, dynamics of each individual cell is described in terms of two variables: the fast variable x_i ($i = 1, 2$) models the behavior of the action potential whereas the slow y_i plays the role of the membrane recovery variable.

The governing equations are:

$$\begin{aligned}\frac{dx_1}{dt} &= x_1 - \frac{x_1^3}{3} - y_1 + \gamma_1 x_2 \\ \frac{dy_1}{dt} &= \varepsilon_1(x_1 + a_1) \\ \frac{dx_2}{dt} &= x_2 - \frac{x_2^3}{3} - y_2 - \gamma_2 x_1 \\ \frac{dy_2}{dt} &= \varepsilon_2(x_2 + a_2)\end{aligned}\tag{1}$$

Note that the neurons share the value of the parameter ε . When the coupling is switched off ($\gamma_1 = \gamma_2 = 0$), each oscillator is governed by two parameters: the small positive value of ε ensures the separation of dynamical timescales between x_i and y_i , whereas a_i can be viewed as the “excitability parameter”: its value determines whether the cell is in the excitatory (stable equilibrium, $|a_i| > 1$) or in the oscillatory ($|a_i| < 1$) state.

As soon as coupling is switched on, the voltage variable of each cell influences the evolution of voltage in the adjoint cell; these mimics electric coupling between the neuronal membranes (“gap junction”). By prescribing the signs before the coefficient $\gamma_{1,2}$ we deliberately restrict ourselves to the asymmetric interaction: the second neuron produces excitatory effect on the first one, whereas the action of the first neuron upon the second one is inhibitory.

Below, the system (1) is treated under fixed values of $\varepsilon_{1,2}$ as well as fixed coupling strengths γ_1 and γ_2 . In fact, we fix values of excitability parameters $a_{1,2}$ as well, but before proceeding that far, we need to characterize the stability of the state of rest.

Equations (1) possess the unique equilibrium at

$$x_1 = -a_1, \quad y_1 = \frac{a_1^3}{3} - a_1 - \gamma_1 a_2, \quad x_2 = -a_2, \quad y_2 = \frac{a_2^3}{3} - a_2 + \gamma_2 a_1\tag{2}$$

if the values of $|a_{1,2}|$ are sufficiently large, this state of rest is asymptotically stable; decrease of $|a_{1,2}|$ destabilizes it via the Andronov-Hopf bifurcation. on the parameter plane of a_1 and a_2 this event occurs on the circle $a_1^2 + a_2^2 = 2$. The peculiarity of Eqs (1) is the degeneracy of the Andronov-Hopf bifurcation: at strong coupling $\gamma_1 \gamma_2 > 1$, the Jacobian of the equilibrium at the critical set of

parameter values possesses not one but two, in general different, pairs of imaginary eigenvalues (see Fig. 1).

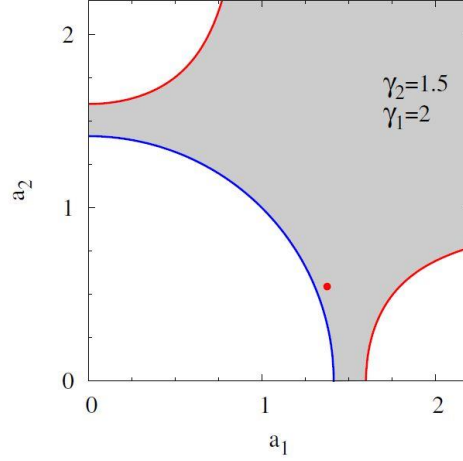


Figure 1. Stability borders for the equilibrium of Eqs. (1) on the parameter plane of a_1 and a_2 , for $\gamma_1\gamma_2 > 1$. Gray color indicates stability region. Thin solid lines (red): conventional Andronov-Hopf bifurcations. Thick solid line (blue): degenerate Andronov-Hopf bifurcation, where all four eigenvalues of the Jacobian are imaginary. Red filled circle: fixed set of parameter values, used for simulations and experiments.

Below, we fix all parameter values inside the stability domain of the equilibrium (file red circle in Fig. 1; $\varepsilon = 0.1$). Although we were unable to present the mathematical proof that at these parameter values the state of rest is stable not only linearly, but also globally asymptotically (in other words, that non-stationary attractors are absent), numerical experiments with large set of randomly chosen initial conditions invariably display convergence to the state of rest. In particularly, no bursting behavior has been observed at these parameter values.

3. Transient bursting in presence of noise: results of numerical simulations

Let additive white Gaussian noise with intensity T act upon the voltage variables of both interacting neurons:

$$\begin{aligned}\frac{dx_1}{dt} &= x_1 - \frac{x_1^3}{3} - y_1 + \gamma_1 x_2 + \sqrt{2T}\xi_1(t) \\ \frac{dy_1}{dt} &= \varepsilon_1(x_1 + a_1)\end{aligned}\tag{3}$$

$$\begin{aligned}\frac{dx_2}{dt} &= x_2 - \frac{x_2^3}{3} - y_2 - \gamma_2 x_1 + \sqrt{2T}\xi_2(t) \\ \frac{dy_2}{dt} &= \varepsilon_2(x_2 + a_2)\end{aligned}$$

where the stochastic terms $\xi_i(t)$ are delta-correlated: $\langle \xi \rangle_i(t_1) \langle \xi \rangle_j(t_2) = \delta_{i,j} \delta(t_1 - t_2)$.

Recall that at in the absence of noise ($T = 0$), the only attractor of the system is the equilibrium. Accordingly, one might expect that numerical integration of the stochastic differential equations (3) should display random oscillations around this equilibrium. Instead, however, we observe the characteristic bursting state: violent fast oscillations, separated by segments of relatively slow evolution. At large and moderate values of T the system does not cease to burst during the whole integration interval. At smaller intensities of noise, the regime of bursting has transient character: after a finite number of bursts, the system settles in the vicinity of the equilibrium. Remarkably, even under fixed intensity of noise and fixed initial conditions in the phase space, duration of the transient appears to be unpredictable: sometimes relaxation to the equilibrium begins already after a few bursts, whereas in other trials tens and hundreds of bursts are required. The number of bursting episodes varies with every new realization of noise. This phenomenon is illustrated in Fig. 2.

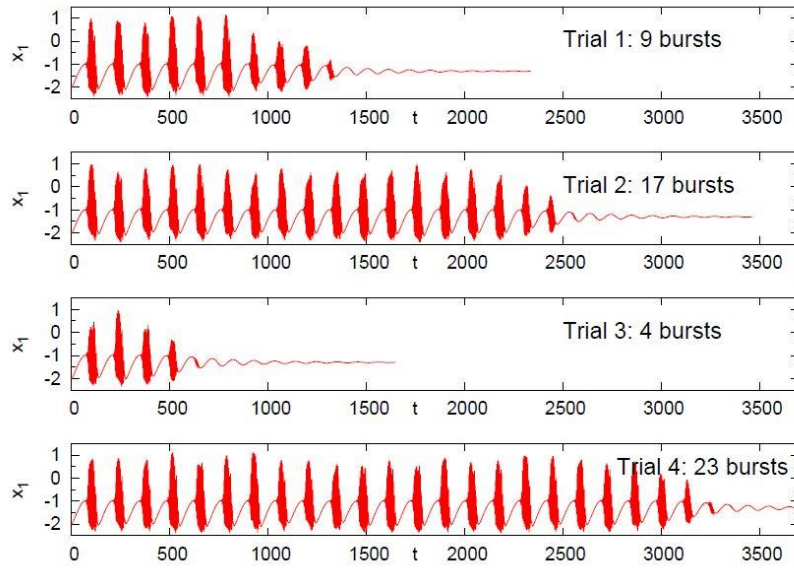


Figure 2. Variation of the number of bursting episodes for different realizations of additive noise in Eq.(3). Noise intensity: $T = 2 \times 10^{-10}$. All trials start at the same position in the phase space.

A large sample of noise realizations delivers the ensemble of different lifetimes of the transient bursting states. We quantify this distribution of lifetimes by calculating the probability $p(N_0)$ that at least N_0 bursts occur before the ultimate relaxation to the state of rest. Results of these calculations for a range of noise intensities T are displayed in Fig. 3.

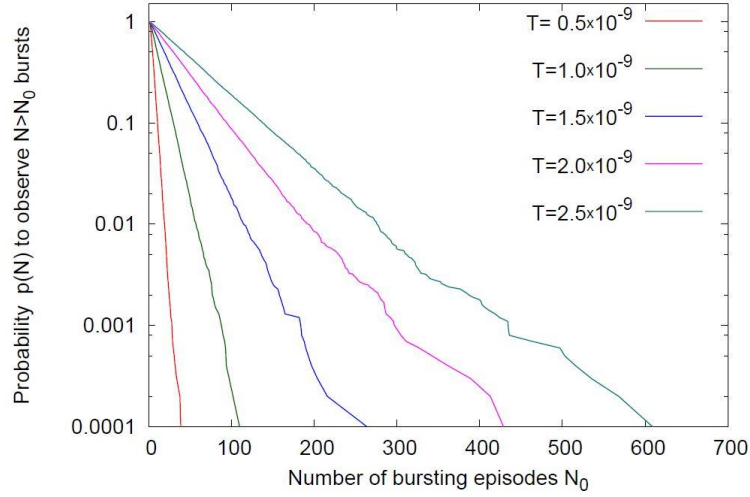


Figure 3. Distributions of lifetimes of the bursting transients at different values of the noise intensity T . For every shown value of T , 10^5 realizations of noise have been used.

Presentation in semi logarithmic coordinates shows that in all cases the distributions are close to exponential:

$$p(N_0) \sim e^{-\kappa N_0} \quad (4)$$

The slope of the distribution κ yields the inverse average number of bursting episodes. As seen from the plot, the value of κ decreases when the noise intensity T is raised. Further calculations have disclosed that the value of κ also depends on the distance to the stability border of the equilibrium in the state diagram: the further from the border (deeper into the shaded domain in Fig. 1), the steeper the distribution. Results of estimation of κ for two combinations of parameters of the deterministic system are shown in Fig. 4.

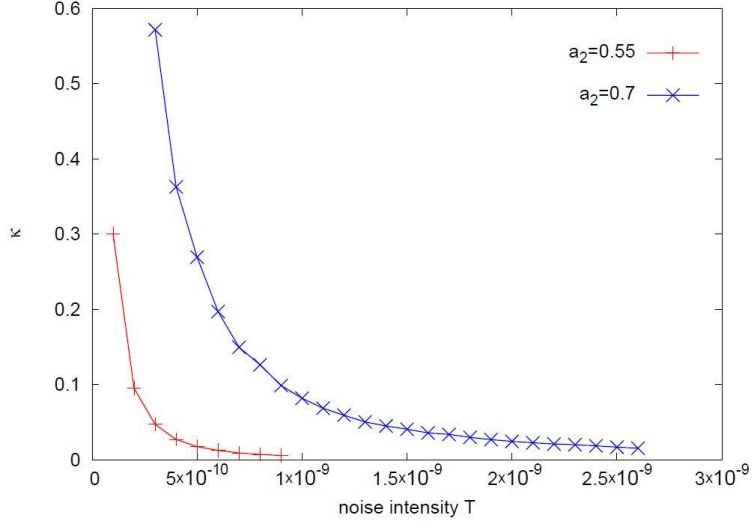


Figure 4. Slope of exponential distributions of the transient bursting lifetimes for different values of T and two different values of the parameter a_2 in Eqs (1).

4. Experimental setup and measurements

It is known that all natural neural systems are analog. In this regard, we decided to check whether we get the same effects in the analog system that we observe in the system of two connected FitzHugh-Nagumo neurons, solving the corresponding equations by numerical methods. For this purpose, we collected an analog electronic circuit simulating the equations (1) and (3). Figure 5 shows an analog electronic circuit corresponding to equation (3). But there is a slight difference from equation (3), in the circuit, noise is added only to the variable x_2 .

And Fig. 6 shows a diagram of the noise generator, which used in our experimental setup [6].

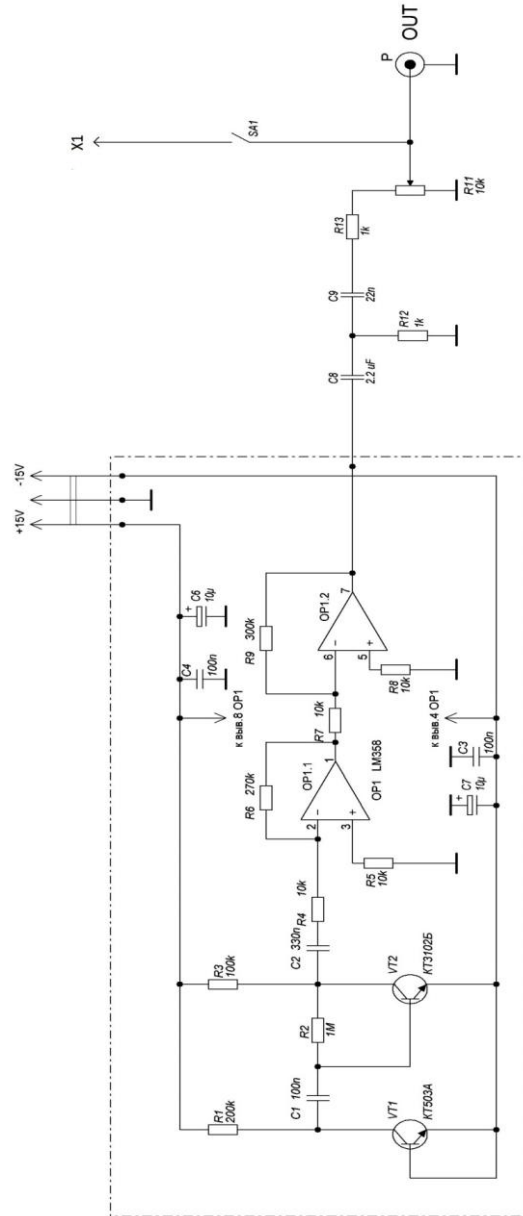


Figure 6. Scheme of an analog electronic circuit simulating a system.

To exclude the influence of various external conditions and increase the stability of the electronic installation, the analog circuit was assembled on a printed circuit board and closed in an aluminum case. Figure 7 shows the inside view of this installation.

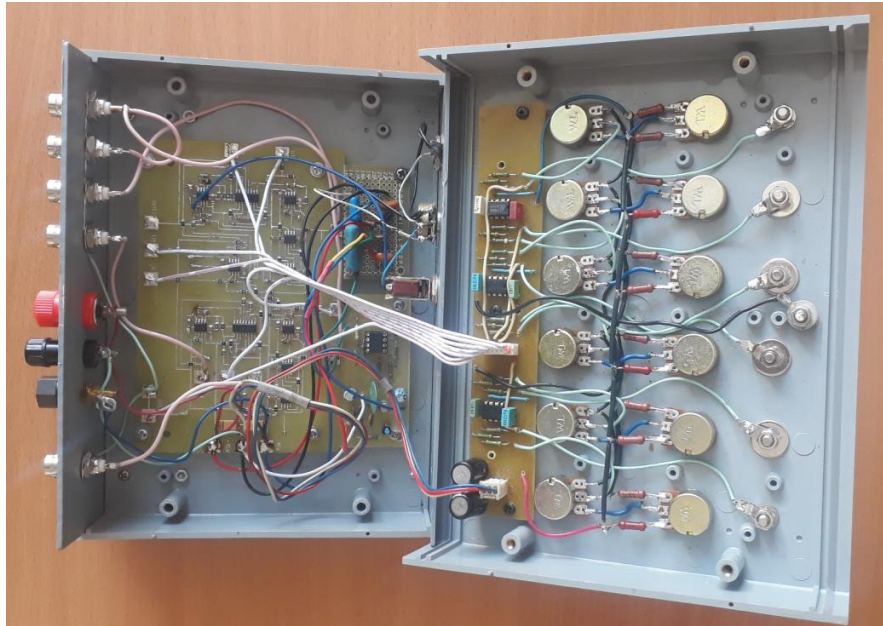


Figure 7. The inside view of an electronic installation for analog system simulation.

To digitize and write to the computer the signals obtained from this electronic installation, the platform of the educational and laboratory complex NI Elvis II + [7] and the LabVIEW software [8] were used.

For each noise level and system parameter values (Eq. 3), we repeated the experiment 5,000 times. At the same time, the duration for one experiment was set to 10 seconds, since such a length of time is sufficient for all bursts barks to calm down in the system and the system can go to rest.

Further, the obtained data, which were previously recorded in separate files for each experimental measurement, were processed using a program developed in the MatLab environment. This program first of all recognizes bursts in the signal and counts them. Recognition of burst is carried out using spectral analysis of a signal fragment. Such a method of recognizing bursts works quite steadily, since in the spectrum of bursts there is always one pronounced energetic peak corresponding to the spike repetition rate.

Figure 8 shows several graphs of the temporary implementation of experimental data corresponding to the values of the variable x_1 . All these implementations were obtained with the same values of the system parameters (Eq. 3) and the same noise level.

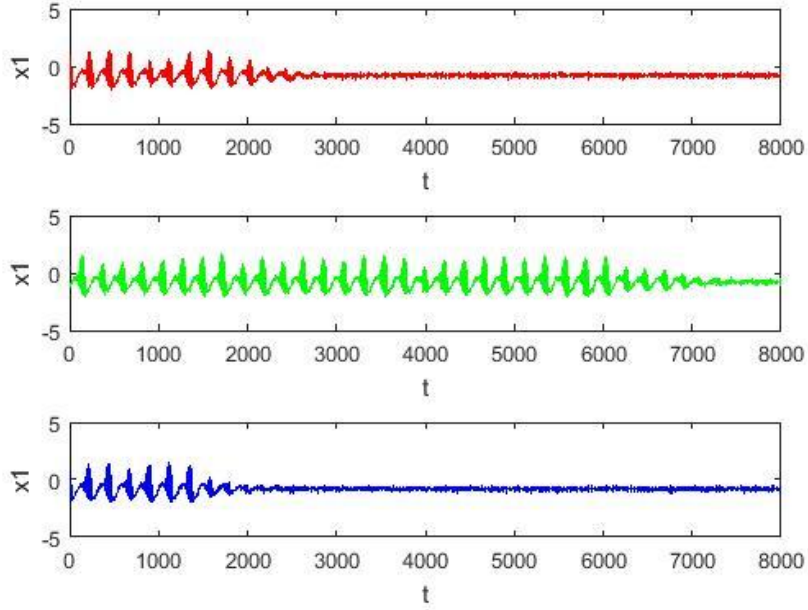


Figure 8. Temporary implementations of signals obtained from an experimental setup. The values of system parameters and noise level are the same in all cases.

As the graphs in Figure 8 show, the number of bursts before attenuation, as well as in the case of numerical studies, turns out to be different when using the same values of the system parameters and noise level. Further analysis of the distribution of the number of bursts before attenuation in the data obtained from an analog experiment also showed that it obeys an exponential law. Experiments show that with a low level of noise, the bursts fade out faster.

One can easily be convinced that the distribution of the number of bursts according to experimental data obeys an exponential law. For this, graphs of this distribution are plotted on a logarithmic scale along the ordinate. The graphs are shown in Figure 9.

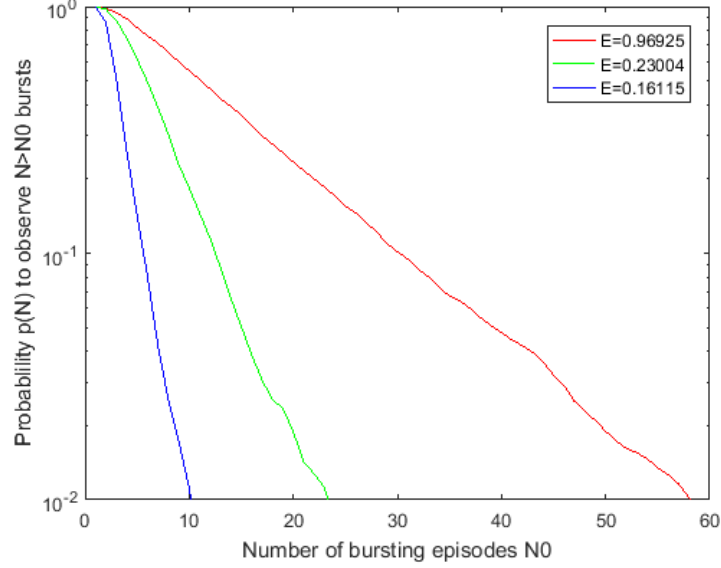


Figure 9. Distribution of the number of bursts before attenuation depending on the noise level according to data obtained from an analog device, where E is the noise level. The logarithmic scale is used along the ordinate.

5. Conclusions

Here, we briefly comment on the mechanism that stands behind the exponential distribution of lifetimes. Like bursting itself, it appears to be enrooted in the slow-fast nature of the deterministic dynamical system (Eq. 1) at small values of ε . In the four-dimensional phase space of (Eq. 1) there is a two-dimensional surface S^S , corresponding to the slow motions. Upon this surface, both dx_1/dt and dx_2/dt vanish; hence, algebraically S^S is defined by the equations

$$y_1 = x_1 - \frac{x_1^3}{3} + \gamma_1 x_2, \quad y_2 = x_2 - \frac{x_2^3}{3} - \gamma_2 x_1 \quad (5)$$

The state of rest (Eq. 2) lies on S^S . In the deterministic setup, the typical phase trajectories rapidly reach the vicinity of S^S and then slowly converge to the equilibrium (which, under the employed parameter values, is a stable focus), to stay there forever. Introduction of noise distorts this picture; the reason is of geometric character: the slow surface (Eq. 5) is not flat, but folded. Whenever a trajectory, slowly evolving along S^S , reaches the fold, it “slides off” into the space of fast motions and performs there several violent large-scale oscillations before returning to S^S again; taken together, these oscillations correspond to a single bursting episode. In a sense, this construction is akin to the textbook mechanism of relaxation oscillations in the Van der Pol equation, where the segments of

slow evolution are interrupted by fast flights between the branches of the slow curve. The stronger the noise, the higher are the chances that the trajectory, in the course of approaching the state of rest, gets kicked to the fold and leaves the slow surface, starting the next bursting event. Notably, once the trajectory has reached the sufficiently small neighborhood of the equilibrium, it becomes “safe”: there the deterministic motion towards the stable state of rest dominates, and the noisy departure to the fold becomes virtually improbable.

At fixed intensity of noise there is a well-defined probability p_{esc} that the trajectory, arriving at the slow surface S^S and tending to the state of rest, will, on its way, escape: reach the fold, with subsequent bursting. [The value of p_{esc} can be estimated e.g. by means of constructing the Fokker-Planck formalism for the motion along S^S ; this problem lies outside the scope of the current paper]. Consider a large ensemble of orbits: M trajectories, starting in the appropriate region of S^S . Approximately $M(1 - p_{esc})$ trajectories march to the equilibrium directly, without bursting; their evolution is effectively ended at the state of rest. The remaining $\approx M p_{esc}$ trajectories participate in the first burst and subsequently return to the slow surface. Part of them is then directly absorbed by the stable equilibrium, but $\approx M p_{esc}^2$ orbits perform the second burst, $\approx M p_{esc}^3$ trajectories feature the third one, and so on. This is a geometric progression: for a randomly chosen trajectory from the original ensemble, the probability $p(N_0)$ to perform at least N_0 bursts equals $p_{esc}^{N_0} = e^{(\log p_{esc})N_0}$, resulting in the exponential distribution of the lifetimes of bursting transients. The slope k of the distribution equals $-\log p_{esc}$. Apparently, p_{esc} is the monotonically growing function of the noise intensity T ; if the noise is strong, p_{esc} approaches 1, and k , respectively, shrinks: the decay of the distribution becomes rather slow, so that the observed numbers of the bursting episodes reach thousands and hundreds of thousands. In this situation, within the maximal available computational/observational time intervals, it is hardly possible to distinguish between the transient (albeit extremely durable) bursting states and the non-decaying bursting regime.

The necessary ingredients of the described mechanism are: (a) the slow-fast dynamics involving the stable state of equilibrium, (b) the folded surface of slow motions in the phase space, and (c) existence of fast large-scale oscillations with subsequent reinjection close to the slow surface. We expect this kind of transient bursting dynamics, obeying the exponential distribution of lifetimes, to occur in the large class of neuronal models. Noteworthy, exponential distributions for the lifetimes of bursting transients were reported in [9] for large ensembles of randomly linked neurons; apparently, there the “quenched disorder”, owing to the randomness of connections, plays a role, similar to the action of time-dependent noise in the small ensemble, considered in the current paper.

References

- [1] Keener J., Sneyd, J. *Mathematical physiology*. Springer, New York, 1998.
 - [2] Rinzel J. *Bursting oscillations in an excitable membrane model*. *Lecture Notes Math.* 1151. Springer, New York, 1985, 304–316.
 - [3] Medetov, B., Weiß, R. G., Zhanabaev, Z. Z., Zaks, M. A. Numerically induced bursting in a set of coupled neuronal oscillators. *Communications in Nonlinear Science and Numerical Simulation* 20.3 (2015), 1090-1098.
 - [4] FitzHugh R.A. Impulses and physiological states in theoretical models of nerve membrane. *Biophys J* 1, (1961), 445–466.
 - [5] FitzHugh R.A. *Mathematical models of excitation and propagation in nerve*. In: Schwan H.P., editor. *Biological engineering*. McGraw-Hill Book Co., New York, 1969 (chapter 1).
 - [6] Douce, J. L., Shackleton J. M. LF random-signal generator. *Electronic and Radio Engineer* 35.8 (1958), 295-297.
 - [7] Tawfik, M., Sancristobal, E., Martin, S., Gil, R., Diaz, G., Colmenar, A., Hakansson, L. Virtual instrument systems in reality (VISIR) for remote wiring and measurement of electronic circuits on breadboard. *IEEE Transactions on learning technologies* 6(1), (2012), 60-72.
 - [8] Bitter, R., Mohiuddin T., Nawrocki M. *LabVIEW: Advanced programming techniques*. Crc Press, Boca Raton, 2017.
 - [9] Tomov, P., Pena, R. F., Roque, A. C., Zaks, M. A. Mechanisms of self-sustained oscillatory states in hierarchical modular networks with mixtures of electrophysiological cell types. *Frontiers in Computational Neuroscience* 10, (2016), 23.
- Nurtay Albanbay, Ph.D. student: Kazakh National Research Technical University named after K.I.Satpayev, Institute of Information and Telecommunication Technologies. Satpayev Str., 22. 050013 Almaty, Kazakhstan (*nurtay.a90@gmail.com*). The author gave a presentation of this paper during one of the conference sessions.
- Bekbolat Medetov, Ph.D: al-Farabi Kazakh National university, 71 al-Farabi Avenue, 050013 Almaty, Kazakhstan (*bm02@mail.ru*).
- Michael A. Zaks, Dr. Sc.: Humboldt University of Berlin, Newtonstr. 15, 12489 Berlin, Germany (*zaks@physik.hu-berlin.de*).

On backward whirl excitation in linear time-variant intact and cracked rotor systems

Tariq Alzarooni, Mohammad AL-Shudeifat, Oleg Shiryayev, C. Nataraj

Abstract: The appearance of backward whirl (BW) phenomena in cracked rotor systems that are exposed to recurrent transitions through the critical forward whirl rotational speeds during startup and coast down operations could result in a catastrophic failure, which, in turn, poses serious economical and safety complications. This phenomenon is investigated here for rotor systems with a breathing crack model. The Finite Element Model (FEM) is used to develop the equations of motion of the considered cracked rotor systems in which startup acceleration is considered. In addition to incorporating the breathing crack, the effect of anisotropic and isotropic bearings on the excitation of this BW phenomena is also examined. The appearance of BW zones is more prominent at increased angular acceleration rates for the anisotropic bearing case of the cracked rotor. It is found that the BW zones are captured at nearly all values of crack depth ratios for the anisotropic bearing case. However, these zones only appear at relatively high crack depths for the isotropic bearing case.

1. Introduction

Backward whirl (BW) or backward precession in rotary systems is a dangerous phenomenon, which could eventually result in a catastrophic failure which would have serious environmental, health and safety implications. Therefore, early fault detection is essential to sustain safe working conditions and to minimize the cost burden due to potential equipment breakdowns and disruption of operation. Bearing damage, sometimes coupled with a propagating crack, could potentially excite backward whirling in rotors. Accordingly, studying the dynamic behavior of cracked rotor systems has gained broad interest in fracture mechanics and asset integrity fields.

Switching, or a hinged crack model, was first introduced by Gasch [1] to simulate fatigue crack behavior via abrupt stiffness change from a fully open to a fully closed crack at a certain shaft rotation angle within a complete revolution cycle. On the other hand, a breathing crack model proposed by Jun et al. [2] represents the behavior of a fatigue crack via gradual opening and closure over a complete revolution cycle. Considering intensive unbalance excitation and static loads of the rotor system, the breathing crack model better replicates real world rotor behavior. Consequently, the breathing crack model is further pursued in the current paper.

Breathing cracks have been extensively investigated by many researchers since early 1980's, vast majority of whom have modeled the breathing crack behavior in the form of a stiffness variation using a simple cosine function [3-21]. This method was originally proposed by Mayes and Davies [3]. An alternate explicit breathing function was proposed in [5] to account for saturation of crack breathing behavior using a softly-clipped cosine function. The aforementioned breathing function allows lower lateral displacement amplitudes due to energy being dissipated among a higher number of harmonic response components.

Another modified cosine function was introduced in [6] to prevent total crack closure. In a separate direction of work, the breathing mechanism was modeled using a steering function, which induces periodic local variation in stiffness parameters [10-12]. The steering function is obtained from a combination of theory-based stress-strain linear correlation assumption and previously performed experimental tests. Breathing cracks were also modeled using a harmonically varying stiffness within a revolution in two coordinate directions [13]. The study showed that high accuracy was attained using only two harmonic terms.

Al-Shudheifat et al. have developed three new breathing functions [22,23,25], which were based on a Fourier Series expansion for representing time varying moment of inertia for the cracked rotor element. The breathing functions are used in formulating the actual time-varying stiffness matrix of the cracked element. Two breathing functions were derived in [25], which represent stiffness variation in lateral and transversal rotor directions, while the third breathing function was derived in [23], which represents the coupling behavior in the form of the product of inertia. The proposed functions are arguably more precise in resembling the actual breathing mechanism compared to cosine or steering functions. More details regarding the theoretical basis of these breathing functions and their comparison with traditional cosine function representation is discussed in [25].

Whirl orbit analysis associated with the breathing crack model has been studied in depth by many researchers [4, 16-17, 23, 25, 26-30]. In [23] the whirling orbits were studied at $1/3$ and $1/2$ of the 1st critical rotor speed in correlation with the presence of breathing cracks. It was found that the appearance of two inner loops during rotor speed passage at $1/3$ of 1st critical speed can represent a clear signature for presence of a breathing crack in the shaft. Further, the appearance of a single whirl orbit during rotor speed passage through $1/2$ of 1st critical speed was found as an additional indicator for the presence of the breathing crack. Similar studies have been performed in [27] on a cracked rotor system whereby analytical and experimental analysis of orbital plots were performed. Analytical results showed 180° shift in phase orientations before and after passages through $1/2$ and $1/3$ critical speeds. Experimental results have not yielded the same orientation shift mainly due to the excessive damping present in the system.

In [16] a rotor dynamic analysis was conducted, in which the breathing crack model is assumed to be independent of the shaft's weight dominance for governing the breathing crack mechanism. Instead, an angle between the crack direction and the shaft whirling direction is used for determining the opening and closing behavior in the model for the breathing crack. It was concluded that the steady-state response amplitude peak is determined by the imbalance orientation angle regardless of the rotor's condition in terms of the crack presence.

In [25] the position of the orbit loops was studied as a function of the BW and FW frequencies. It was found that the outer loops appear during the passage through the subcritical backward whirl speed, while the inner loops appear during the passage through the subcritical forward whirl speed. It was also reported that the orientation and the number of these loops can be indicatively used for rotor crack diagnosis. Experimental analysis was also used to verify analytical and numerical findings of whirl analysis. In [4] the shift in FW and BW frequencies was studied in the presence of multiple cracks. It was found that their relevant frequencies decrease with increasing crack depths and orientations.

Whirl orbit shape has also been extensively investigated in [17] using general harmonic balance technique followed by experimental verification. It was found that the shaft's amplitude corresponding to BW frequency appears to be larger than the one corresponding to FW frequency at a very low crack depth. The results also showed the appearance of the shaft's BW at lower frequency values than FW frequency within the subcritical speed range.

In [26] whirl orbits for a cracked rotor were obtained from simulations by considering two scenarios: with and without the unbalance effect. In the absence of the unbalance effect, BW was observed for a short instant near the critical speed range and following a steep reduction in shaft's amplitude. This phenomenon was attributed to presence of a crack in the shaft as interpreted in [28]. However, BW was not observed in the second scenario where the unbalance effect was incorporated in the model.

In [31-34], a numerical solution using Runge-Kutta integration technique was employed to solve for the dynamic response of a rotor during transient operation. A constant acceleration was assumed to replicate start-up operation, which would result in a speed linearly varying in time. FE model was used in [31-32], whereas a 4-DOF model was used in [33] as an enhanced feature to a simple 2-DOF Jeffcott model incorporating gyroscopic effects. These studies were mainly focused on capturing backward whirl zones for open crack problems at various crack depths and unbalance force orientation with respect to the transverse crack direction.

To the best of the authors' knowledge, no previous studies of backward whirl phenomena during transient operation of a rotor with a breathing crack have been reported in the literature. Furthermore, it is suspected that the occurrence of backward whirl forms a good indication for presence of a crack since it cannot be excited in a crack-free shaft [35]. In the present paper, the transient rotor operation

in the form of rotor startup will be simulated at various constant acceleration rates for various crack depths. The same simulation is intended to be executed at various unbalance force orientation angles with respect to the transversal crack direction. The dynamic response of the rotor will be examined to identify effects on the critical forward speed, fundamental amplitude, transient amplitude, and local peaks. The obtained results will be compared with the results of analysis obtained in [31-33] for open crack cases.

2. Rotor-disk-bearing system modeling with breathing crack

The breathing crack model, proposed in [25] is considered here, where its schematic representation is shown in Fig. 1. The crack's opening and closure mechanism is solely dominated by the static deflection of the rotor system. This happens due to variation in compression and tension stress states at the periphery of the shaft, which results in the crack breathing phenomenon. The schematic of the shaft's cracked cross-section is shown in Fig. 2, where the transverse crack depth h is normalized by the radius of the shaft R , which results in a non-dimensional representation of the crack depth $\mu=h/R$.

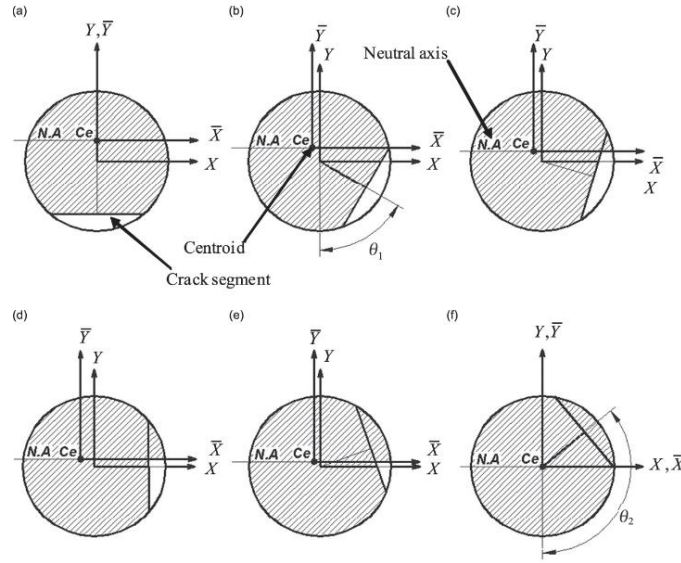


Figure 1. Breathing crack mechanism and relevant shifting in centroid [25].

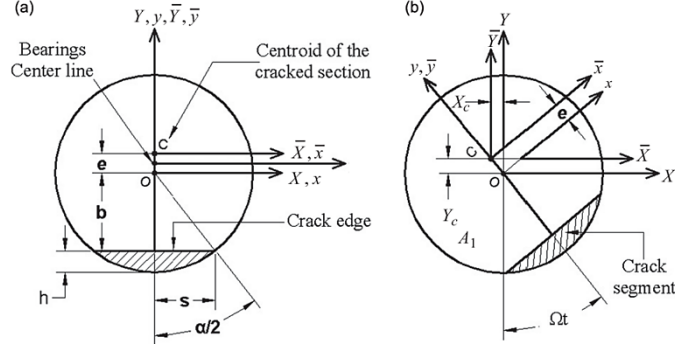


Figure 2. Schematic diagrams of the cracked element cross-section: (a) before rotation and (b) after the shaft rotates [23].

The orientation of the unbalance force vector F_u is located at angle β with respect to the crack opening direction. Considering $t = 0$ at negative Y axis, and for a complete revolution cycle, the crack is assumed to be fully open for the range of angles $-\theta_1 \leq \theta \leq \theta_1$, partially open for $\theta_1 \leq \theta < (\pi + \alpha)/2$ and $\pi - \alpha/2 \leq \theta < 2\pi - \theta_1$; and, fully closed at $(\pi + \alpha)/2 \leq \theta \leq (3\pi - \alpha)/2$. Detailed derivation of the breathing crack functions can be found in [25].

The underlying physics is that the gradual opening/closure of the cracked element leads to variation in centroidal axes location, which, in turn, leads to variation in the stiffness parameter of the cracked shaft. Thus, gradual opening and closure of the cracked shaft element within a complete cycle of rotation dictates smooth increasing and reduction of the shaft's stiffness, respectively. In the context of analytical modeling using the FE approach, the element containing the breathing crack will undergo variation in stiffness based on centroidal shift, whereas the remaining elements shall be treated as intact shaft elements based on Euler-Bernoulli beam with circular cross-section. The following schematic shown in Fig. 3 represents the FE model used in the simulation. Transverse displacements were measured at the 2nd node from the left.

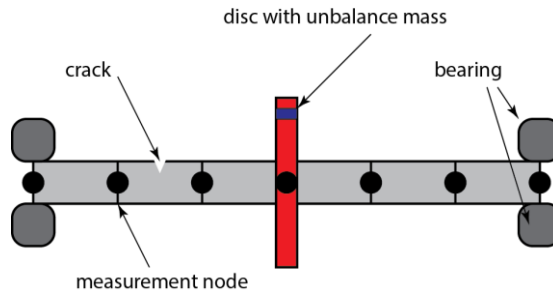


Figure 3. Schematic diagrams of the finite element disk-shaft-bearing-rotor system (not to scale).

The rotor of mass M and length L is divided into finite N -elements with $N + 1$ nodes and the finite element equation of motion is described as follows:

$$\mathbf{M}\ddot{\mathbf{q}}(t) + \widehat{\mathbf{C}}\dot{\mathbf{q}}(t) + \mathbf{K}\mathbf{q}(t) = \mathbf{F}_u(t) + \mathbf{F}_g \quad (1)$$

where \mathbf{M} , $\widehat{\mathbf{C}}$, \mathbf{K} are $4(N+1) \times 4(N+1)$ global mass, damping and gyroscopic, and stiffness matrices, respectively. \mathbf{M} resembles the addition of rotor's classical mass and inertial matrices. $\widehat{\mathbf{C}}$ resembles the rotor's total gyroscopic and proportional damping matrices as $\widehat{\mathbf{C}} = \Omega\mathbf{G} + \mathbf{C}$, where Ω is the rotor's angular speed and \mathbf{C} is a proportional damping matrix obtained via $\mathbf{C} = \gamma\mathbf{M} + \xi\mathbf{K}$ where $\gamma = 0.0005 \text{ s}^{-1}$ and $\xi = 0.00005 \text{ s}$. These matrices are omitted in this paper for conciseness. The overall system unbalance force vector $\mathbf{F}_u(t)$ has a size of $4(N+1) \times 1$. Considering 2D rectangular coordinates, the unbalance force will have two components on i -th node, at which it is added as per the following relations:

$$\mathbf{f}_i = [f_i^u \quad f_i^v \quad 0 \quad 0] \quad (2)$$

$$f_i^u = m_e d \Omega(t)^2 \cos(\theta(t) + \beta) \quad (3)$$

$$f_i^v = m_e d \Omega(t)^2 \sin(\theta(t) + \beta) \quad (4)$$

where m_e is the unbalance mass, d is the distance between the unbalance mass location and the shaft center, $\theta(t)$ is angular displacement, and β is the orientation of unbalance force vector with respect to the transversal crack direction. The elements of $\mathbf{F}_u(t)$ at the node corresponding to the disc location are given in Eqs. (3-4), while other nodal unbalance forces are set equal to zero. The gravity force vector is also included in \mathbf{F}_g . Bearings were included in the model through addition of stiffness and damping at the corresponding nodes and incorporating them in the global stiffness and damping matrices.

Analogous to the derivation of the cracked element stiffness matrix in [36] for the open cracked model in the stationary coordinates, the following elemental stiffness matrix of the cracked element with a breathing crack model is obtained and merged with the j -th cracked element matrix of the global stiffness matrix:

$$\mathbf{k}(t) = \frac{E}{l^3} \begin{bmatrix} 12I_{\bar{y}}(t) & 12I_{\bar{x}\bar{y}}(t) & -6I_{\bar{x}\bar{y}}(t) & 6I_{\bar{y}}(t) & -12I_{\bar{y}}(t) & -12I_{\bar{x}\bar{y}}(t) & -6I_{\bar{x}\bar{y}}(t) & 6I_{\bar{y}}(t) \\ 12I_{\bar{x}\bar{y}}(t) & 12I_{\bar{x}}(t) & -6I_{\bar{x}}(t) & 6I_{\bar{x}\bar{y}}(t) & -12I_{\bar{x}\bar{y}}(t) & -12I_{\bar{x}}(t) & -6I_{\bar{x}}(t) & 6I_{\bar{x}\bar{y}}(t) \\ -6I_{\bar{x}\bar{y}}(t) & -6I_{\bar{x}}(t) & 4I_{\bar{x}}^2(t) & -4I_{\bar{x}\bar{y}}^2(t) & 6I_{\bar{x}\bar{y}}(t) & 6I_{\bar{x}}(t) & 2I_{\bar{x}}^2(t) & -2I_{\bar{x}\bar{y}}^2(t) \\ 6I_{\bar{y}}(t) & 6I_{\bar{x}\bar{y}}(t) & -4I_{\bar{x}\bar{y}}^2(t) & 4I_{\bar{y}}^2(t) & -6I_{\bar{y}}(t) & -6I_{\bar{x}\bar{y}}(t) & -2I_{\bar{x}\bar{y}}^2(t) & 2I_{\bar{y}}^2(t) \\ -12I_{\bar{y}}(t) & -12I_{\bar{x}\bar{y}}(t) & 6I_{\bar{x}\bar{y}}(t) & -6I_{\bar{y}}(t) & 12I_{\bar{y}}(t) & 12I_{\bar{x}\bar{y}}(t) & 6I_{\bar{x}\bar{y}}(t) & -6I_{\bar{y}}(t) \\ -12I_{\bar{x}\bar{y}}(t) & -12I_{\bar{x}}(t) & 6I_{\bar{x}}(t) & -6I_{\bar{x}\bar{y}}(t) & 12I_{\bar{x}\bar{y}}(t) & 12I_{\bar{x}}(t) & 6I_{\bar{x}}(t) & -6I_{\bar{x}\bar{y}}(t) \\ -6I_{\bar{x}\bar{y}}(t) & -6I_{\bar{x}}(t) & 2I_{\bar{x}}^2(t) & -2I_{\bar{x}\bar{y}}^2(t) & 6I_{\bar{x}\bar{y}}(t) & 6I_{\bar{x}}(t) & 4I_{\bar{x}}^2(t) & -4I_{\bar{x}\bar{y}}^2(t) \\ 6I_{\bar{y}}(t) & 6I_{\bar{x}\bar{y}}(t) & -2I_{\bar{x}\bar{y}}^2(t) & 2I_{\bar{y}}^2(t) & -6I_{\bar{y}}(t) & -6I_{\bar{x}\bar{y}}(t) & -4I_{\bar{x}\bar{y}}^2(t) & 4I_{\bar{y}}^2(t) \end{bmatrix} \quad (5)$$

The rotordynamic transient whirl response is obtained by numerical simulation based on constant angular acceleration rate α . The change in rotation angle and angular velocity during the shaft's ramp up are described as $\theta(t) = \alpha t^2/2$ and $\Omega = \alpha t$ respectively. Subsequently, the gyroscopic matrix becomes a time-varying matrix. Furthermore, the two components of the unbalance force vector $\mathbf{F}_u(t)$ become nonlinear. The maximum simulation time was set when the shaft reaches the angular speed of $\Omega(t_{max}) = 470$ rad/s, or approximately 4500 rpm. The peak whirl amplitude is obtained from $z = \sqrt{u^2 + v^2}$ where u and v represent the horizontal and vertical whirl vibration amplitudes, respectively, at the second node from the left bearing.

3. Numerical simulation results

Transient responses of the considered cracked single disk configuration (SDC) rotor in Fig. 3 are obtained by numerical simulation for the startup operation. The FE model of the cracked rotor-bearing-disk system is carried out with the physical parameters as listed in Table 1.

Table 1: Physical parameters of the considered rotor-disk system.

Description	Value	Description	Value
Length of the rotor, L	0.7 m	Disk outer radius,	0.075 m
Radius of the rotor, R	$19.06 \cdot 10^{-3}$ m	Disk Inner radius, R_i	0.019 m
Density of rotor, ρ_r	7850 kg/m ³	Density of disk, ρ_d	2700 kg/m ³
Modulus of elasticity, E	210 GPa	Mass of the disk, m_d	0.663 kg
Bearing stiffness, k_{xx}, k_{yy}	5×10^6 N/m, 7×10^7 N/m	Mass unbalance, $m_e d$	10^{-3} kg · m
Bearing damping, c_{xx}, c_{yy}	5×10^2 N·s/m	Mass unbalance	varying

Numerical simulation results for startup operation of SDC for asymmetric bearings are shown in Fig. 4. The plots are obtained for two crack depth ratios of $\mu = 0.1$ and 0.4 for two different unbalance force orientation angles $\beta = 0$ and $2\pi/3$ rad. It is observed that in all cases, as acceleration increases new local peaks of whirl amplitudes start appearing after passing through the fundamental FW speed. It is also observed that zones of BW orbits start appearing prominently following the passage through the critical FW speed once the cracked shaft and anisotropic bearings models are incorporated. It can also be observed that more zones of BW orbits are captured in the case of $\mu = 0.4$, suggesting a higher chance of occurrence of BW at a higher crack depth.

Furthermore, it is observed that the maximum peak amplitude is directly proportional to the crack depth ratio μ . It can also be observed that the maximum FW amplitude is indirectly proportional to the rate of angular acceleration. The peak of the critical FW speed is shifted towards higher rotation speeds at an increased angular acceleration rate. These findings align well with the findings of earlier work

that used the open-crack model [31]. One last important observation is that for the same crack depth ratio μ and varied unbalance force vector orientation β , the captured BW zones vary accordingly, which suggests that the unbalance force orientation vector has an impact on the extent of BW zones captured after the fundamental FW amplitude peak.

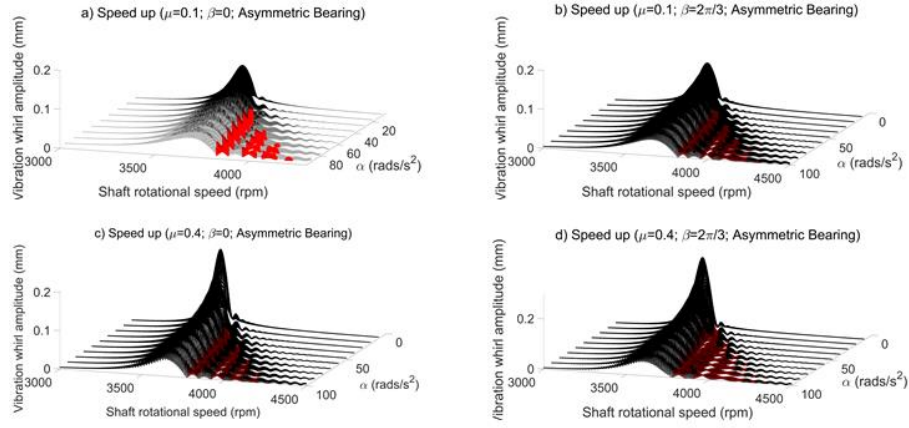


Figure 4. Dynamic response of cracked rotor with asymmetric bearing at a) $\mu=0.1$, $\beta=0$ rad; b) $\mu=0.1$, $\beta=2\pi/3$ rad; c) $\mu=0.4$, $\beta=0$ rad; d) $\mu=0.4$, $\beta=2\pi/3$ rad (red color represents BW zones).

Fig. 5 shows an example of BW orbits (in red) which takes place at minima between fundamental and subsequent local FW amplitude peaks in the case of asymmetric bearing conditions.

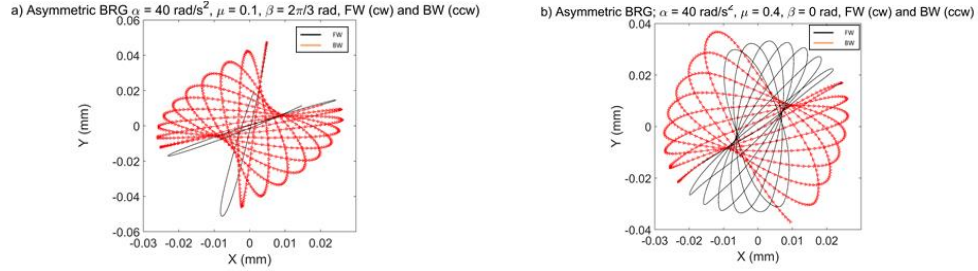


Figure 5. Backward whirl orbits for cracked rotor and symmetric bearing

For isotropic bearings, Fig. 6 illustrates the effect of an ideal bearing condition on the BW zones. Similar findings are observed here with regards to capturing of BW zones as in anisotropic bearings conditions except for the minor difference that BW zones are only observed at higher crack depth ratio (≥ 0.55) compared to the anisotropic bearing condition. Furthermore, the captured BW zones appear in the narrower speed range for the isotropic bearing case.

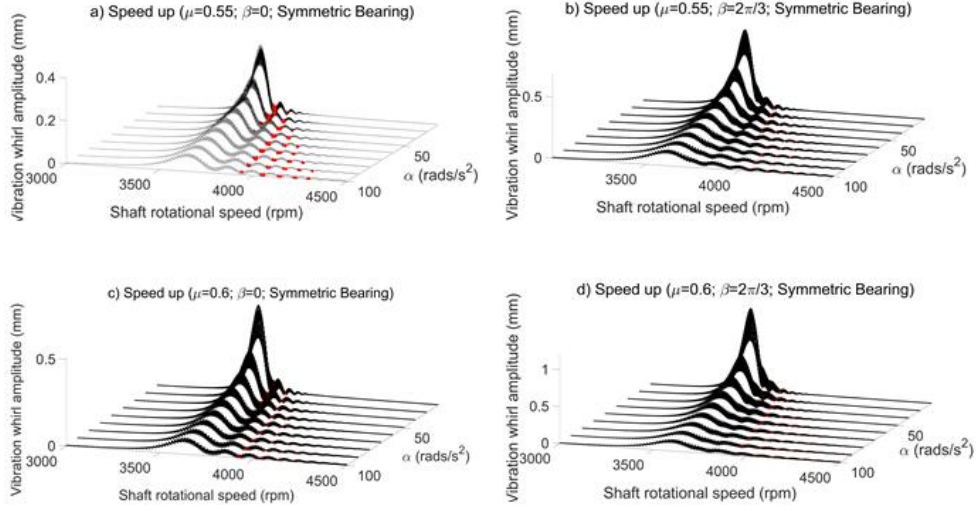


Figure 6. Dynamic response of cracked with symmetric bearings at a) $\mu=0.55$, $\beta=0$ rad; b) $\mu=0.55$, $\beta=2\pi/3$ rad; c) $\mu=0.6$, $\beta=0$ rad; d) $\mu=0.6$, $\beta=2\pi/3$ rad.

Fig. 7 shows examples of BW orbits (in red) for the cracked rotor with isotropic bearings, which also take place at minima between fundamental and subsequent local FW peaks. This observation indicates that the BW zones can be observed for isotropic bearings, but at a significantly lower extent.

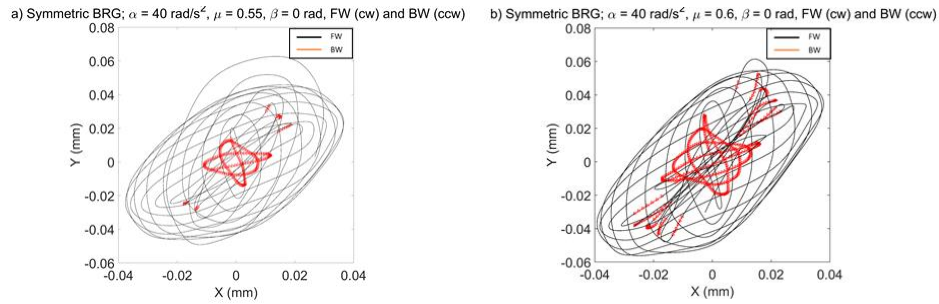


Figure 7. Backward whirl amplitude for cracked rotor and symmetric bearing

4. Conclusion

The BW phenomenon is studied here in accelerated cracked rotor systems with a breathing crack model. The study was based on numerical simulation using finite element equations of motions (EOM) for startup rotor operation. The time-varying stiffness matrix of the cracked element was superimposed in the FE model to simulate the breathing behavior of the crack. The obtained linear-time-varying EOMs

were numerically integrated to compute the whirl response of the cracked rotor system during startup operation. Whirl behaviors were analyzed during and after the passage of the critical FW speed zones. It was found that following the immediate reduction of whirl amplitude after the fundamental FW peak, small transient FW peaks start evolving. The extent of these local peaks was found to be directly affected by the rate of angular acceleration, unbalance force vector orientation and the crack depth. Further, BW orbits were found to be captured in the vicinity of these local transient peaks, particularly at the minima between the fundamental FW and the subsequent local transient peaks. BW zones were found to be affected significantly by the condition of the bearings. In other words, the extent of BW zones was found to be larger with anisotropic bearings condition regardless of the rotor's crack condition. However, for symmetric bearings, BW zones were only captured at relatively high crack depth ratio, which suggests the significance of bearing's condition influence on BW zones. The unbalance force orientation vector was also found to have significant impact on the shape of these BW orbits. It is necessary to study the combination of BW and FW transient phenomena because it will help to develop novel condition monitoring approaches for rotor systems with a goal of early detection of rotor crack or bearing damage.

References

- [1] R. Gasch. Dynamic behaviour of a simple rotor with cross sectional crack. *Transactions of Institution of Mechanical Engineers, International Conference on Vibration in Rotating Machinery*. Paper C178/76 (1976), pp. 123–128.
- [2] O.S. Jun, H.J. Eun, Y.Y. Earmme, C.W. Lee, Modelling and vibration analysis of a simple rotor with breathing crack. *Journal of Sound and Vibration* 155 (1992), 273–290.
- [3] I. Mayes, W. Davies. The vibrational behavior of a rotating shaft system containing a transverse crack. *Institution of Mechanical Engineers, International Conference on Vibration in Rotating Machinery*. Paper C168/76 (1976), pp. 53–64.
- [4] D. Gayen, D.Chakraborty, R.Tiwari. Finite Element Analysis for a Functionally Graded Rotating Shaft with Multiple Breathing Cracks. *International Journal of Mechanical Science* 134 (2017), 411–423.
- [5] H. Khorrami, S. Rakheja, R. Sedaghati. Vibration behavior of a two-crack shaft in a rotor disc-bearing system. *Mechanism and Machine Theory* 113 (2017), 67–84.
- [6] M.J. Gomez, C. Castejon, J.C. Garcia-Prada. Crack detection in rotating shafts based on 3x energy: analytical and experimental analyses. *Mechanism and Machine Theory* 96 (2016), 94–106.
- [7] A.A. Cavalini Jr, L. Sanches, N. Bachschmid, V. Steffen Jr. Crack identification for rotating machine based on a nonlinear approach. *Mechanical Systems and Signal Processing* 79 (2016), 72–85.
- [8] Z. Kulesza, J.T. Sawicki. Damping by parametric excitation in a set of reduced-order cracked rotor systems. *Journal of Sound and Vibration* 354 (2015), 167–179.
- [9] Z. Kulesza. Dynamic behavior of cracked rotor subjected to multisine excitation. *Journal of Sound and Vibration* 333 (2014), 1369–1378.

- [10] R.T. Liong, C. Proppe. Application of the cohesive zone model for the evaluation of stiffness losses in a rotor with a transverse breathing crack. *Journal of Sound and Vibration* 332 (2013), 2098-2110.
- [11] R. Ricci, P. Pennacchi. Discussion of the dynamic stability of a multi-degree-of-freedom rotor system affected by transverse crack. *Mechanism and Machine Theory* 58 (2012), 82-100.
- [12] H. D. Nelson and C. Nataraj. Dynamics of a rotor system with a cracked shaft. *Journal of Vibration, Acoustics, Stress, and Reliability in Design* 108(1986), 189-196.
- [13] D.J. Han; Vibration analysis of periodically time-varying rotor system with transverse crack. *Mechanical Systems and Signal Processing* 21 (2007), 2857-2879.
- [14] J-J Sinou, B. Faverjon. The vibration signature of chordal cracks in a rotor system including uncertainties. *Journal of Sound and Vibration* 331 (2012), 138-154.
- [15] J.T. Sawicki, M.I. Friswell, Z. Kulesza, A. Wroblewski, J.D. Lekki. Detecting cracked rotors using auxiliary harmonic excitation. *Journal of Sound and Vibration* 330 (2011), 1365-1381.
- [16] L. Cheng, N. Li, X-F Chen, Z-J He. The Influence of crack breathing and imbalance orientation angle on the characteristics of the critical speed of a cracked rotor. *Journal of Sound and Vibration* 330 (2011) 2031-2048.
- [17] M.A. Al-Shudeifat, E.A. Butcher, C.R. Stern. General harmonic balance solution of a cracked rotor-bearing-disk system for harmonic and sub-harmonic analysis: analytical and experimental approach. *International Journal of Engineering Science* 48 (2010), 921-935.
- [18] J-J Sinou. Detection of cracks in rotor based on the 2X and 3X super-harmonic frequency components and the crack-unbalance interactions. *Communication in Nonlinear Science and Numerical Simulation* 13 (2008), 2024-2040.
- [19] J.-J. Sinou, A.W. Lees. A non-linear study of a cracked rotor. *European Journal of Mechanics A/Solids* 26 (2007), 152-170.
- [20] J.-J. Sinou. Effects of a crack on the stability of a non-linear rotor system. *International Journal of Non-Linear Mechanics* 42 (2007), 959-972.
- [21] J-J Sinou, A.W. Lees. The influence of cracks in rotating shafts. *Journal of Sound and Vibration* 285 (2005), 1015-1037.
- [22] C. Guo, M.A. Al-Shudeifat, J. Yan, L.A. Bergman, D.M. McFarland, E.A. Butcher. Stability analysis for transverse breathing cracks in rotor systems. *European Journal of Mechanics A/Solids* 42 (2013), 27-34.
- [23] C. Guo, M.A. Al-Shudeifat, J. Yan, L.A. Bergman, D.M. McFarland, E.A. Butcher. Application of empirical mode decomposition to a Jeffcott rotor with a breathing crack. *Journal of Sound and Vibration* 332 (2013), 3881-3892.
- [24] Q. Han, F. Chu. Parametric instability of a rotor-bearing system with two breathing transverse cracks. *European Journal of Mechanics A/Solids* 36 (2012), 180-190.
- [25] M.A. Al-Shudeifat, E.A. Butcher. New breathing functions for the transverse breathing crack of the cracked rotor system: approach for critical and subcritical harmonic analysis. *Journal of Sound and Vibration* 330 (2011), 526-544.
- [26] O.S. Jun, M.S. Gadala. Dynamic behavior analysis of cracked rotor. *Journal of Sound and Vibration* 309 (2008), 210-245.
- [27] A.K. Darpe, K. Gupta, A. Chawla. Transient response and breathing behavior of a cracked Jeffcott rotor. *Journal of Sound and Vibration* 272 (2004), 207-243.

- [28] N. Bachschmid, Pennacchi, E. Tanzi. Some remarks on breathing mechanism, on non-linear effects and on slant and helicoidal cracks. *Mechanical Systems and Signal Processing* 22 (2008), 879-904.
- [29] Q. Han, F. Chu. The effect of transverse crack upon parametric instability of a rotor-bearing system with an asymmetric disk. *Communications in Nonlinear Science and Numerical Simulation* 17 (2012), 5189-5200.
- [30] A.D. Nembhard, J.K. Sinha, A. Yunusa-Kaltungo. Experimental observations in the shaft orbits of relatively flexible machines with different rotor related faults. *Measurements* 75 (2015), 320-337.
- [31] M.A. AL-Shudeifat. New backward whirl phenomena in intact and cracked rotor systems. *Journal of Sound and Vibration* 443 (2019), 124-138.
- [32] M.A. AL-Shudeifat, H. Al Hosani, A.S. Saeed, S. Balawi. Effect of unbalance force vector orientation on the whirl response of cracked rotors. *Journal of Vibration and Acoustics* 141 (2019), VIB-18-1053.
- [33] F.K. Alhammadi, M.A. AL-Shudeifat, O. Shiryayev. Effect of angular acceleration and unbalance force orientation on the backward whirl in cracked rotors. *Proceedings of the IMECE 2018-87476* (2018).
- [34] K.T. Millsaps, G.L. Reed. Reducing lateral vibration of a rotor passing through critical speeds by acceleration scheduling. *Journal of Engineering for Gas Turbines and Power* 120 (1997), 615-620.
- [35] A.S. Sekhar, B.S. Prabhu. Transient analysis of a cracked rotor passing through critical speed. *Journal of Sound and Vibration* 173 (1994), 415-421.
- [36] M.A. AL-Shudeifat. On the finite element modeling of an asymmetric cracked rotor. *Journal of Sound and Vibration* 332 (2013), 2795–2807.

Tariq Alzarooni, (Ph.D. student): Khalifa University of Science and Technology, Department of Aerospace Engineering, Mushrif Campus, PO Box 127788, Abu Dhabi, United Arab Emirates (tariq.alzarooni@ku.ac.ae) The author gave a presentation of this paper during one of the conference sessions.

Mohammed AL-Shudeifat, Associate Professor: Khalifa University of Science and Technology, Department of Aerospace Engineering, Mushrif Campus, PO Box 127788, Abu Dhabi, United Arab Emirates (mohd.shudeifat@ku.ac.ae)

Oleg Shiryayev, Assistant Professor: University of Alaska Anchorage, Department of Mechanical Engineering, ECB 301J, 3211 Providence Dr., Anchorage, AK 99508, USA (oshiryayev@alaska.edu)

C. Nataraj, Moritz Chair Professor: Villanova University, Mechanical Engineering, 800 Lancaster Avenue, Villanova, PA 19085, USA (nataraj@villanova.edu)

Estimation of the domain of attraction for a nonlinear mechanical system

Jan Awrejcewicz, Dmytro Bilichenko, Akram Khalil Cheib,
Nataliya Losyeva, Volodymyr Puzyrov

Abstract: The paper deals with the problem of obtaining estimates of the domains of attraction and stability for a nonlinear mechanical system. It is based on special procedure of polynomial Lyapunov function construction. This procedure is applied to estimate the domain of attraction for a single DoF system (Duffing oscillator) and 3-DoF system. The latter consists of two coupled linear oscillators, to one of which a dynamic absorber with damping and nonlinear stiffness is connected. Possible advantages and drawbacks of suggested approach are discussed.

1. Introduction

The stability of a dynamic system to disturbances is a prerequisite for the stable operation of most technical systems. Therefore, in the theory of control, the problem of asymptotic stabilization, which consists in finding an admissible control providing the required motion of a closed system with asymptotic stability, has become especially important. As a rule, the problem of asymptotic stabilization has many solutions, so there is a need to choose one that provides the best performance for a closed system. One of the most important quantitative characteristics of asymptotically stable motion is the domain of attraction (DA) or region of attraction, i.e., the set of those and only those initial perturbations for which there is an asymptotic tendency of the perturbed motions to the unperturbed. In this regard, the tasks of accurately constructing the region of attraction or even its estimation are relevant. When synthesizing the stabilization law, it is advisable to maximize the region of attraction of the desired equilibrium state, since the larger the region of attraction, the easier it is to get into it when external disturbances arise. In other words, the larger the area of attraction, the more robust the control will be.

Over the past decades, many authors have investigated various aspects of this problem [1, 2, 4, 5, 6, 8, 9, 10, 11, 13, 14, 15, 16]. Several methods have been proposed for calculating the approximation for DoA, which can be broadly divided into Lyapunov and non Lyapunov methods. Lyapunov approaches include, for example, sum-squared programming (SOS) [2], methods that use both simulation and SOS programming [15], and procedures using moment

theory [5]. In this approach, the appropriate Lyapunov function (LF) is first chosen to show the asymptotic stability of the system in a small neighborhood of equilibrium. Further, the largest set of sub-levels of this Lyapunov function, in which its time derivative is negative definite, is calculated as an estimate for DoA. Non-Lyapunov methods include, for example, changing the trajectory approach [4] and occupation measures [6].

This report proposes a procedure for a kind of normalization of PL (terms having an order of smallness above the second) in order to eliminate the presence of “optional” terms in the derivative and thereby improve the estimate for the region $dV/dt < 0$. The examples of Duffing equation and 3-DoF mechanical system are considered.

2. Description the approach

2.1. Formulation of the problem

Let the origin $\mathbf{x} = \mathbf{0}$ be an asymptotically stable equilibrium point for the nonlinear system

$$\dot{\mathbf{x}} = \mathbf{f}(\mathbf{x}) \quad (1)$$

where $\mathbf{f} : D \rightarrow \mathbb{R}^n$ is locally Lipschitz function, and $D \subset \mathbb{R}^n$ is a domain containing the origin.

Definition 2.1 [8]. Let $\phi(t, \mathbf{x})$ be the solution of system (1) that starts at initial state \mathbf{x}_0 at time $t = 0$. The region of attraction of the origin, denoted by R_a , is defined by

$$R_a = \{\mathbf{x} \in D : \phi(t, \mathbf{x}) \rightarrow \mathbf{0} \text{ as } t \rightarrow \infty\}. \quad (2)$$

For most nonlinear systems, the exact determination of region (2) is not possible, therefore, the task is to obtain an estimate

$$S \subset R_a, \quad \mathbf{0} \in S, \quad (3)$$

so that S can be represented in a fairly simple form. Such an estimate can be obtained using the Lyapunov function for system (1). Consider a locally positive definite function $V(\mathbf{x})$ whose derivative $\dot{V}(\mathbf{x})$ is locally negative in a neighborhood of origin.

Statement 2.1 [12] Let S be a compact set, and the following conditions hold:

$$1) \exists c : 0 < V(\mathbf{x}) \leq c, \forall \mathbf{x} \in S(\mathbf{x} \neq \mathbf{0}), \text{ and } \forall \mathbf{x} \in \partial S : V(\mathbf{x}) = c; \quad (4)$$

$$2) \forall \mathbf{x} \in S : \dot{V}(\mathbf{x}) < 0(\mathbf{x} \neq \mathbf{0}), \quad (5)$$

then $S \subset R_a$.

Note that the set $\mathbf{x} : V(\mathbf{x}) \leq c$ may not be compact, it is enough only that condition (4) is satisfied in the considered region S .

An estimate of the form (4) substantially depends on the choice of the function V , the choice of an arbitrary Lyapunov function for system (1) in the general case may turn out to be ineffective. Such function V (satisfying conditions (4)) will give some estimate of the attraction region, however, an estimate obtained can be arbitrarily small.

2.2. Construction of the Lyapunov function

In the case when all the eigenvalues of the system linearized in a neighborhood of the equilibrium are located in the left half-plane, this equilibrium is asymptotically stable regardless of the nonlinear expansion terms of the right-hand side. In terms of the direct Lyapunov method, it is sufficient to use quadratic LF. However, when estimating the region of attraction, the influence of nonlinear terms is significant. To obtain an effective estimate, it is necessary to add terms of a higher order to the LF $V(\mathbf{x})$ that can improve the properties of the derivative dV/dt .

Consider the following model system

$$\frac{d\mathbf{x}}{dt} = \mathbf{A}\mathbf{x} + P^{(3)}(\mathbf{x}), \quad (6)$$

where \mathbf{A} is a stable (Hurwitz) matrix, $P^{(3)}$ is a polynomial of third order.

With non-degenerate linear transformation

$$\mathbf{x} = \mathbf{S} \begin{pmatrix} z \\ \bar{z} \end{pmatrix}$$

system (1) can be converted to the form

$$\frac{dz}{dt} = \mathbf{J}z + P^{(3)}(z, \bar{z}), \quad \frac{d\bar{z}}{dt} = \bar{\mathbf{J}}\bar{z} + \bar{P}^{(3)}(z, \bar{z}). \quad (7)$$

Here $\mathbf{J} \oplus \bar{\mathbf{J}} = \text{diag}(-h_1 + i\omega_1, \dots, -h_n + i\omega_n, -h_1 - i\omega_1, \dots, -h_n - i\omega_n)$ – Jordan normal form of matrix \mathbf{A} ($h_j \geq 0, j = \overline{1, n}$).

Adhering the results of works [3, 7], we introduce the following notation. Let $\mathbf{L} = (l_1, \dots, l_n)$ is the n -dimensional subscript, $l = |\mathbf{L}| = l_1 + \dots + l_n$, then the homogeneous form of order s may be presented as following

$$\sum_{l+m=s} k_{\mathbf{L}, \mathbf{M}} z^{\mathbf{L}} \bar{z}^{\mathbf{M}} = \sum_{l+m=s} k_{l_1, \dots, l_n, m_1, \dots, m_n} z_1^{l_1} \dots z_n^{l_n} \bar{z}_1^{m_1} \dots \bar{z}_n^{m_n}. \quad (8)$$

Consider the Lyapunov function

$$V(z, \bar{z}) = \sum_{j=1}^m \alpha_j z_j \bar{z}_j + V^{(4)}(z, \bar{z}) = \sum_{j=1}^m \alpha_j z_j \bar{z}_j + \sum_{l+m=4} k_{\mathbf{L}, \mathbf{M}} z^{\mathbf{L}} \bar{z}^{\mathbf{M}}, \quad (9)$$

where α_j are arbitrary positive constants and $k_{L,M}$ are some coefficients (unknown at this point). The full derivative of LF with respect to system (7) has the following view

$$\dot{V}^{(2)}(\mathbf{z}, \bar{\mathbf{z}}) = -\sum_{j=1}^n \alpha_j h_j z_j \bar{z}_j, \quad \dot{V}^{(4)}(\mathbf{z}, \bar{\mathbf{z}}) = \left\langle \frac{\partial V^{(4)}}{\partial \mathbf{z}}, \mathbf{J}\mathbf{z} \right\rangle + \sum_{j=1}^n \alpha_j z_j P_j(\mathbf{z}, \bar{\mathbf{z}}) + c.c., \quad (10)$$

$$\dot{V}^{(6)}(\mathbf{z}, \bar{\mathbf{z}}) = \left\langle \frac{\partial \tilde{V}^{(4)}}{\partial \mathbf{z}}, \mathbf{P}(\mathbf{z}, \bar{\mathbf{z}}) \right\rangle + c.c. \quad (11)$$

Here the acute parentheses mean the scalar product, abbreviation “c.c.” means complex conjugate part of expression.

The coefficients k_{KM} can be selected so that conditions

$$\dot{V}^{(4)}(\mathbf{z}, \bar{\mathbf{z}}) = \sum_{l=2} G_L \mathbf{z}^L \bar{\mathbf{z}}^L \quad (12)$$

are met, where G_L are some real constants. In fact, the condition (12) is equivalent to the following equalities:

A) all coefficients in terms $\mathbf{z}^L \bar{\mathbf{z}}^M$ ($L \neq M$) are equal to zero, which imply

$$\sum_{j=1}^n \alpha_j (b_{L,M-\delta_j} + b_{L-\delta_j,M}) + (-\langle l+m, h \rangle + i(\langle l-m, \omega \rangle)) k_{L,M} = 0. \quad (13)$$

Remind that

$$\langle l+m, h \rangle \triangleq \sum_{j=1}^n (l_j + m_j) h_j, \quad \langle l-m, \omega \rangle \triangleq \sum_{j=1}^n (l_j - m_j) \omega_j. \quad (14)$$

Since $\langle l+m, h \rangle + i(\langle l-m, \omega \rangle) \neq 0$ (neither real part nor imaginary one), the coefficients $k_{L,M}$ unambiguously can be found from equalities (13).

B) The coefficients in terms $\mathbf{z}^L \bar{\mathbf{z}}^L$ are equal to $G_{L,L}$, which imply

$$\sum_{j=1}^n \alpha_j (b_{L,L-\delta_j} + b_{L-\delta_j,L}) - 2\langle l, h \rangle k_{L,L} = G_L, \quad (15)$$

and, hereafter, we have

$$k_{L,L} = \frac{1}{\langle l, h \rangle} \left[\sum_{j=1}^n \alpha_j \text{Re}(b_{L,L-\delta_j}) - \frac{1}{2} G_L \right]. \quad (16)$$

Such procedure may be continued by adding to function V the form of order six and normalizing the $V^{(6)}$. Obviously, it requires the bigger portion of calculations, so the common dilemma “cost – profit” is an essential factor.

Remark 1. This approach is valid in case when some of values h_j are equal to zero, but the origin remains asymptotically stable. This is the critical case on pure imaginary roots according to Lyapunov classification, and the procedure is the same. The only difference is that $V'^{(2)}$ is semi-negative definite now, but V' is still negative definite.

2.3. Example of a single DoF system

Consider, as an illustration of the procedure described above, the Duffing equation

$$\ddot{x} + c\dot{x} + k^{lin}x - k^{nonlin}x^3 = 0, \quad (17)$$

where positive constants c , k^{lin} , k^{nonlin} represent the coefficient of damping and stiffness (the case of softening spring). We suppose that

$$c^2 < k_{lin},$$

i.e the origin

$$x = 0, \dot{x} = 0$$

is classified as stationary point of spiral type.

Introducing the dimensionless variable, parameters and time according to formulas

$$\omega = \sqrt{k^{lin} - c^2/4}, \quad h = \frac{c}{2\omega}, \quad x_1 = \frac{\sqrt{k^{nonlin}}}{\omega}x, \quad \tau = \omega t, \quad (18)$$

we can rewrite equation (17) as a system (6)

$$x_1' = x_2, \quad x_2' = -x_1 - 2hx_2 + x_2^3, \quad (19)$$

where the prime means the differentiation on time τ .

Hereafter the matrix \mathbf{A} is

$$\mathbf{A} = \begin{pmatrix} 0 & 1 \\ -1 & -2h \end{pmatrix}. \quad (20)$$

and their eigenvalues and eigenvectors are:

$$\lambda_{12} = -h \pm i, \quad \beta_{12} = (1, \lambda_{12})^T.$$

The upper subscript “ T ” means the transpose operation. With transformation

$$x_1 = z + \bar{z}, \quad x_2 = \lambda_1 z + \lambda_2 \bar{z}$$

we have a system in form (7), herewith

$$\mathbf{J} = \text{diag}(\lambda_1, \lambda_2), \quad P^{(3)}(z, \bar{z}) = -\frac{1}{2}i(z + \bar{z})^3. \quad (21)$$

According to formulas (13), (16) we have

$$k_{40} = \frac{1 - ih}{8(1 + h^2)}, \quad k_{31} = \frac{1 - 2ih}{1 + 4h^2}, \quad k_{22} = -\frac{1}{4h}G_2 \quad (b_{30} = -\frac{1}{2}i, \quad b_{21} = -\frac{3}{8}i, \quad \alpha_1 = 1). \quad (22)$$

Function V and its derivative V' in real variables are

$$V(x_1, x_2) = (x_1^2 + x_2^2) + \frac{1}{4}[(\frac{\sigma_3}{\sigma_1\sigma_2} + k_{22})x_1^4 + \frac{4h\sigma_3}{\sigma_1\sigma_2}x_1^3x_2 + (-\frac{6}{\sigma_2} + 8k_{22})x_1^2x_2^2 + 12h\frac{12h}{\sigma_1\sigma_2}x_1x_2^3 + (-\frac{3}{\sigma_1\sigma_2} + 4k_{22})x_2^4], \quad (23)$$

$$V' = -2h(x_1^2 + x_2^2)[1 + 2k_{22}(x_1^2 + x_2^2)] + 4x_1^3[\frac{h\sigma_3}{\sigma_1\sigma_2}x_1^3 + x_1^2x_2(-\frac{3}{\sigma_1} + 4k_{22}) + \frac{9}{\sigma_1\sigma_2}x_1x_2^2 + (-\frac{3}{\sigma_1\sigma_2} + 4k_{22})x_2^3], \quad \sigma_1 = 1 + h^2, \sigma_2 = 1 + 4h^2, \sigma_3 = 5 + 8h^2. \quad (24)$$

Here the unknown arbitrary value b_{22} (or G_2) is a kind of “tuning” parameter. It has some influence on size of both domains where V is positive and V' is negative. Its value is chosen with the aim to maximize the corresponding estimation of the R_a . As it follows from formulas (23), (24), the positive value of b_{22} is welcomed, because it gives some additional effect to functions V, V' (first of them becomes “more positive”, and second one becomes “more negative”). The typical view of the domains $0 < V \leq c$, $V' < 0$ is presented in Fig.1a ($h = 0.3, b_{22} = 0.5, c = 0.5$). Varying the parameter b_{22} brings different approximations of DA. The optimal value is about 0.96 (solid line in Fig.1b).

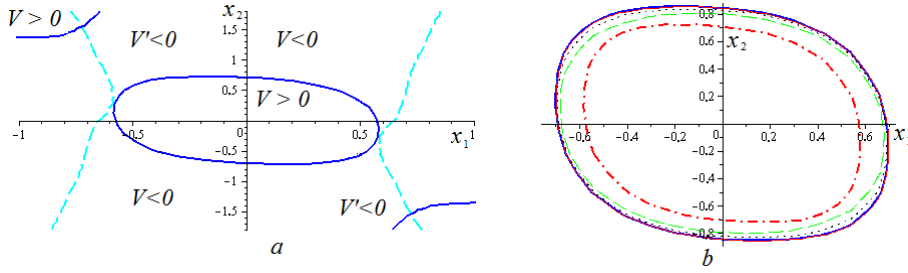


Figure 1. a: Boundaries of domains $0 < V \leq c$, $V' < 0$. b: Estimates of region of attraction for different values of tuning parameter: $b_{22} = 0.5$ – dot-dash line; $b_{22} = 0.8$ – dash line; $b_{22} = 0.96$ – solid line; $b_{22} = 1.05$ – dot line.

3. Application to 3-DoF system

We consider the 3-Degrees-of-Freedom mechanical system which is schematically presented on fig.2. It consists of two masses connected to each other and to fixed supports by springs (linear) and an absorber connected to one of them.

The motion equations of the mechanical system considered are

$$m\ddot{x}_1 + c(\dot{x}_1 - \dot{x}_a) + kx_1 + k(x_1 - x_2) - k_a^{lin}(x_1 - x_a) + k_a^{nonlin}(x_1 - x_a)^3 = 0,$$

$$m\ddot{x}_2 + k(x_2 - x_1) + kx_2 = 0, \quad (25)$$

$$m_a\ddot{x}_a + c(\dot{x}_a - \dot{x}_1) + k_a^{lin}(x_a - x_1) - k_a^{nonlin}(x_a - x_1)^3 = 0.$$

Here x_1 and x_2 refer to the displacements of the primary 2-DoF system, while x_a refers to the displacement of the absorber; m is the mass of the bodies, and k — the stiffness of the springs; $c, k_a^{lin}, k_a^{nonlin}$ are the absorber damping coefficient, linear spring coefficient and cubic (positive) spring coefficient respectively. It is supposed that parameters of main system are given, parameters of absorber are tunable, and the mass of the absorber m_a is much less then m .

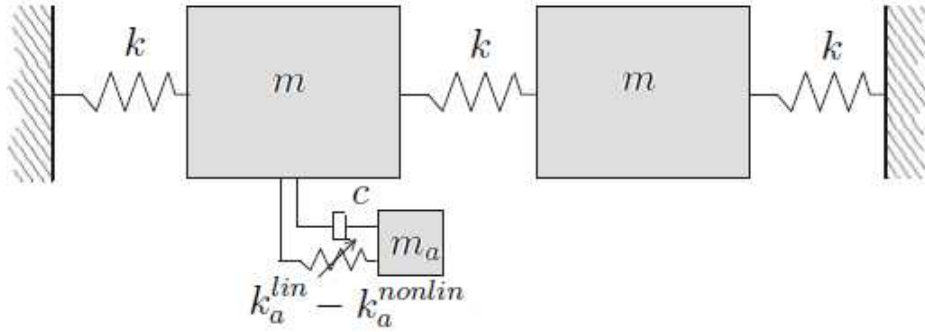


Figure 2. The 3-Degrees-of-Freedom mechanical system.

Let us introduce the dimensionless parameters and time with formulas

$$\mu = \frac{m_a}{m}, \quad \omega = \sqrt{\frac{k}{m}}, \quad h = \frac{c}{m_a\omega}, \quad \varkappa = \frac{k_a^{lin}}{m_a\omega^2}, \quad \tau = \omega t. \quad (26)$$

Here $\omega_1 = \omega, \omega_2 = \sqrt{3}\omega$ are the natural frequencies of the main system.

With substitution

$$x_a = x_1 + x_3 \quad (27)$$

the linearized system in the vicinity of origin is associated with the following λ - matrix

$$\begin{pmatrix} \lambda^2 + 2 & -1 & -\mu(h\lambda + \varkappa) \\ -1 & \lambda^2 + 2 & 0 \\ -\mu(h\lambda + \varkappa) & 0 & \lambda^2 + h\lambda + \varkappa \end{pmatrix}. \quad (28)$$

Accordingly, the characteristic polynomial is as follows

$$f(\lambda) = \lambda^6 + h\lambda^5 + (4 + \varkappa - \mu^2 h^2)\lambda^4 + 2h(2 - \mu^2 \varkappa)\lambda^3 + \quad (29)$$

$$(3 + 4\kappa - 2\mu^2 h^2 - \mu^2 \kappa^2)\lambda^2 + h(3 - 4\mu^2 \kappa)\lambda + \kappa(3 - 2\mu^2 \kappa).$$

The transformation matrix is determined as following $\mathbf{S} = (\beta_1, \dots, \beta_6)$, and the components of column β_j are:

$$\begin{aligned} \beta_{j1} &= \mu(h\lambda_j + \kappa)(\lambda_j^2 + 2), \beta_{j2} = \mu(h\lambda_j + \kappa), \beta_{j3} = (1 + \lambda_j^2)(3 + \lambda_j^2), \\ \beta_{jq+3} &= \lambda_j \beta_{jq} \quad (q = 1, 2, 3). \end{aligned} \quad (30)$$

Here λ_j is the corresponding eigenvalue.

The single cubic term in system (25) is x_3^3 , then

$$x_3 = \beta_{31}z_1 + \beta_{32}z_2 + \beta_{33}z_3 + c.c \quad (31)$$

For instance with $h = 0.14$, $\kappa = 1.49$ the eigenvalues are

$$\begin{aligned} \lambda_{1,2} &= -0.0000396 \pm 0.9995627i, \quad \lambda_{3,4} = -0.0000399 \pm 1.732127i, \\ \lambda_{5,6} &= -0.06992 \pm 1.21889i. \end{aligned} \quad (32)$$

The corresponding matrix \mathbf{S} is given in Appendix.

Of course, the calculation for the multi-DoF system is very cumbersome, so here we restrict ourselves to listing the main stages of obtaining an estimate.

Step 1. Finding the eigenvectors and linear transformation matrix.

Step 2. Writing the equations of motion in new variables.

Step 3. Construction the LF according to the procedure described in Section 2 (finding the coefficients $b_{\mathbf{L}, \mathbf{M}}$).

Step 4. Variation of values $G_{\mathbf{L}}$ in order to obtain the maximal (within the framework of this approach) estimate for the attraction region.

Step 5. Visualization of the results obtained.

Remark. The last paragraph is a separate rather nontrivial problem due to the dimension of the phase space ($n = 6$ in our case). It may be useful here to go to the polar coordinates $z_j = \rho_j \exp(i\varphi_j)$ and build the corresponding region in space ρ_1, ρ_2, ρ_3 .

4. Conclusions

In this paper, we propose a method for constructing the polynomial Lyapunov function in order to obtain approximations of the attraction region for nonlinear mechanical systems. This method uses the procedure of normalizing the terms of the higher terms of the PL decomposition in order to eliminate the presence of optional terms in the derivative and thereby improve the estimate for the region. This approach seems quite effective, although

like other well-known methods it is computationally costly and time-consuming, especially for systems of high dimension and/or with uncertain parameters. This approach is applied to estimation of DA for single DoF and three DoF mechanical systems.

APPENDIX.

The transformation matrix in case $h = 0.14$, $\varkappa = 1.49$ is

$$\begin{pmatrix} 0.029826 + 0.002799i & -0.029807 - 0.004855i & 0.015952 - 0.003274i \\ 0.029800 + 0.002799i & 0.029800 + 0.004850i & 0.029604 + 0.003413i \\ 0.001750 - 0.000159i & 0.000528 + 0.000276i & -0.759487 - 0.176995i \\ -0.002799 + 0.029813i & 0.008411 - 0.051629i & 0.002875 + 0.019673i \\ -0.002799 + 0.029787i & -0.008402 + 0.051617i & -0.006230 + 0.035846i \\ 0.000159 + 0.001749i & -0.000479 + 0.000915i & 0.268841 - 0.913356i \end{pmatrix},$$

(three absent columns are complex conjugate to presented ones).

References

- [1] CHESI, G. *Domain of attraction: analysis and control via SOS programming*. Springer, 2011.
- [2] CHESI, G., GARULLI, A., TESI, A., AND VICINO, A. Lmi-based computation of optimal quadratic lyapunov functions for odd polynomial systems. *Int. J. Robust Nonlinear Control* 1, 15 (2005), 35 – 49.
- [3] CHETAEV, N. *The stability of motion*. New York: Pergamom Press, 1961.
- [4] GENESIO, R., TARTAGLIA, M., AND VICINO, A. On the estimation of asymptotic stability regions: state of the art and new proposals. *IEEE Trans. Autom. Control* 8, 30 (1985), 747 – 755.
- [5] HACHICHO, O., AND TIBKEN, B. Estimating domains of attraction of a class of nonlinear dynamical systems with lmi methods based on the theory of moments. *Proceedings of the 41-st IEEE Int. Conf.on Decision and Control*, 3 (2002), 3150 – 3155.
- [6] HENRION, D., AND KORDA, M. Convex computation of the region of attraction of polynomial control systems. *IEEE Trans. Autom. Control* 2, 59 (2014), 297 – 312.
- [7] KAMENKOV, G. *Stability and oscillations of nonlinear systems*. Moscow: Nauka, 1972.
- [8] KHALIL, H. *Nonlinear systems*. 3-rd ed. New Jewsey: Prentice hall, 2002.

- [9] LIU, Y., AND PANG, G. The basin of attraction of the liu system. *Commun. Nonlinear Sci. Numer. Simul.* 4, 16 (2011), 2065 – 2071.
- [10] NAJAFI, E., BABUSKA, R., AND LOPES, G. A fast sampling method for estimating the domain of attraction. *Nonlinear Dyn.*, 86 (2016), 823 – 834.
- [11] PRAKASH, S., VANUALAILAI, J., AND SOMA, T. Obtaining approximate region of asymptotic stability by computer algebra: a case study. *South Pac. J. Nat. Appl. Sci.* 1, 20 (2002), 56 – 61.
- [12] ROUCHE, N., HABETS, P., AND LALOY, M. *Stability theory by Liapunov's direct method*. New York: Springer-Verlag, 1977.
- [13] STACEY, A., AND STONIER, R. Analytic estimates for the boundary of the region of asymptotic attraction. *Dynamics and Control*, 8 (1998), 177 – 189.
- [14] TIBKEN, B., AND DILAVER, K. Computation of subsets of the domain of attraction for polynomial systems. *Proceedings of the 41-st IEEE Int. Conf.on Decision and Control*, 3 (2002), 2651 – 2660.
- [15] TOPCU, U., PACKARD, A., AND SEILER, P. Local stability analysis using simulations and sum-of-squares programming. *Automatica* 10, 44 (2008), 2669 – 2675.
- [16] TOPCU, U., PACKARD, A., SEILER, P., AND BALAS, G. Robust region-of-attraction estimation. *IEEE Trans. Autom. Control* 1, 55 (2010), 137 – 142.

Jan Awrejcewicz, Professor: Lodz University of Technology, 1/15 Stefanowski Str., 90-924 Lodz, Poland, Poland (PL) (*jan.awrejcewicz@p.lodz.pl*).

Dmytro Bilichenko, Student: Vasyl Stus Donetsk National University, 600-richia 21, Vinnitsia, Ukraine, Ukraine (UA) (*bilichenko.d@donnu.edu.ua*).

Akram Khalil Cheib, PhD Student: Vasyl Stus Donetsk National University, 600-richia 21, Vinnytsia, Ukraine, Ukraine (UA) (*akram_cheib@hotmail.com*).

Nataliya Losyeva, Professor: Vasyl Stus Donetsk National University, 600-richia 21, Vinnitsia, Ukraine, Ukraine (UA) (*natalie.loseva@gmail.com*).

Volodymyr Puzyrov, Professor: Vasyl Stus Donetsk National University, 600-richia 21, Vinnitsia, Ukraine, Ukraine (UA) (*v.puzyryov@donnu.edu.ua*). The author gave a presentation of this paper during the conference in the special session “Innovative strategies for vibration control and mitigation” organized by G. Failla and R. Santoro.

Nonlinear dynamics of flexible nanobeams taking into account the Casimir, van der Waals and Coulomb forces

Jan Awrejcewicz, Olga A. Saltykova, Vadim A. Krysko, Anton V. Krysko

Abstract: A mathematical model of a flexible nanobeam, described by the kinematic hypothesis of the first approximation and located in the field of action of the forces of Casimir, van der Waals, and Coulomb, is proposed. Using the methods of nonlinear dynamics, we studied the influence of the scale parameter on the forced vibrations of nanobeam made of nitrogen.

1. Formulation of the problem

Currently, MEMS and NEMS are widely used in various instrumentations [1]. As an element of such systems, a beam having dimensions of the order of nano can be considered, which is under the influence of external mechanical and electric fields, such as the forces of Casimir, Van der Waals, or Coulomb [2, 3]. In the present work, we construct a mathematical model of a nanobeam located in the field of action of these forces. Classical solid mechanics does not take into account the size-dependent behavior occurring in nano-scale structures. Among the theories that allow modeling scale effects in a continuum, we note the couple stress theory of elasticity [4, 5], nonlocal theory of elasticity [6], and gradient theory of elasticity [7]. The paper uses couple stress theory of elasticity to take into account a size-dependent behavior.

The structure under consideration is a two-dimensional region of the space \mathbb{R}^2 with a Cartesian coordinate system, introduced as follows: in the body of the beam, a cast line, called the median line, is fixed $z=0$, the OX axis is directed from left to right along the median line, whereas the OZ axis is down, perpendicular to OX. Between the beam and the electrode there is a gap h_1 . In the indicated coordinate system, the beam as a two-dimensional domain Ω is defined as follows (Fig. 1):

$$\Omega = \{x \in [0, a], -h \leq z \leq h + h_1\}, \quad 0 \leq t \leq \infty.$$

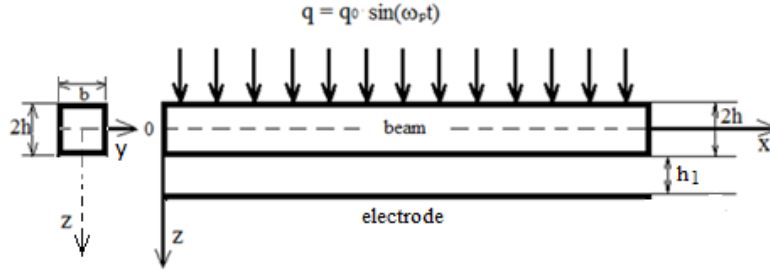


Figure 1. The settlement scheme

The equations of beam motion, in displacements, described by Euler-Bernoulli hypotheses, in dimensionless form (1):

$$\begin{aligned} \frac{\partial^2}{\partial x^2} \left[- \left(\frac{1}{12} + \frac{\gamma}{2(1+\nu)} \right) \frac{\partial^2 w}{\partial x^2} \right] + \frac{\partial}{\partial x} \left\{ \left[\left(\frac{\partial u}{\partial x} + \frac{1}{2} \left(\frac{\partial w}{\partial x} \right)^2 \right) \right] \left(\frac{\partial w}{\partial x} \right) \right\} + q &= \frac{\partial^2 w}{\partial t^2}, \\ \lambda^2 \frac{\partial}{\partial x} \left[\left(\frac{\partial u}{\partial x} + \frac{1}{2} \left(\frac{\partial w}{\partial x} \right)^2 \right) \right] &= \frac{\partial^2 u}{\partial t^2}, \end{aligned} \quad (1)$$

where w is the deflection functions of the beam, u is the functions of moving the middle surface,

$\lambda = \frac{a}{2h}$ is the geometric parameter, $\gamma = \left(\frac{l}{2h} \right)^2$ is the size-dependent parameter, l is the material length scale parameter.

The boundary conditions corresponding to the rigid sealing of the ends of the beam follow

$$w(0, t) = w(1, t) = 0, \quad \frac{\partial w(0, t)}{\partial x} = \frac{\partial w(1, t)}{\partial x} = 0, \quad u(0, t) = u(1, t) = 0, \quad (2)$$

and we take the initial conditions:

$$w(x, 0) = \frac{\partial w(x, 0)}{\partial t} = 0; \quad u(x, 0) = \frac{\partial u(x, 0)}{\partial t} = 0. \quad (3)$$

The system of nonlinear partial differential equations is reduced to a system of ordinary differential equations by the finite difference method with approximation $O(c^2)$, where c is the step along the spatial coordinate. The obtained Cauchy problem in time is solved by the Runge – Kutta type methods (4th, 2nd order Runge – Kutta method, 4th order Runge – Kutta – Fehlberg method, 4th order Cash – Karp method, Runge – Kutta – Prince – Dormand method of 8th order, implicit Runge-Kutta method of the 2nd and 4th order [8-9]). Based on the described algorithm, a software package has been created that allows you to solve the problem, depending on the control parameters $\{q_0, \omega_p\}$.

A transverse alternating load of the form distributed on the surface acts on the beam:

$$q = q_0 \sin(\omega_p t) + q_k + q_w + q_c, \quad (4)$$

where q_0 is the amplitude, ω_p is the frequency of the forced oscillations, $q_k = \frac{\hbar c_1 \pi^2}{240(h_1 - w)^4}$ is the

Casimir force, $q_w = \frac{A}{6\pi(h_1 - w)^3}$, $q_c = \frac{1.202}{4k_b * 298.15(h_1 - w)^2}$ is the van der Waals force, Coulomb

force. Here \hbar is the Planck constant, c_1 is the speed of light in vacuum, k_b is the Boltzmann constant, and A is the Hamaker constant. To study the dynamics of the described structure, nonlinear dynamics analysis methods are used: Fourier power spectra are constructed, phase portraits are calculated, the values of the highest Lyapunov exponent are calculated using the Wolf, Kantz, Rosenstein algorithms, the Lyapunov exponents spectra are estimated using the Sano-Savada algorithms and using neural networks, Poincaré sections are built, wavelet spectra based on the mother wavelets of Morlet, Gauss 16–32 are also employed [10-13].

2. Numerical results

We study the nonlinear dynamics of a beam under the action of the Casimir force in vacuum. The system is conservative. The geometric and physical parameters of the mechanical structure are as follows: $a = 400 \mu m$, $h = 4 \mu m$, $h_1 = 6 \mu m$, $\lambda = a/2h = 100$. The material of beam is silicon, with the following physical parameters $\nu = 0,28$, $E = 131 GPa$, $\rho = 2.33 g/sm^2$. In addition to the Casimir force, an external alternating load acts on the beam. The natural frequency of the beam ω_p was calculated, with the above geometric and physical parameters, and it was found that $\omega_p = 22.5$.

Tables 1–3 show Fourier power spectra, Morlet wavelet spectra, and signals for various amplitudes of the driving oscillations. In Table 1, the size-dependent parameter $\gamma = 0$, in Table 2 - $\gamma = 0,1$, in Table 3 - $\gamma = 0,3$.

When exposed to an external load beam with an oscillation amplitude $q_0 = 10^{-4}$ of the beam, two-frequency response with $\omega_p = 22.537$ and $\omega_1 = 22.375$ is obtained. Frequency values are linearly independent. The maximum amplitude of the oscillations is $3 \cdot 10^{-5}(2h)$. Increasing the load does not lead to the appearance of new frequencies up to $q_0 = 0.3$. At a given amplitude of the driving oscillations, a third frequency $\omega_2 = 22.23$ occurs, the amplitude of the oscillations is $0.1(2h)$.

Table 1. The dynamic characteristics of the beam structure at $\gamma = 0$

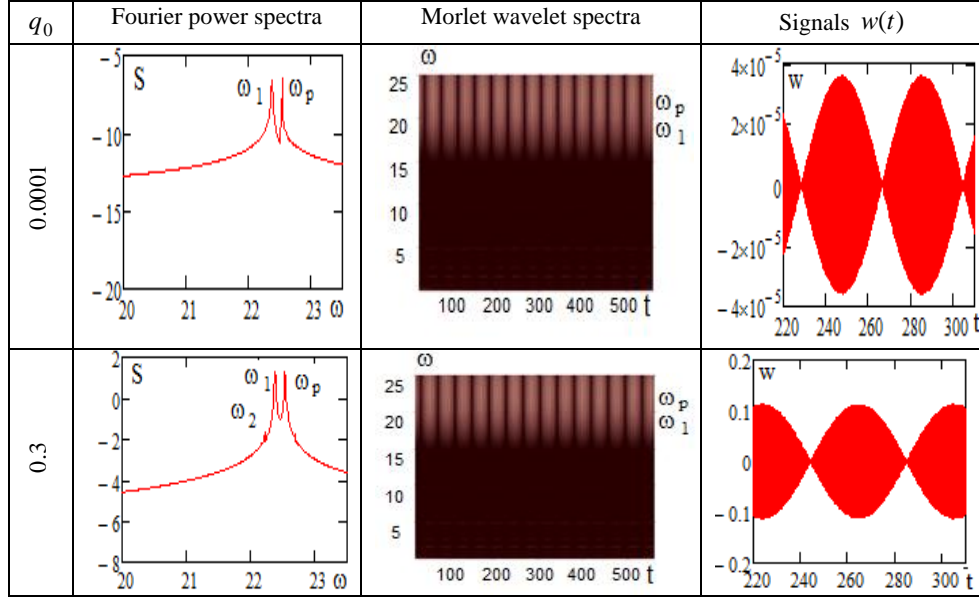
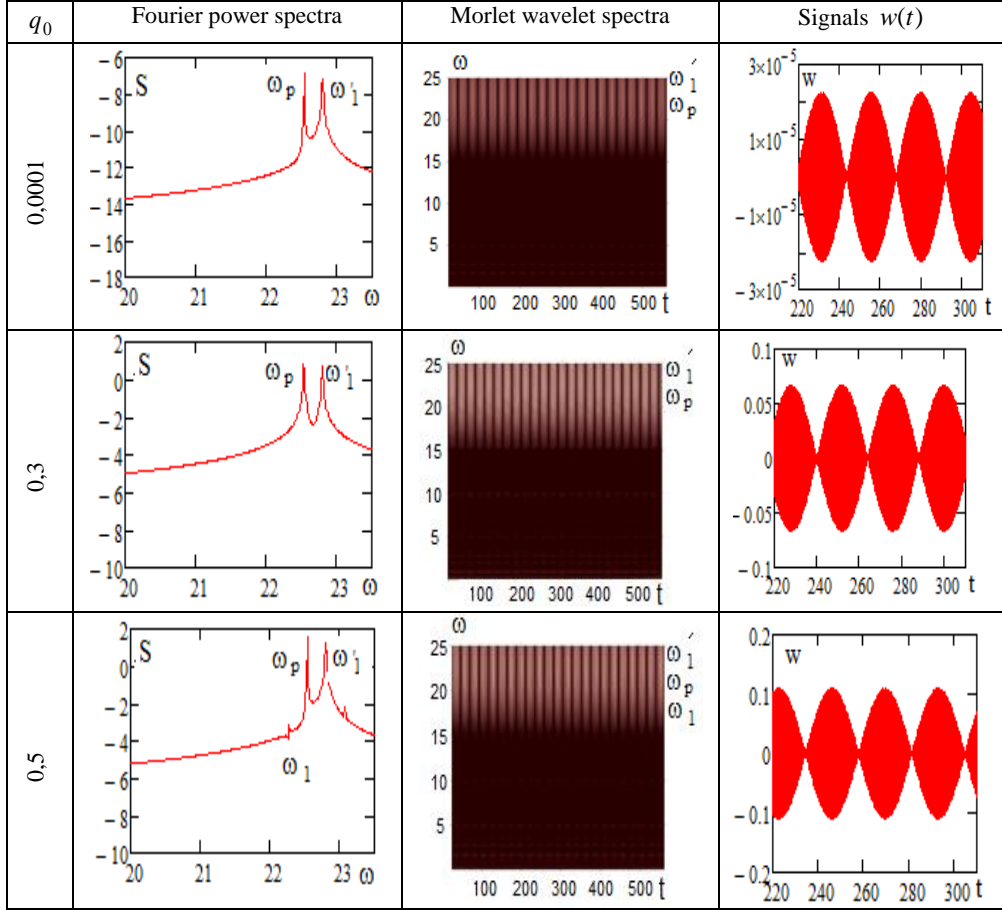


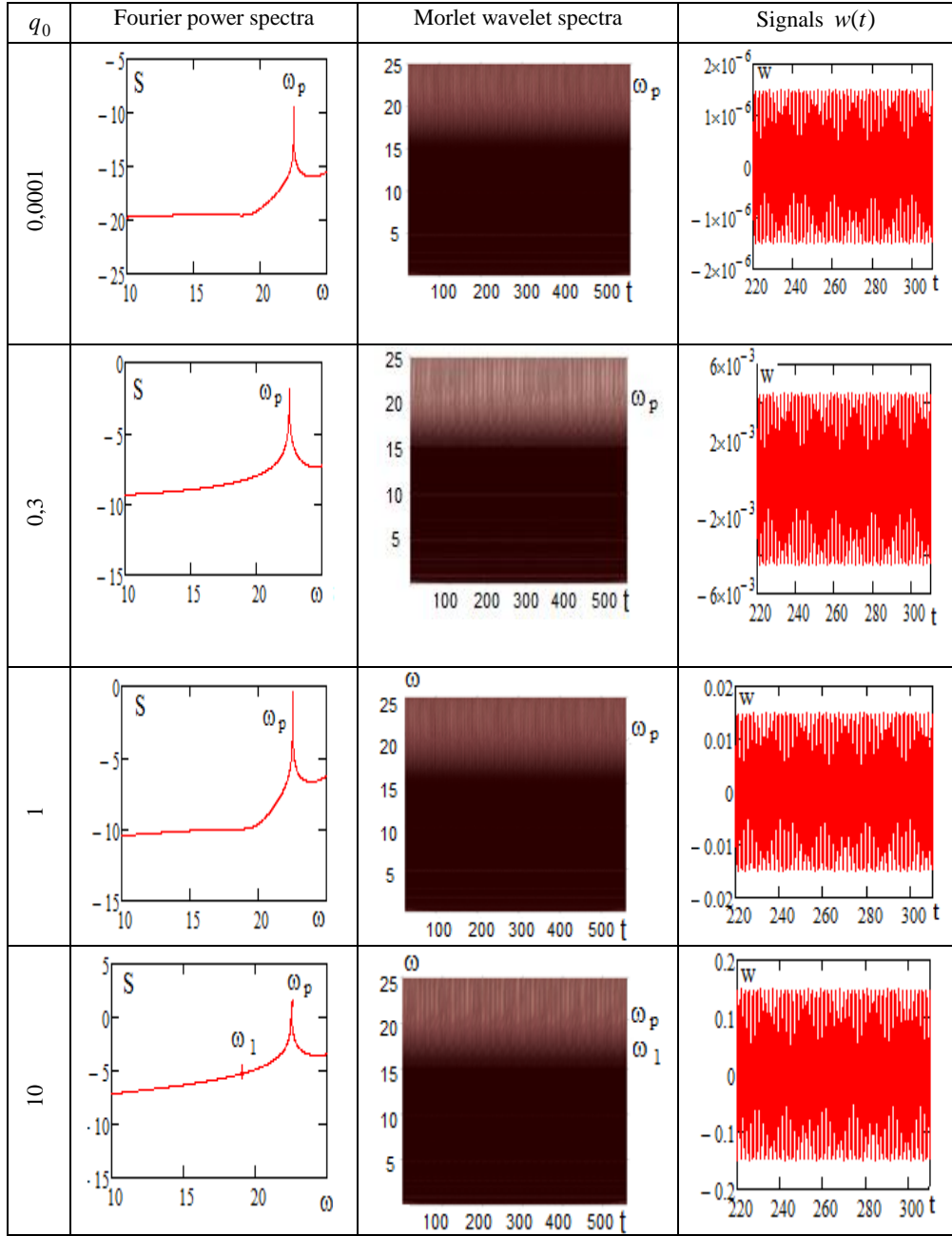
Table 2 and Table 3 show the results where the size-dependent parameter γ is taken into account. Under the action of an external load with an amplitude $q_0 = 10^{-4}$, the oscillations are two-frequency, however, the frequency $\omega_1' = 22.8$, i.e. frequency has become larger in value than frequency $\omega_p = 22.53$. The amplitude of the oscillations decreased to $2 \cdot 10^{-5}$, compared with the results given in Table 1 (for $q_0 = 10^{-4}$). Changes in the frequency characteristics does not occur, but the amplitude of the oscillations decreased by almost two times. This makes it possible to increase the amplitude of the driving load up to $q_0 = 0.5$ where the frequency ω_1 occurs, and at the following resonance conditions $\omega_1' - \omega_p = \omega_p - \omega_1$.

Table 2. The dynamic characteristics of the beam structure at $\gamma = 0.1$



An increase in the size-dependent parameter leads to a decrease in the amplitude of oscillations of the beam, if $\gamma = 0.3$, $q_0 = 10^{-4}$ the amplitude of oscillations is $3 \cdot 10^{-6}(2h)$, which is an order of magnitude smaller than for $\gamma = 0$ (Table 1). In contrast to the cases considered above, when $\gamma = 0.3$ the power spectrum contains only $\omega_p = 22.53$ frequency. For $q_0 = 10$ there is a frequency $\omega_1 = 19.127$.

Table 3. The dynamic characteristics of the beam structure at $\gamma = 0.3$



Changing the γ parameter implies decrease in the time periods of frequency of intermittency. This can be seen on the Morlet wavelet spectra. For $\gamma = 0$ the number of periods is 14 (Table 1), $\gamma = 0.1$ - 22 (Table 2), and for $\gamma = 0.3$ is no intermittency of frequencies (Table 3). The wavelet spectra contain frequencies that are not reflected in the Fourier power spectra, but it is also impossible to determine frequencies whose values are close in value to the frequency of the forcing oscillations on the wavelet spectra.

For all cases considered, the values of the spectrum of Lyapunov exponents were calculated using the Sano-Savada algorithm. As a result, we can conclude that the increase of the γ parameter leads to a regularization of beam vibrations.

3. Conclusions

The influence of the parameter and the amplitude of the driving load on the nonlinear dynamics of the beam, described by the kinematic hypothesis of the first approximation located in the field of action of the Casimir force, is investigated. The beam is made of silicon. Summarizing, it was found that an increase in the parameter leads to a regularization of beam vibrations and to a decrease in the beam deflection under the action of the same external load.

Acknowledgments

The work was supported by the RSF, № 16-11-1038

References

- [1] Bouchaala, A., Jaber, N., Shekhah, O., Chernikova, V., Eddaoudi, M., Younis, M.I. A smart microelectromechanical sensor and switch triggered by gas. *Applied Physics Letters*, 109(1) (2016) 013502.
- [2] Parsegian, V.A. *Van Der Waals Forces: A Handbook for Biologists, Chemists, Engineers and Physicists*. Cambridge Iniversity Press, Cambridge. 2005.
- [3] Borgad, M., Klimchitskaya, G.L., Mohideen, U., Mostepanenko, V.M. *Advances in the Casimir effect*. Oxford Iniversity Press, Oxford. 2009.
- [4] Mindlin, R.D., Tiersten, H.F. Effects of couple-stress in linear elasticity. *Arch. Ration. Mech. Anal.* 11 (1962) 415-448.
- [5] Yang, F., Chong, M., Lam, D.C.C., Tong, P. Couple stress based strain gradient theory for elasticity. *International Journal of Solid and Structures* 39 (2002) 617-621.
- [6] Eringen, A.C. Nonlocal polar elastic continua. *International Journal of Engeenering and Sciences* 10 (1972) 252-282.

- [7] Aifantis, E.C. Strain gradient interpretation of size effects. *Int. J. Fract.* 95 (1999) 299-314.
- [8] Kalogiratou, Z., Monovasilis, T., Psihoyios, G., Simos, T.E. Runge–Kutta type methods with special properties for the numerical integration of ordinary differential equations. *Physics Reports* 536(3) (2014) 75-146.
- [9] Tang, W., Sun, Y. Construction of Runge–Kutta type methods for solving ordinary differential equations. *Applied Mathematics and Computation* 234 (2014) 179-191.
- [10] Krysko, V.A., Awrejcewicz, J., Krylova, E.Y., Papkova, I.V., Krysko, A.V. Non-symmetric forms of non-linear vibrations of flexible cylindrical panels and plates under longitudinal load and additive white noise. *Journal of Sound and Vibration* 423 (2018) 212-229.
- [11] Saltykova, O.A., Krysko, V.A. The contact interaction of two Timoshenko beams. *Nonlinear Dynamics* 13(1) (2017) 41-53.
- [12] Krysko, V.A., Awrejcewicz, J., Papkova, I.V., Saltykova, O.A., Krysko, A.V. Chaotic contact dynamics of two microbeams under various kinematic hypotheses. *International Journal of Nonlinear Sciences and Numerical Simulation* 20(3-4) (2019) 373-386.
- [13] Krylova, E.Y., Papkova, I.V., Erofeev, N.P., Zakharov, V.M., Krysko, V.A. Complex fluctuations of flexible plates under longitudinal loads with account for white noise. *Journal of Applied Mechanics and Technical Physics* 57(4) (2016) 714-719.

Jan Awrejcewicz, Professor: Lodz University of Technology, Faculty of Mechanical Engineering, Department of Automation, Biomechanics and Mechatronics, 1/15 Stefanowskiego Str., 90-924 Lodz, Poland (jan.awrejcewicz@p.lodz.pl);

Olga A. Saltykova Associate Professor: Department of Mathematics and Modeling, Yuri Gagarin State Technical University of Saratov, Politehnicheskaya 77, 410054 Saratov, Russian Federation (olga_a_saltykova@mail.ru);

Anton V. Krysko, Professor: Applied Mathematics and Systems Analysis, Yuri Gagarin State Technical University of Saratov, Politehnicheskaya 77, 410054 Saratov, Russian Federation (anton.krysko@gmail.com).

Vadim A. Krysko, Professor: Department of Mathematics and Modeling, Yuri Gagarin State Technical University of Saratov, Politehnicheskaya 77, 410054 Saratov, Russian Federation (tak@san.ru).

Vibration of nonlinear lumped systems with serially connected elastic elements

Jan Awrejcewicz, Roman Starosta, Grażyna Sypniewska-Kamińska

Abstract: The mechanical system with the nonlinear springs connected in series is considered in the paper. The mathematical model of that kind of systems consists of the differential and algebraic equations (DAEs). Adequately modified multiple scales method (MSM) in time domain have been applied to solve effectively the problem of harmonically forced vibration governed by DAEs. The obtained approximate solution in the analytical form allows for qualitative study of the considered system, among others for identification of the resonance conditions. The case of the main resonance is analysed in details. The modulation equations of the amplitudes and phases which are the integral part of the MSM solution allow one to study both steady and unsteady resonant motion. The stability of the resonant curves concerning the steady states has been tested and verified by comparison with the numerically obtained solutions.

1. Introduction

The massless springs in various configurations serve as a widely used models of the elastic effects in many structures. They occur not only in pure mechanical systems but also in mechatronical devices and in micro-electro-mechanical systems as well. The springs arranged in various configurations can be a source of manifold and sometimes unexpected dynamical phenomena, especially near resonances.

Our research deals with the one dimensional lumped system containing two springs with nonlinear properties and connected in series. The system seems to be quite simple, however its governing equations contain both differential and algebraic equation, therefore the appropriate modification of the asymptotic approach is necessary. We are focused on the forced vibration both far from resonance as well as in the resonance conditions. The alike system but containing one nonlinear and one linear spring was analyzed by Telli and Kopmaz [1]. The one dimensional oscillator with two nonlinear springs connected in series was analyzed in the paper [2], where the solutions dealing with only the non-resonant case are analyzed.

2. Mechanical system and mathematical model

Let us consider a body of mass m attached to the immovable wall by two springs connected in series, which can move in the horizontal path. The physical model of the analyzed system is given in Fig.1.

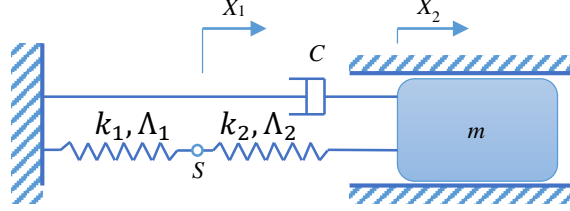


Figure 1. The analyzed mechanical system.

Let X_1 and X_2 are the elongation of the springs, whose nominal length are L_{01} and L_{02} , therefore the absolute displacement of the body equals $X_1 + X_2$. We assume the nonlinear character of the restoring forces in the springs in the following form

$$F_i = k_i(X_i + \Lambda_i X_i^3) \text{ for } i = 1, 2, \quad (1)$$

where k_i is the stiffness coefficient and Λ_i stands for the nonlinearity parameter for the i -th spring.

The kinetic energy of the system is

$$T = \frac{1}{2}m(\dot{X}_1 + \dot{X}_2)^2, \quad (2)$$

while the potential energy

$$V = k_1 \left(\frac{1}{2}X_1^2 + \frac{1}{4}\Lambda_1 X_1^4 \right) + k_2 \left(\frac{1}{2}X_2^2 + \frac{1}{4}\Lambda_2 X_2^4 \right). \quad (3)$$

The forces connected with the external excitation and the damping effects are introduced into model as generalized force

$$Q = F_0 \cos(\Omega t) + C(\dot{X}_1 + \dot{X}_2). \quad (4)$$

Since the springs are connected serially, the equilibrium equation for the weightless connecting point S is as follows

$$k_1 X_1 (1 + \Lambda_1 X_1^2) = k_2 X_2 (1 + \Lambda_2 X_2^2). \quad (5)$$

The equation of motion, derived using the Lagrang'e formalism, and the equation (5) are transferred to the convenient dimensionless form, so the governing equations supplemented with the initial conditions take the following form

$$\ddot{x}_1 + \ddot{x}_2 + c(\dot{x}_1 + \dot{x}_2) + (1 + \lambda)x_2(1 + \alpha_2 x_2^2) = f_0 \cos(p \tau), \quad (6)$$

$$x_1(1 + \alpha_1 x_1^2) = \lambda x_2(1 + \alpha_2 x_2^2), \quad (7)$$

$$x_1(0) + x_2(0) = x_0, \quad \dot{x}_1(0) + \dot{x}_2(0) = v_0, \quad (8)$$

where

$$\lambda = \frac{k_2}{k_1}, \alpha_1 = \Lambda_1 L^2, \alpha_2 = \Lambda_2 L^2, c = \frac{c}{m \omega}, f_0 = \frac{F_0}{L m \omega^2}, p = \frac{\Omega}{\omega}, L = L_{01} + L_{02}.$$

The overdot denotes the differentiation with respect to the dimensionless time $\tau = t \omega$, where $\omega = \sqrt{k_e/m}$ and $k_e = \frac{k_1 k_2}{k_1 + k_2}$ is the effective stiffness of two linear springs connected in series which plays the role of a characteristic coefficient.

Differentiating twice the algebraic equation (7) the following relation between the second derivatives of the unknown functions is obtained

$$\ddot{x}_1(1 + 3\alpha_1 x_1^2) + 6\alpha_1 x_1 \dot{x}_1^2 = \ddot{x}_2 \lambda (1 + 3\alpha_2 x_2^2) + 6\alpha_2 \lambda x_2 \dot{x}_2^2, \quad (9)$$

which allows to eliminate, for example, the function $x_1(\tau)$ from the equation (6).

3. Analytical solution to the problem

The differential-algebraic problem (6) – (8) is solved in the asymptotic way using the Multiple Scale Method (MSM). Since we assume the smallness of some parameters, so we formally introduce the parameters with the tilde over the symbol:

$$\alpha_1 = \varepsilon \tilde{\alpha}_1, \alpha_2 = \varepsilon \tilde{\alpha}_2, c = \varepsilon \tilde{c}, f_0 = \varepsilon \tilde{f}_0, \quad (10)$$

where $0 < \varepsilon \ll 1$ is a so called small parameter.

Each of the solutions are assumed in the form of the sum containing the new unknown functions dependent on two time scales, i.e. we have

$$x_1(\tau; \varepsilon) = \xi_{10}(\tau_0, \tau_1) + \varepsilon \xi_{11}(\tau_0, \tau_1), \quad (11)$$

$$x_2(\tau; \varepsilon) = \xi_{20}(\tau_0, \tau_1) + \varepsilon \xi_{21}(\tau_0, \tau_1), \quad (12)$$

where $\tau_0 = \tau$ is the fast time scale, and $\tau_1 = \varepsilon \tau$ is the slow time scale. The differential operators take the form

$$\frac{d}{d\tau} = \frac{\partial}{\partial \tau_0} + \varepsilon \frac{\partial}{\partial \tau_1}, \quad \frac{d^2}{d\tau^2} = \frac{d}{d\tau} \left(\frac{d}{d\tau} \right) = \frac{\partial^2}{\partial \tau_0^2} + 2\varepsilon \frac{\partial^2}{\partial \tau_0 \partial \tau_1} + o(\varepsilon^2). \quad (13)$$

Substituting expressions (10) – (13) into equations (6) – (7) yields the algebraic-differential system in which the small parameter ε appears in various powers. This leads to the first and the second order approximation equations:

- approximation of the order ε^0

$$(1 + \lambda) \xi_{20} + \frac{\partial^2 \xi_{10}}{\partial \tau_0^2} + \frac{\partial^2 \xi_{20}}{\partial \tau_0^2} = 0, \quad (14)$$

$$\lambda \xi_{20} - \xi_{10} = 0, \quad (15)$$

- approximation of the order ε^1

$$\frac{\partial^2 \xi_{11}}{\partial \tau_0^2} + \frac{\partial^2 \xi_{21}}{\partial \tau_0^2} + (1 + \lambda) \xi_{21} + (1 + \lambda) \tilde{\alpha} \xi_{20}^3 + \tilde{c} \left(\frac{\partial \xi_{10}}{\partial \tau_0} + \frac{\partial \xi_{20}}{\partial \tau_0} \right) + 2 \left(\frac{\partial^2 \xi_{10}}{\partial \tau_0 \partial \tau_1} + \frac{\partial^2 \xi_{20}}{\partial \tau_0 \partial \tau_1} \right) = \tilde{f}_0 \cos(p \tau_0), \quad (16)$$

$$\lambda \tilde{\alpha}_2 \xi_{20}^3 + \lambda \xi_{21} - \tilde{\alpha}_2 \xi_{10}^3 - \xi_{11} = 0. \quad (17)$$

The above set of the differential-algebraic equations is solved in the recursive way, i.e. the solutions to the lower order approximation equations are substituted into the higher order ones.

The solution to the equations (14) – (15) are

$$\xi_{10} = \lambda B(\tau_1) e^{i\tau_0} + \lambda \bar{B}(\tau_1) e^{-i\tau_0}, \quad (18)$$

$$\xi_{20} = B(\tau_1) e^{i\tau_0} + \bar{B}(\tau_1) e^{-i\tau_0}, \quad (19)$$

where $B(\tau_1)$ and its complex conjugate $\bar{B}(\tau_1)$ are the unknown complex functions.

4. Vibration far from resonance

After substituting the solutions (18) – (19) into the equations (16) – (17), the secular terms should be eliminated, which leads to the following solvability conditions

$$2 i \frac{\partial B}{\partial \tau_1} + i B \tilde{c} + \frac{3 B^2 \bar{B} (\lambda^3 \tilde{\alpha}_1 + \tilde{\alpha}_2)}{1 + \lambda} = 0, \quad (20)$$

$$2 i \frac{\partial \bar{B}}{\partial \tau_1} + i \bar{B} \tilde{c} - \frac{3 \bar{B}^2 B (\lambda^3 \tilde{\alpha}_1 + \tilde{\alpha}_2)}{1 + \lambda} = 0. \quad (21)$$

Substituting solutions (18) and (19) into (16) – (17) and taking into consideration the conditions (20) – (21), the following solution to the second order approximation equations is found

$$\xi_{11} = -\frac{e^{i p \tau_0} \lambda \tilde{f}_0}{2(p^2 - 1)(1 + \lambda)} + \frac{e^{3 i \tau_0} \lambda B^3 (\lambda^2 (\lambda - 8) \tilde{\alpha}_1 + 9 \tilde{\alpha}_2)}{8(1 + \lambda)} - 3 e^{i \tau_0} \lambda B^2 \bar{B} (\lambda^2 \tilde{\alpha}_1 - \tilde{\alpha}_2) + CC \quad (22)$$

$$\xi_{21} = -\frac{e^{i p \tau_0} \tilde{f}_0}{2(p^2 - 1)(1 + \lambda)} + \frac{e^{3 i \tau_0} B^3 (9 \lambda^3 \tilde{\alpha}_1 - 8 \tilde{\alpha}_2)}{8(1 + \lambda)} + CC \quad (23)$$

where CC stands for the complex conjugates.

There is convenient to express the complex functions $B(\tau_1)$ and $\bar{B}(\tau_1)$ in the exponential form

$$B(\tau_1) = \frac{1}{2} a(\tau_1) e^{i\psi(\tau_1)}, \quad \bar{B} = \frac{1}{2} a(\tau_1) e^{-i\psi(\tau_1)}, \quad (24)$$

where $a(\tau_1)$ and $\psi(\tau_1)$ are unknown real valued functions and stand for the amplitude and the phase of the oscillations, respectively.

Introducing relationships (24) into the solvability conditions (20) – (21), returning to the original notations according to (10) and using the definition of operator (13)₁ allow us to write the modulation equations in the following form

$$\frac{da(\tau)}{d\tau} = -\frac{1}{2}c a(\tau), \quad (25)$$

$$\frac{d\psi(\tau)}{d\tau} = \frac{3(\alpha_2 + \lambda^3 \alpha_1)a(\tau)^2}{8(1+\lambda)}. \quad (26)$$

Assuming the initial conditions in the form

$$a(0) = a_0, \quad \psi(0) = \psi_0, \quad (27)$$

we obtain the solution to the problem (25) – (27) as follows

$$a(\tau) = a_0 e^{-\frac{c\tau}{2}}, \quad \psi(\tau) = \psi_0 + \frac{3a_0^2(1-e^{-c\tau})(\alpha_2 + \alpha_1\lambda^3)}{8c(1+\lambda)}. \quad (28)$$

The amplitude and phase determined by (28) are then introduced into the solutions (18) – (19), (22) – (23) of the first and second order approximation. Then the relationships (24) are taken into account. Afterwards, using expressions (11) – (12) and returning to the original denotations according to (10), we obtain the approximate solution to the original problem (6) – (8). The absolute dimensionless displacement of the body obtained in this way follows

$$x(\tau) = x_1(\tau) + x_2(\tau) = -\frac{f_0 \cos(p\tau)}{(p^2 - 1)} + (1 + \lambda)a(\tau) \cos(\tau + \psi(\tau)) + \frac{1}{32}a(\tau)^3 \cos(\tau + \psi(\tau)) \left(24\alpha_2\lambda - \alpha_2 - 25\alpha_1\lambda^3 + 2(\alpha_2 + \alpha_1\lambda^3) \cos(2(\tau + \psi(\tau))) \right), \quad (29)$$

where $a(\tau)$ and $\psi(\tau)$ are the solutions (28) to the modulation problem (25) – (27).

The comparison of the time course of the body displacement determined by the solution (29) with the analogic one obtained numerically is presented in Fig.2 and Fig.3 for the transient and the steady state vibration, respectively.

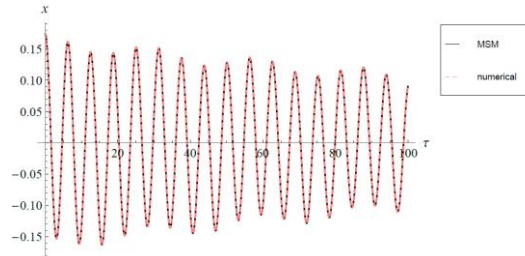


Figure 2. Body displacement in time for the transient non-resonant vibration.

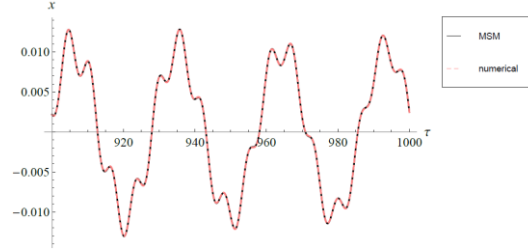


Figure 3. Body displacement in time for the steady-state non-resonant vibration.

The results presented are obtained for the following data: $\alpha_1 = 0.87, \alpha_2 = 1.21, \lambda = 0.63, f_0 = 0.01, p = 0.215, c = 0.009, a_0 = 0.1, \psi_0 = 0$. The compatibility of the two approaches, i.e. MSM and numerical solution, is very high which confirms the correctness of the derived analytical solutions. The relationship between initial conditions (8) and (27) has been determined using the analytical form of the solution (29).

5. Vibration at resonance

Let us analyze the case of the main resonance when $p \approx 1$. In order to investigate the behaviour of the system near resonance, the detuning parameter σ is introduced as follows

$$p = 1 + \sigma. \quad (30)$$

The assumption (30) is inserted into equation (6) and then the procedure similar to that of the previous section is carried out. In result, the modulation equations are obtained of the following form

$$\frac{da(\tau)}{d\tau} = -\frac{1}{2}c a(\tau) + \frac{f_0 \sin(\sigma\tau - \psi)}{2(1+\lambda)}, \quad (31)$$

$$\frac{d\psi(\tau)}{d\tau} = \frac{3(\alpha_2 + \lambda^3 \alpha_1)a(\tau)^2}{8(1+\lambda)} - \frac{f_0 \cos(\sigma\tau - \psi)}{2(1+\lambda)a(\tau)}. \quad (32)$$

Observe that equations (31) – (32), supplemented by initial conditions (27), cannot be solved analytically. The numerical treatment is required in this case. The absolute dimensionless body displacement obtained in the way similar to the one described in the previous section is as follows

$$x(\tau) = x_1(\tau) + x_2(\tau) = (1 + \lambda)a(\tau) \cos(\tau + \psi(\tau)) + \frac{1}{32}a(\tau)^3 \cos(\tau + \psi(\tau)) \left(24\alpha_2\lambda - \alpha_2 - 25\alpha_1\lambda^3 + 2(\alpha_2 + \alpha_1\lambda^3) \cos(2(\tau + \psi(\tau))) \right), \quad (33)$$

where $a(\tau)$ and $\psi(\tau)$ denote the solutions to the modulation equations (31) – (32).

Time history of the body displacement in the case of the main resonance is presented in Figs. 4, 5 for the transient and the steady state. The data assumed for the calculations are as follows: $\alpha_1 = 0.87, \alpha_2 = 1.21, \lambda = 0.63, f_0 = 0.009, \sigma = 0.008, c = 0.008, a_0 = 0.2, \psi_0 = 0$.

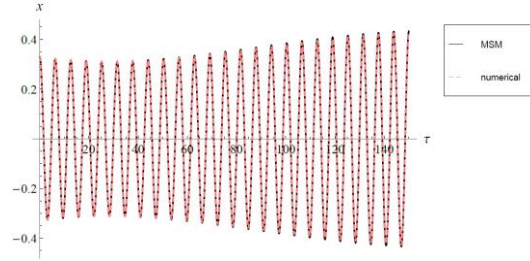


Figure 4. Time courses of the body (transient vibration) obtained analytically and numerically (resonance case).

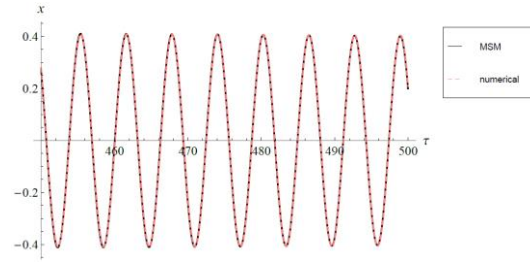


Figure 5. Time course of the body (steady state vibration) obtained analytically and numerically (resonance case).

The obtained results clearly exhibit powerful of the employed approximate analytical method.

5.1. Steady-state resonant responses

When the transient processes disappear, the forced system can reach the steady state oscillations. In order to study this case it is convenient to introduce the modified phase $\theta = \sigma\tau - \psi(\tau)$ into equations (31) – (32) which allows to transform them into the following counterpart autonomous form

$$\frac{da(\tau)}{d\tau} = -\frac{1}{2}c a(\tau) + \frac{f_0 \sin(\theta)}{2(1+\lambda)}, \quad (34)$$

$$\frac{d\theta(\tau)}{d\tau} = \sigma - \frac{3(\alpha_2 + \lambda^3 \alpha_1)a(\tau)^2}{8(1+\lambda)} + \frac{f_0 \cos(\theta)}{2(1+\lambda)a(\tau)}. \quad (35)$$

Fixation of the values of the amplitude and the modified phase is characteristic for the steady state solutions. Consequently, zeroing the derivatives of both the amplitude and the modified phase in

modulation equations (34) - (35) yields the conditions of the steady state in the form of the set of two following equations

$$-\frac{1}{2}c a(\tau) + \frac{f_0 \sin(\theta)}{2(1+\lambda)} = 0, \quad (36)$$

$$\sigma - \frac{3(\alpha_2 + \lambda^3 \alpha_1) a(\tau)^2}{8(1+\lambda)} + \frac{f_0 \cos(\theta)}{2(1+\lambda) a(\tau)} = 0. \quad (37)$$

The resonance curves with regard to the amplitude and the modified phase, obtained through equations (36) – (37) are presented in Figs. 6, 7 for the following fixed parameters: $\alpha_1 = 0.87, \alpha_2 = 1.21, \lambda = 0.63, f_0 = 0.009, c = 0.008$.

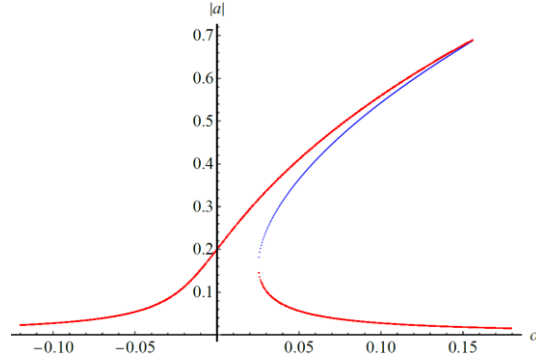


Figure 6. Resonance curve for the amplitude of $x(\tau)$.

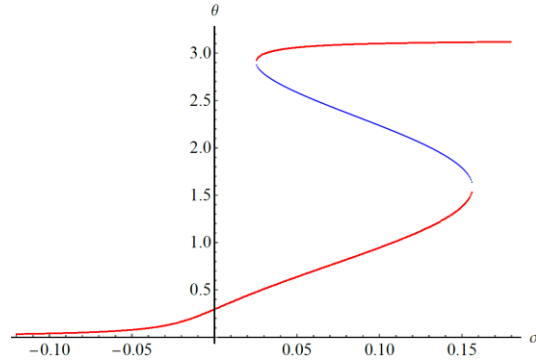


Figure 7. Resonance curve for the modified phase of $x(\tau)$.

In Figures 6 - 7 the stable branches are depicted in red color, whereas unstable ones in blue color.

5.2. Stability of the resonance curves

In order to examine the stability of the steady-state solution in the sense of Lyapunov, we analyze the non-stationary solutions of equations (34) – (35) that are close to the steady state solutions (a_s, θ_s) .

Introducing the functions $\tilde{a}(\tau), \tilde{\theta}(\tau)$ that can be treated as small perturbations, one can assume the following non-stationary solution

$$a(\tau) = a_s + \tilde{a}(\tau), \quad \theta(\tau) = \theta_s + \tilde{\theta}(\tau). \quad (38)$$

Next, substituting expressions (38) into equations (34) – (35), linearizing the obtained equations and noting that (a_s, θ_s) are the steady-state solutions, we get

$$\frac{d\tilde{a}(\tau)}{d\tau} = -\frac{1}{2}c \tilde{a}(\tau) + \frac{f_0 \cos(\theta_s)}{2(1+\lambda)} \tilde{\theta}(\tau), \quad (39)$$

$$\frac{d\tilde{\theta}(\tau)}{d\tau} = -\frac{3a_s(\alpha_2 + \lambda^3 \alpha_1)}{4(1+\lambda)} \tilde{a}(\tau) - \frac{f_0 \cos(\theta_s)}{2(1+\lambda)a_s^2} \tilde{a}(\tau) - \frac{f_0 \sin(\theta_s)}{2(1+\lambda)a_s} \tilde{\theta}(\tau). \quad (40)$$

The characteristic matrix of the homogeneous differential equations (39) – (40) has the form

$$\mathbf{A} = \begin{bmatrix} -\frac{c}{2} & \frac{f_0 \cos(\theta_s)}{2(1+\lambda)} \\ -\frac{3a_s(\alpha_2 + \lambda^3 \alpha_1)}{4(1+\lambda)} - \frac{f_0 \cos(\theta_s)}{2(1+\lambda)a_s^2} & -\frac{f_0 \sin(\theta_s)}{2(1+\lambda)a_s} \end{bmatrix}. \quad (41)$$

If the real parts of all eigenvalues of the matrix \mathbf{A} are negative, then the fixed point (a_s, θ_s) relating to the steady state solution is asymptotically stable in the sense of Lyapunov.

The analytical form of equations (36) – (37) which determine the resonance response functions allows for predict behavior of the system in various conditions. In Figs. 8, 9 there is presented the influence of the external excitation amplitude on the shape of the response curves ($\alpha_1 = 0.87, \alpha_2 = 1.21, \lambda = 0.63, c = 0.008$).

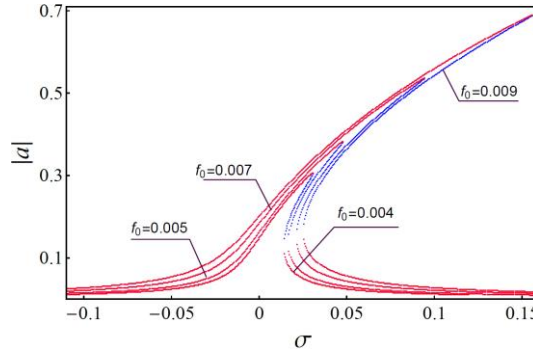


Figure 8. Influence of the external force amplitude on the system response amplitude.

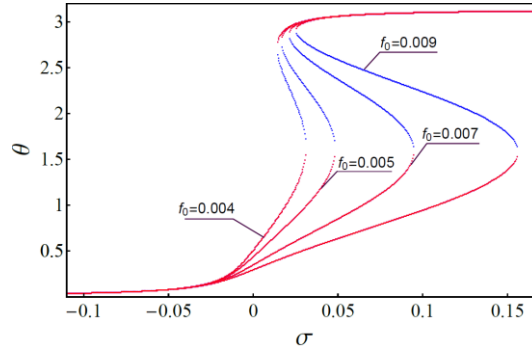


Figure 9. Influence of the external force amplitude on the modified system phase.

6. Conclusions

The dynamics of the lumped system containing two serially connected nonlinear springs has been investigated. The mathematical model consists of the differential and algebraic equations, which requires the appropriate modification of the asymptotic approach in order to deal with the considered mechanical system. The forced vibration in two cases have been analyzed: far from resonance and in the resonance conditions. The approximate analytical solution to the governing equations has been achieved. Its analytical form allows for quantitative and qualitative analysis of the behavior of the system for wide range of the characteristic parameters. The correctness of the results has been confirmed by the numerical calculations.

Acknowledgments

This work was supported by the grant of the Ministry of Science and Higher Education in Poland, 02/21/DSPB/3544 and 02/21/SBAD/3558.

References

- [1] Telli, S., Kopmaz, O., Free vibrations of a mass grounded by linear and nonlinear springs in series, *J.Sound.Vib.* 289 (2006), 689–710.
- [2] Starosta, R., Awrejcewicz, J., Sypniewska-Kamińska, G., Quantifying non-linear dynamics of mass-springs in series oscillators via asymptotic approach, *Mech.Syst.Signal.Pr.* 89 (2017), 149–158

Roman Starosta, Ph. D: Poznań University of Technology, Institute of Applied Mechanics, ul. Piotrowo 3, 60-965 Poznań, Poland (roman.starosta@put.poznan.pl). The author gave a presentation of this paper during one of the conference sessions.

Jan Awrejcewicz, Professor: Technical University of Łódź, Department of Automatics and Biomechanics, ul. Stefanowskiego 90-924, Łódź, Poland (awrejcew@p.lodz.pl).

Grażyna Sypniewska-Kamińska, Ph. D: Poznań University of Technology, Institute of Applied Mechanics, ul. Piotrowo 3, 60-965 Poznań, Poland, (grazyna.sypniewska-kaminska@put.poznan.pl).

Nonlinear dynamics of thermoelastic Sheremetiev-Pelekh nanobeams with topologically optimal microstructure

Jan Awrejcewicz, Maxim V. Zhigalov, Sergey P. Pavlov, Vadim A. Krysko

Abstract. Non-uniform structural elements with complex microstructure or varying material properties, such as rods, beams, plates and shells, are widely used in micro-electro-mechanical (MEMS) and nano-electro-mechanical systems (NEMS). Topological optimization of mechanical structures is becoming a common tool in the design of structures with improved physical characteristics. In the present work, at the first stage, for specific loading conditions, heating conditions and fastening of the mechanical structure, one of the dimensions of which is much larger than the other two, a topological optimization of its microstructure by the criterion of maximum stiffness is carried out. In each of these cases, the optimal microstructure is original. The obtained microstructure (values of the elastic modulus, density, etc.) are used at the second stage in the study of nonlinear dynamics. At the second stage, a mathematical model of the nano beam is constructed on the basis of the Sheremet'ev-Pelekh-Reddy kinematic hypothesis, taking into account the size-dependent behavior on the basis of the modified couple stress theory and geometric nonlinearity of von Kármán. On the basis of the constructed mathematical model, the static and dynamic behavior of inhomogeneous (optimal) and homogeneous beams is studied. The paper compares the static and dynamic results for optimal and homogeneous beams, taking into account the size-dependent behavior, and without it, for different boundary conditions, temperature distribution and types of the applied load. It is shown that for a homogeneous beam and a beam with an optimal microstructure, the stress-strain state, the magnitude of the natural frequencies and the nature of the dynamic regimes differ significantly, both for linear and nonlinear cases.

1. Introduction

Structurally inhomogeneous materials (NM) are composites with properties varying in any desired direction. This allows the new material to have better strength characteristics without causing unwanted stress concentration. Due to these features, NM beams are widely used in various engineering structures such as gas turbines, wind turbines, helicopter rotor blades, ship propellers, space and marine structures. Recently, the creation of beam elements from NM mainly by the methods of topological optimization.

Topological optimization of composite structures is becoming a common tool in the design of metamaterials with improved physical characteristics. To average the complex microstructural behavior of an elastic medium, the method of asymptotic homogenization [1, 2], created in the 80

years of the last century, is mainly used. Recently, however, the most widely used methods for topological optimization of structures are explicit parameterization methods, which are known as density-based methods. These methods work on a region broken down into finite elements. Instead of a set of elastic properties of a microstructure, each finite element contains only one design variable. This variable is often understood as the density of the element material. The basic idea is to define the element parameters as design variables, and to calculate the parameters in the optimization problem. A relationship is established between local parameters (for example, density) and global physical properties of the material (for example, Young's modules or thermal conductivity coefficients).

In general, the following methods are employed while designing of microstructure objects: solid isotropic material with penalization (SIMP) [3], evolutionary structural optimization (ESO) [4], level set method [5], and the rational approximation of material properties (RAMP) [6]. By means of various algorithms of search of an optimum, for example, such as a method of optimum criterion (OC) [7], a method of mobile asymptotes (MMA) [8], materials in the field of optimization are redistributed so that desirable functional characteristics of a material are reached. Elastic, thermal or thermoelastic criteria are taken into account in the design of the NM. The elasticity criteria take into account only the mechanical load [1], the thermal criteria take into account the thermal load [9], whereas the thermoelastic criteria cover both mechanical and thermal loads [10].

As mentioned above, the construction of KM are widely used in various industries. One of the directions is the creation of elements of nanoelectromechanical systems (NEMS). Nanosensors (cantilevers, nanoequilibrium, resonators, etc.) and nanoactuators (nanomotors, gears, etc.) are used in physics, biology, chemistry, medicine (diagnostics, cellular nano - and microsurgery, drug delivery to the affected area of the body) and many other areas. The dependences of elastic behavior on size can be explained using molecular dynamics (MD) modeling or higher order continuum mechanics. While the molecular dynamics approach can provide more accurate approximations to real objects, it is too computationally expensive. Therefore, the higher-order continuum mechanics approach has been widely used in modeling small-scale structures. In general, these theories can be divided into three different classes, namely: the family of deformation gradient theories, micro continuum theory, and nonlocal elasticity theories. One of the most popular theories is the modified couple stress theory, proposed by Young et al. [11] are based on the change in the theory of moments. One of the most important aspects of the use of the couple stress theory of elasticity is its application to the problems of statics and dynamics of beams. This is due to the fact that the beams are the main element of nanodetectors, nanowires and switches. The hypotheses of Bernoulli-Euler, Timoshenko, Sheremetiev-Pelekh-Reddy are used to construct mathematical models of beams.

The analysis of the literature shows that the studies of dimension-dependent beams on the Bernoulli-Euler, Timoshenko, Sheremetiev-Pelekh-Reddy models are carried out mainly based on the

Duffing-type equations, which are obtained by applying the Bubnov-Galerkin method in the first approximation to the original partial differential equations. Linear problems on determination of natural frequencies and static problems on research of influence of size-dependent parameters are considered. Studies of nonlinear chaotic dynamics, especially for inhomogeneous beams of the Sheremetiev-Pelekh-Reddy model have not been carried out.

It is shown that for a homogeneous beam and a beam with an optimal microstructure, the stress-strain state and eigenfrequencies differ significantly for both linear and nonlinear cases.

2. Mathematical background

Consider a two-dimensional elastic region $\Omega = \left\{ x \in [0, a]; -\frac{h}{2} \leq z \leq \frac{h}{2} \right\}$, bounded by a closed surface $\Gamma = \Gamma_1 \cup \Gamma_2 \cup \Gamma_3$, which is under a plane stress state (Fig. 1). On the Γ_1 there are given boundary conditions of different types, whereas Γ_2 is not fixed and not loaded. At the border Γ_3 there is a vertical load F , directed downwards. It is assumed that the material is linearly elastic and isotropic.

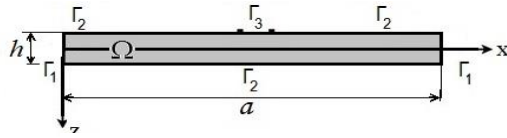


Fig.1. Computational model.

The area is under a constant temperature field $T(\mathbf{x}), \mathbf{x} = \{x, z\}$. We denote by $\theta = T(\mathbf{x}) - T_0$ the change in temperature relative to the initial temperature T_0 .

For the displacement field (u_1, u_3) , the equilibrium equation has the following form

$$\sigma_{ij,j} = 0 \text{ in } \Omega, \quad (1)$$

where σ_{ij} is the stress tensor. The relationship between linear deformations and displacements is determined by the following relations

$$\varepsilon_{ij} = \frac{1}{2} (u_{i,j} + u_{j,i}), i, j = 1, 2. \quad (2)$$

The stress-strain relation satisfies the Duhamel-Neumann law

$$\sigma_{ij} = E(\mathbf{x})(\varepsilon_{ij} - \alpha \theta \delta_{ij}), \quad (3)$$

where $E(\mathbf{x}), \alpha(\mathbf{x}), \theta(\mathbf{x})$ and δ_{ij} denote the Young's modulus of elasticity and thermal expansion coefficient of the inhomogeneous material of region Ω the difference between the current and the initial temperature field and the Kronecker symbol, respectively. The displacement and temperature fields are coupled via equation (3).

The purpose of topological optimization is to find the optimal material distribution that maximizes the stiffness or minimizes the flexibility of the thermoelastic body. The problem of topological optimization in its counterpart thermoelastic formulation obeys the following formal description [12]:

$$\min_{0 \leq r(x) \leq 1} C = \iint_{\Omega} \beta \theta u_{i,i} d\Omega + \int_{\Gamma} F u_3 d\Gamma, \quad (4)$$

and is subjected to the following constraint

$$\int_{\Omega} \rho(x) d\Omega \leq A(\Omega) \gamma, \quad (5)$$

where: $\beta(\mathbf{x}) = \alpha(\mathbf{x}) E(\mathbf{x})$; $\rho(\mathbf{x})$ – beam material density, γ – coefficient associated with the basic material of the beam.

The projection variable $r(\mathbf{x})$ is coupled with Young's moduli $E(\mathbf{x})$, with $\beta(\mathbf{x})$, and with the volume material density $\rho(\mathbf{x})$ of each element, following the scheme for minimum compliance topology optimization (the so-called ramp scheme) [6]:

$$E(\mathbf{x}) = \frac{E_0 r(\mathbf{x})}{(1 + p \cdot (1 - r(\mathbf{x})))}, \quad \beta(\mathbf{x}) = \frac{\alpha_0 E_0 r(\mathbf{x})}{(1 + q \cdot (1 - r(\mathbf{x})))}, \quad \rho(x) = \frac{\rho_0 r(\mathbf{x})}{(1 + p \cdot (1 - r(\mathbf{x})))}, \quad \mathbf{x} \in \Omega, \quad (6)$$

where: p, q - penalty parameters used to guarantee the compact material distribution; $r(\mathbf{x})$ – field of the projection variables $0 < r_0 \leq r(\mathbf{x}) \leq 1$; r_0 – small number guaranteeing non-zero stiffness of the finite elements. Observe that for $r(\mathbf{x})=1$ the whole space is filled with the reinforced basic material. After applying the topological optimization procedure, the values of the elastic modulus $E(\mathbf{x})$, coefficient $\beta(\mathbf{x})$ and bulk density of the material for the optimal topology of the microstructure $\rho(\mathbf{x})$ are determined. The obtained values $E(\mathbf{x})$, $\beta(\mathbf{x})$ и $\rho(\mathbf{x})$ were further used in the construction of a mathematical model of a inheterogeneous nano-beam of Sheremetiev-Pelekh-Reddy.

A mathematical model nano-beam Sheremetiev-Pelekh-Reddy to homogenous beams have been firstly proposed in the work [13]. We give below the equations for the inhomogeneous beam:

$$\begin{aligned}
& k_1 \left(\frac{\partial^2 u}{\partial x^2} + \frac{\partial w}{\partial x} \frac{\partial^2 w}{\partial x^2} \right) + \frac{\partial k_1}{\partial x} \left(\frac{\partial u}{\partial x} + \frac{1}{2} \left(\frac{\partial w}{\partial x} \right)^2 \right) = b_1 \frac{\partial^2 u}{\partial t^2} \\
& k_2 \frac{\partial^2 \psi}{\partial x^2} - k_3 \frac{\partial^3 w}{\partial x^3} - k_5 \left(\psi + \frac{\partial w}{\partial x} \right) + \frac{\partial k_2}{\partial x} \frac{\partial \psi}{\partial x} - \frac{\partial k_3}{\partial x} \frac{\partial^2 w}{\partial x^2} = b_3 \frac{\partial^2 \psi}{\partial t^2} \\
& k_1 \left(\frac{\partial^2 u}{\partial x^2} \frac{\partial w}{\partial x} + \frac{\partial u}{\partial x} \frac{\partial^2 w}{\partial x^2} + \frac{3}{2} \left(\frac{\partial w}{\partial x} \right)^2 \frac{\partial^2 w}{\partial x^2} \right) + k_3 \frac{\partial^3 \psi}{\partial x^3} - k_4 \frac{\partial^4 w}{\partial x^4} + k_5 \left(\frac{\partial \psi}{\partial x} + \frac{\partial^2 w}{\partial x^2} \right) + \\
& + \frac{\partial k_1}{\partial x} \left[\frac{\partial u}{\partial x} \frac{\partial w}{\partial x} + \frac{1}{2} \left(\frac{\partial w}{\partial x} \right)^2 \frac{\partial w}{\partial x} \right] + 2 \frac{\partial k_3}{\partial x} \frac{\partial^2 \psi}{\partial x^2} - 2 \frac{\partial k_4}{\partial x} \frac{\partial^3 w}{\partial x^3} + \frac{\partial k_5}{\partial x} \left(\psi + \frac{\partial w}{\partial x} \right) + \frac{\partial^2 k_3}{\partial x^2} \frac{\partial \psi}{\partial x} - \\
& - \frac{\partial^2 k_4}{\partial x^2} \frac{\partial^2 w}{\partial x^2} + q(x, t) = b_1 \frac{\partial^2 w}{\partial t^2}.
\end{aligned} \tag{7}$$

where: $k_1(x) = \int_A (\lambda + 2\mu) dA$; $k_2(x) = \int_A (\lambda + 2\mu) \left(z^2 - \frac{z^4}{3h^2} + \frac{z^6}{9h^4} \right) + \frac{1}{4} \mu l^2 \left(1 + \frac{z^2}{h^2} \right)^2 dA$;

$k_3(x) = \int_A (\lambda + 2\mu) \left(\frac{z^4}{3h^2} - \frac{z^6}{9h^4} \right) + \frac{1}{4} \mu l^2 \left(1 - \frac{z^4}{h^4} \right) dA$; $k_4(x) = \int_A (\lambda + 2\mu) \frac{z^6}{9h^4} + \frac{1}{4} \mu l^2 \left(1 - \frac{z^4}{h^4} \right)^2 dA$;

$k_5(x) = \int_A \mu \left(1 - \frac{z^2}{h^2} \right)^2 + \mu l^2 \frac{z^2}{h^4} dA$; $b_1 = \rho A$; $b_3 = \frac{68}{315} A h^2$.

Boundary conditions of different types are reported in [13]. In this paper we will consider the boundary condition of the form:

$$\begin{aligned}
& w(0, t) = w(a, t) = 0; \partial w(0, t) / \partial x = \partial w(a, t) / \partial x = 0; \\
& u(0, t) = u(a, t) = 0; \psi(0, t) = \psi(a, t) = 0.
\end{aligned} \tag{8}$$

and the following initial conditions are taken

$$w(x, 0) = \partial w(x, 0) / \partial t = 0; u(x, 0) = \partial u(x, 0) / \partial t = 0; \psi(x, 0) = \partial \psi(x, 0) / \partial t. \tag{9}$$

3. Results and discussions

Based on the solution of the optimization problem, the distribution of the elastic modulus and density along the length of the beam was obtained. The obtained values of physical quantities were used for the study of static and dynamic problems of the nonlinear beam of the Sheremetiev-Pelekh-Reddy model. Numerical study of static and dynamic problems, the results of which are described below, was carried out for dimensionless equations [13] and the following parameters: relative length $\gamma_1 = a/h = 40$, size-dependent parameter $\gamma_2 = l/h = 0; 0.3$.

3.1. Methods of solution

To reduce the partial differential equation (2) to the system of ordinary differential equations we have employed the Cauchy problem, and the method of finite differences in spatial variables with


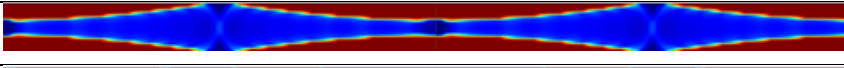
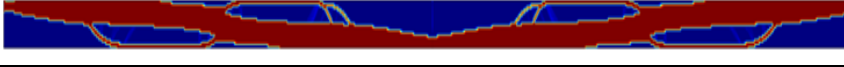
approximation $O(h^2)$. The Cauchy problem was solved by the Runge-Kutta method of the 4th order and selection of the optimal step in the numerical method was carried out using the Runge principle.

3.2. Obtaining the optimal topology

In this paper, two types of problems with boundary conditions (8) and two types of load were considered. In what follows we consider both problems separately.

Case study 1. A beam with boundary conditions (8) and loaded with a force distributed over the entire length of the beam

Table 1 Microstructures of optimal beams.

$\theta = -100$	
$\theta = 0$	
$\theta = 100$	

Case study 2. Beam with boundary conditions (8) and loaded with force concentrated in the center of the beam

Table 2 Microstructures of optimal beams.

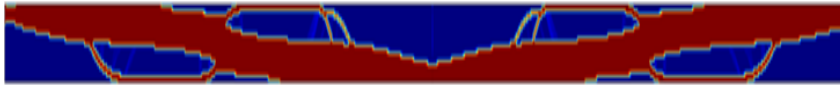
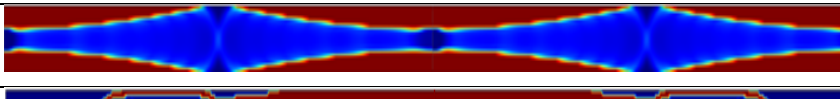

$\theta = -100$	
$\theta = 0$	
$\theta = 100$	

Table 1, 2 shows the optimal material distribution topology for beams exposed to different temperatures θ . Here, the red color is associated with the reinforcing base material, whereas the blue color is the matrix, which has a low stiffness.

3.3. The study of nonlinear dynamics with maps of the characters of the oscillations

Map comparison for case study 1, temperature = + 100

Table 3. Comparison of oscillation mode maps

	$\gamma_2 = 0$	$\gamma_2 = 0.3$
optimal		
homogeneous		

The area of zones of harmonic vibrations on maps of modes of vibrations both for homogeneous (suboptimal beam) and for optimal beam taking into account the size-dependent behavior ($\gamma_2 = 0.3$) is larger, and the area of zones of chaotic and other zones of vibrations is larger on maps of modes of oscillations at ($\gamma_2 = 0$). In addition, for optimal beams, both taking into account the size dependent behavior ($\gamma_2 = 0.3$), and when ($\gamma_2 = 0$) the harmonic vibrations zone is significantly less than for a non-optimal beam. Common to all cards is the presence of vibrations at an independent frequency (marked in green) in the frequency range from 7.5 to 8.5 over the entire load interval. It should also be noted the shift of bifurcation zones (marked in yellow) from areas of small loads ($q < 3 \cdot 10^4$) for non-optimal beams, both taking into account the size-dependent behavior ($\gamma_2 = 0.3$), and at ($\gamma_2 = 0$), to areas of large loads ($q > 3 \cdot 10^4$) for optimal beams. On maps of suboptimal beams, both taking into account the size-dependent behavior ($\gamma_2 = 0.3$), and at ($\gamma_2 = 0$), there is a much smaller number of harmonic vibration zones (marked in blue) than for maps of optimal beams.

Map comparison for case study 2, temperature = + 100

Table 4. Comparison of various charts of the vibration regimes

	$\gamma_2 = 0$	$\gamma_2 = 0.3$
optimal		
homogeneous		

The area of zones of harmonic vibrations on the maps of the modes of vibrations for both homogeneous (non-optimal beams) and for the optimum beam taking into account the size dependent behavior ($\gamma_2 = 0.3$) more, and square zones of chaotic areas and other fluctuations more maps modes of vibrations ($\gamma_2 = 0$). In addition, for optimal beams, both taking into account the size dependent behavior ($\gamma_2 = 0.3$), and when ($\gamma_2 = 0$) the harmonic vibrations zone is significantly less than for a non-optimal beam.

Common to all cards is the presence of oscillations at an independent frequency (green color) in the frequency range from 7.5 to 8.5 over the entire load interval. It should also be noted that the largest bifurcation (yellow color) zones are distributed for non-optimal beams, both taking into account the size-dependent behavior ($\gamma_2 = 0.3$), and at ($\gamma_2 = 0$) frequencies from 4 to 7. For optimal beams, bifurcation zones are located over the entire load interval for certain frequency values, and the main part is located for loads from $3 \cdot 10^4$. On maps of suboptimal beams, both taking into account the size-dependent behavior ($\gamma_2 = 0.3$), and at ($\gamma_2 = 0$), there is a much smaller number of harmonic oscillation zones (blue color) than for maps of optimal beams.

4. Concluding remarks

The paper presents a mathematical model for obtaining the optimal topology of beams under given loads and fastening conditions. Algorithms and programs allowing to receive optimum distribution of a material of a beam on criterion of a minimum of elasticity are developed. As a result of static and dynamic studies, the influence of the optimal structure of the beam on the change of deflection, natural frequencies and dynamic characteristics is shown. The analysis of the results showed that the frequency-deflection dependence $\omega(w)$ for all cases of the temperature field ($\theta = \pm 100, 0$) demonstrate a qualitative and quantitative difference between the results of static and dynamic problems for optimal and homogeneous beams. At the same time, for the optimal beam deflection w , for the same load, is less than for a homogeneous (non-optimal) beam, both taking into account and without taking into account the size-dependent behavior. In this case, in the problems taking into account the temperature field for large deflections (large loads), there is a convergence of results between beams with optimal microstructure and non-optimal (homogeneous) problems.

Taking into account the topological optimal material allows for more than 10% increase in the bearing capacity of the beam.

Comparative analysis of the maps of the modes of vibrations showed that the area of the zones of harmonic maps for homogeneous (non-optimal beams) and for the optimum beam taking into account the size-dependent behavior ($\gamma_2 = 0.3$) more, and square zones of chaotic areas and other fluctuations more maps modes of oscillations ($\gamma_2 = 0$).

In addition, for optimal beams both with ($\gamma_2 = 0.3$) and without dimension dependent behavior ($\gamma_2 = 0$), the harmonic oscillation zones are significantly smaller than for a non-optimal beam.

Note the common location of bifurcation zones for optimal and suboptimal zones regardless of the load and the type of boundary condition.

Acknowledgements

This work has been supported by the grant RSF № 16-11-10138-II

References

- [1] Bendsøe, M., Kikuchi, N. Generating optimal topologies in optimal design using a homogenization method. *Computational Methods in Applied Mechanics and Engineering* 71 (1988) 197–224.
- [2] Sanchez-Palencia, E. Non-homogeneous media and vibration theory. Springer Verlag, Berlin, 1980.

- [3] Bendsøe, M. Optimal shape design as a material distribution problem. *Structural Optimization* 1 (1989) 193–202.
- [4] Xie, Y., Steven, G. A simple evolutionary procedure for structural optimization. *Computers and Structures* 49 (1993) 885–896.
- [5] Sethian, J., Wiegmann, A. Structural boundary design via level set and immersed interface methods. *Journal of Computational Physics* 163(2) (2000) 489–528.
- [6] Barroqueiro, B., Andrade-Campos, A., Valente, R.A.F. Designing self supported SLM structures via topology optimization. *Journal of Manufacturing and Materials Processing* 3(3) (2019) 68.
- [7] Zhou, M., Rozvany, G. Dcoc: an optimality criteria method for large systems, part i: theory. *Structural Optimization* 5 (1993) 12–25.
- [8] Svanberg, K. The method of moving asymptotes – a new method for structural optimization. *International Journal for Numerical Methods in Engineering* 24 (1987) 359–373.
- [9] Jonsmann, J., Sigmund, O., Bouwstra, S. Compliant thermal microactuators. *Sensors and Actuators* 76 (1999) 463–469.
- [10] Li, Q., Steven, G., Xie, Y. Thermoelastic topology optimization for problems with varying temperature fields. *Journal of Thermal Stresses* 24 (2001) 347–366.
- [11] Yang, F, Chong, A.C.M., Lam, D.C.C., Tong, P. Couple stress based strain gradient theory for elasticity. *International Journal of Solids and Structures* 39 (2002) 2731–43.
- [12] Deaton, J.D., Grandhi, R.V. Stress-based Topology Optimization of Thermal Structures. *10th World Congress on Structural and Multidisciplinary Optimization*, May 19 -24, 2013, Orlando, Florida, USA.
- [13] Krysko, A.V., Awrejcewicz, J., Zhigalov, M.V., Pavlov, S.P., Krysko, V.A. Nonlinear behaviour of different flexible size-dependent beams models based on the modified couple stress theory. Part 1. Governing equations and static analysis of flexible beams. *International Journal of Non-Linear Mechanics* 93 (2017) 96–105.

Jan Awrejcewicz: Department of Automation, Biomechanics and Mechatronics, Lodz University of Technology, 1/15 Stefanowski St., 90-924 Lodz and Department of Vehicles, Warsaw University of Technology, 84 Narbutta Str., 02-524 Warsaw, POLAND; (awrejcew@p.lodz.pl). The author gave a presentation of this paper during one of the conference sessions

Sergey P. Pavlov: Department of Mathematics and Modeling, Saratov State Technical University, Politehnikhskaya 77, 410054, Saratov, Russian Federation, (pspsar@yandex.ru).

Maxim V. Zhigalov: Department of Mathematics and Modeling, Saratov State Technical University, Politehnikhskaya 77, 410054, Saratov, Russian Federation, (max.zhigalov@gmail.com).

Vadim A. Krysko: Department of Mathematics and Modeling, Saratov State Technical University, Politehnikhskaya 77, 410054, Saratov, Russian Federation, (tak@san.ru)

Gravity waves in channels with corrugated bottom: asymptotic approaches

Włodzimierz Bielski, Ryszard Wojnar

Abstract: We consider a propagation of long one-dimensional gravity waves of a homogeneous incompressible fluid in a rectangular channel with corrugated (wavy) bottom, while we assume a micro-periodic corrugation. The term "asymptotic" is used in two meanings: firstly, in a linear problem for an asymptotic transition to find the equivalent channel depth h^{eff} , and secondly to derive the nonlinear gravity wave equation from Euler's equations.

1. Introduction

A gravity wave arises when fluid is displaced from a position of equilibrium. In fluid dynamics, gravity waves are generated in a fluid medium or at the interface between two media when the force of gravity or buoyancy tries to restore equilibrium, [1]. This type of waves include huge floating elevations of the sea water level (ocean tides) which, with regularity dictated by the lunar rotation, roll over the surface of the water and sometimes even fall into river beds and run against their currents. Also gravity waves are a mechanism that produce the transfer of momentum from the troposphere to the stratosphere and mesosphere, [2].

1.1. Flow in the channel with uneven bottom

The important problem is a fluid flow upon an uneven bottom. It concerns propagation of gravity waves in a canal with uneven bottom, and relates to the problem of flows in beds of rivers (canals, pipes, lakes) with obstacles at the bottom (such as stones, plants or other structures), which are not susceptible to outer influences, cf. [3, 4].

The older book by M. W. Dingemans and the recent book by I. Popescu are providing a review of techniques available for the problems of wave propagation in regions with uneven beds as they are encountered in coastal areas, [5, 6].

The problem of the linear description of gravity waves in a shallow channel dates back to Lagrange's work from 1781, [7].

When it comes to the description of gravity waves in a shallow channel, when the influence of a nonlinear term should be included in the Euler equation, the issue goes back to the Russell report of 1841, [8, 9]. A long period of efforts of scholars such as Rayleigh, Boussinesq, McCowan was crowned with the famous paper by Korteweg and de Vries [10]. Since then, a plethora of works have appeared on solitary waves in shallow channels, [11, 12, 13].

1.2. Plan of the paper

In this paper we are dealing with *long* gravity waves travelling in channels with corrugated (wavy) bottom.

The article consists of two parts. In the first part (Sections 2 and 3) we treat a linear description of gravity wave reaching back to Lagrange's work on the gravity waves, [7], and by the method of asymptotic homogenization we find the effective channel depth h^{eff} , and hence the gravity wave velocity $\sqrt{gh^{\text{eff}}}$. In the second part (Section 4) we give the asymptotic derivation of KdV equation for a rectangular channel with a wavy bottom, [10].

2. Long gravity waves in an infinite channel

Let us examine first the propagation of long waves in a rectangular channel with corrugated (wavy) bottom. The channel is supposed to of the constant width b , and of infinite length along the x_1 - axis,. The depth h of the fluid in the channel is supposed to be small in comparison with the length L of the considered fluid wave, $h \ll L$, see Fig.1.

The waviness of the bottom is described by the periodic function $\beta = \beta(x_1)$. The mean value of β , is $\langle \beta(x_1) \rangle = 0$, and the mean depth of the fluid in channel in equilibrium is h_0 .

The function $\beta = \beta(x_1)$ and the function $\eta = \eta(x_1, t)$ describing the profile of the considered gravity wave (it is the elevation of the wave surface above the equilibrium free surface level) are small in comparison with the fluid depth, $\beta \ll h_0$ and $\eta \ll h_0$. The cross-section area of the liquid in the channel is given by $S(x_1, t) = b \cdot h(x_1, t)$. We shall here consider longitudinal waves, in which the liquid moves along the channel. In such waves the velocity component $v_1 \equiv u$ along the channel is large compared with the components $v_2 \equiv v$.

We omit small terms, and we omit terms quadratic in the velocity, since the amplitude of the wave is supposed small. The x_1 and x_2 - components of Euler's equation can be written in the form

$$\rho \frac{\partial u}{\partial t} = - \frac{\partial p}{\partial x_1} \quad \text{and} \quad \frac{\partial p}{\partial x_2} = -\rho g.$$

From the latter equation we have $p = p_{\text{At}} + \rho \cdot g \cdot (y_{\text{A}} - x_2)$, since the pressure at the free surface ($x_2 = y_{\text{A}} = h_0 + \eta$) must be equal to the atmospheric pressure p_{At} . We distinguish here and elsewhere by the the suffix (\cdot_{A}) those quantities which refer to the free surface.

Substituting the last expression in the first Euler's equation, we obtain

$$\frac{\partial u}{\partial t} = -g \frac{\partial y_{\text{A}}}{\partial x_1}.$$

Finally, we have

$$\frac{\partial u}{\partial t} = -g \frac{\partial \eta}{\partial x_1} \tag{1}$$

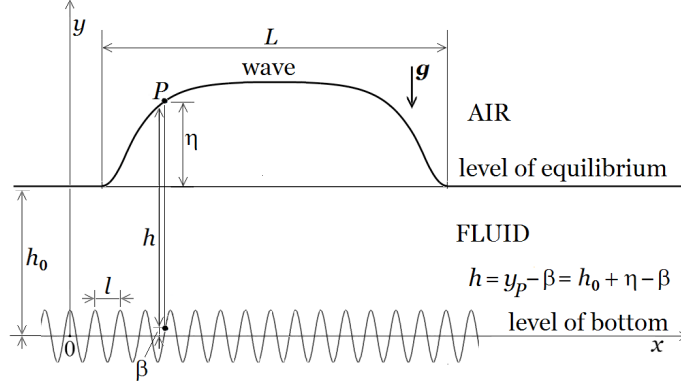


Figure 1. One-dimensional gravity wave moving past the channel with uneven sinusoidal bottom resulting in variations of the fluid depth $h = h(x)$. In the phenomenon described in this paper $h \ll L$ and $\beta \ll h$. Also $l \ll L$. The free surface of the fluid is described by the equation $y = y(x)$. The height of the point P at the free surface above the bottom is $h = y_P - \beta$

The second equation needed to eliminate one of the two unknowns u and η is essentially the equation of continuity for the case in question. The real depth of the fluid is, cf. Fig.1,

$$h = h(x_1, t) \equiv y_A(x, t) - \beta(x_1) \equiv h_0 + \eta(x_1, t) - \beta(x_1) \quad (2)$$

We consider a volume of liquid bounded by two plane cross-sections of the channel at a distance dx_1 apart. The change per unit time in the volume of liquid between the two planes considered is $(\partial S / \partial t) dx_1$. We can therefore write

$$\frac{\partial S}{\partial t} + \frac{\partial(Su)}{\partial x_1} = 0 \quad (3)$$

This is the required global *equation of continuity*.

Let S_0 be the mean equilibrium cross-sectional area of the liquid in the channel. Then

$$S = S_0 + S' + S'' \quad (4)$$

where S_0 is the channel cross-section in equilibrium $S_0 = b h_0$, where b is the width of the channel, S' is the change in the cross-sectional area caused by the fluid wave $S' = b \eta(x_1, t)$ and S'' is the change in the cross-sectional area caused by the uneven bottom $S'' = -b \beta(x_1)$. The continuity equation becomes

$$\frac{\partial \eta}{\partial t} + \frac{\partial \{(h_0 + \eta - \beta) u\}}{\partial x_1} = 0 \quad (5)$$

Differentiating the latter equation with respect to t and substituting $\partial u/\partial t$ from Eq.(1) we obtain

$$\frac{\partial^2 \eta}{\partial t^2} + \frac{\partial}{\partial x_1} \left\{ \frac{\partial \eta}{\partial t} u - g (h_0 + \eta - \beta) \frac{\partial \eta}{\partial x_1} \right\} = 0$$

This is a nonlinear equation. We linearize it by assumption that η and β are small in comparison with the mean depth of the channel h_0 receiving

$$\frac{\partial^2 \eta}{\partial t^2} - gh_0 \frac{\partial^2 \eta}{\partial x_1^2} = 0 \quad (6)$$

This is a *wave equation*; the velocity of propagation of long gravity waves in channels is

$$c = \sqrt{gh_0} \quad (7)$$

In sequel we arrive at similar relations by another ways, cf. Eq.(2) and Eq. (36).

3. Homogenising equations in linear approximation

The method of asymptotic expansions is also known as the homogenisation method. This method described, for example in the book by E. Sanchez-Palencia [14] was recently developed by Igor Andrianov and Jan Awrejcewicz, [15].

3.1. General principles for one-dimensional gravity waves

Notice, in this section we write simply x instead of x_1 .

We consider long gravity waves in the channel with a wavy bottom. The amplitude and period of these wavy variations are small, and we call it the micro-waviness. Let $\mathcal{L} \subset \mathbb{R}^1$ be a section of x -axis. We introduce a parameter $\varepsilon = l/\mathcal{L}$, where l is a typical length scale of the waviness spacing.

The one dimensional domain \mathcal{L} is assumed to have an εY - periodic structure. The set \mathcal{L} is covered by a regular mesh of size ε , each one-dimensional cell being a segment Y . Accordingly to two-scale asymptotic approach, instead of one space variable x , we introduce two variables, macroscopic x and microscopic y , where $y = x/\varepsilon$, and instead of a function $f(x)$ consider the function $f(x, y)$. Taking into account the formula for the total derivative (known as the chain rule) we have

$$\frac{\partial f(x, y)}{\partial x} \rightsquigarrow \frac{\partial f(x, y)}{\partial x} + \frac{1}{\varepsilon} \frac{\partial f(x, y)}{\partial y} \quad \text{with} \quad y = \frac{x}{\varepsilon}$$

where the superscript ε denotes the micro-periodicity of the relevant quantities.

We study one-dimensional gravity wave propagation in a channel, whose bottom exhibits a periodic micro-waviness, and the fluid cross-section S_0 is of the form $S_0^\varepsilon = S_0(y, t)$, or what is equivalent for the rectangular cross-section

$$h\left(\frac{x}{\varepsilon}, t\right) = h^\varepsilon(y, t) \quad (8)$$

The small parameter ε characterizes the micro-structure of the bottom. Hence, the coefficients and the fields are functions of the ε , what is indicated by the superscript ε .

According to the method of two-scale asymptotic expansions we write

$$\eta^\varepsilon = \eta^{(0)}(x, y) + \varepsilon^1 \eta^{(1)}(x, y) + \varepsilon^2 \eta^{(2)}(x, y) + \dots \quad (9)$$

where functions $\eta^{(i)}(x, y)$, $i = 0, 1, 2, \dots$ are assumed to be Y - periodic. For shortness we omit the argument t in the terms of this expansion. In full description we should write obviously $\eta^{(i)} = \eta^{(i)}(x, y, t)$.

Now, we perform asymptotic homogenisation of the problem.

Our equation of motion reads

$$\frac{\partial^2 \eta^\varepsilon}{\partial t^2} - g \frac{\partial}{\partial x} \left(h_0^\varepsilon \frac{\partial \eta^\varepsilon}{\partial x} \right) = 0 \quad (10)$$

or

$$\begin{aligned} \frac{\partial^2}{\partial t^2} \left(\eta^{(0)}(x, y) + \varepsilon^1 \eta^{(1)}(x, y) + \varepsilon^2 \eta^{(2)}(x, y) + \dots \right) &= g \left(\frac{\partial}{\partial x} + \frac{1}{\varepsilon} \frac{\partial}{\partial y} \right) \times \\ &\times \left\{ h_0(y) \left(\frac{\partial}{\partial x} + \frac{1}{\varepsilon} \frac{\partial}{\partial y} \right) \left(\eta^{(0)}(x, y) + \varepsilon^1 \eta^{(1)}(x, y) + \varepsilon^2 \eta^{(2)}(x, y) + \dots \right) \right\} \end{aligned} \quad (11)$$

The argument t is omitted again. According to the method of asymptotic homogenisation we compare the terms associated with the same power of ε . We successively obtain:

At ε^{-2}

$$0 = \frac{\partial}{\partial y} \left(h_0(y) \frac{\partial \eta^{(0)}(x, y)}{\partial y} \right) \quad (12)$$

This equation is satisfied provided that $\eta^{(0)}$ does not depend on the local variable y , it is

$$\eta^{(0)} = \eta^{(0)}(x) \quad (13)$$

This statement holds true under the assumption that the coefficient $h_0(y)$ is Y - periodic.

At ε^{-1} we receive

$$0 = \frac{\partial}{\partial y} \left\{ h_0(y) \left(\frac{\partial \eta^{(0)}(x)}{\partial x} + \frac{\partial \eta^{(1)}(x, y)}{\partial y} \right) \right\} \quad (14)$$

and at ε^0

$$\begin{aligned} \frac{\partial^2 \eta^{(0)}(x, y)}{\partial t^2} &= g \frac{\partial}{\partial x} \left\{ h_0(y) \left(\frac{\partial \eta^{(0)}(x)}{\partial x} + \frac{\partial \eta^{(1)}(x, y)}{\partial y} \right) \right\} + \\ &+ g \frac{\partial}{\partial y} \left\{ h_0(y) \left(\frac{\partial \eta^{(1)}(x)}{\partial x} + \frac{\partial \eta^{(2)}(x, y)}{\partial y} \right) \right\} \end{aligned} \quad (15)$$

3.2. Results of the (one-dimensional) homogenisation

Equation (14) is satisfied if

$$\eta^{(1)} = \psi(y) \frac{\partial \eta^{(0)}(x)}{\partial x} \quad (16)$$

where $\psi(y)$ satisfies the equation

$$\frac{\partial}{\partial y} \left\{ S_0(y) \left(1 + \frac{\partial \psi(y)}{\partial y} \right) \right\} = 0 \quad (17)$$

known as a *local problem*.

We submit the expression (16) into Eq.(15), integrate over Y and obtain

$$\frac{\partial^2 \eta^{(0)}(x)}{\partial t^2} = g \frac{\partial}{\partial x} \frac{1}{|Y|} \int_Y \left\{ h_0(y) \left(\frac{\partial \eta^{(0)}(x)}{\partial x} + \frac{\partial \eta^{(1)}(x, y)}{\partial y} \right) \right\}$$

or

$$\frac{\partial^2 \eta^{(0)}(x, y)}{\partial t^2} = g h_0^{\text{eff}} \frac{\partial^2 \eta^{(0)}(x)}{\partial x^2} \quad (18)$$

where

$$h_0^{\text{eff}} = \frac{1}{|Y|} \int_Y h_0(y) \left(1 + \frac{\partial \psi(y)}{\partial y} \right) dy \quad (19)$$

Equation (18) presents the homogenised equation of the long gravity wave in the channel with the effective depth h_0^{eff} . We have also

$$c^{\text{eff}} = \sqrt{g h_0^{\text{eff}}} \quad (20)$$

the effective velocity of the gravity wave in the channel with a corrugated bottom.

4. Nonlinearity of gravity waves

4.1. Bernoulli's equation for potential flow in channel with the wavy (corrugated) bottom

We consider a potential two-dimensional flow of an incompressible fluid of the density ρ . In potential flow we can express the velocity as a gradient of scalar function Φ , *viz.* potential,

$$\mathbf{v} = \nabla \Phi$$

Euler's equation $\partial \mathbf{v} / \partial t + (\mathbf{v} \cdot \nabla) \mathbf{v} = -(1/\rho) \nabla p + \mathbf{g}$ can be written in the form of Bernoulli's type equation, [1],

$$\frac{1}{2} (u^2 + v^2) + \frac{p}{\rho} + gh = \chi(t) \quad (21)$$

where the potential energy ρgh is calculated from the bottom of the fluid, and $\chi = \chi(t)$ is an arbitrary function of the time t only. In the case of the wavy bottom in one-dimensional flow in the direction of the axis x we have $h = h(x, t)$.

4.2. Long gravity wave in a shallow channel

In accordance with the method of successive approximations, [9, 10], we start from the supposition that the horizontal and vertical fluid velocity components, u and v may be expressed by convergent series of the form

$$\begin{aligned} u &= f - \frac{1}{2}h^2 \frac{\partial^2 f}{\partial x^2} + \frac{1}{24}h^4 \frac{\partial^4 f}{\partial x^4} - \dots \\ v &= -h \frac{\partial f}{\partial x} + \frac{1}{6}h^3 \frac{\partial^3 f}{\partial x^3} - \frac{1}{120}h^5 \frac{\partial^5 f}{\partial x^5} + \dots \end{aligned} \quad (22)$$

where h denotes the actual height of a fluid particle above the bottom of the channel, the function $f = f(x, t)$, and the axis x represents direction of the flow.

So defined components u and v satisfy the incompressibility condition and the potentiality of the flow (the absence of rotation)

$$\frac{\partial u}{\partial x} + \frac{\partial v}{\partial y} = 0 \quad \text{and} \quad \frac{\partial u}{\partial y} - \frac{\partial v}{\partial x} = 0 \quad (23)$$

The introduced series for long waves are rapidly convergent: for the discussed waves the state of motion changes slowly with x and therefore the successive derivatives of f with respect to this variable, must rapidly decrease.

4.3. Boundary conditions and the wave velocity

The upper boundary of the fluid is a free surface, and is described, as previously, by the relation, see Fig.1,

$$y_A = y_A(x) = h_0 + \eta(x, t) \quad (24)$$

while the depth of the fluid at a given point x is

$$h(x) = y_A(x) - \beta(x) = h_0 + \eta(x, t) - \beta(x) \quad (25)$$

Both quantities $\beta(x)$ and $\eta(x, t)$ are very small

$$\beta \ll h_0, \quad \eta \ll h_0 \quad \text{and moreover} \quad h_0 \ll L \quad (26)$$

Passing to the conditions at the free boundary, let p_{At} be the constant atmospheric pressure, p_A - the pressure at a point just below the surface where the capillary forces cease to act, and τ - the surface tension. We have then, [1],

$$p_{At} - p_A = \tau \frac{\partial^2 y}{\partial x^2} \quad (27)$$

Similarly as in Section 3, we distinguish here and elsewhere by the suffix (\cdot_A) those quantities which refer to the free surface.

According to Bernoulli's equation (21)

$$\frac{\partial \Phi_A}{\partial t} + \frac{1}{2} (u_A^2 + v_A^2) + \frac{p_A}{\rho} + gy_A = \chi(t)$$

Therefore

$$\frac{p_{At}}{\rho} = \chi(t) - \frac{\partial \Phi_A}{\partial t} - \frac{1}{2} (u_A^2 + v_A^2) - gy_A + \frac{\tau}{\rho} \frac{\partial^2 y}{\partial x^2} \quad (28)$$

or, after using the series (22) representing the velocity and regrouping

$$\frac{p_{At}}{\rho} = L(x, t) - gy_A + M(x, t)y_A^2 + \dots + \frac{\tau}{\rho} \frac{\partial^2 y}{\partial x^2} \quad (29)$$

where

$$L = L(x, t) = \chi(t) - \int \frac{\partial f}{\partial t} dx - \frac{1}{2} f^2 \quad (30)$$

$$M = M(x, t) = \frac{1}{2} f \frac{\partial^2 f}{\partial t^2} + \frac{1}{2} \frac{\partial^2 f}{\partial x \partial t} - \frac{1}{2} \left(\frac{\partial f}{\partial x} \right)^2$$

Remember that the atmospheric pressure p_{At} is a constant. By differentiation of (29) with respect to x we receive the first necessary equation

$$\frac{\partial L}{\partial x} + h^2 \frac{\partial M}{\partial x} + \dots - g \frac{\partial h}{\partial x} + \frac{\tau}{\rho} \frac{\partial^3 z}{\partial x^3} = 0 \quad (i)$$

Moreover, a second equation must hold good at the surface. Namely, we have, cf. Eq.(24), $y_A = h_0 + \eta(x, t)$. Therefore

$$\frac{dy_A}{dt} = \frac{\partial \eta}{\partial t} + \frac{\partial \eta}{\partial x} \frac{dx}{dt} \quad \text{or} \quad v_A = \frac{\partial \eta}{\partial t} + u_A \frac{\partial \eta}{\partial x}$$

Hence we get the second equation

$$-u_A \frac{\partial y_A}{\partial x} + v_A - \frac{\partial y_A}{\partial t} = 0 \quad (ii)$$

The bottom corrugation $\beta = \beta(x)$ does not appear in this relation.

4.4. Linear step of approximation

Dealing with the fact that for long waves (whose length is great in comparison with the depth of the canal) every new differentiation with respect to x gives rise to continually smaller quantities, we reduce Eqs. (i) and (ii) in the following manner.

In the lowest approximation from Eq.(i) we get

$$\frac{\partial L}{\partial x} - g \frac{\partial h}{\partial x} = 0$$

or

$$\frac{\partial f}{\partial t} + f \frac{\partial f}{\partial x} + g \frac{\partial h}{\partial x} = 0 \quad (31)$$

From (ii) we have

$$\frac{\partial h}{\partial t} + h \frac{\partial f}{\partial x} + f \frac{\partial h}{\partial x} = 0 \quad (32)$$

In order to satisfy Eqs.(i) and (ii) by the method of successive approximation we put

$$h = h_0 + \eta - \beta \quad \text{and} \quad f = f_0 + \varphi \quad (33)$$

where the quantities h_0 and f_0 are constant, and the η, β and φ are small.

After using expressions (33) the linearized version of the system of Eqs.(31) and (32) reads

$$\frac{\partial \varphi}{\partial t} + f_0 \frac{\partial \varphi}{\partial x} + g \frac{\partial(\eta - \beta)}{\partial x} = 0 \quad (34)$$

$$\frac{\partial \eta}{\partial t} + h_0 \frac{\partial \varphi}{\partial x} + f_0 \frac{\partial(\eta - \beta)}{\partial x} = 0$$

Equations (34) can be satisfied by taking $\partial \varphi / \partial t = 0$ and $\partial \eta / \partial t = 0$. Then

$$f_0 \frac{\partial \varphi}{\partial x} + g \frac{\partial(\eta - \beta)}{\partial x} = 0 \quad (35)$$

$$h_0 \frac{\partial \varphi}{\partial x} + f_0 \frac{\partial(\eta - \beta)}{\partial x} = 0$$

The condition of non-contradiction of the last two equations is the disappearance of their determinant, it is

$$f_0 = \sqrt{gh_0} \quad (36)$$

while the solution of the set (35) is

$$\varphi = -\frac{f_0}{h_0}(\eta - \beta + \alpha) \quad (37)$$

where α is an arbitrary constant.

4.5. Non-linear step of approximation

If we wish to proceed to a second (non-linear) step of approximation we put

$$f = f_0 - \frac{f_0}{h_0}(\eta - \beta + \alpha + \gamma) \quad (38)$$

where γ is a correction, small compared with η and α . We write in short

$$f = f_0 - \frac{f_0}{h_0}(\tilde{\eta} + \alpha + \gamma) \quad (39)$$

where

$$\tilde{\eta} \equiv \eta - \beta \quad (40)$$

On substituting this in (i) and (ii) (from Section 4.3) and on writing out the result we find respectively

$$\frac{f_0}{h_0} \frac{\partial \tilde{\eta}}{\partial t} + g \frac{\partial \gamma}{\partial x} - \frac{g}{h_0}(\tilde{\eta} + \alpha) \frac{\partial \tilde{\eta}}{\partial x} - \left(\frac{1}{2} g h_0^2 - \frac{\tau}{\rho} \right) \frac{\partial^3 \tilde{\eta}}{\partial x^3} = 0 \quad (41)$$

$$\frac{f_0}{h_0} \frac{\partial \tilde{\eta}}{\partial t} - g \frac{\partial \gamma}{\partial x} - \frac{g}{h_0}(2\tilde{\eta} + \alpha) \frac{\partial \tilde{\eta}}{\partial x} + \frac{1}{6} g h_0^2 \frac{\partial^3 \tilde{\eta}}{\partial x^3} = 0$$

To obtain Eqs.(41) we rejected all terms which are small with any one of the remaining terms. For instance, the terms with

$$\frac{\partial \tilde{\eta}}{\partial x} \cdot \frac{\partial^2 \tilde{\eta}}{\partial x^2} \quad \text{and} \quad \left(\frac{\partial \tilde{\eta}}{\partial x} \right)^2$$

are rejected in comparison with

$$\tilde{\eta} \frac{\partial \tilde{\eta}}{\partial x}$$

which is retained in the equations, those with

$$\frac{\partial \gamma}{\partial t} \quad \text{and} \quad \frac{\partial^2 \tilde{\eta}}{\partial x \partial t} \quad \text{against} \quad \frac{\partial \tilde{\eta}}{\partial t}$$

In eliminating $\partial \gamma / \partial x$ from Eqs.(41) we obtain

$$\frac{\partial \tilde{\eta}}{\partial t} = \frac{3f_0}{2h_0} \frac{\partial}{\partial x} \left(\frac{1}{2} \tilde{\eta}^2 + \frac{2}{3} \alpha \tilde{\eta} + \frac{1}{3} \sigma \frac{\partial^2 \tilde{\eta}}{\partial x^2} \right) \quad (42)$$

where

$$\tilde{\eta} \equiv \eta - \beta \quad \text{and} \quad \sigma = \frac{1}{3}h_0^2 - \frac{\tau h_0}{\rho g} \quad (43)$$

This result is a generalisation of the *KdV equation*, [10], for the flow in shallow channel with the wavy bottom.

5. Comments

We have proposed a method estimating the influence of the corrugated bottom on the propagation of the long gravity waves in two cases: linear and non-linear.

For the linear case we have shown that the equation describing such waves is formally the same as in the case of the flat bottom, but the velocity of the wave is modified, because the depth of a channel is replaced by its effective value.

What concerns the nonlinear description of the gravity waves in a channel with the corrugated bottom, we have found that formally it is still the same KdV equation, in which the wave elevation η is substituted by the modified elevation $\tilde{\eta} \equiv \eta - \beta$. Hence, some results obtained for the KdV equation can be transferred to the description of gravity waves in the channels with corrugated bottom.

Acknowledgments

This work was partially supported within statutory activities No 3841/E-41/S/2018 of the Ministry of Science and Higher Education of Poland.

References

- [1] Landau, L. D., and Lifshitz, E. M. *Fluid mechanics*. transl. by J. B. Sykes and W. H. Reid, Second edition. Pergamon Press, Oxford - New York 1987.
- [2] Gill A. E. *Gravity wave*. Atmosphere Ocean Dynamics, Academic Press, 1982.
- [3] Kubrak E., Kubrak J., Rowiński P. M. Application of one-dimensional model to calculate water velocity distributions over elastic elements simulating Canadian waterweed plants (*Elodea canadensis*). *Acta Geophysica* **61** (1) (2013) 194–210.
- [4] Wojnar R., Bielski W. Flow in the canal with plants on the bottom, in: *Complex analysis and potential theory with applications*, editors: T. Aliev Azerogly, A. Golberg, S.V. Rogosin, Cambridge Scientific Publishers, 167–183, 2014.
- [5] Dingemans M. W. *Water Wave Propagation Over Uneven Bottoms*. Part 1; *Water Wave Propagation Over Uneven Bottoms*. Part 2. Advanced Series on Ocean Engineering: Volume 13, Delft 1997.

- [6] Popescu, I. *Computational Hydraulics - numerical methods and modelling*. IWA Publishing Alliance House, London 2014.
- [7] Lagrange, J.- L. *Mémoire sur la théorie du mouvement des fluides*. Nouveaux mémoires de l'Académie royale des sciences et belles-lettres de Berlin, année 1781.
- [8] Russell, J. S. Report on Waves. (Report of the British Association for the Advancement of Science, York, September 1844 (London 1845), pp 311-390).
- [9] Lamb, G. L., Jr. *Elements of soliton theory*. John Wiley & Sons, New York - Chichester - Brisbane - Toronto 1980.
- [10] Korteweg, D. J. and de Vries, G. On the change of form of long waves advancing in a rectangular canal, and on a new type of long stationary waves, *Phil. Mag.* (5) 39 (1895) 422-443.
- [11] Li, J., Jeng, D.-S. Note on the propagation of a shallow water wave in water of variable depth, *Ocean Engineering* 34 (2007) 1336-1343.
- [12] Karim, R., Alim, A., Andallah, L.S. Dispersion effect on traveling wave solution of K-dV equation. *American Journal of Computational Mathematics*, 3 (4), December 20, 2013.
- [13] Infeld, E., Karczewska, A., Rowlands, G., and Rozmej, P. Exact cnoidal solutions of the extended KdV equation, *Acta Physica Polonica A* **133** (5) (2018) 1191-1199.
- [14] Sanchez-Palencia, E. *Non-homogeneous media and vibration theory*, Springer Verlag, Berlin, Heidelberg, New York 1980.
- [15] Andrianov, I. V., Awrejcewicz, J., Danishevskyy, V. V. *Asymptotical Mechanics of Composites: Modelling Composites without FEM*, Springer International Publishing AG, Cham 2018.

Włodzimierz Bielski, Prof.: Institute of Geophysics, Polish Academy of Sciences, 01-452 Warsaw, ul. Księcia Janusza 64 (wbielski@igf.edu.pl).

Ryszard Wojnar, Ph.D.: Institute of Fundamental Technological Research, PAS, 02-106 Warsaw, ul. Pawińskiego 5B, Poland (rwojnar@ippt.pan.pl).

Nonholonomic acceleration and chaotic dynamics of locomotion

Ivan Bizyaev, Alexey Borisov, Alexander Kilin, Ivan Mamaev, Elena Pivovarova

Abstract: An analysis is made of the dynamics of nonholonomic systems with mass distribution periodically varying with time. This analysis is carried out by considering the rolling of a rigid body and the motion of a wheeled vehicle. In these problems, various types of motion, including those associated with strange attractors, are observed. A detailed treatment is given of the problem of unbounded acceleration (an analog of Fermi's acceleration) by periodic action. We also show the possibility of chaotic dynamics related to strange attractors of equations for generalized velocities, which is accompanied by a two-dimensional random walk of the platform in a laboratory reference system.

1. Equations of motion

Consider the rolling of a dynamically asymmetric unbalanced ball on a horizontal plane within the framework of the model of a rubber body [6, 7, 9] (Fig. 1). That is, we assume that there is no slipping at the point of contact, and the vertical component of the angular velocity is zero. Denote by R and m the radius and the mass of the ball, respectively; let $\mathbf{a} = (a_1, a_2, a_3)$ be the displacement vector of the center of mass of the ball relative to the geometric center, and let $\mathbf{I} = \text{diag}(I_1, I_2, I_3)$ be the central inertia tensor of the ball. We assume that noncoplanar rotors are put inside the ball, and they generate a variable gyrostatic moment $\mathbf{K}(t)$, but do not affect the mass distribution in the system.

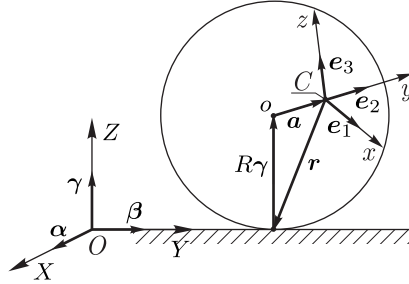


Figure 1.

To describe the dynamics of the top, we introduce two coordinate systems:

- a fixed system $OXYZ$ with orthogonal unit vectors α, β, γ ,

- a moving system $Cxyz$ with orthogonal unit vectors $\mathbf{e}_1, \mathbf{e}_2, \mathbf{e}_3$ rigidly attached to the body, and with origin at the center of mass of the body.

It is further assumed that all vectors are referred to the moving coordinate system $Cxyz$.

Conditions for the absence of slipping at the point of contact and of spinning around the vertical are described, respectively, by the following constraints equations:

$$\mathbf{v} + \boldsymbol{\omega} \times \mathbf{r} = 0, \quad (\boldsymbol{\omega}, \boldsymbol{\gamma}) = 0,$$

where \mathbf{v} and $\boldsymbol{\omega}$ are, respectively, the velocity of the center of mass and the angular velocity of the ball, $\boldsymbol{\gamma}$ is the normal vector to the plane of support, and $\mathbf{r} = -R\boldsymbol{\gamma} - \mathbf{a}$ is the radius vector of the point of contact.

The equations of motion of the system can be obtained from the d'Alembert–Lagrange principle and written in quasi-velocities with undetermined multipliers in the following form (for a detailed derivation of the equations, see [4])

$$\begin{aligned} \tilde{\mathbf{I}}\dot{\boldsymbol{\omega}} + \dot{\mathbf{K}} &= (\tilde{\mathbf{I}}\boldsymbol{\omega} + \mathbf{K}) \times \boldsymbol{\omega} - m\mathbf{r} \times (\boldsymbol{\omega} \times \dot{\mathbf{r}}) + mg(\boldsymbol{\gamma} \times \mathbf{a}) + \lambda_0\boldsymbol{\gamma}, \\ \dot{\boldsymbol{\gamma}} &= \boldsymbol{\gamma} \times \boldsymbol{\omega}, \end{aligned} \quad (1)$$

where $\tilde{\mathbf{I}} = \mathbf{I} + m(\mathbf{r}, \mathbf{r}) \cdot \mathbf{E} - m\mathbf{r} \cdot \mathbf{r}^T$ is the inertia tensor of the ball with respect to the point of contact, \mathbf{E} is the unit 3×3 matrix, and g is the acceleration of gravity. The undetermined multiplier λ_0 corresponds to the no-spin constraint and has the form

$$\lambda_0 = - \frac{(\tilde{\mathbf{I}}^{-1}\boldsymbol{\gamma}, (\tilde{\mathbf{I}}\boldsymbol{\omega} + \mathbf{K}) \times \boldsymbol{\omega} - m\mathbf{r} \times (\boldsymbol{\omega} \times \dot{\mathbf{r}}) + mg(\boldsymbol{\gamma} \times \mathbf{a}) - \dot{\mathbf{K}})}{(\boldsymbol{\gamma}, \tilde{\mathbf{I}}^{-1}\boldsymbol{\gamma})}.$$

For a complete description of the motion of the top in absolute space, equation (1) needs to be supplemented with quadratures describing the orientation of the top in space and the trajectory of the contact point,

$$\begin{aligned} \dot{\boldsymbol{\alpha}} &= \boldsymbol{\alpha} \times \boldsymbol{\omega}, & \dot{\boldsymbol{\beta}} &= \boldsymbol{\beta} \times \boldsymbol{\omega}, \\ \dot{X} &= R(\boldsymbol{\omega}, \boldsymbol{\beta}), & \dot{Y} &= -R(\boldsymbol{\omega}, \boldsymbol{\alpha}). \end{aligned} \quad (2)$$

Here X and Y are the coordinates of the point of contact (or of the geometric center of the ball) in the fixed system of coordinates.

Since, in the general case, the vector of gyrostatic moment \mathbf{K} is a given time function, it follows that system (1) is a nonautonomous system of six differential equations of the first order.

System (1) admits two first integrals:

- the geometric one,

$$\boldsymbol{\gamma}^2 = 1; \quad (3)$$

– and the constraint forbidding the spin about the vertical,

$$(\boldsymbol{\omega}, \boldsymbol{\gamma}) = 0. \quad (4)$$

Thus, on the given level set of the integrals of motion, the system reduces to a nonautonomous system of four differential equations.

For the case in which the gyrostatic moment \mathbf{K} is constant, the system also admits the integral of energy,

$$\mathcal{E} = \frac{1}{2}(\boldsymbol{\omega}, \tilde{\mathbf{I}}\boldsymbol{\omega}) - mg(\mathbf{r}, \boldsymbol{\gamma}).$$

In the general case of a variable gyrostatic moment, the energy depends on time. Below we consider the question concerning the possibility of unbounded growth of energy when the ball rolls.

2. Speedup

1°. Let us formulate the main question of the possibility of accelerating the system in question as follows:

Is it possible to choose the mass-geometric parameters of the ball and the law of change of the gyrostatic moment in such a way that bounded changes of the gyrostatic moment lead to an unbounded growth in energy (and speed) of the ball?

To answer this question, we consider an initial system which does not depend on time, and attempt to draw conclusions about the presence or absence of speedup in the system using some of its properties. To this end we introduce the notion of *frozen system*. By a frozen system we mean a system in which the gyrostatic momentum \mathbf{K} is a constant quantity and is equal to the value of the gyrostatic momentum of the initial problem at different instants of time.

The equations of motion of the frozen system, for $\mathbf{K} = \text{const}$, are of the form

$$\begin{aligned} \tilde{\mathbf{I}}\dot{\boldsymbol{\omega}} &= (\tilde{\mathbf{I}}\boldsymbol{\omega} + \mathbf{K}) \times \boldsymbol{\omega} - m\mathbf{r} \times (\boldsymbol{\omega} \times \dot{\mathbf{r}}) + mg(\boldsymbol{\gamma} \times \mathbf{a}) + \lambda_0\boldsymbol{\gamma}, \\ \dot{\boldsymbol{\gamma}} &= \boldsymbol{\gamma} \times \boldsymbol{\omega}, \end{aligned} \quad (5)$$

where

$$\lambda_0 = - \frac{(\tilde{\mathbf{I}}^{-1}\boldsymbol{\gamma}, (\tilde{\mathbf{I}}\boldsymbol{\omega} + \mathbf{K}) \times \boldsymbol{\omega} - m\mathbf{r} \times (\boldsymbol{\omega} \times \dot{\mathbf{r}}) + mg(\boldsymbol{\gamma} \times \mathbf{a}))}{(\boldsymbol{\gamma}, \tilde{\mathbf{I}}^{-1}\boldsymbol{\gamma})}.$$

Equations (5) admit three integrals of motion, namely,

– the geometric integral,

$$\boldsymbol{\gamma}^2 = 1; \quad (6)$$

– the constraint forbidding rotation with respect to the vertical,

$$(\boldsymbol{\omega}, \boldsymbol{\gamma}) = 0; \quad (7)$$

– and the energy

$$\mathcal{E} = \frac{1}{2}(\boldsymbol{\omega}, \tilde{\mathbf{I}}\boldsymbol{\omega}) - mg(\mathbf{r}, \boldsymbol{\gamma}). \quad (8)$$

This system can be reduced to the fixed level set of first integrals of motion (3), (4). As a result of the reduction, we obtain an autonomous system of four differential equations that preserve the energy integral (8).

Choosing the level set of the energy integral \mathcal{E} and taking the section in the form of the plane $g = \text{const}$, we can construct for this system, in the standard way [4], the Poincaré map

$$\Pi_2^g : \{(l, y)\} \rightarrow \{(l, y)\}.$$

Let us formulate the following hypothesis.

Hypothesis. *An acceleration in nonholonomic systems using periodic changes of parameters in the course of time is possible if the corresponding frozen system at an arbitrary point of time admits simple attractors (repellers) and, under the periodic change of parameters, a periodic alternation of an attractor and a repeller on the phase plane occurs.*

Numerical experiments have shown that for the system of interest such a speedup, which satisfies the hypothesis, is possible when the following conditions are simultaneously satisfied:

1. the center of mass of the ball is displaced in one of the principal planes of inertia;
2. the principal moments of inertia corresponding to the plane in which the center of mass is displaced are not equal to each other;
3. the gyrostatic momentum vector rotates uniformly in the same principal plane of inertia in which the center of mass of the ball is displaced.

As an example, we consider the speedup of the ball with the mass-geometric parameters

$$m = 1, \quad R = 3, \quad \mathbf{I} = \text{diag}(2, 6, 5), \quad \mathbf{a} = (-1, 0, 1.5), \quad g = 9.8 \quad (9)$$

by means of control actions of the form

$$\mathbf{K} = k(-\sin \Omega t, 0, \cos \Omega t), \quad k = 1, \quad \Omega = 0.1, \quad (10)$$

where k and Ω are constant parameters. Thus, in the coordinate system attached to the ball, the gyrostatic momentum vector rotates in a circle of radius k in the plane $\mathbf{e}_1\mathbf{e}_3$.

Remark. In the general case, the direction of the gyrostatic momentum vector at the initial instant of time is given by the additional parameter α_0

$$\mathbf{K} = k(-\sin(\Omega t + \alpha_0), 0, \cos(\Omega t + \alpha_0)),$$

but in numerical experiments we assume that $\alpha_0 = 0$, since the initial position of the vector \mathbf{K} does not influence the dynamics of the system at large times.

2°. To investigate and visualize the system dynamics, we perform a reduction of the equations of motion (1) to the level set of the integrals (3), (4) by making a change of variables to those similar to the Andoyer–Deprit variables [4]:

$$\begin{aligned}\omega_1 &= G\sqrt{1-y^2}\sin l, & \gamma_1 &= y\cos g\sin l + \sin g\cos l, \\ \omega_2 &= G\sqrt{1-y^2}\cos l, & \gamma_2 &= y\cos g\cos l - \sin g\sin l, \\ \omega_3 &= Gy, & \gamma_3 &= -\sqrt{1-y^2}\cos g.\end{aligned}\tag{11}$$

The equations of motion in the new variables (11) are a system of four differential equations with time-periodic coefficients. In the four-dimensional phase space $\mathcal{G}^4 = \{(l, y, g, G)\}$ the phase flow of the reduced system generates a four-dimensional map for each period $T = 2\pi/\Omega$

$$\Pi_4^t : \mathcal{G}^4 \rightarrow \mathcal{G}^4.\tag{12}$$

To visualize this map, we shall present its projection into the space $\mathcal{G}^3 = \{(l, y, G)\}$.

We consider an example of motion of the ball with parameters (9) and controls (10) at which speedup is observed. We define the initial conditions as follows:

$$l = \pi, \quad y = 0.5, \quad g = \pi, \quad G = 5.\tag{13}$$

Figure 2 shows a projection of the map (12) into the space \mathcal{G}^3 under the above-mentioned initial conditions. The figure demonstrates a growth of the absolute value of the angular velocity of the top, G , and a decrease in the amplitude of oscillations of projections ω_1, ω_3 (i.e., the width of the “tube”).

The dependence of the energy of the system for the trajectory with initial conditions (13) is shown in Fig. 3. It can be seen that the energy grows linearly in time, hence, the angular velocity must increase as $t^{1/2}$.

Remark. It is interesting that in another nonholonomic problem of speeding up a sleigh by periodic oscillations of the moving mass [2, 3] or by rotation of a gyrostat [1] the velocity of the system increases as $t^{1/3}$.

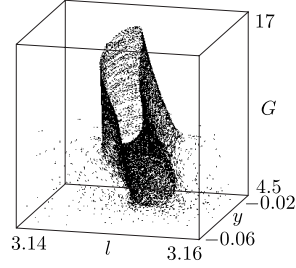


Figure 2. Projection of a map for each period $T = 2\pi/\Omega$ under the initial conditions (13).

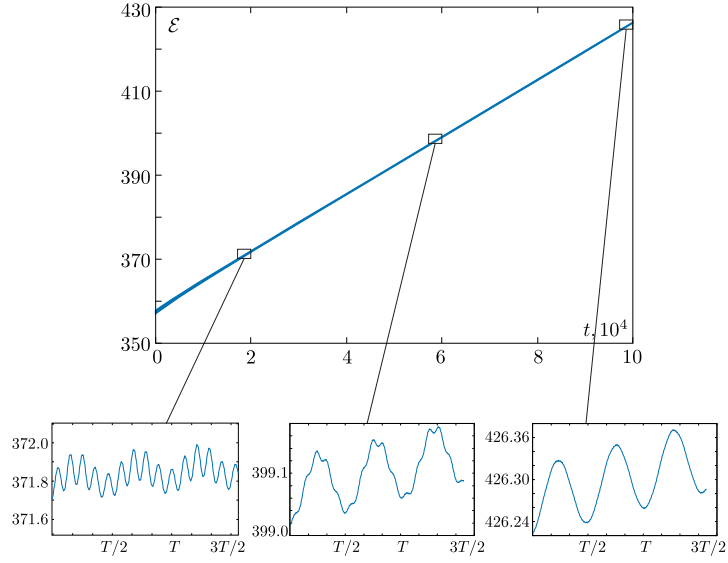


Figure 3. Energy of the system versus time, and its enlarged fragments.

Numerical experiments show that the amplitude of oscillations of angular velocities ω_1, ω_3 decreases with time. However, the question of the asymptotics of these amplitudes as $t \rightarrow \infty$ remains open, and its solution requires application of asymptotic methods of analysis.

For the above-mentioned mass-geometric parameters (9), control (10) and initial conditions (13), the ball executes in absolute space rotations close to permanent ones and rolls, on average, along a straight line. The trajectory of the contact point of the ball on the plane (X, Y) is shown in Fig. 4.

Remark. We have not been able to detect a speedup in the system for system parameters that do not satisfy the proposed hypothesis. For example, we could not detect it when we chose the parameters (9), but let the displacement of the center of mass be $\mathbf{a} = (0, 0, 1.5)$,

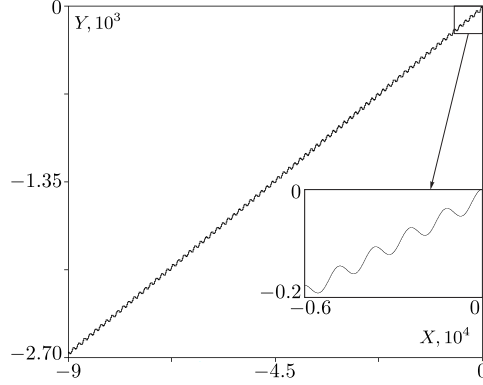


Figure 4. Trajectory of the contact point of the ball on the plane (X, Y) .

or when we took the parameters (9) and chose the tensor of inertia to be axisymmetric $\mathbf{I} = \text{diag}(5, 6, 5)$. In both cases the frozen system with $\mathbf{a} \perp \mathbf{K}$ or $\mathbf{a} \parallel \mathbf{K}$ had no simple attractors (repellers) and no speedup was observed.

3. Asymptotic behavior

We have investigated the existence of accelerated trajectories depending on initial conditions of the system. To do this, we integrate the equations of motion of the system for various initial conditions and indicate the existence or absence of acceleration by various colors.

Figure 5(a) shows the map of the asymptotic regimes of the system for the initial value $G(0) = G_0 = 5$. In this figure, black corresponds to the growth of energy. White corresponds to the decrease in energy. The shades of gray (in the chart) correspond to the changes in energy that are close to zero.

It can be seen from the figure that there are three domains of initial conditions on the chart that correspond to different asymptotic regimes:

1. Domains colored black and dark-gray. Under all initial conditions in this domain, a linear growth of energy is observed.
2. Domains colored white and light-gray. Under all initial conditions in this domain, at large times, the phase trajectory converges to the attractor.
3. The domains of mixed behavior exhibit points of different shades of gray. This mixing is due to the fact that the boundaries between different types of asymptotic behavior are of fractal nature, which results in color mixing.

Figure 5(b) shows a typical projection of a chaotic attractor to the space (l, y, G) which

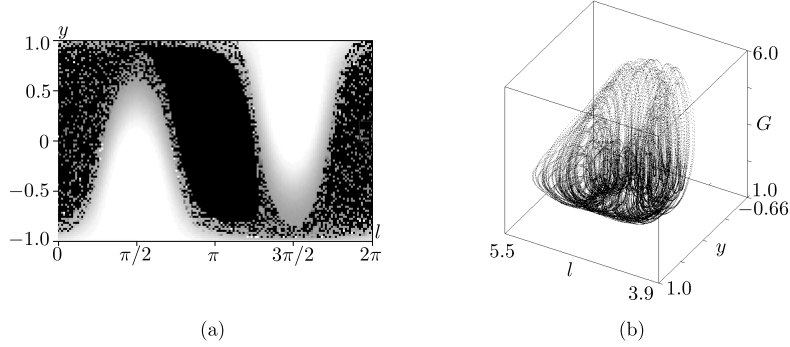


Figure 5. (a) Chart of asymptotic regimes of the system on the plane of the initial conditions (l, y) for $G_0 = 5$. (b) The projection of the phase portrait of a chaotic attractor.

the trajectory of the system reaches in the absence of acceleration.

Numerical experiments show that, when integrating a trajectory for the times $t \gg t_{max}$ from the initial conditions corresponding to the white areas in Fig. 5(a), two cases are possible:

1. All trajectories are eventually accelerating, i.e., after some period of chaotic regime, the system exhibits acceleration. Most likely, this behavior is observed due to the accumulated error caused by the integration at large times.
2. There are trajectories that move towards the attractor and do not descend from it; however, due to the fractal structure of the plane of the initial conditions, the selection of the initial conditions becomes a rather complicated problem.

The Lyapunov exponents for this attractor take the following values (due to the presence of singularities in the Andoyer–Deprit variables, these exponents were calculated in the variables ω, γ):

$$\begin{aligned} \Lambda_1 &= 0.01755, \quad \Lambda_2 = 0.002089, \quad \Lambda_3 = 0.00059, \quad \Lambda_4 = -0.000477, \\ \Lambda_5 &= -0.002236, \quad \Lambda_6 = -0.016431, \quad \sum \Lambda_i = 0.001103. \end{aligned}$$

For the attracting trajectory corresponding to the acceleration of the system, the Lyapunov exponents take the following values:

$$\begin{aligned} \Lambda_1 &= 0.000189, \quad \Lambda_2 = -4.2 \cdot 10^{-5}, \quad \Lambda_3 = -4.6 \cdot 10^{-5}, \quad \Lambda_4 = -0.000195, \\ \sum \Lambda_i &= -9.5 \cdot 10^{-5}. \end{aligned}$$

4. Chaotic dynamics

In previous sections we consider a system which can be modeled as an unbalanced rigid shell with a frame rigidly attached to the shell. Orthogonal rotors are installed on the frame. These rotors rotate with time-periodic angular velocity and do not change the mass distribution of the system.

Here we consider a system close to the previous one, but with some differences. We consider a balanced rigid shell with a frame, which rotates with constant angular velocity. On the frame an orthogonal rotor is installed which also rotates with constant angular velocity.

To specify the orientation of the shell, we introduce a *noninertial coordinate system* $Cxyz$ which is attached to the shell. We denote its unit vectors by \mathbf{e}_x , \mathbf{e}_y and \mathbf{e}_z . Let the unit vector $\mathbf{e}_z = (0, 0, 1)$ be directed along the axis of dynamical symmetry of the shell. Then the angular velocity of the frame relative to the shell is defined by the relation $\Omega(t)\mathbf{e}_z$.

Nonholonomic constraints. Let \mathbf{u} and \mathbf{w} be, respectively, the translational velocity and the angular velocity of the shell, referred to the axes $Cxyz$. As is well known, the conditions that there is no slipping and no spinning at the contact point P are defined by the following relations:

$$\mathbf{u} + a\mathbf{\Gamma} \times \mathbf{w} = 0, \quad (\mathbf{w}, \mathbf{\Gamma}) = 0, \quad (14)$$

where $\mathbf{\Gamma}$ is the normal to the plane projected to the axes $Cxyz$.

The rotation matrix $\mathbf{P}(t)$ which defines the transition to the coordinate system $Cx_1x_2x_3$ (attached to the frame) has the form

$$\mathbf{P}(t) = \mathbf{R}\Phi(t),$$

$$\Phi(t) = \begin{pmatrix} \cos \varphi(t) & \sin \varphi(t) & 0 \\ -\sin \varphi(t) & \cos \varphi(t) & 0 \\ 0 & 0 & 1 \end{pmatrix}, \quad \varphi(t) = \int_0^t \Omega(\tau) d\tau,$$

where \mathbf{R} is the constant matrix.

The transition to the velocities \mathbf{v} and $\boldsymbol{\omega}$ (in the coordinate system $Cx_1x_2x_3$) is defined by the following relations (see [4] for details):

$$\hat{\mathbf{w}} = \mathbf{P}^T \hat{\boldsymbol{\omega}} \mathbf{P} + \dot{\mathbf{P}}^T \mathbf{P}, \quad \mathbf{v} = \mathbf{P} \mathbf{u},$$

$$\hat{\boldsymbol{\omega}} = \begin{pmatrix} 0 & \omega_3 & -\omega_2 \\ -\omega_3 & 0 & \omega_1 \\ \omega_2 & -\omega_1 & 0 \end{pmatrix}, \quad \hat{\mathbf{w}} = \begin{pmatrix} 0 & w_3 & -w_2 \\ -w_3 & 0 & w_1 \\ w_2 & -w_1 & 0 \end{pmatrix}. \quad (15)$$

The angular velocity vector of the frame and the normal to the plane in $Cx_1x_2x_3$ have the form

$$\mathbf{\Omega}(t) = \Omega(t)\mathbf{P}\mathbf{e}_z, \quad \boldsymbol{\gamma} = \mathbf{P}\boldsymbol{\Gamma}.$$

Taking these relations into account, we represent the equations for constraints (14) in the form

$$\begin{aligned} \mathbf{v} + a\boldsymbol{\gamma} \times (\boldsymbol{\omega} - \mathbf{\Omega}(t)) &= 0, \\ (\boldsymbol{\omega} - \mathbf{\Omega}(t), \boldsymbol{\gamma}) &= 0. \end{aligned} \tag{16}$$

Kinetic energy. We represent the kinetic energy of the shell as follows:

$$T_s = \frac{1}{2}m_s\mathbf{u}^2 + \frac{1}{2}(\mathbf{w}, \mathbf{I}_s\mathbf{w}),$$

where m_s and $\mathbf{I}_s = \text{diag}(I_s, I_s, J_s)$ are the mass and the principal moments of inertia of the shell, respectively.

In the coordinate system $Cx_1x_2x_3$, up to an additive function of time, we obtain

$$T_s = \frac{1}{2}m_s\mathbf{v}^2 + \frac{1}{2}(\boldsymbol{\omega}, \mathbf{R}\mathbf{I}_s\mathbf{R}^T\boldsymbol{\omega}) - J_s(\boldsymbol{\omega}, \mathbf{\Omega}(t)).$$

The kinetic energy of the frame in the coordinate system $Cx_1x_2x_3$ can be represented as

$$T_f = \frac{1}{2}m_f\mathbf{v}^2 + \frac{1}{2}(\boldsymbol{\omega}, \mathbf{I}_f\boldsymbol{\omega}),$$

where m_f and \mathbf{I}_f are the mass and the tensor of inertia of the frame, respectively.

The kinetic energy of the i th rotor has the form

$$T_i = \frac{1}{2}\mu_i\mathbf{v}^2 + \frac{1}{2}(\boldsymbol{\omega} + \dot{\phi}_i(t)\mathbf{n}_i, \mathbf{j}_i(\boldsymbol{\omega} + \dot{\phi}_i(t)\mathbf{n}_i)),$$

where m_i and \mathbf{j}_i are the mass and the tensor of inertia of the i th rotor, respectively, and \mathbf{n}_i is the unit vector defining its direction of rotation.

Using the fact that the axis of rotation of the rotor coincides with the axis of dynamical symmetry, i.e., $\mathbf{j}_i\mathbf{n}_i = j_i\mathbf{n}_i$, we obtain the kinetic energy of the system in the form

$$T = T_s + T_f + \sum_{i=1}^n T_i = \frac{1}{2}m\mathbf{v}^2 + \frac{1}{2}(\boldsymbol{\omega}, \mathbf{I}\boldsymbol{\omega}) + (\mathbf{k}(t), \boldsymbol{\omega}), \tag{17}$$

where m is the mass of the entire system, and \mathbf{I} and $\mathbf{k}(t)$ are its moment of inertia and gyrostatic momentum, respectively:

$$\begin{aligned} m &= m_s + m_f + \sum_{i=1}^n \mu_i, \quad \mathbf{I} = \mathbf{R}\mathbf{I}_s\mathbf{R}^T + \mathbf{I}_f + \sum_{i=1}^n \mathbf{j}_i, \\ \mathbf{k}(t) &= \sum_{i=1}^n j_i \dot{\phi}_i(t)\mathbf{n}_i - J_s\mathbf{\Omega}(t). \end{aligned} \tag{18}$$

Since the matrix \mathbf{I} is symmetric and positive definite, one can always choose the matrix \mathbf{R} in such a way that $\mathbf{I} = \text{diag}(I_1, I_2, I_3)$ is a diagonal matrix.

In the general case, we represent the equations of motion in the form of Poincaré–Suslov equations (for details, see [5, 8]):

$$\begin{aligned} \frac{d}{dt} \left(\frac{\partial T}{\partial \boldsymbol{\omega}} \right) + \boldsymbol{\omega} \times \frac{\partial T}{\partial \boldsymbol{\omega}} + \mathbf{v} \times \frac{\partial T}{\partial \mathbf{v}} + \boldsymbol{\gamma} \times \frac{\partial T}{\partial \boldsymbol{\gamma}} &= \sum_{i=1}^3 \lambda_i \frac{\partial f_i}{\partial \boldsymbol{\omega}} + \lambda_0 \frac{\partial f_0}{\partial \boldsymbol{\omega}}, \\ \frac{d}{dt} \left(\frac{\partial T}{\partial \mathbf{v}} \right) + \boldsymbol{\omega} \times \frac{\partial T}{\partial \mathbf{v}} &= \sum_{i=1}^3 \lambda_i \frac{\partial f_i}{\partial \mathbf{v}} + \lambda_0 \frac{\partial f_0}{\partial \mathbf{v}}, \end{aligned} \quad (19)$$

where $\boldsymbol{\lambda} = (\lambda_1, \lambda_2, \lambda_3)$ and λ_0 are the undetermined multipliers defining the reaction of the constraints (16).

Substituting the kinetic energy (17) in equations of motion (19) and supplementing by the Poisson equation for $\boldsymbol{\gamma}$, we obtain a system of 6 equations which admits three integrals of motion

$$F_0 = \boldsymbol{\gamma}^2, \quad F_1 = (\mathbf{M}, \boldsymbol{\gamma}), \quad f = \mathbf{M}^2,$$

where

$$\mathbf{M} = \boldsymbol{\gamma} \times (\tilde{\mathbf{I}}\boldsymbol{\omega} - \mathbf{K}(t)), \quad \mathbf{K}(t) = \mathbf{k}(t) - ma^2\boldsymbol{\Omega}(t). \quad (20)$$

Thus, we obtain a three-dimensional phase flow which generates a two-dimensional Poincaré map Φ_{f,g_0} . At some parameters of the system, a strange attractor arises on the map Φ_{f,g_0} (see Fig. 6).

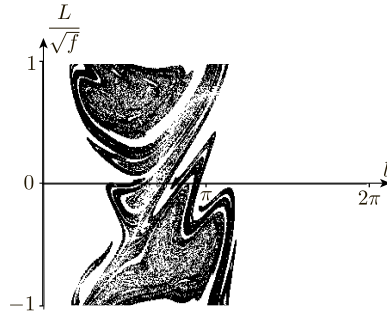


Figure 6. An example of the strange attractor on the Poincaré map.

This attractor corresponds to the following Lyapunov exponents:

$$\Lambda_1 \approx 0.11, \quad \Lambda_2 \approx 0, \quad \Lambda_3 \approx 0, \quad \Lambda_4 \approx 0, \quad \Lambda_5 \approx 0, \quad \Lambda_6 \approx -0.13.$$

Its Kaplan–Yorke dimension on the Poincaré map is

$$D = 1 + \frac{\Lambda_1}{|\Lambda_6|} \approx 1.84.$$

Acknowledgments

This work is carried out at MIPT under project 5–100 for state support for leading universities of the Russia and supported by the RFBR grants 18-08-00999-a and 18-29-10051-mk.

References

- [1] BIZYAEV, I., BORISOV, A., KOZLOV, V., AND MAMAEV, I. The chaplygin sleigh with parametric excitation: Chaotic dynamics and nonholonomic acceleration. *Nonlinearity* **32**, 9 (2019), 3209–3233.
- [2] BIZYAEV, I., BORISOV, A., AND KUZNETSOV, S. Chaplygin sleigh with periodically oscillating internal mass. *EPL* **119**, 6 (2017), 60008.
- [3] BIZYAEV, I., BORISOV, A., AND MAMAEV, I. The chaplygin sleigh with parametric excitation: Chaotic dynamics and nonholonomic acceleration. *Regul. Chaotic Dyn.* **22**, 8 (2017), 955–975.
- [4] BORISOV, A., AND MAMAEV, I. *Rigid Body Dynamics: Hamiltonian Methods, Integrability, Chaos*. R&C Dynamics, Institute of Computer Science, Izhevsk, 2005.
- [5] BORISOV, A., AND MAMAEV, I. Symmetries and reduction in nonholonomic mechanics. *Regul. Chaotic Dyn.* **20**, 5 (2015), 553–604.
- [6] BORISOV, A., MAMAEV, I., AND BIZYAEV, I. The hierarchy of dynamics of a rigid body rolling without slipping and spinning on a plane and a sphere. *Regul. Chaotic Dyn.* **18**, 3 (2013), 277–328.
- [7] CENDRA, H., AND ETCHECHOURY, M. Rolling of a symmetric sphere on a horizontal plane without sliding or slipping. *Rep. Math. Phys.* **57**, 3 (2006), 367–374.
- [8] FEDOROV, Y., AND KOZLOV, V. Various aspects of n -dimensional rigid body dynamics. *Amer. Math. Soc. Transl. (2)* (1995).
- [9] KOILLER, J., AND EHLERS, K. Rubber rolling over a sphere. *Regul. Chaotic Dyn.* **12**, 2 (2007), 127–152.

Alexey Borisov, Professor: Moscow Institute of Physics and Technology, 141701 Dolgoprudny, Institutskiy per., 9, Russia (*borisov@rtd.ru*).

Ivan Mamaev, Professor: Kalashnikov Izhevsk State Technical University, 426034 Izhevsk, Universitetskaya str., 1, Russia (*mamaev@rtd.ru*).

Ivan Bizyaev, Professor: Moscow Institute of Physics and Technology, 141701 Dolgoprudny, Institutskiy per., 9, Russia (*bizyaev_90@mail.ru*).

Alexander Kilin, Professor: Udmurt State University, 426034 Izhevsk, Universitetskaya str., 1, Russia (*aka@rtd.ru*). The author gave a presentation of this paper during one of the conference sessions.

Elena Pivovarova, Ph.D.: Udmurt State University, 426034 Izhevsk, Universitetskaya str., 1, Russia (*archive@rtd.ru*).

Nonlinear dynamics of laser systems: Chaos, bifurcations and strange attractors

Vasily Buyadzhi, Anna Buyadzhi, Alexey Chernyshev, Evgeniya Plisetskaya,
Eugeny Pavlov and Sergey Kir'yanov

Abstract: An advanced chaos-geometric computational approach to analysis, modelling and prediction of the non-linear dynamics of quantum and laser systems with elements of the deterministic chaos is briefly presented and applied to study of a chaos generation in the one-ring erbium fiber laser. The approach is based on using the techniques such as a wavelet analysis, multi-fractal formalism, mutual information approach, correlation integral analysis, false nearest neighbour algorithm, the Lyapunov's exponents analysis, surrogate data method, prediction models etc. There are listed the advanced numerical data on the topological and dynamical invariants (correlation, embedding, Kaplan-York dimensions, the Lyapunov's exponents, Kolmogorov's entropy etc) of chaotic dynamics for the one-ring erbium fiber laser with the control parameters: the modulation frequency and dc bias voltage of the additional electro-optical modulator.

1. Introduction

In modern computational quantum electronics, laser physics etc dynamical systems (such as atomic and molecular systems in an electromagnetic field, multi-element semiconductors and gas lasers etc) are intensively studied in the last years. Especial interest attracts dynamics of the laser systems, which can exhibit chaotic dynamical behaviour. These systems can be considered in the first approximation as a grid of autogenerators (quantum generators), coupled by different way [1-8]. A quantitative study of the chaos phenomenon features is of a great interest and importance for many scientific and technical applications. At the present time it became one of the most actual and important problems of computational physics of the complex systems. Chaotic fluctuations in the laser diodes dynamics deserve much attention because of their potential for unprecedented application of the technologies, secure communication, the construction of chaotic lidars, optical reflectometers, true random number generators etc [1-21]. It is known that a transition to chaos in dissipative regime of functioning of NMR-maser provides the construction based on a new type of detecting signals with unprecedented sensitivity especially when approaching control parameter to the point of doubling bifurcation.

In this work we present the advanced results of application of a uniform chaos-geometric formalism (CGF) to analysis and modelling of non-linear dynamics of some laser systems. The CGF

is based on using the advanced generalized techniques such as the wavelet analysis, multi-fractal formalism, mutual information approach, correlation integral analysis, false nearest neighbour algorithm, the Lyapunov's exponents analysis, and surrogate data method, prediction models etc (see details in Refs. [4,5,17-41]). We present the advanced results of study of chaos generation dynamics in the one-ring erbium fiber laser (EFL) with the control parameters: the modulation frequency f and dc bias voltage V of the additional electro-optical modulator (EOM). The values of the topological and dynamical invariants for the EFL dynamics are listed.

2. Universal chaos-dynamical approach to analysis of dynamics of the complex laser systems

As many blocks of the used approach have been developed earlier and needed only to be reformulated regarding the problem studied in this paper, here we are limited to presenting the key moments following to Refs. [4-6,12,29-39]. The important step of the quantitative studying chaotic dynamics of different dynamical systems is a numerical analysis of the characteristic time series, i.e. the time series of key dynamical characteristics. Let us formally consider scalar measurements $s(n) = s(t_0 + n\Delta t) = s(n)$, where t_0 is the start time, Δt is the time step, and is n the number of the measurements. In a general case, $s(n)$ is any time series, particularly, the series for an amplitude level. Packard et al. [22] introduced the method of using time-delay coordinates to reconstruct the phase space of an observed dynamical system. The direct use of the lagged variables $s(n + \tau)$, where τ is some integer to be determined, results in a coordinate system in which the structure of orbits in phase space can be captured. Then using a collection of time lags to create a vector in d dimensions,

$$\mathbf{y}(n) = [s(n), s(n + \tau), s(n + 2\tau), \dots, s(n + (d-1)\tau)], \quad (1)$$

the required coordinates are provided. In a nonlinear system, the $s(n + j\tau)$ are some unknown nonlinear combination of the actual physical variables that comprise the source of the measurements. The dimension d is called the embedding dimension, d_E . Two methods are usually used to determine this parameter. First approach is based on computing the autocorrelation function. Another approach is based on using an average mutual information. The next principal step is to reconstruct a Euclidean space R^d large enough so that the set of points d_A can be unfolded without ambiguity. In accordance with the embedding theorem, the embedding dimension, d_E , must be greater, or at least equal, than a dimension of attractor, d_A , i.e. $d_E > d_A$. In other words, we can choose a fortiori large dimension d_E , e.g. 10 or 15, since the previous analysis provides us prospects that the dynamics of our system is probably chaotic. However, two problems arise with working in dimensions larger than really required by the data and time-delay embedding [24]. Firstly, many of computations for extracting interesting properties from the data require search and other operations in R^d whose computational

cost rises exponentially with d . Secondly, but more significant from the physical viewpoint, in the presence of noise or other high dimensional contamination of the observations, the extra dimensions are not populated by dynamics, already captured by a smaller dimension, but entirely by the contaminating signal. In too large an embedding space one is unnecessarily spending time working around aspects of a bad representation of the observations which are solely filled with noise. Further it is necessary to determine the dimension d_A . There are a few methods to reconstruct an attractor dimension (see, e.g., [1-8]), but usually there are applied only two methods. The first correlation integral analysis uses the correlation integral, $C(r)$, to distinguish between chaotic and stochastic systems. To compute the correlation integral, the algorithm of Grassberger and Procaccia [26] is the most commonly used approach, where the correlation integral is

$$C(r) = \lim_{N \rightarrow \infty} \frac{2}{N(n-1)} \sum_{\substack{i,j \\ (1 \leq i < j \leq N)}} H(r - \|\mathbf{y}_i - \mathbf{y}_j\|) \quad (2)$$

where H is the Heaviside step function with $H(u) = 1$ for $u > 0$ and $H(u) = 0$ for $u \leq 0$, r is the radius of sphere centered on \mathbf{y}_i or \mathbf{y}_j , and N is the number of data measurements. The correlation exponent d can be determined as the slope of line in the coordinates $\log C(r)$ versus $\log r$ by a least-squares fit of a straight line over a certain range of r , called the scaling region. To verify the results obtained by the correlation integral analysis, one can use surrogate data method. This method (look for example, [3,4]) is an approach that makes use of the substitute data generated in accordance to the probabilistic structure underlying the original data.

The next important step is computing the Lyapunov's exponents, which are the dynamical invariants of a nonlinear system. In a general case, the orbits of chaotic attractors are unpredictable, but there is the limited predictability of chaotic physical system, which is defined by the global and local Lyapunov's exponents. In a chaos theory, the spectrum of the Lyapunov's exponents is considered a measure of the effect of perturbing the initial conditions of a dynamical system. Note that both positive and negative Lyapunov's exponents can coexist in a dissipative system, which is then chaotic. In fact, if one manages to derive the whole spectrum of the Lyapunov's exponents, other invariants of the system, i.e. Kolmogorov entropy and attractor's dimension can be found. The Kolmogorov entropy, K , measures the average rate at which information about the state is lost with time. An estimate of this measure is the sum of the positive Lyapunov's exponents. The inverse of the Kolmogorov entropy is equal to the average predictability. The estimate of the dimension of the attractor is provided by the Kaplan and Yorke conjecture:

$$d_L = j + \frac{\sum_{\alpha=1}^j \lambda_\alpha}{|\lambda_{j+1}|}, \quad (3)$$

where j is such that $\sum_{\alpha=1}^j \lambda_{\alpha} > 0$ and $\sum_{\alpha=1}^{j+1} \lambda_{\alpha} < 0$, and the Lyapunov's exponents λ_{α} are taken in

descending order. There are a few approaches to computing the Lyapunov's exponents. One of them is based on the Jacobi matrix of system. In the case where only observations are given and the system function is unknown, the matrix has to be estimated from the data. In this case, all the suggested methods approximate the matrix by fitting a local map to a sufficient number of nearby points. In our work we use the method with the linear fitted map proposed by Sano and Sawada, although the maps with higher order polynomials can be also used. To calculate the spectrum of the Lyapunov's exponents from the amplitude level data, one could determine the time delay τ and embed the data in the four-dimensional space. In this point it is very important to determine the Kaplan-York dimension and compare it with the correlation dimension, determined by the Grassberger-Procaccia algorithm. It is worth to remind that results of state-space reconstruction are highly sensitive to the length of data set (i.e. it must be sufficiently large) as well as to the time lag and embedding dimension determined. Indeed, there are limitations on the applicability of chaos theory for observed (finite) time series arising from the basic assumptions that the time series must be infinite.

3. Results and conclusions

Below we present the numerical results of a quantitative study of the chaos generation dynamics in the EFL with the control parameters: a modulation frequency f and dc bias voltage V of the additional EOM. Feng et al. [1] experimentally observed generation of chaos in the EFL (laser parameters: the output power 20.9 mW, wavelength 1550.190 nm) with the EOM which is made from crystal LiNbO₃. In the first series of measurements by Feng et al. [1] the DC bias voltage is maintained at 10V, frequency modulation control parameters was $f=64-75$ MHz. Figure 1 (column I) shows the measured time dependence of the output voltage V_{out} of the frequency modulation: A. $f=75$ MHz (one-period state); B. $f=68$ MHz (double-period state); C. $f=64$ MHz (chaotic state) [1]. In a second series of measurements by Feng et al. [1] the modulation frequency is kept at 60 MHz, and its dc bias voltage V was changed from 4 to 10V (Figure 1, column II). Theoretical examination shows that depending on the values of f , V laser device is in turn in the one-period ($f=75$ MHz, $V=10$ V or $f=60$ MHz, $V=4$ V), double-period ($f=68$ MHz, $V=10$ V or $f=60$ MHz, $V=6$ V), chaotic ($f=64$ MHz, $V=10$ V and $f=60$ MHz, $V=10$ V) states [1]. Using our version of the CGF [4-6,12,29] we calculated values of Lyapunov's exponents (LE), correlation dimension, embedding dimension, the Kaplan-York dimension, the Kolmogorov entropy (KE) K_{entr} for two time series. The relevant data are listed in the Table 1. In general, our theoretical analysis shows that the chaos in the EDFL device is generated via scenario of intermittency by increasing the DC bias voltage and period-doubling bifurcation sequence by reducing the EOM modulation frequency.

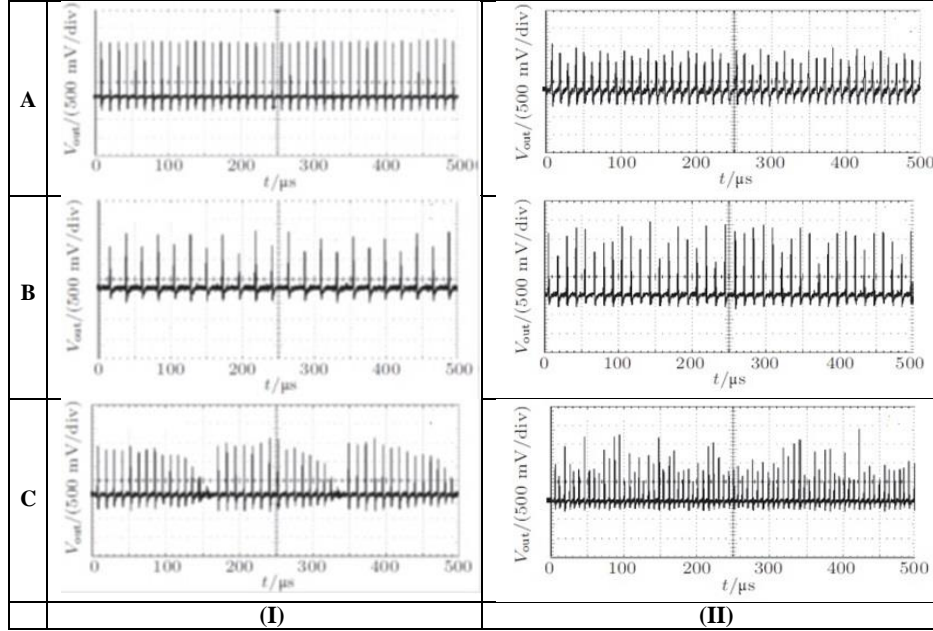


Figure 1. Temporal dependence V_{out} (I): A. $f = 75$ MHz (1-period state); B. $f = 68$ MHz (2-period); C. 64 MHz (chaotic); (II): A. $V = 4B$ (3-period); B. $V = 6B$ (intermittency); C. $V = 10B$ (chaotic).

Table 1. Results of calculation of the LE amplitude level: λ_i in descending order, d_L - Kaplan-York dimension, K_{entr} - KE

Row	λ_1	λ_2	λ_3	d_L	K_{entr}
I	0.168	0.0212	-0.223	2.85	0.19
II	0.172	0.0215	-0.220	2.88	0.19

To conclude, we presented the results of the CGF version (which includes the advanced techniques such as multi-fractal formalism, mutual information, correlation integral and the Lyapunov's exponents analysis, false nearest neighbors, surrogate data algorithms etc [4,5,17-41]) application to analysis and modeling the chaos generation dynamics in the EFL using the experimental data by Feng et al [1]. The values of the topological and dynamical invariants (correlation, embedding, Kaplan-York dimensions, the Lyapunov's exponents etc) for the EFL dynamics are listed.

Acknowledgments

The authors would like to thank Prof. Jan Awrejcewicz and colleagues for invitation to make contributions to DSTA-2019 (Łódź, Poland). The useful comments of the anonymous referees are very much acknowledged too.

References

- [1] Feng, C., Yu-Ling, F., Zhi-Hai, Y., Jian, F., Yuan-Chao, S., Yu-Zhu, Z. Experimental investigation on chaos generation in erbium-doped fiber single-ring lasers. *Chin. Phys. B.* 21 (2013), 100504.
- [2] Glushkov, A.V., Buyadzi, V.V., Kvasikova, A.S., Ignatenko, A.V., Kuznetsova, A.A., Prepelitsa, G.P., Ternovsky, V.B. Nonlinear chaotic dynamics of Quantum systems: Molecules in an electromagnetic field and laser systems. *Quantum Systems in Physics, Chemistry, and Biology. Series: Progress in Theoretical Chemistry and Physics*, ed. A.Tadger, R.Pavlov, J.Maruani, E.Brändas, G.Delgado-Barrio. Springer, Cham. 30 (2017), 169-180.
- [3] Fischer, I., Hess, O., Elsaber, W., Gobel, E. High-dimensional chaotic dynamics of an external cavity semiconductor laser. *Phys. Rev. Lett.* 73 (1994) 2188-2191.
- [4] Glushkov, A.V., Ternovsky, V.B., Buyadzi, V.V., Prepelitsa, G.P., Geometry of a Relativistic Quantum Chaos: New approach to dynamics of quantum systems in electromagnetic field and uniformity and charm of a chaos. *Proc. Intern. Geom. Center.* 7, 4 (2014), 60-71
- [5] Prepelitsa, G.P., Glushkov, A.V., Lepikh, Ya.I., Buyadzi, V.V., Ternovsky, V.B., Zaichko P.A. Chaotic dynamics of non-linear processes in atomic and molecular systems in electromagnetic field and semiconductor and fiber laser devices: new approaches, uniformity and charm of chaos. *Sensor Electr. and Microsyst. Techn.* 11, 4 (2014), 43-57.
- [6] Buyadzi, V.V., Belodonov, A.S., Mironenko, D., Mashkantsev, A.A., Kir'yanov, S.A., Buyadzi, A.A., Glushkov, A.V. Nonlinear dynamics of external cavity semiconductor laser system with elements of a chaos. *Engineering Dynamics and Life Sciences*, Eds. J. Awrejcewicz, M. Kaźmierczak and J. Mrozowski. Lodz Univ., Lodz. 3 (2017), 89-96.
- [7] Glushkov A.V., Khetselius O.Yu., Kuzakon V.M., Prepelitsa G.P., Solyanikova E.P., Svinarenko A.A., Modeling of interaction of the non-linear vibrational systems on the basis of temporal series analyses (application to semiconductor quantum generators). *Dynamical Systems - Theory and Applications*. Lodz Univ., Lodz. (2011) BIF110.
- [8] Glushkov, A.V. *Methods of a chaos theory*. Astroprint, Odessa, 2012.
- [9] Glushkov, A.V. *Relativistic quantum theory. Quantum mechanics of atomic systems*. Astroprint, Odessa, 2008.
- [10] Khetselius, O.Yu. *Hyperfine structure of atomic spectra*. Astroprint, Odessa, 2008.
- [11] Khetselius, O.Yu. Hyperfine structure of radium. *Photoelectronics.* 14 (2005), 83-85
- [12] Buyadzi, V.V., Glushkov, A.V., Mansarliysky, V.F., Ignatenko, A.V., Svinarenko A.A. Spectroscopy of atoms in a strong laser field: New method to sensing AC Stark effect, multiphoton resonances parameters and ionization cross-sections. *Sensor Electr. and Microsyst. Techn.* 12, 4 (2015), 27-36.
- [13] Glushkov, A.V., Khetselius, O.Yu., Bunyakova, Yu.Ya., Buyadzi, V.V., Brusentseva, S.V., Zaichko P.A. Sensing interaction dynamics of chaotic systems within a chaos theory and microsystem technology Geomath with application to neurophysiological systems. *Sensor Electr. and Microsyst. Techn.* 11, 3 (2014), 62-69.
- [14] Glushkov, A.V., Mansarliysky, V.F., Khetselius, O.Yu., Ignatenko, A.V., Smirnov, A.V., Prepelitsa, G.P. Collisional shift of hyperfine line for thallium in an atmosphere of the buffer inert gas. *J. Phys.: Conf. Ser.* 810 (2017), 012034.

- [15] Svinarenko, A.A., Glushkov, A.V., Khetselius, O.Yu., Ternovsky, V.B., Dubrovskaya, Yu.V., Kuznetsova, A.A., Buyadzh, V.V. Theoretical Spectroscopy of Rare-Earth Elements: Spectra and Autoionization Resonances. *Rare Earth Element*, ed. Jose E. A. Orjuela, InTech. (2017), 83-104.
- [16] Glushkov, A.V., Khetselius, O.Yu., Svinarenko, A.A., Buyadzh, V.V., Ternovsky, V.B., Kuznetsova, A.A., Bashkarev, P.G. Relativistic Perturbation Theory Formalism to Computing Spectra and Radiation Characteristics: Application to Heavy Element. *Recent Studies in Perturbation Theory*, Ed. D.I.Uzunov. InTech. (2017), 131-150.
- [17] Glushkov, A.V., Safranov, T.A., Khetselius, O.Yu., Ignatenko, A.V., Buyadzh, V.V., Svinarenko A.A. Analysis and forecast of the environmental radioactivity dynamics based on methods of chaos theory: General conceptions. *Environmental Problems*. 1, 2 (2016), 115-120.
- [18] Glushkov, A.V., Khetselius, O.Y., Brusentseva, S.V., Zaichko, P.A., Ternovsky, V.B. Studying interaction dynamics of chaotic systems within a non-linear prediction method: application to neurophysiology. *Advances in Neural Networks, Fuzzy Systems and Artificial Intelligence, Series: Recent Advances in Computer Engineering*, Ed. J.Balicki. WSEAS Pub., Gdansk. 21 (2014), 69-75.
- [19] Glushkov, A.V., Svinarenko, A.A., Buyadzh, V.V., Zaichko, P.A., Ternovsky, V.B. Chaos-geometric attractor and quantum neural networks approach to simulation chaotic evolutionary dynamics during perception process. *Advances in Neural Networks, Fuzzy Systems and Artificial Intelligence*, Ed. J.Balicki. WSEAS Pub., Gdansk. 21 (2014), 143-150.
- [20] Glushkov, A.V., Prepelitsa, G.P., Svinarenko, A.A., Zaichko, P.A. Studying interaction dynamics of the non-linear vibrational systems within non-linear prediction method (application to quantum autogenerators). *Dynamical Systems Theory*, ed. J. Awrejcewicz, M. Kazmierczak, P. Olejnik, J. Mrozowski. Lodz Univ., Łódź. T1 (2013), 467-477.
- [21] Gottwald, G.A., Melbourne, I. Testing for chaos in deterministic systems with noise. *Physica D*. 212 (2005), 100–110.
- [22] Packard, N.H., Crutchfield, J.P., Farmer, J.D., Shaw, R.S. Geometry from a time series. *Phys. Rev. Lett.* 45 (1980), 712–716.
- [23] Kennel, M.B., Brown, R., Abarbanel, H. Determining embedding dimension for phase-space reconstruction using a geometrical construction. *Phys. Rev. A* 45 (1992) 3403-3411.
- [24] Abarbanel, H.D.I., Brown, R., Sidorowich, J.J., Tsimring, L.Sh. The analysis of observed chaotic data in physical systems. *Rev. Mod. Phys.* 65 (1993), 1331–1392.
- [25] Schreiber, T. Interdisciplinary application of nonlinear time series methods. *Phys. Rep.* 308 (1999), 1–64.
- [26] Grassberger, P., Procaccia, I. Measuring the strangeness of strange attractors. *Physica D*. 9 (1983), 189–208.
- [27] Fraser, A.M., Swinney, H.L. Independent coordinates for strange attractors from mutual information. *Phys. Rev. A*. 33 (1986), 1134–1140.
- [28] Glushkov, A.V., Svinarenko, A.A., Loboda, A.V. *Theory of neural networks on basis of photon echo and its program realization*. TEC, Odessa, 2003.
- [29] Khetselius, O.Yu. *Quantum structure of electroweak interaction in heavy finite Fermi-systems*. Astropoint, Odessa, 2011.
- [30] Glushkov, A.V., Kuzakon, V.M., Ternovsky, V.B., and Buyadzh, V.V. Dynamics of laser systems with absorbing cell and backward-wave tubes with elements of a chaos. *Dynamical Systems Theory*, ed. J. Awrejcewicz, M. Kazmierczak, P. Olejnik, J. Mrozowski. Lodz Univ., Łódź. T1 (2013), 461-466.

- [31] Khetselius, O.Yu. Forecasting evolutionary dynamics of chaotic systems using advanced non-linear prediction method. *Dynamical Systems Applications*, ed. J. Awrejcewicz, M. Kazmierczak, P. Olejnik, J. Mrozowski. Lodz Univ., Łódź. T2 (2013), 145-152.
- [32] Bunyakova, Yu.Ya., Glushkov, A.V. *Analysis and forecast of the impact of anthropogenic factors on air basein of an industrial city*. Ecology, Odessa, 2010.
- [33] Bunyakova, Yu.Ya., Khetselius, O.Yu. Non-linear prediction statistical method in forecast of atmospheric pollutants. *Proc. of 8th Intern. Carbon Dioxide Conference (Germany)*. T2-098 (2009).
- [34] Khetselius, O.Yu., Brusentseva, S.V., Tkach, T.B. Studying interaction dynamics of chaotic systems within non-linear prediction method: Application to neurophysiology. *Dynamical Systems Applications*, ed. J. Awrejcewicz, M. Kazmierczak, P. Olejnik, J. Mrozowski. Lodz Univ., Łódź. T2 (2013), 251-259.
- [35] Glushkov, A.V., Khetselius, O.Y., Bunyakova, Yu.Ya., Prepelitsa, G.P., Solyanikova, E.P., and Serga E.N. Non-linear prediction method in short-range forecast of atmospheric pollutants: low-dimensional chaos. *Dynamical Systems - Theory and Applications*, Lodz. (2011), LIF111.
- [36] Prepelitsa, G.P., Buyadzhi, V.V., Ternovsky, V.B. Non-linear analysis of chaotic self-oscillations in backward-wave tube. *Photoelectronics*. 22 (2013), 103-107.
- [37] Glushkov, A., Khetselius, O., Svinarenko, A., Serbov, N., The sea and ocean 3D acoustic waveguide: rays dynamics and chaos phenomena. *J. Acoust. Soc. America*. 123, 5 (2008), 3625
- [38] Gubanova, E.R., Glushkov, A.V., Khetselius, O.Yu., Bunyakova, Yu.Ya., Buyadzhi, V.V., Pavlenko, E.P. *New methods in analysis and project management of environmental activity: Electronic and radioactive waste*. FOP, Kharkiv, 2017.
- [39] Khetselius, O., Glushkov, A., Dubrovskaya, Yu., Chernyakova, Yu., Ignatenko, A., Serga, I., Vitavetskaya, L. Relativistic quantum chemistry and spectroscopy of exotic atomic systems with accounting for strong interaction effects. *Concepts, Methods and Applications of Quantum Systems in Chemistry and Physics*. Springer, Cham, 31 (2018), 71-91.
- [40] Glushkov, A.; Khetselius, O.; Svinarenko, A.; Buyadzhi, V. *Spectroscopy of autoionization states of heavy atoms and multiply charged ions*. TEC, Odessa, 2015.
- [41] Glushkov, A.V., Khetselius, O.Yu., Svinarenko, A.A., Buyadzhi, V.V., *Methods of computational mathematics and mathematical physics. P.1*. TES, Odessa, 2015.
- Vasily V. Buyadzhi, Assoc.-Prof. (PhD): Odessa State Environmental University, Pure and Applied Mathematics Department, L'vovskaya str. 15, 65009 Odessa, Ukraine (buyadzhivv@gmail.com) The author gave a presentation of this paper during one of the conference sessions.
- Anna A. Buyadzhi, M.Sc. (Ph.D. student): Odessa State Environmental University, Pure and Applied Mathematics Department, L'vovskaya str. 15, 65009 Odessa, Ukraine (buyadzhiaa@gmail.com)
- Alexey Chernyshev, Senior Lecturer: Odessa State Environmental University, Pure and Applied Mathematics Department, L'vovskaya str. 15, 65009 Odessa, Ukraine
- Evgeniya Plisetskaya, M.Sc. (Ph.D. student): Odessa State Environmental University, Pure and Applied Mathematics Department, L'vovskaya str. 15, 65009 Odessa, Ukraine
- Eugeny V. Pavlov, M.Sc. (Ph.D. student): Odessa State Environmental University, Pure and Applied Mathematics Department, L'vovskaya str. 15, 65009 Odessa, Ukraine
- Sergey V. Kir'yanov, M.Sc. (Ph.D. student): Odessa State Environmental University, Pure and Applied Mathematics Department, L'vovskaya str. 15, 65009 Odessa, Ukraine.

Thermographic analysis of the additional load influence on the muscle activation during gait

Jarosław Chruściel, Anna Frątczak, Angelika Puchalska, Siam Streibl,
Bartłomiej Zagrodny

Abstract: Carrying loads in asymmetrical ways (on one shoulder, across the body or with one hand) has become a common practice. This study aims to introduce the effects of the aforementioned load carrying methods on muscle activation with the use of infrared thermography. Experimental results reveals differences in temperature symmetry distribution along upper part of the body. Also it was observed, that with higher asymmetrical load bigger temperature difference between left and right side was obtained.

1. Introduction

Physical activity leads to increased blood flow in order to supply the activated muscles with all necessary nutrients and oxygen as well as to remove metabolites, a by-product of muscular contractions [1, 2]. The energy produced by muscles, caused by its relatively low efficiency, is expressed in the form of heat. The human body aims to dissipate it in order to prevent internal organs and muscles itself from overheating, also known as hyperthermia [3]. It does so through a process referred to as thermoregulation in which the skin plays a key role and involves vasoconstriction, sweating and shivering [4]. With that being said, skin temperature should reflect the level of heat dissipation and is correlated with muscle activation.

An increasingly popular method to assess muscle activation by analysing skin temperature is thermal imaging [5, 6]. Infrared thermography (IRT) is a technique which is based on the fact that every matter with a temperature greater than absolute zero emits infrared radiation. A thermographic camera, by means of its optical system, detects radiation emitted in the long-infrared range and creates a visual representation of temperature distribution, called a thermogram [7].

Another popular method used for assessing muscle activation is surface electromyography (sEMG). This technique measures the electrical activity of skeletal muscles by detecting their electric potential when muscle cells are activated. It is possible to investigate the activity of a particular muscle with a pair of electrodes attached or inserted on the skin above the muscle [8].

Influence of different types of additional load on muscle activation have been determined in numerous studies. Load in a form of a hockey bag of different sizes [9] or backpack worn in different positions [10-13] was examined. The influence of carrying an additional load in one and both hands on muscle activation was investigated [14]. In most cases muscle activity was assessed by sEMG. To the best knowledge of authors, a study concerning the influence of additional load in form of a laptop bag

carried in different forms on muscle activity by means of IRT has not been done yet.

Currently women and men keep their personal belongings, documents, electronic devices and everyday life items in bags. They use their hands or shoulders as a support or put a long strap across their torso. Carrying backpacks on one shoulder is also popular among students [15]. These four modes of carrying additional loads are going to be examined. Infrared thermography was chosen as it allows researchers to analyse a whole area at once, contrary to EMG. It is also a non-invasive and requires no contact what is its main advantage.

This study aims to determine the relationship between different types of asymmetrical loads and muscle activation with the use of IRT. The muscles chosen to be analysed are: *latissimus dorsi*, *trapezius* and *obliquus abdominis*.

2. Materials and methods

A group of four college students were used in the study, aged 23 ± 1 , height 180 ± 3.4 cm and weight 76 ± 11.6 kg. They were without any injuries and visible asymmetry/faulty posture.

Infrared thermography measures skin temperature, which is highly influenced by a large number of external factors. Activities such as sunbathing or exercising can affect skin temperature, even several days after. Moreover, substances such as specific food or drinks, when consumed, may influence blood pressure and thus skin temperature. Showering or applying lotion on the skin, along with many skin-related activities must be strictly regulated in order to improve the quality and coherence of results obtained through thermography. To carry out this study, participants followed a standardised procedure [16]. The experiments were conducted in a 5×10 m room, which fulfills the standards of thermal imaging in medicine and physiotherapy - with a temperature between 22°C and 24°C and humidity levels between 24% and 28%. Experimental procedures was also identical for each participant.

Firstly, volunteers were asked to remove their tops and wait 20 minutes in order to acclimate their bodies to the study environment. Next, initial upper-body thermograms were taken (anterior and posterior) with the InfReC R300SR thermal camera positioned 3 m away from subjects and supported by a tri-pod. Once completed, the gait on a motorised treadmill (York Fitness T500 6010) was held for 1 km with a velocity equal to 4 km/h. A second thermograph was taken right after the gait sequence. A third thermograph was taken 5 minutes after the second one due to the presence of sweat on the skin after the activity, which has a cooling effect on the skin [17]. Each participant was assigned to carry the additional load in one of four different ways, as shown in Fig. 1.

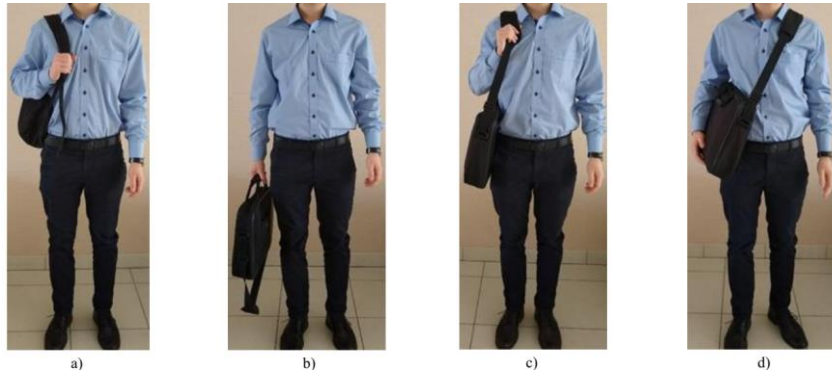


Figure 1. Four investigated modes of carrying load a) backpack carried on one shoulder b) laptop bag held in one hand c) laptop bag carried on one shoulder d) laptop bag with strap across torso

Each volunteer was required to walk with an additional weight value equal to 5%, 10% and 15% of their bodyweight as well as perform a control gait without additional load in order to determine the effects of each experiment. One sequence of measures took approximately 45 minutes per person and had to be done on separate days or after a one hour break so as not to disrupt the results. This resulted in about 3 h of measurements in total for each person. Every volunteer walked on a treadmill with one type of load. Types of load are assigned to the subjects according to the description:

Subject 1 - backpack carried on one shoulder

Subject 2 - laptop bag held in one hand

Subject 3 - laptop bag carried on one shoulder

Subject 4 - laptop bag with strap across torso

After all measurements were done, the results were analysed in the thermal imaging software InfReC Analyzer NS9500 Standard. Each approximate area of the 6 examined muscles was marked in the software as shown in Fig. 2.

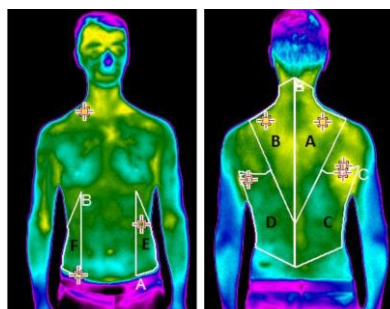


Figure 2. Muscles marked in thermal image software, A/B- *trapezius* - right/left, C/D- *latissimus dorsi* - right/left, E/F- *obliquus abdominis* - left/right

Additionally, the overall skin temperature average was measured for before and 5 minutes after gait, separately for the anterior and posterior torso and defined by the polygons traced.

3. Results

Table 1 presents the average temperature difference before and 5 minutes after gait between right and left side of investigated muscles. For Subject 1, difference in temperature between right and left *latissimus dorsi* after gait with no load is -0.11°C , which indicates bigger activation of the left *latissimus dorsi*. However, for gait with load, the temperature difference is positive, increases and reaches 0.21°C for load equal to 15% of body weight (Fig. 3). Changes in temperature difference for *trapezius* between no load and 15% body weight load is 0.01°C , therefore these changes are insignificant. Temperature difference between right and left *obliquus abdominis* decreases from 5% body weight with increasing load and obtains value of -0.31°C , which indicates that left obliquus abdominis is activated more during gait with load bigger than 5% of body weight.

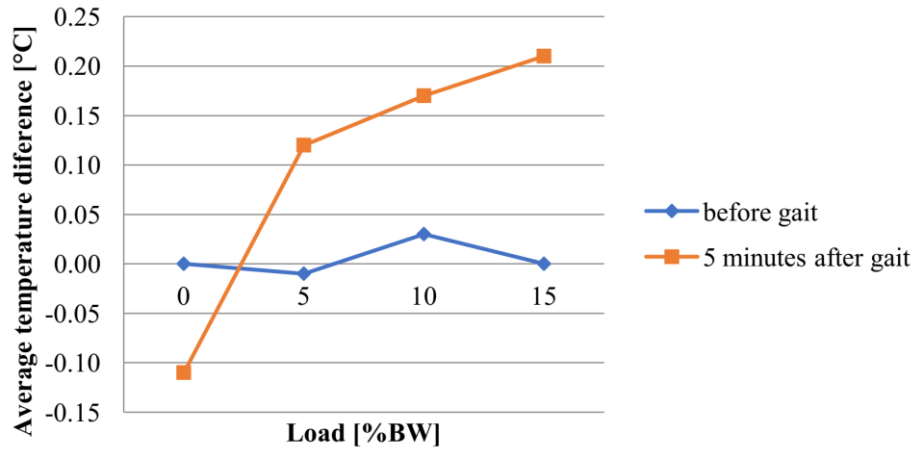


Figure 3. Average temperature difference between right and left *latissimus dorsi* for Subject 1

For Subject 2 difference in temperature between right and left side of the examined posterior muscles (*latissimus dorsi* and *trapezius*) rises with increasing load. It can be observed that left muscles are more active during no load gait and the right muscles become more active with increasing weight of the load. The right *latissimus dorsi* and *trapezius* become more active than left for 15% body weight load, as the temperature difference reaches 0.06°C and 0.18°C for *latissimus dorsi* and *trapezius* respectively. Opposite phenomenon is observed in *obliquus abdominis* as shown in Fig. 4. With increasing weight

of the load the difference between right and left muscles decreases and obtains value of -0.37°C , which indicates increase in left *obliquus abdominis* activation.

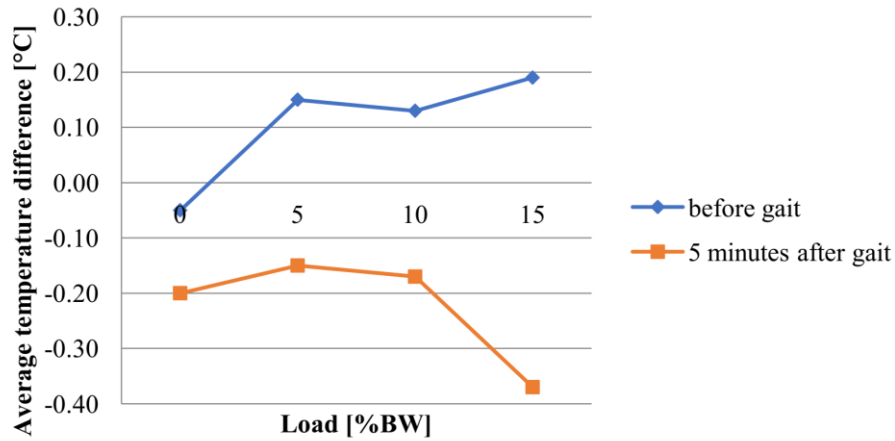


Figure 4. Average temperature difference between right and left *obliquus abdominis* for Subject 2

For Subject 3 increase in temperature difference after gait is observed for *latissimus dorsi* and *trapezius* throughout experiments which is interpreted as continuous growth in right side muscles activation. The temperature difference between right and left side for gait with no load is -0.33°C and -0.31°C , whereas for gait with 15% body weight load is 0.06°C and 0.20°C for *latissimus dorsi* and *trapezius* respectively. It may be caused by the asymmetry in muscle activity before gait shown in Fig. 6. Increase of temperature difference of *trapezius* is shown in Fig. 5. Investigated posterior muscles are more activated on left side for loads below around 10% of body weight, because the temperature difference between right and left *latissimus dorsi* is -0.08°C and *trapezius* -0.05°C . Right side muscles activation dominates for greater loads. *Obliquus abdominis* presents reversed trend and right side muscles are stronger activated.

For Subject 4 continuous growth in temperature difference after gait is observed for all attempts with load. Gait without load causes temperature difference to fall for *latissimus dorsi* and *obliquus abdominis* muscles. The decrease is 0.03°C for *latissimus dorsi* and 0.10°C for *obliquus abdominis*. *Trapezius* and *obliquus abdominis* muscles are continually more activated on right side of the body. The increase of temperature difference for *trapezius* is shown in Fig. 7. *Latissimus dorsi* on left side side is stronger activated for loads up to around 10% of body weight. With further increasing load right side side is dominant. The total increase of temperature difference between right and left *latissimus dorsi*, *trapezius* and *obliquus abdominis* is 0.15°C , 0.36°C and 0.09°C respectively.

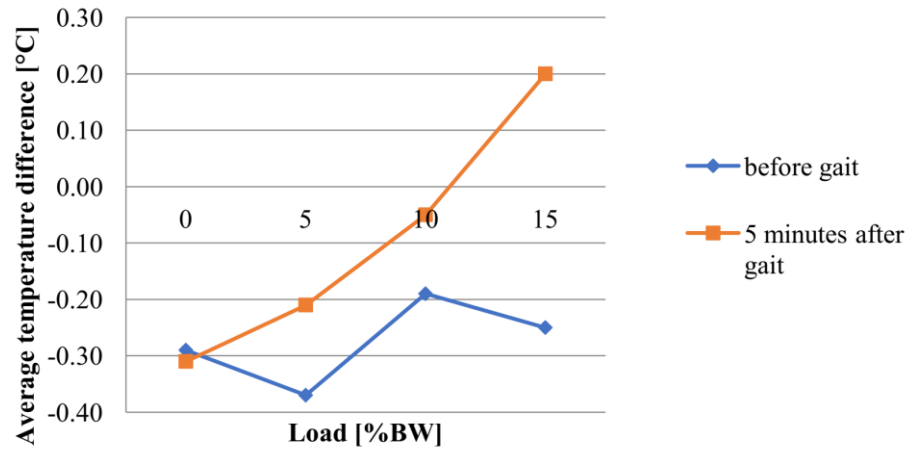


Figure 5. Average temperature difference between right and left trapezius for Subject 3

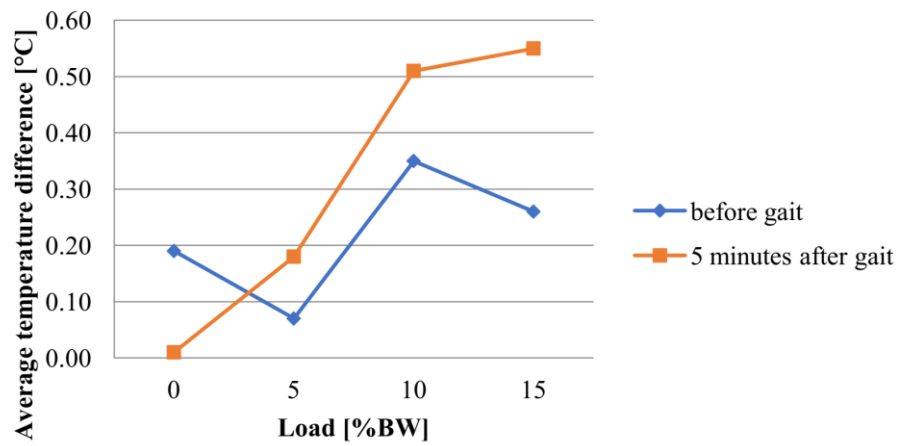


Figure 7. Average temperature difference between right and left trapezius for Subject 4

Table 1 Average temperature difference between right and left muscle in °C

	no load		5% of body weight		10% of body weight		15% of body weight	
	before	after	before	after	before	after	before	after
Subject 1								
latissimus dorsi	0.00	-0.11	-0.01	0.12	0.03	0.17	0.00	0.21
trapezius	0.00	0.05	0.01	0.00	0.07	0.02	0.05	0.06
obliquus abdominis	0.01	-0.03	-0.06	0.04	-0.01	-0.10	0.04	-0.31
Subject 2								
latissimus dorsi	-0.11	-0.32	0.07	-0.19	0.00	-0.16	0.24	0.06
trapezius	-0.22	-0.27	-0.16	-0.31	-0.12	-0.18	-0.06	0.18
obliquus abdominis	-0.05	-0.20	0.15	-0.15	0.13	-0.17	0.19	-0.37
Subject 3								
latissimus dorsi	-0.21	-0.33	-0.07	-0.12	0.17	-0.08	0.14	0.06
trapezius	-0.29	-0.31	-0.37	-0.21	-0.19	-0.05	-0.25	0.20
obliquus abdominis	0.42	0.19	0.25	0.08	0.32	-0.03	0.47	0.01
Subject 4								
latissimus dorsi	-0.06	-0.09	-0.02	-0.18	0.08	0.02	0.06	0.09
trapezius	0.19	0.01	0.07	0.18	0.35	0.51	0.26	0.55
obliquus abdominis	0.24	0.34	0.18	0.19	0.20	0.29	0.24	0.33

4. Discussion

As a result of thermoregulation being activated, the average body temperature decreased after gait in all cases. Since the experiment is focused on the effects of an asymmetrical load on the specified muscles, temperature difference between left and right muscles after gait with different loads is considered and compared. Additionally, temperature difference between left and right muscles before

the gait is also taken into consideration, because the experiments with different load were done on separate days. One can observe fluctuation of the aforementioned temperature difference in many cases.

As stated, skin temperature highly depends on external factors. For Subject 1 no significant difference is noticed in the temperature between left and right *trapezius*. This muscle is responsible for raising the upper limbs. Therefore, the volunteer does not raise the shoulder while carrying backpack on it. However, the center of gravity is changed during the gait with load on the right hand side and to keep the balance the body activates more the right *latissimus dorsi* and left *obliquus abdominis*. Similar testing procedure was applied by [18] but the measuring technique was electromyography. Results in presented study deny conclusions stated in the article which proves the significant difference only for *trapezius* and no changes in lower muscles (*latissimus dorsi* and *obliquus abdominis*). In our study such dependence is observed in all cases except of the cross body laptop bag. For Subject 2 it is visible that all left side muscles are more activated after the gait with no load, however, before gait those temperature differences were smaller. It may be caused by asymmetrical movement during gait. It would be reasonable to check the activity of leg muscles or feet pattern during gait. Such asymmetry may be caused by hip, knee or ankle injury that the body wants to compensate. Only when the load equal to 15% of body weight is applied the right *latissimus dorsi* and right *trapezius* are more active than left correspondent. According to the experiment carried by [19] the biggest differences should be visible for the volunteer carrying bag much lower than the level of the shoulder. In presented study this theory is not proven. The Subject 2 does not show any significant differences even for 15% of body weight. For Subject 3 it may be concluded that the posture is not exactly symmetrical according to the sagittal plane. From the numerical data it can be seen that before gait *obliquus abdominis* are more activated on the right side. At the same time the left *trapezius* is more activated. The volunteer admits that most of the time all the belongings are held in the bag on the right shoulder what may cause permanent spine curvature. The experiment carried by [20] proves the asymmetrical muscle activity among children with problem of scoliosis with one curve as well as double curve [20]. In presented study the temperature difference between right and left muscles before any activity is not near the zero value, therefore, it may be concluded that the Subject 3 suffers from one side scoliosis what was also proven by the Adams test. For Subject 4 as it was mentioned before, this is the only case where all examined muscles are more activated on the right hand side than those on the left side. *Trapezius*, the muscle responsible for elevation of the scapula, is more and more activated with increasing load to carry some part of the additional weight. If the load is not distributed bilaterally, there is an increased muscle activity of the *trapezius* muscle on the shoulder that the bag is worn on. The same conclusion was found in the paper written by [18]. In all examined cases where the additional load was distributed nonuniformly the *trapezius* was more activated on the side where the strap was held on. This is due to the Subject trying to maintain the proper scapula position to ensure the strap of the bag is kept over the

shoulder while the trunk is laterally flexed so that the centre of mass of the body remains over the base of support during gait.

5. Conclusions

Obtained results show that during gait with additional load held in asymmetrical manner, right and left muscle activity changes. With increasing weight of the carried load, the differences become larger in order to compensate the change of the centre of gravity. The compensation appears in some muscles only when the load reaches 10% of body weight, because for lower loads by other muscles. Different types of loading cause different patterns of compensation. Additionally, it was shown that for different type of carrying the bag/backpack subjects activate their muscles in a different way. The common phenomenon is increased right or left *latissimus dorsi*, *trapezius* and *obliquus abdominis* activity in the majority of cases. Since the thermal camera measures the temperature of the surface of the skin, it is impossible to assess from which muscle the heat comes from if there are two muscles overlapping one another. The temperature on the skin results from the heat conduction between the two aforementioned muscles. The results indicate that walking with the load in each of the four examined manners increase possibility of muscle injury as well as lead to or increase faulty posture.

Acknowledgments

This paper is an effect of the Research Project conducted by the students of Advanced Mechanical Engineering at the Faculty of Mechanical Engineering Łódź University of Technology under the supervision of PhD Bartłomiej Zagrodny and was supported supported by the Grant for Young Scientists Lodz University of Technology

References

- [1] Johnson J., Exercise and the cutaneous circulation. *Exerc. Sport Sci Rev.*, (1992), 59-97.
- [2] Joyner M. and Casey D., Regulation of increased blood flow (hyperemia) to muscles during exercise: a hierarchy of competing physiological needs. *Physiol Rev.* 95(2) (2015), 549-601.
- [3] Nagashima K., et al. Exercise and thermoregulation. *J. Phys Fitness Sports Med* 1(1) (2012), 73-82
- [4] Lenhardt R., et al. Thermoregulation and Hyperthermia. *Acta Anaest. Scand Suppl*, 109(34) (1996)
- [5] Escamilla-Galindo V., et al. Skin temperature response to unilateral training measured with infrared thermography. *J. Exerc Rehabil*, 13(5) (2017), 526-534.
- [6] Rodriguez D., et al. Infrared thermography applied to lower limb muscles in elite soccer players with functional ankle equinus and nonequinus condition. *Peer. J.*, 25(7) (2017)
- [7] Singh M. H., Principle and Operation of Thermal Imaging Systems. *Sensors* 17(5) (2017)
- [8] Mills K., The basics of electromyography. *J. of Neurol. Neurosurg. & Psych.* 2(2) (2005), 32-35.

- [9] Corrigan L., The Effect of Unilateral Load Carriage on the Muscle Activities of the Trunk and Lower Limbs of Young Healthy Males during Gait. Ottawa, 2012.
- [10] Devroey C., et al. Evaluation of the effect of backpack load and position during standing and walking using biomechanical, physiological and subjective measures. *Ergonomics* 50(5) (2007), 728-742
- [11] Chow D., et al. The effect of backpack load on the gait of normal adolescent girls. *Ergonomics* 48(6) (2005), 642-656
- [12] Hong Y. et al. Effect of prolonged walking with backpack loads on trunk muscle activity and fatigue in children. *Journal of Electromyography and Kinesiology* 18(6) (2008), 990-996.
- [13] Simpson K., et al. Backpack load affects lower limb muscle activity patterns of female hikers during prolonged load carriage. *J. of Electromyog. and Kinesiol.* 21(5) (2011), 782-788.
- [14] McGill S., et al. Low back loads while walking and carrying: comparing the load carried in one hand or in both hands. *Ergonomics* 56(2) (2013), 293-302.
- [15] Alami A., et al. A Study of Features of Backpack Carrying Methods by Schoolchildren: A Population Based Study. *Int. J. of Pediatrics* 6(11) (2018), 8517-8525.
- [16] Bauer J. and E. Dereń. Standardization of infrared thermal imaging in medicine and physiotherapy. *Acta Bio-Optica et Informatica Medica* 20(1) (2014), 11-20.
- [17] Akimov D., Skin temperature and lactate threshold during muscle work in athletes. *Human Physiology*. 37(5) (2011), 621-628.
- [18] Hardie G.R., The effects of bag style on muscle activity of the trapezius, erector spinae and latissimus dorsi during walking in female University Students. *J. of Human Kinetics* 45 (2015), 39-47.
- [19] Grimmer K., Adolescent standing postural response to backpack loads: a randomised controlled experimental study. *BMC Musculo Disord.* 3 (2002), 74-84.
- [20] Dragan S., Application of thermography in diagnostics and prognostication of scoliosis treatment. *Acta Bioeng. Biomech.*, 4(1) (2002), 63- 70.

Jarosław Chruściel, M.Sc.: Łódź University of Technology, Stefanowskiego 1/15, Łódź, Poland

Anna Frątczak, M.Sc.: Łódź University of Technology, Stefanowskiego 1/15, Łódź, Poland

Angelika Puchalska, M.Sc.: Łódź University of Technology, Stefanowskiego 1/15, Łódź, Poland

Siam Streibl, M.Sc.: Łódź University of Technology, Stefanowskiego 1/15, Łódź, Poland

Bartłomiej Zagrodny, Ph.D.: Faculty of Mechanical Engineering, Łódź University of Technology, Department of Automation, Biomechanics and Mechatronics, Stefanowskiego 1/15, Łódź, Poland

Finding globally optimal combinations of cranes drive mechanisms by the method of exhausting alternative design structures of mechanisms

Stefan Chwastek

Abstract: During certain crane operations: hoisting or lowering the payload connected with a slewing jib, generated are Euler and Coriolis forces whose impacts should be minimized already at the stage of selection of the system parameters and mechanism structure. The Machine and Mechanism Theory provides a method of exhausting kinematic chains which involves identification of all possible alternatives of kinematic structures with respect to the required number of degrees of freedom and field of work. This article outlines a methodology of selecting optimal structure from a set of possible solutions. Optimization of a multi-drive machine, needs to take into account the interactions between cooperating mechanisms. By introducing a certain quality criterion, a set of parameters optimized for the full range of motion is determined for each structure. Accordingly, each structure is assigned a value of the optimum quality index. The method was illustrated for a one-link crane with lever mechanisms, and comparison was made with ropes mechanisms. Optimization tasks were formulated assuming the ideal stiffness of the structure in quasi-static conditions. Effectiveness was verified under dynamic impact conditions, taking into account rope flexibility. Finding globally optimal design solution it comes to the best combination of different mechanisms allows the dynamic overload values to be significantly reduced at the stage of design of the steel structure.

1. Introduction

Similar issues were addressed in [4, 5]. In the work [4] the minimum deviation of the vertical load is sought for a finite number of boom positions, basing on the linearized form of the objective function. The study [4] summarizes the efforts to find the optimal position of blocks in a compensation mechanism such that the boom unbalance moment should be minimized. Optimization of the crane luffing mechanism based on Gray Fuzzy Optimal Model is described in [7]. The study [5] explores the trajectory optimization of a double-rocker four-bar mechanism with an objective to minimize the amplitude of its trajectory. After analyzing the sensitivity of the system, the number of decision variables was reduced from six to four. The searching method was applied to handle the set of 3^4 elements. A set of lengths of movable cells of the crane mechanism was obtained from the minimum deviation of the vertical load condition. In fact the method presented in [3] gives a nearly identical solution. In order to ensure realizability of the movement within the assumed angular range, certain

restrictions arising from the Grashoff conditions were introduced in the optimization problem. However, none of the previously mentioned works explore the, potential use of alternative structures of mechanisms when searching for globally optimal solutions. Optimization of a multi-drive machine, needs to take into account the interactions between mechanisms. Tower cranes with the luffing boom are machines, where individual mechanisms: slewing boom, load lifting and counterbalance mechanisms can operate simultaneously. Multi-stage optimization consists in the best adjustment of parameters of the subsequent mechanism connected to the structure of previously configured mechanisms. The order in which the mechanisms are connected is of great importance. Parametric optimization involving the exploration of alternative design structures of mechanisms is aimed to yield the best combination of independent drive mechanisms from a previously selected set of structures with optimum parameters.

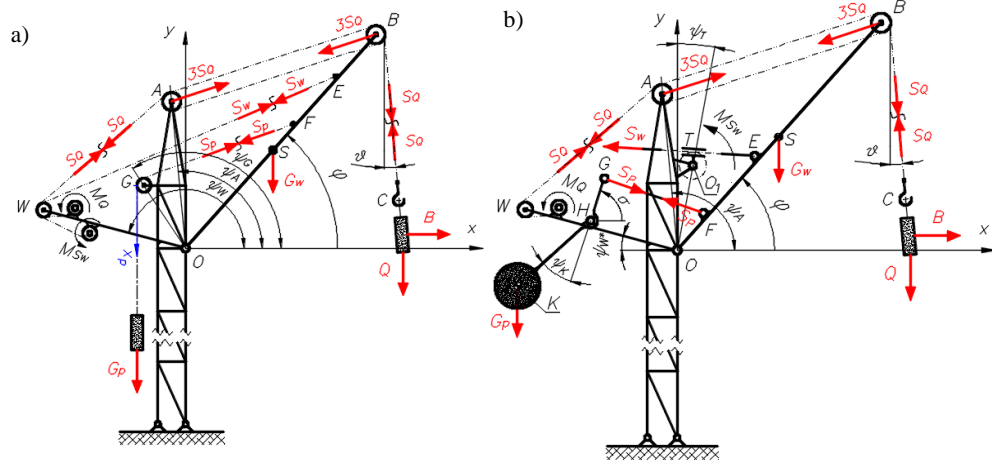
2. Optimization by the method of exploring alternative design structures of mechanisms

The primary focus in structural design of modern cranes is on minimization of forces acting in hoist ropes and reduction of energy consumption involved in crane operation. The method of exhausting kinematic chains which involves identification of all possible alternatives of kinematic structures with respect to the required number of degrees of freedom and field of work [1, 2]. Method of selective analysis of mechanism structures in this approach was developed into the method of synthesizing globally optimal configurations of cooperating mechanisms. The structure and optimal parameters of the slewing mechanism were adopted on the basis of the work [3]. Optimization of slewing mechanism discussed in [3] in fact could be applied to the rope mechanism in a winch. The main objective in optimization of the luffing mechanism was to ensure such roping configuration so as to minimize the horizontal hook trajectory error for the full variability range of the angle of the jib horizontal inclination when the winch is blocked. Apparently, for a crane with a pivoting boom, there is no good alternative for a luffing mechanism based on a roping system, yet as far as lifting jib mechanisms and counterweights are concerned, novel solutions can be sought among available mechanical structures. Consequently, the research task now will involve the search for globally optimal selection of crane mechanisms. And so for counterbalance mechanisms of any structure, the residual moment of imbalance depends on the angular position of the boom and the p_i parameters (where $i = 1, 2, \dots, k$) of the counterbalance mechanism. The set of optimal parameters is determined by the condition whereby the square functional $J(p_1, p_2, \dots, p_k)$ ought to be minimized. In the optimization procedure, p_i –parameters become optimization variables belonging to a limited set of allowable solutions – Ω , where $\Omega \subset R^{k+r}$. Each structure was assigned a value of the optimum quality index – L_m . The optimum quality index represents the value of the slewing work of the unloaded boom which will be performed by the mechanism with optimum parameters. Index – m represents

the number of the counterweight mechanism. Obviously, this will be the lowest value of work for a given structure, assuming the length and weight of the boom remain unchanged. Optimization of the boom lifting mechanism is carried out for a particular counterbalance mechanism. Thus we get some variants of solutions and optimization tasks are possible. When these are solved, the values of the optimum quality index – S_{Wmn} can be determined. Index n – represents the number of the boom lifting mechanism. The optimum quality index becomes the maximum value of the force acting in the lifting cable – S_W at the full slewing cycle of the boom under the nominal load – Q . The indices m, n identify the correlation: m - th counterbalance mechanism with the n - th boom lifting mechanism in the given crane structure variant. The set of optimal parameters is determined by the imposed condition that the square functional $J(p_{k+1}, p_{k+2}, \dots, p_{k+r})$ be minimized. All parameters determined in previous sections remain constant throughout the entire optimization procedure. Parametric optimization in the enumeration of alternative structures of mechanisms is aimed to yield the best combination of different mechanisms in a given structure from a previously selected set of structures with optimum parameters Ω_0 . Where $\Omega_0 \subset \Omega$. The sets of decision variables for different optimization problems should be independent. If it is not possible, the combined criterion should be derived in the form of a functional with weighting factors

3. Cranes with a pivoting jib as complex dynamic systems

Material handling operations give rise to Euler and Coriolis forces whose impacts should be minimized already at the stage of selection of the system parameters and mechanism structure.



Optimization of a multi-drive machine, i.e. a tower crane with a pivoting boom, needs to take into account the interactions between cooperating mechanisms. For each investigated crane mechanisms, the specific optimization task is formulated by defining the objective function, typically in the form of quadratic functionals. Thus, for the assumed lifting capacity and distance jaunt we get the structure of the crane mechanism that guarantees the minimal energy consumption. This study investigates the energy efficiency of the jib lift mechanism structures: that with unilateral constraints (rope mechanisms) – see Figure 1.a) and with bilateral constraints (eg. lever mechanisms) see Figure 1.b), so that they can be optimized together with the jib-balancing mechanism. Thus obtained optimal sets of parameters for the mentioned mechanisms were optimized for the full range of the slewing motion. The angle variability range $\varphi \in [15^\circ \div 75^\circ]$. Major parameters include the length and weight of the boom $L_{OB} = 30$ m and $G_W = 45$ kN and the weight of the load $Q = 50$ kN. Respective forces acting in ropes due to lifting load – S_Q , jib lifting – S_W , counterweight – S_P act at acute angles to the jib: $\alpha = \alpha(\varphi)$, $\beta = \beta(\varphi)$, $\gamma = \gamma(\varphi)$ - not indicated in Figure 1. The physical model of a one-link crane is governed by the following equations of motion:

$$\begin{cases} J_{WO} \varepsilon_\varphi = L_{OB} \left[3 \sin(\alpha) \cdot S_Q - \cos(\varphi - \nu) \cdot S_Q + \kappa_{OE} \sin(\beta) \cdot S_W + \kappa_{OF} \cdot \sin(\gamma) \cdot S_P - \kappa_{OS} \cos(\varphi) \cdot G_W \right] & (1) \\ m_Q \left[a_{BC} - L_{BC} \cdot \omega_\nu^2 - L_{OB} \sin(\varphi - \nu) \cdot \varepsilon_\varphi + L_{OB} \cos(\varphi - \nu) \cdot \omega_\varphi^2 \right] = \cos(\nu) \cdot Q - S_Q & (2) \\ m_Q \left[L_{BC} \cdot \varepsilon_\nu + 2 \cdot \omega_\nu \cdot v_{BC} - L_{OB} \cos(\varphi - \nu) \cdot \varepsilon_\varphi - L_{OB} \sin(\varphi - \nu) \cdot \omega_\varphi^2 \right] = -\sin(\nu) \cdot Q & (3) \end{cases}$$

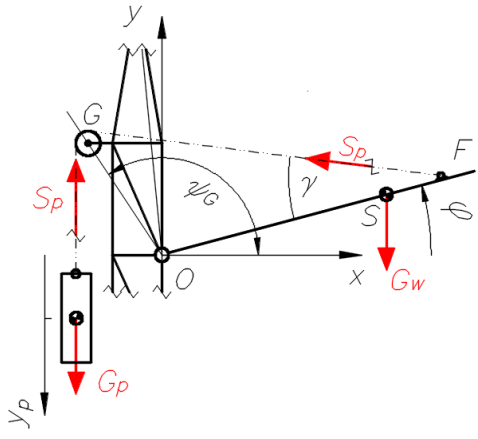
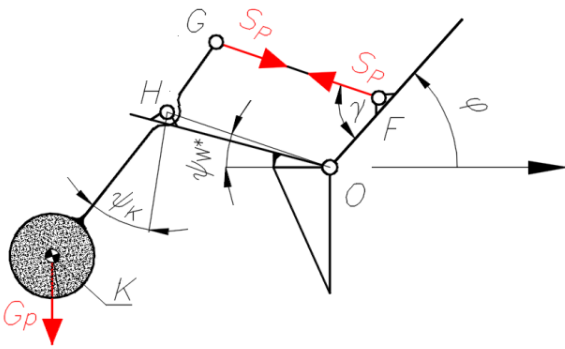
where: ε_φ , ω_φ – angular acceleration and angular velocity of the jib, ε_ν , ω_ν – angular acceleration and angular velocity of the load Q , a_{BC} , v_{BC} – acceleration and velocity of the longitudinal motion of the load Q , a_{XP} – vertical acceleration of the counterweight G_P , κ_{OE} , κ_{OF} , κ_{OS} – normalized with respect to L_{OB} distances: $|OE|$, $|OP|$, $|OS|$.

The first equations govern the motion of the boom and the load respectively. For a fixed structure of the slewing mechanism, these equations remain unchanged. Changing the structure of the boom lifting mechanism does not alter the form of these equations. Changing the structure of the counterweight mechanism requires the alteration of equation of motion. The motion of the specific counterbalance mechanism, describes equations (4) and (5) in Table 1.

4. Exhausting the alternative structures of counterweight mechanisms

For the purpose of this study, two structures of counterbalance mechanisms are considered whose structures are shown in Table 1, together with the governing equations. Each structure was assigned a value of the optimum quality index - L_m . (index m – represents the number of the counterweight mechanism according to Table 1). The optimum quality index represents the value of the slewing work of the unloaded boom which will be performed by the mechanism with optimum parameters. Obviously, this will be the lowest value of work for a given structure, assuming the length and weight of the boom remain unchanged.

Table 1. Selected structures of counterweight mechanisms and they optimum quality indexes

Nr	Diagram of the counterbalance mechanism, equation of motion	Optimal parameters	L_m
1	 <p>Figure 2. Rope counterbalance mechanism</p> $m_P \cdot a_{y_P} = G_P - S_P \quad (4)$	$p_1 = L_{OG} = 7.065 \text{ m}$ $p_2 = L_{OF} = 30 \text{ m}$ $p_3 = \psi_G = 85.489^\circ$ $p_4 = G_P = 67 \text{ kN}$	$L_{11} = 51.43 \text{ kJ}$
		$p_1 = L_{OG} = 7.065 \text{ m}$ $p_2 = L_{OF} = 30 \text{ m}$ $p_3 = \psi_G = 85.489^\circ$ $p_4 = G_P = 76.5 \text{ kN}$	$L_{12} = 0.72 \text{ kJ}$
2	 <p>Figure 3. Counterbalance lever mechanism</p> $J_P \varepsilon = G_P L_{HK} \cos(\varphi + \psi_K) + S_P L_{OF} \sin(\varphi - \psi_W) \quad (5)$	$p_1 = L_{OF} = 4 \text{ m}$ $p_2 = L_{HK} = 5 \text{ m}$ $p_3 = \psi_K = 0^\circ$ $p_4 = G_P = 115.7 \text{ kN}$ $L_{OH} = L_{GF}$ $L_{OF} = L_{GH}$	$L_{21} = 44.95 \text{ kJ}$
		$p_1 = L_{OF} = 4 \text{ m}$ $p_2 = L_{HK} = 5 \text{ m}$ $p_3 = \psi_K = 0^\circ$ $p_4 = G_P = 103 \text{ kN}$ $L_{OH} = L_{GF}$ $L_{OF} = L_{GH}$	$L_{22} = 0 \text{ kJ}$

The optimum index can be calculated from the following dependence:

$$L_m = \int_{\varphi_{min}}^{\varphi_{max}} M(\varphi) d\varphi \quad (6)$$

Where $M(\varphi)$ is the residual moment of the boom unbalance (for $Q = 0$):

$$M(\varphi) = G_W L_{OS} \cos(\varphi) - S_P(\varphi) L_{OF} \sin(\gamma) \quad (7)$$

The moment $M(\varphi) = M(\varphi, p_1, p_2, \dots, p_k)$ depends on the angular position of the boom and the p_i parameters (where $i = 1, 2, \dots, k$) of the counterbalance mechanism. The set of optimal parameters is determined by the condition whereby the square function ought to be minimized:

$$J(p_1, p_2, \dots, p_k) = \int_{\varphi_{min}}^{\varphi_{max}} [M(\varphi, p_1, p_2, \dots, p_k)]^2 d\varphi. \quad (8)$$

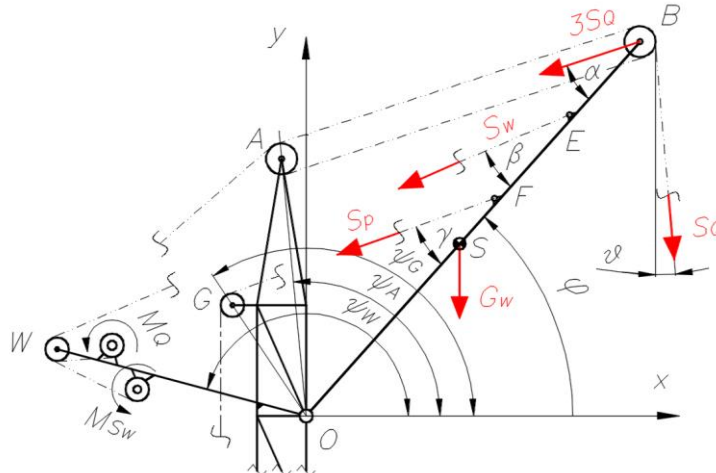
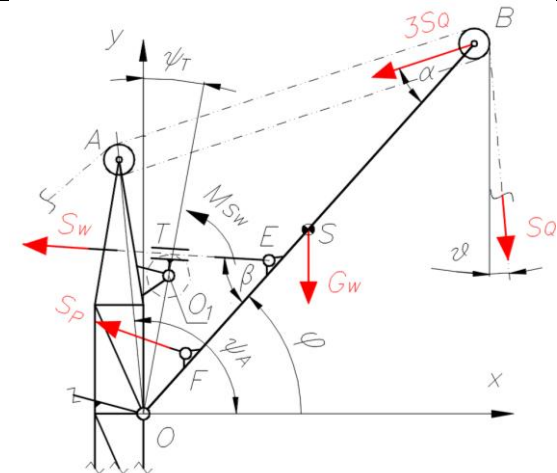
Thus the limitations imposed on the parameters p_i , need to be taken into account, as explained in more detail in [3]. Dimensions (G_w, L_{OS}) present in the dependence (7), as unrelated to the counterbalance mechanism – are considered as constant parameters in the optimization procedure. Rearranging the equation (4) or (5) (depending on the type of mechanism under consideration) we obtain a formula representing the force acting in the cable in equations (1). However, in the optimization procedure, the influence of the counterweight acceleration in equations (4) and (5) is neglected in order to determine its dependence on force – S_p . Comparing the quality index of the two optimized mechanisms shown in Table 1, the choice of the lever counterweight mechanism is obvious. It should be noted, however, that the optimization procedure takes into account only the mechanical properties of each solution, without considering the involved costs. The rope mechanism, due to unilateral constraints, excludes the occurrence of compressive forces in the line and therefore the optimum quality index has a relatively high value. When costs are considered in the optimization model, the functional (8) can be transformed into a weight criterion.

5. Exploring the alternative options of the jib lifting mechanism

Exploration of alternative design solutions of the boom lifting mechanisms was confined to two structures. It is worthwhile to mention that optimization of the boom lifting mechanism is carried out for a particular counterbalance mechanism. Thus we get four variants of solutions and four optimization tasks are possible. When these are solved, the values of the optimum quality index – $S_{w_{mn}}$ can be determined (index n – represents the number of the boom lifting mechanism according to Table 2). Table 2 shows the kinematic diagrams of boom lifting mechanisms: rope and rack mechanics, alongside the values of the optimum quality index – $S_{w_{mn}}$. The optimum quality index becomes the maximum value of the force acting in the jib lifting cable – S_w at the full slewing cycle of the boom under the nominal load – Q . The indices: m, n identify the correlation: m – th counterbalance mechanism with the n – th boom lifting mechanism in the given crane structure variant. The set of optimal parameters is determined by the imposed condition that the functional be minimized:

$$J(p_{k+1}, p_{k+2}, \dots, p_{k+r}) = \int_{\varphi_{min}}^{\varphi_{max}} [S_w(\varphi, p_{k+1}, p_{k+2}, \dots, p_{k+r})]^2 d\varphi. \quad (9)$$

Table 2. Selected structures of counterweight mechanisms and they optimum quality indexes

<i>n</i>	Diagram of the boom lifting mechanism, optimal parameters		
1	 <p>Figure 4. Boom-lifting rope mechanism</p>		
	<i>m</i>	Optimal parameters for a given configuration (<i>m</i> ,1)	S_{Wm1}
	1	$p_4 = G_P = 67 \text{ kN}$ $p_5 = L_{OE} = 30 \text{ m}$, $p_6 = L_{OW} = 10 \text{ m}$, $p_7 = \psi_W = 116.49^\circ$	17.67 kN
	2	$p_4 = G_P = 103 \text{ kN}$ $p_5 = L_{OE} = 30 \text{ m}$, $p_6 = L_{OW} = 10 \text{ m}$, $p_7 = \psi_W = 116.879^\circ$	14.64 kN
2	 <p>Figure 5. Boom lifting lever mechanism</p>		
	<i>m</i>	Optimal parameters for a given configuration (<i>m</i> ,2)	S_{Wm2}
	1	$p_4 = G_P = 76.5 \text{ kN}$, $p_5 = L_{OE} = 3.75 \text{ m}$, $p_6 = L_{OT} = 3 \text{ m}$, $p_7 = \psi_T = 5^\circ$	60.55 kN
	2	$p_4 = G_P = 115.71 \text{ kN}$, $p_5 = L_{OE} = 3.75 \text{ m}$, $p_6 = L_{OT} = 3.75 \text{ m}$, $p_7 = \psi_T = 13.5^\circ$	27.33 kN

The formula expressing the force S_W in the optimization problem involving the boom lift mechanism is derived from equation (1) for zero angular acceleration, ie for $\varepsilon = 0$. The force $S_W(\varphi) = S_W(\varphi, p_{k+1}, p_{k+2}, \dots, p_{k+r})$ depends on the boom angle and parameters p_j (where $j = k+1, k+2, \dots, k+r$) of the boom lifting mechanism. All parameters determined in previous sections remain constant throughout the entire optimization procedure. The total value of the nominal lifting work – L_{Qmn} depends on the type and parameters of the counterbalance mechanism, and is independent on the type and parameters of the boom lifting mechanism. For the counterweight mechanisms with optimum parameters according to Table 1, we will get: $L_{Q11} = 58.7$ kJ, $L_{Q12} = 7.353$ kJ, $L_{Q21} = 44.9$ kJ, $L_{Q22} = 6.6$ kJ. The value $L_{Q21} = 44.9$ kJ is associated with the need to reduce the weight of the counterweight to 103 kN in the ropes mechanism lifting the boom combined with lever mechanism of counterweight.

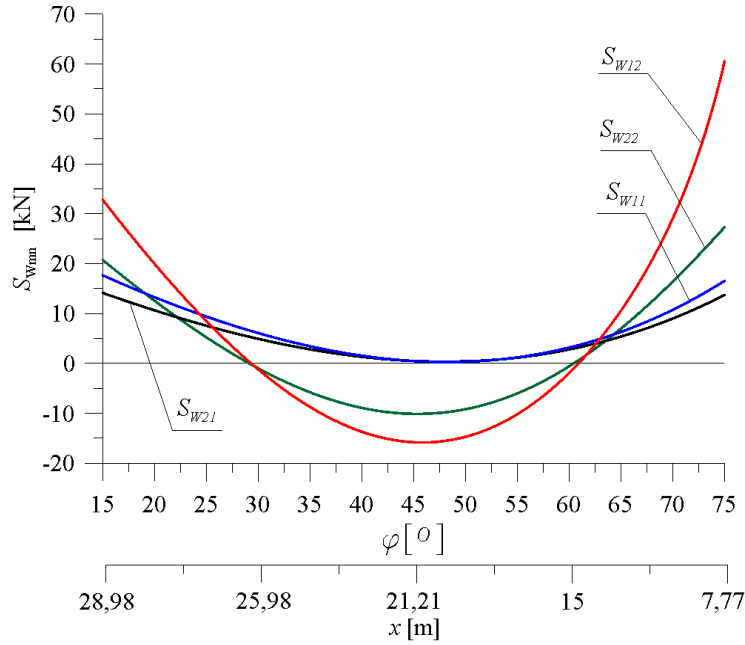


Figure 6. Forces acting in the cables of the jib-lifting mechanism during the slewing motion

Figure 6 confirms that in the task involving the synthesis of crane boom lifting mechanism, S_{Wmn} - is a better indicator of the optimality than the value of lifting work - L_{Qmn} .

Advantages of minimizing the force acting in the rope in the jib lifting mechanism are:

- Small rope diameter → small pulley → low resistance during rope winding,
- Low-power electric motors (approximately 8 kW) → reduced energy demand,
- Small force variations in ropes → less overloading of electric motors → little overheating of engines.

6. Verification of optimization results under dynamic conditions

To verify the optimization results in dynamic conditions it is required that flexibility in the system, including rope flexibility, should be taken into account. Rope flexibility is inversely proportional to its effective length (sag – l). Assuming the averaged value of the Young modulus $E = 125$ GPa for ropes with a non-metallic core, in accordance with [8], the modulus of elasticity of the rope is obtained from the formula:

$$k(l) = i_k \frac{EA}{l} \quad (10)$$

where: A – effective cross-section area of the rope, i_k – multiplicity of the pulley block.

Rope cross-section areas in rope mechanisms are calculated basing on [9] and taken to be identical, ie. $A_p = A_{sw} = A_Q = 3.83$ cm². Damping in the ropes is assumed to be proportional to the modulus of elasticity through the dimensionless damping factor ζ_0 (in this paper been assumed: $\zeta_0 = 0$). The effects of rope tension on its stiffness and damping are neglected. The duty cycle of each mechanism involves the following stages: start, steady-state motion and braking, yielding a trapezoidal characteristics of drive velocity.

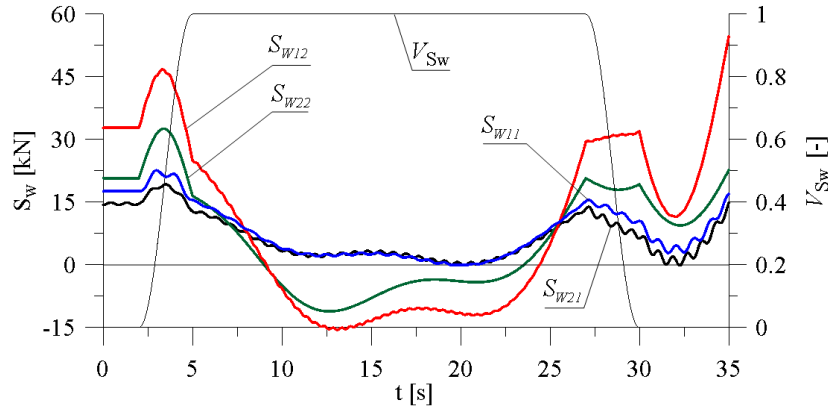


Figure 7. Comparison of dynamic forces acting in ropes of the hoisting boom

Basing on the catalogue data, the universal model of kinematic excitations is adopted differing in the steady-state velocity values for specific mechanisms. For the winch in the luffing mechanism steady-state velocity values is $V_{sw11} = V_{sw21} = 24$ m/min, whilst for the rack-and-pinion lift mechanism combined with combined with lever mechanism of counterweight $V_{sw22} = 9$ m/min, but combined with rope mechanism of counterweight $V_{sw21} = 7.2$ m/min. The steady-state velocity for the cargo winch $V_Q = 27$ m/min. The start-up and braking times are taken to be identical $t_{s/b} = 3$ s. Solving the Matlab-Simulink system of differential equations (1) yields the rope tension variations. Of particular importance is comparison of forces acting in ropes and power consumption in the crane with the rope lifting mechanism and various counterbalance mechanisms under dynamic conditions. It appears (see Figure 7) that dynamic forces acting in ropes whilst lifting the boom in the entire motion range are

smaller in the variant solution incorporating a counterweight lever mechanism, i.e. $S_{w21}(t) < S_{w11}(t)$ and $S_{w22}(t) < S_{w12}(t)$ for $T = 30$ s. The global optimal solution provides the lever counterbalance mechanism correlated with the rope mechanism of boom lifting. In the context of energy consumption, of particular importance are bilateral constraints in the boom-lifting mechanism. It is well demonstrated in Figure 8, indicating that that $P_{w22}(t) < P_{w12}(t) < P_{w21}(t) < P_{w11}(t)$ for $t \in [0; T]$. In this study the load characteristics of the drive motors are neglected, and for the purpose of comparison a more universal kinematic model governed by trapezoidal characteristics of velocity in normalized form – V_{Sw} is considered. Multiplying the normalized speed values by the specific steady-state velocity – V_{Swmn} , we obtain the drive characteristic for the relevant boom lifting mechanism. As shown in Figure 6, forces acting in the toothed rack in cranes incorporating a rack-pinion lift mechanism are greater than forces acting in ropes.

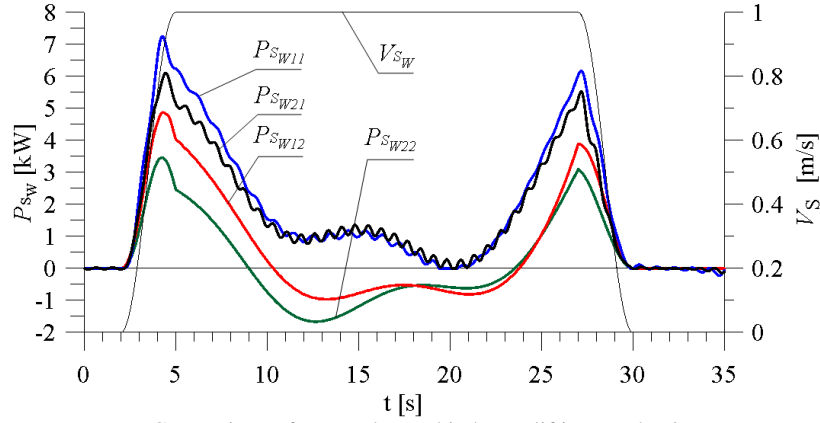


Figure 8. Comparison of power demand in boom lifting mechanisms

In terms of energy consumption, the optimal approach is to correlate the lever type counterbalance mechanism with the rack-pinion lifting mechanism, which is assumed to be self-locking.

7. Conclusions

Optimization tasks involving the two rope mechanisms and two lever mechanisms in a slewing jib crane lead us to the following conclusions:

- Parametric optimization in the enumeration of alternative structures of mechanisms is aimed to yield the best combination of different mechanisms in a given structure from a previously selected set of structures with optimum parameters Ω_0 . Where $\Omega_0 \subset \Omega$.
- For the assumed lifting capacity and distance jaunt we get such combination of counterbalance mechanisms with the crane lifting mechanism that guarantees minimal dynamic force and minimal energy consumption.
- By minimizing forces acting in ropes in the boom lifting mechanism, we improve the controllability of dynamic processes. This is particularly important in the context of effectiveness of active vibration reduction methods.

- The extended method of exploring alternative structures of mechanisms for parametric optimization, outlined in this paper, allows for finding globally optimal design solution and the method is a universal.
- Effective optimization, confirmed by dynamic analysis, allows the dynamic overload values to be significantly reduced at the stage of design of the steel structure, resulting in a lighter and cheaper structure.
- Application of dedicated software (such as Mathcad) to solve variational problems such as finding a minimum of properly formulated quadratic functionals proves to be very effective and rapid solution to parametric optimization problems.
- The main advantage of the presented method lies in its simplicity and universality, there is no need to simplify optimization criteria and the mathematical formulae are elegant and concise.
- The presented methodology was used in the optimization of the mechanism relieving the load from the movable seat in a heavy machine operator seat simulator and in the project aimed at modification of the multi-support structure of the malt conveyor.

8. Directions for future research

Solving the parametric optimization task with regard to a crane mechanism (or mechanisms) actually involves the optimization of the materials handling process carried out in a given space and time. If the optimization criterion in the luffing mechanism in the form of a quadratic functional is expanded to incorporate the condition imposed on the derivative $dy/d\varphi$, vibrations of the payload suspended on the hook can be thus reduced [3], which is clearly our objective and not an accidental effect. In precise transport operations, when utmost care is taken to comply with very strict regimes regarding the position and orientation of the payload, passive vibration reduction methods, including parametric optimization, may prove insufficient. In these cases active vibration reduction methods have to be implemented alongside the optimal control strategies of the payload movement based on variation methods, the Hamilton principle or the Pontriagin maximum principle. Parametric optimization should always precede functional optimization (i.e. optimization of control strategy).

References

- [1] Adamczyk E.: *Synteza strukturalna i geometryczna wielocłonowych ustrojów nośnych maszyn roboczych*. Wydawnictwo Politechniki Wrocławskiej. Wrocław 1982, ISSN 0324 -962X. (in polish)
- [2] Gronowicz A., Miller S.: *Mechanisms. Methods for creating alternative solutions, catalog of structural and kinematic diagrams*, Wydawnictwo Politechniki Wrocławskiej, Wrocław, 1997, ISBN 83-7085-257-2. (in polish)
- [3] Chwastek S.: *Optimisation of Crane Mechanisms – Selected Problems*; Key Engineering Materials, 2013, Vol. 542, pp. 43-58, Trans Tech Publications, Switzerland, DOI: 10.4028/www.scientific.net/ KEM.542.43.
- [4] Xue Y., Ji M.S., Wu N.: *The Dimensionless-Parameter Robust Optimization Method Based on Geometric Approach of Pulley Block Compensation in luffing Mechanism*; International Conference of Electrical, Automation and Mechanical Engineering, 2015, ISBN: 978-1-5108-0652-8.

- [5] Dong Soo Kim Jongsoo Lee: *Structural Design of a Level-luffing Crane Through Trajectory Optimization and Strength-based Sized Optimization*. Structural and Multidisciplinary Optimization, pp. 515–531, 2015, DOI: 10.1007/s00158-014-1139-2.
- [6] Cheng Wenming: *Optimization of cylindrical drum compensation luffing system for portal crane[J]; Hoisting and Conveying Machinery*; International Conference of Electrical, Automation and Mechanical Engineering, 2015, ISBN: 978-1-5108-0652-8.
- [7] Fei Ye, Zhu Tianen, Yu Haiyang: *Multi-objective Optimization of Crane Luffing Mechanism Based on Gray Fuzzy Optimal Model*; International Conference Applied Informatics and Communication - International Conference, 2011, Xi'an, China, Proceedings, Part II, Springer-Verlag GmbH Berlin Heidelberg 2011, ISBN 978-3-642-23219-0.
- [8] http://www.drumet.pl/pl,kat2,liny_specjalistyczne,8.html. (Ropes catalogue)

Stefan Chwastek PhD, MSc, assistant professor: Cracow University of Technology, Faculty of Mechanical Engineering, Kraków, Poland (stefan.chwastek@mech.pk.edu.pl).
The author gave a presentation of this paper during one of the conference sessions.

Adaptive fractional order control of a quadrotor

Eva-H. Dulf, Cristina-I. Muresan, Daniel D. Timis

Abstract: Due to their exceptional flying maneuverability and simple dynamics, multi rotor systems are widely used for various applications. Such systems vary overtime due to external disturbances or unmeasured changes to which they are subjected. In this case, a simple PID controller cannot provide the desired response, unless the controller parameters are re-tuned. An adaptive control algorithm responds to this need. Moreover, to increase robustness, fractional order controllers are designed, being recognized for this property. Such control provides the entire process with good robustness and ensures good operation for major process changes. The present paper describes a comparison between such an algorithm and a classical PID applied in an adaptive scheme to a quadrotor system.

1. Introduction

In the last few year researchers have shown an increased interest in developing control algorithms for multi rotor systems, due to their multiple applications in both military and civilian domains. Such aerial vehicles are used in surveying objects and ground on the basis of orthographic photos to generate point clouds, volume calculations, digital height and 3D models; industrial inspection of solar parks, wind parks, power lines, engines and plants, industrial parks; bridge inspection, visual structure assessment and monitoring, inspection and survey of structures; aerial images and photography; aerial movies and videography; condition-analysis and target-analysis to document construction sites, structural monitoring, sound barrier and wall monitoring, excavation documentation, plant and wildlife preservation and conservation, or any kind of first-responder activities in crisis regions [1, 2]. This was the motivation for the present work: to design and implement a laboratory platform to simulate the operation of a quadrotor system and to perform experimental tests for evaluating different control strategies. There are a series of prototypes [3, 4], each of these having advantages and also some drawbacks. The available laboratory scaled systems are much too expensive and created for some particular behavior. The main challenge in the control of these equipments arises from their special features like strong coupling subsystems, unknown physical parameters, nonparametric uncertainties and external disturbances. Therefore, with the goal of finding the optimal solution, the researchers developed various, linear and nonlinear, control techniques, such as PID control, orientation by vision, sliding mode control, fuzzy logic, predictive, feedback linearization, adaptive control, etc. [5]. Very good results are obtained with fractional order

controllers [6]. An application of fractional order sliding mode controller and neural networks to attitude control of a quadrotor is proposed in [7]. A fractional order filter with two-degrees-of-freedom PID controller for the pitch control of an UAV is presented in [8]. A fractional order proportional-integral controller design for the roll-channel or lateral direction control of a fixed-wing unmanned aerial vehicle is presented in [9, 10] and for the pitch control of a vertical takeoff and landing in [11]. Fractional order sliding mode controller is presented in [12] in path tracking, with an adaptive correcting coefficient in mass parameter of quadrotor. No results are reported with fractional order adaptive attitude control of quadrotors.

The present paper describes the quadrotor prototype realized by our team and the designed fractional order adaptive control, based on the experience gained in our previous research [13-16].

The paper is structured in five sections. After this short introductory part, section 2 describes the quadcopter prototype. Section 3 discusses the proposed control strategy, while the obtained results are presented in Section 4. The work ends with conclusions.

2. The quadrotor prototype

The simplified scheme of the quadcopter is presented in Fig.1, while the prototype is in Fig.2. The purpose of this experimental stand is to design and simulate, on physical equipment, the performance of certain algorithms and control methods. That was the main criteria in choosing the dimensions and the components.

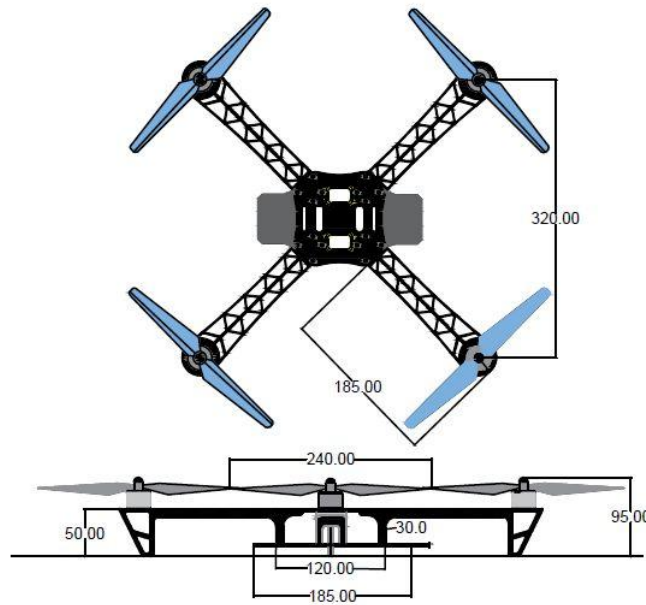


Figure 1. The simplified scheme of the designed quadrotor

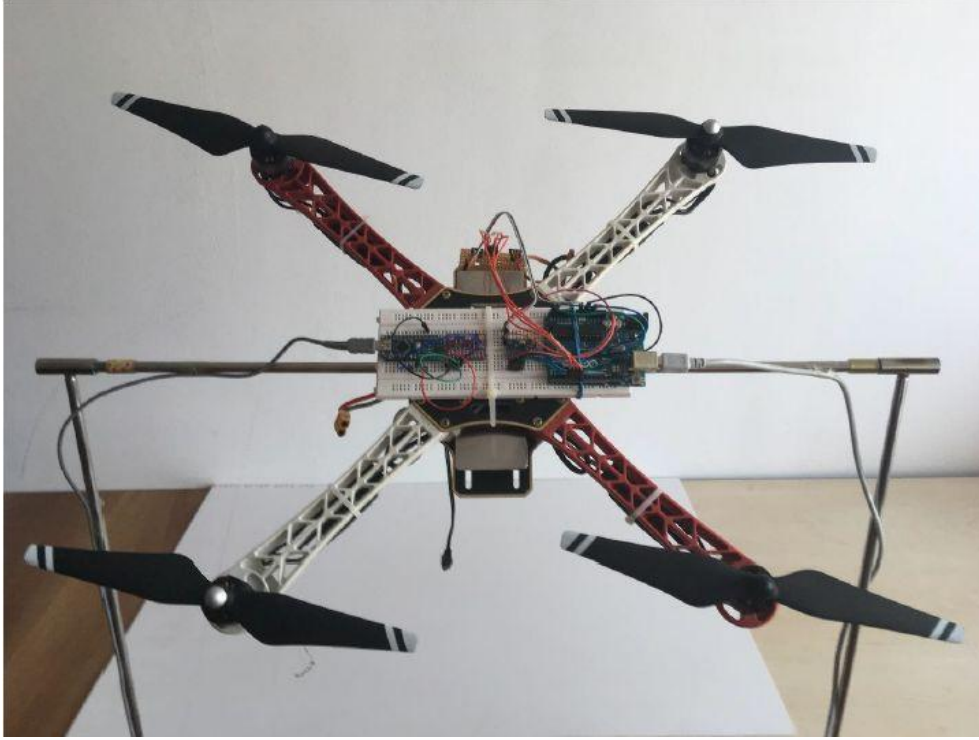


Figure 2. The prototype of the quadrotor

The framework of the quadcopter was purchased from a specialized manufacturer, type DJI F450 [17], having a total weight of 282g. The used rotors are DJI 2212, whit a diameter of 28mm, voltage of 11,1-14,8V, weight 56g. The propeller is a DJI 9450 type, having a diameter of 240mm, pitch of 127mm and 13g weight. The battery is DJI – PTM12 [17], with a capacity of 2200 mAh and a nominal voltage of 11.1V, which guarantees a flight time of about 15 minutes. The main advantage of the battery is the 176g weight. The electronic speed control element is DJI E300 [17], with a voltage of 11,1 – 14,8V, 15A current, frequency of 30 – 450Hz and 30g weight. As radio control kit a Hobby King model was selected, with 6 channels, model HK T6A V2 [17]. As sensors, a 9-axis sensor, type MPU 9150 [17], was chosen, which contains an accelerometer, a gyroscope and a magnetometer. The control unit is an Arduino UNO development board [17].

3. The proposed control strategy

For the constructed experimental quadcopter , the corresponding nonlinear mathematical model is established, based on general equations from [18]:

$$\ddot{\phi} = \frac{\cos\Psi}{I_{xx}} U_2 - \frac{\sin\Psi}{I_{yy}} U_3. \quad (1)$$

$$\ddot{\Theta} = \frac{\sin\Psi}{\cos\Phi I_{xx}} U_2 + \frac{\cos\Psi}{\cos\Phi I_{yy}} U_3. \quad (2)$$

$$\ddot{\Psi} = \frac{\sin\Psi \operatorname{tg}\Phi}{I_{xx}} U_2 + \frac{\cos\Psi \operatorname{tg}\Phi}{I_{yy}} U_3 + \frac{1}{I_{zz}} U_4. \quad (3)$$

where (ϕ) , (θ) and (ψ) represents the angular positions around the axes x, y and z; (U_i) , with $i=1,2,3,4$ are the rotor voltages, while (I_{xx}) , (I_{yy}) and (I_{zz}) are the inertia moments around the three axes. Due to the fact that the quadcopter is symmetric, both in terms of geometry and mass distribution, it can be stated that $I_{xx}=I_{yy}$.

The proposed control structure is depicted in Fig.3. The main elements are: the identification block, establishing the process parameters at each sampling period, the adaptation block establishing the new parameters of the controller and the recursive equation of the controller with adapted coefficients.

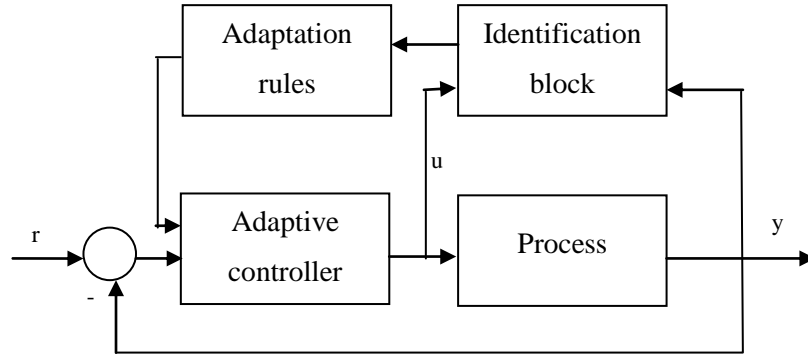


Figure 3. The adaptive control structure.

The used controller is a fractional order PID (FO-PID) controller, being recognized for their superiority over classical PID controllers [19]. The used form is:

$$H_{FO-PID}(s) = k_p \cdot (1 + k_d \cdot s^\mu + \frac{k_i}{s^\lambda}) \quad (4)$$

where $\mu, \lambda \in (0,1]$ are the derivative and integral order, k_p , k_d and k_i are the proportional, derivative and integral gains.

The controller tuning is based on the cost function expressed to satisfy the criteria of gain crossover frequency (ω_{gc}), phase margin (ϕ_m) and iso-damping property [16]:

$$|H_d(j\omega_{gc})| = |H_{FO-PID}(j\omega_{gc}) \cdot H_P(j\omega_{gc})| = 1 \quad (5)$$

$$\angle H_d(j\omega_{gc}) = \angle [H_{FO-PID}(j\omega_{gc}) \cdot H_P(j\omega_{gc})] = -\pi + \varphi_m \quad (6)$$

$$\left(\frac{d(\angle [H_{FO-PID}(j\omega) \cdot H_P(j\omega)])}{d\omega} \right)_{\omega=\omega_t} = 0 \quad (7)$$

where with (H_p) is the process model, (ω_{gc}) is the gain crossover frequency and (φ_m) represents the phase margin. Additionally, in the cost function control signal minimization is introduced.

$$CF = |f_1(x)| + |f_2(x)| + \dots + |f_n(x)| \quad (8)$$

where $[f_1(x) \ f_2(x) \ \dots \ f_n(x)]^T = 0$ is the system of nonlinear equations and $x = [k_p \ k_i \ k_d \ \lambda \ \mu]^T$ are the controller parameters.

The resulting nonlinear equation system is solved using a modified Particle Swarm Optimization (PSO) algorithm based on a technique developed by Eberhart and Kennedy [20].

The corresponding Simulink/Matlab® scheme for a single rotor is given in Fig.4.

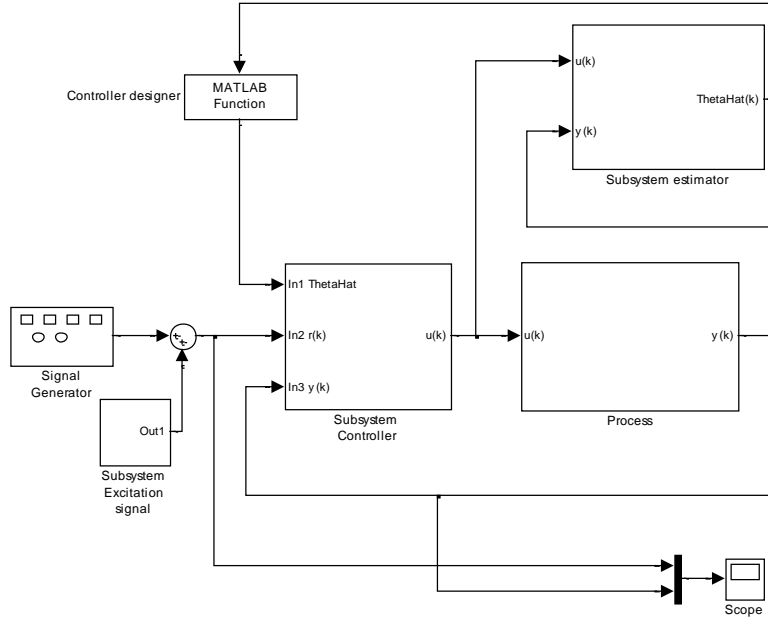


Figure 4. The control structure for a single rotor in Simulink/Matlab®.

4. Simulation results

In order to highlight the advantages of the proposed control strategy, a comparison between the results obtained with an adaptive PID controller and the fractional order adaptive controller was made. The classical controller was designed with approximately the same performances as the fractional order, but having less degree of freedom, the control signal minimization is not realized.

In Fig.5 –Fig.8 the obtained experimental results for a square reference signal are presented. The time scale is expressed in number of sample times. It can be observed that both adaptive PID and adaptive fractional order PID controllers presents good results for pitch and yaw motion of the quadrotor. This is an expected result, the controllers being designed for the same performances. The main difference is in the control signal. Using classical PID controller in the adaptive structure the control signal reaches 180 units for the pitch motion and 165 for the yaw, while the fractional order controller, due to the additional degree of freedom, ensures a control value of 48 unit for pitch and 43 for yaw motion.

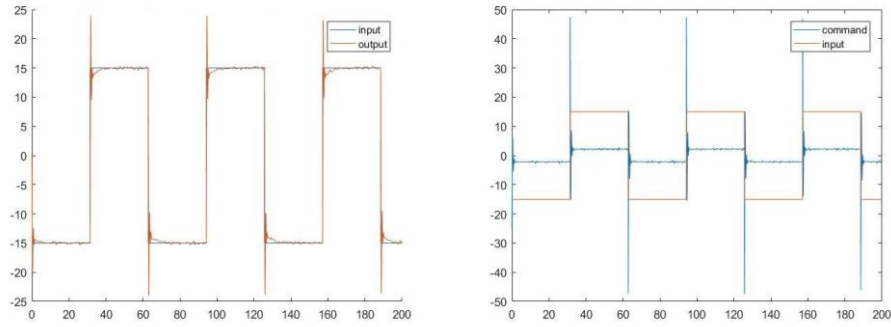


Figure 5. Output and control signal for pitch motion with adaptive fractional order PID controller

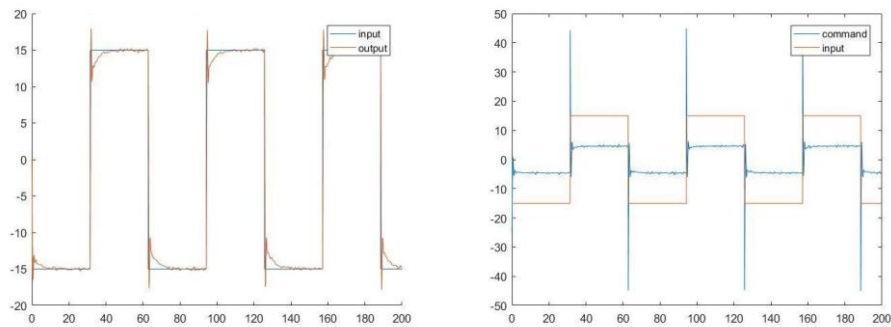


Figure 6. Output and control signal for yaw motion with adaptive fractional order PID controller

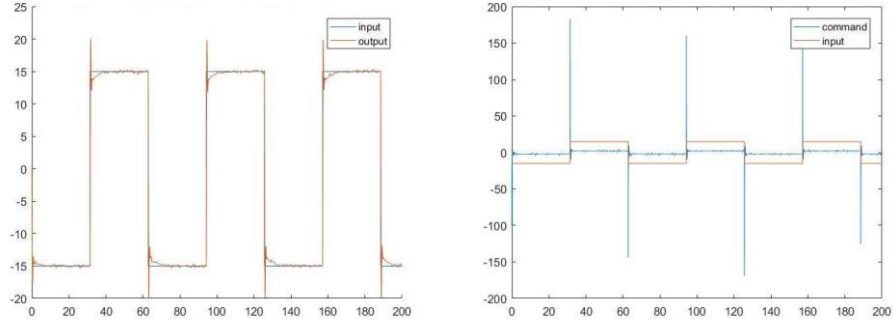


Figure 7. Output and control signal for pitch motion with adaptive PID controller

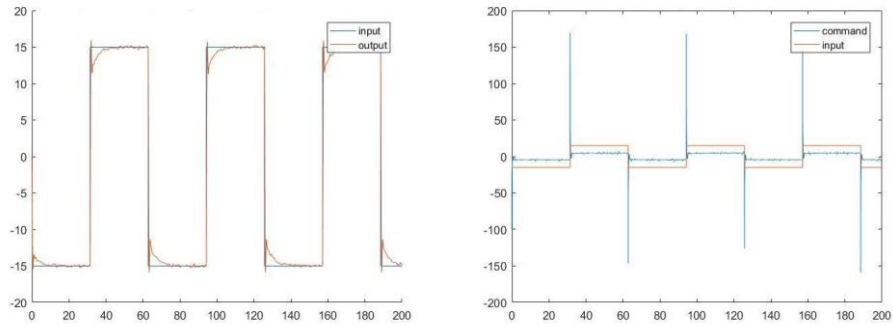


Figure 8. Output and control signal for yaw motion with adaptive PID controller

The next research step consisted in analyzing the performance measures in case of disturbances. Fig.9-Fig. 12 presents these results. Are highlighted the same good performances for both controllers, the fractional order one having the advantage of small control effort.

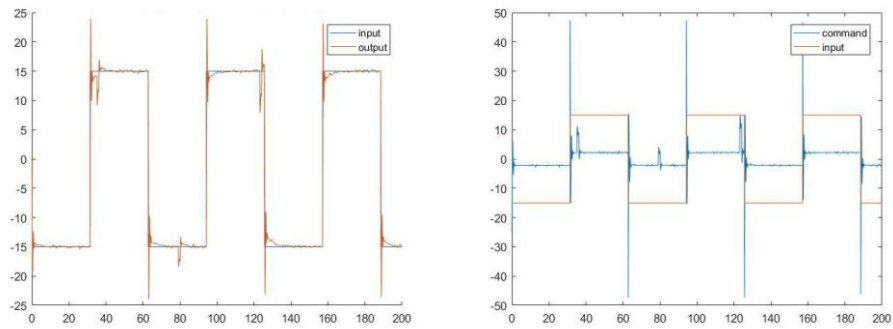


Figure 9. Output and control signal for disturbed pitch motion with adaptive fractional order PID controller

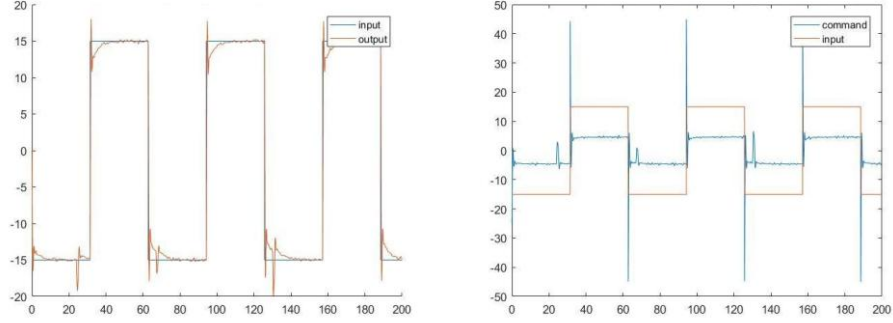


Figure 10. Output and control signal for disturbed yaw motion with adaptive fractional order PID controller

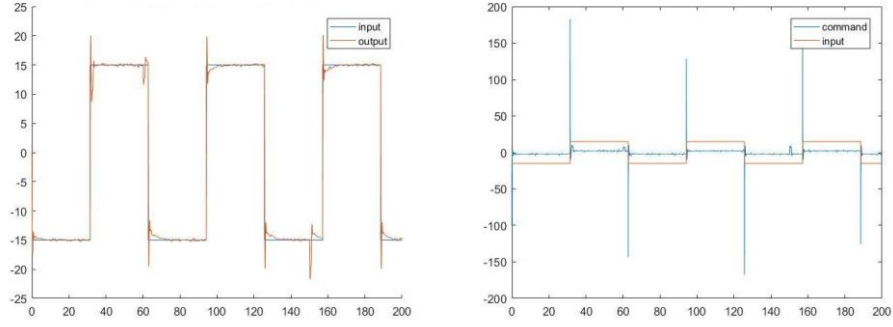


Figure 11. Output and control signal for disturbed pitch motion with adaptive PID controller

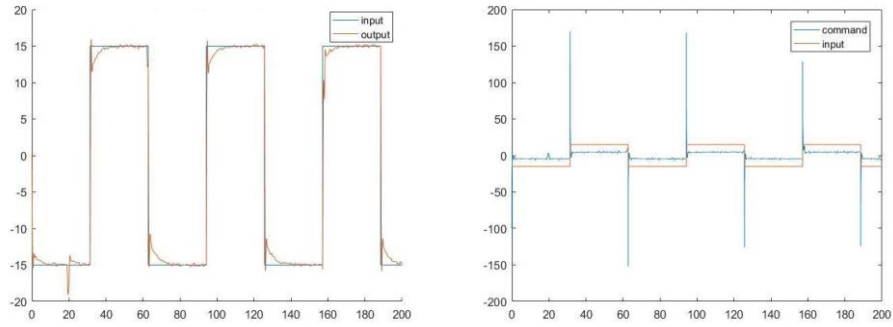


Figure 12. Output and control signal for disturbed yaw motion with adaptive PID controller

The control peak occurring in the transient of the control signal is another concern of the authors. With this regard next research step consist in implementing a constrained optimization algorithm using fractional order controllers.

With these good results the first step toward autonomic system, vehicle that do not require human interactions, is done. Flight planning and image processing features will be added in order to obtain a surveillance application.

5. Conclusions

The paper presents a designed, laboratory scale prototype for an unmanned aerial vehicle. The control strategy is implemented in a microcontroller in order to test real life behaviors. As control strategy an adaptive structure using fractional order controllers is proposed. These are designed to ensure robustness to gain variations and to minimize the control effort, while the adaptive structure eliminates the inherent disturbances between the pitch, roll and yaw motions. The effectiveness of the proposed adaptive fractional order control structure is investigated by experimental results. In order to highlight the advantages of fractional order controllers, comparison with a classical PID controller in the same adaptive structure is provided. Future works include testing different fractional order control strategies and applications of the unmanned aerial vehicle.

Acknowledgments

This work was supported by the János Bolyai Grant of Hungarian Academy of Science.

References

- [1] Shakhathreh, Hazim & Sawalmeh, Ahmad & Al-Fuqaha, Ala & Dou, Zuochao & Almaita, Eyad & Khalil, Issa & Othman, Noor & Khreishah, Abdallah & Guizani, Mohsen., Unmanned Aerial Vehicles: A Survey on Civil Applications and Key Research Challenges, *IEEE Access*, 7, 2018 10.1109/ACCESS.2019.2909530.
- [2] Hosseini, Nozhan & Jamal, Hossein & Matolak, David & Haque, Jamal & Magesacher, Thomas., "UAV Command and Control, Navigation and Surveillance: A Review of Potential 5G and Satellite Systems", IEEE Aerospace Conference March 2019
- [3] Becerra, S.M., Autonomous Control of Unmanned Aerial Vehicles, *Electronics*, 2019, 8, 452; doi:10.3390/electronics8040452
- [4] Abdulkader Joukhadar, Mohammad Alchehabi and Adnan Jeje, Advanced UAVs Nonlinear Control Systems and Applications, *Aerial Robotic Systems*, DOI: 10.5772/intechopen.86353
- [5] Sumaila Musa, Techniques for Quadcopter Modelling & Design: A Review, *Journal of Unmanned System Technology*, 2017, DOI: 10.21535/just.v5i3.981, pp.66-75.
- [6] Cajo, R. et al., A Survey on Fractional Order Control Techniques for Unmanned Aerial and Ground Vehicles, *IEEE Access*, 2019, Vol.7, pp. 66864 – 66878.
- [7] Efe, M. Ö., Battery power loss compensated fractional order sliding mode control of a quadrotor UAV, *Asian J. Control*, 2012, vol. 14, no. 2, pp. 413-425.
- [8] G. Feng, Z. Xiao-ping, Research on fractional order two-degrees-of-freedom flight control technology of unmanned air vehicle, *Proc. Int. Conf. Comput. Sci. Inf. Process. (CSIP)*, 2012, pp. 807-812.

- [9] Chao, H.; Luo, Y.; Di, L.; Chen, Y.Q., Roll-channel fractional order controller design for a small fixed-wing unmanned aerial vehicle, *Control Eng. Pract.*, 2010, vol. 18, no. 7, pp. 761-772.
- [10] Luo, Y.; Chao, H.; Di, L.; Chen, Y.Q., Lateral directional fractional order (PI) control of a small fixed-wing unmanned aerial vehicles: Controller designs and flight tests, *IET Control Theory Appl.*, 2011, vol. 5, no. 18, pp. 2156-2167.
- [11] Han, J.; Di, L.; Coopmans, C.; Chen, Y., Pitch loop control of a vtol UAV using fractional order controller, *J. Intell. Robot. Syst.*, 2014, vol. 73, no. 1, pp. 187-195.
- [12] Mohsen Vahdanipour, Mahdi Khodabandeh, Adaptive fractional order sliding mode control for a quadrotor with a varying load, *Aerospace Science and Technology*, 2019, Vol. 86, pp.737-747.
- [13] Dulf, E.H., Muresan, C.I., Both-Rusu, R., Dulf, F.V., Robust Auto-tuning Fractional Order Control of an Aerodynamical System, Advances in Engineering Research, *Proceedings of the 2016 International Conference on Mechatronics, Control and Automation Engineering*, DOI: 10.2991/mcae-16.2016.11
- [14] Dulf, E.H., Timis, D.D., Szekely, L., Miclea, L.C., Adaptive Fractional Order Control Applied to a Multi-rotor System, *Proceedings of the 22nd International Conference on Control Systems and Computer Science*, May 28-30, 2019, University POLITEHNICA of Bucharest, Romania
- [15] Dulf, E.H., Timis, D.D., Muresan C.I., Robust Fractional Order Controllers for Distributed Systems, *Acta Polytechnica Hungarica* 2017, 14(1), pp.163-176.
- [16] Muresan, C.I., Dulf, E.H., Rusu-Both, R., Vector-based tuning and experimental validation of fractional-order PI/PD controllers, *Nonlinear Dynamics*, 2016, 84(1), pp. 179-188.
- [17] Laporte-Fauret Q. et al, Low-Cost UAV for high-resolution and large-scale coastal dune change monitoring using photogrammetry, *Journal of Marine Science and Engineering*, 2019, 7(3), pp.63-69.
- [18] Balas, C., *Modelling and linear control of a quadrotor*, Cranfield, 2007.
- [19] Podlubny, I., Fractional-order systems and $PI^\lambda D^\mu$ –controllers, *IEEE Transactions on Automatic Control*, 1999, 44, pp. 208–213.
- [20] Eberhart, R. and J. Kennedy, A new optimizer using particle swarm theory. *Proceedings of the 6th International Symposium Micro Machine and Human Science (MHS)*, 1995, pp. 39–43.

Eva-Henrietta Dulf, Professor: Technical University of Cuj-Napoca, Department of Automation, Memorandumului str. 28, 400014 Cluj-Napoca, Romania (Eva.Dulf@aut.utcluj.ro).

Cristina Ioana Muresan, Assoc. Professor: Technical University of Cuj-Napoca, Department of Automation, Memorandumului str. 28, 400014 Cluj-Napoca, Romania (Cristina.Muresan@aut.utcluj.ro). The author gave a presentation of this paper during one of the conference sessions.

Daniel Dumitru Timis, MSc: Technical University of Cuj-Napoca, Department of Automation, Memorandumului str. 28, 400014 Cluj-Napoca, Romania (Daniel.Timis@aut.utcluj.ro).

The use of mechanical resonance for the reduction of torque pulsation and energy demand in machines with crankshaft systems

Wiesław Fiebig

Abstract. In the crankshaft system without spring the inertia forces are steady increasing by increase of the rotational speed, what cause higher amplitudes of the dynamical torque on the driving wheel of the motor. With use of mechanical resonance the amplitudes of the dynamical torque in the crankshaft systems can be significantly reduced. The experimental results have confirmed the reduction of the dynamic torque amplitudes and energy demand in the crankshaft system at the resonance conditions.

1. Introduction

Resonance in mechanical systems is in most cases an unwanted phenomenon. Increased vibrations lead to higher dynamic loads acting on components of mechanical systems. The related overload and fatigue may strongly affect the integrity of structures and systems such as suspension bridges (cf. the Tacoma Narrows Bridge collapse) or shafts rotating at critical speeds. In contrast to mechanical systems, positive effects of resonance are used in many other applications such as acoustics, medical science (magnetic resonance), electrical machines, radio communication, laser technology, etc. [1].

An interesting example of the use of mechanical resonance is a new drilling technique called the resonance hammer drilling (RHD) [2] as an alternative to increase the rate of penetration in hard rocks drilling. The technique uses the axial vibration due to the cutting process to generate a harmonic load on the bit and an excitation in a steel mass (hammer). When the excitation frequency is near to the natural frequency of the steel mass, the bit is subject to cyclic impacts.

Mechanical resonance is used in vibratory conveyors [3]. Experimental results show that the resonant mode of a vibratory conveyor with electromagnetic excitation is very advantageous since then it consumes the least energy to maintain the system in the state of oscillation.

Pick-and-place robots [4], for example, should be accelerated and decelerated not by means of large strong actuators but rather by an exchange between kinetic and potential energy. In such robots, savings of up to 56% due to the use of resonance energy have been observed. Positive effects of mechanical resonance are also used for establishing optimal parameters of micro-propulsion systems to drive flying objects [5].

The energy flow at resonance conditions has been investigated in a number of publications [12–14] in which it has been stated that the absorbed average mechanical power evolution could be used to describe the dynamical behavior of the vibratory system.

In reciprocating machines with crankshaft systems, there are inertia forces from the unbalance of the first and second order which cause vibrations and variable loads. These loads can be partially reduced by applying counterweights [??]. Such counterweights do not need to be used in resonant reciprocating machines in which the piston would be connected to the spring element. Results of experiments carried out on a dedicated test bench confirmed a reduction of energy demand of the resonance press in comparison with the conventional eccentric press and a reduction of dynamic torque amplitudes in the crankshaft system at resonance conditions.

2. The crankshaft system with and without resonance

The basis of the theory of hydrodynamic lubrication (HD) is Reynolds equation [4, 5] that describes the flow of a viscous fluid in an arrow gap between the surfaces of a regular curvature.

In sliding bearing the journal 1 slides on the bearing surface 2. The crankshaft systems in machines are used for the transformation of the linear motion into the rotational motion. It can be considered that the mass representing piston will be attached to the spring element. This has an significant influence on the torque pulsation on the drive shaft of the motor at resonance conditions. In Fig. 1 the schematic views of a crankshaft system with and without the spring element are shown. In a crankshaft system without spring (Fig 1b) there is a damper, which represents the forces due to the friction.

In the arrangement shown in Fig. 1a, the resonance takes place when the frequency resulting from the crank rpm is equal to the natural frequency resulting from the reduced piston mass and spring stiffness. During resonance, a compensation of the inertial force due to the piston mass by the force in spring occurs that contributes to a reduction of the amplitude of the torque pulsation on the crankshaft. The spring absorbs energy and gives it back in the same way as in the oscillator. At the resonance conditions, the force amplitude in the connecting rod as well as the torque pulsation in the crankshaft system will be minimal, depending on damping in the system.

Technical solution based on the above-described phenomena can be used in various piston machines working at constant rotational speed. The possibility of eliminating the inertia forces in the connecting rod systems is very important because these forces reach high values, especially at higher rotational speeds, and in some applications are comparable to those resulting from working loads. This makes a huge difference compared to conventional crankshaft systems in which counterbalance masses and flywheels are needed to reduce the dynamic forces and the torque pulsation [].

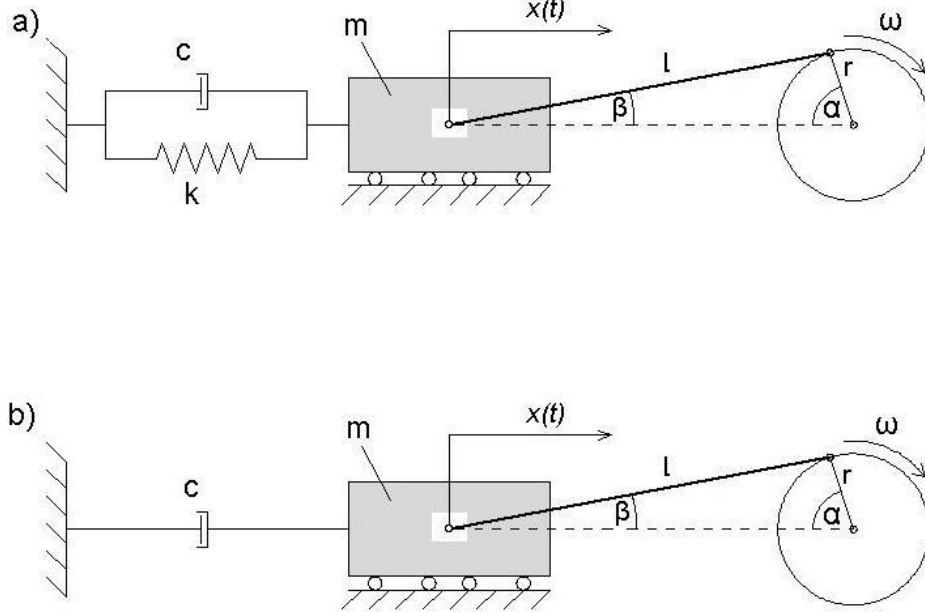


Figure 1. Schematic view of: a) crankshaft with a spring, b) crankshaft without a spring.

Authors of [18] deal with dynamics of the connecting rod. Their paper presents the dependencies of forces acting on this component and the resulting kinematic relationships, as well as the distribution of forces in its individual parts during the working cycle. In order to verify the above-presented formulae, the crankshaft model was implemented in Adams simulation software. The analysis of the crankshaft systems in Adams environment has been presented in [??, ??, ??–??]. The crankshaft-slide model was imported to Adams from a CAD model. Between base and the crank, a revolute joint was created, while between the rod and the crank journal, a revolute joint was defined. Further, between the rod and the pin, a revolute joint was used, a fixed point between the pin and the slide, and a translational joint was created between the mass and the slide. The model was ran at different angular velocities and load forces. A view of the model in Adams can be seen in Fig. 2.

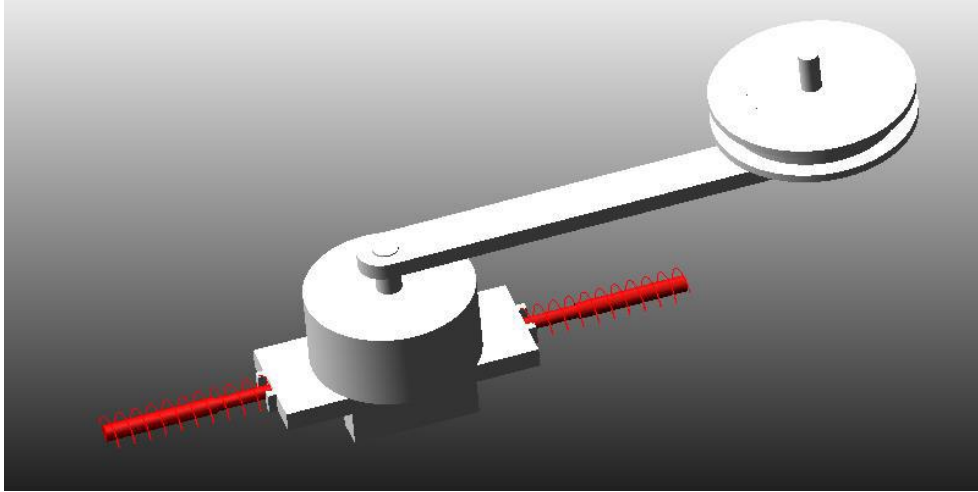


Figure 2. A model of the crankshaft system in Adams.

Fig. 3 shows a comparison of the torque courses to both the crankshaft system with a spring (Fig. 1a) and without a spring (Fig. 1b). It should be noted that the presented analytical model does not take into account possible non-linearities occurring in the system, e.g. non-linear friction between the guide and the mass. These non-linearities, however, occurring in real-life systems should not be expected to reach magnitudes large enough to change the behavior of the system during resonance.

Fig. 3 shows a comparison of the torque waveforms for the crankshaft system with and without a spring. The following values of system parameters were adopted for simulation:

- $m = 1$ kg — mass of the piston;
- $r = 0.30$ m — the crank radius;
- $c = 3$ Ns/m — the damping coefficient;
- $k = 1000$ N/m — the stiffness coefficient of spring elements.

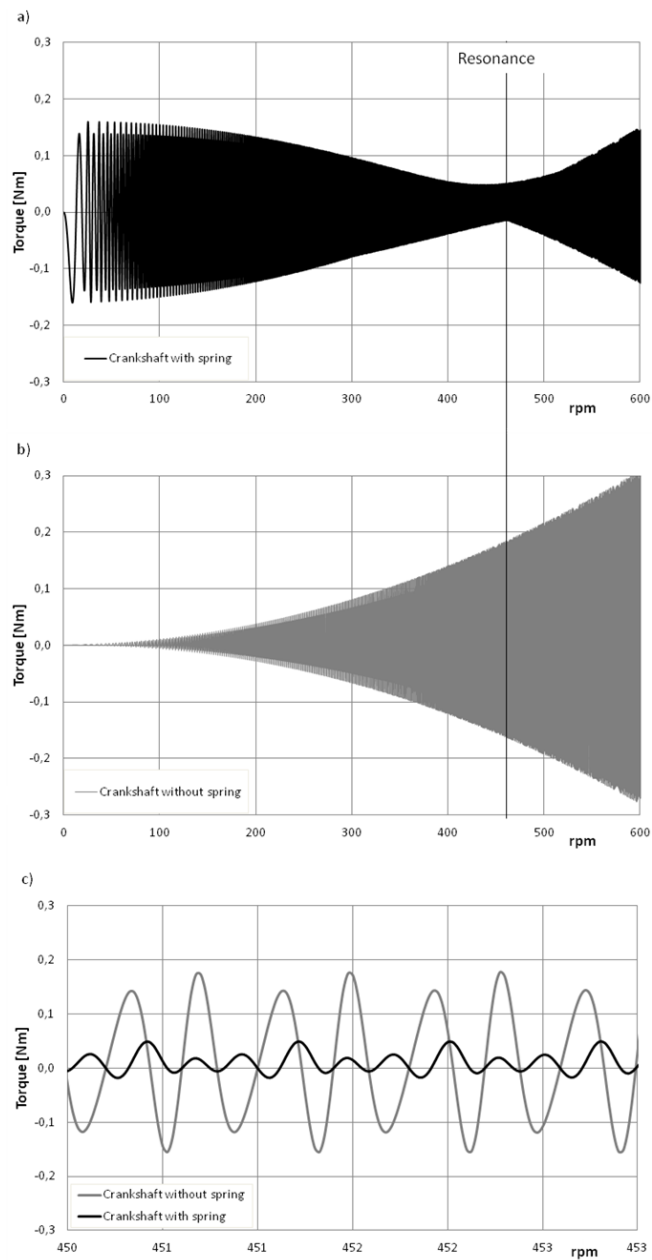


Figure 3. Torque vs. rotational speed for the crankshaft with and without a spring.

In the waveforms in Fig. 3 can be seen that for the crankshaft system with a spring, for which resonance occurs at 452 rpm, the torque amplitude will be reduced by around 5 times. For the crankshaft system without a spring there is an constantly increasing of torque amplitude in the investigated rpm range.

Due to the phenomenon of resonance, the energy in the crankshaft system without load is only used to overcome frictional forces. For crankshaft systems without resonance, an increase in mass leads to increase of torque amplitude. This increase is several times smaller for crankshaft systems with a spring at resonance than in the system without a spring.

In Fig. 4 the influence of the frequency on torque amplitude is shown. It can be seen that the influence of the frequency is similar to the influence of the crank radius.

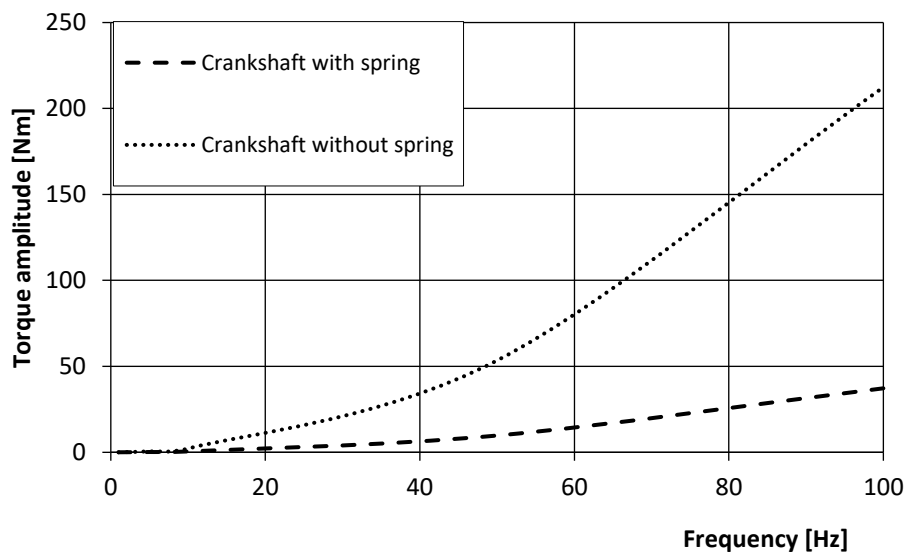


Figure 4. Torque amplitude vs. frequency,

From Fig. 4 it can be seen that with an increase of frequency, differences between the torque amplitudes for the respective systems are increasing. For a frequency of 10 Hz, differences between the crankshaft system with and without resonance are 4,18 times higher than for the crankshaft system without the spring.

In Fig. 5 the influence of the load on the torque amplitude is shown. The load in form of half sine has been considered. The ratio of the amplitude of excitation force to the amplitude of spring force will be defined as:

$$k_F = F_L / F_s \quad (1)$$

where

F_L - amplitude of excitation (load) force

F_s - amplitude of spring force.

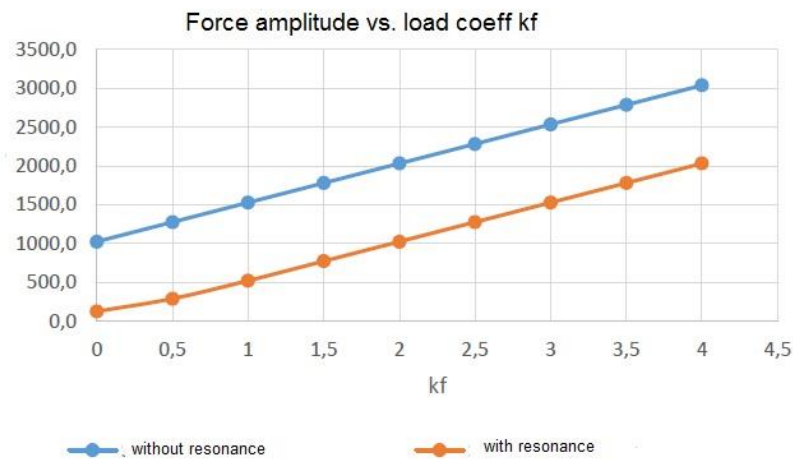


Figure 5. Torque amplitude in crankshaft loaded with half sine wave force. Resonance at 1500 rpm (25 Hz), mass 5kg, spring stiffness 123 kN/m , damping ratio 3 Ns/m.

It can be seen, that the torque amplitudes without resonance at ratio $k_F=1$ (amplitude of load force is equal the spring force) are 3 times higher than with resonance. These differences are lower at higher values of load coefficient k_F . It should be noted that at higher loads, the effect of resonance becomes percentage lower and is higher at lower frequencies (rpm).

3. An experiment with physical model

Figure 6 presents the schematic view of the physical model in which both crankshaft systems were investigated. The physical model consists of the oscillating mass connected with the crankshaft system and with the set of 4 springs. The rpm of the AC asynchronous motor was controlled with the frequency inverter. The force in the crankshaft was measured with the force sensor. The mass is mounted on the slide with a low friction.

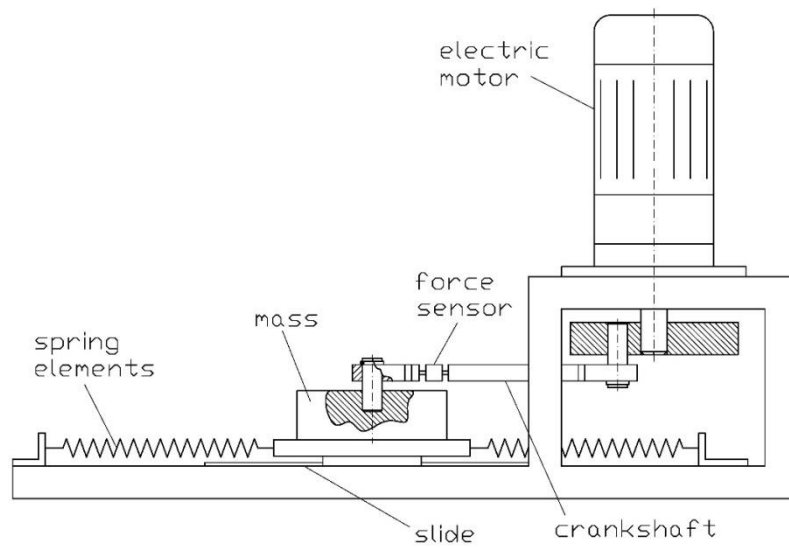


Figure 6. Schematic view off the test bench.

A view of the test bench is shown in Fig 7.



Figure 7. View of the test bench.

In Fig. 8 the measured time waveforms of the displacement of the mass and the force in the crankshaft are shown. It can be seen that the amplitudes of the force on the crankshaft with spring decrease with increasing of rpm and reach their minimum values at the resonance, where the inertial forces of the masses are compensated by the spring forces and by absence of load the driving force is needed to overcome the friction force only. For the crankshaft without spring the steady increase of the amplitudes of the force in the crankshaft is observed, due mainly to the inertial forces and friction forces.

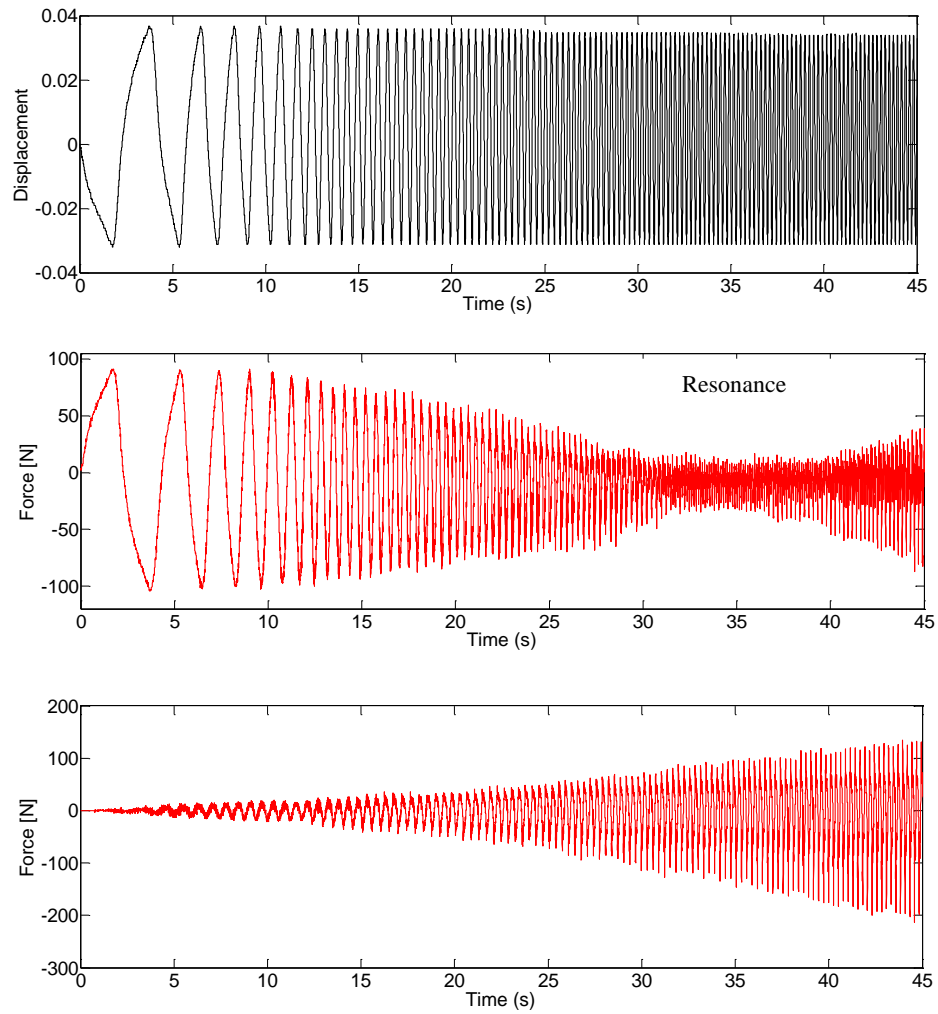


Figure 8. The measured waveforms of: a) displacement of the mass, b) force with the spring, c) force.

Compensation of inertia forces at resonance should have an impact on efficiency of machines of that type. The effect of the torque pulsation amplitude reduction in resonance was confirmed experimentally. The use of mechanical resonance in machines with crankshaft systems can thus eliminate flywheels in some applications where reduction of the torque pulsation in crankshaft drives is required.

Measurements of the power absorbed by the drive motor in the crankshaft system (on the test bench of Fig. 7) with a spring and without spring were carried out.

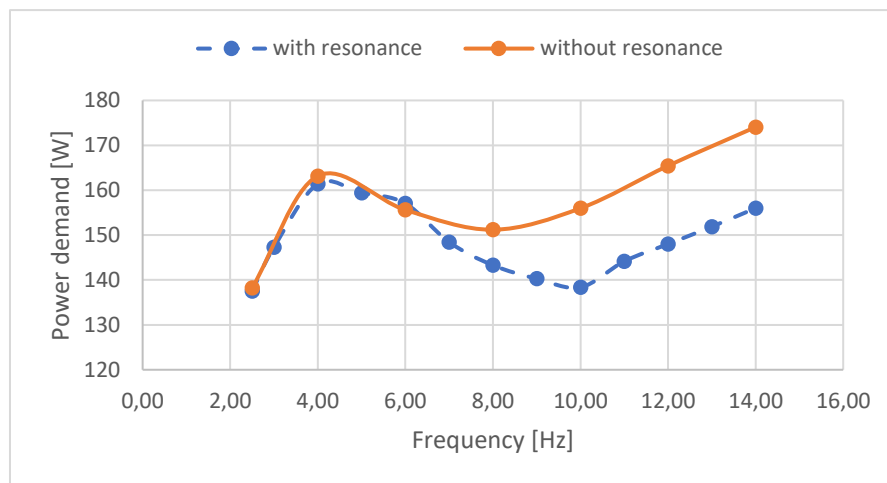


Figure 9. Comparison of power demand in the crankshaft system with and without spring.

Comparison of results shown in Fig. 9 proves that due to resonance at around 10 Hz, reduction of power consumption in the drive system by about 13% occurred.

4. Conclusions

The paper presents the possibilities to use the mechanical resonance to minimize the torque pulsation in the crankshaft systems of machines like piston compressors, combustion motors and other machines in which translational motion is transferred into rotational motion. The torque amplitudes of crankshaft systems with and without resonance have been analyzed and compared.

It was found that under conditions of resonance in the crankshaft system occurs a significant reduction of the amplitudes of the dynamic torque on the motor. The influence of oscillator mass, damping factor, displacement amplitude (radius of crank), frequency and load forces on the amplitude of torque has been shown.

Measurements of the force in the crankshaft system based on a physical model have been carried out. The results of experimental investigations have confirmed the reduction of the amplitudes of the dynamic force and dynamic torque in the crankshaft system.

The use of mechanical resonance in crankshaft systems has the following advantages: the mass of the oscillator is smaller than the mass of the flywheel, especially at lower frequencies. This ability can be used for resonance systems can be used for mass miniaturization in drive systems, in resonance systems, the load from the inertia forces is compensated by the spring force and the power supplied is used to overcome the work load and the friction resistance. For this reason, the dynamic forces in the individual components of the crankshaft system will be smaller, particularly the forces present in the bearings, which may affect the durability of the system.

To determine how the reduction of the torque amplitudes at resonance conditions leads to a reduction of power demand of the electric motor further investigations will be carried out.

References

- [1] Crocker, M.J. Handbook of Noise and Vibration Control. John Wiley & Sons, Hoboken, New Jersey, 2007, 528–545.
- [2] Yang, J.N., Akbarpour, A., Ghaemmaghami, P. Instantaneous Optimal Control Law for Tall Buildings Under Seismic Excitations. Technical Report NCEER-87-0007, 1987.
- [3] Horodincu, M., Saghedin, N.E. Experimental Investigations of Power Absorbed at Mechanical Resonance. Experimental Techniques SEM, 2011, 1-11.
- [4] Harris, C.M., Piersol A.G. Shock and Vibration Handbook. McGraw-Hill, New York, 2002.
- [5] Glynne-Jones, P., Tudor, M.J., Beeby, S.P., White, N.M. An electromagnetic, vibration-powered generator for intelligent sensor systems. Sensors and Actuators, A 110, 2004, 344–349.
- [6] Goldner, R.B., Zerigian, P. A Preliminary Study of Energy Recovery in Vehicles by Using Regenerative Magnetic Shock Absorbers. SAE Technical Paper Series 2001-01-2071, 2001.
- [7] Plooij, M.C., Wisse, M. A Novel Spring Mechanism to Reduce Energy Consumption of Robotic Arms. Intelligent Robots and Systems (IROS), IEEE/RSJ International Conference, 2012, 2901-2908.
- [8] Baek, S., Ma, K., Fearing R. Efficient Drive of Flapping - Wing Robots. IEEE/RSJ International Conference on Intelligent Robots and Systems October 11-15, 2009 St. Louis, USA
- [9] Despotovic, Z, Ribic, A. A comparion of Energy Efficiency of SCR Phase Control and Switch Mode Regulated Vibratory Conveying Drives. IX Symposium Industrial Electronics, INDEL, 2012, Banja Luka, Nov. 01-03, 2012

- [10] Fiebig, W., Wrobel, J. Simulation of Energy Flow at Mechanical Resonance. 22nd ICSV Conference, July 12-16, 2015, Florence, Italy

Wieslaw Fiebig, Professor, Wrocław University of Science and Technology, Faculty of Mechanical Engineering, Łukasiewicza 7/9, 50-370 Wrocław, Poland (wieslaw.fiebig@pwr.edu.pl). The author gave a presentation of this paper during one of the conference sessions.

Finite element analysis of magneto-rheological fluid embedded on journal bearings

Gustavo de Freitas Fonseca, Ailton Nabarrete

Abstract: In this work, the influence of magneto-rheological fluid embedded on journal bearings in the dynamic behavior of rotors is considered. The modified Reynolds equations for Bingham viscoplastic materials are used for determination of the nonlinear hydrodynamic forces. Flexible rotors are modeled by the finite element method. The proper weight of the structure, unbalance and bearing hydrodynamic forces are included in the equation of motion as external excitations. Non-linear hydrodynamic forces calculation depends on the relative position between the shaft and the journal bearing. For this reason, the system response is determined by the modified Newmark method, which contemplates the determination of the equilibrium at any time step by the incorporation of the Newton-Raphson method. The whole model was developed in the MATLAB® programming environment. The results of the case studies are presented as orbital graphs, displacements versus time and frequency responses.

1. Introduction

Rotating systems are invariably subjected to high vibration level, which can reduce the components durability, increase downtime and elevate the operation and production costs. The vibrations sources can be related to foundation problems, weak design, shaft friction, unbalance, misalignment and many others. For many years machines have required the development of vibration control, either with passive or active devices. Recently smart materials have been developed and applied to different dynamic systems withstanding different load conditions and variations to diminish the vibrations caused during their operation. In one of these cases magneto-rheological (MR) fluids have been developed and incorporated directly in journal bearings that support rotating shafts. Experimental tests of different conceptions have been presented in the literature [1,2].

For more than one decade, researchers have demonstrated the nonlinear vibration of rotary shafts supported by squeeze film journal bearings [3,4]. Wang et al. proposed an iterative method that depends on the circumferential mass flow to determine the pressure distribution [5]. On the other hand Irannejad and Ohadi have produced an expression of pressure distribution considering the effects of the squeeze film [8]. He has determined the hydrodynamic forces by the use of numerical

integrations in the axial and circumferential directions. In the recent past Castro employed direct equations for the determination of nonlinear hydrodynamic forces [4], representing a significant reduction in time to process the numerical analysis.

This research aims at the nonlinear vibration control of a rotating shaft supported by squeeze film journal bearings. To show this effect a numerical analysis of a rotating shaft supported by journal bearings with magneto-rheological squeeze film damper (MRSFD) is demonstrated. The modified Reynolds equations for a viscoplastic Bingham material are derived to determine the fluid film pressure distribution [5]. The behavior of the squeeze film damper described by Tichy is used to calculate the magnetic pull force [6]. A finite element model considers beam elements in the discretization of the rotary shaft. A disc is placed at the end of the shaft and unbalance forces appear during the shaft rotation. Time responses are obtained by the Newmark integration method. This method has been modified because of the nonlinear behavior and the position dependence of the MRSFD journal forces. As in a previous work, the Newton-Raphson method is incorporated to guarantee the equilibrium of forces at each time step [3].

2. Mathematical model of the magneto-rheological squeeze damper

Reynolds equations of conventional viscous fluid have been modified in velocity profile and pressure distribution by treating the MR fluid as Bingham viscoplastic fluid [7]. Another work was developed based on the previous paper. It has detailed a rigid rotor mathematical model considering the short bearing approach embedded by MR fluid [8]. The author has provided the transient response for different electric currents setups induced in the bearings. WANG et al. presented the whole Reynolds equation deduction and the particularization to a viscoplastic Bingham material problem [5]. The pressure distribution expressions were deduced, concerning the short and long bearing approaches. The authors presented a simulation of a flexible rotor, using the finite element method to model a rotating system supported by the foundation and a single MRSFD journal bearing. The time responses of the system were obtained by the Newmark classic integration method. In this work the pressure distribution expression is expressed as presented in [5] but neglecting the cavitations' effects.

The fluid film thickness can be expressed by

$$h = c(1 + \varepsilon \cos \theta) \quad (1)$$

According to [5] and [6], the MR fluid viscosity can be considered as a Bingham viscoplastic material, as shown in Fig. 1.

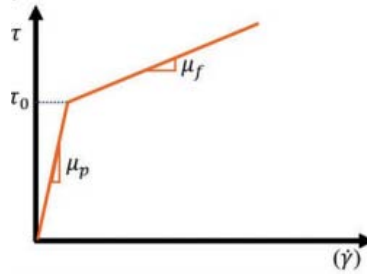


Figure 1. Bingham fluid biviscosity model. Adapted from [5].

Thus, the two dynamic viscosity of the MR fluid can be written as

$$\mu = \begin{cases} \mu_p, & \dot{\gamma} \leq \frac{\tau_0}{\mu - \mu_p} \\ \mu_f + \frac{\tau_0(H)}{\dot{\gamma}}, & \dot{\gamma} > \frac{\tau_0}{\mu - \mu_p} \end{cases} \quad (2)$$

where μ_p is the plastic viscosity and μ_f is the Newtonian viscosity, after the yield shear stress τ_0 is achieved. It is remarked by [5] that $\mu_p \gg \mu_f$. During the simulations performed by [2], $\mu_p = 100 \mu_f$ has been adopted. In this paper, it is assumed that $\mu_p = 20 \mu_f$. The yield shear stress depends on the electromagnetic field in the journal area. According to [6], this quantity can be estimated by

$$\tau_0 = AH^2 \quad (3)$$

where A is the electromagnetic induction device performance coefficient. It is suggested by [7] a range between $10^{-10} \sim 10^{-9} N/A^2$. The electromagnetic intensity can be calculated by

$$H = \frac{IN}{2h} \quad (4)$$

where I is the electric current and N is the number of coil turns.

Then, the pressure distribution in a MRSFD journal bearing is expressed in the form

$$p(\theta, z) = \begin{cases} -\frac{6\mu\omega\varepsilon \sin \theta}{c^2 (1 + \varepsilon \cos \theta)^3} \left(z^2 - \frac{L^2}{4} \right), & \dot{\gamma} \leq \frac{\tau_0}{\mu - \mu_p} \\ -\frac{6\omega\varepsilon \sin \theta (\dot{\gamma}\mu_f + \tau_0(H))}{c^2 (1 + \varepsilon \cos \theta)^3} \left(z^2 - \frac{L^2}{4} \right), & \dot{\gamma} > \frac{\tau_0}{\mu - \mu_p} \end{cases} \quad (5)$$

The cavitation effects are neglected by adopting the Gumbel boundary condition. It was concluded by [8] that the cavitation area equals the atmospheric pressure, whilst the dynamic pressure presented in (5) is considered in the remaining region

$$p = \begin{cases} p = p_{atm}, & 0 \leq \theta < \pi \\ p = p(\theta, z), & \pi \leq \theta \leq 2\pi \end{cases} \quad (6)$$

Next, the hydrodynamic forces in radial and tangential directions are determined by integrating the pressures distribution through the axial z and circumferential θ directions

$$\begin{aligned} F_r &= \left| R \int_{-L/2}^{L/2} \int_{\pi}^{2\pi} p(\theta, z) \cos \theta d\theta dz \right| \\ F_t &= \left| R \int_{-L/2}^{L/2} \int_{\pi}^{2\pi} p(\theta, z) \sin \theta d\theta dz \right| \end{aligned} \quad (7)$$

Fig. 2 shows the pressure distribution in the circumferential direction, neglecting the cavitation effects, the coordinate system $\mathbf{x-y}$ of the journal bearing and the forces scheme, considering radial, indicated by \mathbf{N} , and tangential, indicated by \mathbf{T} .

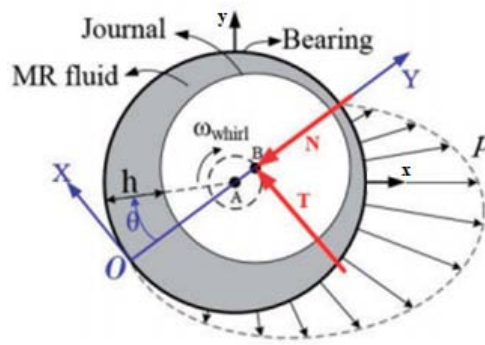


Figure 2. Pressure distribution in journal bearing. Adapted from [5].

In addition, the magnetic pull force appears due to eccentricity between the two magnetic poles: the rotating shaft and the bearing [6]. The magnetic pull force direction aligns with the radial hydrodynamic forces, as shown in Fig. 3.

Then, the expression of the magnetic pull force is written

$$F_m = \mu_f U_m^2 \frac{\pi R L e_B}{(c^2 - e_B^2)^{3/2}} \quad (8)$$

where μ_f is the relative permeability of MR fluid and U_m the magnetic motion force.

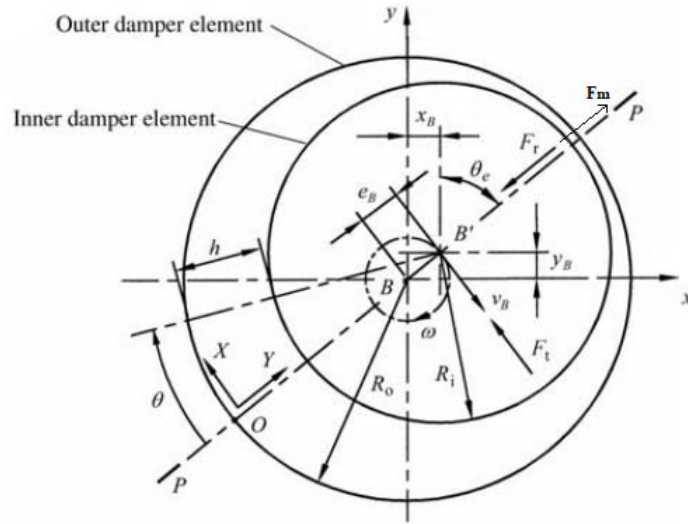


Figure 3. Acting forces in a MRSFD forces. Adapted from [6]

Neglecting the magnetic field outer the journal bearing, this quantity can be calculated by

$$U_m = IN \quad (9)$$

Besides, the eccentricity e_B is a function of the relative position between the shaft and the bearing, which can be determined by

$$e_B = \sqrt{x_B^2 + y_B^2} \quad (10)$$

Thereby, the radial effective force can be calculated by subtracting the hydrodynamic radial force and the magnetic pull force

$$F_{r\,eff} = F_r - F_m \quad (11)$$

Putting the radial effective force and the tangential hydrodynamic forces in a convenient coordinate system (i.e. $\mathbf{x}\text{-}\mathbf{y}$ directions in Fig. 2)

$$\begin{aligned} F_x &= F_{r\,eff} \cos\psi - F_t \sin\psi \\ F_y &= F_{r\,eff} \sin\psi + F_t \cos\psi \end{aligned} \quad (12)$$

where,

$$\psi = \tan^{-1}\left(\frac{y}{x}\right) \quad (13)$$

3. Nonlinear rotor model

A finite element model of a flexible shaft supported by two MRSFD journal bearings is developed. The model has five beam elements, each one having eight degrees of freedom, i.e. four per node. The model supports a rigid disk at the end. Fig. 4 shows the structure idealization.

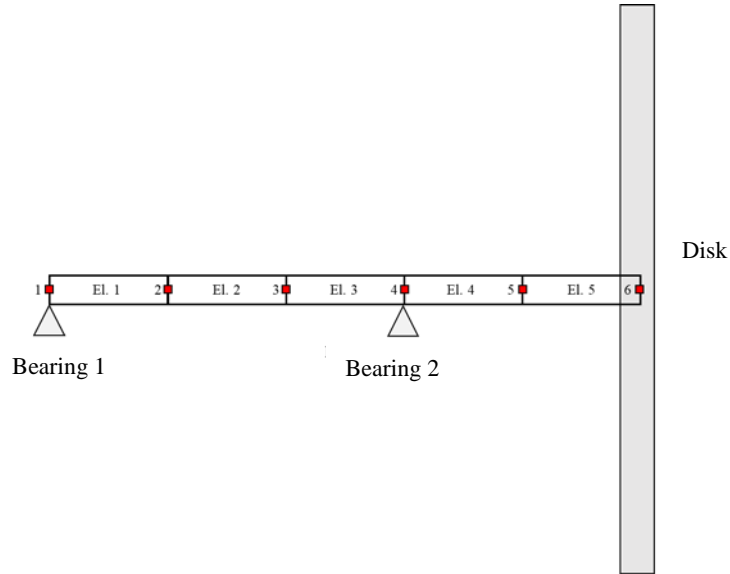


Figure 4. Finite element model of the rotary shaft.

The rotary shaft properties are presented in Table 1.

Table 1. Properties of the model

Property	Value	Unity
Young Modulus. E	206.7	GPa
Density. ρ	7800	kg/m ³
Poisson Coefficient. ν	0.3	-
Damping Coefficient. β	2.5×10^{-5}	-
Shat Diameter. D_s	50.8×10^{-3}	m
Shaft Length. L_s	1.25	m
Disk Mass. m_d	200	kg
Disk Diameter. D_d	1.0	m
Disk Length. L_d	0.2	m
Imbalance Mass. m_u	2.5	kg
Imbalance Eccentricity. e	0.01	m
Journal Diameter. D_b	55.9×10^{-3}	m
Journal Length. L_b	40.0×10^{-3}	m
Radial Clearance. c	1.0×10^{-3}	m
MR Newtonian Viscosity. μ	0.09	Pa.s
Coil Number of Turns. N	570	-
Electric Current. I	0.0 to 1.0	A

After assembling the stiffness, mass, gyroscopic and damping matrices of each beam element, the governing motion equation of the full model is shown

$$[M]\{\ddot{q}\} + ([C] + \omega[G])\{\dot{q}\} + [K]\{q\} = \{F_{MRSFD}\} + \{F_d\} + \{W\} \quad (14)$$

where, $[M]$, $[C]$, $[G]$, $[K]$ are the mass, damping, gyroscopic and stiffness matrices, respectively. The vectors $\{F_{MRSFD}\}$ and $\{F_d\}$ represent the MRSFD journal bearing hydrodynamic and the unbalance forces, respectively, and $\{W\}$ represent the rotor weight.

$$F_d = me\omega^2 \begin{Bmatrix} \cos \omega t \\ \sin \omega t \\ 0 \\ 0 \end{Bmatrix} \quad (15)$$

4. Dynamic response to the disc unbalance

The waterfall diagram in Fig. 5 has been determined for the Bearing 2, where the position is depicted in Fig. 4. Over the 1.0X line there is a peak at 1600 rpm or 27 Hz, corresponding to the critical speed of the system. However, the 0.5X line presents higher displacements above 3600 rpm with values at least 3 times the ones observed in the critical speed.

For a better understanding of the dynamic behavior of the rotor it has been done a runup simulation, when the angular speed is increased systematically. Fig. 6 shows the vertical displacement in Bearing 2 as a function of the rotation speed. The first peak occurs at 27 Hz (1600 rpm) approximately, which is the critical speed previously demonstrated in the waterfall diagram. After that, the system stabilizes in a rotation speed window corresponding 40 Hz to 70 Hz. However, when the rotation speed reaches 70 Hz (4200 rpm) the vertical displacements starts to increase, reaching the whip instability above 80 Hz (4800 rpm).

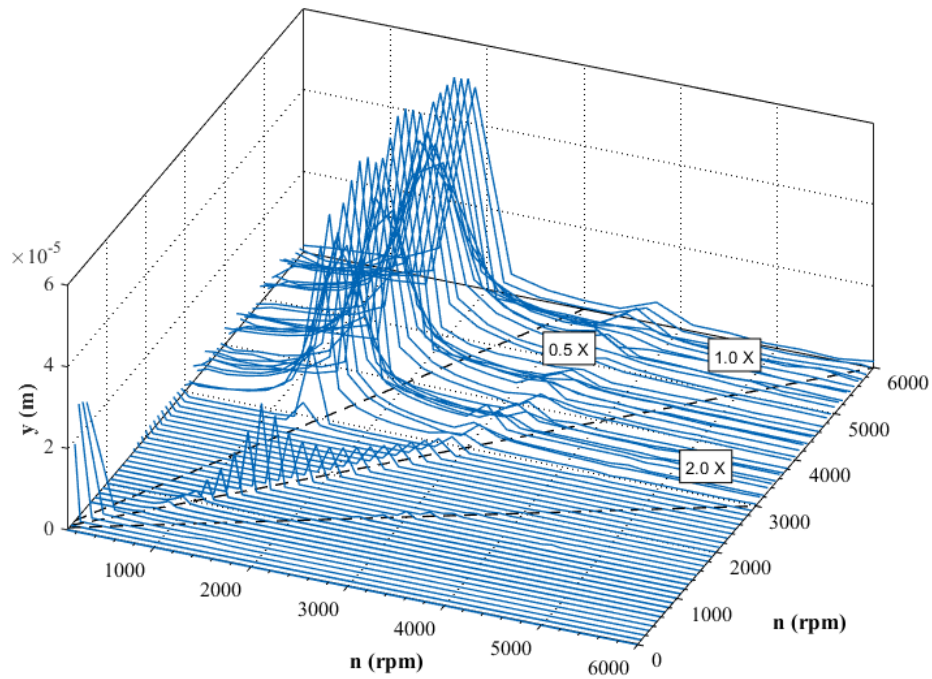


Figure 5. Waterfall without any current applied – Nonlinear effects.

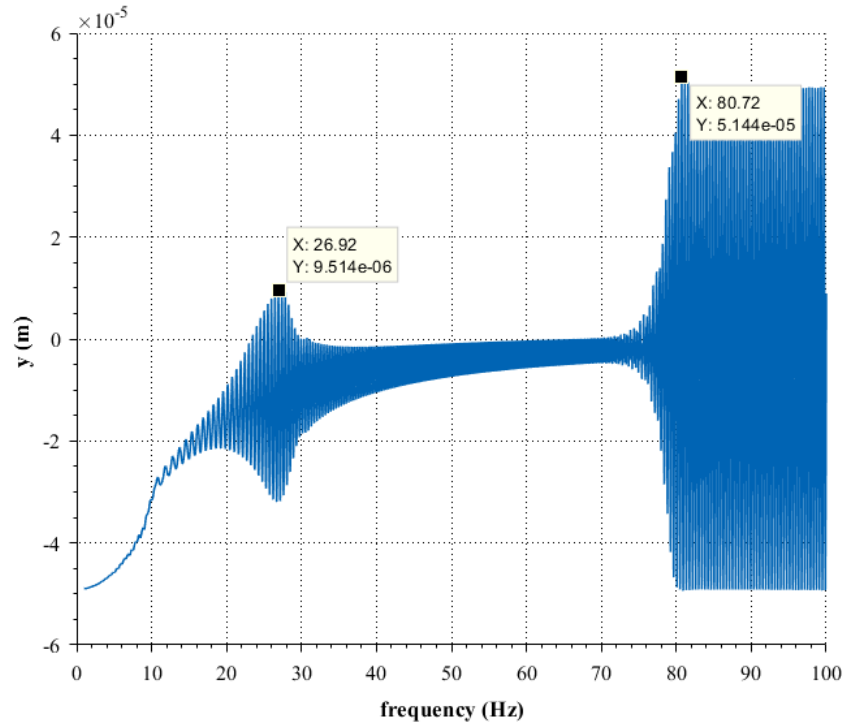


Figure 6. Run-up response without any current applied – Nonlinear effects.

The time response has been determined at 800 rpm for 1.0 A of electric current. The vertical displacements of bearing 2, which represent the MRSFD journal bearing is shown in Fig. 7. The response represents a nonlinear behavior, since presents a variable period. On the other hand, the displacement amplitude demonstrates stabilization in 0.8×10^{-6} m after 0.3 seconds.

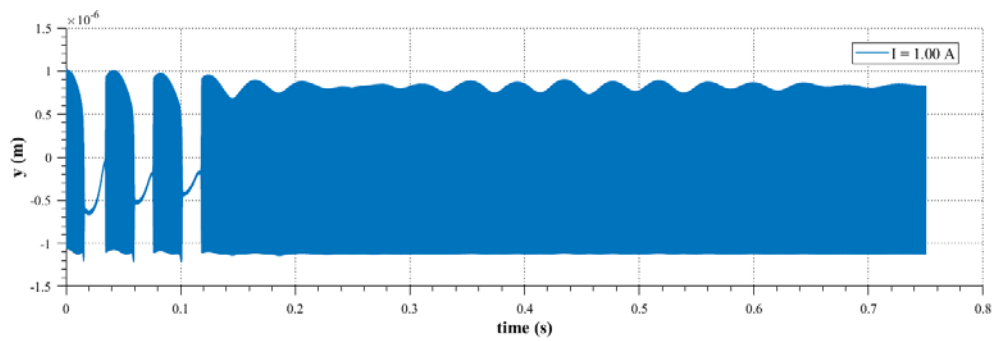


Figure 7. Time response on node 4 @ 1.0 A and 800 rpm.

For the same bearing operating at zero electric current, the orbit is concentrated in the fourth quadrant (Fig. 8) and it assumes a quasi-elliptical shape. Activating the electric current at 1.0 A the orbit takes a circular shape with the center at the origin.

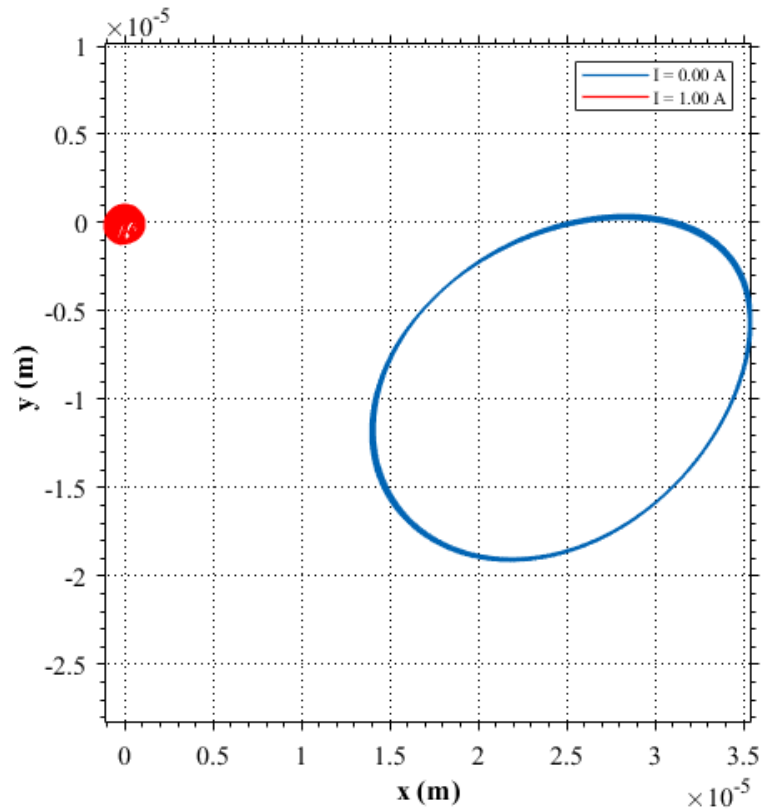


Figure 8. Orbit @ 800 rpm – 0.0 A and 1.0 A – Node 4.

Finally, it has been done a run-up simulation at an electric current of 1.0 A and increased unbalance of 10 kg.m. The electric current activation increases the system critical speed to 33 Hz or 2000 rpm, which is 23 % higher when no electric current is activated. Thus, it can be assumed that the electromagnetic induction resulted in higher system stiffness. Moreover, there is no longer oil whip instability corresponding to 0 to 100 Hz frequency range.

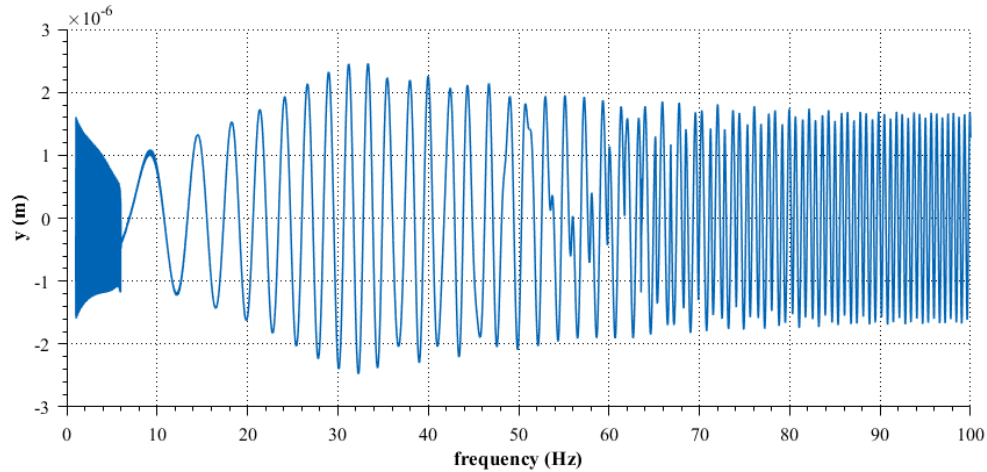


Figure 9. Run-up simulation at an electric current of 1.0 A.

5. Conclusions

The rotary shaft operating supported by MRSFD journal bearings is analyzed without electric current to take as reference. The cascading diagrams show the critical speed at 1600 rpm and the emergence of whip instability at 3200 rpm. The presence of gravity acceleration delays the onset of fluid-induced instability. The simulations performed considering the electromagnetic induction in MRSFD bearings showed the systematic reduction of the displacement amplitudes. In addition, the shape of the orbits is no longer elliptical as in the current-free case, but circumferential after the actuation of electric currents. Finally, the simulation of the run-up shows that current of 1.0 A provides an increase in critical rotation (33.3 Hz). In addition, this actuation provides a reduction in response amplitudes.

Acknowledgments

The authors are grateful to the Fundação de Amparo à Pesquisa do Estado de São Paulo (FAPESP) for funding this research, grant no. 2015/20363-6.

References

- [1] Wang, J.; Meng, G.; Hahn, E. Experimental Study on Vibration Properties and Control of Squeeze Mode MR Fluid Damper-Flexible Rotor System. ASME 2003 Design Engineering Technical Conferences and Computers and Information in Engineering Conference, Chicago, 2-6 September (2003) p.1-5.
- [2] Bompos, D. A.; Nikolakopoulos, P. G., CFD simulation of magnetorheological fluid journal bearings. Simulation Modelling Practice and Theory, v. 19 (2011) p. 1035-1060.

- [3] Nabarrete, A., Melo, V., Balthazar, J.M., Tusset, M.A., Nonlinear analysis of rotors with rigid coupling misalignment. 14th International Conference of Dynamical Systems - Theory and Applications - DSTA 2017. Vibration, Control and Stability of Dynamical Systems (2017) Lodz.
- [4] De Castro, H.F., Cavalca, K.L., Nordmann, R. Whirl and whip instabilities in rotor-bearing system considering a nonlinear force model. *Journal of Sound and Vibration* 317 (2008) 273–293.
- [5] Wang, J., Feng, N., Meng, G., Hahn, E. J., Vibration Control of Rotor by Squeeze Film Damper with Magnetorheological Fluid. *Journal of Intelligent Material Systems and Structures*, v. 17 (2006) p. 353-357.
- [6] Tichy, J. A., Behavior of a Squeeze Film Damper with an Electrorheological Fluid. *Tribology Transactions*, v. 36, n. 1 (1993) p.127-133.
- [7] Zapomel, J.; Ferfecki, P.; Forte, P. A computational investigation of the transient response of an unbalanced rigid rotor flexibly supported and damped by short magnetorheological squeeze film dampers. *Smart Materials and Structures*, v. 21 (2012) p.1-12.
- [8] Irannejad, M.; Ohadi, A. Vibration analysis of a rotor supported on magnetorheological squeeze film damper with short bearing approximation: A contrast between short and long bearing approximations. *Journal of Vibration Control*, v. 23, n. 11 (2017) p. 1972-1808.

Influence of control system parameters and it's disturbances on lane change process

Mirosław Gidlewski, Leszek Jemioł, Dariusz Żardecki

Abstract: Automatic control of lane change is a key to automate more complex maneuvers. According authorial concept the lane change controller has a mixed structure. In the open-loop structure it works as a set-point signal generator which generates three variables determining the lane change maneuver: a set-point input signal of steering system angle, and two set-point output signals describing desirable vehicle's trajectory (lateral and angular shifts of the car). In the closed-loop structure it works as a steering signal corrector which corrects on-line (by two Kalman regulators) the steering system angle signal. Error signals are calculated by comparison of reference (generated) and real (measured) signals expressing vehicle's trajectory. The set-point reference signals, as well as regulators are based on a simple linear reference model (simplified "bicycle model"). For validation of the controller algorithm extensive simulation investigations have been executed. In these investigations, as the virtual object of control – the very detailed (MBS-type, 3D, nonlinear, and verified experimentally) mathematical model of medium-duty truck has been used. The authors' model of a conceptual control system and extensive simulation investigations were presented at several authors' papers. This paper presents unpublished results of the studies, which are concerned on sensitivity of the control system to it's delay of data processing.

1. Introduction

Many researches is engaged on works on control system which automate car's manoeuvres. Especially difficult seems to be the manoeuvres performed with high speeds (e.g. obstacle avoidance or overtaking) Usually, the road manoeuvres may be treated as a sequence of elementary lane changes. Therefore, the automation of the lane change is a fundamental problem of the automation of the car.

Steering wheel control is a subject of numerous scientific papers (examples in [1], [3]). The control algorithms and control systems are usually based on a concept that includes the designation of the path and the execution of the trajectory in the tracking process using the appropriate sensors and regulators. Trajectory planning is then considered as a parametric optimization task for the assumed geometric form of a path shape function. Controllers proposed in these works are based on well known regulation structures and algorithms.

The authors' conception (details in [4], [5], [6]) is based on the optimal control theory implemented to the simplest version of the "bicycle model" describing the vehicle lateral dynamics. Such simple motion model (reference model) enables analytical forms of reference signals, as well as analytical forms of regulators' algorithms to be used to correct a steering signal with using real trajectory measurements. Thanks to analytical forms of reference signals and regulators, the automatic lane change control process can be computerized in real time.

This conception requires a lot of simulation investigations for sensitivity analysis of the control system. Sensitivity investigations have been reported in several authors' papers due to vehicle parameters changes (masses, wheel-road friction coefficients, vehicle speed), due to simplification of the reference model (neglected inertia parameters in a steering system), due to disturbances (noise, offset) of signals measured in the system.). In such studies, as a control object occurred a medium size lorry modeled with many details as automatically controlled multibody system. For sensitivity analysis special indexes were used. This paper continue sensitivity investigations of elaborated control system and fragmentary unpublished results of the studies are presented. Here, they concern the sensitivity of the lane-change controller to time delay of data processing.

It is well known, that delay effects are especially pernicious (possible instability !) in feedback systems and very important for control systems with regulators working in real time. Literature on control systems with delay is very rich (extensive lists in [2]). For synthesis control algorithms dedicated to systems with delay special methods have been elaborated. Generally, they are based on the concept of predictor (eg. Smith predictor) joined in the control system. But in many cases, if the time delay is small, a control with delay effects neglected (as in our case) turns out enough to ensure stability and good steering action. Of course, this requires a lot of simulation investigations. Fragments of such calculations are presented in the paper.

2. Automatic control of lane change process

Suppose that a car moves with a significant speed on a straight even road and suddenly an obstacle springs up in front of it. The driver or the Automatic Cruise Control (ACC) system applies brakes. If a collision cannot be avoided by braking and the automatic dodging system may be used, the lane-change control system is automatically operated by means of an active steering system. In result of the system operation, the vehicle dodges the obstacle with a preset speed resulting from the braking process. The analysis of the situation and the instant of operating the steering system constitute a complicated optimization problem, which is not covered herein. The scope of this analysis is narrowed to controlling the lane-change process.

The plane vehicle motion in the lane-change process is described by two variables: position of the centre of vehicle mass relative to the road centreline $Y(t)$ and angular position of the vehicle body

relative to the road centreline (yaw angle) $\psi(t)$. According to drivers' experience, as well as to the control theory, the steering wheel angle curve minimizing the manoeuvre time should be close to the "bang-bang" curve (according to the terminology used in the theory of time-optimal systems) and the control process may be decomposed into two phases, i.e. transposition and angular stabilization (Fig.1)

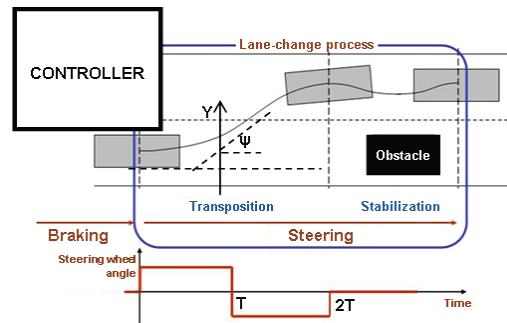


Figure 1. Two-phase lane change control process.

The lane change controller is composed by a reference signal generator and two regulators acting in a switchable structure (fig.2). The generator provides three reference signals $\delta_{HR}(t)$ (bang-bang type waveform signal of the steering system angle), $Y_R(t)$ and $\psi_R(t)$ (waveform signals of the linear and angular vehicle positions computed for $\delta_{HR}(t)$ signal) which describe the lane change maneuver according to a simple reference model of the vehicle motion. The signals $Y_R(t)$, $\psi_R(t)$ are set-point

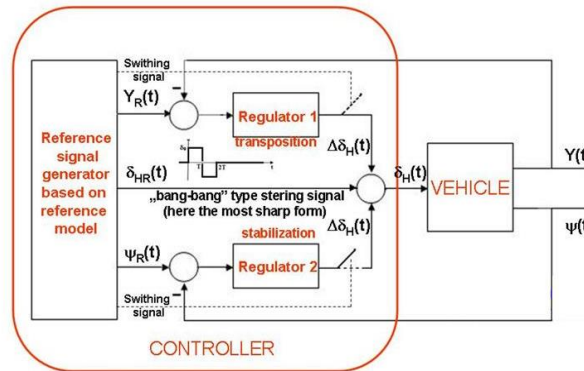
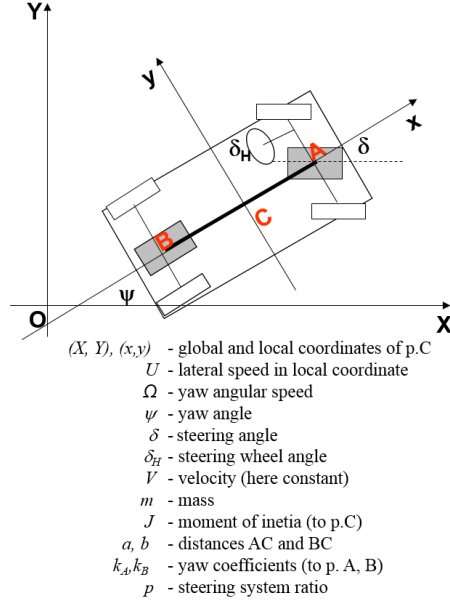


Figure 2. Block diagram of the automatic control system.

signals for two Kalman - type regulators which correct the real steering angle signal $\delta_H(t)$ to minimize errors between measured and desired waveforms of the variables. In the first phase of the control process, the transposition system is ON (activated) and the angular stabilization system is OFF

(deactivated); in the second phase, these connections are reversed. The switching strategies can be also more sophisticated.



Classic „bicycle model”
in local coordinates
+ **Standard approach**
Transformation
to global coordinates

$$m\dot{U}(t) + \frac{k_A + k_B}{V} U(t) + \frac{mV^2 + k_A a - k_B b}{V} \Omega(t) = k_A \delta(t)$$

$$J\dot{\Omega}(t) + \frac{k_A a^2 + k_B b^2}{V} \Omega(t) + \frac{k_A a - k_B b}{V} U(t) = k_A a \delta(t)$$

$$X(t) = \int_0^t \dot{X}(\tau) d\tau = \int_0^t (V \cos(\psi(\tau)) - U(\tau) \sin(\psi(\tau))) d\tau$$

$$Y(t) = \int_0^t \dot{Y}(\tau) d\tau = \int_0^t (V \sin(\psi(\tau)) + U(\tau) \cos(\psi(\tau))) d\tau$$

$$\psi(t) = \int_0^t \Omega(\tau) d\tau$$

$$\delta_H(t) = p \cdot \delta(t)$$

Linearization
Laplace transformation
Transfer functions $G_{Y\delta}(s), G_{\psi\delta}(s)$
Reduced transfer functions

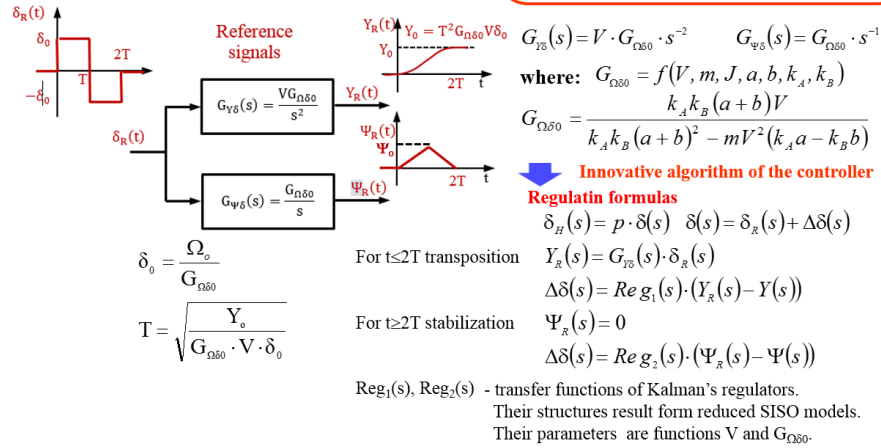


Figure 3. The concept of the lane change control system synthesis.

The concept of synthesis of controller's algorithms (reference signal generator for $\delta_{HR}(t)$, $Y_R(t)$, $\Psi_R(t)$, as well as both regulators for $\Delta\delta(t)$) is expressed in Figure 3.

A special feature of the developed controller algorithm is an analytical linking of its parameters with the parameters of the reference model and lane-change description. So, changing the parameters like Y_0 , V , ..., the controller can changes its parameters like δ_0 , T , ... automatically.

3. Delay-type disturbances in control system

The conceptual control system is a base for elaboration of real mechatronic system containing real sensors, real data processing, real actuators. These mechatronic devices can treated as ideal elements working with disturbances. Disturbances in the system can be different, and not only due to signals' noises and offsets but also due to time delays in transmission, and generally to time delay in data processing.

It is interesting that delay effects in data processing can be caused by actions of non-linear elements having characteristics with "dead zone". In mechanical systems such behaviour is well known as "clearance" or "backlash". Transmission of signals through dead zone element can result not only in their distortion but also in their delay. Delay effects are especially visible for signals which appear suddenly. This is expressed in fig. 4.

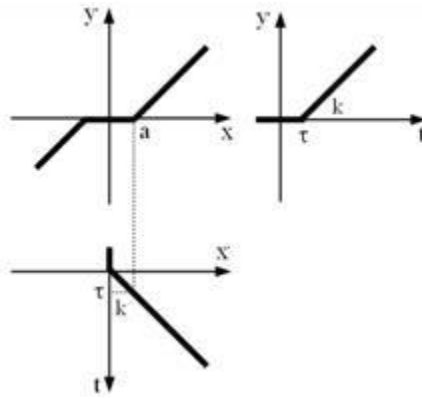


Figure 4. The effect of time delay for signal $x(t)$ which is processed to the form $y(t)$ in the element having characteristics $y(x)$ with dead zone described by a parameter a .

Analytical description [7]: $x(t) = kt1(t)$, $y(t) = kt1(t-\tau)$, $1(t)$ – Heaviside function, $\tau = a/k$

Therefore delay effects seem to be especially important for analysis of disturbances in our conceptual control system. In such studies block diagram of the automatic control system presented in fig.2 is modified to more realistic form presented in fig. 5.

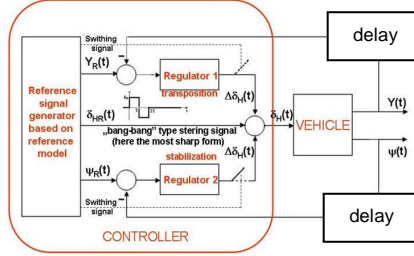


Figure 5. Block diagram of the automatic control system with delay.

4. Example simulation investigations

Examinations of the control system have been worked on simulation tests where the controller model controlled a lane-change manoeuvre of virtual vehicle modelled in detail (3D multi-body non-linear mathematical model of a two-axle motor truck of medium load capacity). The object's model requires about 200 parameters (note, that the reference model in the controller demands only 7 parameters). Thank to many investigations the model was verified with success, for many datasets describing the controller, vehicle, and road conditions (including “difficult” cases).

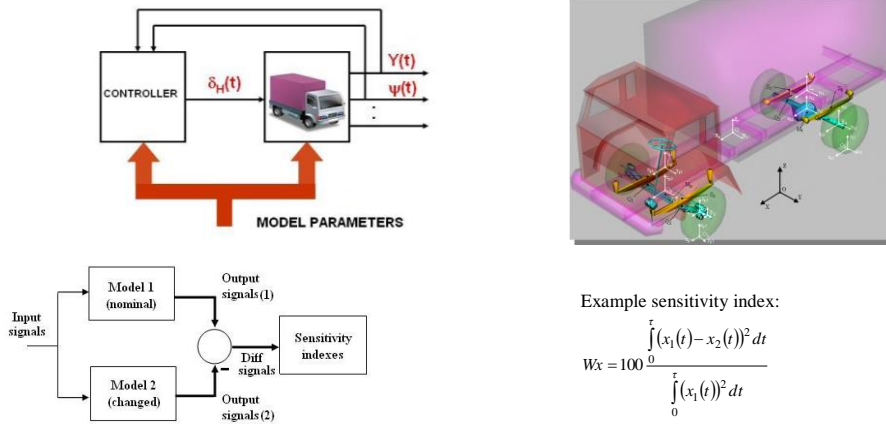


Figure 6. The concept of sensitivity studies basing on simulation investigations.

For simulation tests an authorial package of programs has been elaborated. This software is useful for sensitivity studies, because it ensures also calculations of special sensitivity indexes (fig. 6).

In the studies reported in the paper, the nominal model concerns the system without delay effects, and the model changed – with delay $\tau \in \{0.03, 0.06, 0.09\}$ s in the regulators' action. Example results of investigations are presented below (fig.7). In all these simulations operation conditions have been rather difficult for the car (speed about 70 km/h, wet asphalt road).

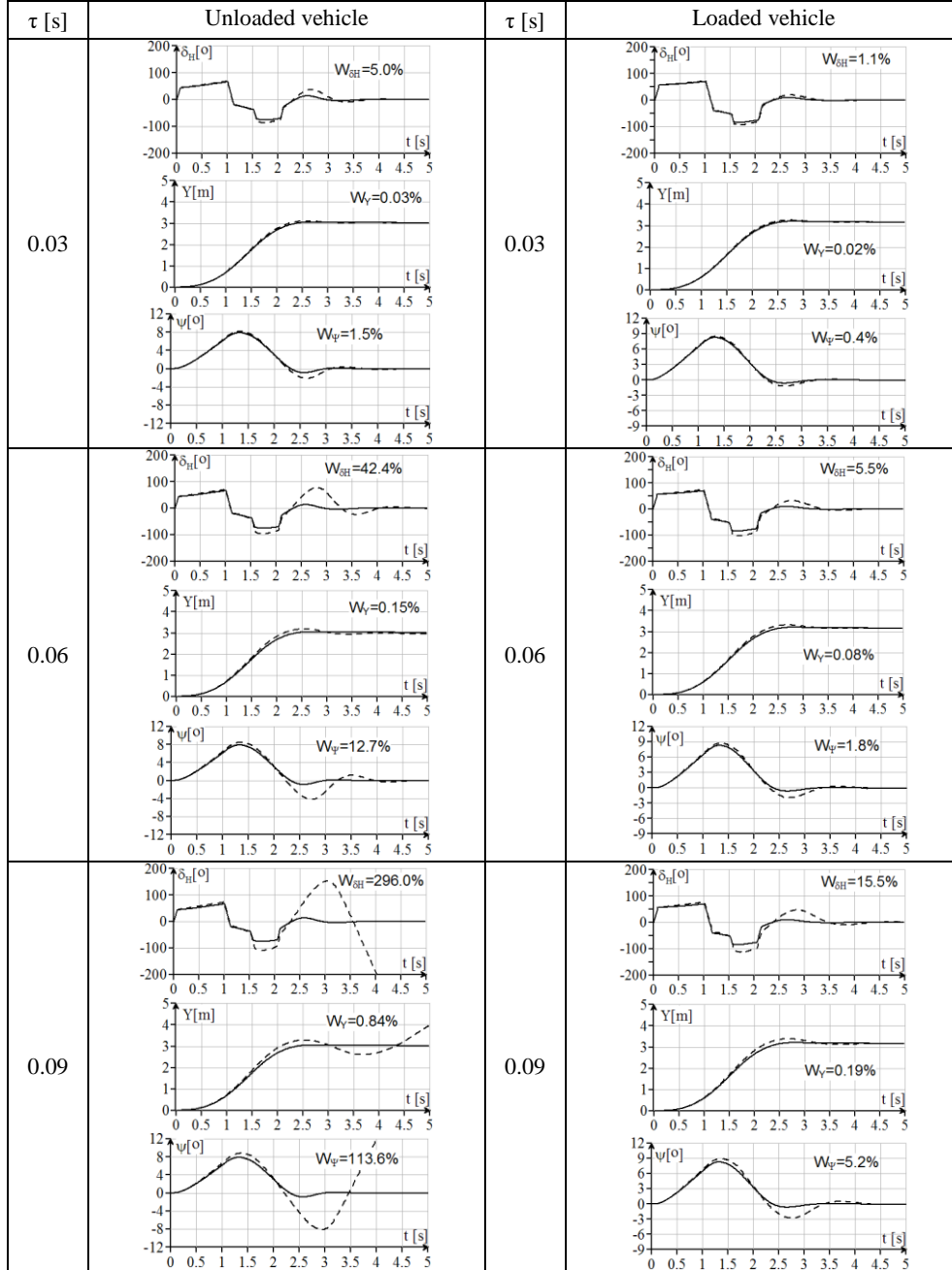


Figure 7. Results of simulations when measured signals have been delayed.

Notation: solid lines for the system without delays, dashed lines for the system with delays.

5. Summary

The presented simulation results show that the lane change maneuver has been successfully carried out, in spite of the measurement delay-type disturbances of signals. Satisfying results have been observed when the delay parameter τ was small ($\tau \in \{0.03, 0.06\}$). Of course increasing the delay worsens the quality of the control. The area of stability depends on vehicle parameters, and road conditions, Especially difficult for stability were extreme difficult operating conditions (lightly loaded lorry and very wet road). For $\tau > 0.2$ the system was instable practically in all conditions.

Finally, it can be stated that the proposed control system have proven to be enough robust to the measurement delays and varying operating conditions when the differences between nominal and changed model are not too large.

References

- [1] Bevan, G. P.; Gollee, H.; O'Reilly, J: *Trajectory generation for road vehicle obstacle avoidance using convex optimization*. Proceedings of the Institute of Mechanical Engineers Part D – Journal of Automobile Engineering, Vol. 224 (4), 2010.
- [2] Fridman E.: *Tutorial on Lyapunov-based methods for time-delay systems*. European Journal of Control, Vol.20, pp. 271-283, 2014.
- [3] Gao, Y.; Lin, T.; Borrelli, F.; Tseng, E.; Hrovat, D.: *Predictive control of autonomous ground vehicles with obstacle avoidance on slippery roads*. Dynamic Systems and Control Conf. 2010.
- [4] Gidlewski, M.; Żardecki, D.: *Investigation of vehicle motion control process due to the linearization of the lateral dynamics reference model used in the controller*. Mechanics Research Communications, 82, 2017.
- [5] Gidlewski, M.; Jankowski, K.; Muszyński, A.; Żardecki, D.: *Vehicle Lane Change Automation with Active Steering – Theoretical Studies and Numerical Investigations*. SAE Paper 2017-01-1555, 2017.
- [6] Gidlewski M., Jemioł L., Żardecki D.: Sensitivity investigations of the automated lane-change manoeuvre – selected issues. Journal-article. Proceedings of the Institution of Mechanical Engineers, Part I: Journal of Systems and Control Engineering. Vol. 233/2019, Issue 4.
- [7] Żardecki D.: Modelowanie luzu i tarcia oparte na odwzorowaniach $\text{luz}(\dots)$ i $\text{tar}(\dots)$ – podstawy teoretyczne i zastosowanie w symulacji drgań nieliniowych w układach kierowniczych samochodów. (Rozprawa habilitacyjna). Wyd. WAT, Warszawa 2007. (in Polish)

Mirosław Gidlewski, PhD. Eng.: ŁUKASIEWICZ Research Network – Automotive Industry Institute (ŁUKASIEWICZ – PIMOT), ul. Jagiellońska 55, 03-301 Warszawa, Poland (m.gidlewski@pimot.eu).

Leszek Jemioł, MSc. Eng.: University of Technology and Humanities in Radom, Malczewski Street 29, 26-600 Radom, Poland (leszek.jemiol@uthrad.pl).

Dariusz Żardecki, Prof.: Military University of Technology (WAT), Kaliski Street 2, 00-908 Warsaw, ŁUKASIEWICZ Research Network – Automotive Industry Institute (ŁUKASIEWICZ – PIMOT), ul. Jagiellońska 55, 03-301 Warszawa, Poland (d.zardecki4@upcpoczta.pl), dariusz.zardecki@wat.edu.pl).

Experimental nonlinear localisation in a system of two coupled beams

Aurélien Grolet, Zein Shami, Sadaf Arabi, Olivier Thomas

Abstract: This study presents results showing experimental non-linear localisation in a (macro) system of two coupled beams. First a reduced order model of the system is introduced, using the so called STEP method, leading to a two dof model with cubic non-linearity. This model allows to show that non-linear localisation is possible through a 1:1 internal resonance mechanism. Moreover, one can show, using Harmonic Balance Method, that the forced localised solution stems from the principal resonance curve through pitchfork bifurcation, and the numerical model allows to compute the amplitude of bifurcation as well as the bifurcated branch. The experimental results are presented and compared to the numerical ones showing very good agreements.

1. Introduction

This study deals with the non-linear vibration of structural systems. The objective is to present both numerical and experimental results related to non-linear localisation. Localisation corresponds to vibration states where the energy is localised to a spatial subset of the structure, and is related to symmetry breaking bifurcation. Many studies have demonstrated numerically that localisation can occur in system of coupled non-linear oscillators (e.g. [7]). Some experimental results related to localisation are available for nano/micro system of beams array (e.g. [8, 1]), but a small amount of experimental results are available for macro structure. In this study, we design a macroscopic plate structure that can be considered as two coupled non-linear beams. Considering numeric and experimental results, we show that the structure allows for a non-linear modal interaction leading to symmetry breaking bifurcation and localisation.

2. Two beams system and reduced order model

2.1. Description of the system

The system considered here consists of a circular plate that has been machined in order to create two parallel beams as indicated on Fig. 1. In this study, we will consider only transverse vibrations. The body of the circular plate provides a coupling between the beams, and it also restrains the axial displacement of the beams ends, so that the behaviour of the beams is similar to clamped-clamped beams, i.e. non-linearity occurs due to a coupling between axial and transverse motions.

To observe non-linear localisation, we will consider two particular eigen-modes of the structure depicted on Fig. 1. For those modes, the beams vibrate over a first bending mode shape (in phase or out of phase) and the rest of the plate remains at quite low amplitude. The idea is to design the structure such that both mode interacts non-linearly to give a localized mode (i.e. with broken symmetry). Indeed, if one looks only at the mid-beam amplitude, both modes can be described with the shape $\phi_1 = (1, 1)$ and $\phi_2 = (1, -1)$. The idea is to generate a modal interaction of the form $q_1(t)\phi_1 + q_2(t)\phi_2$, where q_1 and q_2 are the time varying modal amplitudes. If q_1 and q_2 are in phase, then the interaction will lead to a shape of the form $(a_1 + a_2, a_1 - a_2)$ which tends to the localised shape $(1, \epsilon)$ as the amplitude of the first mode a_1 tend to the amplitude of the second mode a_2 .

In order to prevent interaction with other modes, we set the structure dimension such that the two previous modes are consecutive (i.e. there is no other modes in between). This can be achieve to a certain extend by increasing the distance between the beams. The structure was also designed such that the vibration amplitude for symmetry breaking bifurcation is quite small (about 0.23 mm at the center of the beams) in order to be observed with reasonably low forcing amplitude. The design was realized in an iterative way using a reduced order model presented briefly hereafter.

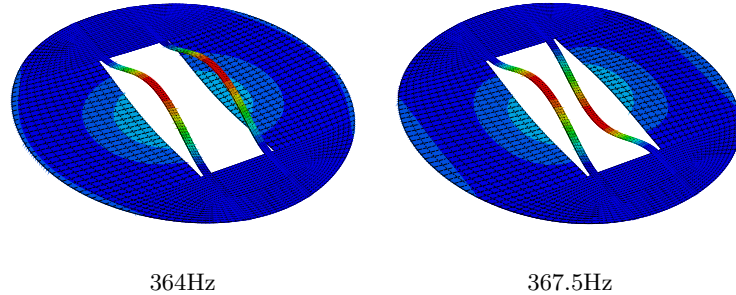


Figure 1. Linear mode shapes of interest (magnitude of the displacement) and their FEM natural frequencies

2.2. Reduced order model for plate structure

In theory, the system could be modelled by finite element method, but in practice the resolution time for non-linear computations would be prohibitive. An approximation of the system behaviour can be obtained by a so called Reduced Order Model (ROM). Here, only the form of the ROM equation for plate structure will be given, more details about the ROM procedure can be found in [3].

We consider that the solution to the FEM plate model is expanded over the linear mode

shapes basis computed with free boundary conditions. We denote q_j (reps. p_k) the modal amplitude of the j -th transverse mode (resp. the k -th in-plane mode). Neglecting in-plane inertia and using a condensation procedure (so that the p_k 's can be expressed as a function of the q_j 's, [3]), it can be shown that the reduced set of equation for the FEM plate model can be put under the following form (i.e. only considering modal amplitudes of transverse modes) [3]:

$$\ddot{q}_j + \omega_j^2 q_j + \sum_{k,l,m=1}^{N_t} \Gamma_{jklm} q_k q_l q_m = f_j(t), \quad \forall j \in [1, N_t] \quad (1)$$

where ω_j is the natural angular frequency of the j -th transverse mode, N_t is the number of transverse modes kept in the reduction basis and f_j is the j -th transverse modal force. The Γ_{jklm} are coefficients that can be evaluated using the so called STiffness Evaluation Procedure (STEP) which is based on a series of static non-linear FEM computations [6, 3].

In this study we are interested in the interaction between the two modes described on Fig.1, so that only those two modes are kept in the reduced order model. Based on Eq.(1), the reduced set of equation have the following form:

$$\begin{aligned} \ddot{q}_1 + \omega_1^2 q_1 + G_1 q_1^3 + E_1 q_1^2 q_2 + C_1 q_1 q_2^2 + D_1 q_2^3 &= f_1(t) \\ \ddot{q}_2 + \omega_2^2 q_2 + G_2 q_2^3 + E_2 q_1 q_2^2 + C_2 q_1^2 q_2 + D_2 q_1^3 &= f_2(t) \end{aligned} \quad (2)$$

When computing the values of the coefficient, one finds that some of them are order of magnitudes smaller than the others, and are therefore neglected (see table 1).

coeff.	G_1	C_i	E_i	D_i
$i = 1$	$9.26 \cdot 10^{10}$	$3.46 \cdot 10^{11}$	≈ 0	≈ 0
$i = 2$	$1.09 \cdot 10^{11}$	$3.46 \cdot 10^{11}$	≈ 0	≈ 0

Table 1. Non-linear coefficients for the reduced order model of the final design

3. Analytic and numeric results

3.1. Equation of motion and solution methods

Based on the previously presented ROM, we consider the following equation of motion (with periodic forcing):

$$\begin{aligned} \ddot{q}_1 + 2\xi_1 \omega_1 \dot{q}_1 + \omega_1^2 q_1 + G_1 q_1^3 + C_1 q_1 q_2^2 &= f_1 \sin(\Omega t) \\ \ddot{q}_2 + 2\xi_2 \omega_2 \dot{q}_2 + \omega_2^2 q_2 + C_2 q_1^2 q_2 + G_2 q_2^3 &= f_2 \sin(\omega t) \end{aligned} \quad (3)$$

where q_i is the modal amplitude of the i -th transverse mode ($i = 1$: in phase mode, $i = 2$ out of phase mode, see Fig.1), ξ_i 's are the modal damping ratio, ω_i 's are the natural frequencies,

f_i 's are the modal forces amplitude and Ω is the excitation frequency. G_1, G_2 and C are the non-linear coefficients obtained through the reduced order model procedure.

In this study, approximated solutions to the system in Eq.(3) are obtained using the Harmonic Balance Method (HBM), coupled with a numerical continuation procedure based on the Asymptotic Numeric Method (ANM) [2]. The solution is searched for as a truncated Fourier series, and the coefficients of the Fourier series are obtained by solving an algebraic equation depending on a parameter (here the frequency). The use of the MANLAB package [4] allows to compute the solution as the parameter is varied, along with its stability.

In addition, in order to design the structure, a single harmonic approximation has been used to derive analytical conditions resulting in the appearance of a modal interaction, which will be presented hereafter.

3.2. Non-linear modal analysis

In this section, we consider the undamped, unforced version of the equation of motion (3). We search for a single harmonic solution under the form $q_n(t) = A_n e^{i\omega t} + c.c.$ (where *c.c.* stands for complex conjugate). The following polar representation is introduced: $A_n = a_n e^{i\gamma_n}$. The derivatives \dot{q}_n and \ddot{q}_n are computed and substituted into (the unforced and undamped version of) (3) leading to the following (after separation of real and imaginary parts):

$$\begin{aligned} a_1 (-\omega^2 + \omega_1^2 + 3G_1 a_1^2 + C_1 a_2^2 (\cos(2\gamma_2 - 2\gamma_1) + 2)) &= 0 \\ a_2 (-\omega^2 + \omega_2^2 + C_2 a_1^2 (\cos((2\gamma_1 - 2\gamma_2) + 2) + 3G_2 a_2^2) &= 0 \\ a_1 a_2^2 C_1 \sin(2\gamma_1 - 2\gamma_2) &= 0 \\ a_1^2 a_2 C_1 \sin(2\gamma_2 - 2\gamma_1) &= 0 \end{aligned} \tag{4}$$

The free HBM solutions can be separated into uncoupled and coupled solutions.

The uncoupled solutions are obtained by setting $a_2 = 0$ (mode 1) or $a_1 = 0$ (mode 2) in Eq.(4), leading to the expression of the backbone curves for the first and the second mode:

$$\begin{aligned} \omega_{nl,1}^2 &= \omega_1^2 + 3G_1 a_1^2, \quad \text{and } a_2 = 0 \\ \omega_{nl,2}^2 &= \omega_2^2 + 3G_2 a_2^2, \quad \text{and } a_1 = 0 \end{aligned} \tag{5}$$

The coupled solutions are obtained by setting $\sin(2\gamma_2 - 2\gamma_1) = 0$ in Eq.(4). There is two cases to be considered, namely $\cos(2\gamma_2 - 2\gamma_1) = \pm 1$, referred to as "linear coupling" (+1, the modes interact in phase, or in phase opposition) and "elliptic coupling" (-1, the modes interact in phase quadrature).

- For the linear coupling, the following equation can be obtained from Eq.(4):

$$3(G_1 - C_2)a_1^2 + 3(C_1 - G_2)a_2^2 = \omega_2^2 - \omega_1^2 \tag{6}$$

It shows that a linear-coupled solution can bifurcate from mode one only if $G_1 - C_2 > 0$, and from mode 2 only if $C_1 - G_2 > 0$. The amplitudes of bifurcation are respectively $a_1^2 = \frac{\omega_2^2 - \omega_1^2}{3(G_1 - C_2)}$ and $a_2^2 = \frac{\omega_2^2 - \omega_1^2}{3(C_1 - G_2)}$

- For the elliptic coupling, the following equation can be obtained from Eq.(4):

$$(3G_1 - C_2)a_1^2 + (C_1 - 3G_2)a_2^2 = \omega_2^2 - \omega_1^2 \quad (7)$$

It shows that a elliptic-coupled solution can bifurcate from mode one only if $3G_1 - C_2 > 0$, and from mode 2 only if $C_1 - 3G_2 > 0$. The amplitudes of bifurcation are respectively $a_1^2 = \frac{\omega_2^2 - \omega_1^2}{3G_1 - C_2}$ and $a_2^2 = \frac{\omega_2^2 - \omega_1^2}{C_1 - 3G_2}$

Different behaviour may happen, based on the values of the non linear coefficients (see e.g. [5]). In this study, the structure has been designed to allow both modes to interact in order to generate localisation. Indeed, using the coefficients of the reduced order model given in table 1, one has the following:

- $G_1 - C_2 < 0$ and $C_1 - G_2 > 0$, so that a linear-coupled mode can bifurcate only from the out-of-phase mode when the mid-beam amplitude is close to 0.23mm.
- $3G_1 - C_2 \approx 0$ and $C_1 - 3G_2 \approx 0$ so that the "elliptic-coupled" bifurcation points are at very high amplitude (considered here as infinity)

The summary of the non-linear analysis is given on Fig.2. The backbone curve of both modes are represented, along with the bifurcated solution stemming from the out-of-phase mode. A stability analysis, similar to the one use in the multiple scale method, allows to draw an instability zone for the out-of-phase mode, defined by the following:

$$(2\omega\xi_1\omega_1)^2 + (\omega_1^2 - \omega^2 + 2C_1a_2^2)^2 = (a_2^2C_1)^2 \quad (8)$$

As soon as the second mode enter the instability zone, it bifurcates to a coupled solution where the first mode gets more and more activated though non-linear interaction. In the physical domain, this correspond to a solution where both beams vibrate out-of-phase with (increasing) different amplitude (see Fig.2, left panel), indicating the break of symmetry and the localisation.

3.3. Forced response

In order to evaluate the structure of the forced response the MANLAB package is used [4]. In order to see clearly the non-linear interaction with the first mode, only the second mode is excited (i.e. $f_1(t) = 0$ in Eq.(3)). Fig.3 shows the forced response of the second mode

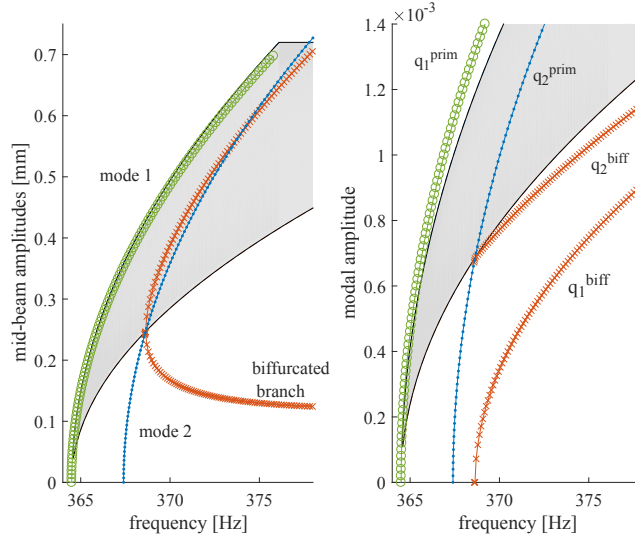


Figure 2. Backbone curves for the two uncoupled modes (○: in-phase mode, ·: out-of-phase mode) along with the bifurcated solution (×) and the instability zone of the out-of-phase mode (shaded area). left panel: physical representation, right panel: modal representation

for several amplitude of forcing (for $f_2(t)$), along with the instability zone presented in the previous section. As the forcing amplitude increase, the response becomes more and more non-linear, and turning points appear. As the amplitude increases even further the response enters the shaded area and becomes unstable.

MANLAB allows to compute the bifurcated branch as depicted on Fig.4 (for a forcing amplitude of $f_2 = 2$). It turns out that, for this forcing amplitude, the bifurcated solution is stable, then experiments a Neimark-Saker bifurcation, then gets stable again until the turning point to the right. This stability analysis indicates that the bifurcated solution could be observed in practice, as will be demonstrated by the experimental measurements.

The right panel of Fig.4 depicts the same forced response results using the physical representation, i.e. the amplitude at the middle of each beam. It clearly shows that the bifurcated branch corresponds to a non-symmetric state, which gets more and more localised as the amplitude increases.

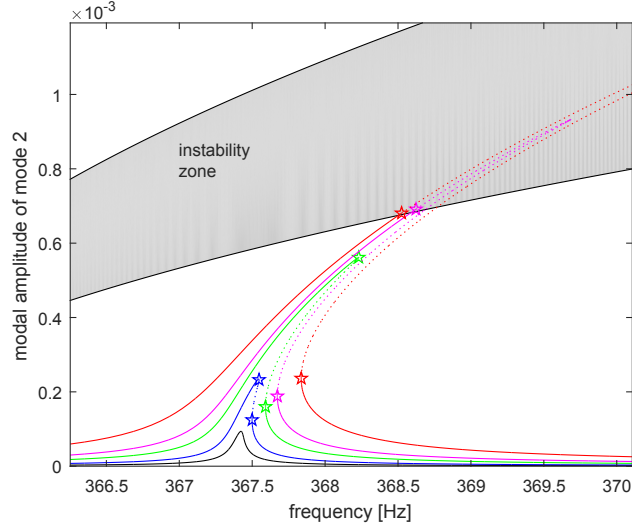


Figure 3. Numerical forced response for an excitation on the second mode only, for several amplitude of modal forcing ($f_2 = 0.1, 0.25, 0.6, 1.0, 2.0$). Solid lines: stable, dotted lines: unstable. The stars indicate the changes of stability.

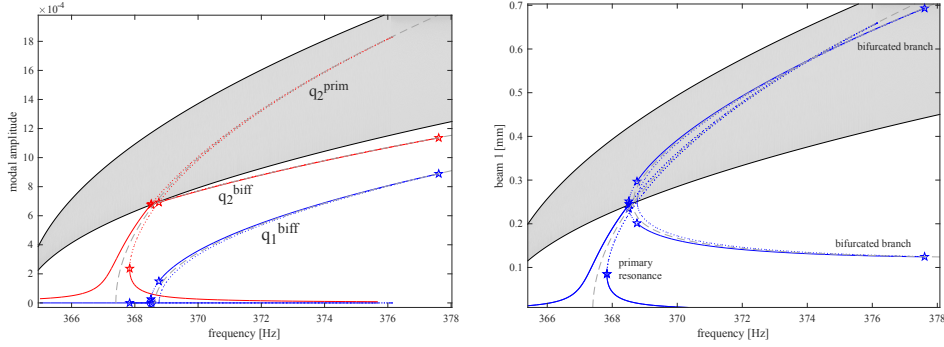


Figure 4. Numerical forced response for an excitation on the second mode with an amplitude of $f_2 = 2.0$). Solid lines: stable, dotted lines: unstable, the stars indicate the change of stability. The dashed lines represents the backbone curves obtained in the modal analysis. Right panel: modal representation, Left panel: Physical representation

4. Experimental set-up and protocols

4.1. Description of the experimental setup

The plate structure depicted on Fig.5 has been machined out of a stainless steel plate (thickness $e = 1.5$ mm, density $\rho = 7850 \text{ kg.m}^{-3}$, Young modulus $E = 190 \text{ GPa}$) using wire cutting.

For the experiments, the structure is hanged using four nylon wires, which allows to be close to free boundary conditions.

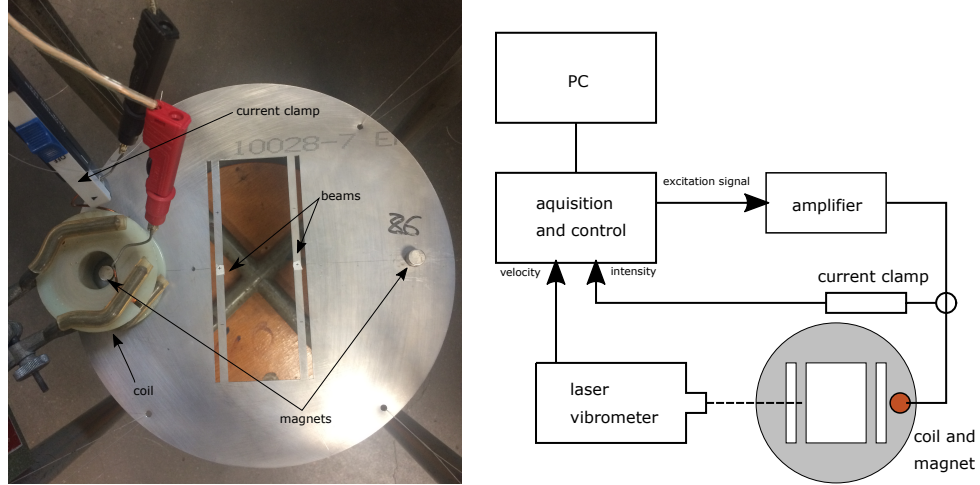


Figure 5. Picture of the experimental setup and scheme of the measurement chain

In order to provides excitation to the structure, a small magnet (about 6 grams) is stuck at a given excitation point, and a coil is then placed around it. Sending periodic current through the coil allows to transmit a force without having an actual physical contact with the structure (Lorentz/Laplace forces). The amplitude of the force is controlled by the intensity of the current sent to the coil, which is monitored using a current clamp.

Velocity measurements are carried out using a laser vibrometer, which allows to measure the transverse velocity at each user-defined points on the top surface of the structure (most of the time at the middle of the beams).

4.2. Measurement protocols

In this study, the measurement are made using swept sine excitation. The scheme of the experimental set-up is depicted on Fig.5. For the analysis, a sinusoidal current with fixed intensity is sent to the coil, and the velocity amplitude is measured at the center of a particular beam. Then the excitation frequency is slightly increased (or decreased) and the velocity measurements is repeated, until a given excitation frequency has been reached. For a given excitation level, this allows to plots the amplitude of the displacement at the middle of each beam as as function of the excitation frequency (forced response).

Note that since only one laser vibrometer was available, the measurements are done one after another (i.e. for a given level of excitation, the measurements is done for beam 1, then

the experiment is reset and the measurement is done for beam 2).

4.3. Location of the excitation

Following the numerical analysis of the previous section, the excitation point is chosen such that it excites only the out-of-phase modes. This is done by positioning the magnets at a node of the in-plane modes. In order to keep the structure symmetric, the magnet is positioned on a node of the in-plane mode belonging to the horizontal axis of symmetry, and a second magnet (without coil) is positioned in a symmetrical position with relation to the vertical axis (see Fig.5).

5. Results and discussion

5.1. Linear modal analysis

An experimental modal analysis is conducted on the structure in order to evaluate its symmetry. The experimental natural frequencies are approximately 364Hz and 367Hz, which is in good agreement as compared to the FEM frequencies given in Fig.1. The modal damping ratios are estimated approximately using the -3dB bandwidth, leading to $\xi_1 = \xi_2 = 10^{-4}$.

The experimental mode shapes of the out-of-phase mode are evaluated by sending a low intensity sinusoidal current to the coil (at the natural frequency) and scanning the velocity over the structure. The results are depicted on Fig.6. The mode shape is very close to the FEM mode shape presented in Fig.1. The maximum amplitudes at the middle of the beam are respectively $2.2 \cdot 10^{-3}$ and $1.9 \cdot 10^{-3}$ mm (about 10% difference), which indicates a small disturbance in the symmetry, mainly due to the magnet positioning.

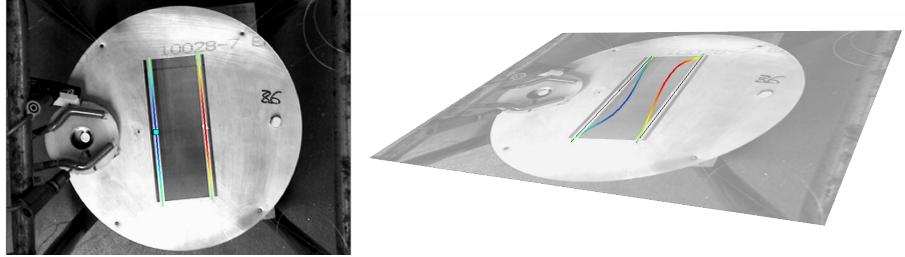


Figure 6. Experimental mode shape for the out-of phase mode (top view and 3D view), only the velocity amplitude of the beams have been depicted

5.2. Forced response

The results of the sweep-sine analysis are presented on Fig.7, where the mid-beam amplitudes are plotted as a function of the excitation frequency for several current amplitudes.

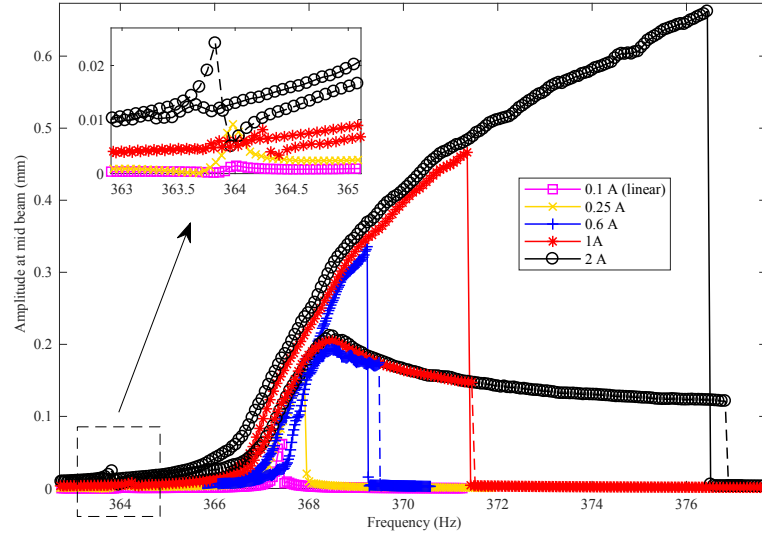


Figure 7. Mid-beam amplitude as a function of frequency for several current intensity (solid line: beam one, dashed line: beam 2)

It can be observed that the response of the first mode (around 364Hz) is very low, which indicates that the magnets are well positioned, and that the coil excites mainly the out-of-phase mode. Since each measurement is carried out one after another, over time, it might happen that the natural frequencies of the structure change a bit (about 0.5Hz) due to temperature variations or other reasons (as observed for the resonance peak of the in-phase mode in the zoom of Fig.7).

For low intensity currents ($I=0.1\text{A}$ and $I=0.25\text{A}$), only the mid-beam amplitude of beam 1 is depicted on Fig.7 (solid lines). For $I=0.1\text{A}$, the behaviour of the structure is linear, and both beams vibrate with the same amplitude. For $I=0.25\text{A}$, the non-linearity starts to be activated, and a jumps occurs as the excitation frequency is increased.

For higher intensity, both the amplitude of beam one (solid lines) and two (dashed lines) are depicted. For the three cases ($I=0.6\text{A}$, $I=1\text{A}$ and $I=2\text{A}$) the behaviour is similar and can be interpreted as follows. When the mid-beam amplitude is below 0.2mm, both beams vibrate out-of-phase with roughly the same amplitude. However, when the vibration amplitude increases, there is a break of symmetry in the vibration shape of the structure, both beams vibrates with clearly different amplitude. As the current increases, the difference in the beam amplitude increases as well leading to a localisation. For the highest excitation current, one can see that the first beam vibrates with an amplitude 7 times greater than the

second beam.

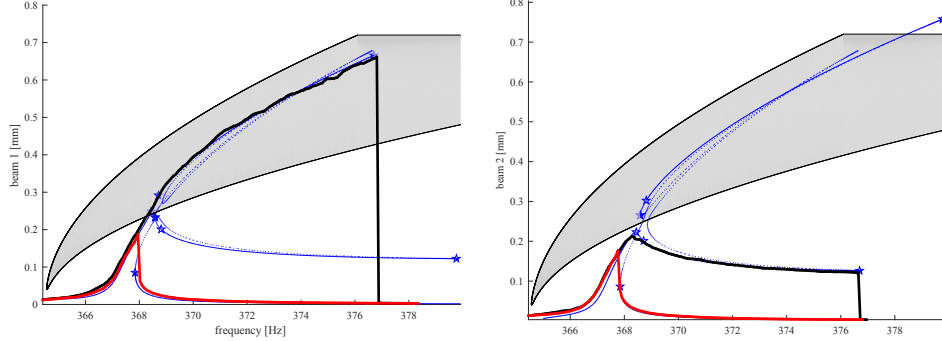


Figure 8. Comparison between experimental and numerical results for a current of 2A (left: beam 1, right beam 2). The thick lines represent experimental sweep-sine responses (upward and downward sweep). The thin lines represent numerical responses (solid: stable, dotted: unstable). The stars indicate the stability changes

A comparison to the numerical results obtained using the reduced order model is given on Fig.8. The current in the coil is fixed to the maximum tested amplitude (i.e. $I = 2A$). In the experimental case both an upward and a downward sweep-sine analysis is carried out for both beam (thick lines). In the numerical case, the solution to Eq.(2) is computed using the HBM and the ANM (thin lines). In order to take into account the fact that magnet is not exactly positioned at a node of the in-phase mode, we consider that the in-phase mode is also forced, with an amplitude ten times smaller than the out-of-phase modes. This perturbation leads to the destruction of the branching points, and the localisation appears in a continuous way, as in the experimental data. One can see that the numerical simulations agree very well with the experimental results, which validates the reduced order model procedure and the theoretical analysis.

6. Conclusion

In this paper, we considered the transverse non-linear vibration of a system of coupled beams. Numerical simulations based on a reduced model of the structure have shown that a non-linear modal interaction can occur, leading to symmetry breaking bifurcation and localisation. Experimental measurements using swept sine excitation were carried out, and demonstrate that the modal interaction can be observed in practice (with good repeatability), if the excitation amplitude is high enough. The numerical and the experimental results agree very well, showing that the reduced order model procedure is able to generate a good representation of the physical system with only a few degree of freedom. Further study

should consider systems with more than two beams, in order to generate travelling waves and/or breathers.

References

- [1] CHATANI, K., WANG, D. F., IKEHARA, T., AND MAEDA, R. Vibration mode localization in coupled beam-shaped resonator array. In *2012 7th IEEE International Conference on Nano/Micro Engineered and Molecular Systems (NEMS)* (2012), pp. 69–72.
- [2] COCHELIN, B., DAMIL, N., AND POTIER-FERRY, M. *Méthode asymptotique numérique. Methodes numériques*. Hermes Lavoissier, 2007.
- [3] GIVOIS, A., GROLET, A., THOMAS, O., AND DEÜ, J.-F. On the frequency response computation of geometrically nonlinear flat structures using reduced-order finite element models. *Nonlinear Dynamics* 97, 2 (2019), 1747–1781.
- [4] GUILLOT, L., COCHELIN, B., AND VERGEZ, C. A taylor series-based continuation method for solutions of dynamical systems. *Nonlinear Dynamics* (2019).
- [5] MANEVICH, A. I., AND MANEVITCH, L. I. *The Mechanics of Nonlinear Systems with Internal Resonances*. Imperial college press, 2005.
- [6] MIGNOLET, M. P., PRZEKOP, A., RIZZI, S. A., AND SPOTTSWOOD, S. M. A review of indirect/non-intrusive reduced order modeling of nonlinear geometric structures. *Journal of Sound and Vibration* 332, 10 (2013), 2437 – 2460.
- [7] PAPANGELO, A., FONTANELA, F., GROLET, A., CIAVARELLA, M., AND HOFFMANN, N. Multistability and localization in forced cyclic symmetric structures modelled by weakly-coupled duffing oscillators. *Journal of Sound and Vibration* 440 (2019), 202 – 211.
- [8] SATO, M., HUBBARD, B. E., ENGLISH, L. Q., SIEVERS, A. J., ILIC, B., CZAPLEWSKI, D. A., AND CRAIGHEAD, H. G. Study of intrinsic localized vibrational modes in micromechanical oscillator arrays. *Chaos: An Interdisciplinary Journal of Nonlinear Science* 13, 2 (2003), 702–715.

Aurelien GROLET, (Ph.D.): ENSAM Lille/LISPEN, , 8 Boulevard Louis XIV, 59000 Lille.
(aurelien.grolet@ensam.eu).

The author gave a presentation of this paper during one of the conference sessions.

Zein SHAMI, (M.Sc.): ENSAM Lille/LISPEN, 8 Boulevard Louis XIV, 59000 Lille ().

Sadaf ARABI, (M.Sc.): ENSAM Lille/LISPEN, 8 Boulevard Louis XIV, 59000 Lille ().

Olivier THOMAS, (Pr.): ENSAM Lille/LISPEN, 8 Boulevard Louis XIV, 59000 Lille ().

Stability and control of a hybrid walking robot on planar, unstable and vibrating terrain

Dariusz Grzelczyk, Jan Awrejcewicz

Abstract: In this study we developed and investigated numerically a general kinematical model of a hybrid robot consisting of both crab-like and mammal-like legs. The simulation model implemented in Mathematica allowed us for virtual experiments and visualization the control process of the robot. We especially considered more precisely possibility of control the position and the orientation of the robot body on planar, unstable and vibrating ground. The used control algorithm is suitable to simultaneous control of all robot's legs in order to control of all six spatial degrees-of-freedom of the robot's body, i.e. three rotations and three linear displacements, respectively. Especially, this method can be successfully used for coordination and control all robot's legs on a planar, vibrating and unstable ground, for instance during stabilization of the robot's spatial position. Since the used version of the Mathematica computer program allows to communicate with different modern microcontrollers, the developed control algorithm can be simply adopted to control real constructions of different multi-legged robots.

1. Introduction

Different type of multi-legged robots were extensively investigated in the last years by numerous researches. These mobile machines can reproduce animals or humans movements and substitute humans in different activities [1]. Among numerous robots met in the literature, especially we can distinguish constructions with leg structure inspired on the basis of the anatomy of mammals and insects. Large numbers of the robot's limbs with different kinematic structures are suitable to overcome complex obstacles found in natural environment, without losing stability of the robot.

Walking robots were the subject of our investigations in the last years (for instance, see papers [2-9]). Recently, also different control strategies of the walking robots were commonly tested by other researches, employing different commercial software [10-16]. It shows that studies on walking robots are still challenging for researches. Therefore, in this paper we developed and implemented in Mathematica a general full parametric simulation model of a hybrid walking robot, i.e. the robot with different numbers of the limbs biologically inspired by insects or mammals. Especially, we considered the problem of control all six spatial degrees-of-freedom of the robot's body (i.e. three linear displacements and three rotations along and around three different axes, respectively) and control of all robot's legs on planar, unstable and vibrating ground. Such control possibilities can be especially

suitable in a natural environment of the robot, when it comes to both obstacle avoidance and the navigation process.

2. Prototypes of crab-like and mammal-like hexapod robots

In this study we designed two types of hexapod walking robots, with different leg's structures, i.e. crab-like robot (Fig. 1 on the left) and mammal-like robot (Fig 1 on the right). The presented designs were created in Inventor Professional 2019 software. As can be seen, each robot consists of the main body part (i.e. trunk) and six (hexapod) legs. In order to avoid mutual collisions, the robot's legs are symmetrically distributed on the robot's body. Each joint of the robot's leg is actuated by Power HD AR-1201MG servomotor controlled by the pulse-width-modulation (PWM) technique. These servomotors have inner closed loop feedback of the position control.



Figure 1. CAD models of bio-inspired walking robots created in Inventor Professional 2019 software: crab-like hexapod robot (on the left), and mammal-like hexapod robot (on the right).

In this study we focused especially on a mathematical formulations regarding full control of the robot on a planar, unstable and vibrating ground. To do it, we developed and implemented in Mathematica a general, three-dimensional, fully parametric simulation model of a hexapod robot. This model can be suitable to visualize kinematic behavior of the investigated robot and control the correctness of the simulated results, i.e. the spatial position of individual elements of the robot and the configurations of its legs. Moreover, through the appropriate choosing of the parameters, dimensions and different configurations of the robot's limbs, we are able to quickly generate also other types of walking machines, including four- or eight-legged walking robots.

3. Kinematic model of the robot

Figure 2 shows the example of a generated simulation model of a hybrid hexapod robot. In the presented case, four of its legs (two front and two hind) have mammal-like structures, whereas two middle legs have crab-like structures. The considered model of the robot is located in a global coordinate system $Oxyz$. The local coordinate system $O'x'y'z'$ is fixed to the robot, which is associated with the center

of the robot's trunk. In turn, other local coordinate systems are fixed to robot's limbs (here is presented only one local coordinate system $O''x''y''z''$ fixed to a single leg).

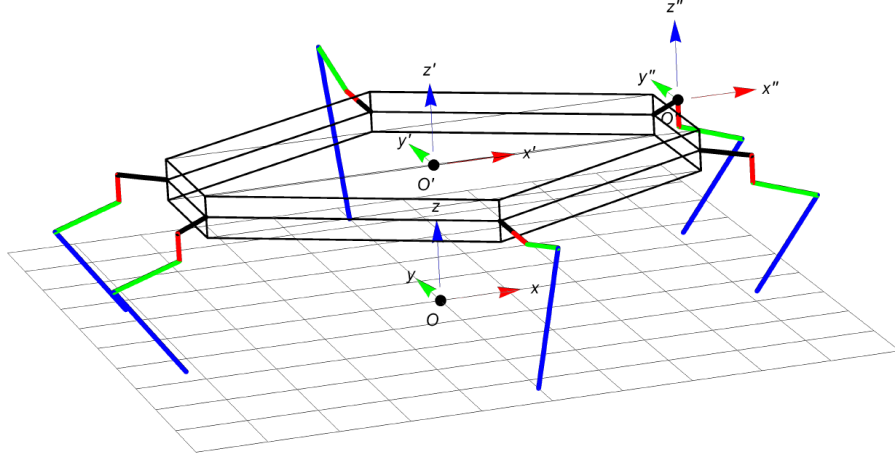


Figure 2. Simulation model of a hybrid hexapod robot implemented in Mathematica.

In our study we considered irregular/unstable ground of the robot, where a height (z – component of the ground) is a function of the coordinates x and y as well as the t , and have the following general form:

$$z = z_G(x, y, t). \quad (1)$$

The angles $\alpha_G, \beta_G, \gamma_G$ describe rotations of the ground, whereas $\Delta x_G, \Delta y_G, \Delta z_G$ denote linear deviations of the ground, with respect to x -, y - and z - axes of the global coordinate system, respectively. In turn, the angles $\alpha_R, \beta_R, \gamma_R$ describe rotations of the robot's body, whereas $\Delta x_R, \Delta y_R, \Delta z_R$ denote linear deflection of the robot, with respect to x -, y - and z - axes of the global coordinate system, respectively. Then, the vectors \mathbf{r}_G describing positions of all points on the ground in the global coordinate system $Oxyz$ can be calculated as follows:

$$\mathbf{r}_G = \mathbf{R}_G(\alpha_G, \beta_G, \gamma_G) \cdot \mathbf{r}_G^{init} + \Delta \mathbf{r}_G, \quad (2)$$

where $\Delta \mathbf{r}_G = [\Delta x_G, \Delta y_G, \Delta z_G]^T$, \mathbf{r}_G^{init} are vectors describing positions of points of the ground in the initial time, and

$$\mathbf{R}_G(\alpha_G, \beta_G, \gamma_G) = \mathbf{R}_G^{(z)}(\gamma_G) \cdot \mathbf{R}_G^{(y)}(\beta_G) \cdot \mathbf{R}_G^{(x)}(\alpha_G) \quad (3)$$

is the rotation matrix, whereas

$$\mathbf{R}_G^{(x)}(\alpha_G) = \begin{bmatrix} 1 & 0 & 0 \\ 0 & \cos \alpha_G & -\sin \alpha_G \\ 0 & \sin \alpha_G & \cos \alpha_G \end{bmatrix}, \quad (4)$$

$$\mathbf{R}_G^{(y)}(\beta_G) = \begin{bmatrix} \cos \beta_G & 0 & \sin \beta_G \\ 0 & 1 & 0 \\ -\sin \beta_G & 0 & \cos \beta_G \end{bmatrix}, \quad (5)$$

$$\mathbf{R}_G^{(z)}(\gamma_G) = \begin{bmatrix} \cos \gamma_G & -\sin \gamma_G & 0 \\ \sin \gamma_G & \cos \gamma_G & 0 \\ 0 & 0 & 1 \end{bmatrix}, \quad (6)$$

are elementary rotation matrices of the ground, respectively. All vectors \mathbf{r}_R of the robot in the global coordinate system $Oxyz$ can be expressed by the formula:

$$\mathbf{r}_R = \mathbf{R}_R(\alpha_R, \beta_R, \gamma_R) \cdot \mathbf{r}_R^{init} + \Delta \mathbf{r}_R, \quad (7)$$

where $\Delta \mathbf{r}_R = [\Delta x_R, \Delta y_R, \Delta z_R]^T$, \mathbf{r}_R^{init} are vectors describing positions of points of the robot in the initial time, and

$$\mathbf{R}_R(\alpha_R, \beta_R, \gamma_R) = \mathbf{R}_R^{(z)}(\gamma_R) \cdot \mathbf{R}_R^{(y)}(\beta_R) \cdot \mathbf{R}_R^{(x)}(\alpha_R) \quad (8)$$

is the rotation matrix, whereas

$$\mathbf{R}_R^{(x)}(\alpha_R) = \begin{bmatrix} 1 & 0 & 0 \\ 0 & \cos \alpha_R & -\sin \alpha_R \\ 0 & \sin \alpha_R & \cos \alpha_R \end{bmatrix}, \quad (9)$$

$$\mathbf{R}_R^{(y)}(\beta_R) = \begin{bmatrix} \cos \beta_R & 0 & \sin \beta_R \\ 0 & 1 & 0 \\ -\sin \beta_R & 0 & \cos \beta_R \end{bmatrix}, \quad (10)$$

$$\mathbf{R}_R^{(z)}(\gamma_R) = \begin{bmatrix} \cos \gamma_R & -\sin \gamma_R & 0 \\ \sin \gamma_R & \cos \gamma_R & 0 \\ 0 & 0 & 1 \end{bmatrix}, \quad (11)$$

are elementary rotation matrices of the ground, respectively. The computation of all coordinates describing positions of the feet of all the robot's legs requires consideration of the vectors \mathbf{r}_G of the ground in contact points between the robot's feet and the ground, and the inverse matrix \mathbf{R}_R^{-1} . Finally, the appropriate articulated variables for all joints of the robot's legs can be calculated.

4. Simulation results

4.1 Control of the robot walking on a planar ground

First, we considered the robot standing on a planar, stable and not vibrating ground (i.e. $z_G(x, y, t) = 0$, $\Delta x_G = \Delta y_G = \Delta z_G = 0$ and $\alpha_G = \beta_G = \gamma_G = 0$). In turn, we applied non-zero excitations of all six degrees-of-freedom of the robot's body, i.e. $\Delta x_R \neq 0$, $\Delta y_R \neq 0$, $\Delta z_R \neq 0$, $\alpha_R \neq 0$, $\beta_R \neq 0$, $\gamma_R \neq 0$. Configurations of the robot and its legs captured in regular time intervals are depicted in Fig. 3.

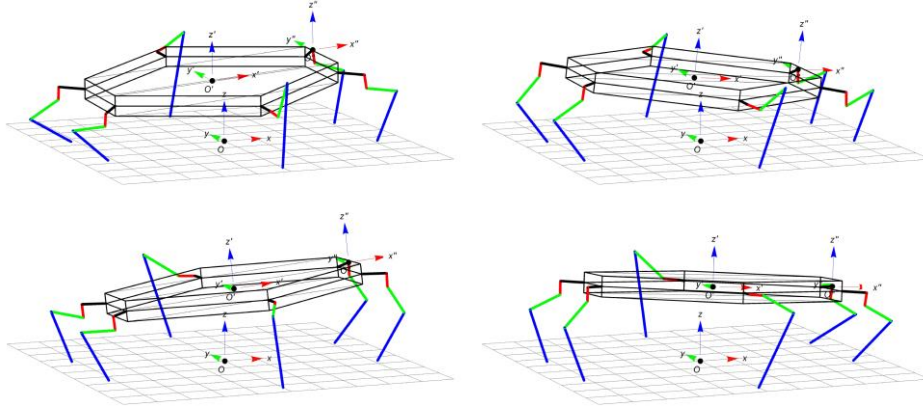


Figure 3. The chosen configurations of the investigated hexapod robot standing on a planar surface, controlled independently by linear deviations Δx_R , Δy_R , Δz_R , and rotations α_R , β_R , γ_R of the robot's body.

In the presented case, linear deviations Δx_R , Δy_R , Δz_R , as well as rotations α_R , β_R , γ_R of the robot controlling all six degrees-of-freedom of the robot are accurately reflected based on the predefined functions Δx_R , Δy_R , Δz_R , α_R , β_R , γ_R , respectively. Moreover, it should be emphasized that at any time the robot is supported by all six legs. The presented simulations show that the analyzed construction can be used as a fully controlled Stewart platform. As a result, we solved the control problem of the robot, including all six spatial degrees-of-freedom of the robot's body, i.e. independent controlling of three deviations and three rotations along and around three different axes of the robot.

4.2 Control of the robot on unstable ground

In this subsection we considered the control problem of the robot on unstable ground. Figure 4 presents configurations of the robot standing on unstable ground (i. e. $z_G(x, y, t) \neq 0$), captured in

regular time intervals. To better illustrate the process of controlling individual legs of the robot on unstable ground, we assumed first that $\Delta x_R = \Delta y_R = \Delta z_R = 0$ and $\alpha_R = \beta_R = \gamma_R = 0$ (i.e. full, both linear and angular spatial stabilization of the robot's trunk).

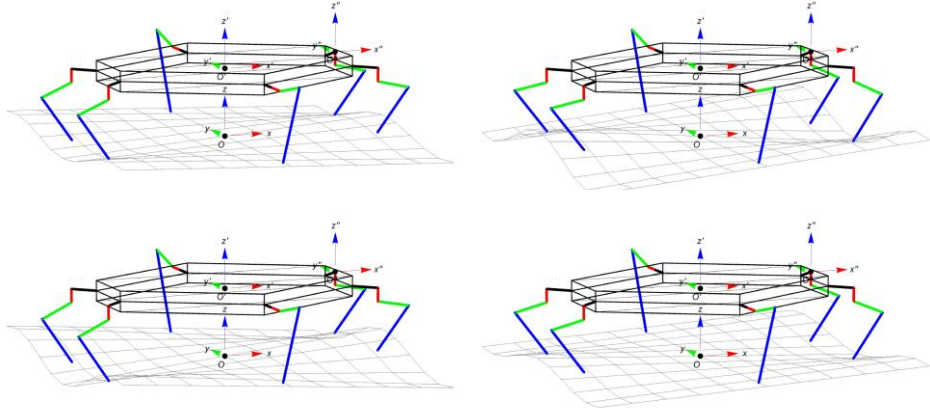


Figure 4. Configurations of the investigated hexapod robot on unstable ground, captured in regular time intervals for $\Delta x_R, \Delta y_R, \Delta z_R = 0$ and $\alpha_R, \beta_R, \gamma_R = 0$.

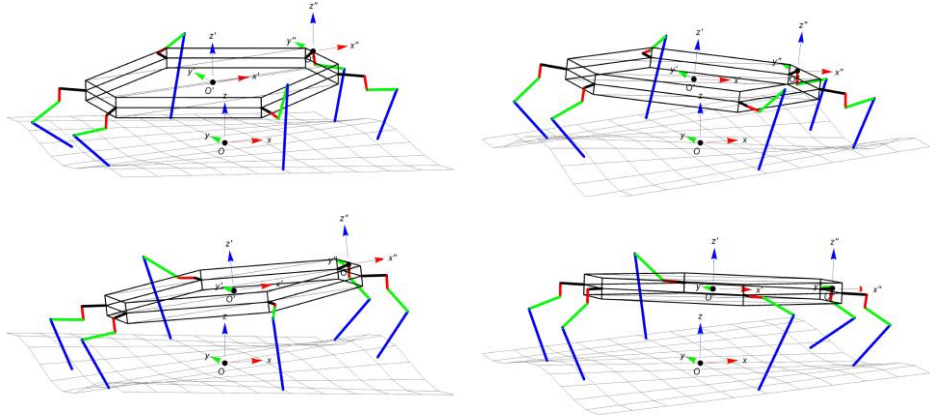


Figure 5. Configurations of the investigated hexapod robot on unstable ground, captured in regular time intervals for $\Delta x_R, \Delta y_R, \Delta z_R \neq 0$ and $\alpha_R, \beta_R, \gamma_R \neq 0$.

In this case we can observe the process of stabilizing both linear and angular positions of the robot, when the supporting ground is unstable. As we can see, at any time the robot is supported by all six legs, through the appropriate changing of the configurations of its legs, depending on the changes of the ground. Of course, it has a positive effect on the robot's stable position. Concluding, it should be noted that the presented control algorithm also works for $\Delta x_R, \Delta y_R, \Delta z_R \neq 0$ and $\alpha_R, \beta_R, \gamma_R \neq 0$ (see

Fig. 5). As a result, the considered construction can play a role of a Stewart platform, also on unstable ground.

4.3 Control of the robot on vibrating ground

Here we considered the control problem of the robot on vibrating ground. As in previous subsection, to better illustrate the process of controlling individual legs of the robot, first we taken into account that $\Delta x_R = \Delta y_R = \Delta z_R = 0$ and $\alpha_R = \beta_R = \gamma_R = 0$ (i.e. full, both linear and angular spatial stabilization of the robot's trunk). In turn, we taken into account non-zero harmonic excitations of the ground, i.e. $\Delta x_G \neq 0, \Delta y_G \neq 0, \Delta z_G \neq 0$ and $\alpha_G \neq 0, \beta_G \neq 0, \gamma_G \neq 0$. Simulation results captured in regular time intervals are reported in Fig. 6. As in previous cases, in each time the robot is supported by all six legs, thanks to the appropriate changing of the configurations of its all legs, depending on the vibrating ground. The robot keeps its position and orientation in the global coordinate system, regardless of the vibrating ground. The presented control algorithm also works for $\Delta x_R, \Delta y_R, \Delta z_R \neq 0$ and $\alpha_R, \beta_R, \gamma_R \neq 0$ (see Fig. 7). As a result, this construction can play a role of a Stewart platform, also on vibrating ground.

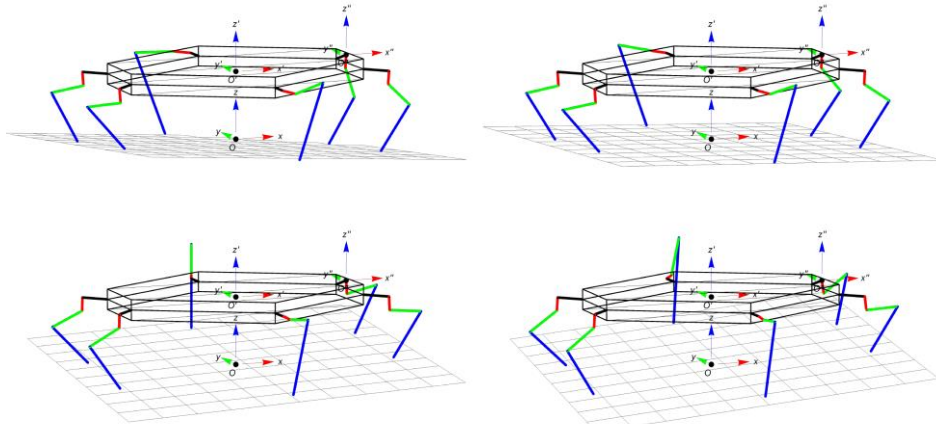


Figure 6. Configurations of the investigated hexapod robot on vibrating ground, captured in regular time intervals for $\Delta x_R, \Delta y_R, \Delta z_R = 0$ and $\alpha_R, \beta_R, \gamma_R = 0$.

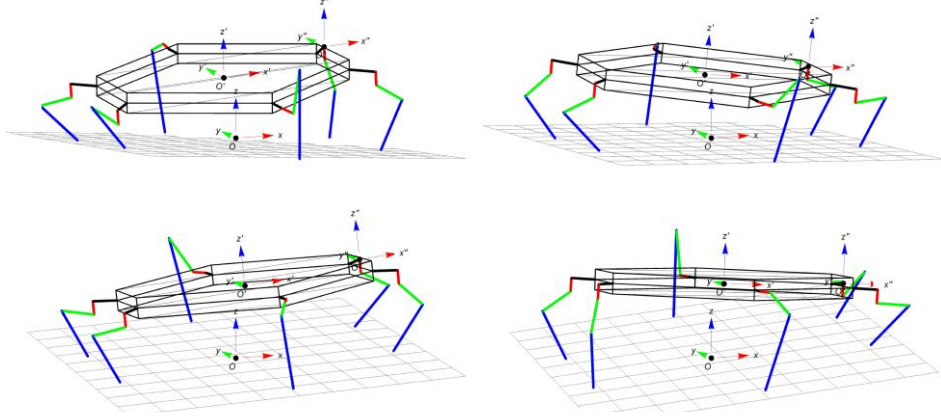


Figure 7. Configurations of the investigated hexapod robot on vibrating ground, captured in regular time intervals for $\Delta x_R, \Delta y_R, \Delta z_R \neq 0$ and $\alpha_R, \beta_R, \gamma_R \neq 0$.

5. Concluding remarks

In this paper we developed and numerically investigated a model of a multi-legged robot. As an example we considered six-legged hexapod robot with both crab-like and mammal-like legs. Using the simulation model implemented in Mathematica, we conducted some virtual experiments regarding stabilization and control of the position and orientation of the robot on planar, unstable and vibrating ground.

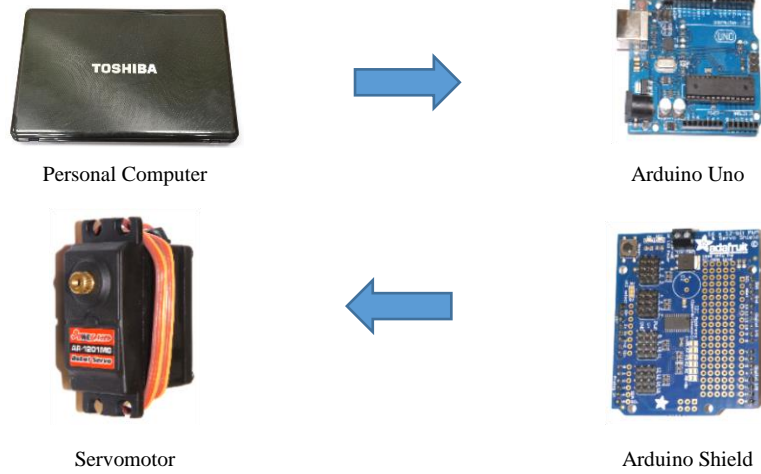


Figure 8. A general scheme of the control the robots' servomotors of a robot prototype using a simulation model implemented in Mathematica.

The possibilities of the Mathematica concerning 3D animation of simulated objects are available in the recent versions of this environment (in this paper we used Mathematica 11.2 version). Thanks to the developed visualization, we can observe exactly the configuration of all robot legs at any time, and this can be treated as a virtual experiment. The most recent versions of the Mathematica program also allow to relatively simple operation and communications with different modern microcontrollers connected to a computer such as Arduino Uno or Raspberry Pi. In addition, simpler versions of Mathematica software can also be installed, for instance, in the internal memory of the above mentioned Raspberry Pi microcontroller. As a result, using both the appropriate microcontroller and motor drivers, it is possible to directly apply the calculated articulated variables into all robot's joints, in order to real verification of the proposed algorithms controlling individual limbs of the robot. The obtained results show that the presented control possibility can be employed for full control of the robot position and orientation in space. As a result, the robot can be used as a fully control walking Stewart platform. The developed simulation model can be relatively simple and successfully adopted to control the constructed prototypes of different kinds of multi-legged machines. It is schematically shown in Fig. 8. This task will be the goal of our further research related to the problem of control the robot's legs, using real constructions made on the basis of the designs shown in Fig. 1.

Acknowledgments

The work has been partially supported by the National Science Centre of Poland under the grant OPUS 9 no. 2015/17/B/ST8/01700 for years 2016-2019.

References

- [1] Lagaza K, Pandey A. A literature review on motion planning of hexapod machines using different soft computing methods. *Global Journal of Engineering, Science and Social Science Studies*. 2018;3(1):1-10.
- [2] Grzelczyk D, Stańczyk B, Awrejcewicz J. On the hexapod leg control with nonlinear stick-slip vibrations. *Applied Mechanics and Materials*. 2015;801:12-24.
- [3] Grzelczyk D, Stańczyk B, Awrejcewicz J. Power consumption analysis of different hexapod robot gaits. In: *Dynamical Systems - Mechatronics and Life Sciences*. (Eds.) J. Awrejcewicz, M. Kaźmierczak, J. Mrozowski, P. Olejnik. TU of Lodz, Lodz, 2015, 197-206 (ISBN 978-83-7283-707-3).
- [4] Grzelczyk D, Stańczyk B, Awrejcewicz J. Estimation on the contact forces between the hexapod legs and the ground during walking in the tripod gait. *Vibrations in Physical Systems*. 2016;27:107-114.
- [5] Grzelczyk D, Stańczyk B, Szymanowska O, Awrejcewicz J. Simulation of the octopod robot controlled by different central patterns generators. In: *Engineering Dynamics and Life Sciences*. (Eds.) J. Awrejcewicz, M. Kaźmierczak, J. Mrozowski, P. Olejnik. DAB&M of TUL Press, Lodz, 2017, 229-238 (ISBN 978-83-935312-4-0).

- [6] Grzelczyk D, Szymanowska O, Awrejcewicz J. Kinematic and dynamic simulation of an octopod robot controlled by different central pattern generators. *Proceedings of the Institution of Mechanical Engineers, Part I: Journal of Systems and Control Engineering*. 2019;233(4):400-417.
- [7] Grzelczyk D, Awrejcewicz J. Analysis of contact forces between the ground and the hexapod robot legs during tripod gait. *Machine Dynamics Research*. 2018;42(2),17-26.
- [8] Grzelczyk D, Awrejcewicz J. Modeling and control of an eight-legged walking robot driven by different gait generators. *International Journal of Structural Stability and Dynamics*. 2019;19(5):1941009-1-1941009-23.
- [9] Grzelczyk D, Awrejcewicz J. Dynamics, stability analysis and control of a mammal-like octopod robot driven by different central pattern generators. *Journal of Computational Applied Mechanics*. 2019;50(1):76-89.
- [10] Rong X, Li Y, Ruan J, Li B. Design and simulation for a hydraulic actuated quadruped robot. *Journal of Mechanical Science and Technology*. 2012;26(4):1171-1177.
- [11] Burkus E, Odry P. Mechanical and walking optimization of a hexapod robot using PSO. In: *Proceedings of the IEEE 9th International Conference on Computational Cybernetics (ICCC '13)*, 8-10 July 2013, Tihany, Hungary, art. no. 6617583:177-180.
- [12] Linnemann R, Klaassen B, Kirchner F. Walking robot scorpion – experiences with a full parametric model. In: *Proceedings of the European Simulation and Modelling Conference (ESM '01)*, 6-9 June 2001, Prague, Czech Republic: 7 pages.
- [13] Guan X, Zheng H, Zhang X. Biologically inspired quadruped robot biosbot: modeling, simulation and experiment. In: *Proceedings of the 2nd International Conference on Autonomous Robots and Agents*, 13-15 December 2004, Palmerston North, New Zealand: 261-266.
- [14] Chen W, Ren G, Zhang J, Wang J. Smooth transition between different gaits of a hexapod robot via a central pattern generators algorithm. *Journal of Intelligent & Robotic Systems*. 2012;67(3-4):255-270.
- [15] Koo IM, Tran DT, Kang TH, Vo GL, Song YK, Lee CM, Choi HR. Control of a quadruped walking robot based on biologically inspired approach. In: *Proceedings of the 2007 IEEE/RSJ International Conference on Intelligent Robots and Systems (IROS '07)*, October 29 - November 2, 2007., San Diego, CA, USA: 2969-2974.
- [16] Koo IM, Kang TH, Vo GL, Trong TD, Song YK, Choi HR. Biologically inspired control of quadruped walking robot. *International Journal of Control, Automation and Systems*. 2009;7(4):577-584.
- Dariusz Grzelczyk, Ph.D.: Lodz University of Technology; Department of Automation, Biomechanics and Mechatronics; 1/15 Stefanowski Street, 90-924 Lodz, Poland (dariusz.grzelczyk@p.lodz.pl). The author gave a presentation of this paper during one of the conference sessions.
- Jan Awrejcewicz, Prof.: Lodz University of Technology; Department of Automation, Biomechanics and Mechatronics; 1/15 Stefanowski Street, 90-924 Lodz, Poland (jan.awrejcewicz@p.lodz.pl).

A rotational energy harvester for propulsion systems: design and experimental validation

B. Gunn, S. Theodossiades, S. J. Rothberg

Abstract: Modern control systems in propulsion applications can ensure the smooth and efficient operation and assist in detecting failures at early stages. The implementation of these control systems is restricted by the availability of sensor data, such as the stress experienced by a rotating shaft. Wireless sensor technology could be mounted to rotating components but nevertheless powering these sensors is a technical challenge. Traditionally batteries or slip rings would be used but these have a relatively short service life, which could lead to unacceptable maintenance demands. Energy harvesters may solve this issue by utilising vibration energy and converting it to useable electrical energy. In the present work, the prototype of a duffing-type rotational electromagnetic energy harvester is designed and tested, based on a previously published model of the authors. The harvester takes energy from the torsional speed fluctuations of a rotating shaft, commonly found in propulsion systems. The experimental results show a broadband response of the energy harvester to achieve useful power generation across a wide range of shaft speeds, which agrees well with the numerical model predictions.

1. Introduction

Rotating shafts in automotive, aeronautical and industrial applications regularly encounter torsional fluctuations about a mean speed. In many cases, these unavoidable fluctuations have speed dependent frequency content. Typically, the torsional oscillations are undesirable and represent waste energy lost from the system. In addition, there is a growing demand for wireless sensors in a variety of applications. Sophisticated control and health monitoring systems require an ever increasing amount of data in the internet of things. Often these sensors need to be in inaccessible places where maintenance (e.g. of batteries) would be too costly for wireless sensors to be viable. Vibration energy harvesters address these issues by extracting small amounts of ambient (otherwise waste) energy to power low consumption wireless sensor nodes.

Several examples of energy harvesters for rotating environments can be found in the literature. Commonly, a piezoelectric cantilever is mounted to the shaft pointing radially outwards [5, 2, 15]. As the shaft speed increases, the centripetal acceleration on the tip mass has a stiffening effect on the system which can be used to broaden the resonant frequency

range. However, the beam's stiffness properties mean that the harvester cannot be exactly at resonance throughout the whole operating speed range of the shaft. To combat this, Gu and Livermore used a highly flexible beam to strike a piezoelectric transducer [3]. Zhang et al [14] added a magnetic tip mass which repelled a fixed magnet resulting in a bistable oscillator which improved performance at low frequencies.

Another approach seen in the literature is to use offset pendulum dynamics to power wireless tyre pressure monitoring systems [13, 10]. These pendulums are tuned to the dominant frequency of the host at all speeds. However, they can experience non-linearity at high displacements.

So far, most of the mentioned harvesters extract their energy from the mean speed of the rotating host as opposed to the torsional fluctuations. Oil drilling rigs have been studied with both piezoelectric patches [9] and electromagnetic harvesters [12] used to power wireless sensors.

Kim [6] used the cantilever beam mentioned above to harness the torsional speed fluctuations of an internal combustion engine. This was tuned to a broad frequency range but was deemed insufficient to power the sensor of choice.

This paper is a continuation of a previous paper published by the same authors [4]. In that paper, a numerical model was presented for an energy harvester which used an electric motor with a cubic non-linear stiffness. In the present work, a physical realisation of the energy harvester is modelled, manufactured and tested. Conical springs are used to provide the non-linear stiffness and a new method of electromechanical coupling is used.

2. Overview of design

Figure 1 shows a 3D rendering of the intended prototype design and the constituent parts are labelled in the exploded view of figure 1. Working from left to right, two stator fins are mounted rigidly to the rotating shaft such that they rotate with the shaft's motion. Between these two stator fins are two pairs of conical springs which have non-linear stiffness characteristics as described in section 3.1. Sandwiched between the coil springs are the rotor fins. These fins stick through a slot in the back of the rotor and are held in place by small screws. The magnets then fit into recesses in the rotor and stick to the steel fins by magnetic attraction. Each magnet has opposing polarity to the one directly adjacent to it so that as the rotor rotates, the flux flowing through the coil alternates between North and South and the net flux through the coil is zero when the rotor is in its neutral position. The coil bobbin is also rigidly mounted to the shaft at a desired distance from the rotor. Coils of wire are wrapped around protrusions in the plane of the magnet surfaces. The rotor is made from aluminium rather than iron or some ferromagnetic steel to prevent the attractive forces

affecting the motion of the rotor. Finally, the motion of the shaft and rotor will be measured using laser Doppler vibrometers. To enable the rotor motion to be accurately measured, a collar made from acrylonitrile butadiene styrene (ABS) is glued to the rotor. Reflective tape is then wrapped around the collar to reflect the laser beam.

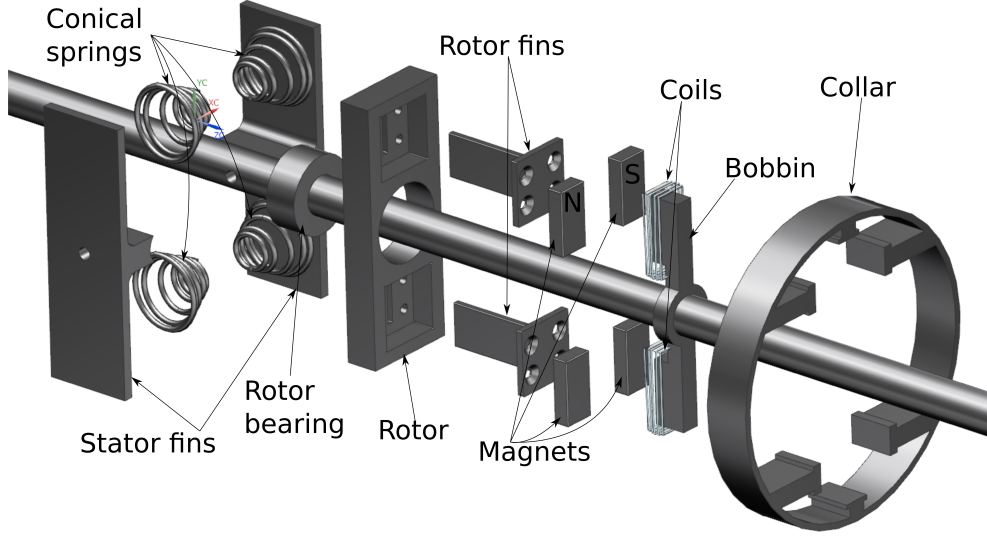


Figure 1. 3D rendering of the prototype energy harvester exploded view

The energy harvester equation of motion is given by [4]

$$J\ddot{\varphi} = -k_1\varphi - k_3\varphi^3 - c_{mech}\dot{\varphi} + \hat{\Theta}I + J\ddot{\alpha} \quad (1)$$

Where φ denotes the relative displacement of the rotor with respect to the stator and an overdot denotes differentiation with respect to time. J is the mass moment of inertia of the rotor, k_1 and k_3 are the linear and cubic components of the non-linear spring stiffness respectively. The mechanical damping coefficient is denoted by c_{mech} . $\hat{\Theta}$ is the electromechanical coupling factor and the electrical current flowing through the circuit is given by I . The angular acceleration of the host structure is denoted as $\ddot{\alpha}$.

The acceleration of the shaft is assumed to be accurately described by Eq. (2)

$$\ddot{\alpha} = A\omega^2 \cos(\omega t) \quad (2)$$

where A is a scalar, ω is the frequency of oscillation which in this case is assumed to be

twice the shaft speed. Such an acceleration is present in a shaft driven through a universal joint by a motor with constant rotational velocity.

3. Experimental prototype

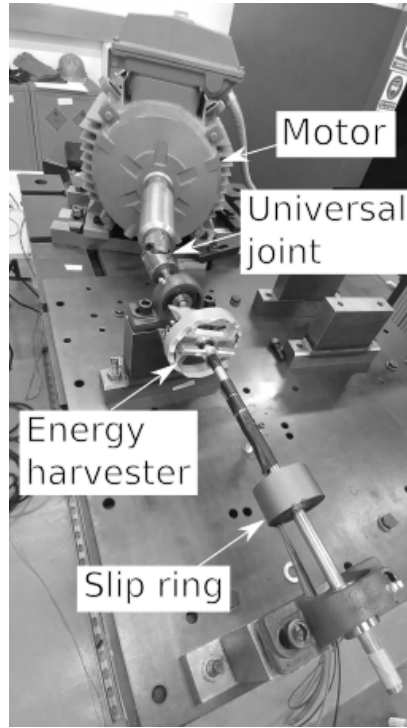


Figure 2. Photograph of experimental rig

A prototype model of the design described in section 2 was manufactured. In the published literature [4], part of the optimisation process required a physical prototype to be made to determine an approximate mechanical damping coefficient for the design upon which the optimisation is based. Therefore, parameters used for this prototype are not optimal; however, they can be used to validate the numerical models and improve the design accordingly.

Figure 2 shows a photograph of the apparatus used to test the energy harvester. A three phase electric motor drives an unloaded shaft to which the energy harvester is mounted. Between the motor and the energy harvester shaft sits a universal joint which is intentionally offset at an angle to induce second order speed fluctuations in the shaft [11]. These speed fluctuations are approximately sinusoidal with an amplitude that increases with shaft speed, similar to the vibrations of a four cylinder internal combustion engine.

3.1. Spring stiffness

The spring force is calculated using the MITCalc tool [7]. Figure 3 shows a comparison between the force calculated using the MITCalc versus the force measured using an Instron compressive test machine with a 1kN load cell. At low deflections, the spring stiffness is linear until a critical force is reached. Beyond this load, the stiffness becomes non-linear and progressively stiffer.

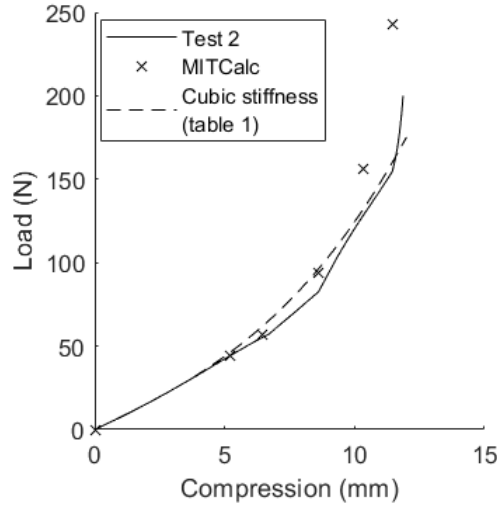


Figure 3. Comparison between predicted and experimental spring force

In the original model, it was assumed that the stiffness could be accurately described by a cubic polynomial resulting in a duffing type frequency response. Whilst the experimental and numerical results agree well, the progressing stiffness seems to be piecewise linear rather than smoothly stiffening as assumed in the cubic stiffness polynomial.

3.2. Constant speed test

Based on the results of section 3.3, the experimental test rig was run at a mean speed of 1600 rpm. The test was run for approximately 30 *seconds* to allow any transients to be eliminated before a sample of data was taken for 6 *seconds*. A restoring force surface method was used to determine the stiffness coefficients, k_1 and k_3 and the mechanical damping coefficient, c_{mech} . The mechanical damping ratio, ζ_{mech} is then calculated using Eq (3). The parameters calculated using this method are summarised in table 1.

$$\zeta_{mech} = \frac{c_{mech}}{2\sqrt{k_1 J}} \quad (3)$$

Table 1. Results of system identification at 1600 rpm

Parameter (units)	k_1 (Nm/rad)	k_3 (Nm/rad ³)	ζ_{mech}
Value	10.203	44.803	0.0351

When these parameters were fed into the numerical model of Eq (4), the resulting time series data for the open circuit harvester are shown in figure 4. The results show good agreement for the full cycle of the rotor.

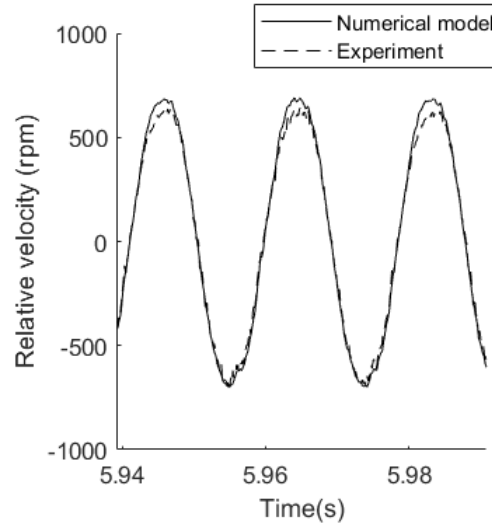


Figure 4. Comparison of time series data for numerical model and experimental relative velocity of rotor

3.3. Shaft speed sweep

Using the experimental apparatus of figure 2, a new test was conducted to assess the frequency response of the harvester. The motor was accelerated linearly from rest to 2500 rpm in 60 seconds, then decelerated linearly back to zero in another 60 seconds. Two Polytec OFV 400 laser vibrometers were used to measure the rotational velocity of the shaft and the rotor. These measurements were then used to calculate the relative velocity which was integrated numerically to get the relative displacement of the rotor with respect to the shaft. Figure 5 shows how the maximum relative velocity varies with shaft speed. This plot was obtained by extracting all the peaks of the relative velocity time series data and plotting against the mean shaft speed. The figure shows a clear non-linearity in the behaviour of the rotor with the experimental jump down occurring at 1877 rpm on the up-sweep and

experimental jump up at 1772 *rpm* on the down-sweep.

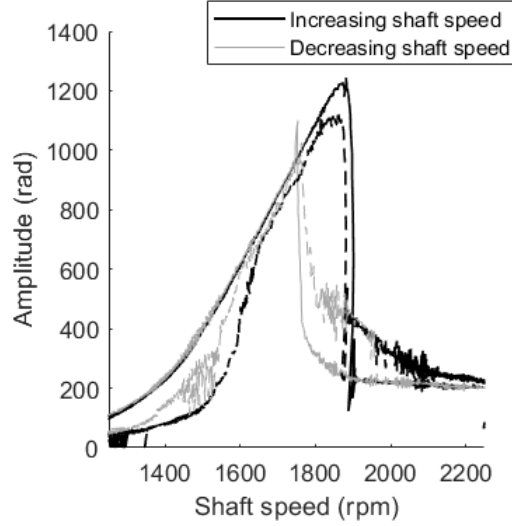


Figure 5. Frequency response of the energy harvester through a sweeping manoeuvre. Solid lines show numerical predictions, dashed lines show experimental results.

The solid lines represent the numerical model results and the dashed lines show the experimental results. The numerical model is run using the measured shaft speed as input and results in a jump-down speed 1903*rpm* on the up-sweep and jump up at 1748*rpm* on the down-sweep.

Furthermore, the numerical and experimental results follow the same curve from 1600*rpm* to 1877*rpm* showing excellent agreement between the numerical and experimental models. The deviation below around 1500 rpm is likely due to the unavoidable linear region of the conical spring. The rotor must first reach resonance to achieve a high enough displacement for the non-linearity to initiate.

3.4. Coupling factor

In the previous work [4], the electromechanical coupling mechanism was assumed to be a permanent magnet motor. However, as shown in figure 1, this prototype uses magnets with axial facing poles. Thus, a new model for the electromagnetic coupling is now needed. The same approach is used as Owens and Mann [8] except the equations for the magnetic flux density are different because, in the present work, rectangular magnets and coils are used.

Faraday's law states that an electromotive force (e.m.f.) is generated in a coil of con-

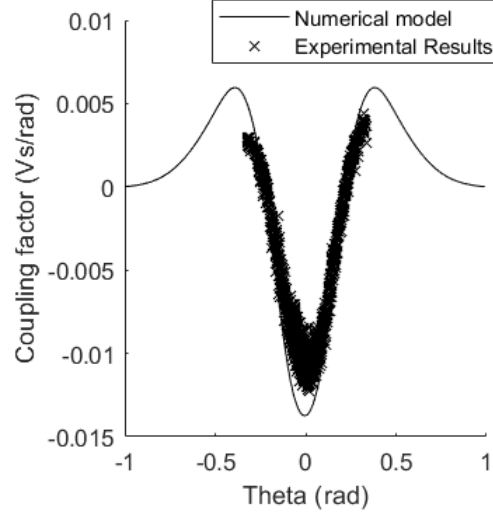


Figure 6. Comparison between numerical and experimental coupling factors

ductor when the magnetic flux flowing through it changes.

$$\varepsilon = \frac{d\Phi}{dt} \quad (4)$$

The flux through a single coil turn is found by integration of the magnetic flux density, B , through the area it encloses. Since the furthest turns of the coil are at a large distance relative to the size of the magnet, it cannot be assumed that the flux is constant through the whole coil. Only the magnetic field component perpendicular to the coil area contributes the the generated e.m.f. Hence, only the z component of the magnetic field is calculated. The magnetic flux density at any point in space around a rectangular bar magnet (perpendicular to its face) is given by [1]:

$$B_z(x, y, z) = \frac{\mu_0 M_s}{4\pi} \sum_{k=1}^2 \sum_{m=1}^2 \sum_{n=1}^2 (-1)^{k+n+m} \arctan \left[\frac{(x - x_n)(y - y_m)}{(z - z_k)} g(x, y, z; x_n, y_m, z_k) \right] \quad (5)$$

where $g(x, y, z; x_n, y_m, z_k)$ is given by

$$g(x, y, z; x_n, y_m, z_k) = \frac{1}{[(x - x_n)^2 + (y - y_m)^2 + (z - z_k)^2]^{1/2}} \quad (6)$$

where (x, y, z) is the infinitesimal point on the coil that is of interest and (x_n, y_m, z_k) is the point defining the boundaries of the magnet.

Eq. (5) is integrated over a single coil turn to give

$$\Phi = \int_{x_{min}}^{x_{max}} \int_{y_{min}}^{y_{max}} B_z dx dy \quad (7)$$

The average flux per turn for a uniform coil is given by

$$\Phi_{mean} \frac{1}{A_c} \int_{x_1}^{x_2} \int_{z_1}^{z_2} \Phi dx dz \quad (8)$$

Finally, the total flux through the coil is found by multiplying the total number of coil turns by the mean flux

$$\Phi_{total} = N_{total} \Phi_{mean} \quad (9)$$

Differentiation of Eq. (9) with respect to time shows that all parameters of Eq. (5) are constant with respect to time except the position of the coil relative to the magnets. Hence Eq. (4) can be written

$$\varepsilon = \frac{d\Phi}{dt} = \frac{d\Phi}{d\varphi} \frac{d\varphi}{dt} = \hat{\Theta}(\varphi) \dot{\varphi} \quad (10)$$

This model was tested experimentally by extracting the relative displacement, voltage and relative velocity at each point in the time series data where the relative velocity was within a small range (53 – 54 *rad/s*). The experimental coupling factor was calculated by dividing the voltage by the velocity at these points in accordance with Eq. (10). The numerical model was calculated by integrating Eq. (5) as described and taking account of the rotation of the coil with respect to the magnets. Discrepancies between the numerical model and the physical prototype are thought to be caused by poor coil formation in the physical prototype.

3.5. Voltage

Using results given in table 1 and the coupling factor as demonstrated in figure 6, the time series integration was run again and the predicted voltage compared to the experimental results in the highest resonant range around 1850 *rpm*.

Based on sections 3.2, 3.3 and 3.4, the main cause of error in the prediction of the voltage arises because of the inaccuracy of the coupling factor. This is mostly due to limitations in the manufacture of the physical coil which was wound by hand on a flat bobbin. In future, if coil winders with more accurate and repeatable winding can be used, the coupling factor will be greatly improved.

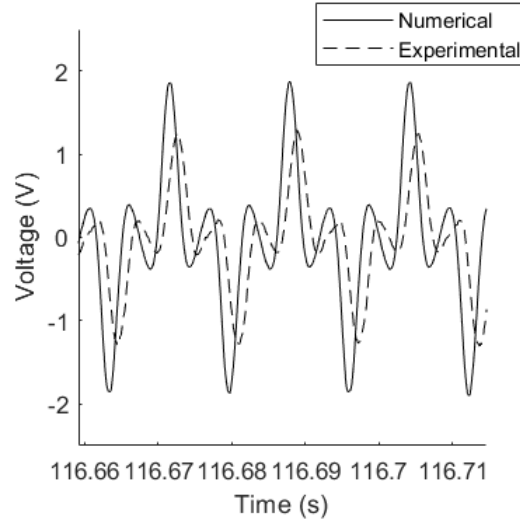


Figure 7. Comparison of time series voltage data for numerical model and experiment

4. Conclusions

This report presents an experimental validation of a previously published model for an energy harvester. It has been shown that conical spring stiffness can be approximated by a cubic polynomial to appropriately model the behaviour of the energy harvester except for at low speeds where it is thought that the springs operate in their linear regimen.

The electromechanical coupling mechanism has been modified (since the last published work) and an updated calculation of the coupling factor has been validated experimentally. Limitations in coil formation are thought to be the reason behind discrepancies between the physical prototype and the numerical model.

Also, a mechanical damping ratio of $\zeta_{mech} = 3.51\%$ has been measured using experimental data and the force surface restoration method. This damping ratio could be used to better optimise the next iteration of the design with a view to designing a coil that will maximise the power transferred to the electrical circuit by matching the mechanical and electrical damping ratios.

Future work will require a new energy harvester to be designed using the experimentally determined mechanical damping ratio. New springs and optimised inertia will help broaden the resonant frequency range to include the whole shaft operating range. The next prototype will also include a better wound coil for improved coupling factor which will be connected to an electrical load to get a power measurement and verify the effect of electrical damping.

Acknowledgments

The authors would like to thank F. Porras-Robles for his contribution to the design and test of the physical prototype.

References

- [1] FURLANI, E. P. *Permanent magnet and electromechanical devices : materials, analysis, and applications*, illustrate ed. Academic Press, San Diego, California, 2001.
- [2] GU, L., AND LIVERMORE, C. Passive self-tuning energy harvester for extracting energy from rotational motion. *Applied Physics Letters* 97, 8 (2010).
- [3] GU, L., AND LIVERMORE, C. Compact passively self-tuning energy harvesting for rotating applications. *Smart Materials and Structures* 21, 1 (2012), 015002.
- [4] GUNN, B. E., THEODOSSIADES, S., AND ROTHBERG, S. J. A Nonlinear Concept of Electromagnetic Energy Harvester for Rotational Applications. *Journal of Vibration and Acoustics* 141, 3 (2019), 031005.
- [5] HSU, J.-C., TSENG, C.-T., AND CHEN, Y.-S. Analysis and experiment of self-frequency-tuning piezoelectric energy harvesters for rotational motion. *Smart Materials and Structures* 23, 7 (jul 2014), 075013.
- [6] KIM, G. W. Piezoelectric energy harvesting from torsional vibration in internal combustion engines. *International Journal of Automotive Technology* 16, 4 (aug 2015), 645–651.
- [7] MITCALC. Spring calculation. <http://www.mitcalc.com/doc/springs/help/en/springs.htm>. Accessed: 2019-08-13.
- [8] OWENS, B. A. M., AND MANN, B. P. Linear and nonlinear electromagnetic coupling models in vibration-based energy harvesting. *Journal of Sound and Vibration* 331, 4 (2012), 922–937.
- [9] QIAN, F., ZHOU, W., KALUVAN, S., ZHANG, H., AND ZUO, L. Theoretical modeling and experimental validation of a torsional piezoelectric vibration energy harvesting system. *Smart Materials and Structures* 27, 4 (2018).
- [10] ROUNDY, S., AND TOLA, J. Energy harvester for rotating environments using offset pendulum and nonlinear dynamics. In *Smart Materials and Structures* (2014), vol. 23, IOP Publishing, p. 105004.
- [11] SCHMELZ, F., SEHERR-THOSS, C. H.-C., AND AUCTION, E. *Universal Joints and Driveshafts*, english ed ed. Springer-Verlag, Berlin, 1992.
- [12] TRIMBLE, A. Z., LANG, J. H., PABON, J., AND SLOCUM, A. A Device for Harvesting Energy From Rotational Vibrations. *Journal of Mechanical Design* 132, 9 (2010), 091001.

- [13] WANG, Y. J., CHEN, C. D., AND SUNG, C. K. System design of a weighted-pendulum-type electromagnetic generator for harvesting energy from a rotating wheel. *IEEE/ASME Transactions on Mechatronics* 18, 2 (2013), 754–763.
- [14] ZHANG, Y., NAKANO, K., ZHENG, R., AND CARTMELL, M. P. Adjustable Nonlinear Mechanism System for Wideband Energy Harvesting in Rotational Circumstances. *Journal of Physics: Conference Series* 744, 1 (2016), 012079.
- [15] ZHU, B., HAN, J., ZHAO, J., AND DENG, W. Practical Design of an Energy Harvester Considering Wheel Rotation for Powering Intelligent Tire Systems. *Journal of Electronic Materials* 46, 4 (2017), 2483–2493.

B. Gunn, M.Eng. (Ph.D. student): Wolfson School of Mechanical, Electrical and Manufacturing Engineering, Loughborough University, University Road, Loughborough, Leicestershire, LE11 3TU, UNITED KINGDOM (*b.e.gunn@lboro.ac.uk*). The author gave a presentation of this paper during one of the conference sessions.

S. Theodossiades, Professor: Wolfson School of Mechanical, Electrical and Manufacturing Engineering, Loughborough University, University Road, Loughborough, Leicestershire, LE11 3TU, UNITED KINGDOM (*s.theodossiades@lboro.ac.uk*).

S. J. Rothberg, Professor: Wolfson School of Mechanical, Electrical and Manufacturing Engineering, Loughborough University, University Road, Loughborough, Leicestershire, LE11 3TU, UNITED KINGDOM (*exact postal address*). *s.j.rothberg@lboro.ac.uk*

A new analytical approach to nonlinear free vibration of microtubes

Nicolae Herisanu, Vasile Marinca

Abstract: Based on Hamiltonian principle and a modified couple stress theory, a nonlinear differential equation of motion is presented. The analytic approximate solution to nonlinear free vibration is obtained by means of the Optimal Auxiliary Functions Method (OAFM). The influence of internal material length scale parameter, outer diameter, flow velocity and Poisson's ratio on the dynamic behaviour is considered.

1. Introduction

Microtubes have been widely used and studied in different applications such as capacitive switches, signal filtering, biology, information technology and semiconductor technology, cancer therapy, resonant sensors and so on. In the last years, there has been a great deal of interest in dynamic behaviour of micro-pipes or microtubes. Younis and Nayfeh [1] investigated the response of a resonant microbeam to an electric actuation. A nonlinear model is used to account for the mid-plane stretching a DC electrostatic force and an AC harmonic force. Also, Zand et al. [2] studied nonlinear oscillations of microbeams actuated by suddenly applied electrostatic force. Effects of electrostatic actuation, residual stress, midplane stretching and fringing fields are considered in modelling. Large amplitude flexural vibration behavior is presented by Shen [3] for microtubes embedded in an elastic matrix of cytoplasm. The microtube is modeled as a nonlocal shear deformable cylindrical shell which contains small scale effect. Formulation are based on shell theory with a von Karman-Donnell-type of kinematic nonlinearity. Zeverdejani and Beni [4] analysed the free vibration of protein microtubes embedded in the cytoplasm by using Euler-Bernoulli model based on modified strain gradient theory. The protein microtube is modeled as a simply supported or clamped-clamped beam and the elastic medium is modeled with Pasternak support foundation. The microfluid-induced nonlinear free vibration of microtubes is studied by Yang et al. [5]. Based on Hamilton's principle and a modified couple stress theory and taking into consideration the geometric nonlinearity, a derivation of the nonlinear equation of motion is obtained. A mathematical formulation is proposed by Semnani et al. [6] to investigate the nonlinear flow-induced dynamic characteristics of a cantilevered pipe conveying fluid from macro to micro scale. Hosseini and Bahaadini [7] investigated the size dependent stability of cantilevered micro pipes. They used the modified strain gradient theory in

conjunction with the Bernoulli-Euler beam model when two of three length scale parameters or all of them are zero. The micro Coriolis flow meters are extensively used by Ghazanu et al. [8] in fluidic micro-circuits. The out-of-plane vibration and stability of curved microtubes are investigated to study the dynamic behaviour of curved Coriolis flow meters. The structural analysis of microtube vibration modes calculated by an atomistic approach is reported by Havelka et al. [9]. Molecular dynamics was applied to refine the atomic structure of a microtube including its anisotropy. A size-dependent Timoshenko beam model is used by Bahaadini et al. [10] for the study of free vibration and instability analysis of a nanotube conveying nanoflow. To capture the size effects, nonlocal strain gradient theory and Knudsen number are applied.

In the present study, starting to an elastic pinned-pinned Euler-Bernoulli beam resting on an elastic foundation with a linear torsional spring at one end, we will determine an analytical approximate solution of nonlinear free vibration. The influence of internal material, outer diameter, flow velocity and Poisson's ratio are considered.

2. Problem formulation

The system under consideration is a pinned-pinned straight and slender microtube with length L , flexural rigidity EI , and mass per unit length m , as shown in Fig.1. The internal flow in the microtube is due to an incompressible fluid of mass per unit length M , flowing with velocity V_f .

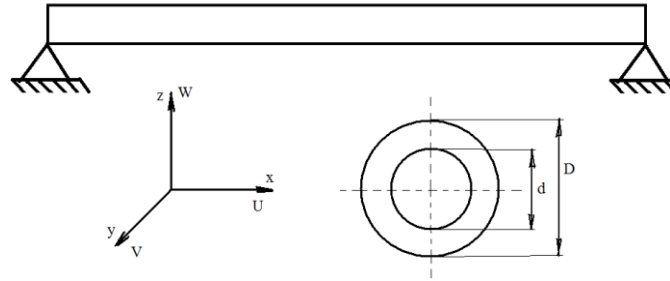


Figure 1. Schematic view of a fluid-conveying microtube.

The displacement of the Bernoulli-Euler beam can be assumed to be:

$$U = -Z\psi(x,t), \quad V = 0, \quad W = W(x,t) \quad (1)$$

where U , V and W are the displacement components in the x -, y -, and z -directions, respectively. ψ is the rotation angle of the central axis of the microtube given by

$$\psi(x,t) = \frac{\partial W(x,t)}{\partial x} \quad (2)$$

Based on the Hamilton's principle [5]

$$\delta \int_{t_1}^{t_2} (T_p + T_f - Q - U_s) dt = 0 \quad (3)$$

and on a modified couple stress elasticity theory, we have:

$$T_p = \frac{m}{2} \int_0^L \left(\frac{\partial W}{\partial x} \right)^2 dx \quad (4)$$

$$T_f = \frac{M}{2} \int_0^L \left[\left(\frac{\partial W}{\partial t} + V_f \frac{\partial W}{\partial x} \right)^2 + V_f^2 \right] dx \quad (5)$$

$$Q = \int_0^L (EI + GA l^2) \left(\frac{\partial^2 W}{\partial x^2} \right)^2 dx \quad (6)$$

$$U_s = - \int_0^L P \left(\frac{\partial W}{\partial x} \right)^2 dx \quad (7)$$

where I is the area moment of inertia, A is cross-sectional area and P is the additional axial force

$$P = \frac{EA}{2L} \int_0^L \left(\frac{\partial W}{\partial x} \right)^2 dx \quad (8)$$

Applying the variational technique, the dynamic equation of motion of this microbeam can be derived as

$$(EI + GA l^2) \frac{\partial^4 W}{\partial x^4} + (M + m) \frac{\partial^2 W}{\partial t^2} + 2MV_f \frac{\partial^2 W}{\partial x \partial t} + \frac{\partial^2 W}{\partial x^2} \left[MV^2 - \frac{EA}{2L} \int_0^L \left(\frac{\partial W}{\partial x} \right)^2 dx \right] = 0 \quad (9)$$

The boundary conditions for the pinned-pinned microbeam are

$$\frac{\partial^2 W(0,t)}{\partial x^2} = W(0,t) = \frac{\partial^2 W(L,t)}{\partial x^2} = W(L,t) = 0 \quad (10)$$

Defining the following dimensionless variables and expressions:

$$\begin{aligned} x^* &= \frac{x}{L}, \quad y = \frac{W}{L}, \quad t^* = \frac{t}{L^2} \sqrt{\frac{EI}{m+M}}, \quad v = LV_f \sqrt{\frac{M}{EI}}, \quad \beta = \frac{M}{m+M}, \quad k^2 = \frac{EAL^2}{EI}, \\ \xi &= \frac{GA l^2}{EI}, \quad \eta = \frac{l}{D}, \quad h = \frac{d}{D}, \quad \delta = \frac{L}{D}, \quad A = \frac{\pi D^2}{4} (1 - h^2), \quad I = \frac{\pi D^4}{64} (1 - h^4) \end{aligned} \quad (11)$$

and omitting the star, Eq.(9) may be written in dimensionless form

$$(1 + \xi) \frac{\partial^4 y}{\partial x^4} + \frac{\partial^2 y}{\partial x^2} + 2\sqrt{\beta}v \frac{\partial^2 y}{\partial x \partial t} + v^2 \frac{\partial^2 y}{\partial x^2} = \frac{1}{2} k^2 \frac{\partial^2 y}{\partial x^2} \int_0^1 \left(\frac{\partial y}{\partial x} \right)^2 dx \quad (12)$$

Then the boundary conditions (10) are:

$$y(0,t) = \frac{\partial^2 y(0,t)}{\partial x^2} = y(1,t) = \frac{\partial^2 y(1,t)}{\partial x^2} = 0 \quad (13)$$

3. Free vibration of the microtube

In what follows, the free vibration of a pinned-pinned straight and slender microtube will be analyzed. Galerkin-Bubnov decomposition method is used to convert the nonlinear partial differential equation of motion (12) into a nonlinear ordinary differential equation. Assuming that the displacement expression is of the form

$$y(x,t) = X(x)T(t) \quad (14)$$

where $X(x)$ is the eigenfunction of the free undamped vibrations of a beam which satisfies the boundary conditions (13). In this paper, we consider $X(x) = \sin \pi x$, and $T(t)$ is the generalized coordinate of the discretized system. Multiplying Eq.(9) with $X(x)$ and then integrating this new equation on the domain $x \in [0,1]$ and taking into account the identities

$$\begin{aligned} \int_0^1 \frac{\partial^4 y(x,t)}{\partial x^4} X(x) dx &= \frac{1}{2} \pi^4 T(t), \quad \int_0^1 \frac{\partial^2 y(x,t)}{\partial x^2} X(x) dx = -\frac{\pi^2}{2} T(t) \\ \int_0^1 \frac{\partial^2 y}{\partial x^2} \int_0^1 \left(\frac{\partial y}{\partial x} \right)^2 X(x) dx &= -\frac{\pi^4}{4} T^3(t), \quad \int_0^1 \frac{\partial^2 y}{\partial x \partial t} X(x) dt = 0, \quad \int_0^1 \frac{\partial^2 y}{\partial t^2} X(x) dt = \frac{1}{2} \ddot{T} \end{aligned} \quad (15)$$

where the dot defines the derivative with respect to t , we obtain the nonlinear ordinary differential equation

$$\ddot{T}(t) + \omega_n^2 T(t) + \alpha T^3(t) = 0 \quad (16)$$

where

$$\omega_n^2 = (1 + \xi) \pi^4 - \pi^2 v^2, \quad \alpha = \frac{1}{4} \pi^4 k^2 \quad (17)$$

The corresponding initial conditions for Eq.(16) are

$$T(0) = a, \quad \dot{T}(0) = 0 \quad (18)$$

We mention that Eq.(16) is a well-known Duffing nonlinear differential equation, with strongly or weakly nonlinear cases, depending on the value of the parameter k . In our work, we will obtain an approximate analytical solution for Eq.(16) and (18). For this purpose, we apply a novel approach, namely the Optimal Auxiliary Functions Method in a proper manner, completely different in comparison with other methods.

4. Basics of the Optimal Auxiliary Functions Method (OAFM)

The Eqs.(16) and (18) can be rewritten in the more general form [11-15]

$$L[T(t)] + N[T(t)] + g(t) = 0 \quad (19)$$

in which L is a linear differential operator, N is a nonlinear operator and $g(t)$ is a known function, t being the independent variable and $T(t)$ is an unknown function. The boundary/initial conditions are

$$B\left(T(t), \frac{\partial T(t)}{\partial t}\right) = 0 \quad (20)$$

Henceforward, $\tilde{T}(t)$ will be the approximate analytical solution of Eq.(19) and (20) and assume that

$$\tilde{T}(t) = T_0(t) + T_1(t, C_1, C_2, \dots, C_p) \quad (21)$$

in which $T_0(t)$ is the initial approximation and $T_1(t, C_1, C_2, \dots, C_p)$ is the first approximation which will be determined as described in what follows. Inserting Eq.(21) into Eq.(19) one obtain

$$L[T_0(t)] + L[T_1(t, C_i)] + N[T_0(t) + T_1(t, C_i)] + g(t) = 0, \quad i = 1, 2, \dots, p \quad (22)$$

Obviously, we should choose the initial approximation $T_0(t)$ to be solution of equation

$$L[T_0(t)] + g(t) = 0 \quad (23)$$

with the corresponding boundary/initial conditions

$$B\left(T_0(t), \frac{\partial T_0(t)}{\partial t}\right) = 0 \quad (24)$$

We propose that the first approximation $T_1(t, C_i)$ be determined from the nonlinear differential equation

$$L[T_1(t, C_i)] + N[T_0(t) + T_1(t, C_i)] = 0, \quad i = 1, 2, \dots, p \quad (25)$$

with the boundary conditions

$$B\left(T_1(t, C_i), \frac{\partial T_1(t, C_i)}{\partial t}\right) = 0 \quad (26)$$

where C_i are p unknown parameters at this moment. The nonlinear term in (25) can be expanded as

$$N[T_0(t) + T_1(t, C_i)] = N[T_0(t)] + \sum_{j \geq 1} \frac{T_1^j}{j!} N^{(j)}[T_0(t)] \quad (27)$$

To avoid the difficulties that can appear in solving the nonlinear differential equation (25) and to accelerate the convergence of the first approximation $T_1(t, C_i)$ and implicitly of the approximate solution $\tilde{T}(t)$, instead of the last term arising in Eq.(25), we propose another expression, such that Eq.(25) can be rewritten in the form

$$L[T_1(t, C_i)] + \sum_{i=1}^p f_i(t) C_i = 0, \quad B\left(T_1(t, C_i), \frac{dT_1(t, C_i)}{dt}\right) = 0 \quad (28)$$

where f_i are known auxiliary functions depending on the initial approximation $T_0(t)$, on the functions which appear in the composition of $N[T_0(t)]$ or are combination of such expressions. The auxiliary functions f_i are not unique and it should be emphasized that we have a great freedom to choose these auxiliary functions. After using the previous considerations we can read that for example if $T_0(t)$ and $N[T_0(t)]$ are polynomial functions, then f_i are sums or quotient of polynomial functions; if T_0 and $N[T_0]$ are exponential functions, then f_i are sums or quotient of exponential functions; if $T_0(t)$ are trigonometric functions and $N[T_0(t)]$ are polynomial functions, then f_i are sums or quotient of combinations of trigonometric and polynomial functions, and so on. As a conclusion, the auxiliary functions f_i are of the same form as $T_0(t)$ and $N[T_0(t)]$. In other words, $T_0(t)$ and $N[T_0(t)]$ are sources for the auxiliary functions f_i . It is very important to remark that if $N[T_0(t)] = 0$, then it is clear that $T_0(t)$ is an exact solution for Eqs.(16) and (17).

Now, the unknown parameters C_i can be optimally identified via rigorous mathematical methods, such as the least square method, Ritz method, collocation method, Galerkin method, Kantorovich method, and the preferred approach would be to minimize the square residual error by computing

$$J(C_1, C_2, \dots, C_p) = \int_{(D)} R^2(t, C_1, C_2, \dots, C_p) dt \quad (29)$$

where

$$R(t, C_1, C_2, \dots, C_p) = L[\tilde{T}(t)] + N[\tilde{T}(t)] + g(t) \quad (30)$$

and $\tilde{T}(t)$ is given by Eq.(21). The values of the parameters C_i are obtained from the system:

$$\frac{\partial J}{\partial C_1} = \frac{\partial J}{\partial C_2} = \dots = \frac{\partial J}{\partial C_p} = 0 \quad (31)$$

By this novel procedure, the approximate analytical solution $\tilde{T}(t)$ is well determined after identification of the optimal values of the initial unknown convergence-control parameters C_i . It will be proved that our procedure is a very powerful tool for solving nonlinear problems without small or large parameters into initial Eqs. (19) and (20).

5. OAFM for Eqs. (16) and (18)

If Ω is the frequency of the system (21) and making the transformation $\tau = \Omega t$ into (16), we obtain

$$T''(\tau) + \frac{\omega_n}{\Omega^2} T(\tau) + \frac{\alpha}{\Omega^2} T^3(\tau) = 0 \quad (32)$$

where prime denotes derivative with respect to τ . For (32) we choose linear and nonlinear operators

$$L[T(\tau)] = T''(\tau) + T(\tau) \quad (33)$$

$$N[T(\tau)] = \left(\frac{\omega_n^2}{\Omega^2} - 1 \right) T(\tau) + \frac{\alpha}{\Omega^2 T^3}(\tau) \quad (34)$$

We assume that the approximate analytical solution $\tilde{T}(\tau)$ for Eqs. (32) and (18) is

$$\tilde{T}(\tau) = T_0(\tau) + T_1(\tau, C_1, C_2, C_3, C_4) \quad (35)$$

in which the initial approximation $T_0(\tau)$ and the first approximation T_1 will be defined as follows:

$$T_0''(\tau) + T_0(\tau) = 0, \quad T_0(0) = a, \quad T_0'(0) = 0 \quad (36)$$

The solution of Eq.(36) is

$$T_0(\tau) = a \cos \tau \quad (37)$$

Substituting Eq.(37) into Eq.(21), one can get:

$$N[T_0(\tau)] = A_1 \cos \tau + A_2 \cos 3\tau \quad (38)$$

$$A_1 = \frac{a}{\Omega^2} \left(\omega_n^2 - \Omega^2 + \frac{3\alpha a^2}{4} \right), \quad A_2 = \frac{\alpha}{4} a^2 \quad (39)$$

Taking into consideration the form of Eqs.(37) and (38), we define the auxiliary functions as

$$f_1(\tau) = C_1, \quad f_2 = 2C_2 \cos 2\tau, \quad f_3(\tau) = 2C_3 \cos 4\tau, \quad f_4(\tau) = 2C_4 \cos 6\tau \quad (40)$$

such as the first approximation $T_1(\tau, C_1, C_2, C_3, C_4)$ is obtained from the equation

$$\begin{aligned} T_1''(\tau) + T_1(\tau) &= (C_1 + C_3 \cos 2\tau + 2C_3 \cos 4\tau + 2C_4 \cos 6\tau)(A_1 \cos \tau + A_2 \cos 3\tau) \\ T_1(0) &= T_1'(0) = 0 \end{aligned} \quad (41)$$

where C_1, C_2 and C_3 are unknown parameters at this moment. The Eq.(41) can be rewritten as

$$\begin{aligned} T_1'' + T_1 &= [A_1(C_1 + C_2) + A_2C_2 + A_3C_3 + A_2C_4] \cos \tau + [A_1(C_2 + C_3) + A_2C_1] \cos 3\tau + \\ &+ A_1(C_3 + C_4) + A_2C_2] \cos 5\tau + A_1C_4 \cos 7\tau + A_2C_3 \cos 9\tau + A_2C_4 \cos 11\tau \end{aligned} \quad (42)$$

Avoiding the presence of secular a term in Eq.(42) needs

$$\Omega^2 = \omega_n^2 + \frac{3\alpha}{4} a^2 + \frac{\alpha a^2}{4} \frac{C_2 + C_3 + C_4}{C_1 + C_2} \quad (43)$$

Taking into account Eq.(43), from Eq.(42) we find the following solution:

$$\begin{aligned} T_1(\tau, C_i) &= \frac{A_1(C_2 + C_3) + A_2C_1}{8} (\cos \tau - \cos 3\tau) + \frac{A_1(C_3 + C_4) + A_2C_2}{24} (\cos \tau - \cos 5\tau) + \\ &+ \frac{A_1C_4}{48} (\cos \tau - \cos 7\tau) + \frac{A_2C_3}{80} (\cos \tau - \cos 9\tau) + \frac{A_2C_4}{120} (\cos \tau - \cos 11\tau) \end{aligned} \quad (44)$$

From (35),(37),(44) and $\tau = \Omega t$, one can get the first-order approximate solution.

$$\begin{aligned} T_1(t, C_1, C_2, C_3, C_4) &= a \cos \Omega t + \frac{A_1(C_2 + C_3) + A_2C_1}{8} (\cos \Omega t - \cos 3\Omega t) + \\ &+ \frac{A_1(C_3 + C_4) + A_2C_2}{24} (\cos \Omega t - \cos 5\Omega t) + \\ &+ \frac{A_1C_4}{48} (\cos \Omega t - \cos 7\Omega t) + \frac{A_2C_3}{80} (\cos \Omega t - \cos 9\Omega t) + \frac{A_2C_4}{120} (\cos \Omega t - \cos 11\Omega t) \end{aligned} \quad (45)$$

where Ω is given by Eq.(43) and the optimal values of the convergence-control parameters will be determined by minimizing the residual of the initial differential equation.

6. Numerical example

To show the validity of our technique, we consider a particular case, when

$$a = 0.03, \eta = 0.1, h = 0.8, \delta = 20, v = 3, \mu = 0.38 \quad (46)$$

the optimal values of the convergence-control parameters and the frequency are:

$$\begin{aligned} C_1 &= -0.0037510868, C_2 = -0.0005173432, C_3 = -0.0018105005, \\ C_4 &= -0.0012962683, \quad \Omega = 3.933145 \end{aligned} \quad (47)$$

It is easy to verify the accuracy of the obtained results by plotting the approximate analytical solution given by Eqs. (42) and (44). Fig.2 show the comparison between the present solution and the numerical integration results obtained using a fourth-order Runge-Kutta method.

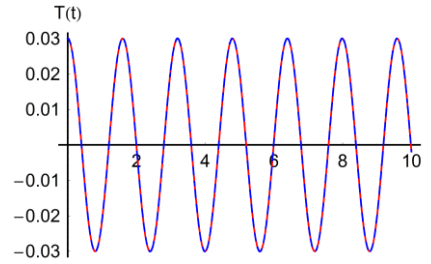


Figure 2. Comparison between the approximate solution (45) with the parameters given by (47) and numerical integration results of Eqs.(16) and (18): — numerical; - - - analytical.

From fig.2 it can be seen that the solution obtained by OAFM is very accurate being nearly identical with the numerical integration results.

7. Conclusions

The main goal of the present work has been to construct an explicit analytical approximation to the solution of the generalized coordinate T of the considered discretized system. Our approach is based on a new construction of the solution and especially on the involvement of the convergence-control parameters C_i via auxiliary functions f_i . The optimal values of these parameters lead to an excellent agreement between our approximate analytical solution and numerical results. The proposed procedure leads to very accurate results for the generalized coordinate and also for the frequency of the system under investigation with a moderate number of convergence-control parameters. It was proved that OAFM is very effective and rapidly convergent to the exact solution using only the first iteration. The construction of the first iteration is different from any other approaches, especially referring to the linear operator L and the auxiliary convergence-control functions f_i which ensure a

fast convergence. The main advantage of the proposed technique is a simple but rigorous way to control and adjust the convergence of the solution.

References

- [1] Younis, M.I., and Nayfeh, A.H. A study of the nonlinear response of a resonant microbeam to an electric actuation. *Nonlinear Dynamics* 31 (2003), 91-117
 - [2] Zand, M.M., Ahmadian, M.T., and Rashidian, R. Semi-analytic solutions to nonlinear vibrations of microbeams under suddenly applied voltages. *Journal of Sound and Vibration* 325 (2009), 389-396
 - [3] Shen, H.S. Nonlinear vibration of microtubes in living cells. *Current Applied Physics* 11 (2011), 812-821
 - [4] Zeverdejani, M.K., and Beni, Y.T. The nano scale vibration of protein microtubes based on modified strain gradient theory. *Current Applied Physics* 13 (2013), 1566-1576
 - [5] Yang, T.Z., Ji, S., Yang X-D., and Fang, B. Microfluid induced nonlinear free vibration of microtubes. *International Journal of Engineering Science* 76 (2014), 47-55
 - [6] Semnani, A.M.D., Zafari, H., and Dehdashri, E. A parametric study on nonlinear flow-induced dynamics of a fluid-conveying cantilever pipe in a post flutter region from macro to micro scale. *International Journal of Nonlinear Mechanics* 85 (2016), 207-225
 - [7] Hosseini, M., and Bahaadni, R. Size-dependent stability analysis of cantilever micro-pipes conveying fluid based on modified strain gradient theory. *Int. J. Eng. Science* 101 (2016), 1-13
 - [8] Ghazani, M.R., Molki, H., and Beigloo, A.A. Nonlinear vibration and stability analysis of the curved microtube conveying fluid as a model of the micro Coriolis flow meters based on strain gradient theory. *Applied Mathematical Modelling* 45 (2017) 1020-1030
 - [9] Havelka, D., Deriu, M., Cifra, M., and Kucera, D. Deformation pattern in vibrating microtube: Structurate mechanics study based on atomistic approach. *Scientific Reports* 7 (2017) 4227
 - [10] Bahaadni, R., Saidi, A.R., and Hosseini, M. On dynamics of nanotubes conveying nanoflow. *International Journal of Engineering Science* 123 (2018), 181-196
 - [11] Herisanu, N., Marinca, V., Madescu, G., Dragan, F. Dynamic response of a permanent magnet synchronous generator to a wind gust, *Energies* 12 (2019), 915
 - [12] Marinca, V., Herisanu, N. The nonlinear thermomechanical vibration of a functionally graded beam on Winkler-Pasternak foundation, *MATEC Web of Conferences* 148 (2018), 13004
 - [13] Marinca, V., Herisanu, N. Vibration of nonlinear nonlocal elastic column with initial imperfection, *Springer Proceedings in Physics* 198 (2018), 49-56
 - [14] Herisanu, N., Marinca, V., Madescu, G. Application of the optimal auxiliary functions method to a permanent magnet synchronous generator, *Int.J.Nonlinear Sci.Num. Simulation* 20 (2019), 399-406
 - [15] Marinca, B., and Marinca V. Approximate analytical solution for thin film flow of a fourth grade fluid down a vertical cylinder. *Proceedings of the Romanian Academy. Series A.* 19 (2018), 69-76
- Nicolae Herisanu, Professor: University Politehnica Timisoara, Department of Mechanics and Vibration, Bd. Mihai Viteazu 1, 300222 Timisoara, Romania (nicolae.herisanu@upt.ro). The author gave a presentation of this paper during one of the conference sessions.
- Vasile Marinca, Professor: Centre for Advanced Technical Research, Romanian Academy – Timisoara Branch, Bd. Mihai Viteazu 24, 300222 Timisoara, Romania (vasile.marinca@upt.ro).

Dynamics and vibration analysis of a spatial linkage model with flexible links and joint friction subjected to position and velocity motion constraints

Elżbieta Jarzębowska, Krzysztof Augustynek, Andrzej Urbaś

Abstract: In the paper a spatial linkage composed of rigid and flexible links subjected to work dependent velocity programmed constraints is analysed. The friction in joints is taken into account. The key tool for the spatial linkage dynamics derivation is an automated computational procedure for constrained dynamics generation. It serves systems subjected to holonomic and first order nonholonomic constraints and proved its effectiveness to open chain models. The distinction between this procedure and others, usually Lagrange based, is that final equations are in the reduced state form, i.e. constraint reaction force are eliminated during derivation. This is the essential advantage of the procedure. It provides the smallest set of dynamic equations, which may serve motion analysis and control. The paper presents extension of the procedure on linkages composed of flexible links with closed-loop kinematics, for which a spanning tree can have a serial or tree structure. Also, analysis of dynamics and vibrations of the linkage motion subjected to programmed constraints is presented. Motions and vibrations caused by adding the programmed constraints, enable designing proper velocity ranges for the linkage in its work regimes and assessing kinematic parameters needed to follow these motions. The theoretical development of automated generation of constrained dynamics is illustrated by an example of the linkage model.

1. Introduction

Generation and analysis of constrained system dynamical models are used in so many engineering applications, e.g. in ground, space and underwater robotics, control and performance analysis of industrial mechanical systems and many others, that methods, mostly computational, for their derivations and solutions became separate research areas, see e.g. [1-3] and references there. Definitely most of derivation methods of motion equations for mechanical systems serve these systems subjected to position and first order material constraints and these methods are based upon the Lagrange approach and its modifications, i.e. upon classical mechanics approaches; see e.g. [1,3,4] and references there. The task based constraints, control and performance constraints and, in a more general sense, motion requirements are not merged into these models and as such are not handled in a general manner. There are also specialized computational packages for the generation of constrained system dynamic models. Generally, they are either Newton-Euler or Lagrange equations

based; see e.g. [1,3]. Some of these packages are developed for specific classes of constrained systems like the one presented in [4] dedicated to nonholonomic wheeled systems. Also, there are many methods that use specific derivation approaches like in [2,5,6]. The consequences of application of these derivation methods to constrained system models are that the resulting equations of motion are not convenient for many applications directly, e.g. Lagrange multipliers need to be eliminated for most motion analysis and control applications. The same problems are related to constrained flexible system models, for which classical modeling methods are applied.

For constrained rigid component multibody systems, subjected to variety of control goals specified by algebraic or differential constraint equations, the dynamic models derivation method is developed in [7,8]. The method is referred to as the generalized programmed motion equations (GPME) method and it enables generating constrained dynamics for models subjected to programmed or task based constraints of an arbitrary order. The dynamics is referred to as reference dynamics and its solutions provide the system behavior when the task based constraints are on. It may serve two main purposes [8,9]. The first one enables assessment of velocities and accelerations needed by the system to follow the desired motion. It enables verification whether the desired motion is feasible for the given system, e.g. if possible power sources needed for reaching desired velocities are available. The second one serves control. The GPME provides the so called reference dynamics, whose outputs are inputs to a model based controller [9]. Tracking control architecture developed in [8-10] for systems constrained by first order and higher order constraints proved to be effective, however, algorithms for generation reference and control dynamics models presented there are based upon analytical based scheme what is a disadvantage when a complex multibody mechanical system is to be modeled.

An automated Computational Procedure for Constrained Dynamics (CoPCoD) generation, for which the constraints may be first order, material and nonmaterial, i.e. programmed, is developed in [11,12]. The CoPCoD is based upon the GPME method and may be applied to system models that consist of rigid and flexible components with open kinematic chains. The essential distinctions between the GPME method and the CoPCoD based upon it and methods presented in the literature are that the constraints may be first order material or nonmaterial, holonomic or nonholonomic, and the final equations of motion are derived in the reduced state form, i.e. constraint reaction forces are eliminated at the derivation level. This is the essential difference in the final form of the motion equations, since the one CoPCoD may serve reference and control oriented dynamics.

In the paper a spatial linkage (SL), i.e. a serial closed-loop kinematic chain composed of rigid and flexible links with friction in joints subjected to work regime velocity programmed constraints (VPC) is analyzed. The key tool for the SL dynamics derivation is the CoPCoD, extended to rigid or flexible close chain models. The contribution of our research is twofold. Firstly, it extends the CoPCoD on SL models composed of rigid-flexible links with closed-loop kinematics, for which a

spanning tree can have a serial or tree structure. The SL is converted into two open-loop kinematic chains by using the cut-joint technique. Such approach requires adding closing constraint equations for a joint at which a closed-loop kinematic chain is separated. Secondly, it analyzes dynamics and vibration of the SL motion with VPC that come from work regime or requirements on it. The CoPCoD provides the smallest set of dynamics equations, which may serve for motion analysis and planning. Analysis of desired motion and vibrations caused by adding VPC, enable designing proper velocity ranges for the SL in work regimes and assessing kinematic parameters needed to follow these motions. The theoretical development of automated CoPCoD generation is illustrated by an example of the SL model.

The paper is then organized as follows. After Introduction, Section 1 delivers a short report on the background for the presented computational scheme. Section 2 presents the CoPCoD generation for the SL structure subjected to position and first order constraints. The CoPCoD is applied to a selected SL model in Section 3. The paper ends with conclusions and the list of references.

2. Constrained dynamics model of the 2 degrees of freedom SL

The two-dof SL as presented in Fig. 1, is considered. The linkage is formed of five links. It is assumed that link (2,3) can be treated as rigid or flexible. The cut-joint technique is used in order to derive the dynamics equations. The SL is cut at the spherical joint S and two open-loop kinematic chains ($n_c = 2$), built of two and three links are obtained. The motion of the considered linkage is limited by kinematic constraints resulting from geometry as well as regime velocity programmed constraints of link (2,1).

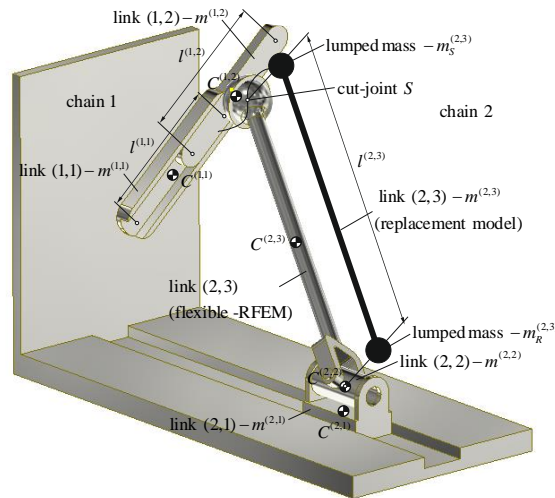


Figure 1. Model of the SL

2.1. Generalized coordinates and homogeneous transformation matrices

The kinematics of the model considered is described by the formalism of joint coordinates and homogeneous transformation matrices (Fig. 2) [13].

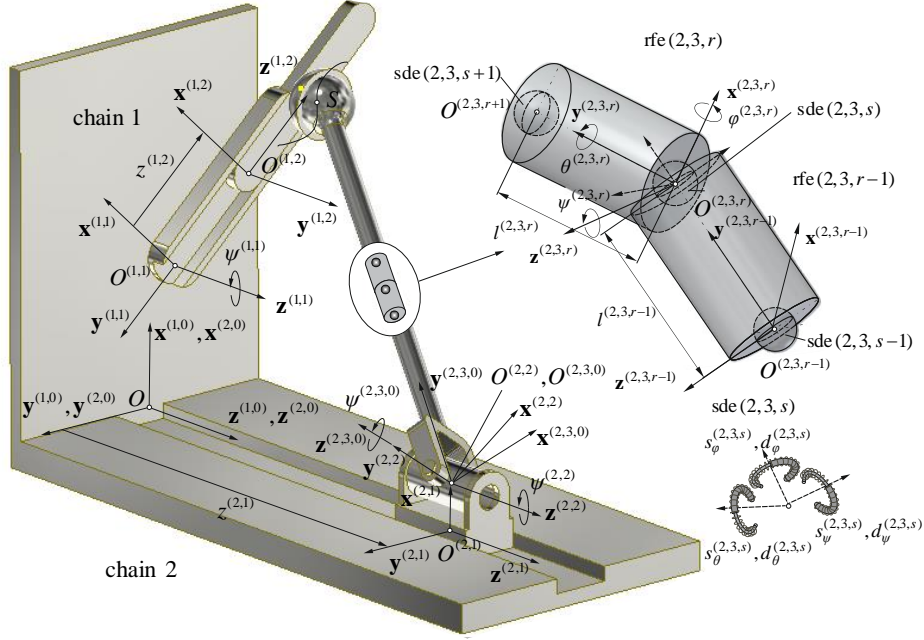


Figure 2. Local frames and joint coordinates assigned to the SL

Vector of the generalised coordinates is defined as follows:

$$\mathbf{q} = (q_i)_{i=1, \dots, n_{def}} = \begin{bmatrix} \mathbf{q}^{(1)T} & \mathbf{q}^{(2)T} \end{bmatrix}^T, \quad (1)$$

where:

$$\text{-- chain 1: } \mathbf{q}^{(1)} = (q_i^{(1)})_{i=1, \dots, n_{def}^{(1)}} = \begin{bmatrix} \psi^{(1,1)} & z^{(1,2)} \end{bmatrix}^T,$$

$$\text{-- chain 2: } \mathbf{q}^{(2)} = (q_i^{(2)})_{i=1, \dots, n_{def}^{(2)}} = \begin{bmatrix} z^{(2,1)} & \psi^{(2,2)} & \psi^{(2,3,0)} & \tilde{\mathbf{q}}_f^{(2,3)T} \end{bmatrix}^T,$$

$$\tilde{\mathbf{q}}_f^{(2,3)} = \begin{bmatrix} \psi^{(2,3,r)} & \theta^{(2,3,r)} & \phi^{(2,3,r)} \end{bmatrix}^T \Big|_{r=1, \dots, n_{def}^{(2,3)}}$$

The transformation matrices to the global reference system $\{c, 0\}_{c=1,2}$ are calculated using the following formulas:

$$\mathbf{T}^{(1,i)} \Big|_{i=1,\dots,n_l^{(1)}} = \prod_{j=1}^i \tilde{\mathbf{T}}^{(1,j)}, \quad (2.1)$$

$$\mathbf{T}^{(2,i)} \Big|_{i=1,2} = \prod_{j=1}^i \tilde{\mathbf{T}}^{(1,j)}, \quad (2.2)$$

$$\mathbf{T}^{(2,3,r)} \Big|_{r=0,\dots,n_{ge}^{(2,3)}-1} = \mathbf{T}^{(2,2)} \prod_{j=0}^r \tilde{\mathbf{T}}^{(2,3,r)}, \quad (2.3)$$

where: $\tilde{\mathbf{T}}^{(c,j)} = \begin{bmatrix} \tilde{\mathbf{R}}^{(c,j)} & \mathbf{r}_{O^{(c,j)}}^{(c,j-1)} \\ \mathbf{0} & 1 \end{bmatrix}$, $\tilde{\mathbf{R}}^{(c,j)}$ is the rotation matrix of link (c,j) with respect to the system $\{c,j-1\}$, $\mathbf{r}_{O^{(c,j)}}^{(c,j-1)}$ is the position vector of point $O^{(c,j)}$ in the system $\{c,j-1\}$, $\tilde{\mathbf{T}}^{(2,3,0)} = \begin{bmatrix} \tilde{\mathbf{R}}^{(2,3,0)} & \mathbf{r}_{O^{(2,3,0)}}^{(2,2)} \\ \mathbf{0} & 1 \end{bmatrix}$, $\tilde{\mathbf{R}}^{(2,3,0)}$ is the rotation matrix of rfe $(2,3,0)$ with respect to the system $\{2,2\}$, $\mathbf{r}_{O^{(2,3,0)}}^{(2,2)}$ is the position vector of point $O^{(2,3,0)}$ in the system $\{2,2\}$, $\tilde{\mathbf{T}}^{(2,3,r)} \Big|_{r=1,\dots,n_{ge}^{(2,3)}-1} = \begin{bmatrix} \tilde{\mathbf{R}}^{(2,3,r)} & \mathbf{r}_{O^{(2,3,r)}}^{(2,3,r-1)} \\ \mathbf{0} & 1 \end{bmatrix}$, $\tilde{\mathbf{R}}^{(2,3,r)}$ is the rotation matrix of rfe $(2,3,r)$ with respect to the system $\{2,3,r-1\}$, $\mathbf{r}_{O^{(2,3,r)}}^{(2,3,r-1)}$ is the position vector of point $O^{(2,3,r)}$ in system $\{2,3,r-1\}$.

2.2. The Generalized Programmed Motion Equations for the SL

The GPME equations for the position constraints take the form [8,9]:

$$\frac{\partial R_1}{\partial \dot{q}_i} \Big|_{i \in i_c} + \sum_{j \in i_d} \frac{\partial R_1}{\partial \dot{q}_j} \frac{\partial \dot{q}_j}{\partial \dot{q}_i} = 0, \quad (3)$$

where: i_c, i_d are indices of independent and dependent coordinates, respectively,

$$R_1 = \sum_{c=1}^{n_c} R_1^{(c)}, \quad R_1^{(1)} = \dot{E}_k^{(1)} - 2 \sum_{i=1}^{n_{def}^{(1)}} \frac{\partial E_k^{(1)}}{\partial q_i^{(1)}} \dot{q}_i^{(1)} + \sum_{i=1}^{n_{def}^{(1)}} \frac{\partial E_{p,g}^{(1)}}{\partial q_i^{(1)}} \dot{q}_i^{(1)} + \sum_{i=1}^{n_{def}^{(1)}} f_{fr}^{(1)} \dot{q}_i^{(1)},$$

$$R_1^{(2)} = \dot{E}_k^{(2)} - 2 \sum_{i=1}^{n_{def}^{(2)}} \frac{\partial E_k^{(2)}}{\partial q_i^{(2)}} \dot{q}_i^{(2)} + \sum_{i=1}^{n_{def}^{(2)}} \left(\frac{\partial E_{p,g}^{(2)}}{\partial q_i^{(2)}} + \frac{\partial E_{p,f_i}^{(2)}}{\partial q_i^{(2)}} + \frac{\partial R_{f_i}^{(2)}}{\partial \dot{q}_i^{(2)}} \right) \dot{q}_i^{(2)},$$

$E_k^{(c)}, E_{p,g}^{(c)} \Big|_{c=1,2}$ are kinetic energy and potential energy of gravity forces, $\mathbf{f}_{fr}^{(1)}$ is friction force,

$E_{p,f_i}^{(2)}, R_{f_i}^{(2)}$ are potential energy of spring deformation and the Rayleigh function of the flexible link.

In order to derive the GPME equations, it is required to choose the independent and dependent coordinates, as well as defining the kinetic energy, potential energy of the gravity force of the system, quantities describing the flexibility of the link (2,3) and friction in joint (1,2).

2.3. Selection of independent and dependent coordinates

The vector \mathbf{q} contains independent and dependent coordinates:

$$\mathbf{q} = (q_i)_{i \in i_c \cup i_{d_c}} \in \{\mathbf{q}_{i_c}, \mathbf{q}_{d_c}\}, \quad (4)$$

The selection these coordinates can be carried out arbitrarily, but the number of the dependent coordinates is equal to the number of constraint equations.

It is assumed that coordinate partitioning is performed as follows:

$$i_c \in \{3, \dots, n_{dof}\} \rightarrow \mathbf{q}_{i_c} = \begin{bmatrix} \mathbf{z}^{(1,2)} & \tilde{\mathbf{q}}_f^{(2,3)} \end{bmatrix}^T, \quad (5.1)$$

$$i_{d_c} \in \{1, 2\} \rightarrow \mathbf{q}_{d_c} = \begin{bmatrix} \psi^{(1,1)} & \mathbf{z}^{(2,1)} & \psi^{(2,2)} & \psi^{(2,3,0)} \end{bmatrix}^T. \quad (5.2)$$

2.4. Kinetic energy and potential energy of gravity forces

The kinetic energy of the chains can be expressed as:

$$E_k^{(1)} = \frac{1}{2} \sum_{j=1}^{n_j^{(1)}} \text{tr} \left\{ \dot{\mathbf{T}}^{(1,j)} \mathbf{H}^{(1,j)} \dot{\mathbf{T}}^{(1,j)T} \right\}, \quad (6.1)$$

$$E_k^{(2)} = \frac{1}{2} \left\{ \sum_{j=1}^{n_j^{(2)}-1} \text{tr} \left\{ \dot{\mathbf{T}}^{(2,j)} \mathbf{H}^{(2,j)} \dot{\mathbf{T}}^{(2,j)T} \right\} + \sum_{r=0}^{n_{fe}^{(2,3)}} \text{tr} \left\{ \dot{\mathbf{T}}^{(2,3,r)} \mathbf{H}^{(2,3,r)} \dot{\mathbf{T}}^{(2,3,r)T} \right\} \right\}, \quad (6.2)$$

where: $\mathbf{H}^{(\cdot)}$ is a pseudo-inertia matrix.

The potential energy of the gravity force of the chains can be defined in the following forms:

$$E_{p,g}^{(1)} = \sum_{j=1}^{n_j^{(1)}} m^{(1,j)} g \mathbf{J}_1 \mathbf{T}^{(1,j)} \mathbf{r}_{C^{(1,j)}}^{(1,j)}, \quad (7.1)$$

$$E_{p,g}^{(2)} = \sum_{j=1}^{n_j^{(2)}-1} m^{(2,j)} g \mathbf{j}_1 \mathbf{T}^{(2,j)} \mathbf{r}_{C^{(2,j)}}^{(2,j)} + \sum_{r=0}^{n_{fe}^{(2,3)}} m^{(2,3,r)} g \mathbf{j}_1 \mathbf{T}^{(2,3,r)} \mathbf{r}_{C^{(2,3,r)}}^{(2,3,r)}, \quad (7.2)$$

where: $m^{(c)}$ is mass of link, $\mathbf{r}_{c^{(c)}}^{(c)}$ is a position vector of the mass centre of link and

$$\mathbf{J} = \begin{bmatrix} \mathbf{j}_1 \\ \mathbf{j}_2 \\ \mathbf{j}_3 \end{bmatrix} = \begin{bmatrix} 1 & 0 & 0 & 0 \\ 0 & 1 & 0 & 0 \\ 0 & 0 & 1 & 0 \end{bmatrix}.$$

2.5. Modelling the flexible link (2,3)

The rigid finite element method is applied to discretize the flexible link [13]. The potential energy of spring deformation and a dissipation function of the flexible link are expressed by:

$$E_{p,f_l} = \frac{1}{2} \sum_{s=1}^{n_{dl}^{(2,3)}} \tilde{\mathbf{q}}^{(2,3,s)^T} \mathbf{S}^{(2,3,s)} \tilde{\mathbf{q}}^{(2,3,s)}, \quad (8.1)$$

$$R_{f_l} = \frac{1}{2} \sum_{s=1}^{n_{dl}^{(2,3)}} \dot{\tilde{\mathbf{q}}}^{(2,3,s)^T} \mathbf{D}^{(2,3,s)} \dot{\tilde{\mathbf{q}}}^{(2,3,s)}, \quad (8.2)$$

where: $\mathbf{S}^{(c)}, \mathbf{D}^{(c)}$ are matrices containing stiffness and damping coefficients of spring-damping elements.

2.6. Modelling friction in the slider link (1,2)

The friction phenomenon is modelled in the sense of the LuGre friction model [14]. This model requires to determine state variable $\dot{s}^{(2,1)}$ in each integration step from the following state equation:

$$\dot{s}^{(2,1)} = \dot{z}^{(2,1)} \left(1 - \frac{\sigma_0^{(2,1)} s^{(2,1)} \operatorname{sgn}(\dot{z}^{(2,1)})}{\mu_k^{(2,1)} + (\mu_s^{(2,1)} - \mu_k^{(2,1)}) \exp\left(-\left(\frac{\dot{z}^{(2,1)}}{v_s^{(2,1)}}\right)^2\right)} \right), \quad (9)$$

where $\mu_s^{(2,1)}, \mu_k^{(2,1)}$ are static and kinetic friction coefficients, respectively, $v_s^{(2,1)}$ is the Stribeck velocity and $\sigma_0^{(2,1)}$ is the stiffness coefficient of the bristle. Having the value of the state variable $\dot{s}^{(2,1)}$ at a given integration step, the friction coefficient can be calculated as follows:

$$\mu^{(2,1)} = \sigma_0^{(2,1)} s^{(2,1)} + \sigma_1^{(2,1)} \dot{s}^{(2,1)} + \sigma_2^{(2,1)} \dot{z}^{(2,1)}, \quad (10)$$

where $\sigma_1^{(2,1)}, \sigma_2^{(2,1)}$ are damping and viscous damping coefficients, respectively.

The normal force acting on the slider (1,2) is determined according to the model presented in [15].

2.7. Kinematic and programmed constraints

The kinematic constraints are formulated for the cut-joint located at the spherical joint S and can be written in the following form:

$$\Phi_k(\mathbf{q}) \equiv 0 \Rightarrow \mathbf{J} \left(\mathbf{T}_S^{(1,2)} \mathbf{r}_S^{(1,2)} - \mathbf{T}_S^{(2,3,n_{rfe}^{(2,3)}-1)} \mathbf{r}_S^{(2,3,n_{rfe}^{(2,3)}-1)} \right) = \mathbf{0}, \quad (11.1)$$

$$\dot{\Phi}_k(\mathbf{q}, \dot{\mathbf{q}}) \equiv 0 \Rightarrow \mathbf{C}_k^{(1)} \dot{\mathbf{q}}^{(1)} - \mathbf{C}_k^{(2)} \dot{\mathbf{q}}^{(2)} = \mathbf{0}, \quad (11.2)$$

$$\ddot{\Phi}_k(\mathbf{q}, \dot{\mathbf{q}}, \ddot{\mathbf{q}}) \equiv 0 \Rightarrow \mathbf{C}_k^{(1)} \ddot{\mathbf{q}}^{(1)} - \mathbf{C}_k^{(2)} \ddot{\mathbf{q}}^{(2)} + \mathbf{d}_k = \mathbf{0}, \quad (11.3)$$

where $\mathbf{r}_S^{(\cdot)}$ are position vectors of the cut-joint S in local frames $\{\cdot\}$,

$$\begin{aligned} \mathbf{C}_k^{(1)} &= \begin{bmatrix} (\mathbf{C}_k^{(1)})_1 \\ (\mathbf{C}_k^{(1)})_2 \\ (\mathbf{C}_k^{(1)})_3 \end{bmatrix} = \left((c_k^{(1)})_{ij} \right)_{\substack{i=1,2,3 \\ j=1,\dots,n_{def}^{(1)}}} = \mathbf{J} \left[\mathbf{T}_1^{(1,2)} \mathbf{r}_S^{(1,2)} \quad \dots \quad \mathbf{T}_{n_{def}^{(1)}}^{(1,2)} \mathbf{r}_S^{(1,2)} \right], \\ \mathbf{C}_k^{(2)} &= \begin{bmatrix} (\mathbf{C}_k^{(2)})_1 \\ (\mathbf{C}_k^{(2)})_2 \\ (\mathbf{C}_k^{(2)})_3 \end{bmatrix} = \left((c_k^{(2)})_{ij} \right)_{\substack{i=1,2,3 \\ j=1,\dots,n_{def}^{(2)}}} = \mathbf{J} \left[\mathbf{T}_1^{(2,3,n_{rfe}^{(2,3)}-1)} \mathbf{r}_S^{(2,3,n_{rfe}^{(2,3)}-1)} \quad \dots \quad \mathbf{T}_{n_{def}^{(2)}}^{(2,3,n_{rfe}^{(2,3)}-1)} \mathbf{r}_S^{(2,3,n_{rfe}^{(2,3)}-1)} \right], \\ \mathbf{d}_k &= \mathbf{d}_k \quad i=1,2,3 = \mathbf{J} \left(\left(\sum_{i=1}^{n_{def}^{(1)}} \sum_{j=1}^{n_{def}^{(1)}} \mathbf{T}_{ij}^{(1,2)} \dot{q}_i^{(1)} \dot{q}_j^{(1)} \right) \mathbf{r}_S^{(1,2)} - \left(\sum_{i=1}^{n_{def}^{(2)}} \sum_{j=1}^{n_{def}^{(2)}} \mathbf{T}_{ij}^{(2,3,n_{rfe}^{(2,3)}-1)} \dot{q}_i^{(2)} \dot{q}_j^{(2)} \right) \mathbf{r}_S^{(2,3,n_{rfe}^{(2,3)}-1)} \right). \end{aligned}$$

It is assumed that the velocity of the slider (2,1) has to change according to the assumed function of time $\dot{z}_A^{(2,1)}(t)$. The programmed constraint equations and their time derivatives take the form:

$$\dot{\Phi}_p(t, \dot{\mathbf{q}}) \equiv 0 \Rightarrow \mathbf{C}_p^{(2)} \dot{\mathbf{q}}^{(2)} - \dot{z}_A^{(2,1)}(t) = 0, \quad (12.1)$$

$$\ddot{\Phi}_p(t, \ddot{\mathbf{q}}) \equiv 0 \Rightarrow \mathbf{C}_p^{(2)} \ddot{\mathbf{q}}^{(2)} - \ddot{z}_A^{(2,1)}(t) = 0. \quad (12.2)$$

where $\mathbf{C}_p^{(2)} = [1 \quad \mathbf{0}]$.

Having constraint equations, the relation between independent and dependent velocities can be formulated as follows:

$$\dot{\mathbf{q}}_{d_c} = \mathbf{K}_{d_c}^{-1} \mathbf{K}_{i_c} \dot{\mathbf{q}}_{i_c}. \quad (13)$$

where \mathbf{K}_{i_c} , \mathbf{K}_{d_c} are matrices obtained the from constraint matrix $\mathbf{K} = \begin{bmatrix} \mathbf{C}_k^{(1)} & \mathbf{C}_k^{(2)} \\ \mathbf{0} & \mathbf{C}_p^{(2)} \end{bmatrix}$ by selecting rows and columns corresponding to positions of independent and dependent coordinates in the generalized coordinates vector \mathbf{q} .

2.8. Reference motion dynamic equations for the SL

The GPME equations supplemented by the kinematic and programmed constraint equation can be written in the following matrix form:

$$\begin{bmatrix} \mathbf{M}_i \big|_{i \in i_c} + \sum_{j \in i_{d_c}} \mathbf{M}_j \frac{\partial \dot{q}_j}{\partial \dot{q}_i} \\ \mathbf{K} \end{bmatrix} \ddot{\mathbf{q}} = \begin{bmatrix} \mathbf{h}_i + \mathbf{Q}_i + \sum_{k=1}^{n_{dof}} \dot{q}_k \frac{\partial \mathbf{Q}_k}{\partial \dot{q}_i} + \sum_{j \in i_{d_c}} \left(\mathbf{h}_j + \mathbf{Q}_j + \sum_{k=1}^{n_{dof}} \dot{q}_k \frac{\partial \mathbf{Q}_k}{\partial \dot{q}_j} \right) \frac{\partial \dot{q}_j}{\partial \dot{q}_i} \\ \mathbf{\Gamma} \end{bmatrix}, \quad (14)$$

where:

$(\cdot)_i$ is i-th row of the matrix/vector (\cdot) , \mathbf{M} - mass matrix, \mathbf{h} - vector of dynamic forces, $\mathbf{Q} = -(\mathbf{g} + \mathbf{f}_{fl} + \mathbf{f}_{fr}) + \mathbf{t}_{dr}$, \mathbf{g} - vector of the gravity forces, \mathbf{f}_{fl} - vector of generalized forces resulting in deformation of the flexible link, \mathbf{f}_{fr} - vector of generalized force resulting from the friction in joints, \mathbf{t}_{dr} - vector of driving torques/forces, $\mathbf{\Gamma} = [-\mathbf{d}_k^T \quad \ddot{\mathbf{z}}_A^{(2,1)}]^T$ - vector of the second time derivatives of the constraints. Formulas for determining the components of the dynamics equations of motion are described in detail in paper [11].

3. Numerical studies – the SL programmed motion analysis

It is assumed that crank (1,1) is driven by a driving and resistance torque (Fig. 3). The assumed velocity of slider (2,1) is described by the function shown in Fig. 4.

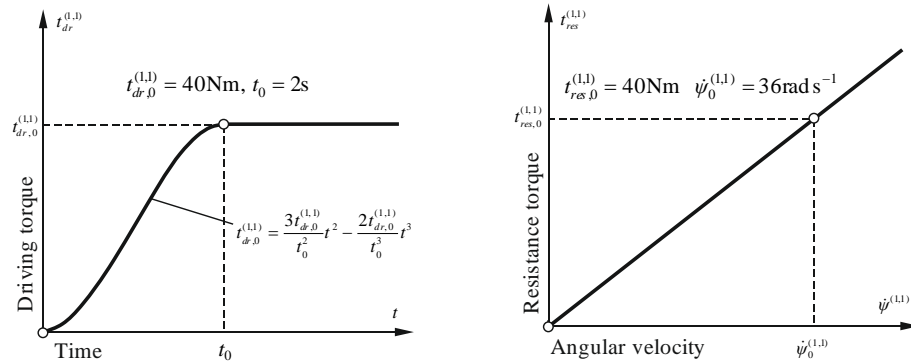


Figure 3. Driving and resistance torque

The static analysis is performed before dynamics to obtain deformation of the flexible link due to gravity forces. After this step, dynamic equations of motion are integrated using 4-th order Runge-Kutta scheme with the constant step size $h=5\times10^{-5}$ s. The flexible links is divided into 4 rfs. The Baumgarte method with constants $\alpha=100$, $\beta=50$ is applied to compensate constraint violations at the position and velocity levels. In simulations, the influence of the friction phenomenon in slider (2,1) and flexibility of the coupler on motion of linkage is analysed. Fig. 5 and 6 show time courses of the displacement and velocity of the crank and slider (1,2). Analyzing the plots, it can be observed that the friction has significant impact on the motion of the linkage, while the impact of links' flexibility is negligible. Lateral deformations of the point located in the middle of the beam length and time course of amplitude of the resultant reaction force at the spherical joint S are shown in Fig. 7. Analyzing deformations, it can be noted that they grow with time and they not exceed 6 mm. Additionally, it can be observed that deformations and reactions forces are smaller when the friction in slider (1,2) is taken into account.

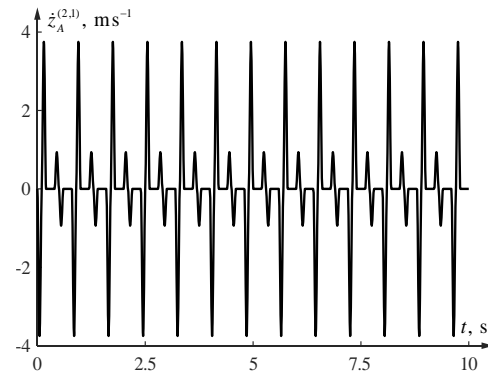


Figure 4. The assumed time course of velocity of slider (2,1)

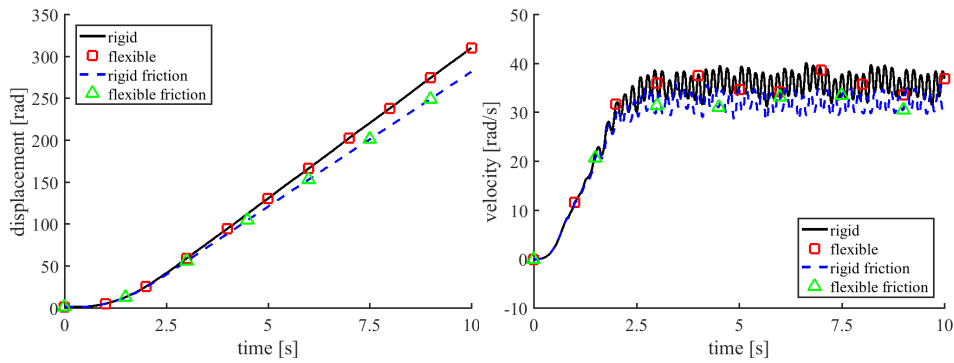


Figure 5. Time course of the displacement and velocity of the crank

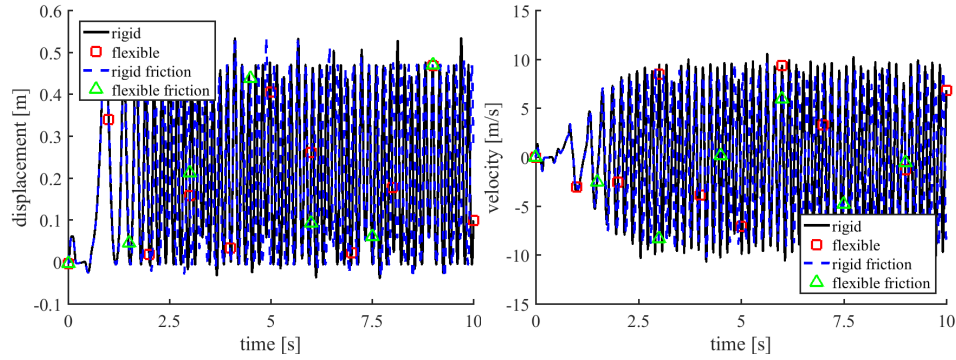


Figure 6. Time course of the displacement and velocity of slider (1,2)

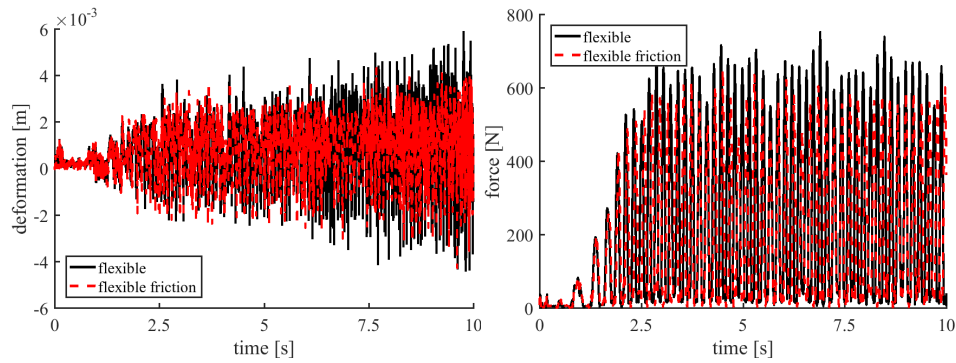


Figure 7. Time course of lateral deformation of the middle point of the coupler and amplitude of the resultant reaction force at the spherical joint

4. Conclusions

The mathematical model the two-dof SL with flexible coupler and friction in joints was presented. Motion of the linkage is limited by kinematic constraint equations formulated for the spherical cut-joint and programmed constraints at the velocity level that represent task based requirements. The CoPCoD based on the GMPE algorithm and joint coordinates with homogeneous transformation matrices is applied to generate dynamic equations of motion. Numerical studies demonstrate that for the considered linkage friction has significant influence on motion of the SL and it reduce level of deformations of the flexible link and as result reaction forces acting joints. Also, the effects of the programmed constraints on the overall SL motion suggest the appropriate desired motion parameter selection.

References

- [1] Schiehlen, W., Guse, N. and Seifried, R. Multibody dynamics in computational mechanics and engineering applications, *Comput. Methods Appl. Mech. Engrg.*, 195 (2006), 5509–5522.

- [2] Richard, M.J., McPhee, J.J., and Anderson, R.J. Computerized generation of motion equations using variational graph-theoretic methods, *Appl. Math. Comp.*, 192 (2007), 135–156.
 - [3] Lot, R. and Dalio, M. Symbolic Approach for Automatic Generation of the Equations of Motion of Multibody Systems, *Multibody System Dynamics*, 12 (2004), 147–172.
 - [4] Kwatny, H.G. and Blankenship, G.L. *Nonlinear control and analytical mechanics. A computational approach*. Birkhauser, Boston, 2000.
 - [5] Guanfeng, L. and Zexiang L. A Unified Geometric Approach to Modeling and Control of Constrained Mechanical Systems, *IEEE Trans. Robot. Automat.*, 18 (2002), 574–587.
 - [6] Aghili, F. A Unified Approach for Inverse and Direct Dynamics of Constrained Multibody Systems Based on Linear Projection Operator: Applications to Control and Simulation, *IEEE Trans. Robot. Automat.*, 21 (2005), 834–849.
 - [7] Jarzębowska, E. Advanced programmed motion tracking control of nonholonomic mechanical systems, *IEEE Trans. Robot.* 24 (2008), 1315–1328.
 - [8] Jarzębowska, E. *Model-Based Tracking Control of Nonlinear Systems*, Taylor & Francis Group, Series: Modern Mechanics and Mathematics, Boca Raton, 2012.
 - [9] Jarzębowska, E. *Advanced Task Tracking Control Design for Robotics-like Systems*, In *Mechatronics - Ideas for Industrial Application*, Awrejcewicz, J. et al. (eds.), 317 series Advances in Intelligent Systems and Computing, Springer, 2015, 203–229.
 - [10] Jarzębowska, E. Model-based control of a third order nonholonomic system, *International Journal of Mathematics and Mechanics of Solids*, (2016) doi: 10.1177/1081286516634827.
 - [11] Jarzębowska, E., Augustynek, K. and Urbaś, A. Automated Generation of Reference Dynamical Models for Constrained Robotic Systems In the Presence of Friction and Damping effects, *Concurrency and Computation: Practice and Experience*, 2018, doi:10.1002/cpe.4452.
 - [12] Jarzębowska, E., Augustynek, K. and Urbaś, A. Programmed task based motion analysis of robotic systems equipped with flexible links and supports, *Matec Web Conf.* 241 (2018), CSNDD, 2018, art. no 01008, <https://doi.org/10.1051/mateconf/201824101008>.
 - [13] Wittbrodt, E., Adamiec-Wójcik, I. and Wojciech, S. *Dynamics of flexible multibody systems. Rigid finite element method*, Springer, Berlin (2006).
 - [14] Canudas de Wit, C., Ollson, H., Åström, K.J. and Lischinsky, P. A new model for control of systems with friction. *IEEE Trans Autom Control* 40 (1995), 419–425.
 - [15] Augustynek, K. and Urbaś, A. Comparison of bristles' friction models in dynamics analysis of spatial linkages. *Mechanics Research Communications* (2017), doi: 10.1016/j.mechrescom.2017.01.003.
- Elżbieta Jarzębowska, Associate Professor: Warsaw University of Technology, 00-665 Warsaw, Nowowiejska 24, Poland (elajarz@meil.pw.edu.pl).
- Krzysztof Augustynek, Ph.D.: University of Bielsko-Biala, 43-309 Bielsko-Biala, Willowa 2, Poland, (kaugustynek@ath.bielsko.pl).
- Andrzej Urbaś, Ph.D.: University of Bielsko-Biala, 43-309 Bielsko-Biala, Willowa 2, Poland, (aurbas@ath.bielsko.pl).

A simple pattern generator for biped walking

Olga Jarzyna, Dariusz Grzelczyk, Jan Awrejcewicz

Abstract: The paper proposes a simple model of a central pattern generator for bipedal walking. The model approximates the angular positions of hip, knee and ankle joints during walking considered in the sagittal plane. The proposed mathematical representation of the walking pattern generator is based on experimental observations of healthy volunteer's gait. It consists of three piecewise-defined continuous and smooth sine-squared-based functions approximating the angular positions of particular joints within a gait cycle. The model can be potentially employed to generate signals controlling motion of an exoskeleton for rehabilitation of lower limbs. It can be easily modified by changing the values of model parameters. The proposed model can be also potentially implemented in control of bipedal robots in the future.

1. Introduction

According to the World Health Organization, about 15% of the world population has some form of disability [1]. As far as the situation in Poland is concerned, the most recent report of the Central Statistical Office of Poland clearly states that the vast majority of the disabled Poles suffer from problems related to the locomotor system [2] – see Fig. 1.

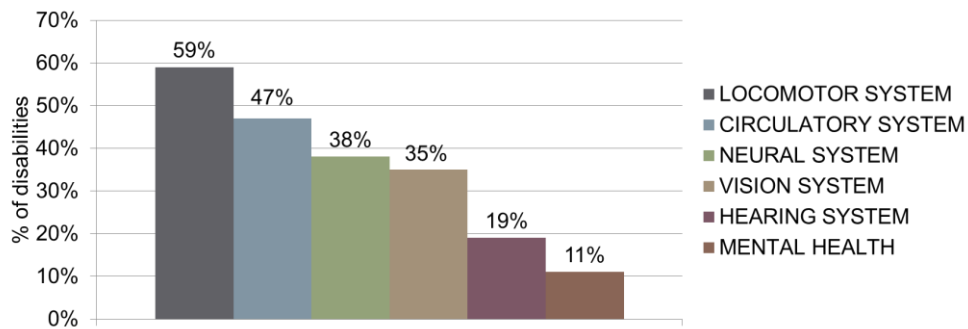


Figure 1. Disabilities in Poland (graph prepared based on [2]).

Irrespective of the reasons, such as different diseases, ageing, or traffic accidents and sports injuries [3], dysfunctions of the locomotor system bring severe consequences not only in medical, but also social aspects since they limit the mobility and living activity of a vast group of the society.

The most common form of rehabilitation of patients with mobility impairment is the work of physiotherapists. However, it is labour-intensive and leads to occupational conditions such as lower-back problems. Therefore, we should aim to develop devices that can both restore motor functions of the disabled and help physiotherapists, which would improve the overall rehabilitation outcomes. For instance, devices such as so-called lower limb exoskeletons (LLEs) can be used for this purpose. Although many research centres have been working on exoskeletons, still much needs to be done before these devices become affordable and broadly available for the public.

The main goal of the present study was to develop a model of a human gait pattern that can be potentially used to control the movement of an exoskeleton. The general idea was to implement a bio-inspired algorithm, called a central pattern generator (CPG). Generally, CPGs are neural circuits that exist in animals' spinal cord and regulate various rhythmic functions such as respiration or locomotion even without receiving sensory feedbacks or brain inputs.

The study is based on a prototype of a lower limb exoskeleton constructed at authors' Department. Although the device allows for rotation in 11 joints, which is supplemented with the ability of moving toes and the trunk, from the point of view of rehabilitation of gait, one should focus on sagittal movements in hips, knees and ankles as they are most significant in the therapy.

2. Simulation model of the LLE

The simulation model of the exoskeleton is shown in Fig. 2. The limb consists of the hip joint A , the thigh of the length l_1 , the knee joint B , the shank of the length l_2 , the ankle joint C , and the foot element CEDF, where E corresponds to the heel, F to the big toe, D is the projection of C on the "sole" EF, l_3 is the height of the foot (equal to the length of CD), l_4 is the length of ED and l_5 is the length of DF. The global coordinate system is fixed on the ground and the local coordinate system is placed between hip joints (see Fig. 2).

Here we consider only the most important movements, which are sagittal movements such as bending and extension in the hip joint (described by the angle $\varphi_1(t)$), bending in the knee (described by the angle $\varphi_2(t)$, which is the angle between the extension of the thigh and the shank), and bending in the ankle (described by $\varphi_3(t)$, which is the angle between the shank and the element l_3). These movements are also accompanied by antero-posterior pelvic tilt β .

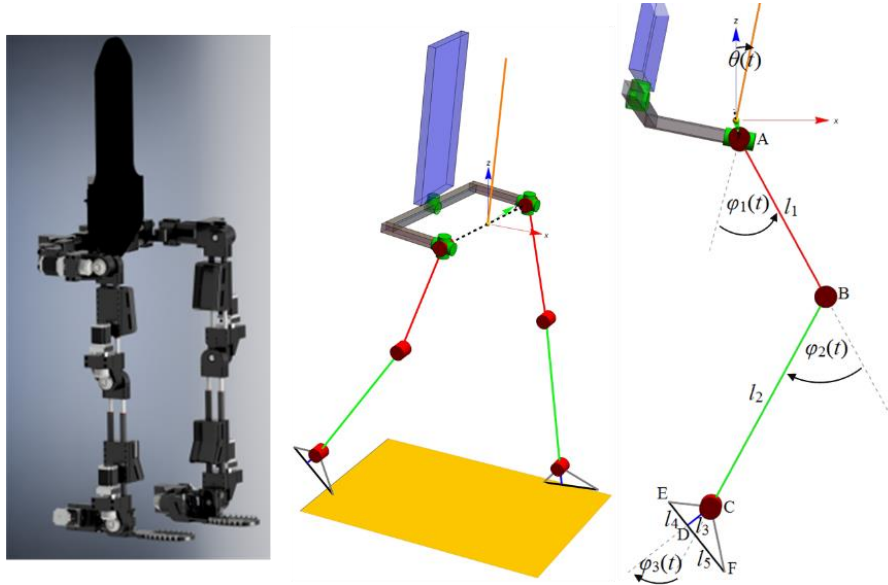


Figure 2. CAD model (left); simulation model developed in Mathematica (middle); kinematic model of a mechanism corresponding to one lower limb (right).

To develop a model that would represent the gait pattern, gait experiments were conducted with the motion capture system. Based on the positions of 37 reflective markers distributed on the volunteer's body, the system reconstructed the human body segments and visualised their movement during the walking process. Then, the changes in the hip, knee and ankle angles for one full gait cycle (this is for the time between two consecutive hits of the heel of the left foot to the ground) were extracted – they are presented in Fig. 3. In all cases, solid lines correspond to the left leg and dashed lines to the right one.

For simplification purposes, it was assumed that the gait is symmetrical, i.e. the patterns of movement of the left and the right lower limb are identical but shifted in phase (they are in antiphase). Hence, solid curves presented in Fig. 3 were obtained experimentally while dashed curves were obtained by shifting the solid signals by 180 degrees (in other words, solid and dashed curves have the same envelopes, but their phases are opposite). Red lines present patterns in the hips, green – in the knees, and blue – in the ankles.

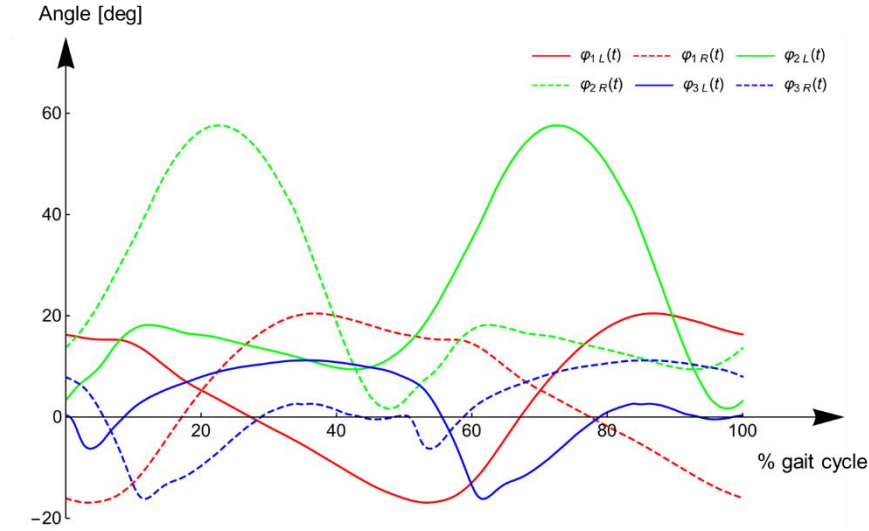


Figure 3. Sagittal plane joint angles during one gait phase – experimental results (red – hip joints, green – knee joints, blue – ankle joints).

The obtained experimental patterns could be used to control the exoskeleton quite successively, but the goal was to model them to be able to modify their shape and adjust them to a particular person. This is particularly important in rehabilitation because at the beginning of the therapy, many patients have their range of motion limited and, for instance, too excessive bending in the knees could possibly damage muscles and tendons.

3. CPG

At first, motion in the hip was modelled. For this purpose, the experimental curve was divided into three intervals, and each of them was approximated with a sine-based function. The angle $\varphi_{1L}(t)$ produces the signal for the left hip joint, while $\varphi_{1R}(t)$ for the right one (the signals are identical but in antiphase):

$$\varphi_{1L}(t) = \varphi_1(t), \quad \varphi_{1R}(t) = \varphi_1(t - 0.5T), \quad (1)$$

where

$$\varphi_1(t) = \phi(\text{mod}[t - T_1, T]), \quad (2)$$

T – duration of one gait phase, and

$$\phi_1(t) = \begin{cases} \phi_{10} + (\phi_{11} - \phi_{10}) \cdot \sin^2\left(\frac{\pi}{2t_{11}}t\right) & \text{if } t \in [0, t_{11}), \\ \phi_{11} - (\phi_{11} - \phi_{12}) \cdot \sin^2\left(\frac{\pi}{2(t_{12} - t_{11})}(t - t_{11})\right) & \text{if } t \in [t_{11}, t_{12}), \\ \phi_{12} - (\phi_{12} - \phi_{10}) \cdot \sin^2\left(\frac{\pi}{2(T - t_{12})}(t - t_{12})\right) & \text{if } t \in [t_{12}, T). \end{cases} \quad (3)$$

The best fit between the proposed approximations and the experimental curve (see Fig. 4) was obtained for the following values of the parameters: $T_1 = 0.545T$, $t_{11} = 0.31T$, $t_{12} = 0.45T$, $\phi_{10} = -16.9^\circ$, $\phi_{11} = 20.5^\circ$, $\phi_{12} = 16.1^\circ$. What is important from the point of view of control of a rehabilitation device, the pattern can be easily modified by changing these values.

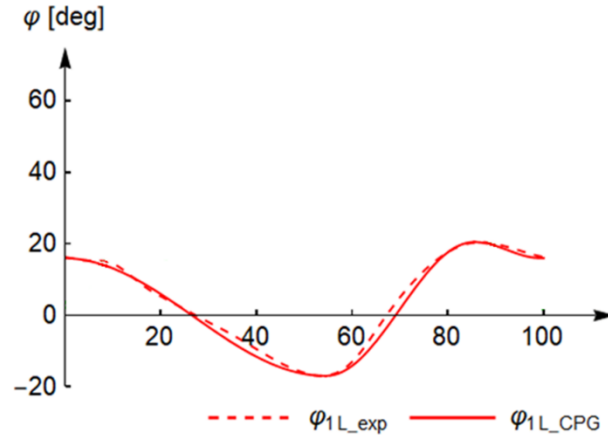


Figure 4. Hip angles during one gait phase – experimental (dashed) vs. simulation (solid) results.

Motion in the knee joints was modelled in the same way, but here, four intervals were distinguished:

$$\varphi_{2L}(t) = \varphi_2(t), \quad \varphi_{2R}(t) = \varphi_2(t - 0.5T), \quad (4)$$

where

$$\varphi_2(t) = \phi_2(\text{mod}[t - T_2, T]), \quad (5)$$

and

$$\phi_2(t) = \begin{cases} \phi_{20} + (\phi_{21} - \phi_{20}) \cdot \sin^2\left(\frac{\pi}{2t_{21}}t\right) & \text{if } t \in [0, t_{21}), \\ \phi_{21} - (\phi_{21} - \phi_{22}) \cdot \sin^2\left(\frac{\pi}{2(t_{22} - t_{21})}(t - t_{21})\right) & \text{if } t \in [t_{21}, t_{22}), \\ \phi_{22} + (\phi_{23} - \phi_{22}) \cdot \sin^2\left(\frac{\pi}{2(t_{23} - t_{22})}(t - t_{22})\right) & \text{if } t \in [t_{22}, t_{23}), \\ \phi_{23} - (\phi_{23} - \phi_{20}) \cdot \sin^2\left(\frac{\pi}{2(T - t_{23})}(t - t_{23})\right) & \text{if } t \in [t_{23}, T). \end{cases} \quad (6)$$

The best fit between the proposed approximations and the experimental curve (see Fig. 5) was obtained for the following values of the parameters: $T_2 = 0.435T$, $t_{21} = 0.30T$, $t_{22} = 0.55T$, $t_{23} = 0.70T$, $\phi_{20} = 9.4$ deg, $\phi_{21} = 57.6$ deg, $\phi_{22} = 1.7$ deg, $\phi_{23} = 18.2$ deg. One can venture to say that the fit is satisfactory as gait patterns differ between people and even between particular gait cycles of an individual.

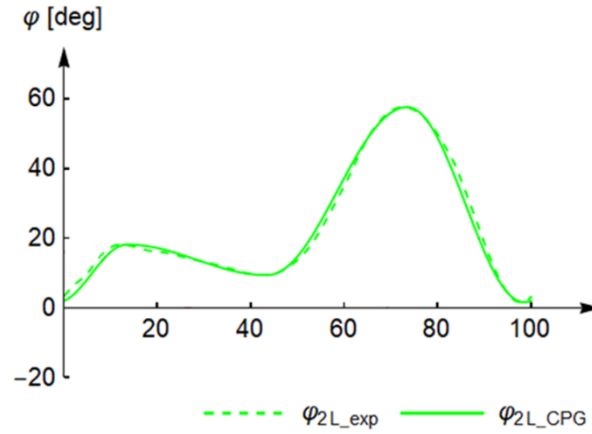


Figure 5. Knee angles during one gait phase – experimental (dashed) vs. simulation (solid) results.

Figure 6 shows the output produced by the proposed CPG for the two joints mentioned above, for both left and right limbs. The signal was repeated 3 times.

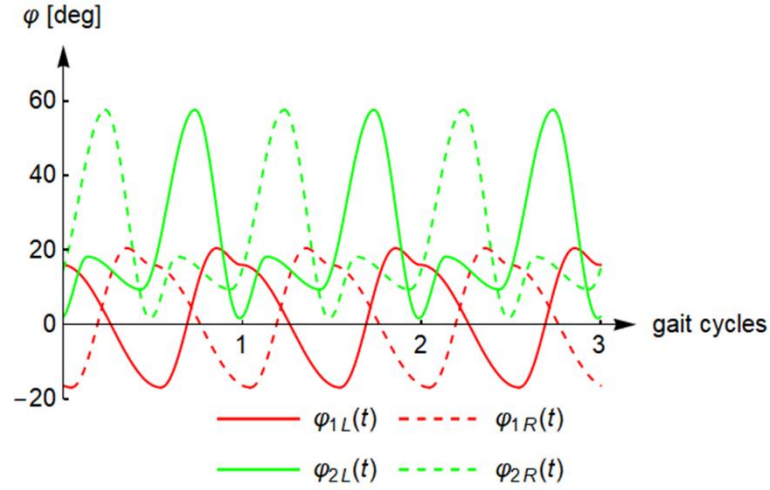


Figure 6. Sagittal plane hip and knee angles during one gait phase – CPG output for the left (solid) and the right limb (dashed), respectively.

In the study, an attempt to model motion in the ankle joint was made, and this task turned out to be more complex than expected. When the simulation model was ran by experimental results, it could be noticed that the foot seem to hit the ground with the heel and then move to the toes immediately. However, in the gait cycle (Fig. 7), the foot should lie flat on the ground for some time.

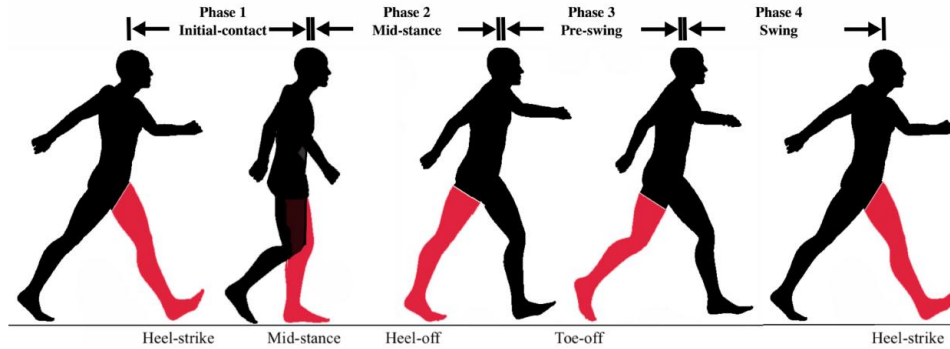


Figure 7. The gait phases [4].

It turned out that different ways of defining the ankle angle can be found in the literature [5-7] (Fig. 8) and, most probably, the definition of the foot angle that we used in our study was different from that used in the software for motion capture system.

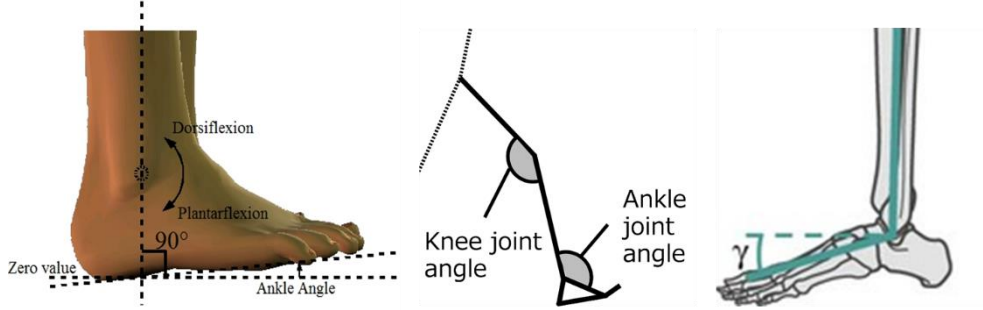


Figure 8. Different exemplary definitions of ankle angle [5-7].

Therefore, the proposed model was modified so as to make the movement of the foot more realistic. For this purpose, the function describing the angle between the ground and the sole of the foot was proposed (see Fig. 9) first, and then, based on this function, the angular position of the hip and the knee as well as the antero-posterior tilt of the pelvis, the ankle angle was calculated:

$$\varphi_{3L}(t) = \varphi_{1L}(t) - \varphi_{2L}(t) - \beta(t) + \varphi_3(t), \quad (7)$$

$$\varphi_{3R}(t) = \varphi_{1R}(t) - \varphi_{2R}(t) - \beta(t) + \varphi_3(t - 0.5T), \quad (8)$$

where

$$\varphi_3(t) = \phi_3(t), \quad (9)$$

and

$$\phi_3(t) = \begin{cases} \phi_{30} + (0 - \phi_{30}) \cdot \sin^2\left(\frac{\pi}{2t_{31}}t\right) & \text{if } t \in [0, t_{31}), \\ 0 & \text{if } t \in [t_{31}, t_{32}), \\ \phi_{31} \cdot \sin^2\left(\frac{\pi}{2(t_{33} - t_{32})}(t - t_{32})\right) & \text{if } t \in [t_{32}, t_{33}), \\ \phi_{31} - (\phi_{31} - \phi_{30}) \cdot \sin^2\left(\frac{\pi}{2(T - t_{33})}(t - t_{33})\right) & \text{if } t \in [t_{33}, T). \end{cases} \quad (10)$$

The signal presented in Fig. 9 was obtained for the following values of the parameters: $t_{31} = 0.10T$, $t_{32} = 0.25T$, $t_{33} = 0.5T$, $\phi_{30} = -10.0$ deg and $\phi_{31} = 30.0$ deg.

Figure 10 shows the comparison of the obtained function and the experimental data. They are not similar, but this was expected because of the mentioned different definitions of ankle angles.

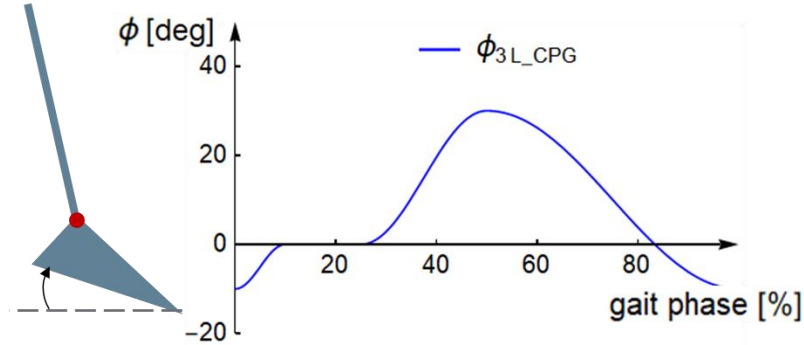


Figure 9. Simulated foot angles in one gait phase.

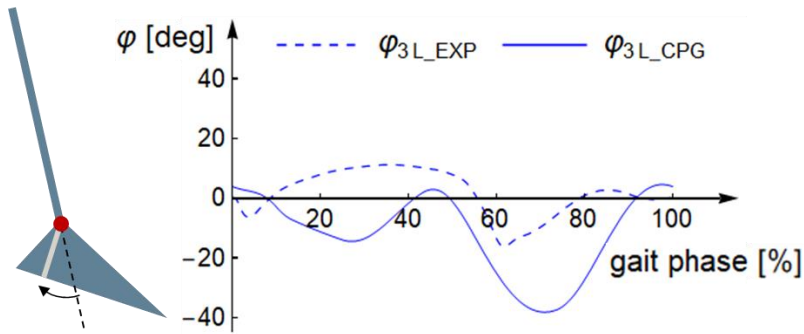


Figure 10. Ankle angles in one gait phase – experimental (dashed) vs. simulation (solid) results.

The introduced modification allowed to model the movement in the feet in a more realistic way. However, it influences vertical fluctuations of the entire structure of the exoskeleton – this effect can be observed in Fig. 11. Therefore, the model has to be subjected to further studies.

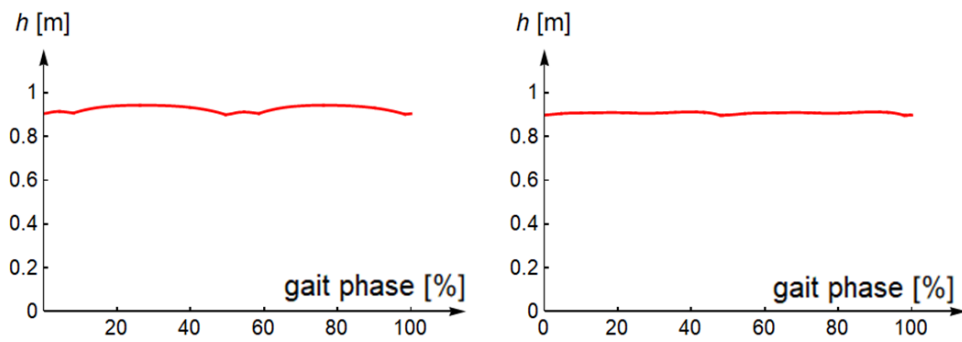


Figure 11. Comparison of vertical fluctuations of the hip joints of the exoskeleton's structure in the global coordinate system; experimental results (on the left) vs. results obtained for the modified CPG model (on the right).

4. Conclusions

To sum up, a simulation model of human gait has been developed based on experimental observations conducted with the motion capture system. A relatively simple gait model using a central pattern generator has been proposed. The model can be potentially used to control the lower limb exoskeleton in the future. It was impossible to obtain a close match between the simulation and experimental results in the entire range of the registered experimental data, which is caused primarily due to the non-repeatability of human movements, as opposed to the simulation model. Last but not least, further investigations related to the foot movement must be conducted.

Acknowledgments

The work has been supported by the National Science Centre of Poland under the grant OPUS 9 no. 2015/17/B/ST8/01700.

References

- [1] World Health Organization, World Report on Disability, 2011.
- [2] Piekarczyńska, M., Wieczorkowski, R., Zajenowska-Kozłowska, A. Health Status of Population of Poland in 2014, Statistical Publishing Establishment, Warsaw, 2016.
- [3] Aguilar-Sierra, H., Yu, W., Salazar, S., Lopez, R. Design and control of hybrid actuation lower limb exoskeleton, *Advances in Mechanical Engineering* 7(6), 2015, 1–13.
- [4] Jiang, X. Chu, K.H., Khoshnam, M., Menon, C. A. Wearable Gait Phase Detection System Based on Force Myography Techniques. *Sensors* 2018, 18, 1279.
- [5] Edrich, T., Riener, R., and Quintern, J. Analysis of Passive Elastic Joint Moments in Paraplegics, *IEEE Trans. Biomed. Eng.* 47(8), 2000, 1058-1065.
- [6] Richards, J., Chohan, A., Erande, R. (Jan 7, 2017) Biomechanics: Chapter 15, Musculoskeletalkey, <https://musculoskeletalkey.com/biomechanics-2/> (accessed on September 10th, 2019).
- [7] Mizushima, J., Seki, K., Keogh, J.W.L., Maeda, K., Shibata, A., Koyama, H., Ohyama-Byun, K. (2018 Jul 13) Kinematic characteristics of barefoot sprinting in habitually shod children, *PeerJ* 6:e5188 [<https://doi.org/10.7717/peerj.5188>].

Olga Jarzyna, M.Sc. (Ph.D. student): Lodz University of Technology, Department of Automation, Biomechanics and Mechatronics, 1/15 Stefanowskiego St., 90-924 Łódź, Poland (olga.jarzyna@edu.p.lodz.pl). The author gave a presentation of this paper during one of the conference sessions.

Dariusz Grzelczyk, Ph.D.: Lodz University of Technology, Department of Automation, Biomechanics and Mechatronics, 1/15 Stefanowskiego St., 90-924 Łódź, Poland (dariusz.grzelczyk@p.lodz.pl).

Jan Awrejcewicz, Professor: Lodz University of Technology, Department of Automation, Biomechanics and Mechatronics, 1/15 Stefanowskiego St., 90-924 Łódź, Poland (jan.awrejcewicz@p.lodz.pl).

Analytical and numerical study of piecewise linear Mathieu equation with non-zero offset

K. R. Jayaprakash, Yuli Starosvetsky

Abstract: The current work is primarily devoted to the analytical and numerical study of instability zones of piecewise linear Mathieu oscillator with a non-zero offset. In this study we invoke the method of averaging to analytically describe the interesting energy dependent instability zones. We show that the derived analytical model provides a fairly good first order approximation to the unstable regions emerging in the vicinity of 1:1 parametric resonance

1. Introduction

The bilinear systems frequently model various engineering structures comprising of moving elements with intermittent contacts. As a simplest bilinear model, one may think of a one degree of freedom (1 DOF) oscillator mounted on the elastic spring with different stiffness characteristics in tension and compression. Theoretical understanding of the response regimes of bi-linear oscillatory models to various types of external loading is crucial in various engineering applications such as machine tool cutting and milling processes [1-2], dynamics of cracked structures [3-6], dynamics of suspension bridges [7], modelling of the topological interlocking structures [8] and more.

Analysis of the response regimes of these special dynamical systems is quite challenging due to their essential nonlinearity and non-smoothness. Many computational and analytical attempts have been devoted to understanding the complex dynamics of a 1DOF bilinear oscillator (BLO) model subject to various types of external excitations such as harmonic and parametric forcing. It is worth noting that in the absence of external forcing - analysis of free vibrations of bilinear oscillator becomes rather simple as the system can be split into two separate linear systems for each state of the response and their solutions can be stitched at the points of transition. In contrast, the situation becomes more complex in the presence of external loading since stitching the solutions of each state (though they are apparently linear) is impossible, because the transition times cannot be calculated explicitly as they are defined through the transcendental equation. Shaw et al. [10] have considered a semi-analytical study of the harmonically forced BLO for the periodic orbits and the ensuing bifurcations. This study has been followed by Thompson et al. [11] who have considered a numerical study of the subharmonic resonances, bifurcations and chaotic regimes of BLO.

The study by Natsiavas [12] considered the forced response of BLO with bi-linear damping and successfully derived a relatively simple, semi-analytic solution for n –periodic orbits and analyzed their stability. Using a similar approach, the author has analyzed the n –periodic response including stability analysis of BLO incorporating the Van-der-Pol type damping [13]. Interestingly, the analytic investigations of the various response regimes of BLOs has not only been confined to the harmonic external forcing. The works of Natsiavas et al. [14-15] present the parametric excitation of piecewise linear oscillator as a typical model of gear backlash and asymmetric stiffness. A thorough computational study by Chatterjee et al. [16] was performed on the model proposed by Natsiavas et al. [14] exploring the regions of stability in the parametric plane of excitation amplitude and frequency ratio. As it was shown by Chatterjee et al. [16], in contrast to the symmetric Mathieu equation, its asymmetric, piecewise linear counterpart may exhibit additional instability regions. However, the above-mentioned study by Chatterjee et al. has not provided any analytical estimates or description of these regions of instability. Some additional analytical studies have been devoted to the analysis of the response regimes of the parametrically and externally forced bi-linear oscillators in the vibro-impact limit [17-19] as well as the dissipative bi-linear oscillator with preload [20].

It is worth noting that all the recent works dedicated to the analysis of this type of dynamical models have applied numerical as well as semi-analytical techniques for the analysis of periodic solutions and assessment of their stability characteristics. Our recent work has shown that the application of some basic asymptotic techniques provides a relatively simple analytical model which adequately approximates and partially explains the complex mechanism governing the unbounded response of a parametric piecewise linear oscillator which essentially depends on the initial energy of the system. Such models can greatly reduce the complex computations and provide better insights of their dynamical behavior. Extension of this technique to a more complex, higher dimensional piecewise linear models subjected to various types of external excitation, opens another new and quite challenging domain of theoretical research.

2. General formulation in terms of AA variables

Let us consider a piecewise linear (PWL) oscillator with a non-zero offset ($a > 0$) subject to the parametric excitation,

$$\ddot{q} + f(q) + \varepsilon P \cos(\Omega_e t) q = 0 \quad (1a)$$

$$f(q) = \begin{cases} q, & q < a \\ \delta^2 q + (1 - \delta^2)a, & q \geq a \end{cases} \quad (1b)$$

The above equation is scaled such that the stiffness coefficient is unity for $q < a$, whereas the corresponding coefficient is $\delta \geq 1$ for $q \geq a$. In what follows δ will be referred to as the ‘asymmetry

parameter' and a as the 'offset parameter'. The corresponding PWL force-displacement curve is shown in Figure. 1. In fact, Eq. (1) or its different variants have been previously considered in several theoretical works for the two important limiting cases.

An asymmetric ($\delta \neq 1$), piecewise linear, Mathieu equation with a zero offset ($a = 0$) has been previously considered by Chatterjee et al. [16]. The study is computationally exhaustive and the authors have demonstrated the formation of additional instability tongues, which are seldom observable on the stability diagram of a classical, symmetric Mathieu equation.

In the other limit, an analytical study of a parametrically excited and damped piecewise linear oscillator has been performed by Babitsky et al. [19] considering the limit of $\delta \rightarrow \infty$ and analyzing the periodic solutions and their stability.

It can be easily verified that the conservative PWL oscillator with zero offset exhibits isochronous oscillations and the frequency of free oscillations is energy independent and equals to $\Omega_{pt} = 2\delta/(1 + \delta)$. However, in the non-zero offset case, the underlying conservative system of (1) exhibits non-isochronous oscillations. In Figure. 2 we illustrate the relations between the frequency of free oscillations and the total energy for the various values of the offset. It is interesting to note that as the total system energy increases the frequency of free oscillations reaches an asymptotic limit of $\Omega_{pt} = 2\delta/(1 + \delta)$ which is essentially the frequency corresponding to the free oscillations of the conservative PWL oscillator with zero offset.

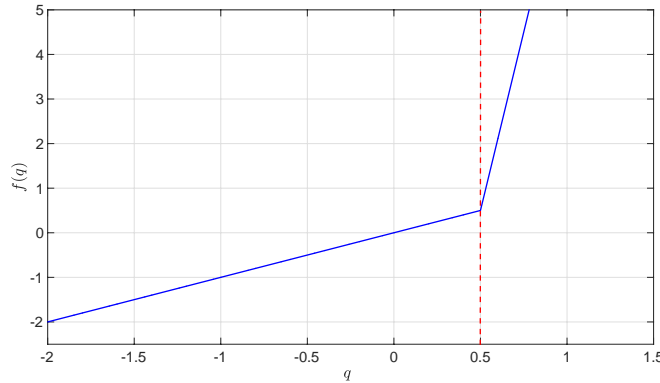


Figure 1. $f(q)$ for an asymmetry parameter of $\delta = 4$ and offset $a = 0.5$

To illustrate the dynamical behavior of PWL Mathieu equation, we provide some time histories corresponding to asymmetric parameter $\delta = 4$ and $\varepsilon = 0.1$. As described previously, if the oscillator response is below the offset, the oscillator behaves as a classical linear Mathieu equation, which exhibits the well-known parametric resonances. Accordingly, once the frequency and amplitude of forcing are inside the resonance tongue (i.e. instability region of the Strutt-Ince diagram), the

response grows exponentially. One such scenario is considered in Figure. 3a wherein the initial displacement is considered below the offset $q(0) < a$ and the excitation frequency is equal to unity ($\Omega_e = 1$). Due to the 1:1 parametric resonance, the response grows exponentially up to the point where the amplitude of the response breaches the offset. Thereafter, there is a sudden escape from resonance, which results in the bounded modulated response. Similarly, in Figure. 3b, we consider the initial displacement $q(0) > a$ and the excitation frequency equal unity ($\Omega_e = 1$). As it will become clear from further analysis, the amplitude of excitation considered in this case is below a certain threshold and as such, the system is quite off the instability zone.

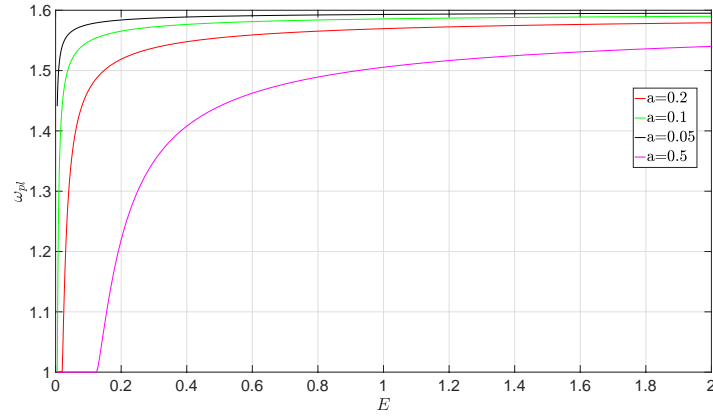


Figure 2. Frequency-energy dependence for PWL oscillator with non-zero offset for the asymmetry parameter $\delta = 4$

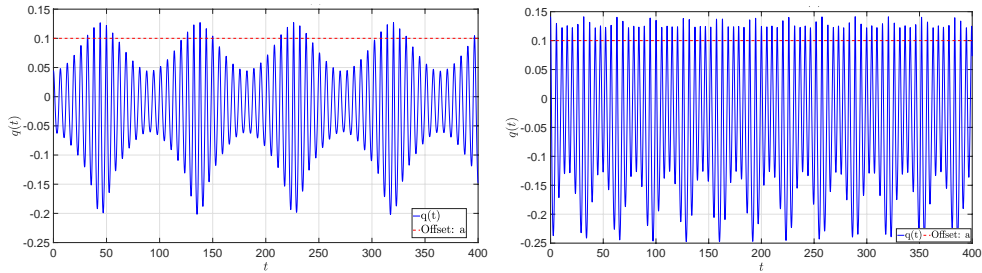


Figure 3. Time histories corresponding to $\varepsilon = 0.1, \delta = 4, P = 5, \Omega_e = 1$ for (a) $q(0) = 0.0447$ (b) $q(0) = 0.1414$

In the second set of simulations, we consider the excitation frequency to be equal to the natural frequency of the PWL oscillator with zero offset i.e. $\Omega_e = \Omega_{pl}$. It is observable that the response in Figure. 4a is bounded for $P = 3.2$. In contrast, for the same initial conditions, an increase in the excitation amplitude to $P = 3.72$ leads to unbounded response.

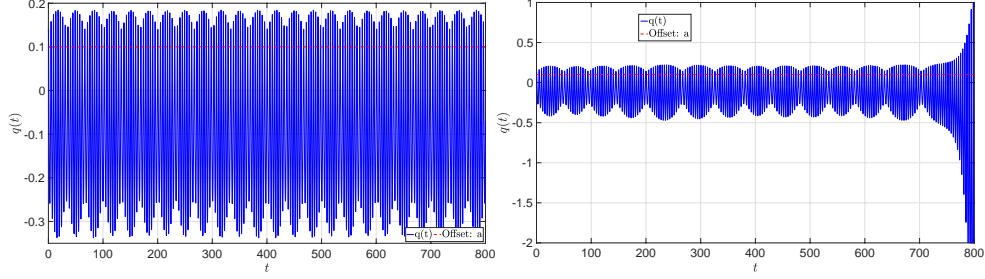


Figure 4. Time histories corresponding to $\varepsilon = 0.1, \delta = 4, q(0) = 0.1414, \Omega_e = \Omega_{pl}$ for (a) $P = 3.2$ (b) $P = 3.72$

Despite the obvious difficulties in the analysis of the dynamics of parametrically excited PWL oscillator, we show that the analytical study of its resonant response regimes is still possible. This is done by the system reformulation in terms of the action-angle (A-A) variables, followed by deducing the averaged flow in the vicinity of a certain (1:1) resonance manifold. Subsequent analysis of the averaged equations reveals the formation of quite interesting, energy dependent instability regions for some general resonance conditions (1:1).

To begin with, the equation of motion in terms of phase space variables are representable in the following form,

$$\begin{aligned} \dot{q} &= p \\ \dot{p} &= -f(q) - \varepsilon P q \cos(\Omega_e t) \end{aligned} \quad (2)$$

The unperturbed Hamiltonian ($\varepsilon = 0$) takes the following form,

$$E = \mathcal{H}_o(p, q) = \begin{cases} \frac{p^2}{2} + \frac{q^2}{2}, & q < a \\ \frac{p^2}{2} + \frac{\delta^2 q^2}{2} + (1 - \delta^2)aq - \frac{a^2}{2}(1 - \delta^2), & q \geq a \end{cases} \quad (3a)$$

whereas, the perturbed Hamiltonian reads,

$$\mathcal{H}(p, q, t) = \mathcal{H}_o(p, q) + \frac{\varepsilon P q^2}{2} \cos(\Omega_e t) \quad (3b)$$

The action-angle variables are defined as,

$$\begin{aligned} I(E) &= \frac{1}{2\pi} \oint p(q, E) dq, \\ \theta &= \frac{\partial}{\partial I} \int_0^q p(q, I) dq \end{aligned} \quad (4)$$

Accordingly, we have,

$$\begin{aligned}
I = \frac{E}{2\pi} & \left\{ \pi + 2 \sin^{-1} \left(\frac{a}{\sqrt{2E}} \right) + \sin \left(2 \sin^{-1} \left(\frac{a}{\sqrt{2E}} \right) \right) \right\} \\
& + \left(\frac{2E\delta^2 + (1 - \delta^2)a^2}{4\pi\delta^3} \right) \left\{ \pi - 2 \sin^{-1} \left(\frac{a}{\sqrt{2E\delta^2 + (1 - \delta^2)a^2}} \right) \right. \\
& \left. - \sin \left(2 \sin^{-1} \left(\frac{a}{\sqrt{2E\delta^2 + (1 - \delta^2)a^2}} \right) \right) \right\}
\end{aligned} \tag{5}$$

From the expression for the action given in (5), it is evident that inverting the expression to obtain $\mathcal{H}_0(I)$ is seldom possible. However, this can be circumvented by transforming to the energy-angle variables in lieu of action-angle variables and will be considered subsequently.

Proceeding with the computation of the angle coordinate we can separately consider the two intervals i.e. $q > a$ and $q \leq a$. Accordingly, the original displacement coordinate represented in terms of energy-angle coordinates, reads

$$q(\theta, E) = \begin{cases} \sqrt{2E^*} \sin(\lambda\delta\vartheta + \psi) + \phi, & 0 \leq \vartheta < \varphi \\ \sqrt{2E} \sin(\lambda(\vartheta - 2\pi) + \kappa), & \varphi \leq \vartheta < 2\pi \end{cases} \tag{6}$$

Where $\psi = \sin^{-1}(a/\delta^2\sqrt{2E^*})$, $\phi = -(1 - \delta^2)a/\delta^2$, $\lambda = \partial I / \partial E$, $\kappa = \sin^{-1}(a/\sqrt{2E})$, $E^* = \frac{E}{\delta^2} + \frac{(1-\delta^2)}{2\delta^4}a^2$ and $\vartheta = \text{mod}(\theta, 2\pi)$, $\varphi = 2\pi - \frac{2}{\lambda} \left\{ \frac{\pi}{2} + \sin^{-1} \left(\frac{a}{\sqrt{2E}} \right) \right\}$.

The perturbed Hamiltonian represented in terms of A-A variables takes the following form

$$\mathcal{H}(I(E), \theta, t) = \mathcal{H}_0(I(E)) + \varepsilon \frac{Pq(\theta, E)^2}{2} \cos(\Omega_e t) \tag{7}$$

As we have already mentioned above, in the absence of perturbation, the system is conservative and in the case of a non-zero offset ($a > 0$) its frequency of oscillations is energy dependent as shown in Figure. 2. As evidenced from the numerical simulations, the system response regimes may exhibit either bounded or unbounded motion. In scope of the present study we are interested in establishing analytically the instability zones, which as it will become clear from the further analysis are energy dependent.

By construction, $q(\theta, E)$ is a 2π - periodic function in terms of the angle variable (θ) and therefore $q^2(\theta, E)$ admits the following Fourier series expansion,

$$q^2(\theta, E) = \sum_{m=-\infty}^{\infty} f_m(E) e^{im\theta} \tag{8}$$

Introducing the above Fourier series expansion in (7), we have

$$\mathcal{H}(I(E), \theta, t) = \mathcal{H}_0(I(E)) + \frac{\varepsilon P}{2} \sum_{m=-\infty}^{\infty} f_m(E) e^{im\theta} \cos(\Omega_e t) \quad (9)$$

The equations of motion in terms of the canonical action-angle coordinates are,

$$\dot{I} = -\frac{\partial \mathcal{H}}{\partial \theta}; \quad \dot{\theta} = \frac{\partial \mathcal{H}}{\partial I} \quad (10)$$

However, as described previously, the inversion of $I(E)$ is seldom possible and the appropriate energy-angle description is,

$$\begin{aligned} \dot{E} &= -\frac{1}{\lambda} \left\{ \frac{i\varepsilon P}{4} \sum_{m=-\infty}^{\infty} m f_m(E) (e^{i\{m\theta + \Omega_e t\}} + e^{i\{m\theta - \Omega_e t\}}) \right\} \\ \dot{\theta} &= \frac{1}{\lambda} \left\{ 1 + \frac{\varepsilon P}{4} \sum_{m=-\infty}^{\infty} \frac{\partial f_m(E)}{\partial E} (e^{i\{m\theta + \Omega_e t\}} + e^{i\{m\theta - \Omega_e t\}}) \right\} \end{aligned} \quad (11)$$

In scope of the present study we consider a 1:1 resonance condition and introduce a resonance slow phase variable v , such that $v = \theta - \Omega_e t$. Here the frequency of excitation (Ω_e) is given by $\Omega_e = \Omega_{pl}$. Further assuming a resonant state and proceeding with the straightforward averaging, we treat v as the slow variable and derive the following averaged equations

$$\dot{E} = \frac{\varepsilon P}{2\lambda} \{\alpha \sin(v) + \beta \cos(v)\} \quad (12a)$$

$$\dot{v} = \frac{1}{\lambda} \left\{ 1 + \frac{\varepsilon P}{2} \{\alpha' \cos(v) - \beta' \sin(v)\} \right\} - \Omega_{pl} \quad (12b)$$

Where $\alpha = \text{Re}(f_1(E))$, $\beta = \text{Im}(f_1(E))$, $\alpha' = \text{Re}\left(\frac{\partial f_1}{\partial E}\right)$, $\beta' = \text{Im}\left(\frac{\partial f_1}{\partial E}\right)$, and $f_{-1} = f_1^*$ (complex conjugate of f_1). It should be noted again, that the derived averaged model is valid only in the vicinity of a certain resonance under consideration. It can be easily shown that the averaged system possesses the following integral,

$$G = \frac{\varepsilon P}{2} \{\alpha \cos(v) - \beta \sin(v)\} + E - I(E)\Omega_{pl} \quad (13)$$

To illustrate the main mechanism of the formation of unbounded response in the strongly nonlinear model under consideration, we have chosen the 1:1 parametric resonance of PWL Mathieu equation. Seeking further for the periodic solutions, we equate both time derivatives of the averaged flow (Eq. 12) to zero to obtain the following algebraic system defining the fixed point of the averaged flow,

$$v = \tan^{-1}\left(-\frac{\beta}{\alpha}\right) \quad (14a)$$

$$\frac{1}{\lambda} \left\{ 1 + \frac{\varepsilon P}{2} \{ \alpha' \cos(v) - \beta' \sin(v) \} \right\} - (\Omega_{pl}) = 0 \quad (14b)$$

In fact, the above derived force - energy relation corresponding to the fixed point provides an absolute threshold for initial energy above which the system will exhibit the unbounded response for the arbitrary chosen initial phase. Correspondingly, the force as a function of the initial energy is presented in Figure. 5 for an asymmetry of $\delta = 4$ for the condition of 1:1 resonance and varying offset parameter α . As observable, with increase in the offset, the force required to induce instability increases. It is worth noting that this force threshold is specific to the initial phase corresponding to the fixed point which is given in Eq. 14a. As it will become clear from the phase portrait of the averaged flow brought below, the change in the initial phase will lead to a change in the critical value of initial energy (assuming the same excitation amplitude and offset) above which the system will exhibit the unbounded response. This behavior is better illustrated by the phase contours corresponding to Eq. (13) as shown in Figure. 6. One can observe a fixed point (saddle) corresponding to Eq. (14) and the phase plane is split into four regions (denoted by A, B, C, D) by the stable and unstable manifolds of the saddle point. If the initial energy is considered in the region A, the oscillator will have bounded, but modulated response. Whereas, the oscillator exhibits unbounded response for any initial energy in the other three regions. As such, for the same excitation amplitude and frequency, the response can be quite varied depending on the initial energy and phase of the oscillator. Thus, the manifolds of the fixed point actually define the unstable region.

In Table 1, we tabulate the threshold energy corresponding to the fixed point (Eq. 14) of the slow flow model. The corresponding threshold energy as observed from the numerical simulation of Eq. 1 is also tabulated considering appropriately transformed initial conditions. The correspondence is found to be extremely good for the lower values of the excitation amplitude of $P = 2$. However, increasing the excitation amplitude further (e.g. $P = 4$, and $\alpha > 0.1$), one starts observing a considerable deviation of the theoretical prediction of the unstable zone vs. the response of the full model. In this case, the mechanism which leads to unbounded response for the values of energy below the predicted threshold is essentially chaotic and cannot be described by the constructed averaged flow.

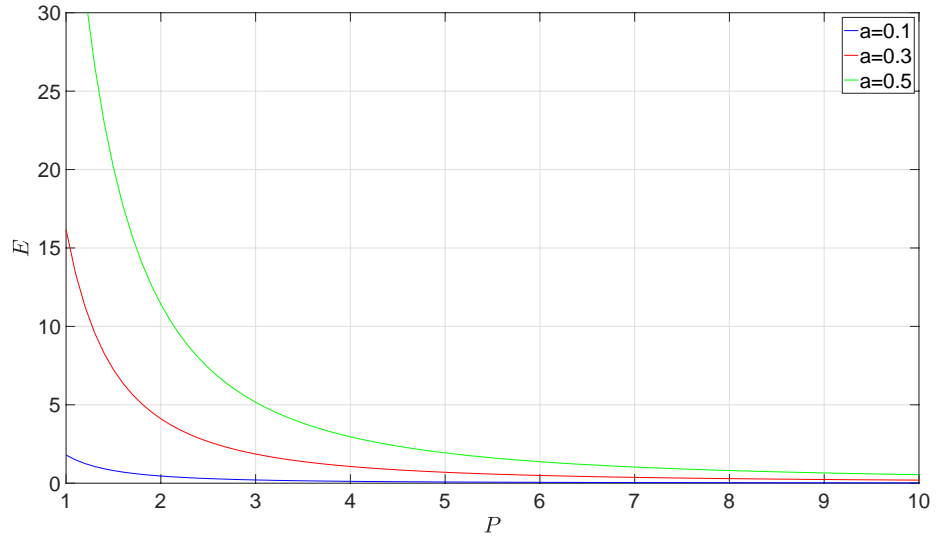


Figure 5. Threshold value of excitation amplitude P as a function of initial energy E corresponding to $\delta = 4$

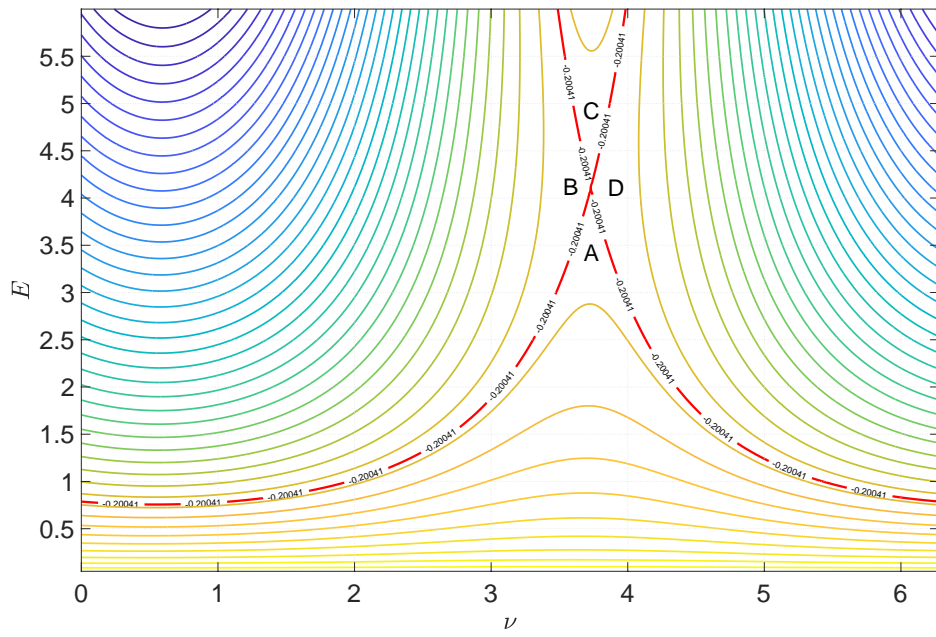


Figure 6. Phase contours corresponding to $a = 0.3, \delta = 4, P = 4.102$

Table 1: Energy threshold for 1: 1 resonance corresponding to $(\delta = 4 \Rightarrow \omega_{pl}(a = 0) = 1.6)$

	$P = 2$		$P = 4$	
	Slow-flow (Eq. 14)	Num (Eq. 1)	Slow-flow (Eq. 14)	Num (Eq. 1)
$a = 0.1$	0.4564	0.449	0.1182	0.117
$a = 0.3$	4.102	4.1	1.065	0.57
$a = 0.5$	11.56	11.32	2.959	2.17
$a = 0.7$	22.36	21.85	5.776	3.46
$a = 0.9$	36.97	36.55	9.588	4.9

3. Conclusions

The current analytical and numerical study is devoted to the study of piecewise linear Mathieu equation with non-zero offset. The description of the instability boundaries of this class of systems is relevant in various engineering systems. However, the essentially nonlinear and non-smooth nature of the oscillator essentially complicates the analysis of the different response regimes arising in this model. To obtain some relatively simple analytical description of the instability zones of a PWL Mathieu equation, we introduce the action-angle variables and apply the method of averaging to deduce a slow-flow model corresponding to a specific resonance case. The study of the slow-flow model provides a clear description of the instability zones. As we have already shown above, these boundaries are not only dependent on the excitation amplitude but also on the initial conditions i.e. initial energy and phase of excitation. The numerical simulations of the full model match extremely well with the deduced slow-flow model for the lower values of the amplitude of parametric excitation. However, the presented analytical model is not devoid of its drawbacks in the sense that it fails to predict the instability boundaries for the higher values of the forcing amplitude. As we have already noted above, in that case the mechanism which leads to unbounded response for essentially low values of energy (i.e. initial energy level below the instability threshold), is strongly chaotic and cannot be described by the constructed averaged flow.

Acknowledgments

JP acknowledges the Department of Science and Technology, India (Grant No. EMR/2017/004094) and YS is grateful to Israel Science Foundation (Grant No. 1079/16) for financial support.

References

- [1] Wiercigroch, M., Chaotic vibration of a simple model of the machine tool-cutting process system. *Journal of Vibration and Acoustics* 119, (1997), 468–475.
- [2] Davies M. A., Balachandran B., Impact dynamics in milling of thin-walled structures. *Nonlinear Dynamics* 22 (2000), 375–392.

- [3] Chati M., Rand R., Mukerjee S., Modal analysis of a cracked beam. *Journal of Sound and Vibration* 207, 2 (1997), pp. 249-270.
- [4] Shen H. H., Pierre C., Natural modes of Bernoulli–Euler beams with symmetric cracks. *Journal of Sound and Vibration* 138 (1990), 115–134.
- [5] Ostachowicz W. M., Krawczuk M., Analysis of the effect of cracks on the natural frequencies of a cantilever beam. *Journal of Sound and Vibration* 150, 191–201.
- [6] Chu Y. C., Shen H. H., Analysis of forced bilinear oscillators and the application to cracked beam dynamics. *AIAA Journal* 10 (1992) 2512–2519.
- [7] Doole S. H., Hogan S. J., A piecewise linear suspension bridge model: Nonlinear dynamics and orbit continuation. *Dynamics and Stability of Systems* 11 (1996), 19–47.
- [8] Dyskin A. V., Pasternak E., Pelinovsky E., Modelling resonances in topological interlocking structures, in: F. Albermani, B. Daniel, J. Griffiths, D. Hargreaves, P. Meehan, A. Tan, M. Veidt (Eds.), *Proceedings of the Fifth Australian Congress on Applied Mechanics, ACAM 2007*, Brisbane, Australia 2, 10–12 December pp. 408–413, (2007).
- [9] Dyskin A. V., Pasternak E., Estrin Y., Mortarless structures based on topological interlocking. *Front. Struct. Civ. Eng.* 6, 2 (2012), 188–197.
- [10] Shaw S. W., Holmes P. J., A periodically forced piecewise linear oscillator. *Journal of Sound and Vibration* 90, 1(1983), 129-155.
- [11] Thompson J. M. T., Bokaian A. R., Ghaffari R., Subharmonic resonances and chaotic motions of a bilinear oscillator. *IMA Journal of Applied Mathematics* 31 (1983), 207–234.
- [12] Natsiavas S., On the dynamics of oscillators with bi-linear damping and stiffness. *International Journal of Non-Linear Mechanics*, 25, 5 (1990), 535-554.
- [13] Natsiavas S., Dynamics of piecewise linear oscillators with Van-der-Pol type damping. *International Journal of Non-Linear Mechanics*, 26, 314 (1991), 349-366.
- [14] Theodossiades S., Natsiavas S., Nonlinear Dynamics of Gear Pair Systems with Periodic Stiffness and Backlash. *Journal of Sound and Vibration* 229 (2000), 287–310.
- [15] Natsiavas S., Theodossiades S., Goudas I., Dynamic analysis of piecewise linear oscillators with time periodic coefficients, *International Journal of Non-Linear Mechanics* 35 (2000), 53-68.
- [16] Marathe A., Chatterjee A., Asymmetric Mathieu equations. *Proc. R. Soc. A* 462 (2006), 1643–1659.
- [17] Dyskin A. V., Pasternak E., Pelinovsky E., Periodic motions and resonances of impact oscillators. *Journal of Sound and Vibration* 331 (2012), 2856–2873.
- [18] Agata G., Dyskin A. V., Pasternak E., Shufrin I., Asymptotic analysis of bilinear oscillators with preload. *International Journal of Engineering Science* 106 (2016), 125–141.

- [19] Babitsky V. I., Krupenin V. L., *Vibration of Strongly Nonlinear Discontinuous Systems*, Springer, Berlin, 2001.
- [20] Dyskin A.V., Pasternak E., Shufrin I., Vertical Vibrations in Rotary Drilling Systems. *Australian Journal of Multi-Disciplinary Engineering* 10, 2 (2015), 198-208.

K. R. Jayaprakash, Assistant Professor: Indian Institute of Technology Gandhinagar, Discipline of Mechanical Engineering, 5/360, IIT Gandhinagar, Palaj, Gandhinagar-382355, Gujarat, India (*jp.kalkunte@iitgn.ac.in*).

Yuli Starosvetsky, Associate Professor: Israel Institute of Technology Technion, Faculty of Mechanical Engineering, D. Dan and Betty Kahn Mechanical Engineering Building, #419, Faculty of Mechanical Engineering, Technion – Israel Institute of Technology, Haifa, 32000, Israel (*staryuli@technion.ac.il*).

Optimization of the spindle speed during milling of large-sized structures with the use of technique of Experiment-Aided Virtual Prototyping

Krzysztof J. Kaliński, Marek Galewski, Michał Mazur, Natalia Morawska

Abstract: In the paper are presented considerations concerning vibration suppression problems during milling of large-sized workpieces with the use of innovative method of matching the spindle speed of cutting tool. It depends on repeatable change of the spindle speed value as soon as the optimal vibration state of the workpiece approaches. The values of dominant “peaks” in the frequency spectra and the Root Mean Square (RMS) values of time domain displacements are evaluated. The efficiency of the proposed approach is evidenced by chosen mechatronic design technique, called Experiment-Aided Virtual Prototyping (E-AVP). Thanks to the results of the identification of the modal subsystem obtained by the Experimental Modal Analysis (EMA) method, it can be stated that the parameters obtained from the experiment and delivered from the computational model have been correctly determined and constitute reliable process data for the simulation tests.

1. Introduction

The methodology of vibration suppression through spindle speed variation awaited a lot of successful applications. For example, the efficiency of the approach was confirmed in case of high-speed milling of rigid workpieces by slender tools even in the potentially unstable regions of spindle speeds, resulting from the position of stability lobes [1]. Vibration suppression using the method of spindle speed variation, however, is ineffective in the case of milling flexible structures [2]. That is why looking for favourable conditions of machining processes performance on a basis of computation of the constant value of optimal spindle speed would produce promising prospects, but it often results in underutilization of production and operating capabilities of modern production machines [3].

Due to the reason above the methods depending on choosing the optimal clamping conditions of the workpiece would be more advisable. Hence a variable stiffness holder in the direction perpendicular to the machined surface, can be installed on the machine table [4]. After appropriate calibration of this holder it is possible to obtain the required stiffness coefficients, depending on the natural frequency of the workpiece [5]. A more practical version of the device is a design with a stiffness coefficient adjustment in the rotational direction [6]. However, the latter means necessity of changing the clamping stiffness during the process which results in difficulty for determination of the optimal condition,

as well in theory as in case of practical applications. The more so that the repetitive change of clamping stiffness coefficients for large-sized workpieces may seem extremely inconvenient, and even – impossible.

To sum up, the only method of reducing level of vibration during as well rough as finishing operations depends on determination of optimal spindle speed. Moreover, the approach reflects its convenience in practical use, because of necessary interference with only technological parameters; all conditions of fixing the workpiece remain unchangeable. The subject of this paper is devoted to a method of searching for conditions of minimizing the vibration level of a tool-large sized flexible workpiece, at unchangeable the clamping stiffness coefficients.

The vibration reduction method, based on the spindle speed and assuming constant clamping stiffness of the workpiece, consists of adjusting the spindle speed to the optimal angle phase shift between subsequent tool passes [7].

Taking into account the influence of the dynamic properties of the workpiece on the amplitude and frequency of vibration implies the necessity of creating a "map" which determines optimal spindle speeds at various points of the clamped workpiece surface on the machine [8, 9], in accordance with the condition of minimum work of the cutting forces, i.e.:

$$\frac{zn_0}{60} = \frac{f_\alpha}{0.25+k}, \quad k = 0,1,2, \dots \quad (1)$$

where: n_0 – subsequent sought spindle speeds, z – number of cutting tool edges, f_α – natural frequency no. α of the workpiece (constant).

However, the above concerns flexible workpieces having small dimensions. In the case of large workpieces, the so called basic optimal spindle speed map does not meet the assumed requirements and is only the first approximation; the optimum spindle speed should be sought under dynamic conditions. One such solution is the proposed authorial technique of the Experiment-Aided Virtual Prototyping (E-AVP), being described below.

2. Hybrid model description

The process of milling large-sized structures can be considered in the convention of a discrete system in hybrid coordinates [2]. Thus, in the hybrid model of the face milling process (Fig. 1) a structural subsystem (i.e. rotating cutting tool, modelled as rotating rigid body or Euler-Bernoulli Bar (EBB) [3]) and a modal subsystem (i.e. a flexible large workpiece idealised as a set of isoparametric finite elements (IFE)) are separated as linear stationary systems.

The main inconvenience of description of the modal subsystem in domain of generalized coordinates is a very large number of degrees of freedom. The structural subsystem has only 6 degrees of freedom, which does not affect too much time spent for computation. After the "synthesis" of both

subsystems, the derived computational model is a linear non-stationary system and has totally 21 hybrid coordinates [3]. The hybrid model also includes time variable position of the contact area between cutting edges and the processed material (CE – coupling elements). The proportional relationship between the cutting force and the instantaneous surface area of the machined layer (so-called *proportional model* [2, 3]) is used for its mathematical description. Clamping stiffness of the workpiece is idealised with the use of a set of massless spring-damping elements (SDE).

Components of generalised displacements in the direction of Cartesian coordinates y_{1l} , y_{12} , y_{13} of CE no. l are related with the generalized coordinates vector \mathbf{q}_s of the structural subsystem and the vector of the modal coordinates \mathbf{a}_m of the modal subsystem using time-dependent constraints equations, respectively described by the matrices \mathbf{T}_l and \mathbf{W}_l [3]. Finally, the dynamics equation of a non-stationary cutting process model in hybrid coordinates takes the form [2, 3]:

$$\begin{aligned} & \begin{bmatrix} \mathbf{M} & \mathbf{0} \\ \mathbf{0} & \mathbf{I} \end{bmatrix} \underbrace{\begin{Bmatrix} \dot{\mathbf{q}}_s \\ \dot{\mathbf{a}}_m \end{Bmatrix}}_{\dot{\boldsymbol{\xi}}} + \begin{bmatrix} \mathbf{L} & \mathbf{0} \\ \mathbf{0} & 2\mathbf{Z}\boldsymbol{\Omega} \end{bmatrix} \underbrace{\begin{Bmatrix} \mathbf{q}_s \\ \mathbf{a}_m \end{Bmatrix}}_{\boldsymbol{\xi}} + \\ & \begin{bmatrix} \mathbf{K} + \sum_{l=1}^{i_l} \mathbf{T}_l^T(t) \mathbf{D}_{Pl}(t) \mathbf{T}_l(t) & - \sum_{l=1}^{i_l} \mathbf{T}_l^T(t) \mathbf{D}_{Pl}(t) \mathbf{W}_l(t) \\ - \sum_{l=1}^{i_l} \mathbf{W}_l^T(t) \mathbf{D}_{Pl}(t) \mathbf{T}_l(t) & \boldsymbol{\Omega}^2 + \sum_{l=1}^{i_l} \mathbf{W}_l^T(t) \mathbf{D}_{Pl}(t) \mathbf{W}_l(t) \end{bmatrix} \underbrace{\begin{Bmatrix} \mathbf{q}_s \\ \mathbf{a}_m \end{Bmatrix}}_{\boldsymbol{\xi}} = \\ & \begin{bmatrix} \sum_{l=1}^{i_l} \mathbf{T}_l^T(t) \mathbf{F}_l^0(t) \\ - \sum_{l=1}^{i_l} \mathbf{W}_l^T(t) \mathbf{F}_l^0(t) \end{bmatrix} + \begin{bmatrix} \sum_{l=1}^{i_l} \mathbf{T}_l^T(t) \mathbf{D}_{Ol}(t) \Delta \mathbf{w}(t - \tau_l) \\ - \sum_{l=1}^{i_l} \mathbf{W}_l^T(t) \mathbf{D}_{Ol}(t) \Delta \mathbf{w}(t - \tau_l) \end{bmatrix} \end{aligned} \quad (2)$$

where: \mathbf{M} , \mathbf{L} , \mathbf{K} – matrices of inertia, damping and stiffness of the structural subsystem, $\boldsymbol{\xi} = \begin{Bmatrix} \mathbf{q}_s \\ \mathbf{a}_m \end{Bmatrix}$ – vector of hybrid coordinates of the hybrid system, $\boldsymbol{\Omega}$ – matrix of angular natural frequencies of the modal subsystem (the stiffness modal matrix); \mathbf{Z} – matrix of dimensionless damping coefficients (the modal damping) of the modal subsystem; i_l – number of „active” coupling elements, i.e. cutting edges currently in contact with the workpiece.

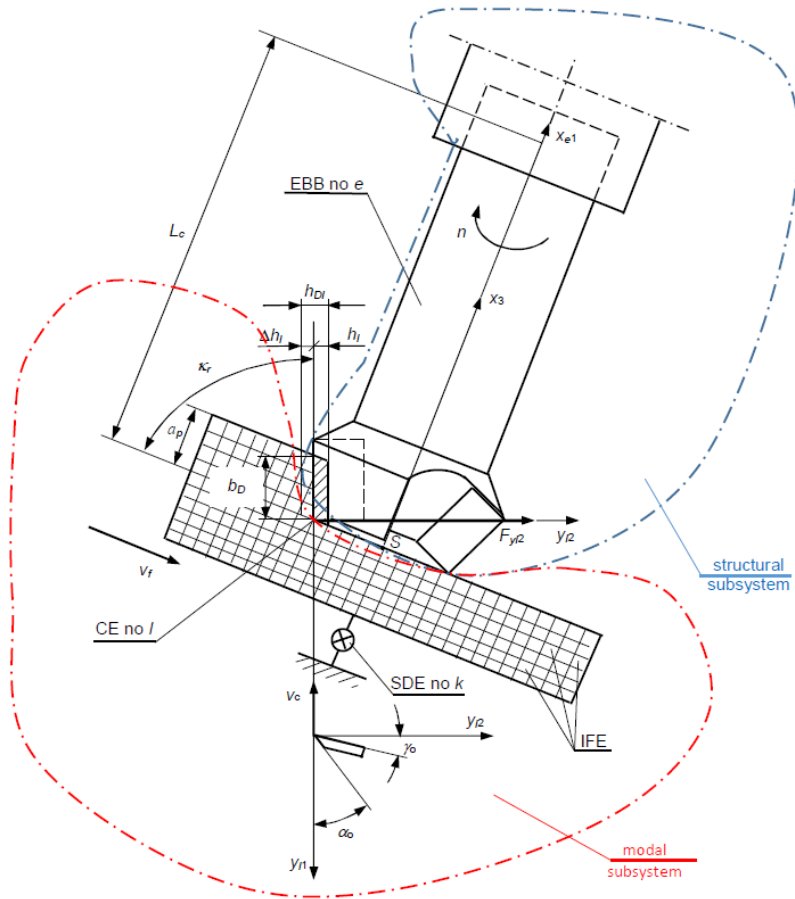


Figure 1. Hybrid model of a face milling process.

3. Optimization of spindle speed during milling of large-sized structures using Experiment-Aided Virtual Prototyping (E-AVP)

The presented procedure (Fig. 2) of changing the spindle speed of the cutting tool means to be more versatile in comparison with the procedure of changing the clamping stiffness, due to no restrictions of a possible use only for rough cutting of large workpiece. The presented procedure has potential use for either rough or finishing cutting of large workpieces. On the other hand, the procedure could be used also in the case of separating many subsystems from the hybrid model.

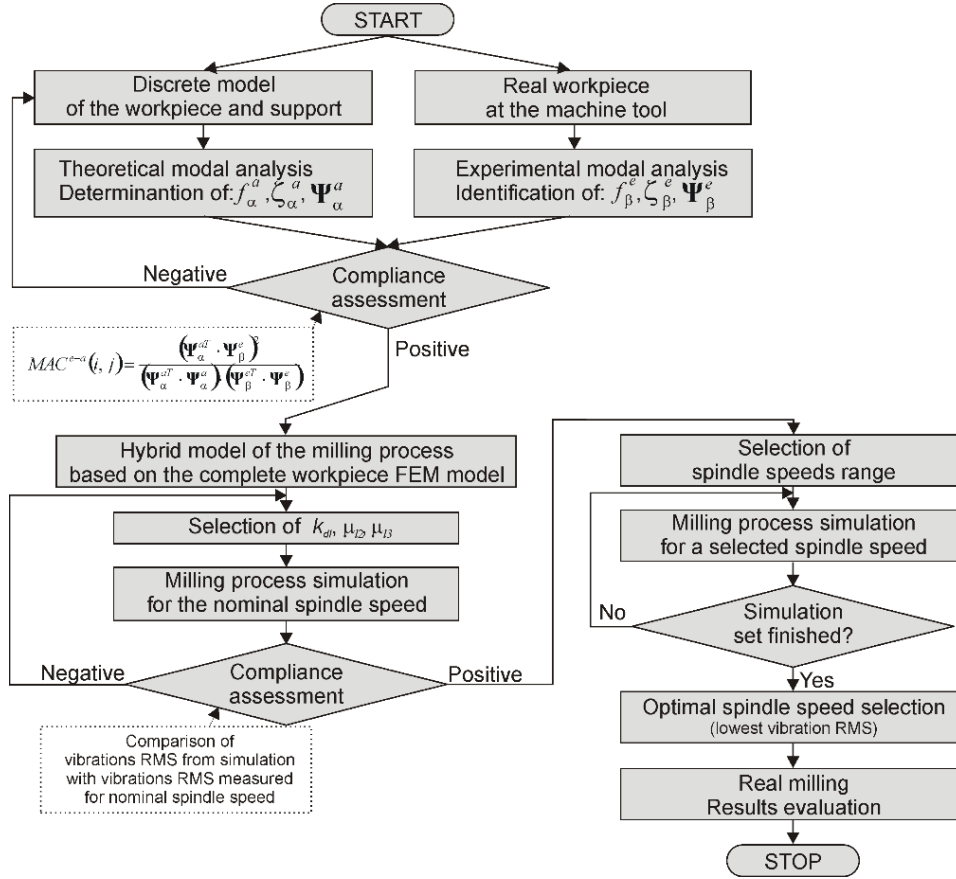


Figure 2. Scheme for finding the optimal spindle speed with the use of the E-AVP technique.

The procedure should begin with the definition of the modal subsystem, modelling it with the use of the finite element method (FEM), theoretical modal analysis (TMA), supported by relevant software MEDINA and PERMAS [3] and validation of the results with respect to real object installed on the machine. This applies in particular to the natural frequencies f of the dominant normal modes, dimensionless damping coefficients ξ and vectors of normal modes Ψ . For a purpose of the latter, experimental modal analysis (EMA) is applied and Modal Assurance Criterion (MAC) is evaluated by the following formula [3]:

$$MAC^{e-a}(\alpha, \beta) = \frac{(\Psi_\alpha^{aT} \cdot \Psi_\beta^e)^2}{(\Psi_\alpha^{aT} \cdot \Psi_\alpha^a)(\Psi_\beta^{eT} \cdot \Psi_\beta^e)} \quad (3)$$

whereas the index is the square of the directional cosine between the Ψ_α^a modal displacements' vector no. α obtained from the calculation, and the Ψ_β^e vector no. β obtained from the experiment. The closer the MAC value is to 1, the more the two eigenvectors match themselves.

The next step in this procedure is to estimate the cutting process parameters, i.e. the average dynamic specific cutting pressure k_{dl} and the coefficients of cutting forces μ_{l2} and μ_{l3} . The selection of their values is iterative, through the implementation of the simulation of the cutting process for nominal spindle speed and comparison of the results with those of vibration measurement during test implementation of real machining for the nominal speed. After adjusting the machining parameters, the allowed range of the spindle speed to be tested is selected, and machining simulations are performed for the selected speeds in this range. After their completion, the spindle speed is selected as the optimal one for which the lowest vibration level or the lowest dominant amplitudes in the spectra, has been reached.

4. Research object

The object of the research was a large-sized workpiece installed on the MIKROMAT 20V portal machining centre at the HYDROTOR PLC in Tuchola (Fig. 3). Relative oscillation was investigated at a conventional contact point of the tool and the workpiece during face milling of the front horizontal surface (i.e. no. 1), length 1778.5 mm, along normal direction to the machined surface.

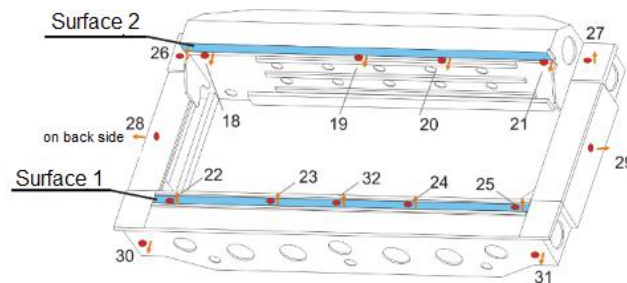


Figure 3. Scheme of test workpiece with marked 1-axis accelerometers positions

In the first stage of the research the correlation of the FEM model with the real workpiece attached to the machine was assessed. In order to eliminate a danger of the results uncertainties, 3 various methods of the modal parameters' identification are applied for this purpose. There were: Eigenvalue Realisation Method (ERA) [3, 10], polyreference Least Squares Complex Frequency Domain (p-LSCFD) [3, 11], and for the purposes of updating the computational model – a new proprietary approach based on Particle Swarm Optimization (PSO) [12]. The results of all the methods really

converged with respect to each other. In the table 1 are shown the MAC coefficients' values for the modal displacements' vectors, identified during the process of EMA with the use of the ERA. 9 normal modes have been identified, although the number of the computed modes is much larger (i.e. 15). However, the latter entitles to conclude that the result of the MAC evaluation appears to be correct.

Table 1. MAC values and natural frequencies for several modes of vibration.

		Computational model MEDINA + PERMAS													
		1	2	3	4	5	6	7	8	9	10	11	12	13	14
ERA	1	0.96	0.0	0.02	0.46	0.1	0.0	0.01	0.23	0.0	0.18	0.02	0.09	0.0	0.02
	2	0.56	0.06	0.01	0.95	0.01	0.0	0.01	0.53	0.01	0.0	0.02	0.03	0.05	0.0
	3	0.0	0.0	0.01	0.0	0.2	0.98	0.02	0.14	0.0	0.01	0.07	0.0	0.0	0.0
	4	0.01	0.05	0.0	0.01	0.04	0.01	0.95	0.0	0.04	0.01	0.0	0.05	0.08	0.07
	5	0.09	0.0	0.0	0.36	0.15	0.02	0.0	0.82	0.0	0.22	0.1	0.01	0.12	0.0
	6	0.23	0.01	0.01	0.0	0.01	0.05	0.03	0.05	0.04	0.82	0.16	0.02	0.16	0.0
	7	0.0	0.08	0.12	0.01	0.0	0.0	0.04	0.02	0.92	0.1	0.06	0.03	0.07	0.01
	8	0.01	0.0	0.0	0.07	0.0	0.01	0.02	0.09	0.0	0.07	0.89	0.51	0.24	0.0
	9	0.0	0.02	0.22	0.0	0.01	0.0	0.01	0.01	0.04	0.01	0.01	0.06	0.05	0.96
ERA		91.3	-	-	151.3	-	234.5	266.7	279.4	313.6	307.1	377.8	-	-	452.0
Computational model MEDINA+PERMAS		90.3	111.0	151.2	153.2	196.9	235.9	263.5	286.3	312.8	331.5	373.4	409.8	426.2	468.3

The next step of the procedure is simulation of the hybrid milling process along with the evaluation of workpiece vibration, based on the dominant values of amplitude “peaks” in the frequency domain and the Root Mean Square (RMS) values of time domain displacements. There was simulated a rough cutting by the Sandvik milling cutter having diameter $D=44$ mm and number of edges $z=4$, at milling depth $a_p=1$ mm.

5. Results of simulations

In tab. 2. are presented for 11 simulations, the RMS values, frequency values f and amplitudes q of dominant “peaks” in the spectrum, observed at instant of time $t_p=10$ s, in the case of rough cutting, spindle speed n_o in the range from 1300 to 1500 rpm and feed rate v_f in the range from 600 to 692 mm/min.

Analysis of the results of the simulated variants based on incremental change of spindle speed (Tab. 2) has allowed to determine the optimal state of cutting. Minimal vibrations were observed in simulation no. 5 ($n_o = 1380$ rpm, Tab. 2, **bold** value). Extremely adverse configuration was observed in case of simulation no. 3 ($n_o = 1340$ rpm, Tab. 2, value underlined). In Figs. 4a-5a are shown time plots of workpiece vibration and the amplitude spectrum for optimal spindle speed. There are observed the harmonics with successively decreasing amplitudes. In Figs. 4b-5b, in case of extremely

unfavourable configuration, harmonic vibrations with successively decreasing amplitudes are observed as well. However, their amplitudes are greater than in case of the optimal solution.

Table 2. Values of RMS in the time domain and dominant amplitudes in the spectra. **Bold** value – optimal result. Value underlined – adverse result.

Number of simulations	n_0 [rpm]	RMS [10^{-4} mm]	f [Hz]	q [10^{-5} mm]
1	1300	4.4681	86.6805	5.1014
			172.1402	2.5931
			258.8207	1.9629
			344.2803	4.1047
2	1320	4.4602	87.9014	6.3043
			175.8027	1.8731
			262.4832	2.0492
			350.3846	3.6023
3	<u>1340</u>	4.4564	89.1222	<u>6.9172</u>
			178.2444	2.8873
			267.3666	2.5430
			356.4888	2.7266
4	1360	4.4617	90.3431	6.3138
			180.6861	2.0148
			272.2500	2.4756
			362.5931	2.1975
5	1380	4.4613	92.7848	4.7775
			184.3487	3.1146
			277.1334	2.6066
			368.6974	1.7229
6	1400	4.4620	94.0056	6.8402
			188.0112	2.9943
			282.0168	<u>3.2191</u>
			376.0225	1.0758
7	1420	4.4559	94.0056	6.8532
			188.0112	<u>3.1969</u>
			282.0168	2.0043
			376.0225	0.9207
8	1440	4.4620	95.2265	6.0986
			191.1155	2.7757
			286.9003	2.1366
			382.1267	1.1042
9	1460	4.4644	97.6682	6.2591
			194.1155	3.0039
			291.7837	2.3184
			389.4518	0.9657
10	1480	4.4614	98.8890	6.3937
			197.7780	2.5276
			297.8879	2.5343
11	1500	4.4564	98.8890	6.4063
			197.7780	1.5484
			297.8879	2.9547

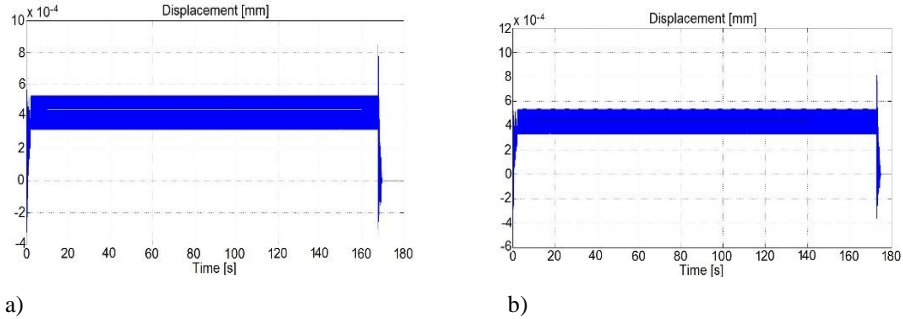


Figure 4. Simulated vibrations in time domain: a) optimal configuration, b) extremely adverse configuration

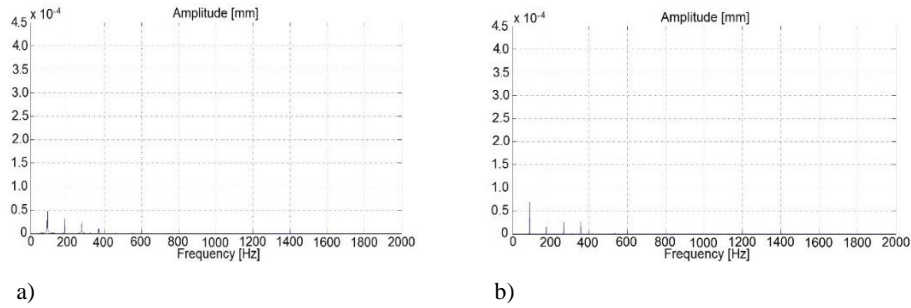


Figure 5. Amplitude spectra, observation time $t_p=10$ s: a) optimal configuration, b) extremely unfavorable configuration

6. Conclusions

Thanks to the obtained results the efficiency of the proposed vibration suppression method has been evidenced by optimizing the spindle speed during high-sized structures milling with the use of a dedicated Experiment-Aided Virtual Prototyping (EAVP) technique.

Thanks to the results of the identification of the modal subsystem obtained by the ERA method, it can be stated that the parameters obtained from the experiment and delivered from the computational model have been correctly determined and constitute reliable process data for the simulation tests. The above is confirmed by 9 natural frequencies identified for the spectrum bandwidth up to 500 Hz.

Acknowledgments

The research has been performed as a part of the tasks financed by the TANGO1/266350/NCBR/2015 project. Experimental investigations on the MIKROMAT 20V portal machining centre were made thanks to cooperation with the HYDROTOR PLC in Tuchola.

References

- [1] K. J. Kaliński, M. A. Galewski, "Chatter vibration surveillance by the optimal-linear spindle speed control", *Mechanical Systems and Signal Processing*, vol. 25, iss. 1, pp. 383–399, 2011.
- [2] K. J. Kaliński, M. A. Galewski, "Optimal spindle speed determination for vibration reduction during ball-end milling of flexible details", *International Journal of Machine Tools and Manufacture*, vol. 92, pp. 19–30, 2015.
- [3] K. J. Kaliński, Nadzorowanie procesów dynamicznych w układach mechanicznych [Vibration surveillance of dynamic processes in mechanical systems]. Gdańsk: Wydawnictwo PG [Publishing House of GUT], 2012 (in Polish).
- [4] K. J. Kaliński, M. Chodnicki, M. R. Mazur, M. A. Galewski, "Vibration surveillance system with variable stiffness holder for milling flexible details", in *Applied Non-Linear Dynamical Systems*, J. Awrejcewicz, Ed. Switzerland: Springer International Publishing, 2014, pp. 175–184.
- [5] K. Kaliński, M. Chodnicki, M. Galewski, M. Mazur, "Vibration surveillance for efficient milling of flexible details fixed in adjustable stiffness holder", *Vibroengineering PROCEDIA*, vol. 3, pp. 215–218, 2014.
- [6] K. J. Kaliński, M. A. Galewski, M. Mazur, M. Chodnicki, "Modelling and simulation of a new variable stiffness holder for milling of flexible details", *Polish Maritime Research*, vol. 24, pp. 115–124, 2017.
- [7] Y. S. Liao, Y. C. Young, "A New On-line Spindle Speed Regulation Strategy for Chatter Control", *International Journal of Machine Tools and Manufacture*, vol. 35, iss. 6, pp. 651–660, 1996.
- [8] K. J. Kaliński, M. Mazur, M. A. Galewski, "The optimal spindle speed map for reduction of chatter vibration during milling of bow thruster blade", *Solid State Phenomena*, vol. 198, pp. 686–691, 2013.
- [9] K. J. Kaliński, M. A. Galewski, M. R. Mazur, "High Speed Milling vibration surveillance with optimal spindle speed based on optimal speeds map", *Key Engineering Materials*, vol. 597, pp. 125–130, 2014.
- [10] N.M.M. Maia, J.M.M. Silva, *Theoretical and Experimental Modal Analysis*. Taunton, Somerset (England): Research Studies Press, 1997.
- [11] W. Heylen, S. Lammens, P. Sas, *Modal Analysis Theory and Testing*. Leuven: KU Leuven, 2007.
- [12] M. A. Galewski, "Spectrum-based modal parameters identification with Particle Swarm Optimization", *Mechatronics*, vol. 37, pp. 21–32, 2016.

Krzysztof Jan Kaliński, Full Professor Eng.: Gdańsk University of Technology, Faculty of Mechanical Engineering, ul. G. Narutowicza 11/12, 80-233 Gdańsk, Poland (kkalinski@o2.pl).

Marek Galewski, DSc. Eng.: Gdańsk University of Technology, Faculty of Mechanical Engineering, ul. G. Narutowicza 11/12, 80-233 Gdańsk, Poland (marek.galewski@pg.edu.pl).

Michał Mazur, Ph.D. Eng.: Gdańsk University of Technology, Faculty of Mechanical Engineering, ul. G. Narutowicza 11/12, 80-233 Gdańsk, Poland (michal.mazur@pg.edu.pl).

Natalia Morawska, M.Sc. Eng. (Ph.D. student): Gdańsk University of Technology, Faculty of Mechanical Engineering, ul. G. Narutowicza 11/12, 80-233 Gdańsk, Poland (natalia.morawska@pg.edu.pl) The author gave a presentation of this paper during one of the conference sessions.

Chaos-geometric approach to analysis and forecasting evolutionary dynamics of complex systems: Atmospheric pollutants dynamics

Olga Yu. Khetselius, Andrey A. Svinarenko, Yuliya Ya. Bunyakova,
Alexander V. Glushkov

Abstract: We present a generalized computational complex approach to studying and forecasting evolutionary dynamics of complex geosystems (city's atmospheric pollution), based on the combined using the non-linear analysis methods and chaos theory such as the mutual information approach, correlation integral analysis, false nearest neighbour algorithm, Lyapunov's exponents analysis, surrogate data method, stochastic propagators method, memory and neural networks, Green's functions approaches. We identify the concentration space-temporary evolution dynamics for the SO₂ in the atmosphere of industrial cities in order to reveal the chaos in the hourly time series at several sites in the Gdansk and Odessa cities during the 2001-2006. We present an advanced computational model to forecasting the atmospheric pollutants evolutionary dynamics (the "Geomath" technology). To determine time delays, the concept of mutual information is used. To determine the attractor dimensions, it is used the correlation integral method and false nearest neighbours algorithm. The data on the Lyapunov's exponents and other topological and dynamical invariants are listed.

1. Introduction

At the present time one of the most actual, important and fundamental problems of modern applied ecology, environmental protection is a problem of the quantitative treating pollution dynamics in the industrial cities and at whole regions and a search of new mathematical tools for analysis, modelling and forecasting a temporal dynamics of the air pollutant (dioxide of nitrogen, sulphur etc) concentrations in an atmosphere of the industrial cities and regions [1-13]. In Refs. [1-3] the detailed review of the results of analysis, modelling and processing the measurement data in different laboratories is presented, in particular, it concerns to analysis of the CO, O₃ concentrations time series. Also, it was shown that O₃ concentrations in Cincinnati (Ohio) and Istanbul are evidently chaotic, and non-linear approach provides satisfactory results. In Refs. [6-10] an analysis of the NO₂, CO, O₃ concentrations time series in a few industrial cities is presented. It has been definitely received an evidence of chaos elements in the corresponding concentrations time series. These studies

show that chaos theory methodology can be applied and the short-range forecast by the non-linear prediction method can be satisfactory.

In this paper we present the results of an advanced analysis, modelling and forecasting a temporal dynamics of the air pollutant (dioxide of sulphur) concentrations in atmosphere of the industrial city (Odessa, Ukraine and Gdansk, Poland) using a chaos-geometric approach, which includes an advanced non-linear analysis technique and modern chaos theory and dynamical systems methods (in versions [5-20]). An accurate short-term forecast of the atmospheric pollutants temporal evolution is presented. All calculations are performed with using “Geomath”, “Superatom” and “Quantum Chaos” computational codes [21-36].

2. Technique of analysis and computing atmospheric pollutants fluctuations temporal dynamics

The key elements of the technique of computing atmospheric pollutants fluctuations dynamics are described in details in Refs. [5-13]. Here we are limited to presenting only the main elements. Let us consider scalar measurements: $s(n)=s(t_0+ n\Delta t) = s(n)$, where t_0 is a start time, Δt is time step, and n is number of the measurements. In our case $s(n)$ is the time series of the atmospheric pollutants concentration. As processes resulting in a chaotic behaviour are fundamentally multivariate, one needs to reconstruct phase space using as well as possible information contained in $s(n)$. The main idea is that direct use of lagged variables $s(n+\tau)$, where τ is some integer to be defined, results in a coordinate system where a structure of orbits in phase space can be captured. Using a collection of time lags to create a vector in d dimensions,

$$\mathbf{y}(n)=[s(n),s(n+\tau),s(n+2\tau),...,s(n+(d-1)\tau)],$$

(where $d=d_E$ is the embedding dimension) the required coordinates are provided.

The goal of the embedding dimension determination is to reconstruct a Euclidean space R^d large enough so that the set of points d_A can be unfolded without ambiguity. To analyse a measured time histories for the sulphur dioxide concentrations, the phase space of the system had been reconstructed by the delay embedding. Further the advanced versions of the mutual information approach, correlation integral analysis, false nearest neighbour algorithm, Lyapunov's exponent's analysis, and surrogate data method are used for comprehensive characterization (c.g., [5,14-17]). The correlation dimension method provides a fractal-dimensional attractor. Statistical significance of the results was confirmed by testing for a surrogate data. The choice of proper time lag is important for the subsequent reconstruction of phase space.

First approach is to compute the linear autocorrelation function $C_L(\delta)$ and to look for that time lag where $C_L(\delta)$ first passes through 0. This gives a good hint of choice for τ at that $s(n+j\tau)$ and

$s(n+(j+1)\tau)$ are linearly independent. Alternative approach is given by a nonlinear concept of independence, e.g. an average mutual information (c.g., [5,14-17]). In order to compute an attractor dimension one should use the correlation integral analysis, which is one of the widely used techniques to investigate the signatures of chaos in a time series.

Further let us note that the spectrum of the Lyapunov's exponents is one of dynamical invariants for non-linear system with chaotic behaviour. The Lyapunov's exponents are related to the eigenvalues of the linearized dynamics across the attractor. For chaotic systems, being both stable and unstable, the Lyapunov's exponents indicate the complexity of the dynamics. The largest positive value determines some average prediction limit. Since the Lyapunov's exponents are defined as asymptotic average rates, they are independent of the initial conditions, and hence the choice of trajectory, and they do comprise an invariant measure of the attractor. An estimate of this measure is a sum of the positive Lyapunov's exponents. The estimate of the attractor dimension is provided by the conjecture d_L and the Lyapunov's exponents are taken in descending order. To compute Lyapunov's exponents, we use a method with linear fitted map (version [1]) , although the maps with higher order polynomials can be used too.

The principally important topic is development of an advanced approach to prediction of chaotic properties of complex systems. Our key idea is in the using the traditional concept of a compact geometric attractor in which evolves the measurement data, plus the implementation of neural network algorithms. The existing so far in the theory of chaos prediction models are based on the concept of an attractor. The meaning of the concept is in fact a study of the evolution of the attractor in the phase space of the system and, in a sense, modelling ("guessing") time-variable evolution.. From a mathematical point of view, it is a fact that in the phase space of the system an orbit continuously rolled on itself due to the action of dissipative forces and the nonlinear part of the dynamics, so it is possible to stay in the neighborhood of any point of the orbit $y(n)$ other points of the orbit $y^r(n)$, $r = 1, \dots, N_B$, which come in the neighborhood $y(n)$ in a completely different times than n . Of course, then one could try to build different types of interpolation functions that take into account all the neighborhoods of the phase space and at the same time explain how the neighborhood evolve from $y(n)$ to a whole family of points about $y(n+1)$. Use of the information about the phase space in the simulation of the evolution of some geophysical (environmental, etc.) of the process in time can be regarded as a fundamental element in the simulation of random processes.

These idea have been used in order to make more advanced the wide spread prediction model which is based on the constructing a parameterized nonlinear function $F(x, a)$, which transform $y(n)$ to $y(n+1) = F(y(n), a)$, and then using different criteria for determining the parameters a . As it is shown by Schreiber [18], the most common form of the local model is very simple :

$$s(n + \Delta n) = a_0^{(n)} + \sum_{j=1}^{d_A} a_j^{(n)} s(n - (j-1)\tau)$$

where Δn - the time period for which a forecast . The coefficients $a_j^{(k)}$, may be determined by a least-squares procedure, involving only points $s(k)$ within a small neighbourhood around the reference point. Thus, the coefficients will vary throughout phase space. The fit procedure amounts to solving $(d_A + 1)$ linear equations for the $(d_A + 1)$ unknowns. Further, since there is the notion of local neighborhoods, one could create a model of the process occurring in the neighborhood, at the neighborhood and by combining together these local models to construct a global nonlinear model that describes most of the structure of the attractor. In order to get more advanced prediction of chaotic dynamics we have applied the polynomial model [5-9,19,20].

3. The advanced data for the sulphur dioxide concentrations time series of the industrial cities and conclusions

We studied the concentration space-temporary evolution dynamics for the SO₂ in the atmosphere of industrial cities in order to reveal the chaos in the hourly time series at several sites in the Gdansk and Odessa cities during the 2001-2006. In our study, we used the sulphur dioxide concentration data observed at several sites of the Gdansk on 2003-2004, namely, the multi year hourly concentrations (one year total of 20x8760 data points) and the Odessa on 2001-2006, namely, the multi year hourly concentrations (one year total of 20 x 6570 data points). The typical temporal series of the SO₂ concentrations at two sites (Gdansk) are presented in Figure 1.

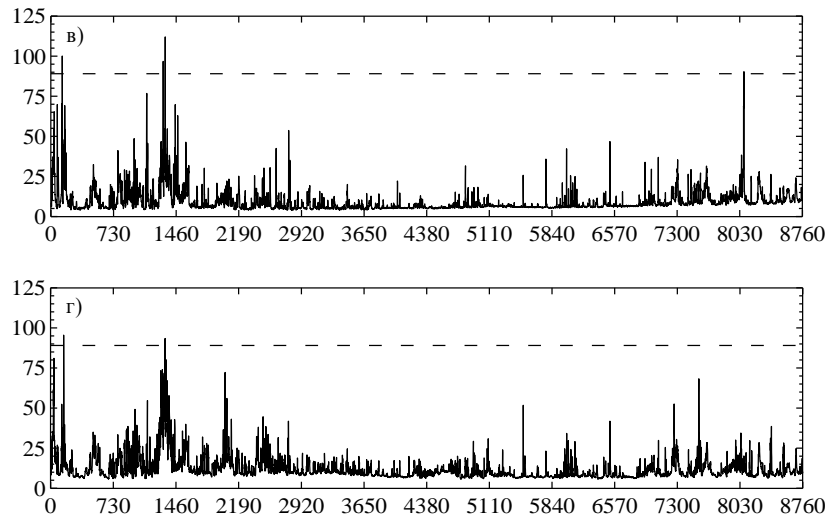


Figure 1. The typical time series of the SO₂ concentrations at two sites (Gdansk), in µg/cm³ (see text)

Let us note that in the Gdansk region, the Agency of Regional Air Quality Monitoring (ARMAAG) provides presently the 24-h forecasts of air quality levels using the model called CALMET/CALPUFF (CALPUFF) (see [2,4] and Refs. therein).

In the Table 1 we present our calculated (advanced) data on some dynamical and topological invariants, in particular, the correlation dimension (d_2), embedding dimension (d_E), the Kaplan-Yorke dimension (d_L), two Lyapunov's exponents (λ_1, λ_2), the Kaplan-Yorke dimension (d_L), and average limit of predictability (Pr_{max} , hours) for the time series of the SO_2 concentration at two sites of the Gdansk (during 2003 year). It should be noted that the analogous data are received for the SO_2 concentration time series at the sites of the Odessa.

Table 1. The correlation dimension (d_2), embedding dimension (d_E), first two Lyapunov's exponents, $E(\lambda_1, \lambda_2)$, Kaplan-Yorke dimension (d_L), and average limit of predictability (Pr_{max} , hours) for the SO_2 concentration time series for the two sites (during 2003)

Site	τ	d_2	d_E	λ_1	λ_2	d_L	Pr_{max}	K
1	19	1.58	6	0.0164	0.0066	5.01	43	0.71
2	17	3.40	6	0.0150	0.0052	4.60	49	0.73

The time series of the SO_2 at the site 2 have the highest predictability (more than 2 days), and other time series have the predictabilities slightly less than 2 days. The concrete example of the prediction model realization (see details in Refs. [19-23]) is presented in Figure 2, where the empirical (solid line) and predicted (dotted line; by the Schreiber-type prediction algorithm with the simple neural networks block) SO_2 concentration curves are listed for the last one hundred points of the time series.

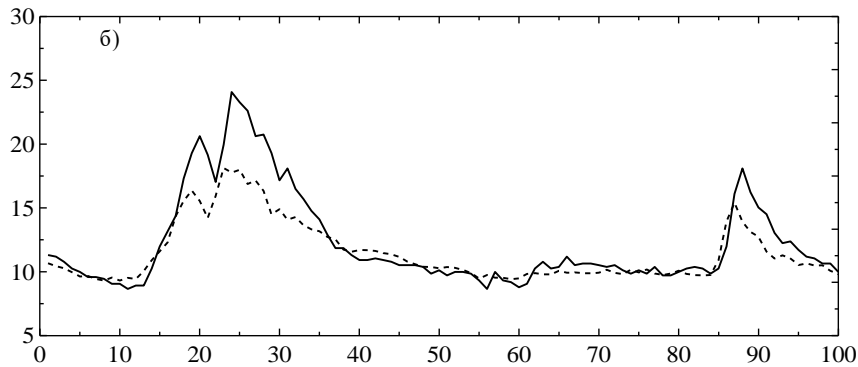


Figure 2. The empirical (solid line) and predicted (dotted line) SO_2 concentration curves for the last one hundred points of the time series (see text).

In whole an analysis shows that almost all the peaks on the actual curve repeated on the prognostic difference between the forecast and the actual data in the event of high concentrations of the ingredients can be quite large. Therefore, one should conclude that the results of our computational forecasting can be considered as quite satisfactory.

Acknowledgments

The authors would like to thank Prof. Jan Awrejcewicz and colleagues for invitation to make contributions to DSTA-2019 (Łódź, Poland). The useful comments of the anonymous referees are very much acknowledged too.

References

- [1] Bunyakova, Yu.Ya., Glushkov, A.V. *Analysis and forecast of the impact of anthropogenic factors on air basein of an industrial city*. Ecology, Odessa, 2010.
- [2] Gubanova, E.R., Glushkov, A.V., Khetselius, O.Yu., Bunyakova, Yu.Ya., Buyadzhi, V.V., Pavlenko, E.P. *New methods in analysis and project management of environmental activity: Electronic and radioactive waste*. FOP, Kharkiv, 2017.
- [3] Glushkov, A.V., Safranov, T.A., Khetselius, O.Yu., Ignatenko, A.V., Buyadzhi, V.V., Svinarenko A.A. Analysis and forecast of the environmental radioactivity dynamics based on methods of chaos theory: General conceptions. *Environmental Problems*. 1, 2 (2016), 115-120.
- [4] CALPUFF, Available from: <http://www.src.com/calpuff/calpuff1.htm>
- [5] Glushkov, A.V. *Methods of a chaos theory*. Astroprint, Odessa, 2012.
- [6] Bunyakova, Yu.Ya., Glushkov, A.V., Khetselius, O.Yu., Ignatenko, A.V., Bykowszczenko, N., Buyadzhi, V.V. New approach and microsystem technology of advanced analysis and forecasting the air pollutant concentration temporal dynamics in atmosphere of the industrial cities. *Sensor Electr. and Microsyst. Techn.* 14, 3 (2017), 65-78.
- [7] Buyadzhi, V.V., Glushkov, A.V., Khetselius, O.Yu., Bunyakova, Yu.Ya., Florko, T.A., Agayar E.V., Solyanikova, E.P. An effective chaos-geometric computational approach to analysis and prediction of evolutionary dynamics of the environmental systems: Atmospheric pollution dynamics. *J.Phys.: Conf. Ser.* 905 (2017), 012036.
- [8] Glushkov, A.V., Khetselius, O.Y., Bunyakova, Yu.Ya., Prepelitsa, G.P., Solyanikova, E.P., Serga E.N. Non-linear prediction method in short-range forecast of atmospheric pollutants: low-dimensional chaos. *Dynamical Systems - Theory and Applications*, Lodz. (2011), LIF111.
- [9] Khetselius, O.Yu., Glushkov, A.V., Bunyakova, Yu.Ya., Buyadzhi, V.V., Bondar, O.I., Vaschenko, V.N., Bykowszczenko, N. New approach and microsystem technology to modelling dynamics of atmosphere ventilation of industrial city and elements of the “Green-City” construction technology. *Sensor Electr. and Microsyst. Techn.* 14, 4 (2017), 37-46.
- [10] Buyadzhi, V., Glushkov, A., Khetselius, O., Ternovsky, V., Serga, I., Bykowszczenko, N., An advanced analysis and modelling the air pollutant concentration temporal dynamics in atmosphere of the industrial cities: Odessa city. *IOP Conf. Series: Earth and Environm. Sci.* 92 (2017), 012006.

- [11] Glushkov, A.V., Khetselius, O.Yu., Agayar, E.V., Buyadzi, V.V., Romanova, A.V., Mansarliysky, V.F. Modelling dynamics of atmosphere ventilation and industrial city's air pollution analysis: New approach. *IOP Conf. Series: Earth and Environm. Sci.* 92 (2017), 012014
- [12] Glushkov, A., Bunyakova, Yu., Buyadzi, V., Dubrovskaya, Yu., Kuznetsova, A., Khetselius, O. New approach and microsystem technology of advanced non-linear analysis and modelling chaotic environmental radioactivity dynamics. *Sensor Electr. and Microsyst. Techn.* 14,3 (2017), 24-37.
- [13] Bunyakova, Yu.Ya., Ternovsky, V.B., Dubrovskaya, Yu.V., Ignatenko, A.V., Svinarenko, A.A., Vitavetskaya, L.A. Analysis of the beryllium-7 activity concentration dynamics in the atmospheric environment time series after the Fukushima Daiichi nuclear power plants emergency. *Sensor Electr. and Microsyst. Techn.* 14, 4 (2017), 73-82.
- [14] Packard, N.H., Crutchfield, J.P., Farmer, J.D., Shaw, R.S. Geometry from a time series. *Phys. Rev. Lett.* 45 (1980), 712–716.
- [15] Abarbanel, H.D.I., Brown, R., Sidorowich, J.J., Tsimring, L.Sh. The analysis of observed chaotic data in physical systems. *Rev. Mod. Phys.* 65 (1993), 1331–1392.
- [16] Fraser, A.M., Swinney, H.L. Independent coordinates for strange attractors from mutual information. *Phys. Rev. A* 33 (1986), 1134–1140.
- [17] Grassberger, P., Procaccia, I. Measuring the strangeness of strange attractors. *Physica D* 9 (1983), 189–208.
- [18] Schreiber, T. Interdisciplinary application of nonlinear time series methods. *Phys. Rep.* 308 (1999), 1–64.
- [19] Khetselius, O.Yu. Forecasting evolutionary dynamics of chaotic systems using advanced non-linear prediction method. *Dynamical Systems Applications*, ed. J. Awrejcewicz, M. Kazmierczak, P. Olejnik, J. Mrozowski. Lodz Univ., Łódź. T2 (2013), 145-152.
- [20] Bunyakova, Yu.Ya., Khetselius, O.Yu. Non-linear prediction statistical method in forecast of atmospheric pollutants. *Proc. of 8th Intert. Carbon Dioxide Conference (Germany)*. T2-098 (2009).
- [21] Serbov, N.G., Glushkov, A.V., Bunyakova, Yu.Ya., Prepelitsa, G.P., Svinarenko, A.A. Sensing the kinetical features of energy exchange in mixture CO₂-N₂-H₂O of atmospheric gases under interacting with laser radiation. *Sensor Electr. and Microsyst. Techn.* N4 (2006), 20-22.
- [22] Glushkov, A., Khetselius, O., Brusentseva, S., Zaichko, P., Ternovsky, V. Studying interaction dynamics of chaotic systems within a non-linear prediction method: application to neurophysiology. *Advances in Neural Networks, Fuzzy Systems and Artificial Intelligence*. Ed. J.Balicki. WSEAS Pub., Gdansk. 21 (2014), 69-75.
- [23] Glushkov, A.V., Svinarenko, A.A., Buyadzi, V.V., Zaichko, P.A., and Ternovsky, V.B. Chaos-geometric attractor and quantum neural networks approach to simulation chaotic evolutionary dynamics during perception process. *Advances in Neural Networks, Fuzzy Systems and Artificial Intelligence*. Ed. J.Balicki. WSEAS Pub., Gdansk. 21 (2014), 143-150.
- [24] Glushkov, A.V., Khetselius, O.Yu., Bunyakova, Yu.Ya., Grushevsky, O.N., and Solyanikova, E.P. Studying and forecasting the atmospheric and hydroecological systems dynamics by using chaos theory methods. *Dynamical Systems Theory*, ed. J. Awrejcewicz, M. Kazmierczak, P. Olejnik, J. Mrozowski. Lodz Univ., Łódź. T1 (2013), 249-258.
- [25] Glushkov, A.V., Prepelitsa, G.P., Svinarenko, A.A., and Zaichko, P.A. Studying interaction dynamics of the non-linear vibrational systems within non-linear prediction method (application to quantum autogenerators). *Dynamical Systems Theory*, ed. J. Awrejcewicz, M. Kazmierczak, P. Olejnik, J. Mrozowski. Lodz Univ., Łódź. T1 (2013), 467-477.

- [26] Glushkov, A.V., Kuzakon, V.M., Ternovsky, V.B., Buyadzh, V.V. Dynamics of laser systems with absorbing cell and backward-wave tubes with elements of a chaos. *Dynamical Systems Theory*, ed. J. Awrejcewicz, M. Kazmierczak, P. Olejnik, J. Mrozowski. Łódź. T1 (2013), 461-466.
- [27] Glushkov, A.V., Ternovsky, V.B., Buyadzh, V.V., Prepelitsa, G.P. Geometry of a Relativistic Quantum Chaos: New approach to dynamics of quantum systems in electromagnetic field and uniformity and charm of a chaos. *Proc. Intern. Geom. Center*. 7, 4 (2014), 60-71.
- [28] Glushkov, A.V., Buyadzh, V.V., Kvasikova, A.S., Ignatenko, A.V., Kuznetsova, A.A., Prepelitsa, G.P., Ternovsky, V.B. Nonlinear chaotic dynamics of Quantum systems: Molecules in an electromagnetic field and laser systems. *Quantum Systems in Physics, Chemistry, and Biology*, ed. A.Tadger, R.Pavlov, J.Maruani, E.Brändas, G.Delgado-Barrio. Springer, Cham. 30 (2017), 169-180.
- [29] Glushkov A.V., Khetselius O.Yu., Kuzakon V.M., Prepelitsa G.P., Solyanikova E.P., Svinarenko A.A., Modeling of interaction of the non-linear vibrational systems on the basis of temporal series analyses (application to semiconductor quantum generators). *Dynamical Systems - Theory and Applications*. Lodz Univ., Lodz. (2011) BIF110.
- [30] Buyadzh, V., Glushkov, A., Mansarliysky, V., Ignatenko, A., Svinarenko A. Spectroscopy of atoms in a strong laser field: New method to sensing AC Stark effect, multiphoton resonances parameters and ionization cross-sections. *Sensor Electr. and Microsyst. Techn.* 12, 4 (2015), 27-36.
- [31] Glushkov, A., Khetselius, O., Bunyakova, Yu., Buyadzh, V., Brusentseva, S., Zaichko P. Sensing interaction dynamics of chaotic systems within a chaos theory and microsystem technology Geomath with application to neurophysiological systems. *Sensor Electr. and Microsyst. Techn.* 11, 3 (2014), 62-69.
- [32] Glushkov, A., Mansarliysky, V., Khetselius, O., Ignatenko, A., Smirnov, A., Prepelitsa, G. Collisional shift of hyperfine line for thallium in an atmosphere of the buffer inert gas. *J. Phys.: Conf. Ser.* 810 (2017), 012034.
- [33] Khetselius, O., Glushkov, A., Dubrovskaya, Yu., Chernyakova, Yu., Ignatenko, A., Serga, I., Vitavetskaya, L., Relativistic quantum chemistry and spectroscopy of exotic atomic systems with accounting for strong interaction effects. *Concepts, Methods and Applications of Quantum Systems in Chemistry and Physics*. Springer, Cham, 31 (2018), 71-91.
- [34] Khetselius, O.Yu. *Quantum structure of electroweak interaction in heavy finite Fermi-systems*. Astroprint, Odessa, 2011.
- [35] Glushkov, A.V., Svinarenko, A.A., Loboda, A.V. *Theory of neural networks on basis of photon echo and its program realization*. TEC, Odessa, 2003.
- [36] Glushkov, A.V., Khetselius, O.Yu., Svinarenko, A.A., Buyadzh, V.V. *Methods of computational mathematics and mathematical physics. P.1*. TES, Odessa, 2015.
- Olga Yu. Khetselius, Professor: Odessa State Environmental University, Pure and Applied Mathematics Department, L'vovskaya str. 15, 65009 Odessa, Ukraine (okhetsel@gmail.com). The author gave a presentation of this paper during one of the conference sessions
- Andrey A. Svinarenko, Professor: Odessa State Environmental University, Pure and Applied Mathematics Department, L'vovskaya str. 15, 65009 Odessa, Ukraine (svinarenkoaa@gmail.com).
- Yuliya Ya. Bunyakova, Assoc.-Professor: Odessa State Environmental University, Environment Economics Department, L'vovskaya str. 15, 65009 Odessa, Ukraine (bunyakovayy@gmail.com)
- Alexander V. Glushkov, Professor: Odessa State Environmental University, Pure and Applied Mathematics Department, L'vovskaya str. 15, 65009 Odessa, Ukraine (glushkovav@gmail.com).

New generalized chaos-geometric and neural networks approach to nonlinear modeling of complex chaotic dynamical systems

Olga Yu. Khetselius, Andrey A. Svinarenko, Anna V. Ignatenko, Anna A. Buyadzhi

Abstract: We present a generalized computational complex approach to studying and forecasting evolutionary dynamics of the complex dynamical systems. The standard nonlinear modeling of chaotic processes in these systems can be based on the concept of compact geometric attractor with using the non-linear analysis and chaos theory methods such as the qualitative theory of differential equations, multi-fractal formalism, wavelet analysis, mutual information approach, correlation integral analysis, false nearest neighbour algorithm, the Lyapunov's exponent's analysis, surrogate data method, stochastic propagators, memory and Green's functions approaches. We elaborate a new approach to analyze and to predict the nonlinear dynamics of chaotic systems based on the concept of geometric attractors, chaos theory methods and the neural network simulation algorithms. The combined using information on the phase space evolution of the physical process in time and the simulation data of the neural network modeling can be considered as one of the fundamentally new approaches in the construction of global nonlinear models of the most effective and accurate description of structure of the corresponding strange attractor. Some illustrative numerical examples are presented.

1. Introduction

The most important and fundamental issue in the description of dynamics of the dynamical systems is its ability to forecast its future evolution, i.e. predictability of a behaviour. It should be recalled that, since the works of Poincare, Kolmogorov, Lorenz, Lyapunov, Einstein, Heisenberg, Feynman, Arnold, Moser, Feigenbaum, Mandelbrot, Sinai and many others, a chaos theory, which actually involves quite a variety of different directions, was developed mostly academically and very separately (qualitative theory of differential equations, ergodic theories, fractal geometry, methods of classical mechanics, etc.). Modern nonlinear dynamics has established the main mechanisms of instability and scenarios of transition to chaos in nonlinear dynamic systems; for example, one of the main scenarios of chaos in a coupled oscillator system is the so-called Ruel-Tacens scenario. But in real, especially very complex devices and systems, chaotic dynamics take on much more complex, partially or not fully understood forms (c.g., [1-14]). If the studied system is more complicated then the greater the equations is necessary for its adequate description. The examples of some systems described by a small amount of differential equations, are known nevertheless, these systems exhibit a

complicated behaviour. Probably the best-known examples of such systems are the Lorenz system, the Sinai billiard, etc. At present time there are developed and implemented a variety of methods, in particular, the nonlinear spectral and trend analysis, the Markov chains analysis, wavelet and multifractal analysis, the formalism of the matrix memory and the method of evolutionary stochastic propagators etc. In a series of papers [15-30] we have attempted to apply some of these methods in a variety of the physical, geophysical, hydrodynamic problems. In connection with this, there is an extremely important task on development of new, more effective approaches to the nonlinear modelling and prediction of chaotic processes in the complex dynamical systems.

In this work we present an advanced computational approach to analysis, modelling, forecasting the temporal evolutionary dynamics of the complex dynamical systems. The standard nonlinear modeling of chaotic processes in these systems can be based on the concept of compact geometric attractor with using the non-linear analysis and chaos theory methods such as the qualitative theory of differential equations, multi-fractal formalism, wavelet analysis, mutual information approach, correlation integral analysis, false nearest neighbour algorithm, Lyapunov exponent's analysis, surrogate data method, stochastic propagators method, memory and Green's functions approach. We elaborate an advanced approach to analyze and to predict the nonlinear dynamics of chaotic systems based on the concept of geometric attractors, chaos theory methods and the neural network simulation algorithms. All calculations are performed with using "Geomath", "Superatom" and "Quantum Chaos" computational codes [11-14, 31-45].

2. New concepts and algorithms in theory of analysis and forecasting dynamics of chaotic processes

The basic idea of the construction of the combined chaos-geometric and neural networks modelling approach to prediction of nonlinear processes in chaotic systems was developed in Refs. [13,14] and resulted in the use of the traditional concept of a compact geometric attractor in which evolves the measurement data, plus the implementation of neural network algorithms. The existing so far in the theory of chaos prediction models are based on the concept of an attractor, and are described in a number of papers (e.g. [1-10]). The meaning of the concept is in fact a study of the evolution of the attractor in the phase space of the system and, in a sense, modelling ("guessing") time-variable evolution.. From the mathematical viewpoint in the phase space of the system an orbit continuously rolled on itself due to the action of dissipative forces and the nonlinear part of the dynamics, so it is possible to stay in the neighborhood of any point of the orbit $y(n)$ other points of the orbit $y^r(n)$, $r = 1, 2, \dots, N_B$, which come in the neighborhood $y(n)$ in a completely different times than n . Here one try to build different types of interpolation functions that take into account all the neighborhoods of the phase space and at the same time explain how the neighborhood evolve from $y(n)$ to a whole family

of points about $y(n+1)$. Use of the information about the phase space in the simulation of the evolution of some nonlinear chaotic process in time can be regarded as a fundamental element in the simulation of random processes. After restoration of the phase space the block of calculating topological (different fractal dimensions, correlation) and dynamic (the local and global Lyapunov's dimensions) invariants is further realized. The latter are very useful in considering the physics of the process and, in addition, determine the limited predictability of the chaotic motion of the physical system. Using only topological or only dynamic invariants to characterize an attractor is unlikely to give a "complete" set of invariants, so they must be used together. Since the Lyapunov's dimensions are defined as asymptotic mean velocities, they are independent of the initial conditions and the choice of trajectory, so they are considered as invariant measures of the attractor. The calculation of the Lyapunov's dimension spectrum is usually performed on the basis of the Jacobian of reflection and the multiplicative ergodic theorem. Calculating the Lyapunov's dimensions, Kolmogorov entropy and Kaplan and York dimensions are further fulfilled.

Further we propose to generalize a description and modelling the nonlinear processes in dynamics of chaotic systems in terms of the modern theory of neural networks and neuroinformatics (c.g., [11]). The key idea is in imitating the temporal evolution of a complex system as the evolution of a neural network with the corresponding elements of the self-study, self-adaptation, etc. Considering the neural network (with a certain number of neurons, as usual, we can introduce the operators S_{ij} synaptic neuron to neuron u_i u_j , while the corresponding synaptic matrix is reduced to a numerical matrix strength of synaptic connections: $W = ||w_{ij}||$. The operator is described by the standard activation neuro-equation determining the evolution of a neural network in time:

$$s'_i = \text{sign}\left(\sum_{j=1}^N w_{ij}s_j - \theta_i\right), \quad (1)$$

where $1 \leq i \leq N$.

From the viewpoint of a chaotic dynamical system theory, the state of the neuron (the chaos-geometric interpretation of the forces of synaptic interactions, etc.) can be represented by currents in the phase space of the system and its topological structure is obviously determined by the number and position of attractors. To determine the asymptotic behaviour of the system it becomes crucial information aspect of the problem, namely, the fact of being the initial state to the basin of attraction of a particular attractor. Modelling each physical attractor by a record in memory, the process of the evolution of neural network, transition from the initial state to the (following) the final state is a model for the reconstruction of the full record of distorted information, or an associative model of pattern recognition is implemented. The domain of attraction of attractors are separated by separatrices or certain surfaces in the phase space. Their structure, of course, is quite complex, but

mimics the chaotic properties of the studied object. Then, as usual, the next step is a natural construction parameterized nonlinear function $F(x, \mathbf{a})$, which transforms:

$$\mathbf{y}(n) \rightarrow \mathbf{y}(n+1) = \mathbf{F}(\mathbf{y}(n), \mathbf{a}), \quad (2)$$

and then to use the different (including neural network) criteria for determining the parameters \mathbf{a} (see below). The easiest way to implement this program is in considering the original local neighborhood, enter the model(s) of the process occurring in the neighborhood, at the neighborhood and by combining together these local models, designing on a global nonlinear model. The latter describes most of the structure of the attractor.

As shown Schreiber [3], the most common form of the local model is very simple :

$$s(n + \Delta n) = a_0^{(n)} + \sum_{j=1}^{d_A} a_j^{(n)} s(n - (j-1)\tau) \quad (3)$$

where Δn - the time period and the coefficients $a_j^{(k)}$ may be determined by a least-squares procedure, involving only points $s(k)$ within a small neighbourhood around the reference point. Thus, the coefficients will vary throughout phase space. The fit procedure amounts to solving $(d_A + 1)$ linear equations for the $(d_A + 1)$ unknowns. The measure of the fitting the curve to the data, which is determined by the condition of exactly how $\mathbf{y}(k+1)$ coincides with $\mathbf{F}(\mathbf{y}(k), \mathbf{a})$, is a local deterministic error: $\varepsilon_D(k) = \mathbf{y}(k+1) - \mathbf{F}(\mathbf{y}(k), \mathbf{a})$. If the map $\mathbf{F}(\mathbf{y}, \mathbf{a})$ is local, then for each adjacent point to \mathbf{y} (k $\mathbf{y}^{(r)}(k)$ ($r = 1, 2, \dots, N_B$)) one could write $\varepsilon_D^{(r)}(k) = \mathbf{y}(r, k+1) - \mathbf{F}(\mathbf{y}^{(r)}(k), \mathbf{a})$, where $\mathbf{y}(r, k+1)$ is the point in the phase space to which $\mathbf{y}(r, k)$ evolves. To measure the quality of the curve to the data, the local cost function looks like (in fact, the cost function for the error):

$$W(\varepsilon, k) = \sum_{r=1}^{N_B} |\varepsilon_D^{(r)}(k)|^2 / \sum_{r=1}^{N_B} [\mathbf{y}(k) - \langle \mathbf{y}(r, k) \rangle]^2, \quad (4)$$

and the parameters determined by minimizing $W(\varepsilon, k)$ will depend on \mathbf{a} . Further, formally, it is possible to start a neural network algorithm, in particular, in the aspect of training an equivalent neural network system with reconstruction and temporary prediction of the state of the neurosystem (accordingly, adjustment of $a_j^{(n)}$). The details of computing procedure are presented in Refs. [11,14].

3. Some illustrative numerical examples and conclusions

As illustration below we present two examples of using a pure geometric attractor prediction model and the combined chaos-geometric and neural networks approach to forecasting the temporal atmospheric pollutants (NO_2) dynamics. The meaning of the latter is precisely the

application of neural network to simulate the evolution of the attractor in phase space, and training most neural network to predict (or rather, correct) the necessary coefficients of the parametric form of functional display. All details regarding the use of the neural network algorithm are described in the Refs. [5,10,11,14]. Here we only note that we used the time series of multiyear hourly concentrations (one year total of 20x8760 data points) observed at a few measurement sites of the Gdansk (Poland). The temporal series of concentrations (in $\mu\text{g}/\text{m}^3$) of the NO_2 are presented in figure 1 (for two sites). These data are presented by the Agency of Regional Air Quality Monitoring (ARMAAG), (see [10,11,46] and Refs. therein).

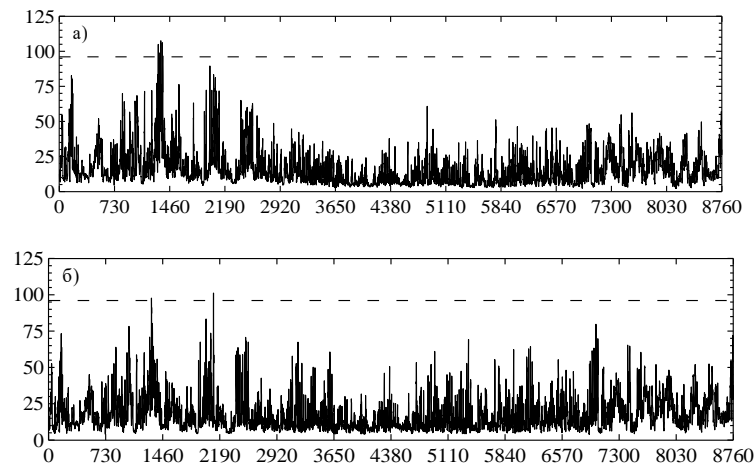


Figure 1. The temporal series of the NO_2 concentration (in $\mu\text{g}/\text{m}^3$): (a) site 1; (b) – site 2(see text).

In the Table 1 we present our advanced data on the correlation dimension (d_2), embedding dimension (d_E), Kaplan-Yorke dimension (d_L), two Lyapunov's exponents (λ_1, λ_2), the Kaplan-Yorke dimension (d_L), and average limit of predictability (Pr_{\max} , hours) for time series of the NO_2 at sites of the Gdansk (2003). The data are received within the standard chaos-geometric approach (c.g., [1-15]).

Table 1. The correlation dimension (d_2), embedding dimension (d_E), first two Lyapunov's exponents, $E(\lambda_1, \lambda_2)$, Kaplan-Yorke dimension (d_L), and average limit of predictability (Pr_{\max} , hours) for time series of NO_2 at the Gdansk sites (during 2003)

Site	τ	d_2	d_E	λ_1	λ_2	d_L	Pr_{\max}	K
1	9	5.31	6	0.0185	0.0060	4.11	41	0.68
2	8	5.31	6	0.0188	0.0052	3.85	42	0.66

The concrete example of computational prediction of the atmospheric pollutant concentration temporal dynamics is presented in Figure 1. In this Figure the empirical (solid line 1) and theoretical forecasting (solid line 2 -by the Schreiber-type algorithm with neural networks block and dotted line 3 - by the standard Schreiber-type algorithm) NO₂ concentration lines (for 10² points) are listed.

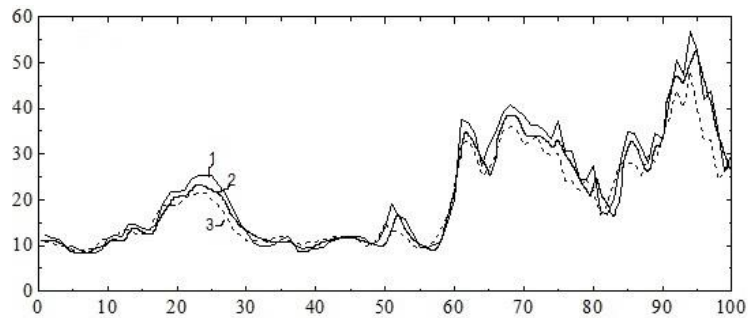


Figure 2. The empirical (solid line 1) and forecasting (solid line 2 and dotted line 3) NO₂ concentration lines for the last one hundred points (see text).

In whole an analysis shows that almost all the peaks on the actual curve repeated on the prognostic difference between the forecast and the actual data in the event of high concentrations of the ingredients can be quite large. The prediction line 2 looks more exact in comparison with actual data. More detailed analysis of this fact will be presented in another paper. Here we only note that the results of our computational forecasting can be considered quite satisfactory.

Acknowledgments

The authors would like to thank Prof. Jan Awrejcewicz and colleagues for invitation to make contributions to DSTA-2019 (Łódź, Poland). The useful comments of the anonymous referees are very much acknowledged too.

References

- [1] Gottwald, G.A., Melbourne, I. Testing for chaos in deterministic systems with noise. *Physica D.* 212 (2005), 100–110.
- [2] Packard, N.H., Crutchfield, J.P., Farmer, J.D., Shaw, R.S. Geometry from a time series. *Phys. Rev. Lett.* 45 (1980), 712–716.
- [3] Kennel, M.B., Brown, R., and Abarbanel, H. Determining embedding dimension for phase-space reconstruction using a geometrical construction. *Phys. Rev. A* 45 (1992) 3403–3411.
- [4] Abarbanel, H.D.I., Brown, R., Sidorowich, J.J., Tsimring, L.Sh. The analysis of observed chaotic data in physical systems. *Rev. Mod. Phys.* 65 (1993), 1331–1392.

- [5] Schreiber, T. Interdisciplinary application of nonlinear time series methods. *Phys. Rep.* 308 (1999), 1–64.
- [6] Fraser, A.M., Swinney, H.L. Independent coordinates for strange attractors from mutual information. *Phys. Rev. A.* 33 (1986), 1134–1140.
- [7] Grassberger, P., Procaccia, I. Measuring the strangeness of strange attractors. *Physica D.* 9 (1983), 189–208.
- [8] Gubanova, E.R., Glushkov, A.V., Khetselius, O.Yu., Bunyakova, Yu.Ya., Buyadzhi, V.V., Pavlenko, E.P. *New methods in analysis and project management of environmental activity: Electronic and radioactive waste.* FOP, Kharkiv, 2017.
- [9] Glushkov, A.V., Svinarenko, A.A., Loboda, A.V. Theory of neural networks on basis of photon echo and its program realization. TEC, Odessa, 2003.
- [10] Bunyakova, Yu.Ya., Glushkov, A.V. *Analysis and forecast of the impact of anthropogenic factors on air basein of an industrial city.* Ecology, Odessa, 2010.
- [11] Glushkov, A.V. *Methods of a chaos theory.* Astroprint, Odessa, 2012.
- [12] Glushkov, A.V., Khetselius, O.Y., Brusentseva, S.V., Zaichko, P.A., Ternovsky, V.B. Studying interaction dynamics of chaotic systems within a non-linear prediction method: application to neurophysiology. *Advances in Neural Networks, Fuzzy Systems and Artificial Intelligence, Series: Recent Advances in Computer Engineering*, Ed. J.Balicki. WSEAS Pub., Gdansk. 21 (2014), 69-75.
- [13] Glushkov, A.V., Svinarenko, A.A., Buyadzhi, V.V., Zaichko, P.A., Ternovsky, V.B. Chaos-geometric attractor and quantum neural networks approach to simulation chaotic evolutionary dynamics during perception process. *Advances in Neural Networks, Fuzzy Systems and Artificial Intelligence, Series: Recent Advances in Computer Engineering*, Ed. J.Balicki. WSEAS Pub., Gdansk. 21 (2014), 143-150.
- [14] Khetselius, O.Yu. Forecasting evolutionary dynamics of chaotic systems using advanced non-linear prediction method. *Dynamical Systems Applications*, ed. J. Awrejcewicz, M. Kazmierczak, P. Olejnik, J. Mrozowski. Lodz Univ., Łódź. T2 (2013), 145-152.
- [15] Bunyakova, Yu.Ya., Khetselius, O.Yu. Non-linear prediction statistical method in forecast of atmospheric pollutants. *Proc. of 8th Intern. Carbon Dioxide Conference (Germany)*. T2-098 (2009).
- [16] Glushkov, A.V., Safranov, T.A., Khetselius, O.Yu., Ignatenko, A.V., Buyadzhi, V.V., Svinarenko A.A. Analysis and forecast of the environmental radioactivity dynamics based on methods of chaos theory: General conceptions. *Environmental Problems*. 1, 2 (2016), 115-120.
- [17] Khetselius, O.Yu. Hyperfine structure of radium. *Photoelectronics*. 14 (2005), 83-85.
- [18] Glushkov, A.V., Khetselius, O.Y., Bunyakova, Yu.Ya., Prepelitsa, G.P., Solyanikova, E.P., Serga E.N. Non-linear prediction method in short-range forecast of atmospheric pollutants: low-dimensional chaos. *Dynamical Systems - Theory and Applications*, Lodz. (2011), LIF111.
- [19] Bunyakova, Yu., Glushkov, A., Khetselius, O., Ignatenko, A., Bykowszczenko, N., Buyadzhi, V. New approach and microsystem technology of advanced analysis and forecasting the air pollutant concentration temporal dynamics in atmosphere of the industrial cities. *Sensor Electr. and Microsyst. Techn.* 14, 3 (2017), 65-78.
- [20] Glushkov, A., Khetselius, O., Svinarenko, A., Serbov, N. The sea and ocean 3D acoustic waveguide: rays dynamics and chaos phenomena. *J. Acoust. Soc. America*. 123, 5 (2008), 3625.

- [21] Buyadzhi, V.V., Glushkov, A.V., Khetselius, O.Yu., Ternovsky, V.B., Serga, I.N., Bykowszczenko, N. An advanced analysis and modelling the air pollutant concentration temporal dynamics in atmosphere of the industrial cities: Odessa city. *IOP Conf. Series: Earth and Environm. Sci.* 92 (2017), 012006.
- [22] Buyadzhi, V.V., Glushkov, A.V., Khetselius, O.Yu., Bunyakova, Yu.Ya., Florko, T.A., Agayar E.V., Solyanikova, E.P. An effective chaos-geometric computational approach to analysis and prediction of evolutionary dynamics of the environmental systems: Atmospheric pollution dynamics. *J.Phys.: Conf. Ser.* 905 (2017), 012036.
- [23] Glushkov, A.V., Khetselius, O.Yu., Agayar, E.V., Buyadzhi, V.V., Romanova, A.V., Mansarliysky, V.F. Modelling dynamics of atmosphere ventilation and industrial city's air pollution analysis: New approach. *IOP Conf. Series: Earth and Environm. Sci.* 92 (2017), 012014
- [24] Glushkov, A.V., Bunyakova, Yu.Ya., Buyadzhi, V.V., Dubrovskaya, Yu.V., Kuznetsova, A.A., Khetselius, O.Yu. New approach and microsystem technology of advanced non-linear analysis and modelling chaotic environmental radioactivity dynamics. *Sensor Electr. and Microsyst. Techn.* 14,3 (2017), 24-37.
- [25] Bunyakova, Yu.Ya., Ternovsky, V.B., Dubrovskaya, Yu.V., Ignatenko, A.V., Svinarenko, A.A., Vitavetskaya, L.A. Analysis of the beryllium-7 activity concentration dynamics in the atmospheric environment time series after the Fukushima Daiichi nuclear power plants emergency. *Sensor Electr. and Microsyst. Techn.* 14, 4 (2017), 73-82.
- [26] Glushkov, A.V., Khetselius, O.Yu., Bunyakova, Yu.Ya., Grushevsky, O.N., Solyanikova, E.P. Studying and forecasting the atmospheric and hydroecological systems dynamics by using chaos theory methods. *Dynamical Systems Theory*, ed. J. Awrejcewicz, M. Kazmierczak, P. Olejnik, J. Mrozowski. Lodz Univ., Łódź. T1 (2013), 249-258.
- [27] Glushkov, A.V., Prepelitsa, G.P., Svinarenko, A.A., Zaichko, P.A. Studying interaction dynamics of the non-linear vibrational systems within non-linear prediction method (application to quantum autogenerators). *Dynamical Systems Theory*, ed. J. Awrejcewicz, M. Kazmierczak, P. Olejnik, J. Mrozowski. Lodz Univ., Łódź. T1 (2013), 467-477.
- [28] Glushkov, A.V., Kuzakon, V., Ternovsky, V., Buyadzhi, V. Dynamics of laser systems with absorbing cell and backward-wave tubes with elements of a chaos. *Dynamical Systems Theory*, ed. J. Awrejcewicz, M. Kazmierczak, P. Olejnik, J. Mrozowski. Lodz Univ., Łódź. T1 (2013), 461-466.
- [29] Glushkov, A.V., Vaschenko, V.N., Gerasimenko, G., and Bunyakova, Yu.Ya. Atmospheric pollutants concentrations temporal dynamics for the industrials ukrainian cities: Low-dimensional chaos. *Dynamical Systems Applications*, ed. J. Awrejcewicz, M. Kazmierczak, P. Olejnik, J. Mrozowski. Lodz Univ., Łódź. T2 (2013), 241-250.
- [30] Khetselius, O.Yu., Brusentseva, S.V., and Tkach, T.B. Studying interaction dynamics of chaotic systems within non-linear prediction method: Application to neurophysiology. *Dynamical Systems Applications*, ed. J. Awrejcewicz, M. Kazmierczak, P. Olejnik, J. Mrozowski. Lodz Univ., Łódź. T2 (2013), 251-259.
- [31] Glushkov, A.V., Buyadzhi, V.V., Kvasikova, A.S., Ignatenko, A.V., Kuznetsova, A.A., Prepelitsa, G.P., and Ternovsky, V.B. Nonlinear chaotic dynamics of Quantum systems: Molecules in an electromagnetic field and laser systems. *Quantum Systems in Physics, Chemistry, and Biology. Series: Progress in Theoretical Chemistry and Physics*, ed. A.Tadger, R.Pavlov, J.Marvani, E.Brändas, G.Delgado-Barrio. Springer, Cham. 30 (2017), 169-180.

- [32] Glushkov A.V., Khetselius O.Yu., Kuzakon V.M., Prepelitsa G.P., Solyanikova E.P., Svinarenko A.A. Modeling of interaction of the non-linear vibrational systems on the basis of temporal series analyses (application to semiconductor quantum generators). *Dynamical Systems - Theory and Applications*. Lodz Univ., Lodz. (2011) BIF110.
- [33] Glushkov, A.V. *Relativistic quantum theory. Quantum mechanics of atomic systems*. Astroprint, Odessa, 2008.
- [34] Khetselius, O.Yu. *Hyperfine structure of atomic spectra*. Astroprint, Odessa, 2008.
- [35] Svinarenko, A.A., Khetselius, O.Yu., Buyadzi, V.V., Florko, T.A., Zaichko, P.A., Ponomarenko, E.L. Spectroscopy of Rydberg atoms in a Black-body radiation field: Relativistic theory of excitation and ionization *J. Phys.: Conf. Ser.* 548,1 (2014), 012048.
- [36] Glushkov, A.V., Ternovsky, V.B., Buyadzi, V.V., Prepelitsa, G.P. Geometry of a Relativistic Quantum Chaos: New approach to dynamics of quantum systems in electromagnetic field and uniformity and charm of a chaos. *Proc. Intern. Geom. Center.* 7,4 (2014), 60-71.
- [37] Buyadzi, V., Glushkov, A., Mansarliysky, V., Ignatenko, A., Svinarenko A. Spectroscopy of atoms in a strong laser field: New method to sensing AC Stark effect, multiphoton resonances parameters and ionization cross-sections. *Sensor Electr. and Microsyst. Techn.* 12, 4 (2015), 27-36.
- [38] Glushkov, A.V., Khetselius, O.Yu., Bunyakova, Yu.Ya., Buyadzi, V.V., Brusentseva, S.V., Zaichko P.A. Sensing interaction dynamics of chaotic systems within a chaos theory and microsystem technology Geomath with application to neurophysiological systems. *Sensor Electr. and Microsyst. Techn.* 11, 3 (2014), 62-69.
- [39] Glushkov, A.V., Mansarliysky, V.F., Khetselius, O.Yu., Ignatenko, A.V., Smirnov, A.V., Prepelitsa, G.P. Collisional shift of hyperfine line for thallium in an atmosphere of the buffer inert gas. *J. Phys.: Conf. Ser.* 810 (2017), 012034.
- [40] Glushkov, A., Buyadzi, V., Ternovsky, V., Geometry of chaos: Consistent combined approach treating of chaotic self-oscillations in backward-wave tube. *Proc. Int. Geom. Center.* 6, 2 (2013), 6-12
- [41] Serbov, N.G., Glushkov, A.V., Bunyakova, Yu.Ya., Prepelitsa, G.P., Svinarenko, A.A. Sensing the kinetical features of energy exchange in mixture CO₂-N₂-H₂O of atmospheric gases under interacting with laser radiation. *Sensor Electr. and Microsyst. Techn.* N4 (2006), 20-22.
- [42] Glushkov, A., Khetselius, O., Ambrosov, S., Bunyakova, Yu., Mansarliysky V. Application of the microsystems technology «Geomath» to modelling balance of the Earth angle moment, atmospheric processes and radiowaveguides: iii. Nonstationary theory. *Sensor Electr. and Microsyst. Techn.* 10,1 (2013), 22-28.
- [43] Glushkov, A., Khetselius, O., Svinarenko, A., Buyadzi, V. *Spectroscopy of autoionization states of heavy atoms and multiply charged ions*. TEC, Odessa, 2015.
- [44] Khetselius, O., Glushkov, A., Dubrovskaya, Yu., Chernyakova, Yu., Ignatenko, A., Serga, I., Vitavetskaya, L., Relativistic quantum chemistry and spectroscopy of exotic atomic systems with accounting for strong interaction effects. *Concepts, Methods and Applications of Quantum Systems in Chemistry and Physics*. Springer, Cham, 31 (2018), 71-91.
- [45] Glushkov, A.V., Khetselius, O.Yu., Svinarenko, A.A., Buyadzi, V.V. *Methods of computational mathematics and mathematical physics. P.I.* TES, Odessa, 2015.
- [46] CALPUFF, Available from: <http://www.src.com/calpuff/calpuff1.htm>

Olga Yu. Khetselius, Professor: Odessa State Environmental University, Pure and Applied Mathematics Department, L'vovskaya str. 15, 65009 Odessa, Ukraine (okhetsel@gmail.com). The author gave a presentation of this paper during one of the conference sessions

Andrey A. Svinarenko, Professor: Odessa State Environmental University, Pure and Applied Mathematics Department, L'vovskaya str. 15, 65009 Odessa, Ukraine (svinarenkoa@gmail.com).

Anna V. Ignatenko, Assoc.-Professor: Odessa State Environmental University, Environment Economics Department, L'vovskaya str. 15, 65009 Odessa, Ukraine (ignatenkoav13@gmail.com)

Anna A. Buyadzhi, M.Sc. (Ph.D. student): Odessa State Environmental University, Pure and Applied Mathematics Department, L'vovskaya str. 15, 65009 Odessa, Ukraine (buyadzhiia@gmail.com).

Nonlinear dynamics of NEMS resonators in temperature field

Anton Krysko, Jan Awrejcewicz, Ilya Kutepov, Vadim Krysko

Abstract: We investigate the nonlinear dynamics of a distributed mechanical system in the form of a flexible curved microbeam described by the kinematic model of the first order approximation (Bernoulli-Euler) in a steady temperature field. Geometric nonlinearity has been introduced according to Kármán's model. The impact of the temperature field is considered according to Duhamel-Neumann. Equations of motion for the flexible Bernoulli-Euler beams are derived from the Hamilton principle, considering the couple stress theory of elasticity. The obtained system of partial differential equations, with regard to displacements motions is reduced to the Cauchy problem by the second-order finite-difference method, which is solved by Runge-Kutta methods of different order. The temperature field is defined from the solution of the steady heat equation using the finite-difference method. Our study is dedicated to the reliable definition of the oscillatory mode of a system using a variety of signal analysis methods, such as Fourier power spectrum, wavelet analysis, analysis of the phase portrait, and Poincaré maps. Analysis of the longitudinal motions allowed establishing a complex oscillatory mode with a harmonic buckling signal. To define the chaotic state, a spectrum of Lyapunov exponents was investigated. In order to check the reliability of the obtained sign of the Lyapunov exponent a few different methods have been used. As a result of the study of nonlinear dynamics of NEMS resonators under the influence of the temperature field, depending on the control parameters, reliable information has been obtained about the mode of oscillation of the system and maps of oscillatory modes have been constructed. The buckling shapes of structures are also investigated.

1. Introduction

The study of nonlinear dynamic processes in micro- and nano-mechanical devices has been a subject of numerous investigations [1–10]. Wang et al. [11] have studied a theoretical analysis and experimental results of the dynamic behavior of the bi-stable resonator of the micro-electro-mechanical system (MEMS) and have shown the existence of a strange attractor and chaos. De Martini [12], Haghighi and Markazi [13], Aghababa [14] used the modified Mathieu equation to simulate the governing equation of motion of the MEMS and used the Melnikov method, describing the region of parameter space where chaos exists. They showed the presence of chaotic behavior in MEMS.

The works [15–16] are dedicated to the study of nonlinear dynamic effects in micromechanical beams, considering temperature effects and initial irregularities. The authors found that the presence of temperature effects leads to loss of stability and investigated resonance phenomena in the system after the loss of stability. The temperature field was taken as a constant value at each point of the beam.

Ebrahimi and Salari [17] developed a consistent non-local microbeam model to analyze longitudinal and free oscillations of functionally gradient nanobeams, within which thermal effects were studied. The authors considered the effect of the temperature field in the linear and nonlinear formulation by obtaining a solution from the one-dimensional heat conduction equation. Reactions to buckling and free vibrations of microbeams with increasing temperature were studied by Nateghi and Salamat-talab [18] using a modified couple stress theory of elasticity. Multiple results showed that the effect of temperature becomes more significant at higher ratios of the thickness of the beam to the parameter of the scale length of the material. In the articles [19-23], application of the finite-element method (FEM), the finite-difference method (FDM) to the problems of modeling vibratory gyroscopes was considered.

When studying the nonlinear dynamics of mechanical structures, it is important to study chaos and stability of the system, which stands for the scope of the article [24], in which one-dimensional mathematical models of beams, panels of infinite length and shells are constructed considering geometric, and constructive kinematic nonlinearity, and various combinations of these nonlinearities. Many problems were solved by various methods: finite differences, Bubnov-Galerkin, Rayleigh-Ritz, etc. Similar to the phenomenon of the universality of the emergence of chaos in simple systems, the existence of a certain universality of the transition to turbulence in the spatial problems of the theory of one-dimensional mechanical structures is shown. However, the book does not consider size-dependent parameters and influence of temperature fields.

Haghighi and Markazi [25] investigated chaotic dynamics of a micromechanical resonator influenced by electrostatic forces. The authors analyzed the phase portrait, Poincaré sections and bifurcation diagrams confirming the analytical forecast and showing the influence of the amplitude of external force on the transition of the system into chaos. Ghayesh and Farokhi [26] analyzed complex dynamic behavior of the system using the construction of fast Fourier transforms (FFT), Poincaré sections, and phase plane diagrams. According to Gulick's [27] definition of chaos, the latter significantly depends on the initial conditions and the sign of the spectrum of the Lyapunov exponents. These initial conditions include temperature effects, which lead the system to a fundamentally new oscillation type, especially at the nano-level. This inquiry has not been previously considered. A review [28] presents a number of papers dedicated to MEMS, however, the question of

studying the chaotic dynamics and stability of curved beam elements of MEMS under the influence of an external load and a temperature field was not considered.

The scope of application of beam MEMS elements is rather wide. These structures are desired for various applications, such as microdrives, microswitches, biosensors, vibration sensors and biomechanical devices. For this reason, the study of sustainability [29] and dynamic behavior [30] of such structures is of particular interest. A relatively new element of MEMS is the arched beam structures, which belong to bistable structures. Bistable structures are required for various applications such as micro-generators, filters, relays, switches, valves, actuators, memory cells and logic. Ramini et al. [31] demonstrated experimentally an efficient approach to excite primary and parametric (up to the 4th) resonance of MEMS arch resonators with large vibrational amplitudes. The authors have shown the possibility of controlling primary and/or parametric resonances, which can be used in various applications, such as resonator logic and storage devices. Hafiz et al. [32] demonstrated the switching between the two vibrational states with the change of the direct current (DC) bias voltage, thereby proving the memory concept. Experimental confirmation of the need to take into account the initial errors of the element curvature was demonstrated by Ramini et al. [33]. The authors noted that if the intentional curvature is not quite as expected after manufacturing, the thermal setting can adjust the curvature as needed. Thus, the study of nonlinear dynamics of curvilinear microbeams in the temperature range is a new and actual task.

Analysis of publications within our subject has revealed that studies of the thermo-mechanical dynamic behavior of microstructures are not sufficiently elaborated. The present study proposes a solution to the following new problem of nonlinear dynamics of micromechanical structures: as the temperature increases, the curved microbeam buckles (deviates to the new state), acquiring a different initial irregularity. The temperature field is proposed to solve the two-dimensional heat equation. The article validates the “truth” of the oscillatory mode definition by applying various methods of the qualitative theory of differential equations and methods for defining the Lyapunov exponents. We have included influence of longitudinal motions to study the nature of oscillations. In addition to the critical states, scenarios of transition from periodic to chaotic oscillations are analyzed.

2. Mathematical model

The beam (Fig. 1) is a curved body, having length L , and height h ; beam section is rectangular with width b and area A , and curvature $k_x = 1/R_x$. Beam with the boundary Γ , occupies the region $\Omega = \{0 < x < L; -h/2 < z < h/2\}$.

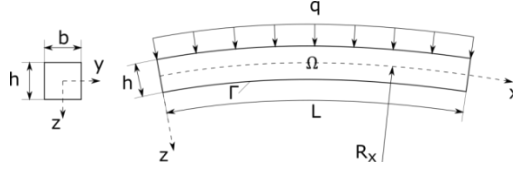


Figure 1. Investigated beam

The mathematical model of the beam is based on the following hypotheses: any cross-section normal to the center line before deformation, remains straight and normal to the center line after the deformation and the section height doesn't change; Kármán's form of nonlinear deformation-motion ratio is used; flatness condition is assumed according to Vlasov [34]; beam material is elastic and isotropic and is subjected to Duhamel-Neumann law; thermal expansion is temperature-independent; physical properties of the material are temperature-independent; there is no temperature field distribution restriction across the thickness of the beam; the propagation velocity of the longitudinal wave in the beam is considered. the motion of continuum points depends on their rigid rotation (Cosserat elasticity).

The equations of motion of the beam, the boundary and initial conditions are obtained from the Hamilton principle. After the transformations, we obtain the resolving motion equations as follows:

$$\begin{aligned} \frac{\partial^2 u}{\partial x^2} - k_x \frac{\partial w}{\partial x} + L_3(w, w) - \frac{\partial N_t}{\partial x} - \frac{\partial^2 u}{\partial t^2} &= 0 \\ \frac{1}{\lambda^2} \left\{ \left(-\frac{1}{12} + \frac{l^2}{4} \right) \frac{\partial^4 w}{\partial x^4} + k_x \left[\frac{\partial u}{\partial x} - k_x w - \frac{1}{2} \left(\frac{\partial w}{\partial x} \right)^2 - w \frac{\partial^2 w}{\partial x^2} \right] + L_1(u, w) + L_2(w, w) \right\} - \frac{\partial^2 M_t}{\partial x^2} - \\ - k_x N_t - \frac{\partial}{\partial x} \left\{ N_t \frac{\partial w}{\partial x} \right\} + q - \frac{\partial^2 w}{\partial t^2} - \varepsilon \frac{\partial w}{\partial t} &= 0, \end{aligned} \quad (3)$$

where: $L_1(u, w) = \frac{\partial^2 u}{\partial x^2} \frac{\partial w}{\partial x} + \frac{\partial u}{\partial x} \frac{\partial^2 w}{\partial x^2}$, $L_2(w, w) = \frac{3}{2} \left(\frac{\partial w}{\partial x} \right)^2 \frac{\partial^2 w}{\partial x^2}$, and $L_3(w, w) = \frac{\partial w}{\partial x} \frac{\partial^2 w}{\partial x^2}$ are nonlinear operators; $w(x, t)w(x, t)$ express element buckling; ε is dissipation factor; h is the beam height; L is beam length; $u(x, t)u(x, t)$ is longitudinal shift of the element; M_x^T is temperature beam bending moment; N_x^T is temperature longitudinal force; t is time; ϑ is volumetric weight of the material; g is gravity acceleration; ρ is density; q is external load.

In case with no temperature and assuming $k_x = 0$, equation (3) is the same as obtained in reference [35].

For the set of equations (3), the following non-dimensional parameters are introduced:

$$\begin{aligned} \bar{w} &= \frac{w}{h}, \quad \bar{u} = \frac{uL}{h^2}, \quad \bar{x} = \frac{x}{L}, \quad \bar{z} = \frac{z}{h}, \quad \bar{q} = q \frac{L^4}{h^4 E}, \quad c = \sqrt{\frac{Eg}{\rho}}, \quad \bar{\varepsilon} = \frac{\varepsilon L}{c}, \quad \bar{t} = \frac{t}{\tau}, \quad \tau = \frac{L}{c}, \quad \lambda = \frac{L}{h}, \\ \gamma &= \frac{l}{h}, \quad \bar{k}_x = \frac{k_x L^2}{h}, \quad \bar{N}_x^T = \frac{N_x^T L^2}{E h^3}, \quad \bar{M}_x^T = \frac{M_x^T}{E h^2}, \quad \bar{T} = \alpha T. \end{aligned} \quad (4)$$

In case when the external transverse load is dynamic, the expression for q is written as $q = q_0 \sin(\omega_p t)$, where q_0 is amplitude of the load and ω_p stands for its frequency. Temperature moments M_x^T and forces N_x^T in the beam motion equation set (3) are defined in the following way

$$N_x^T = \int_{-1/2}^{1/2} T(x, z) dz; \quad M_x^T = \int_{-1/2}^{1/2} T(x, z) z dz. \quad (5)$$

As mentioned above, there is no restriction on the distribution of the temperature field, and the temperature fields are defined by solving the following heat problem:

$$\nabla^2 T(x, z) = \frac{\partial^2 T(x, z)}{\partial x^2} + \lambda^2 \frac{\partial^2 T(x, z)}{\partial z^2} = 0, \quad (6)$$

with the supplemented boundary conditions of the first/second kind

$$T(x, z)|_{\Gamma} = g_1(x, z), \quad (7)$$

$$\left. \frac{\partial T(x, z)}{\partial n} \right|_{\Gamma} = g_2(x, z), \quad (8)$$

where $\frac{\partial}{\partial n}$ is differentiation along the outer normal to the boundary Γ of the beam.

The set of equations (3) should be combined with the boundary conditions equation corresponding to the way of fixing the beam ends:

$$w(0, t) = u(0, t) = w'_x(0, t) = 0, \quad w(1, t) = u(1, t) = w'_x(1, t) = 0, \quad (9)$$

$$w(0, t) = u(0, t) = M_x(0, t) = 0, \quad w(1, t) = u(1, t) = M_x(1, t) = 0. \quad (10)$$

The following initial conditions are employed

$$w(x, 0) = f_1(x); \quad \dot{w}(x, 0) = f_2(x); \quad u(x, 0) = f_3(x); \quad \dot{u}(x, 0) = f_4(x). \quad (11)$$

Table 1. Boundary condition of the heat-transfer equations

Kind	Boundary Condition		
Kind 1	$T(x, z) = g_1(x, z)$	$z = -1/2$	$0 < x < 1$
	$T(x, z) = 0$	$z = 1/2$	$0 < x < 1$
	$T(x, z) = 0$	$x = 1$	$-1/2 < z < 1/2$
	$T(x, z) = 0$	$x = 0$	$-1/2 < z < 1/2$
Kind 2	$T(x, z) = g_1(x, z)$	$z = -1/2$	$0 < x < 1$
	$\partial T / \partial n = g_2(x, z)$	$z = 1/2$	$0 < x < 1$
	$T(x, z) = 0$	$x = 1$	$-1/2 < z < 1/2$
	$T(x, z) = 0$	$x = 0$	$-1/2 < z < 1/2$

The combination of temperature conditions (7) - (8) at the beam boundaries Γ allows considering various cases of temperature exposure. In this article, we simulate a temperature field of the first type,

by the boundary conditions given in Table 1 (a graphic interpretation of the temperature field is also provided herein). The intensity of this temperature effect T varies within $0 \leq T \leq 100^\circ C$. Hereinafter, the temperature T is expressed in dimensional form for steel and it is assumed that, in the investigated temperature range, physical characteristics of the material do not change. To go to the dimensional values of temperature, the following values are used : $E = 2.06 \times 10^5$ mPa, $\alpha = 12.5 \times 10^{-6}$ 1/deg, while temperature is $T = \Delta T + T_0$, where $T_0 = 22^\circ C$, and ΔT is an increment of $T(x, z)$ to be defined from the heat conductivity equation (6).

3. Results of numerical investigations

In order to solve the resulting set of equations (3), we used the finite difference method (FDM) - see [36] for more details.

The following parameters of system (3) are assumed to be fixed: frequency $\omega_p = 5$, curvature $k_x = 24$, the intensity of thermal exposure $g_1(x, z) = 50$, boundary conditions (9), initial conditions (11). The Figure 3 presents a buckling diagram in the beam center for the mentioned parameters. To investigate the state of the system, we analyzed the Fourier power spectra (Tables 4,5,6). For additional analysis of the state of the system, Lyapunov's criterion was applied. Using the general formulation of the problem of stability of the motion of a system according to Lyapunov, the state of the system is considered unstable if the largest Lyapunov exponent (LLE) is positive.

Let us consider the scenario of transition to a chaotic state with $\gamma = 0$ (Table 2). The harmonic mode is observed in the range of load variations from $q_0 = 0$ to $q_0 = 14000$ ($LLE = -0.00389$), afterwards, with the load of $q_0 = 14130$ an independent frequency ω_1 ($LLE = -0.00336$) appears. With a further load increase up to $q_0 = 14500$, ω_2 frequency and two dependent frequencies $\omega_4 = \omega_p - \omega_1$ and $\omega_5 = \omega_p - \omega_2$ ($LLE = -0.01279$) appear. When $q_0 = 21000$ the third frequency ω_3 and three dependent frequencies $\omega_4 = \omega_p - \omega_1$, $\omega_5 = \omega_p - \omega_2$ and $\omega_6 = \omega_p - \omega_3$ appear in the power spectrum. The detected dependence is typical for Ruelle-Takens scenario. In the load change interval from $q_0 = 31000$ to $q_0 = 33000$, there is a periodicity window, however, the Lyapunov exponent has a positive sign ($LLE = 0.00552$), and hence, the beam oscillation is considered as chaotic. Further, for $q_0 = 33000$, six frequencies ω_{1-6} having the similar ratio are observed. When $q_0 = 34000$, a new frequency $\omega_7 = \omega_p/2$ appears in the frequency spectrum. In further range, from $q_0 = 34500$ to $q_0 = 36000$, only such frequencies as ω_p and ω_7 ($LLE = 0.00796$) are exhibited. Up to the $q_0 = 36440$ value, frequency count increases through the period doubling, and the latter phenomenon is characteristic for the Feigenbaum scenario. Further increase of the load up to q_0 makes frequency ω_7 to disappear, the frequency count increases according to Ruelle-Takens. When $q_0 \geq 37000$, many frequencies supplement occurrence of the chaotic mode ($LLE = 0.00842$). Thus,

the transition from periodic to chaotic state is carried out according to the modified Ruelle-Takens scenario throughout a series of appearances of linearly dependent frequencies.

Table 2. Power spectra of the beams dynamics for $\gamma = 0$

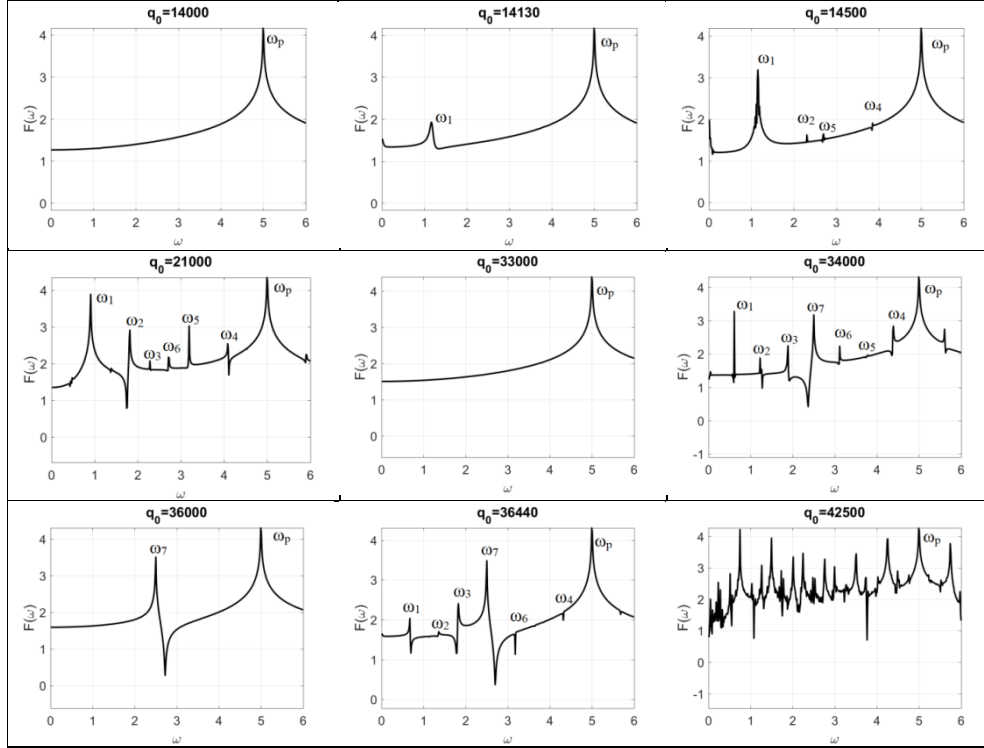
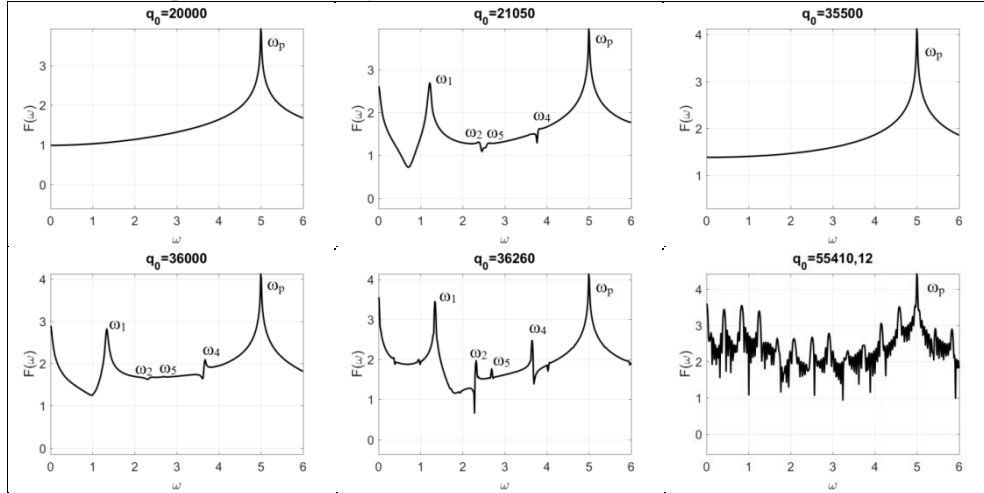


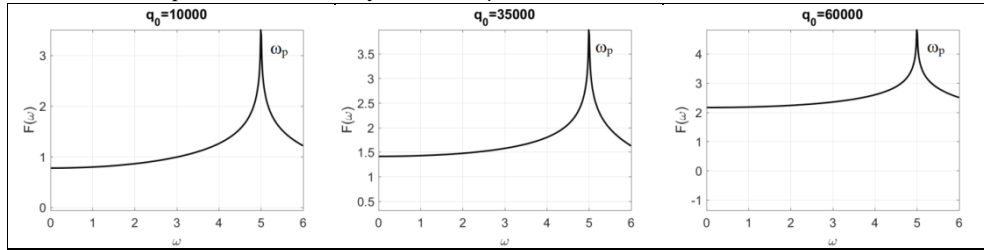
Table 3. Power spectra of the beam dynamics for $\gamma = 0.3$



Let us consider now the scenario of transition into a chaotic state with $\gamma = 0.3$ (Table 3). With the load of $q_0 = 20000$ the system is in the harmonic mode, and oscillations occur at a frequency ω_p ($LLE = -0.01370$). With $q_0 = 21000$, a second frequency ω_1 ($LLE = -0.01248$) appears. Further increase in load leads to the appearance of frequency ω_2 and two dependent frequencies: $\omega_4 = \omega_p - \omega_1$ and $\omega_5 = \omega_p - \omega_2$. Within the range from $q_0 = 24500$ to $q_0 = 35500$, the system is in a harmonic state according to the Fourier power spectrum. Further, frequencies appear in the same order. With $q_0 = 36260$ the power of these frequencies increases ($LLE = 0.13601$), and with $q_0 = 40500$ the spectrum shows multiple frequencies ($LLE = 0.00743$). Further increase of the load to $q_0 = 55410.12$ causes more frequencies to appear, implying chaotic oscillatory mode ($LLE = 0.00932$). The transition from periodic to chaotic dynamics follows occurs the Ruelle-Takens scenario.

Let us consider a scenario of transition into a chaotic state for $\gamma = 0.5$ (Table 4). In the range from $q_0 = 0$ to $q_0 = 60000$, according to the Fourier power spectrum, the system exhibits periodic oscillations. The sign of the Lyapunov exponent changes from negative to positive when the load value is $q_0 = 35000$.

Table 4. Power spectra of the beam dynamics for $\gamma = 0.5$



In the periodicity windows, with $q_0 = 33000$ for $\gamma = 0$, $q_0 = 35500$ for $\gamma = 0.3$ and $q_0 = 35000$ for $\gamma = 0.5$ we observed a harmonic signal $w(0.5, t)$ according to the Fourier power spectrum and the non-harmonic state according to analysis of the largest Lyapunov exponent (LLE). Let us analyze the signal of the longitudinal motion in the quarter of the span of the beam $u(0.25, t)$, Fourier power spectrum is computed for specified values of q_0 and γ . As it can be seen from the figures in the Table 5, the signals for $u(0.25, t)$ are not harmonic, since frequencies on the power spectrum and wavelet appear, as well as complex phase trajectories are shown.

The shape of the beam buckling was investigated with the following system parameters: temperature field of kind 2 (Table 1), $g_1(x, z) = 50$, $g_1(x, z) = -50$, and $g_1(x, z) = 0, k_x = 24$, $q_0 = 30 \times 10^3$, $\omega_p = 5$, with boundary conditions (10) and initial conditions (11). Figure 2 shows the beam deflection $w(x, t)$ for $\gamma = 0$, $\gamma = 0.3$ and $\gamma = 0.5$. It is found that symmetric buckling

shapes are present with a value of the scale parameter $\gamma = 0$, while they are asymmetric with $\gamma = 0.3$ and $\gamma = 0.5$.

Table 5. Time histories and frequency spectra of the beam dynamics of different γ .

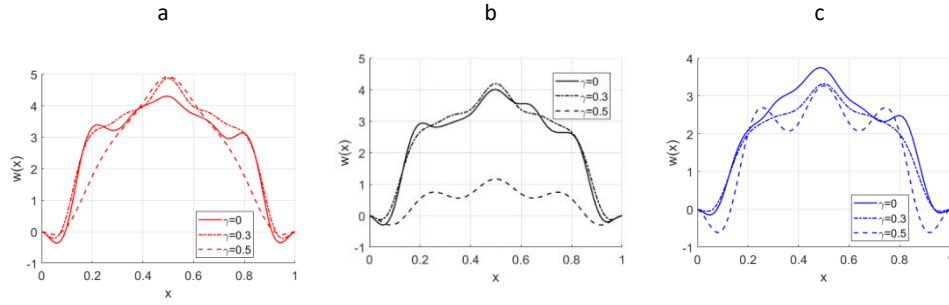
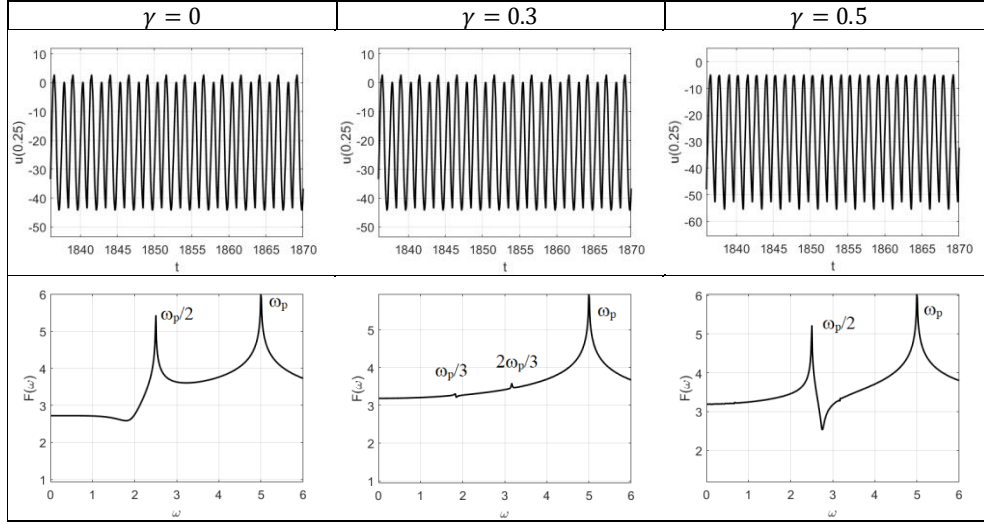


Figure 2. Snapshots of the beam buckling for different γ : a) $g_1(x, z) = 50$, b) $g_1(x, z) = 0$, c) $g_1(x, z) = -50$

In order to study the state of the system in the range of control parameter values $q_0 \in [0; 60 \times 10^3]$ and $\omega_p \in [0; 10]$, a software complex was developed to study the modes of oscillations of a nanobeam based on a heuristic analysis of the Fourier power spectrum. The result of its operation is an image representing a map of oscillatory modes depending on the values of the frequency ω_p and external load amplitude q_0 . Each map has a resolution of 200×200 pixels, that corresponds to 4×10^4 solved and analyzed problems for each parameter.

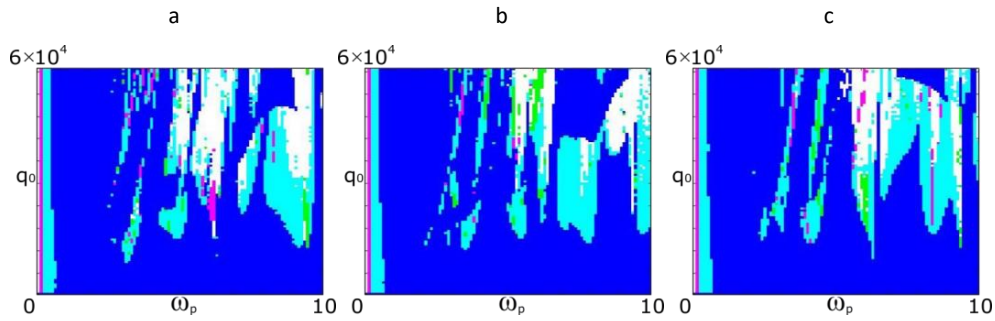


Figure 3. Oscillatory beam mode maps for $k_x = 24$ and different γ : a) $\gamma = 0$, b) $\gamma = 0.3$, c) $\gamma = 0.5$

For $k_x = 24$ (Figure 3), there is an increase of the zone of periodic oscillations in the medium frequency range. Increasing γ parameter implies an increase of the oscillation zone at dependent frequencies in the region of medium and high frequencies. For $k_x = 24$, the map with the maximum harmonic oscillation zone is obtained for $\gamma = 0.3$. It was revealed that with increasing γ , chaotic zone decreases for $k_x = 24$ from 12.27% down to 4.74%. Increasing the curvature k_x from 12 to 36 causes the increase of the chaos zone in the investigated ranges of control parameters. Zone of harmonic oscillations at $k_x = 24$ increases from 64.14% to 67.38%.

4. Concluding remarks

Consideration of the scale parameter length causes a change in the scenario of the system transfer into chaotic state. Reliable estimation of system state requires the introduction of an additional method, such as Lyapunov exponent analysis. Increasing the value of the scale parameter of length contributes to the preservation of the harmonic mode across a longer interval of external load.

All the motion components shall be analyzed to define the system state. For $\gamma = 0$ asymmetric buckling shape is present at the subcritical load, while for $\gamma = 0.3$ and $\gamma = 0.5$ it is detected at the supercritical load.

Acknowledgments

This work was supported by the Russian Science Foundation, № 16-11-10138-II.

References

- [1] Farokhi, H., Ghayesh, M. H., & Amabili, M. (2013). Nonlinear dynamics of a geometrically imperfect microbeam based on the modified couple stress theory. *International Journal of Engineering Science*, 68, 11-23.
- [2] Ke, L. L., & Wang, Y. S. (2011). Size effect on dynamic stability of functionally graded microbeams based on a modified couple stress theory. *Composite Structures*, 93(2), 342-350.

- [3] Buks E. and Roukes M.L. (2001) Metastability and the Casimir effect in micromechanical systems. *Europhys. Lett.*, 54, 220.
- [4] Ke, L. L., Wang, Y. S., Yang, J., & Kitipornchai, S. (2012). Nonlinear free vibration of size-dependent functionally graded microbeams. *International Journal of Engineering Science*, 50(1), 256-267.
- [5] Shafiei, N., Mousavi, A., & Ghadiri, M. (2016). On size-dependent nonlinear vibration of porous and imperfect functionally graded tapered microbeams. *International Journal of Engineering Science*, 106, 42-56.
- [6] Ghayesh, M. H. (2018). Dynamics of functionally graded viscoelastic microbeams. *International Journal of Engineering Science*, 124, 115-131.
- [7] Şimşek, M. (2016). Nonlinear free vibration of a functionally graded nanobeam using nonlocal strain gradient theory and a novel Hamiltonian approach. *International Journal of Engineering Science*, 105, 12-27.
- [8] Shafiei, N., & Kazemi, M. (2017). Nonlinear buckling of functionally graded nano-/micro-scaled porous beams. *Composite Structures*, 178, 483-492.
- [9] Li, L., Han, J., Zhang, Q., & Liu, C. (2018). Stochastic dynamic behavior of electrostatically actuated clamped-clamped microbeams with consideration of thermal field. *International Journal of Non-Linear Mechanics*, 105, 192-199.
- [10] Talimian, A., & Béda, P. (2018). Dynamic stability of a size-dependent microbeam. *European Journal of Mechanics-A/Solids*, 72, 245-251.
- [11] Wang Y.C. et al. Chaos in MEMS, parameter estimation and its potential application. *IEEE transactions on circuits and systems*. 1. *Fundam Theory Appl* 1998;45(10):1013–20.
- [12] De Martini B.E. et al. Chaos for a microelectromechanical oscillator governed by the nonlinear Mathieu equation. *J Microelectromech Syst* 2007;16(6):1314–23.
- [13] 23. Haghighi H.S., Markazi A.H. Chaos prediction and control in MEMS resonators. *Commun Nonlinear Sci Numer Simul* 2010;15(10) : 3091–9.
- [14] Aghababa M.P. Chaos in a fractional-order micro-electro-mechanical resonator and its suppression. *Chin Phys B* 2012;21(10): 100505
- [15] Farokhi, H., & Ghayesh, M. H. (2015). Thermo-mechanical dynamics of perfect and imperfect Timoshenko microbeams. *International Journal of Engineering Science*, 91, 12-33.
- [16] Farokhi, H., & Ghayesh, M. H. (2017). Nonlinear thermo-mechanical behaviour of MEMS resonators. *Microsystem Technologies*, 23(12), 5303-5315.
- [17] Ebrahimi, F., & Salari, E. (2016). Effect of various thermal loadings on buckling and vibrational characteristics of nonlocal temperature-dependent functionally graded nanobeams. *Mechanics of Advanced Materials and Structures*, 23(12), 1379-1397.
- [18] Nateghi, A., & Salamat-talab, M. (2013). Thermal effect on size dependent behavior of functionally graded microbeams based on modified couple stress theory. *Composite Structures*, 96, 97-110.
- [19] Li G., Aluru N.R. Linear, nonlinear and mixed-regime analysis of electrostatic MEMS. *Sensor Actuator A-Phys.* 2001, 91, 278-291.
- [20] Zhang W.M., Meng G. Nonlinear dynamical system of micro-cantilever under combined parametric and forcing excitations in MEMS. *Sensor Actuator A-Phys.* 2005, 119, 291-299. *Sensors* 2010, 10 6168
- [21] Adams S.G., Bertsch F.M., Shaw K.A., MacDonald N.C. Independent tuning of linear and nonlinear stiffness coefficients [actuators]. *J. Microelectromech. Syst.* 1998, 7, 172-180.

- [22] Zhang W.H., Baskaran R., Tumer K.L. Effect of cubic nonlinearity on auto-parametrically amplified resonant MEMS mass sensor. *Sensor Actuator A-Phys.* 2002, 102, 139-150.
- [23] Lee S., Kim J., Moon W., Choi J., Park I., Bae D. A multibody-based dynamic simulation method for electrostatic actuators. *Nonlinear Dyn.* 2008, 54, 53-68.
- [24] Awrejcewicz J., Krysko V.A., Papkova I.V., Krysko A.V. *Deterministic Chaos in One-Dimensional Continuous Systems*. – Singapur, World Scientific series on Nonlinear Science Series, 2016. – 561 p.
- [25] Haghighi, H. S., & Markazi, A. H. (2010). Chaos prediction and control in MEMS resonators. *Communications in Nonlinear Science and Numerical Simulation*, 15(10), 3091-3099.
- [26] Ghayesh, M. H., & Farokhi, H. (2015). Chaotic motion of a parametrically excited microbeam. *International Journal of Engineering Science*, 96, 34-45.
- [27] Gulick, D. (1992). *Encounters with chaos*. McGraw-Hill.
- [28] Thai, H-T., Vo, T.P., Nguyen, T-K., Kim, S-E., A review of continuum mechanics models for size-dependent analysis of beams and plates, *Composite Structures* (2017), doi: <http://dx.doi.org/10.1016/j.compstruct.2017.06.040>
- [29] Ghayesh, Mergen H., Hamed Farokhi, and Gursel Alici. "Subcritical parametric dynamics of microbeams." *International Journal of Engineering Science* 95 (2015): 36-48.
- [30] Li, Zhenkun, et al. "Experimental investigation and theoretical modelling on nonlinear dynamics of cantilevered microbeams." *European Journal of Mechanics-A/Solids* 78 (2019): 103834.
- [31] Ramini, Abdallah, et al. "Efficient primary and parametric resonance excitation of bistable resonators." *AIP Advances* 6.9 (2016): 095307.
- [32] Hafiz, Md, et al. "In-plane MEMS shallow arch beam for mechanical memory." *Micromachines* 7.10 (2016): 191.
- [33] Ramini, Abdallah H., Amal Z. Hajjaj, and Mohammad I. Younis. "Tunable resonators for nonlinear modal interactions." *Scientific reports* 6 (2016): 34717.
- [34] Vlasov, V. Z., *General Theory for Shells and its Application in Engineering*, 1949, Gostekhizdat Publ. Moscow. (translated into English in NACA Technical Translation, 1964)
- [35] A.V. Krysko, J. Awrejcewicz, M.V. Zhigalov, S.P. Pavlov, V.A. Krysko Nonlinear behaviour of different flexible size-dependent beams models based on the modified couple stress theory. Part 1. Governing equations and static analysis of flexible beams, *International Journal of Non-Linear Mechanics*, 93, 2017, 96-105.
- [36] Krysko, V. A., Awrejcewicz, J., Kutepov, I. E., Babenkova, T. V., & Krysko, A. V. (2019). Size-dependent non-linear dynamics of curvilinear flexible beams in a temperature field. *Applied Mathematical Modelling*, 67, 283-296.

Anton Krysko, Professor: Applied Mathematics and Systems Analysis, Yuri Gagarin State Technical University of Saratov, Politehnicheskaya 77, 410054 Saratov, Russian Federation (anton.krysko@gmail.com).

Jan Awrejcewicz, Professor: Lodz University of Technology, Faculty of Mechanical Engineering, Department of Automation, Biomechanics and Mechatronics, 1/15 Stefanowskiego Str., 90-924 Lodz, Poland (jan.awrejcewicz@p.lodz.pl);

Ilya Kutepov: Department of Mathematics and Modeling, Saratov State Technical University, Politehnikhskaya 77, 410054, Saratov, Russian Federation, (iekutepov@gmail.com)

Vadim Krysko: Department of Mathematics and Modeling, Saratov State Technical University, Politehnikhskaya 77, 410054, Saratov, Russian Federation, (tak@san.ru)

Dimension reduction method in nonlinear equations of mathematical physics (MEMS/NEMS problems)

Vadim A. Krysko-jr, Jan Awrejcewicz, Maxim V. Zhigalov, Vadim. A. Krysko

Abstract To simulate the static and dynamic behavior of nanoplates, higher-order continuum theories have been developed: modified couple stress theory of elasticity, nonlocal theory of elasticity, gradient theory of elasticity, and surface elasticity theory. It should be noted that when using these theories, the equations describing the behavior of the plates have a high order, and the desired functions depend on two or more variables. In this regard, there is a need to create methods that can reduce the dimension of the desired functions, i.e. reduce the solution of the partial differential equation to the solution of an ordinary differential equation. The paper provides an overview of methods for reducing partial differential equations to ordinary differential equations based on the Kantorovich-Vlasov method. One such method is the variational iteration method. MVI was widely used by many researchers in solving problems of the theory of shells and plates. The authors of this work, since the 70s of the last century, has been used this method to solve geometrically, physically nonlinear and contact problems of the theory of plates and shells for full-size systems. In a number of their works, the authors provided a justification of this method for a class of equations described by positive definite operators. In the presented paper, MVI is used in plate nanomechanics problems and a proof of MVI convergence for the problems under consideration is given. A numerical example is also added.

1. Introduction

A number of computational methods aimed to solve the most diverse problems of mathematical physics and technology are based on the ideas of Russian scientists I.G. Bubnov and B.G. Galerkin. To date, the Bubnov-Galerkin methods have been applied in solving numerous problems of structural mechanics, structural dynamics, hydromechanics, hydromechanical stability theory, magneto hydrodynamics, heat and mass transfer theory, acoustics, microwave propagation theory, neuron transfer theory, etc. Using the Bubnov - Galerkin approach, ordinary differential equations, partial differential equations, and integral equations were studied. The application of the Bubnov-Galerkin method is connected, among other things, with the search for stationary points of some functional, which is a certain integral of the differential expressions generated by the original problem, which makes it possible to decrease the order of differential operators in the integrand.

The origin of the Bubnov-Galerkin method is usually associated with the name of the outstanding Russian scientist Ivan G. Bubnov (1872 - 1919). Together with A.N. Krylov, he was the creator of the Russian Navy. S.P. Timoshenko in a paper published in 1907 [1] using the example of a central compressed rod considered the stability problem based on minimizing the potential energy of the rod.

This work was sent for feedback to professors N.A. Belevyubsky, S.I. Beletsky, I.G. Bubnov, V.L. Kirpichev and G.V. Kolosov, which were published in 1913 in the "Collection of the Institute of Railway Engineers" [2]. This date is considered the date of the official birth of the Bubnov method, as a general method for solving differential equations. I.G. Bubnov gave two options for solving the problem of reducing partial differential equations (or their systems), i.e. either to algebraic equations (or their systems), or to an ordinary differential equation (or their systems).

In Western literature, this method is associated with the B.G. Galerkin's article [3] published in 1915. The article was devoted to the elastic equilibrium of rods and thin plates. But the above analysis of publications devoted to this method suggests that I.G. Bubnov as a true genius proposed an idea that occurred to him when he was working on a review of S.P. Timoshenko paper. In this review, he already established the identity between the energy method (called the Rayleigh – Ritz – Timoshenko method) and his approach (called the Bubnov – Galerkin method). I.G. Bubnov subsequently used this approach extremely little. This method is well known in the scientific literature due to the works of B.G. Galerkin and his colleagues.

Applying the Bubnov – Galerkin methodology in one of the variables, if the desired function depends on two variables, we arrive at the solution of the ordinary differential equation in the other variable, accordingly, to the Kantorovich – Vlasov method [4, 5]. Such a procedure linked these two

distinguished names, and the method they developed became known as the Kantorovich-Vlasov method (MKV). This method, by its ideology, couples the Fourier method (MF) based on the separation of variables, and the Bubnov-Galerkin method (MBG), which gave impetus to a number of modifications (Fig. 1). Modifications are based on the Weindiner method (MV), the variational iteration method (MVI), the Agranovsky – Baglai – Smirnov method (MABS), and their

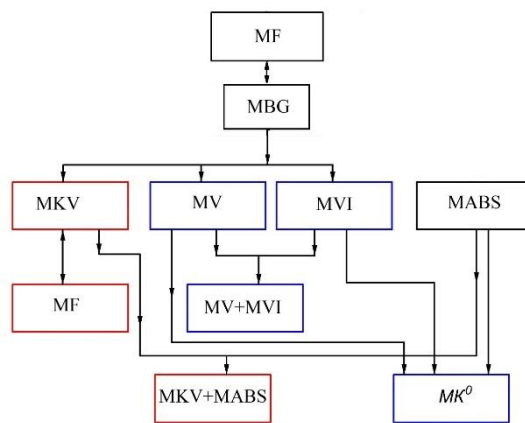


Fig. 1. Interrelation of Bubnov-Galerkin method, Fourier method, the method of Kantorovich-Vlasov and their modifications

combinations are described in a number of papers by the authors of this work [6–8]. These articles provide evidence of convergence and a comparative analysis of the results of these methods.

One of the methods included in the scheme is the variational iterations method (MVI), which saves the researcher from the need to build a system of approximating functions in the procedure while employing the Bubnov-Galerkin method. The functions initially specified in an arbitrary way (obviously satisfying certain well-known smoothness conditions) are refined in the process of calculations by MVI based on the solutions of the original system of differential equations.

This method was first proposed and applied in 1933 by T.E. Shunk [9] for calculating the bending of cylindrical panels. However, the work went unnoticed, and the method was rediscovered again in 1964 by E.E. Zhukov [10], who applied it in calculating thin rectangular plates. Later MVI was widely used by many researchers in solving problems of the theory of shells and plates (a bibliography on this subject is presented in [11]). The justification of this method for the class of equations described by positive definite operators is given in reference [12].

It should be noted the discrepancy in the names. In the Western scientific literature, the variational iterations method is called the extended Kantorovich method thanks to the work of A.D. Kerr [13–15] published 38 years after T.E. Shunk and 5 years after E.E. Zhukov. Thus, the method was reopened.

The variational iterations method (extended Kantorovich method) over the past half century has been used to solve problems of statics, stability, determination of natural frequencies and dynamics. A fairly complete review of Western publications in this area can be found in [16, 17]. In the USSR and Russia, this method was mainly used in the works of V.A. Krysko and his students. For the first time, this scientific group used the approach in 1968 to study the bending of flexible orthotropic plates [18], and it got its name from the variational iterations method in 1970 [19], devoted to the numerical study of flexible plates and comparison with experimental data. Later, scientists of this group used the variational iterations method to solve geometrically and physically nonlinear problems in the theory of shells and plates [20,21], in problems of designing optimal plates [22–24], and on other topics [25–27].

In this paper, the variational iterations method is extended to the study of the static bending of Kirchhoff-Love nano-shells taking into account Kármán geometric nonlinearity and based on a modified couple stress theory.

2. Mathematical background

Let us consider a shallow rectangular shell with dimensions a, b, h along axes x_1, x_2, x_3 , respectively. For a spherical shell, the internal radius, expressed in the shell thickness, can be easily determined with a formula $f = k_1/8$, where k_1 stands for the shell curvature parameter [28].

The origin of the coordinate system is located in the upper left corner of the shell on its middle surface. The axes x_1, x_2 are parallel to the shell sides and the axis x_3 is directed towards the shell curvature (Fig. 2). In the given coordinate system, the shell is treated as a 3D region Ω defined by $\Omega = \{x_1, x_2, x_3 / (x_1, x_2, x_3) \in [0, a] \times [0, b] \times [-h/2, h/2]\}$. The shell middle surface $x_3 = 0$ is defined as $\Gamma = \{x_1, x_2 / (x_1, x_2) \in [0, a] \times [0, b]\}$.

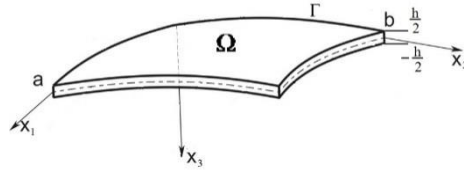


Fig.1. Scheme of the studied shell.

We denote shell displacements along the axes x_1, x_2, x_3 by u_1, u_2, u_3 , respectively, where $u_3 = u_3(x_1, x_2)$. All components of the displacement are assumed to be essentially smaller than the characteristic shell dimension; deformations in the shell middle surface $\varepsilon_{11}, \varepsilon_{22}, \varepsilon_{12}$ are assumed to be negligible with respect to a unit (however, it does not mean that the relationship between displacements and deformations must be linear). Owing to the Kirchhoff-Love hypothesis, the following relations between the deformations of the middle surface ε_{ij} and an arbitrary surface e_{ij} are valid [29]

$$e_{ii} = \varepsilon_{ii} + x_3 \xi_{ii}, \quad i = 1, 2, \quad e_{12} = \varepsilon_{12} + x_3 \xi_{12}, \quad (1)$$

where

$$\begin{aligned} \varepsilon_{ij} &= \frac{\partial u_i}{\partial x_j} + \frac{1}{2} \left(\frac{\partial u_3}{\partial x_i} \right)^2 - k_i u_3, \quad i = 1, 2, \quad \varepsilon_{12} = \frac{\partial u_1}{\partial x_2} + \frac{\partial u_2}{\partial x_1} + \frac{\partial u_3}{\partial x_1} \frac{\partial u_3}{\partial x_2}, \\ \xi_{ij} &= -\frac{\partial^2 u_3}{\partial x_i^2}, \quad i = 1, 2, \quad \xi_{12} = -2 \frac{\partial^2 u_3}{\partial x_1 \partial x_2}, \end{aligned} \quad (2)$$

and k_1, k_2 denote the shell curvatures.

In the modified coupled stress theory [30], the deformation energy U_1 of an elastic body occupying the space Ω , taking into account small deformation, reads

$$U_1 = \frac{1}{2} \int_{\Omega} (\sigma_{ij} \varepsilon_{ij} + m_{ij} \chi_{ij}) dv, \quad (3)$$

where: ε_{ij} – deformation tensor components, χ_{ij} – components of an asymmetric tensor of the curvature gradient. The components are defined as follows

$$\varepsilon_{ij} = \frac{1}{2}(u_{i,j} + u_{j,i} + u_{m,i}u_{m,j}), \quad \chi_{ij} = \frac{1}{2}(\theta_{i,j} + \theta_{j,i}), \quad \theta_i = \frac{1}{2}(\text{rot}(u))_i. \quad (4)$$

Here u_i stands for the components of the displacement vectors \mathbf{u} , θ stands for an infinitely small rotation vector with elements θ_i and δ_{ij} is the Kronecker symbol. In the case of an isotropic elastic material, stresses generated by kinematic parameters occurred in (4) are yielded by the following state equations [30]:

$$\sigma_{ij} = \lambda \varepsilon_{mm} \delta_{ij} + 2\mu \varepsilon_{ij}, \quad m_{ij} = 2\mu l^2 \chi_{ij}, \quad (5)$$

where $\sigma_{ij}, \varepsilon_{ij}, m_{ij}$ и χ_{ij} denote components of the classical tensor of stresses $\boldsymbol{\sigma}$, deformation tensor $\boldsymbol{\varepsilon}$, deviator part of the symmetric tensor of the higher order \mathbf{m} and a symmetric part of the curvature tensor $\boldsymbol{\chi}$, respectively; $\lambda = \frac{E\nu}{(1+\nu)(1-2\nu)}$, $\mu = \frac{E}{2(1+\nu)}$ are the Lamè parameters;

$E(x, y, z, e_i)$, $\nu(x, y, z, e_i)$ is Young's modulus and Poisson's coefficient, respectively, $\rho(x, y, z, e_i)$ – density of the beam material; e_i – the strength of the deformation.

In this model, in addition to the classical Lamè parameters, the additional scale parameter of the length l is employed [30]. This is a simple consequence of the fact that in the couple stress theory, the density of the deformation energy depends only on the deformation tensor and the symmetric curvature tensor. The latter does not explicitly depend on the rotation (nonsymmetric part of the deformation gradient) and the non-symmetric part of the curvature tensor [30].

To obtain the initial differential equations in mixed form we introduce the force function F :

$$T_{ij} = -\frac{\partial^2 F}{\partial x_i \partial x_j}, \quad (6)$$

and then the equations in mixed form will be written with respect to u_3 and the force function F .

We introduce the well-known notation for differential operators

$$\nabla_k^2(.) = k_2 \frac{\partial^2(.)}{\partial x_1^2} + k_1 \frac{\partial^2(.)}{\partial x_2^2}; \quad L(.,.) = \frac{\partial^2(.)}{\partial x_1^2} \frac{\partial^2(.)}{\partial x_2^2} + \frac{\partial^2(.)}{\partial x_2^2} \frac{\partial^2(.)}{\partial x_1^2} - 2 \frac{\partial^2(.)}{\partial x_1 \partial x_2} \frac{\partial^2(.)}{\partial x_1 \partial x_2}. \quad (7)$$

Using the Hamilton principle, we come to a system of differential equations composed of the equations of motion of the nano-shell (8) and the equations of compatibility of deformations (9):

$$\tilde{D} \nabla^4 u_3 - L(u_3, F) - \nabla_k^2 F - q = 0, \quad (8)$$

$$\frac{1}{Eh} \nabla^4 F = -\nabla_k^2 u_3 - \frac{1}{2} L(u_3, u_3), \quad (9)$$

where $\tilde{D} = D + \frac{El^2}{4(1+\nu)}$ (D – cylindrical stiffness, l – size-dependent length parameter of the material).

Scheme of MVI can be formally described in the following way. We are aimed at finding a solution to equation $Aw(x, y) = q(x, y); \quad x, y \in \Omega(x, y)$, where A stands for a certain operator defined on the manifold $D(A)$ of the Hilbert space $L_2(\Omega)$; $q(x, y)$ stands for a given function of two variables x, y , and $w(x, y)$ is a searched function; $\Omega(x, y)$ is a space associated with variations of x and y .

If $\Omega(x, y) = X \times Y$ (X – a certain bounded set of variables x ; Y – a bounded set of y), then a solution to equation has the following form $w_N(x, y) = \sum_{i=1}^N u_i(x)v_i(y)$, where the functions $u_i(x)$ and $v_i(y)$ are defined by the following system of equations

$$\begin{aligned} \int_X (Aw_N - q)u_1(x)dx &= 0, & \int_Y (Aw_N - q)v_1(y)dy &= 0, \\ & \dots\dots\dots \\ \int_X (Aw_N - q)u_N(x)dx &= 0, & \int_Y (Aw_N - q)v_N(y)dy &= 0, \end{aligned}$$

in the following way. A certain system composed of N functions with respect to one of the variables, for instance, $u_1^0(x), u_2^0(x), \dots, u_N^0(x)$ is given. Then, the first N equations of the system yield N functions $v_1^1(x), v_2^1(x), \dots, v_N^1(x)$. Next, the obtained functions are employed to create a new set of functions $x - u_1^2(x), u_2^2(x), \dots, u_N^2(x)$, which is further used to construct a set of new functions with respect to the variable y , i.e. $v_1^3(x), v_2^3(x), \dots, v_N^3(x)$, and so on. In the case of the iterative procedure MVI [12], proves of the theorems constituting the theoretical background of the MVI convergence were given for the problems of the theory of plates.

Theorem 1. If A is a positively defined operator with its action space $D(A) \subset H_A$, then the sequence of elements $\alpha_k = \|w_1^k(x, y) - w_0\|_{H_T}$ is monotonously decreasing, i.e. for arbitrary i and j if only $i \geq j$, then $\|w_1^i - w_0\|_{H_T} \leq \|w_1^j - w_0\|_{H_T}$.

Theorem 2. Let each element of the basis system of the space $W_2^m(X \times Y)$ has the form $\theta_i(x, y) = \varphi_i(x)\psi_i(y)$, where $\{\phi_i(x)\}$ is a basis system in the space $W_2^m(X)$, and respectively $W_2^m(Y)$ in the space $W_2^m(Y)$, and in order to get an arbitrary N -th approximation regarding MVI, the

components of the elements of the basis system $\{\theta_i(x, y)\}$ are taken as initial conditions. Then, for sufficiently large N , the MVI gives a unique approximate solution w_N , and the sequence $\{w_N\}$ is convergent with regard to the norm of the space $W_2^0(X \times Y)$ and tends to the exact solution w_0 independently of a number of steps k , which can be defined for each of the N -th approximation, i.e.

$$\|w_N^k - w_0\|_{W_2^0} \rightarrow 0, \quad N \rightarrow \infty.$$

The resulting system of nonlinear partial differential equations can be solved by one of the methods shown in Fig. 1. Boundary and initial conditions are given in [31].

For a numerical example, the variational iteration method and the combination of the variational iteration method and the Agranovsky – Baglay – Smirnov method [MABS] were used. The Agranovsky-Baglay-Smirnov method is proposed and substantiated in the works of Agranovsky et al. [32]. Let's consider the scheme of application of the Agranovsky-Baglai-Smirnov method on the example of the operator equation:

$$A[w(x_1, x_2)] = q(x_1, x_2). \quad (10)$$

A solution to equation (10) in the first approximation ($w_1 = \phi_1^{(k-1)}(x) \psi_1^{(k)}(y)$) is searched in a way similar to the MVI.

The new equation is defined as follows

$$Aw_2(x, y) = q(x, y) - Aw_1(x, y), \quad (11)$$

i.e. we have changed the right hand side of equation (10). Equation (11) is solved again with the help of MVI, and its first approximation yields

$$w_2(x, y) = \phi_2^{(k-1)}(x) \psi_2^{(k)}(y). \quad (12)$$

The next new equation follows

$$Aw_3(x, y) = q(x, y) - Aw_1(x, y) - Aw_2(x, y). \quad (13)$$

and then one employs the MVI again in the first approximation, and so on.

Finally, the following series is used as the input solution:

$$w(x, y) = \sum_{n=1}^N w_n(x, y). \quad (14)$$

3. Results and discussions.

As a numerical example, we consider the application of the described approaches to solve the problem of bending the nanoplate ($k_1 = k_2 = 0$) and without taking into account the geometric nonlinearity, then equations (8, 9) in dimensionless form will be written as

$$\tilde{D}\Delta\Delta w(x_1, x_2) = q(x_1, x_2), \quad (15)$$

where $\tilde{D} = \frac{1}{12} \frac{(1-\nu)}{(1+\nu)(1-2\nu)} + \frac{1}{4(1+\nu)} \gamma^2$, $\gamma = \frac{l}{h}$ - the dimensionless form of the dimension-dependent coefficient, ν is the Poisson's ratio. We consider the boundary conditions of two kinds:

$$w(x_1, x_2)|_r = 0, \quad \Delta w(x_1, x_2)|_r = 0, \quad (16)$$

$$w(x_1, x_2)|_r = 0, \quad \partial w(x_1, x_2)/\partial n|_r = 0. \quad (17)$$

The load is constant and distributed over the entire surface of the plate and is equal to 50. Ordinary differential equations obtained after the use of MSI and MSI + ABS are reduced by the finite difference method of 2 order of accuracy to a system of algebraic equations which is solved by the Gauss method.

Numerical results for the variational iteration (MVI) and combination (MVI+ABS) method are given in Table 1. The exact solution obtained in double trigonometric series is also reported in [8]:

Table 1.

Boundary condition	Exact solution	γ	MVI			MVI+MABS		
			N=4	N=10	N=20	N=4	N=10	N=20
(16)	0.2028	$\gamma=0$	<u>0.2031</u>	<u>0.2031</u>	<u>0.2030</u>	<u>0.2029</u>	<u>0.2029</u>	<u>0.2028</u>
			-/-	-/-	0.1%	-/-	-/-	0%
(17)	0.0661	$\gamma=0.5$	<u>0.0650</u>	<u>0.0651</u>	<u>0.0653</u>	<u>0.0660</u>	<u>0.0660</u>	<u>0.0661</u>
			1.66%	1.51%	1.21%	-/-	-/-	0%
(16)			0.1074	0.1074	0.1073	0.1066	0.1066	0.1065
(17)			0.0374	0.0375	0.0376	0.0382	0.0382	0.0383

Here N is the number of partitions of the plate NxN. As can be seen from the table, the use of MABS significantly increases the accuracy of the solution and for the value $\gamma=0$, the numerical solution is equal to the exact one. Taking into account the size-dependent behavior leads to the fact that the deflection decreases almost twice, i.e. the plate becomes more rigid.

4. Concluding remarks

The paper deals with the application of the variational iteration method (extended Kantorovich method) to the solution of the problems of the Kirchhoff – Love nano-shells bending on the basis of the modified couple stress theory. Modifications of known methods and their relationship are given. The paper presents a scheme for proving the convergence of the variational iteration method. The numerical implementation of the variational iteration method and the Agranovsky-Baglay-Smirnov method is shown by the example of solving the Sophie-Germain-Lagrange equation. Numerical results prove fast convergence of the methods even with a small number of grid partitions.

Acknowledgements

This work has been supported by the Polish National Science Centre under the Grant PRELUDIUM 16 No. 2018/31/N/ST8/00707.

References

- [1] Timoshenko S.P., On the longitudinal bending of rods in an elastic medium. News of St. Petersburg Polytechnic Institute. Department of Engineering, Natural Sciences and Mathematics 1907, vol. 7, no. 1, pp. 145 - 157.
- [2] Reviews of professors Kirpichev, Beltsenko, Bubnov and Kolosov on the works of Professor Timoshenko, awarded the D.I. Zhuravsky. Collection of St. Petersburg Institute of Railway Engineers of Emperor Alexander I. Edition of the Institute of Railway Engineers. Printing house Yu.N. Erlich, 1913, vol. 81, pp. 1 - 40.
- [3] Galerkin B.G., Rods and plates. Rows in some questions of elastic equilibrium of rods and plates. Vestnik Inzhenerov I Technikov. 915. T.I. № 19. pp. 897-908.
- [4] Kantorovich L.V. Krylov V.I., Approximate methods of higher analysis. M.: Fizmatgiz, 1962.
- [5] Vlasov V.V., General theory of shells. M: Gostekhizdat, 1949.
- [6] Krysko A.V., Awrejcewicz J., Pavlov S.P., Zhigalov M.V., Krysko V.A., On the iterative methods of linearization, decrease of order and dimension of the Karman-type PDEs. The Scientific World Journal Volume 2014 (2014), Article ID 792829, pp. 15.
- [7] Krysko A.V., Awrejcewicz J., Zhigalov M.V., Krysko V.A., On the contact interaction between two rectangular plates. Nonlinear Dynamics DOI 10.1007/s11071-016-2858-2, Vol 84, №4 June 2016, pp. 2729-2748.

- [8] Awrejcewicz J., Krysko V.A., Zhigalov M.V., Krysko A.V., Contact interaction of two rectangular plates made from different materials with an account of physical non-linearity. *Nonlinear Dynamics: An International Journal of Nonlinear Dynamics and Chaos in Engineering Systems*. Volume 85, Number 4. 2016. pp. 2729-2748
- [9] Schunk T.E. Zur Knienfestigkeit schwach gekrummter zylindrischer Schalen/ - *Ing/ Arch.*, 1933, IV, pp. 394 – 414.
- [10] Zhukov E.E., The variational method of successive approximations as applied to the calculation of thin rectangular plates. In the book: *Calculation of thin-walled spatial structures* / Ed. A.R. Rzhantsina. - M.: Stroyizdat, 1964, pp. 27-35.
- [11] Krysko V.A., *Nonlinear statics and dynamics of inhomogeneous shells*. - Saratov: Ed. Saratov. Univ., 1976. pp. 214.
- [12] Kirichenko V. F., Krysko V. A., Substantiation of the variational iteration method in the theory of plates, *Soviet Applied Mechanics*, April 1981, Volume 17, Issue 4, pp. 366-37
- [13] Kerr A.D., An extension of the Kantorovich method. *Q. Appl. Math.*, vol. 26, 1968, pp. 219–229.
- [14] Kerr A.D., Alexander H., An application of the extended Kantorovich method to the stress analysis of a clamped rectangular plate. *Acta Mech.*, vol. 6, 1968, pp. 180–196.
- [15] Kerr A.D., An extended Kantorovich method for the solution of eigenvalue problems, *Int. J. Solids Struct.* vol. 5, 1969, pp. 559–572.
- [16] Singhatanadgid P., Singhanart T., The Kantorovich method applied to bending, buckling, vibration, and 3D stress analyses of plates: A literature review. *Mechanics of Advanced Materials and Structures*. 26(2), 2019, pp. 170-188.
- [17] Banerjee M.M., Mazumdar, J., A Review of Methods for Linear and Nonlinear Vibration Analysis of Plates and Shells. 2016. *Procedia Engineering*. 144, pp. 493-503.
- [18] Krysko V.A., Amelchenko V.V., To the calculation of flexible orthotropic plates by the modified Vlasov-Kantorovich method using an electronic computer. *For Technical Progress (Baku)*.-1968. No. 7. pp. 13-15.
- [19] Krysko V.A., Amelchenko V.V., Calculation of flexible plates by the variational method of iterations and comparison with experimental data. *Three young scientists: Materials of the 3rd inter-university. conf. Saratov*, 1970. pp. 62-66.
- [20] Krysko V.A., Fedorova A.G., Dynamics problems for elastically plastic flexible shallow shells. *Applied Mechanics. USSR Academy of Sciences*. 1979. T. XV, Iss. 2, pp. 71-76.

- [21] Krysko V.A., Fedorova A.G., Stability of shallow shells under the influence of local loads, taking into account geometric and physical nonlinearities. Vestnik Universities. Construction and Architecture, 1978, No. 5, pp. 24-28.
- [22] Krysko V.A., Bochkarev V.V., Designing plates and shells that are close to optimal in weight, taking into account the temperature effect. Applied Mechanics. Academy of Sciences of the Ukrainian SSR, 1981, T. XVII, No 11. pp. 54-59.
- [23] Krysko V.A., Bochkarev V.V., Optimal design of plates and shells, taking into account physical non-linearity. Applied Mechanics. Academy of Sciences of the Ukrainian-SSR. 1982. T.XVIII, No 7. pp. 52-57.
- [24] Krysko V.A., Pavlov S.P., The problem of optimal control of the natural frequency of inhomogeneous shells. Applied Mechanics. USSR Academy of Sciences. 1982. T.XVIII, No. 4. pp. 41-47.
- [25] Krysko V.A., Bochkarev V.V., The stress-strain state of a plate of variable thickness with a flat front surface. Vestnik Vuzov Engineering. 1984. No. 12. pp. 231-235.
- [26] Krysko V.A., Kirichenko V.F., Surova N.S., On projection methods for solving the problems of the theory of flexible gently sloping anisotropic multilayer shells. Materials II All-Union. conf. on scientific and technological products from composite materials. Yerevan, 1984. Part II. pp. 99-107.
- [27] Krysko V.A., Zhigalov M.V. The method of linearization and lowering the order of systems of differential equations in the nonlinear mechanics of heterogeneous structures. Proc. doc. IV International conf. on the mechanics of heterogeneous structures. Ternopol, 1995. pp. 356.
- [28] Vlasov V.Z., General Series of Shells and its Applications in Technique. Gostexizdat, Moscow (1949) (in Russian)
- [29] Novozhilov V. V., Thin Shell Theory, Springer, New York, USA, 2nd edition, 1971.
- [30] Yang F., Chong A. C. M., Lam D. C. C., and Tong P., Couple stress based strain gradient theory for elasticity, Int. J. Solids Struct. 39 (2002), pp. 2731–2743.
- [31] Krysko-jr, V.A., Awrejcewicz, J., Zhigalov, M.V., Kirichenko, V.F., Krysko, A.V., Mathematical Models of Higher Orders. Shells in Temperature Fields. 1st ed. 2019, XII, p. 470.
- [32] Baglay R. D., Smirnov K. K., On the processing of two-dimensional computer signals. Journal of Computational Mathematics and Mathematical Physics. 15:1. 1975. pp. 241–248.

Jan Awrejcewicz: Department of Automation, Biomechanics and Mechatronics, Lodz University of Technology, 1/15 Stefanowski St., 90-924 Lodz and Department of Vehicles, Warsaw University of Technology, 84 Narbutta Str., 02-524 Warsaw, POLAND; (*awrejcew@p.lodz.pl*). The author gave a presentation of this paper during one of the conference sessions

Vadim A. Krysko-jr: Department of Automation, Biomechanics and Mechatronics, Lodz University of Technology, 1/15 Stefanowski St., 90-924 Lodz (*vadimakrysko@gmail.com*).

Maxim V. Zhigalov: Department of Mathematics and Modeling, Saratov State Technical University, Politehnicheskaya 77, 410054, Saratov, Russian Federation, (*max.zhigalov@gmail.com*).

Vadim A. Krysko: Department of Mathematics and Modeling, Saratov State Technical University, Politehnicheskaya 77, 410054, Saratov, Russian Federation, (*tak@san.ru*)

Nonlinear dynamics of flexible nanoplates resting on an elastic foundation in a stationary temperature field

Vadim A. Krysko-jr, Jan Awrejcewicz, Ekaterina Yu. Krylova, Irina V. Papkova

Abstract: In this work a mathematical model of the oscillations of the MEMS/NEMS element is constructed in the form of a flexible, dimensionally dependent, rigidly pinched plate rectangular located in a stationary temperature field. A transverse uniformly distributed alternating load acts on the plate. Geometric nonlinearity is taken into account according to the theory of von Kármán. The motion equations of a mechanical system element, as well as the corresponding boundary and initial conditions, are derived based on the Hamilton principle on the basis of a modified couple stress theory taking into account the Kirchhoff hypothesis. The temperature field is found from the three-dimensional heat equation by the method of variational iterations. It was revealed that the size-dependent parameter significantly affects the dynamics of the beam under the influence of a transverse alternating load and the temperature field. The temperature field at $0 < T < 100$ does not affect the dynamics of the plate.

1. Formulation of the problem

Nanoscale mechanics provides the scientific foundation and infrastructure for nanotechnology and nanoengineering. Over the past decades, explosive worldwide growth has occurred in this area of nanoscience. Nano-plates, such as graphene sheets [1], silver nano-plates [2], and metal coated nano-plates [3] have a wide range of promising applications in various fields of nanotechnology. In such nanoelectromechanical systems (NEMS) as nanomechanical resonators [4–6], nanoscale mass sensors [7–9] and actuators [10]. The mechanical characteristics and behavior of nano-plates, under the influence of various external factors, play an important role in the overall performance of nano-sized devices. Classical continuum models do not take into account the effects of scale at the nano-dimensional level; therefore, many modified theoretical models are used to analyze the nano-plates behavior. A review of such theories is given in [11]. One of the theories that allows one to take into account large-scale effects is the micropolar (asymmetric, moment) theory that is being actively developed now [12–14]. In [15], various theories of plates and shells of the Cosserat type are presented; the features and differences between these theories are discussed. In paper [16] the linear theory describing plane-strain deformations of a micropolar elastic solid which incorporates the additional contribution of surface micropolar elasticity is presented. Two different versions of the surface shell are considered: one gives rise to a fourth-order surface theory and another which, via a

particular form of the Kirchhoff–Love kinematic assumption, results in a second-order surface model. In each case, the interior and exterior mixed boundary value problems are considered and we show that they can have at most one smooth solution despite the presence of boundary conditions of order equal to or higher than that of the governing equations. Augello et al. [17] intend to establish a unified theory of structures based on the micropolar elasticity, which allows taking into consideration the microstructure of the material, through the adoption of four additional material parameters. The considered model is developed in the domain of the Carrera unified formulation (CUF), according to which theories of structures can degenerate into unknown kinematics that makes use of an arbitrary expansion of the generalized variables. CUF is a hierarchical formulation that considers the order of the structural model as input of the analysis, so that no specific approximation and manipulation is needed to implement refined theories. Sargsyan and Sargsyan [18] consider a general model of dynamic bending of isotropic micropolar elastic thin plates with independent fields of displacements and rotations. The model has been justified asymptotically based on the solutions for special cases subject to simplifying assumptions. The model incorporates transverse shear deformations. Neglecting transverse shear, a model of the dynamics for micropolar elastic thin plates is also constructed. To solve the size-dependent differential equations of plate models, various solution methods are used, both analytical and numerical [19] including the Galerkin method [20], and the finite element method [21]. Note that size-dependent models of shells are more complex in terms of mathematical formulas and also solution methods than models of rods, beams [22] and plates. Nayfeh and Younis [23] studied various problems of oscillations and heat transfer processes of a nanoscale resonator taking into account the thermoelastic theory. The influence of temperature fields on nano and micro-elements is considered in [24]. Fazelzadeh et al. [25] investigated the thermo-mechanical vibration characteristics of doubly-curved nano-composite shells reinforced by graphene nanoplates by considering a first-order shear deformation theory. Krysko et al. [26] constructed a mathematical model of vibrations for flexible rectangular plates and shells under the action of transverse shock loads and a temperature field. The dynamic stability under such loads was studied. It is noted that the temperature influence can lead to a dynamic loss of stability. In [27], the nonlinear dynamical system (NDS) of an inhomogeneous isotropic hollow cylinder with a variable modulus of elasticity and thermal conductivity was studied based on the Lord-Shulman theory. The problem was solved numerically using the finite element method. The Laplace transform and potential methods were used to obtain thermoelastic fields of homogeneous isotropic hollow cylinders for the Lord-Shulman model [28]. It is worth noting an article [29] devoted to the thermoelastic behavior of a multilayer shallow cylinder with transitional temperature and mechanical loads applied on its internal and external surfaces. The problem is solved using the Laplace transform and the potential method. It follows from the above review that, despite the large number of publications on thermoelasticity problems, there

are practically no studies on the nonlinear dynamics of geometrically nonlinear nanoplates under conditions of temperature effects. This work aims to fill this gap.

The object of the study is a rectangular plate, occupying in the space \mathbb{R}^3 the region $\Omega = \{0 \leq x \leq a; 0 \leq y \leq b; -\frac{h}{2} \leq z \leq \frac{h}{2}\}$.

The mathematical model of the plate is based on the following hypotheses:

- (i) any cross section normal to the middle plane before deformation remains straight and normal to the middle plane after deformation, but the section height does not change (Kirchhoff hypotheses are used);
- (ii) the nonlinear dependence between deformations and displacements in the von Kármán form is taken into account;
- (iii) the plate material is assumed to be isotropic, elastic and obeys the Duhamel-Neumann law (there are no restrictions on the temperature field over the plate thickness; it is determined from the solution of the three-dimensional heat equation, and it is assumed that the physical parameters of the material are temperature independent);
- (iv) normal stresses on sides parallel to the middle plane of the plate are negligible compared to other stresses and are not taken into account, and Kirchhoff kinematic hypotheses are taken into account.

The components of the symmetric gradient tensor of curvature χ for the Cosserat pseudo-continuum will have the form: $\chi_{ij} = \frac{1}{2}(\theta_{i,j} + \theta_{j,i})$, where $\theta_i = \frac{1}{2}(\text{rot}(u))_i$ are the infinitesimal rotation vector components, and

$$\theta_x = \frac{1}{2}\left(\frac{\partial u_z}{\partial y} - \frac{\partial u_y}{\partial z}\right), \theta_y = \frac{1}{2}\left(\frac{\partial u_z}{\partial x} - \frac{\partial u_x}{\partial z}\right), \theta_z = \frac{1}{2}\left(\frac{\partial u_y}{\partial x} - \frac{\partial u_x}{\partial y}\right).$$

For the case of the Kirchhoff kinematic hypotheses, the χ components are written as follows:

$$\chi_{xx} = \frac{\partial^2 w}{\partial x \partial y}; \chi_{yy} = -\frac{\partial^2 w}{\partial y \partial x}; \chi_{xy} = \frac{1}{2}\left(\frac{\partial^2 w}{\partial y^2} - \frac{\partial^2 w}{\partial x^2}\right); \chi_{xz} = \frac{1}{4}\left(\frac{\partial^2 v}{\partial x^2} - \frac{\partial^2 u}{\partial x \partial y}\right); \chi_{yz} = \frac{1}{4}\left(\frac{\partial^2 v}{\partial y \partial x} - \frac{\partial^2 u}{\partial y^2}\right) \quad (1)$$

Hooke's law is used for an isotropic elastic material. Higher-order tensions m_{ij} , are determined by the following equations [30]: $m_{ij} = \frac{El^2}{1+\nu}\chi_{ij}$, where $i, j = \{x, y, z\}$, E - Young's modulus, ν - Poisson's ratio. The parameter l , that appears in higher-order tensions m_{ij} , plays the role of an additional independent material length parameter associated with the symmetric curvature gradient tensor.

A stationary temperature field is considered. Material properties are temperature independent. Higher order tensions and moments follow

$$\begin{aligned}
Y_{xx} &= \int_{-\frac{h}{2}}^{\frac{h}{2}} m_{xx} dz = \frac{El^2 h}{1+\nu} \frac{\partial^2 w}{\partial x \partial y}; Y_{yy} = \int_{-\frac{h}{2}}^{\frac{h}{2}} m_{yy} dz = -\frac{El^2 h}{1+\nu} \frac{\partial^2 w}{\partial x \partial y}; Y_{xy} = \int_{-\frac{h}{2}}^{\frac{h}{2}} m_{xy} dz = \frac{El^2 h}{2(1+\nu)} \left(\frac{\partial^2 w}{\partial y^2} - \frac{\partial^2 w}{\partial x^2} \right); \\
Y_{xz} &= \int_{-\frac{h}{2}}^{\frac{h}{2}} m_{xz} dz = \frac{El^2 h}{4(1+\nu)} \left(\frac{\partial^2 v}{\partial x^2} - \frac{\partial^2 u}{\partial x \partial y} \right); Y_{yz} = \int_{-\frac{h}{2}}^{\frac{h}{2}} m_{yz} dz = \frac{El^2 h}{4(1+\nu)} \left(\frac{\partial^2 v}{\partial y \partial x} - \frac{\partial^2 u}{\partial y^2} \right); \\
J_{xz} &= \frac{El^2}{1+\nu} \int_{-\frac{h}{2}}^{\frac{h}{2}} \chi_{xz} z dz; J_{yz} = \frac{El^2}{1+\nu} \int_{-\frac{h}{2}}^{\frac{h}{2}} \chi_{yz} z dz.
\end{aligned} \tag{2}$$

In this model, in addition to Young's modulus and Poisson's ratio, it is necessary to take into account one more scale length parameter l [30]. This is a direct consequence of the fact that in the couple stress theory of elasticity, the strain energy density is a function of the strain tensor and the symmetric curvature tensor only. It does not depend explicitly on rotation (the asymmetric part of the deformation gradient) and the asymmetric part of the curvature tensor.

We obtain the resolving equations of motion of the plate, and the boundary and initial conditions from the Hamilton's variational principle: $\int_{t_0}^{t_1} (\delta K - \delta U + \delta W) dt = 0$. Here K - kinetic energy, U - potential energy, $\delta W = \delta W_q + \delta W_\varepsilon$ - variation of the work of external forces W_q and damping forces W_ε . Taking into account the micropolar theory, the potential energy U in an elastic body with infinitely small deformations, is written in the form:

$$U = \frac{1}{2} \int_{\Omega} (\sigma_{ij} \varepsilon_{ij} + m_{ij} \chi_{ij}) dv. \tag{3}$$

Kinetic energy of the system is as follows

$$K = \frac{1}{2} \rho \int_{\Omega} \left[\left(\frac{\partial u_x}{\partial t} \right)^2 + \left(\frac{\partial u_y}{\partial t} \right)^2 + \left(\frac{\partial u_z}{\partial t} \right)^2 \right] dv. \tag{4}$$

Variation of the work of external forces and damping forces takes the following form

$$\delta W_\varepsilon = \int_{\Omega} \left[\varepsilon \frac{\gamma}{g} \frac{\partial w}{\partial t} \delta w \right] dv, \quad \delta W_q = \int_0^a \int_0^b q(x, y, t) \delta w dx dy. \tag{5}$$

where ε is a dissipation coefficient, ρ is the density of the plate material, $q(x, y, t)$ is the external normal load.

From the variational principles, we obtain the resolving equations of motion (6), the boundary and initial conditions. We have

$$\frac{\partial N_{xx}}{\partial x} + \frac{\partial T}{\partial y} + \frac{1}{2} \frac{\partial^2 Y_{yz}}{\partial y^2} + \frac{1}{2} \frac{\partial^2 Y_{xz}}{\partial x \partial y} + 2 \frac{\partial N^T}{\partial x} = \rho h \frac{\partial^2 u}{\partial t^2}, \tag{6}$$

$$\begin{aligned}
& \frac{\partial N_{yy}}{\partial y} + \frac{\partial T}{\partial x} - \frac{1}{2} \frac{\partial^2 Y_{xz}}{\partial x^2} - \frac{1}{2} \frac{\partial^2 Y_{yz}}{\partial x \partial y} + 2 \frac{\partial N^T}{\partial y} = \rho h \frac{\partial^2 v}{\partial t^2}, \\
& \frac{\partial^2 M_{xx}}{\partial x^2} + \frac{\partial^2 M_{yy}}{\partial y^2} + 2 \frac{\partial^2 H}{\partial x \partial y} + \frac{\partial}{\partial x} \left(N_x \frac{\partial w}{\partial x} \right) + \frac{\partial}{\partial y} \left(N_y \frac{\partial w}{\partial y} \right) + 2 \frac{\partial T}{\partial x} \frac{\partial w}{\partial y} + \\
& + 2 \frac{\partial T}{\partial y} \frac{\partial w}{\partial x} + 4T \frac{\partial^2 w}{\partial x \partial y} + 2 \frac{\partial}{\partial x} \left(N^T \frac{\partial w}{\partial x} \right) + 2 \frac{\partial^2 M^T}{\partial x^2} + 2 \frac{\partial}{\partial y} \left(N^T \frac{\partial w}{\partial y} \right) + \\
& + 2 \frac{\partial^2 M^T}{\partial y^2} - \frac{\partial^2 Y_{xx}}{\partial x \partial y} + \frac{\partial^2 Y_{yy}}{\partial y \partial x} + \frac{\partial^2 Y_{xy}}{\partial x^2} - \frac{\partial^2 Y_{xy}}{\partial y^2} + q = \rho h \frac{\partial^2 w}{\partial t^2} + \varepsilon \rho h \frac{\partial w}{\partial t}, \\
& \delta w = 0 \quad \text{or} \quad \left\{ N_{xx}^T \frac{\partial w}{\partial x} + 2T \frac{\partial w}{\partial y} + \frac{\partial Y_{xy}}{\partial x} - \frac{\partial Y_{xx}}{\partial y} + \frac{\partial Y_{yy}}{\partial y} \right\}_{n_x} + \\
& + \left\{ N_{yy}^T \frac{\partial w}{\partial y} + 2T \frac{\partial w}{\partial x} - \frac{\partial Y_{xx}}{\partial x} + \frac{\partial Y_{yy}}{\partial x} - \frac{\partial Y_{xy}}{\partial y} \right\}_{n_y} = 0, \\
& \frac{\partial \delta w}{\partial x} = 0 \quad \text{or} \quad \left\{ M_{xx}^T - Y_{xy} \right\}_{n_x} + \left\{ 2H + Y_{xx} - Y_{yy} \right\}_{n_y} = 0, \\
& \frac{\partial \delta w}{\partial y} = 0 \quad \text{or} \quad \left\{ 2H + Y_{xx} - Y_{yy} \right\}_{n_x} + \left\{ M_{yy}^T + Y_{xy} \right\}_{n_y} = 0, \\
& \delta u = 0 \quad \text{or} \quad \left\{ N_{xx}^T + \frac{1}{2} \frac{\partial Y_{xz}}{\partial y} \right\}_{n_x} + \left\{ T + \frac{1}{2} \frac{\partial Y_{yz}}{\partial y} + \frac{1}{2} \frac{\partial Y_{xz}}{\partial x} \right\}_{n_y} = 0, \\
& \frac{\partial \delta u}{\partial x} = 0 \quad \text{or} \quad \left\{ -\frac{1}{2} Y_{xz} \right\}_{n_y} = 0, \\
& \frac{\partial \delta u}{\partial y} = 0 \quad \text{or} \quad \left\{ -\frac{1}{2} Y_{xz} \right\}_{n_x} + \left\{ -\frac{1}{2} Y_{yz} \right\}_{n_y} = 0, \\
& \delta v = 0 \quad \text{or} \quad \left\{ T - \frac{1}{2} \frac{\partial Y_{xz}}{\partial x} - \frac{1}{2} \frac{\partial Y_{yz}}{\partial y} \right\}_{n_x} + \left\{ N_{yy}^T - \frac{1}{2} \frac{\partial Y_{yz}}{\partial x} \right\}_{n_y} = 0, \\
& \frac{\partial \delta v}{\partial x} = 0 \quad \text{or} \quad \left\{ \frac{1}{2} Y_{xz} \right\}_{n_x} + \left\{ \frac{1}{2} Y_{yz} \right\}_{n_y} = 0, \quad \frac{\partial \delta v}{\partial y} = 0 \quad \text{or} \quad \left\{ \frac{1}{2} Y_{yz} \right\}_{n_x} = 0.
\end{aligned} \tag{7}$$

The nonlinear partial differential equations system with regard to displacements takes the following form

$$\begin{aligned}
& 4(\nu-1)\frac{\partial^2 u}{\partial y^2} - 4(1+\nu)\frac{\partial^2 v}{\partial x \partial y} - 8\frac{b^2}{c^2}\frac{\partial^2 u}{\partial x^2} + 8(\nu-1)\frac{\partial^2 w}{\partial y^2}\frac{\partial w}{\partial x} + 8\frac{\partial w}{\partial y}\frac{\partial^2 w}{\partial x \partial y} - \\
& - 8\frac{b^2}{c^2}\frac{\partial w}{\partial x}\frac{\partial^2 w}{\partial x^2} + l^2(\nu-1)\left(-\frac{h^2}{b^2}\frac{\partial^4 u}{\partial y^4} + \frac{h^2}{b^2}\frac{\partial^4 v}{\partial x \partial y^3} - \frac{h^2}{c^2}\frac{\partial^4 u}{\partial x^2 \partial y^2} + \frac{h^2}{c^2}\frac{\partial^4 v}{\partial x^3 \partial y}\right) - \\
& - \frac{2}{(1-\nu)}\frac{\partial N^T}{\partial x} = 8(\nu^2-1)\frac{\partial^2 u}{\partial t^2}; \\
& - 4(1+\nu)\frac{b^2}{c^2}\frac{\partial^2 u}{\partial x \partial y} + 4(\nu-1)\frac{b^2}{c^2}\frac{\partial^2 v}{\partial x^2} - 8\frac{b^2}{c^2}\frac{\partial w}{\partial x}\frac{\partial^2 w}{\partial x \partial y} + 8(\nu-1)\frac{b^2}{c^2}\frac{\partial w}{\partial y}\frac{\partial^2 w}{\partial x^2} - \\
& - 8\frac{\partial w}{\partial y}\frac{\partial^2 w}{\partial y^2} + l^2(\nu-1)\left(\frac{h^2}{c^2}\frac{\partial^4 u}{\partial x \partial y^3} - \frac{h^2}{c^2}\frac{\partial^4 v}{\partial x^2 \partial y^2} + \frac{h^2 b^2}{c^4}\frac{\partial^4 u}{\partial x^3 \partial y} - \frac{h^2 b^2}{c^4}\frac{\partial^4 v}{\partial x^4}\right) - \\
& - 8\frac{\partial^2 v}{\partial y^2} - \frac{2}{(1-\nu)}\frac{\partial N^T}{\partial y} = 8(\nu^2-1)\frac{\partial^2 v}{\partial t^2}; \\
& (1+6l^2(1-\nu))\frac{c^2}{b^2}\frac{\partial^4 w}{\partial y^4} + (2+12l^2-12l^2\nu)\frac{\partial^4 w}{\partial x^2 \partial y^2} + (1+6l^2(1-\nu))\frac{b^2}{c^2}\frac{\partial^4 w}{\partial x^4} - \\
& - 12\frac{c^2}{b^2}\frac{\partial w}{\partial y}\frac{\partial^2 v}{\partial y^2} - 12\frac{c^2}{b^2}\frac{\partial v}{\partial y}\frac{\partial^2 w}{\partial y^2} - 18\frac{c^2}{b^2}\left(\frac{\partial w}{\partial y}\right)^2\frac{\partial^2 w}{\partial y^2} - 12\nu\frac{\partial^2 w}{\partial y^2}\frac{\partial u}{\partial x} + \\
& + 12(\nu-1)\frac{\partial^2 u}{\partial y^2}\frac{\partial w}{\partial x} - (24-18\nu)\frac{\partial^2 w}{\partial y^2}\left(\frac{\partial w}{\partial x}\right)^2 - 12\frac{\partial w}{\partial y}\frac{\partial^2 u}{\partial x \partial y} - 12\frac{b^2}{c^2}\frac{\partial w}{\partial x}\frac{\partial^2 u}{\partial x^2} - \\
& - 12\frac{\partial w}{\partial x}\frac{\partial^2 v}{\partial x \partial y} + 24(\nu-1)\frac{\partial u}{\partial y}\frac{\partial^2 w}{\partial x \partial y} + 24(\nu-1)\frac{\partial v}{\partial x}\frac{\partial^2 w}{\partial x \partial y} + 12(\nu-1)\frac{\partial w}{\partial y}\frac{\partial^2 v}{\partial x^2} - \\
& - (96-72\nu)\frac{\partial w}{\partial y}\frac{\partial w}{\partial x}\frac{\partial^2 w}{\partial x \partial y} - 12\nu\frac{\partial v}{\partial y}\frac{\partial^2 w}{\partial x^2} + 6(3\nu-4)\left(\frac{\partial w}{\partial y}\right)^2\frac{\partial^2 w}{\partial x^2} - \\
& - 12\frac{b^2}{c^2}\frac{\partial u}{\partial x}\frac{\partial^2 w}{\partial x^2} - 18\frac{b^2}{c^2}\left(\frac{\partial w}{\partial x}\right)^2\frac{\partial^2 w}{\partial x^2} - 24(1+\nu)\left(\frac{\partial N^T}{\partial x}\frac{\partial w}{\partial x} + N^T\frac{\partial^2 w}{\partial x^2} + \frac{\partial N^T}{\partial y}\frac{\partial w}{\partial y} + \right. \\
& \left. + N^T\frac{\partial^2 w}{\partial y^2} + \frac{\partial^2 M^T}{\partial x^2} + \frac{\partial^2 M^T}{\partial y^2}\right) = 12(\nu^2-1)\left(\frac{c^2}{h^2}\frac{\partial^2 w}{\partial t^2} - \frac{c^2}{h^2}\varepsilon\frac{\partial w}{\partial t} - q\right).
\end{aligned}$$

The following dimensionless parameters are used: $x = a\bar{x}$, $y = b\bar{y}$, $w = h\bar{w}$, $u = \frac{h^2}{a}\bar{u}$,

$v = \frac{h^2}{b}\bar{v}$, $l = h\bar{l}$, $t = \frac{ab}{h}\sqrt{\frac{\rho}{E}}\bar{t}$, $\varepsilon = \frac{h}{ab}\sqrt{\frac{E}{\rho}}\bar{\varepsilon}$, $q = \frac{Eh^4}{a^2b^2}\bar{q}$, $T = \frac{h^2}{\alpha ab}\bar{T}$, and α is a linear expansion coefficient.

To study the stress-strain state in conditions of uneven heating, it is necessary to determine first the temperature field. In this regard, there is a need for the formulation and methods development for solving the corresponding problems of thermal conductivity for thin-walled elements.

In this work, we propose to solve the three-dimensional heat equation without an internal heat source to determine the temperature field in the plates

$$\frac{\partial^2 T}{\partial x^2} + \frac{\partial^2 T}{\partial x^2} + \frac{\partial^2 T}{\partial z^2} = 0. \quad (8)$$

To solve the stationary heat equation, boundary conditions of the 1st to 3rd kind should be given. This equation will be solved for the first time by the method of variational iterations [31]. The essence of the variational iteration method is that the solution is represented in the form $T(x, y, z) = X(x)Y(y)Z(z)$. The heat equation is three-dimensional, but the variational iterations method for boundary conditions of the third and third kind makes it possible to obtain an analytical solution. It should be emphasized that the heat equation in a three-dimensional formulation it is used for the first time here in our work.

The obtained solution of the heat equation using the method of variational iterations was compared with the solution obtained by the finite difference method and showed their complete coincidence. To reduce the nonlinear differential equations system to the Cauchy problem, the finite difference method with approximation of the second accuracy order is used. The finite difference method is also applied to the boundary conditions.

In the given equations system, the temperature terms are preliminarily calculated depending on the type of boundary conditions for the heat equation.

The resulting system of ordinary second-order differential equations is reduced to a first order ordinary differential equations system, which is solved by the 4th-order Runge-Kutta method. The application validity of the 4th-order Runge-Kutta method was given in [32].

2. Numeric results

The studies were carried out for a square silver plate with the following physical and geometric parameters: length and width $a=b=2 \cdot 10^{-7}$ m, thickness $h = 4 \cdot 10^{-9}$ m, elastic modulus $E = 1.01972 \cdot 10^8$ kgf/m², $\nu = 0.37$, $l = 0; 0.5$. The problem was solved in two stages: 1. The plate was preheated. The resulting deflection w and displacements u, v were taken as initial conditions. 2. The plate, taking into account the initial conditions, was placed in a constant temperature field and under the action of a transverse uniformly distributed alternating load $q = q_0 \sin(\omega_p t)$, where the excitation frequency is equal to the natural linear oscillations frequency $\omega_p = \omega_0 = 10.6$. The studies were carried out for a plate placed in a temperature field at $T = 0^\circ\text{C}, 50^\circ\text{C}, 100^\circ\text{C}$.

The effect of temperature and size-dependent parameter on the plate dynamics was studied. Table 1 presents the power spectra. Consider plate vibrations with a dimensionally dependent parameter $l = 0$ and $T = 50^\circ\text{C}$. At the load $q_0 \in (0; 68]$, the power spectrum shows harmonic oscillations. The Lyapunov exponents are close to zero. In the load range $q_0 \in (68; 76]$, the oscillations become two-frequency. The first Lyapunov exponent is positive, but close to zero. In the range of loads $q_0 \in$

(76; 78] the frequencies are a linear combination of the excitation frequency ω_p and the independent frequency ω_1 . Further, the system exhibits chaotic oscillations.

Table 1

$q_0 \in (0; 68]$	$q_0 \in (68; 76]$	$q_0 \in (76; 78]$
$Le1 = -3.1082 \cdot 10^{-5}$ $Le2 = -3.1943 \cdot 10^{-5}$ $Le3 = -39 \cdot 10^{-2}$ $Le4 = -59 \cdot 10^{-2}$	$Le1 = 38 \cdot 10^{-5}$ $Le2 = -69 \cdot 10^{-4}$ $Le3 = -15 \cdot 10^{-2}$ $Le4 = -28 \cdot 10^{-2}$	$Le1 = 19 \cdot 10^{-4}$ $Le2 = -58 \cdot 10^{-4}$ $Le3 = -19 \cdot 10^{-4}$ $Le4 = -47 \cdot 10^{-4}$

Table 2

$q_0 \in (0; 118]$	$q_0 \in (118; 128]$
$Le1 = 4.056 \cdot 10^{-5}$; $Le2 = -74 \cdot 10^{-4}$; $Le3 = -41 \cdot 10^{-4}$; $Le4 = -54 \cdot 10^{-4}$	$Le1 = 34 \cdot 10^{-5}$; $Le2 = -9.3136 \cdot 10^{-5}$; $Le3 = -32 \cdot 10^{-3}$; $Le4 = -65 \cdot 10^{-2}$

Table 2 presents the dynamics of the nanoplate ($l = 0.5$) at a temperature of $T = 50^\circ\text{C}$. The plate oscillations are periodic in the range of the load amplitude $q_0 \in (0; 118]$, the first Lyapunov exponent is positive but close to zero. In the range $q_0 \in (118; 128]$ appears a linearly dependent frequency $\omega_1 = \frac{\omega_p}{29}$, the first Lyapunov exponent is positive, but close to zero, the rest of Lyapunov exponents are negative. Figure 2 shows the dependences of the maximum deflection in the plate center on the load amplitude $w_{max}(q_0)$ and the scales of the vibrations type for the silver plate, taking into account the size-dependent parameter $l = 0; 0.5$ at temperature $T = 50^\circ\text{C}$. At $l = 0$ harmonic oscillations are replaced by oscillations at two independent frequencies and bifurcations occur, at which harmonics

appear at the frequency $\frac{\omega_p}{29}$. At $l=0.5$, after harmonic oscillations, frequencies equal to $\frac{\omega_p}{29}$ also appear. Windows of periodic oscillations are replaced by periodic oscillations. The maximum deflection of the oscillations w_{max} is much less than with $l=0$.

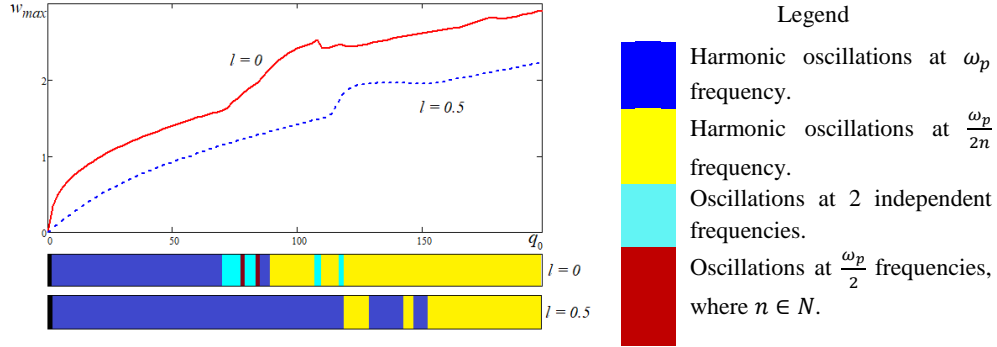


Figure. 2. The dependence of the maximum deflection in the plate center on the load amplitude $w_{max}(q_0)$

Similar results were obtained when studying the dynamics of the plate at a temperature $T = 0^\circ\text{C}$, 100°C and $l = 0; 0.5$.

3. Conclusions

In this work a mathematical model of the nonlinear dynamics for a NEMS plate element under the influence of a temperature field and a transverse uniformly distributed alternating load is derived. The motion equations are obtained taking into account the Kirchhoff hypothesis and the modified couple stress theory of elasticity. It was established that the temperature field in the range $T \in [0; 100]$ does not affect the dynamics of silver nano- and micro-plate under the uniformly distributed alternating load action. Taking into account the size-dependent parameter changes the oscillations nature. For $l = 0$ a transition from harmonic to chaotic oscillations was obtained according to the Ruelle-Takens-Newhouse scenario. At $l = 0.5$, the nanoplate becomes stiffer. Oscillations of a nanoplate are periodic or quasiperiodic.

Acknowledgments

This work has been supported by the Polish National Science Centre under the Grant PRELUDIUM 16 No. 2018/31/N/ST8/00707.

References

- [1] Geim, A. K., Novoselov, K. S., The rise of graphene, in: *Nanoscience and Technology: A Collection of Reviews from Nature Journals*. World Scientific, 2010, pp. 11–19.
- [2] Chen, S., Carroll, D. L., Synthesis and characterization of truncated triangular silver nanoplates. *Nano letters*, 2, 2002, pp. 1003–1007.
- [3] Zhang, S., Wang, Q., Chen, X., Jena, P., Stable three-dimensional metallic carbon with interlocking hexagons. In *Proceedings of the National Academy of Sciences*, 110, 2013, pp. 18809–18813.
- [4] Jiang, L., Yan Z., Timoshenko beam model for static bending of nanowires with surface effects. *Physica E: Low-dimensional systems and Nanostructures*, 42, 2010, pp. 2274–2279.
- [5] Rhoads, J. F., Shaw, S., W., Turner, K. L., Nonlinear dynamics and its applications in micro- and nanoresonators. *ASME 2008 Dynamic Systems and Control Conference*. American Society of Mechanical Engineers, 2008, pp. 1509–1538.
- [6] Asemi, S., Farajpour, A., Mohammadi, M., Nonlinear vibration analysis of piezoelectric nanoelectromechanical resonators based on nonlocal elasticity theory. *Composite Structures*, 116, 2014, pp. 703–712.
- [7] Dai, M. D., Kim, C.W., Eom, K., Nonlinear vibration behavior of graphene resonators and their applications in sensitive mass detection. *Nanoscale research letters*, 7, 2012, pp. 499.
- [8] Shen, H.S., Zhang, C.L., Torsional buckling and postbuckling of double-walled carbon nanotubes by nonlocal shear deformable shell model. *Composite Structures*, 92, 2010, pp. 1073–1084.
- [9] Farajpour, M. R., Rastgoo, A., Farajpour, A., Mohammadi, M., Vibration of piezoelectric nanofilm-based electromechanical sensors via higher-order non-local strain gradient theory. *Micro & Nano Letters*, 11, 2016, pp. 302–307.
- [10] Kong, L., Chen, W., Carbon Nanotube and Graphene based Bioinspired Electrochemical Actuators. *Advanced materials*, 26, 2014, pp. 1025–1043.
- [11] Thai, H.-T., Vo, T.P., Nguyen, T.-K., Kim, S.-E. A review of continuum mechanics models for size-dependent analysis of beams and plates. *Composite Structures*, 177, 2017, pp. 196–219.
- [12] Krylova, E. Yu., Papkova I. V., Yakovleva T. V., Krysko V. A. Theory of Vibrations of Carbon Nanotubes Like Flexible Micropolar Mesh Cylindrical Shells Taking into Account Shift. *Izv. Saratov Univ. (N. S.), Ser. Math. Mech. Inform.*, vol. 19, iss. 3, 2019, pp. 305–316.
- [13] Krylova, E., Yu., Papkova, I. V., Sinichkina, A. O., Yakovleva, T. B., Krysko-yang, V. A., Mathematical model of flexible dimension-dependent mesh plates, *IOP Conf. Series: Journal of Physics: Conf. Series* 1210, 2019, 012073.
- [14] Sarkisyan, S.O., Mathematical model of micropolar elastic thin plates and their strength and stiffness characteristics. *Journal of Applied Mechanics and Technical Physics*, 53(2), 2012, pp. 275–282.
- [15] Altenbach, H., Eremeyev, V.A., *Cosserat-Type Shells CISM International Centre for Mechanical Sciences, Courses and Lectures*, 541, 2013, pp. 131–178.
- [16] Gharahi, A., Schiavone, P., Uniqueness of solution for plane deformations of a micropolar elastic solid with surface effects. *Continuum Mechanics and Thermodynamics*, 2019, pp. 1–14.

- [17] Augello, R., Carrera, E., Pagani, A. Unified theory of structures based on micropolar elasticity *Meccanica* September 2019, Volume 54, Issue 11–12, pp. 1785–1800.
- [18] Sargsyan, A.H., Sargsyan, S.H. Dynamic model of micropolar elastic thin plates with independent fields of displacements and rotations. *Journal of Sound and Vibration*, 333(18), 2014, pp. 4354–4375.
- [19] Mohammadi, M., Goodarzi, M., Ghayour, M., Farajpour, A., Influence of in-plane pre-load on the vibration frequency of circular graphene sheet via nonlocal continuum theory. *Composites Part B: Engineering*, 51, 2013, pp. 121–129.
- [20] Babaei, H., Shahidi, A. Small-scale effects on the buckling of quadrilateral nanoplates based on nonlocal elasticity theory using the Galerkin method. *Archive of Applied Mechanics*, 2011, 81, pp. 1051–1062.
- [21] Zhang, L., Zhang, Y., Liew, K. Vibration analysis of quadrilateral graphene sheets subjected to an in-plane magnetic field based on nonlocal elasticity theory. *Composites Part B: Engineering*, 118, 2017, pp. 96–103.
- [22] Carrera, E., Zozulya, V.V., Carrera unified formulation (CUF) for the micropolar beams: Analytical solutions *Mechanics of Advanced Materials and Structures*, March , 2019.
- [23] Nayfeh AH, Younis MI. Modeling and simulations of thermoelastic damping in microplates. *J Micromech Microeng*, 14(12), 2004, pp.1711–7.
- [24] De S.K., Aluru N.R. Full-Lagrangian schemes for dynamic analysis of electrostatic MEMS. *J. Microelectromech. Syst*, 13, 2004, pp. 737–758.
- [25] S.A. Fazelzadeh, S. Rahmani, E. Ghavanloo, P. Marzocca Thermoelastic vibration of doubly-curved nano-composite shells reinforced by graphene nanoplatelets *Journal of Thermal Stresses* 42(1), 2019, pp. 1-17.
- [26] Krysko, V.A., Awrejcewicz, J., Krysko, A.V. Thermo-dynamics of plates and shells. Springer-Verlag, Berlin, 2007, pp. 777.
- [27] Sherief, H. H., Anwar, M. N., A problem in generalized thermoelasticity for an infinitely long annular cylinder. *Int. J. Eng. Sci.* 1988, 26. pp. 301–6.
- [28] Bagri A., Eslami, M. R., A Unified Generalized Thermoelasticity: Solution for Cylinders and Spheres, *International Journal of Mechanical Sciences*, vol. 49, 2007, pp. 1325–1335.
- [29] Hosseini S.M., Shock-induced thermoelastic wave propagation analysis in a thick hollow cylinder without energy dissipation using mesh-free generalized finite difference (GFD) method. *Acta Mech* 224, 2013, pp. 465–478.
- [30] Yang, F., Chong, ACM., Lam DCC, Tong P., Couple stress based strain gradient theory for elasticity. *Int J Solids Struct*, 39, 2002, pp. 2731–43.
- [31] Krysko, A.V., Awrejcewicz, J., Zhigalov, M.V., Krysko, V.A., On the contact interaction between two rectangular plates, *Nonlinear Dynamics*, 85(4), 2016, pp. 2729–2748.
- [32] Krysko, V.A., Awrejcewicz, J., Papkova, I.V., Saltykova, O.A., Krysko, A.V. On reliability of chaotic dynamics of two Euler-Bernoulli beams with a small clearance *International Journal of Non-Linear Mechanics*, 2018.

Vadim A. Krysko-jr, PhD student Department of Automation, Biomechanics and Mechatronics, Lodz University of Technology, 1/15 Stefanowskiego Str., 90-924 Lodz, Poland; (vadimakrysko@gmail.com).

Jan Awrejcewicz, Professor: Lodz University of Technology, Faculty of Mechanical Engineering, Department of Automation, Biomechanics and Mechatronics, 1/15 Stefanowskiego Str., 90-924 Lodz, Poland (jan.awrejcewicz@p.lodz.pl);

Irina V. Papkova Associate Professor: Department of Mathematics and Modeling, Saratov State Technical University, Politehnicheskaya 77, 410054 Saratov, Russian Federation (ikravzova@mail.ru);

Ekaterina Yu. Krylova, Associate Professor: Department of Mathematics and Modeling, Saratov State Technical University, Politehnicheskaya 77, 410054 Saratov, Russian Federation (kat.krylova@bk.ru);

An optimal control of the gyroscope system in the process of homing an air-to-air missile

Izabela Krzysztofik, Zbigniew Koruba

Abstract: The accuracy of the homing missile depends mainly on the correct determination of the current angle between the Gyroscope System Axis (GSA) and the Line of Sight (LOS). The automatic control system of the gyroscope system should ensure automatic levelling of this angle, and thus continuous directing of the gyro axis to the straight LOS, i.e. tracking of the target through the seeker. The work presents an optimal control algorithm for the gyroscope with a square quality indicator in the conditions of disturbance and kinematic impact of the missile deck. The results of computer simulation tests were obtained in the Matlab-Simulink environment and presented in a graphic form.

1. Introduction

One of the most important air-to-air missile assemblies is the seeker (homing head) [1, 2]. The seekers that use infrared radiation are most commonly used. The seeker intercepts and tracks the air target. Homing of the missile consists primarily in determining the line of sight of the target being attacked – a straight line leaded from the homing seeker to the target.

The basic element of the seeker is the optical target coordinator. The coordinator's optical system is mounted in the gyroscope rotor suspended on the Cardan joint. During the missile's flight, the task of the target coordinator is to determine the angle between the line of sight and the coordinator axis (axis of the gyroscope system) or its components or angular velocities. This operation is carried out automatically, in such a way that the GS control system constantly directs the optical axis to the moving target. At the moment when the axis of the gyroscope system coincides with the line of sight, then we recognize that the missile tracks the target and follows it. Sensors measure the angle between the LOS and the missile axis and pass it to the autopilot. Autopilot, independently, with its apparatus measures the angular position of the missile axis relative to the Earth, and then determines the control signals and feeds them to the steering actuator [3].

The accuracy of determining the current angle between the axis of the gyroscope system and the line of sight therefore has a huge impact on the precision of homing air-to-air missile on the maneuvering air target, and thus increases the efficiency of intercepting and destroying the target [4]. The gyroscope system is subjected to interactions by the missile deck that do not allow long-term maintenance, with a certain accuracy, of the set position of the optical axis. Therefore, the control

system parameters should be optimally selected so as to minimize the mean square error and the dynamic effects of GS appearing in the transient process [5].

The block diagram of the automatic gyro control adjustment system in the homing process is shown in Figure 1.

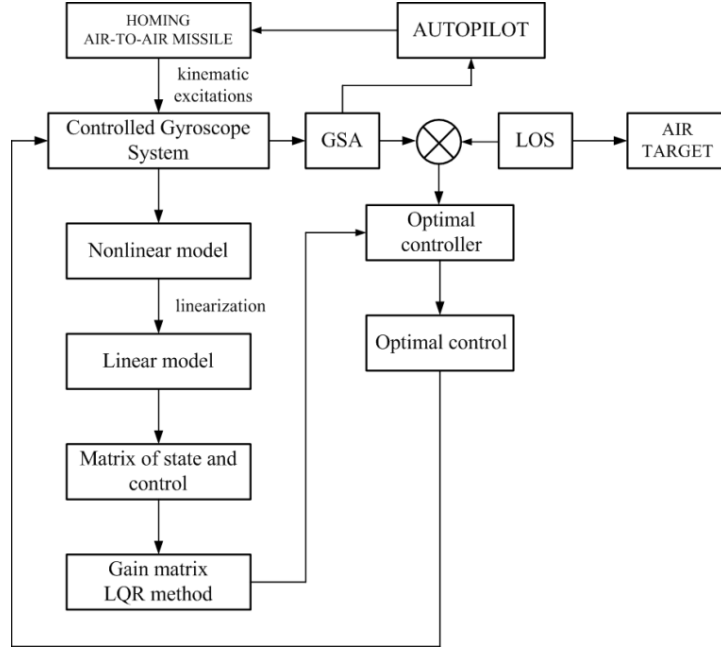


Figure 1. Block diagram of the automatic adjustment system of the gyro system control in the homing process.

This work presents an optimal control algorithm for a gyroscope system with a square quality indicator (minimum error of mean square GSA deviation from LOS) in the conditions of disturbance and kinematic impact of the missile deck. Gain matrices of the optimal controller implementing the developed algorithm were obtained from the Riccati algebraic equation (after linearizing non-linear GS dynamic equations and saving them as state equations).

2. Optimal control of the gyroscope system

A linearized model of a controlled gyroscope system is saved in a vector-matrix form:

$$\frac{dx}{dt} = Ax - Bu \quad (1)$$

where: x – is a vector of state, A – is a state matrix, B – is a control matrix, with components

$$\mathbf{x} = \begin{bmatrix} \vartheta \\ \dot{\vartheta} \\ \psi \\ \dot{\psi} \end{bmatrix}, \mathbf{A} = \begin{bmatrix} 0 & 1 & 0 & 0 \\ 0 & -\eta_b/J_{gk} & 0 & J_{go}n_g/J_{gk} \\ 0 & 0 & 0 & 1 \\ 0 & J_{go}n_g/J_{gk} & 0 & -\eta_c/J_{gk} \end{bmatrix}, \mathbf{B} = \begin{bmatrix} 0 & 0 \\ 1/J_{gk} & 0 \\ 0 & 0 \\ 0 & 1/J_{gk} \end{bmatrix}, \mathbf{u} = \begin{bmatrix} U_b \\ U_c \end{bmatrix}.$$

where: ϑ – inclination angle of GSA, ψ – deflection angle of GSA, $\dot{\vartheta}$ – velocity of inclination angle of GSA, $\dot{\psi}$ – velocity of deflection angle of GSA, η_b – friction coefficient in GS inner frame bearings, η_c – friction coefficient in GS outer frame bearings, J_{gk} – moment of inertia of the GS rotor relative to the transverse axis, J_{go} – moment of inertia of the GS rotor relative to the longitudinal axis, U_b – control moment applied to the GS inner frame, U_c – control moment applied to the GS outer frame.

Let the square quality indicator will be given in the form of:

$$J = \int_0^\infty (\mathbf{x}^T \mathbf{Q} \mathbf{x} + \mathbf{u}^T \mathbf{R} \mathbf{u}) dt \quad (2)$$

where: \mathbf{Q}, \mathbf{R} – weight matrices experimentally matched.

Let us present the control law as follows:

$$\mathbf{u} = -\mathbf{K}(\mathbf{x} - \mathbf{x}_z) \quad (3)$$

where: \mathbf{x}_z – is a vector of set state variables with components $\mathbf{x}_z = [\varepsilon \quad \dot{\varepsilon} \quad \sigma \quad \dot{\sigma}]$ determined from equations (7)–(10).

The \mathbf{K} gain matrix is determined by the following relationship:

$$\mathbf{K} = \mathbf{R}^{-1} \mathbf{B}^T \mathbf{P} \quad (4)$$

In the work, matrix \mathbf{K} was determined using the Matlaba *lqr* function:

$$\mathbf{K} = \text{lqr}(\mathbf{A}, \mathbf{B}, \mathbf{Q}, \mathbf{R}) \quad (5)$$

The \mathbf{P} matrix in equation (4) is determined from the algebraic Riccati equation:

$$\mathbf{A}^T \mathbf{P} + \mathbf{P} \mathbf{A} - \mathbf{P} \mathbf{B} \mathbf{R}^{-1} \mathbf{B}^T \mathbf{P} + \mathbf{Q} = 0 \quad (6)$$

The ε, σ angles occurring in relationship (3) are set angles for the control system when tracking a detected target and are determined from the following system of equations describing the relative positions of the air target and the missile [6-8]:

$$\frac{dr}{dt} = V_c [\cos \chi_c \cos \sigma \cos(\varepsilon - \gamma_c) + \sin \chi_c \sin \sigma] - V_p [\cos \chi \cos \sigma \cos(\varepsilon - \gamma) + \sin \chi \sin \sigma] \quad (7)$$

$$-r \frac{d\varepsilon}{dt} \cos \sigma = V_c \cos \chi_c \cos(\varepsilon - \gamma_c) - V_p \cos \chi \cos \sigma \cos(\varepsilon - \gamma) \quad (8)$$

$$-r \frac{d\sigma}{dt} = V_c [\cos \chi_c \sin \sigma \cos(\varepsilon - \gamma_c) - \sin \chi_c \cos \sigma] - V_p [\cos \chi \sin \sigma \cos(\varepsilon - \gamma) - \sin \chi \cos \sigma] \quad (9)$$

where:

r – the distance between missile and air target;

ε – LOS inclination angle;

σ – LOS deflection angle;

V_p, V_c – missile and target velocities;

χ_c, γ_c – yaw and pitch angles of the target velocity;

χ_p, γ_p – yaw and pitch angles of the missile velocity.

The figure below shows the scheme of determining the optimal controls for the gyroscope system in the homing head of an air-to-air class anti-aircraft missile.

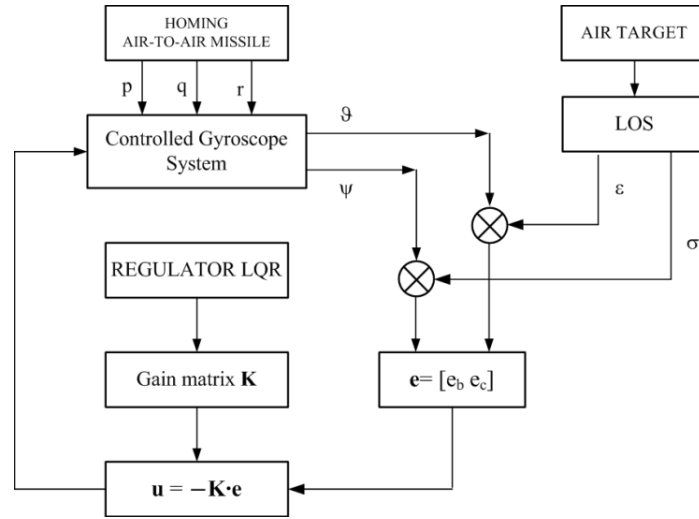


Figure 2. Scheme determining the optimal controls.

In the approaching process, the advance angle changes according to the proportional navigation algorithm:

$$\dot{\gamma} = a_1 \dot{\vartheta}, \dot{\chi} = a_2 \dot{\psi} \quad (10)$$

where: a_1, a_2 – constants of proportional navigation.

3. Results of numerical research of gyroscope system control

Simulation studies of gyroscope system control in the process of air-to-air missile homing to the manoeuvring target were conducted in Matlab/Simulink [9, 10], using *ode45* procedure with a variable integration step, for the following parameters [11]:

Initial parameters of the target and missile

$$X_c = 1500 \text{ m}; Y_c = 500 \text{ m}; Z_c = 350 \text{ m}; V_c = 200 \text{ m/s};$$

$$\gamma_c = 0.0 \text{ rad}; \chi_c = 0.0 \text{ rad}; \Omega_c = 0.15 \text{ rad/s};$$

$$X_p = 1000 \text{ m}; Y_p = 500 \text{ m}; Z_p = 100 \text{ m}; V_p = 50 \text{ m/s}.$$

Maximum value thrust of the rocket engine

$$P_{max} = 1500 \text{ N}$$

Permissible value control force

$$Q_{max} = 1000 \text{ N}$$

Constants value of proportional navigation

$$a_1 = a_2 = 3.5$$

Parameters of the gyroscope system

$$J_{go} = 5 \cdot 10^{-4} \text{ kgm}^2; J_{gk} = 2.5 \cdot 10^{-4} \text{ kgm}^2; n_g = 600 \text{ rad/s}; \eta_b = \eta_c = 0.01 \text{ Nm/s.}$$

LQR parameters

$$Q = \begin{bmatrix} 10 & 0 & 0 & 0 \\ 0 & 100 & 0 & 0 \\ 0 & 0 & 10 & 0 \\ 0 & 0 & 0 & 100 \end{bmatrix}; R = \begin{bmatrix} 5 & 0 \\ 0 & 5 \end{bmatrix}$$

Disturbances p, q, r acting on the gyroscope system from the missile deck were angular velocities about the longitudinal x and transverse y axes, z – respectively.

Figures (3) – (10) show selected results of simulation tests. Figure 3 shows that a missile intercepts a maneuvering air target after a time of 5.3 seconds. Figures 4 and 5 show a good convergence of the angles of flight desired and realized. The same is true of the coincidence of the gyroscope axis with the target line of sight – Figs. 6, 9 and 10.

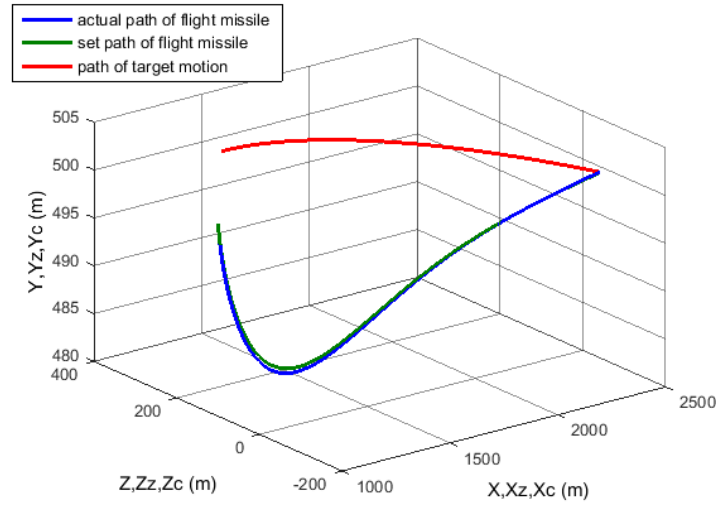


Figure 3. Path-flights of the missile and target.

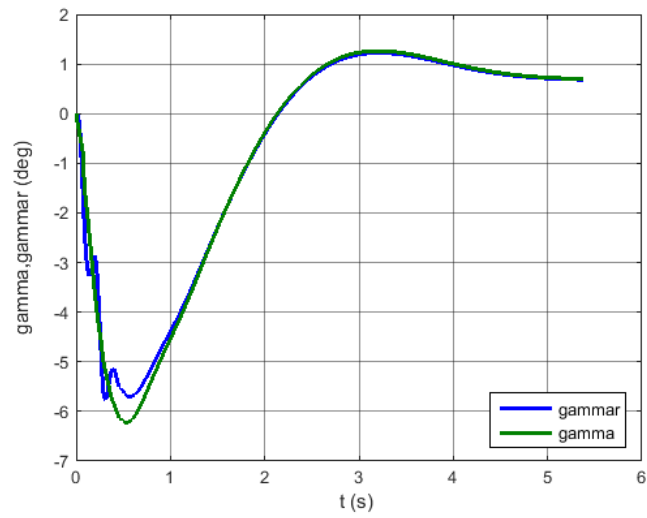


Figure 4. Actual γ_r and set γ angles of missile flight as a function of time.

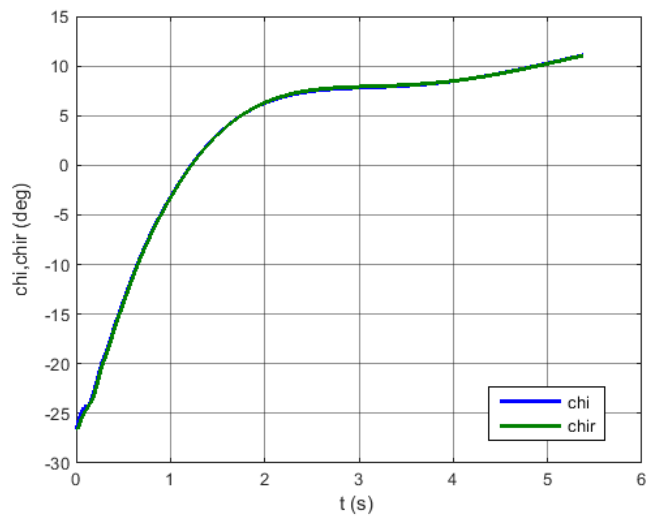


Figure 5. Actual χ_r and set χ angles of missile flight as a function of time.

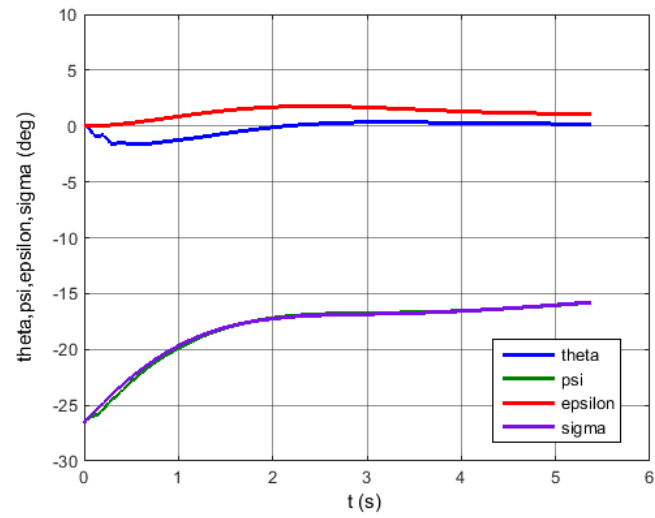


Figure 6. Angles of inclination and deflection of the LOS and gyroscope axis as a function of time.

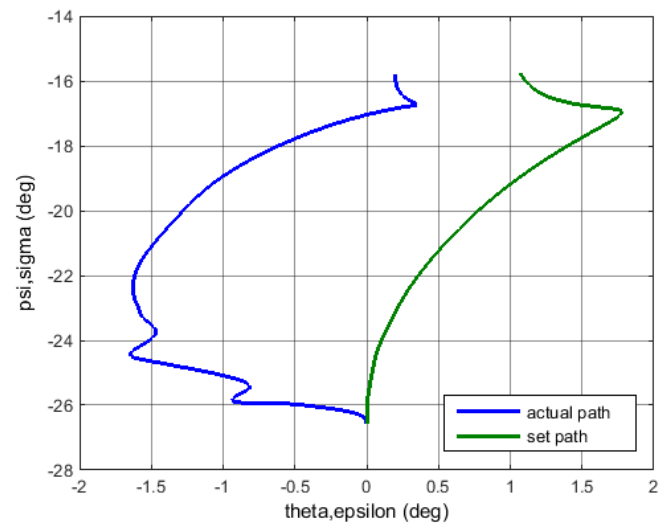


Figure 7. Actual and set paths of the gyroscope system axis.

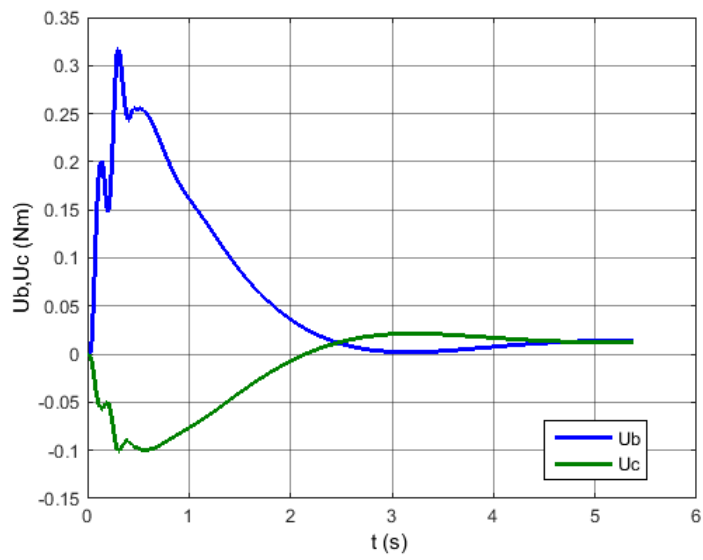


Figure 8. Control moments as a function of time.

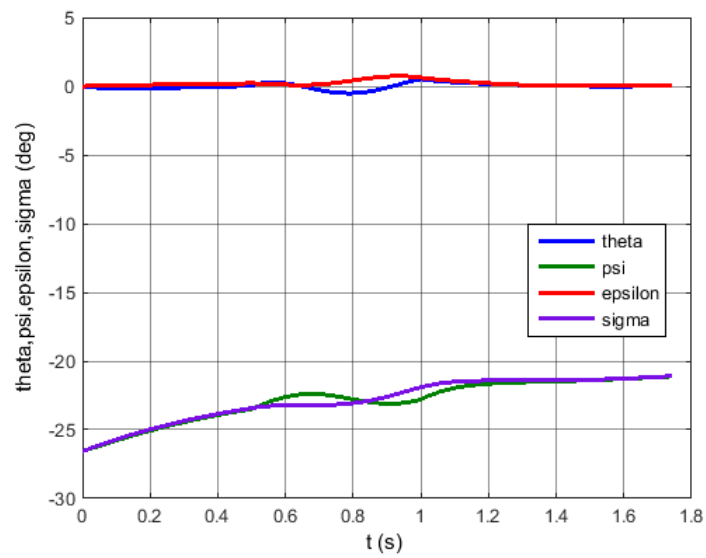


Figure 9. Angles of inclination and deflection of the LOS and gyroscope axis as a function of time.

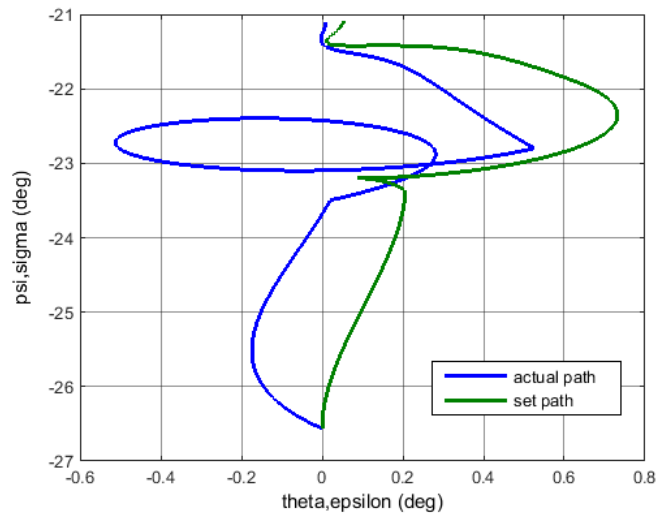


Figure 10. Actual and set paths of gyroscope system axis.

4. Conclusions

The optimal control algorithm presented in the paper demonstrates high effectiveness of gyroscope system control in the process of guiding air-to-air missile to a moving target. Optimal parameters of the regulator allow for stable and continuous maintenance of the target in the field of view of the homing head's optical system (Figs. 6 and 9). This can be particularly important when the target is detected with a significant angular deviation of the missile's longitudinal axis from the target line of sight. It should be emphasised that the control moments are small (Fig. 8), which determines their feasibility under real homing conditions. The optimal gyroscope system controller also operates stable under the influence of missile deck disturbance (Fig. 10).

References

- [1] Zarchan P. *Tactical and Strategic Missile Guidance*. AiAA Inc., Reston, 2012.
- [2] Balakrishnan S. N., Tsourdos A., and White B. A. *Advances in Missile Guidance, Control, and Estimation*. CRC Press Taylor&Francis Group, Boca Raton, 2013.
- [3] Grzyb, M. and Stefański, K. The use of special algorithm to control the flight of anti-aircraft missile. In: *Proceedings of 22th International Conference Engineering Mechanics 2016* (eds. Zolotarev, I. and Radolf, V.), Institute Thermomechanics, Academy Science Czech Republic, Prague, (2016), 174-177.
- [4] Krzysztofik, I., Takosoglu, J. and Koruba Z. Selected methods of control of the scanning and tracking gyroscope system mounted on a combat vehicle. *Annual Reviews in Control* 44, (2017), 173-182.

- [5] Koruba, Z. and Krzysztofik, I. An algorithm for selecting optimal controls to determine the estimators of the coefficients of a mathematical model for the dynamics of a self-propelled anti-aircraft missile system. *Proceedings of the Institution of Mechanical Engineers, Part K: Journal of Multi-Body Dynamics* 227, (2013), 12-16.
- [6] Koruba, Z., Krzysztofik, I. and Dziopa, Z. An analysis of the gyroscope dynamics of an anti-aircraft missile launched from a mobile platform. *Bulletin of the Polish Academy of Sciences: Technical Sciences* 58, (2010), 651-656.
- [7] Koruba, Z. and Ładyżyńska-Kozdraś, E. The dynamic model of a combat target homing system of an unmanned aerial vehicle. *Journal of Theoretical and Applied Mechanics* 48, (2010), 551-566.
- [8] Krzysztofik, I. and Koruba, Z. Mathematical Model of Movement of the Observation and Tracking Head of an Unmanned Aerial Vehicle Performing Ground Target Search and Tracking. *Journal of Applied Mathematics* 2014, (2014), Article ID 934250, 11 pages.
- [9] Lewis, F. L., Vrabie, D. L. and Syrmos, V. L. *Optimal Control*. John Wiley & Sons, Hoboken, 2012.
- [10] Tewari, A. *Modern Control Design with MATLAB and SIMULINK*. John Wiley & Sons, Chichester, 2002.
- [11] Baranowski, L. Effect of the mathematical model and integration step on the accuracy of the results of computation of artillery projectile flight parameters. *Bulletin of the Polish Academy of Sciences: Technical Sciences* 61, (2013), 475-484.
- Izabela Krzysztofik, Dr habil. Eng: Department of Applied Computer Science and Armament Engineering, Kielce University of Technology, 7 Al. Tysiąclecia PP St., 25-314 Kielce, Poland (pssik@tu.kielce.pl).
- Zbigniew Koruba, Professor: Department of Applied Computer Science and Armament Engineering, Kielce University of Technology, 7 Al. Tysiąclecia PP St., 25-314 Kielce, Poland (ksmzko@tu.kielce.pl). The author gave a presentation of this paper during one of the conference sessions.

Discrete-time model reference sliding mode control using an exponential reaching law

Paweł Latosiński, Andrzej Bartoszewicz

Abstract: Discrete time reaching law based sliding mode control is well known to ensure good robustness of the controlled system with respect to any bounded uncertainties. In principle, reaching law methodology involves *a priori* specifying the desired evolution of the system representative point and obtaining a control signal which ensures this evolution. However, since the plant is subject to uncertainties at each time instant, the desired state trajectory specified by the reaching law can get gradually distorted during the control process. This in turn can negatively alter the length of the reaching phase or increase quasi-sliding mode band width. Motivated by this problem, in this paper we describe a novel model reference approach to discrete-time sliding mode controller design. In this approach, a reaching law based control strategy is first applied to a reference model of the plant with the aim of obtaining a desirable state trajectory. Then, a secondary controller is applied to the original plant to drive its state alongside that of the model, thus eliminating the residual effect of disturbance on quasi-sliding motion of the system. In particular, in this paper a non-switching reaching law using an exponential function of the sliding variable has been applied to the model with the aim of obtaining favorable properties of its quasi-sliding motion. It has been demonstrated that, with the use of the proposed model reference approach, these properties are then carried over to the original plant even in the continued presence of uncertainties.

1. Introduction

Discrete-time sliding mode control (DSMC) strategies [11, 15] are a computationally efficient way of ensuring good system performance in the presence of nonlinear uncertainties. Their highly valued robustness property is obtained by confining the system representative point to a vicinity of the sliding hyperplane defined in the state space. Contrary to its older continuous-time equivalent [7, 14], DSMC can effectively compensate for both matched and non-matched uncertainties. Such strategies are conventionally designed by first stating the control law and then proving, via Lyapunov's theorem, that it ensures stability of the sliding motion. However, a more recent approach [9] instead involves defining the desired evolution of the sliding variable in advance and then applying this evolution to synthesize the control signal, therefore omitting the non-trivial proof of stability. This method, referred to as the

reaching law approach, has gained significant recognition in the field of DSMC [1, 6, 8, 10, 12, 13].

An often overlooked downside of reaching law-based DSMC is the fact that the *a priori* specified evolution of the sliding variable gets gradually distorted by uncertainties during the control process. Indeed, since the reaching law specifies values of the sliding variable on a step-by-step basis, residual effect of past disturbances can delay system response or deteriorate its robustness. A very recent approach using a reference model of the controlled plant [4] aims to remedy that problem by eliminating the effect of past uncertainties on sliding motion of the system. Authors of that work have proposed the application of a DSMC strategy (in particular Gao's reaching law [9]) to a reference model of the plant in order to obtain its desired trajectory, and then drive the original system alongside that trajectory using a secondary controller.

In our paper we describe model reference DSMC methodology in a tutorial manner and propose an application of this scheme in conjunction with an exponential reaching law. It is demonstrated that the proposed strategy ensures better robustness of the system than the traditional reaching law approach and ensures that the *a priori* specified evolution of the sliding variable is followed much more closely. In particular, the reaching law applied in our paper ensures an upper bounded, almost constant convergence rate of system representative point to the vicinity of the sliding hyperplane. Furthermore, contrary to the reaching law used in [4], model reference strategy described in this paper ensures non-switching type quasi-sliding motion as defined in [2, 3] rather than conventional switching type discrete-time motion [9]. As a result, our approach produces no chattering in the sliding phase.

2. Model reference strategy

In our paper we consider discrete-time dynamical plants subject to nonlinear disturbance that does not satisfy matching conditions. These conditions state that the uncertainties affect the plant through the same input channel as the control signal and have traditionally been used to ensure good qualities of system sliding motion, but this assumption is not necessary in our work. Dynamics of the considered plants can be expressed as

$$\mathbf{x}_p(k+1) = \mathbf{A}\mathbf{x}_p(k) + \mathbf{b}u_p(k) + \mathbf{d}(k), \quad (1)$$

where $\mathbf{x}_p \in \mathbf{R}^n$ and $u_p \in \mathbf{R}$ represent the system state and the control signal, respectively, the "p" subscript refers to the plant, $\mathbf{d}(k) \in \mathbf{R}^n$ is a vector representing the non-matched disturbance, $\mathbf{A} \in \mathbf{R}^{n \times n}$ is the state matrix and $\mathbf{b} \in \mathbf{R}^n$ is the input distribution vector. The objective of the control process is to drive the state of this plant to a desired \mathbf{x}_d and it is assumed its initial conditions $\mathbf{x}_p(0)$ are known. In our paper a novel model reference sliding

mode control strategy will be applied to such plants. In this approach the following model of the plant is first specified

$$\mathbf{x}_m(k+1) = \mathbf{A}\mathbf{x}_m(k) + \mathbf{b}u_m(k), \quad (2)$$

where the "m" subscript refers to the model, \mathbf{A} and \mathbf{b} are the same as in (1) and $\mathbf{x}_m(0) = \mathbf{x}_p(0)$. Two separate sliding mode controllers will be designed for plant (1) and model (2), respectively. First, a desired evolution of the model state will be obtained with the use of reaching law approach. Then, a simple dead-beat controller will be applied to the original plant with the aim of driving its state towards that of the model. The design process of both controllers begins with defining an appropriate sliding variable and the hyperplane on which this variable equals zero. The considered variables and their corresponding sliding hyperplanes are expressed as

$$\sigma_*(k) = \mathbf{e}_*(k) = \mathbf{c}^T \mathbf{x}_d - \mathbf{c}^T \mathbf{x}_*(k) = 0, \quad (3)$$

where the "*" subscript refers to either plant p or model m , $\mathbf{e}_* \in \mathbf{R}^n$ is the state error and vector $\mathbf{c} \in \mathbf{R}^n$ is selected to guarantee stability of the system. To that end, it must ensure that $\mathbf{c}^T \mathbf{b} \neq 0$ and that all eigenvalues of the closed-loop system state matrix $\mathbf{A}_{cl} = \mathbf{A} - \mathbf{b}(\mathbf{c}^T \mathbf{b})^{-1} \mathbf{c}^T \mathbf{A}$ are inside the unit circle. In order to make the considered strategy applicable to plant (1) it is assumed that total effect of the unpredictable disturbance on sliding variable σ_p is limited. In particular, let this effect be lower and upper bounded in the following way

$$D_{\min} \leq D(k) = \mathbf{c}^T \mathbf{d}(k) \leq D_{\max}. \quad (4)$$

We can then define the mean effect D_1 of this disturbance and its maximum deviation from the mean D_2 in the following way

$$D_1 = \frac{D_{\max} + D_{\min}}{2}, \quad D_2 = \frac{D_{\max} - D_{\min}}{2}. \quad (5)$$

Further in this section a general form of the considered model reference strategy will be discussed. Then, in the next section an example application of this control scheme using a particular reaching law will be described.

2.1. Reaching law applied to the model

In order to obtain a desired model trajectory, a reaching law based control strategy is first applied to design control signal u_m . When using the reaching law approach, target evolution of the sliding variable is defined in advance with a recursive function, and then a control

signal which ensures this evolution is calculated. Reaching law for model (2) has the following general form

$$\sigma_m(k+1) = f[\sigma_m(k), k], \quad (6)$$

where f is a function selected so that stability of the sliding motion is ensured. Since $\sigma_m(0)$ is known and model (2) is free of uncertainties, this function will always define exact subsequent values of the sliding variable. Choice of this function has a direct impact on properties of the system such as its robustness or convergence rate to the sliding hyperplane. In order to obtain control signal u_m which ensures the state evolution defined by (6), sliding variable σ_m is first substituted from (3) into the left hand side of (6), which yields

$$\mathbf{c}^T \mathbf{x}_d - \mathbf{c}^T \mathbf{x}_m(k+1) = f[\sigma_m(k), k]. \quad (7)$$

Then, model dynamics (2) are further substituted into (7), giving

$$\mathbf{c}^T \mathbf{x}_d - \mathbf{c}^T \mathbf{A} \mathbf{x}_m(k) - \mathbf{c}^T \mathbf{b} u_m(k) = f[\sigma_m(k), k]. \quad (8)$$

Finally, relation (8) is solved for u_m , which gives the desired control signal

$$u_m(k) = (\mathbf{c}^T \mathbf{b})^{-1} \{ \mathbf{c}^T \mathbf{x}_d - \mathbf{c}^T \mathbf{A} \mathbf{x}_m(k) - f[\sigma_m(k), k] \}, \quad (9)$$

which drives the output of the model exactly as specified in reaching law (6). In the next section a second controller will be designed with the aim of driving the state of the plant alongside the obtained trajectory of the model.

It should be noted that, since the considered reference model is free of uncertainties, exact evolution of its state can be obtained for any k knowing only the initial conditions of the system. Thus, it is possible to calculate values for $\sigma_m(k)$ ahead of time and store them in a look-up table if one wishes to enhance computational efficiency of the control strategy.

2.2. Control strategy for the plant

Typically, reaching law based strategies similar to (6) are applied directly to the considered plant subject to uncertainties. However, since control signal (9) itself cannot compensate for disturbance in any way, this would cause the desired state trajectory to get gradually distorted in each step. To prevent this, we instead propose a secondary control signal for the original plant which aims to drive its state alongside that of the model. This control signal originates from the simple reaching law

$$\sigma_p(k+1) = \sigma_m(k+1) - D(k) + D_1. \quad (10)$$

It should be noted that this reaching law depends on the unpredictable disturbance and, as a result, does not specify exact values of σ_p in each step but merely the range of its possible values. Nevertheless, it can be applied to design control signal u_p by first substituting sliding variable (3) and system dynamics (1) into the left hand side of (10). This gives

$$\mathbf{c}^T \mathbf{x}_d - \mathbf{c}^T \mathbf{A} \mathbf{x}_p(k) - \mathbf{c}^T \mathbf{b} u_p(k) - \mathbf{c}^T \mathbf{d}(k) = \sigma_m(k+1) - D(k) + D_1. \quad (11)$$

Considering (4), one can solve this equation for u_p and get the control signal

$$u_p(k) = (\mathbf{c}^T \mathbf{b})^{-1} \{ \mathbf{c}^T \mathbf{x}_d - \mathbf{c}^T \mathbf{A} \mathbf{x}_p(k) - \sigma_m(k+1) - D_1 \}. \quad (12)$$

This control signal ensures that output of the original plant will always closely follow the trajectory obtained from the model. Indeed, as seen in reaching law (10), sliding variable σ_p can only deviate from σ_m by a value proportional to the single most recent disturbance term. This property will be formally described in the following theorem.

Theorem 1 *If the control signal for plant (1) is defined by (12), then for all $k > 0$ the absolute difference between $\sigma_p(k)$ and $\sigma_m(k)$ is not greater than D_2 .*

Proof: For any k reaching law (10) implies

$$|\sigma_p(k+1) - \sigma_m(k+1)| = |\sigma_m(k+1) - D(k) + D_1 - \sigma_m(k+1)|. \quad (13)$$

Then, since relations (4) and (5) give $|D(k) - D_1| \leq D_2$ for all k , (13) further gives

$$|\sigma_p(k+1) - \sigma_m(k+1)| = |-D(k) + D_1| \leq D_2. \quad (14)$$

Thus, for any time instant after 0 the difference between $\sigma_p(k)$ and $\sigma_m(k)$ is lower and upper bounded by D_2 . ■

It has been shown that, with the use of the proposed model reference scheme, output of the plant always closely follows that of the model. This is an important property since it means that system robustness ensured by reaching law (6) for the reference model is carried over to the original plant even in the presence of non-matched disturbance. Theorem 1 allows one to draw an additional conclusion on the convergence rate of the sliding variable to zero, which will be outlined below.

Theorem 2 *If the control signal for plant (1) is defined by (12), then for all $k > 0$*

$$|\sigma_p(k+1) - \sigma_p(k)| \leq |\sigma_m(k+1) - \sigma_m(k)| + 2D_2. \quad (15)$$

Proof: It is easy to notice from properties of the absolute value that

$$\begin{aligned} |\sigma_p(k+1) - \sigma_p(k)| &= |\sigma_p(k+1) - \sigma_m(k+1) + \sigma_m(k+1) - \sigma_m(k) + \sigma_m(k) - \sigma_p(k)| \\ &\leq |\sigma_p(k+1) - \sigma_m(k+1)| + |\sigma_m(k+1) - \sigma_m(k)| + |\sigma_m(k) - \sigma_p(k)|. \end{aligned} \quad (16)$$

Then, for any $k > 0$ Theorem 1 further implies

$$|\sigma_p(k+1) - \sigma_p(k)| \leq D_2 + |\sigma_m(k+1) - \sigma_m(k)| + D_2, \quad (17)$$

which is consistent with relation (15). ■

It has been shown that the proposed model reference approach ensures a similar convergence rate of the system representative point to zero as the reaching law applied to the model. In conclusion, Theorems 1 and 2 show that all significant properties of the reaching law applied to the model are carried over to the original plant. In the next section an example application of this control scheme using an exponential reaching law will be proposed. Then, the effectiveness of the new method will be verified in a simulation.

3. Exponential reaching law

In this paper the model reference control scheme proposed in this paper will be used in conjunction with an exponential reaching law first introduced in [5]. This reaching law aims to ensure a limited, almost constant convergence rate of the system representative point to the sliding hyperplane, confine this representative point to a narrow vicinity of the hyperplane and prevent unnecessary switching in the sliding phase to avoid excessive chattering. For the disturbance-free model (2) this reaching law has the following form

$$\sigma_m(k+1) = \sigma_m(k) - \sigma_0 \text{sgn}[\sigma_m(k)]g[\sigma_m(k)], \quad (18)$$

where $\sigma_0 > 0$ is a constant design parameter, function

$$g(\star) = 1 - \exp\left[-\frac{(\star)^2}{\sigma_0^2}\right] \quad (19)$$

and $\text{sgn}(\star)$ is specified so that $\text{sgn}(0) = 0$. According to relation (9) control signal for the reference model is expressed as

$$u_m(k) = (\mathbf{c}^T \mathbf{b})^{-1} \{ \mathbf{c}^T \mathbf{x}_d - \mathbf{c}^T \mathbf{A} \mathbf{x}_m(k) - \sigma_m(k) + \sigma_0 \text{sgn}[\sigma_m(k)]g[\sigma_m(k)] \}. \quad (20)$$

It can be seen that for large values of σ_m reaching law (18) will cause the sliding variable to decrease by a value close to σ_0 in the next step, providing an almost constant convergence

rate to the vicinity of zero in the reaching phase. On the other hand, as σ_m gets closer to zero, function g causes the value of the switching term to diminish, which prevents generating excessive control signals in the sliding phase.

Reaching law based strategy (20) allows one to obtain favorable properties of the sliding motion for the reference model of the plant. Then, reaching law (10) can be used to carry over these properties to the original plant, exactly as described in Section 2.2. Properties of the proposed model reference strategy with reaching law (18) will be discussed in greater detail in the next section.

3.1. Properties of the proposed strategy

Exact properties of system sliding motion with the use of the proposed model reference strategy with exponential reaching law will now be formulated and proven. In the first theorem it will be demonstrated that the proposed strategy always ensures limited sliding variable rate of change.

Theorem 3 *If the control signal for plant (1) is defined by (12) and values of σ_m are obtained from reaching law (18), then for any $k \geq 0$ sliding variable rate of change satisfies*

$$|\sigma_p(k+1) - \sigma_p(k)| \leq \sigma_0 + 2D_2. \quad (21)$$

Proof: Since function g defined as (19) is always upper bounded by 1, then for sliding variable σ_m reaching law (18) implies

$$|\sigma_m(k+1) - \sigma_m(k)| = |-\sigma_0 \text{sgn}[\sigma_m(k)]g[\sigma_m(k)]| \leq \sigma_0. \quad (22)$$

Then, directly from Theorem 2 we obtain

$$|\sigma_p(k+1) - \sigma_p(k)| \leq |\sigma_m(k+1) - \sigma_m(k)| + 2D_2 \leq \sigma_0 + 2D_2, \quad (23)$$

which is consistent with (21). ■

Next, it will be shown that the proposed model reference scheme always drives the system representative point to a specified quasi-sliding mode band around the switching hyperplane.

Theorem 4 *If the control signal for plant (1) is defined by (12) and values of $\sigma_m(k)$ are obtained from reaching law (18), then for any initial conditions of the system, its representative point is at least asymptotically driven to the following band around the sliding hyperplane*

$$\left\{ \mathbf{x}_p : |\mathbf{c}^T \mathbf{x}_d - \mathbf{c}^T \mathbf{x}_p| \leq D_2 \right\}. \quad (24)$$

Proof: It will first be shown that reaching law (18) always ensures asymptotic convergence of $\sigma_m(k)$ to zero. Let k be any time instant for which $\sigma_m(k) > 0$. To simplify notation, we temporarily substitute $s = \sigma_m(k)$. Then, relations (18) and (19) imply

$$\sigma_m(k+1) = f(s) = s - \sigma_0 \left\{ 1 - \exp \left[-\frac{s^2}{\sigma_0^2} \right] \right\} < s = \sigma_m(k), \quad (25)$$

which means the sliding variable will decrease in the next step. It will be further shown that $\sigma_m(k+1)$ cannot become negative. Relation (25) gives

$$\frac{d}{ds} f(s) = 1 - \frac{2s}{\sigma_0} \exp \left[-\frac{s^2}{\sigma_0^2} \right], \quad (26)$$

$$\frac{d^2}{ds^2} f(s) = -\frac{2(\sigma_0^2 - 2s^2)}{\sigma_0^3} \exp \left[-\frac{s^2}{\sigma_0^2} \right]. \quad (27)$$

It is easy to notice that the formula (27) has exactly one zero for positive values of s , namely $\sigma_0/\sqrt{2}$. Change of sign from negative to positive around this zero implies that (26) has a global minimum in this point, which equals

$$\frac{d}{ds} f(\sigma_0/\sqrt{2}) = 1 - \frac{2}{\sqrt{2}} \exp \left(-\frac{1}{2} \right) \approx 0.142 > 0. \quad (28)$$

Since the minimum is positive, one concludes that the first derivative of $f(s)$ is always greater than zero for $s > 0$, which further implies that $f(s)$ itself is a strictly increasing function. Thus, for any $s > 0$ relation (25) gives

$$\sigma_m(k+1) > f(0) = 0 - \sigma_0 [1 - \exp(0)] = 0, \quad (29)$$

which means that $\sigma_m(k+1)$ will never become negative. Since relations (25) and (29) show that sliding variable $\sigma_m(k)$ always decreases but never changes its sign to negative, it must converge to a certain non-negative σ_+ . Naturally, $\sigma_m(k+1)$ also converges to the same value. Consequently, reaching law (18) implies

$$\sigma_+ = \lim_{k \rightarrow \infty} \sigma_m(k+1) = \lim_{k \rightarrow \infty} \{ \sigma_m(k) - \sigma_0 g[\sigma_m(k)] \} = \sigma_+ - \sigma_0 g(\sigma_+). \quad (30)$$

Taking into account (19), relation (30) further gives

$$\sigma_+ - \sigma_0 \left\{ 1 - \exp \left[-\frac{\sigma_+^2}{\sigma_0^2} \right] \right\} - \sigma_+ = 0, \quad (31)$$

which ultimately yields $\sigma_+ = 0$. We conclude that for any initial conditions of the system such that $\sigma_m(0) > 0$ sliding variable σ_m always asymptotically converges to zero. Proof of the same property for initial conditions such that $\sigma_m < 0$ is almost identical to the analysis given in (25)-(31), which is why it will be omitted.

It will now be demonstrated that the representative point of the actual plant always at least asymptotically converges to band (24). Since $\sigma_m(k)$ converges to zero, Theorem 1 implies

$$\lim_{k \rightarrow \infty} |\sigma_p(k)| = \lim_{k \rightarrow \infty} |\mathbf{c}^T \mathbf{x}_d - \mathbf{c}^T \mathbf{x}_p| \leq \lim_{k \rightarrow \infty} |\sigma_m(k)| + D_2 = D_2, \quad (32)$$

which means that the system representative point will either enter the considered quasi-sliding mode band in finite time or approach it asymptotically. ■

It has been proven that the proposed model reference control scheme using exponential reaching law (18) at least asymptotically drives the state of the plant to a narrow vicinity of the sliding hyperplane while at the same time ensuring an upper bounded convergence rate to this vicinity. The band obtained in Theorem 4 is strictly narrower than the one obtained in [5] for reaching law (18) without the use of reference model. This implies that the proposed model reference scheme improves robustness of the plant with respect to disturbance while still ensuring all desirable qualities of system sliding motion. In the next section, the new approach will be compared to an existing control strategy in a simulation example.

4. Simulation results

In this section the proposed model reference strategy will be compared to conventional reaching law approach by means of a simulation. In particular, in this example we consider a fourth-order discrete-time plant with dynamics expressed as

$$\mathbf{x}_p(k+1) = \begin{bmatrix} 1 & 1 & 1/2 & 1/6 \\ 0 & 1 & 1 & 1/2 \\ 0 & 0 & 1 & 1 \\ 0 & 0 & 0 & 1 \end{bmatrix} \mathbf{x}_p(k) + \begin{bmatrix} 1/24 \\ 1/6 \\ 1/2 \\ 1 \end{bmatrix} u_p(k) + \begin{bmatrix} d_1(k) \\ 0 \\ 0 \\ 0 \end{bmatrix} \quad (33)$$

with initial conditions $\mathbf{x}_p(0) = [20 \ 0 \ 0 \ 0]^T$. The objective is to drive the representative point of the system to $\mathbf{x}_d = \mathbf{0}$ in the presence of non-matched disturbance, where $d_1(k) = \sin(k\pi/10)$. To that end, two strategies will be used.

- A) Conventional reaching law approach using strategy (18) originally proposed in [5].
 - B) Our model reference scheme, in which the same reaching law is applied to the model (2).
- For both strategies we select $\sigma_0 = 2$ and $\mathbf{c} = [1 \ 1.5 \ 0.9167 \ 0.25]$. The three figures presented below illustrate the comparison of both strategies. They include comparisons of the sliding variable, the control signal and the first state variable, respectively.

It can be seen from Figure 1 that the proposed model reference strategy ensures an almost constant convergence rate of sliding variable to zero, consistent with the selected

design parameter $\sigma_0 = 2$. Meanwhile, evolution of the variable for strategy B without the reference model is distorted in the reaching phase and convergence to zero is delayed. At the same time, our strategy drives the variable to a narrower quasi-sliding mode band, the width of which is consistent with Theorem 4. Figure 2 illustrates that both strategies generate similar values of the control signal in the initial stages of the control process, but strategy A requires significantly less control effort in the sliding mode. Finally, Figure 3 demonstrates that the proposed model reference strategy ensures faster convergence of the first state variable to its target value and its smaller error in all stages of the control process.

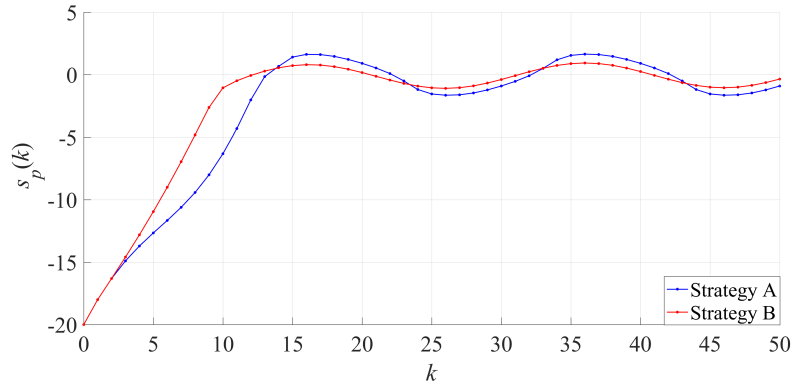


Figure 1. Sliding variable

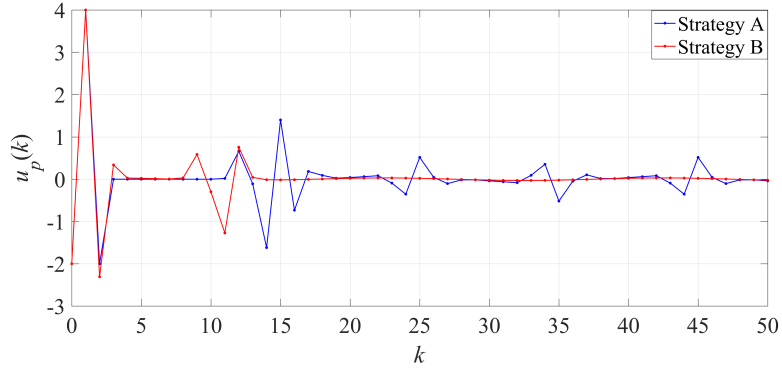


Figure 2. Control signal

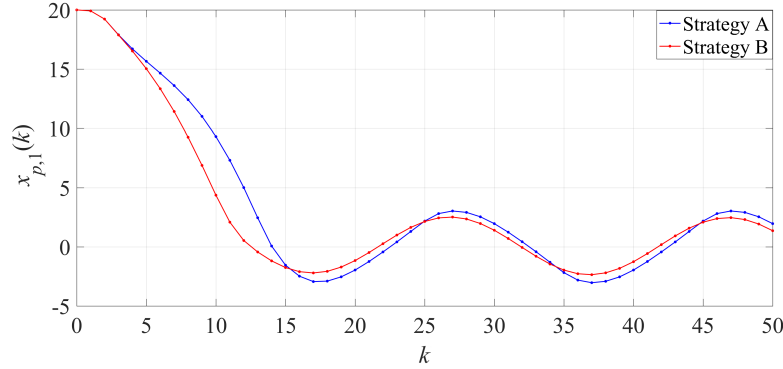


Figure 3. First state variable

5. Conclusions

In our paper we have described a novel model reference sliding mode control strategy for discrete-time systems. In this strategy, a reaching law based controller is first applied to the reference model of the plant with the aim of obtaining the desired state trajectory, then the state of this plant is driven along that trajectory with a secondary controller. In particular, in our paper this desired trajectory has been obtained with an exponential reaching law, which ensures a bounded convergence rate of the system representative point to the sliding hyperplane, good robustness of the plant and no undesirable chattering. It has been demonstrated that the model reference control scheme allows one to improve robustness of the plant by completely rejecting the effect of past uncertainties on its sliding motion. Indeed, it has been shown that when the proposed strategy is applied to the plant, its evolution more closely follows the one specified in the reaching law.

Acknowledgment

Paweł Latosiński gratefully acknowledges financial support provided by the Foundation for Polish Science (FNP).

References

- [1] BANDYOPADHYAY, B., AND FULWANI, D. High-performance tracking controller for discrete plant using nonlinear sliding surface. *IEEE Transactions on Industrial Electronics* 56, 9 (2009), 3628–3637.
- [2] BARTOLINI, G., FERRARA, A., AND UTKIN, V. Adaptive sliding mode control in discrete-time systems. *Automatica* 31, 5 (1995), 769–773.
- [3] BARTOSZEWICZ, A. Discrete time quasi-sliding mode control strategies. *IEEE Trans-*

actions on Industrial Electronics 45, 4 (1998), 633–637.

- [4] BARTOSZEWICZ, A., AND ADAMIAK, K. Model reference discrete-time variable structure control. *International Journal of Adaptive Control and Signal Processing* 32 (2018), 1440–1452.
- [5] BARTOSZEWICZ, A., AND LATOSIŃSKI, P. Sliding mode congestion controller for data transmission networks with unknown and variable packet loss rates. *Studies in Informatics and Control* 25, 1 (2016), 109–121.
- [6] CHAKRABARTY, S., AND BANDYOPADHYAY, B. A generalized reaching law with different convergence rates. *Automatica* 63, 1 (2016), 34–37.
- [7] DRAŽENOVIĆ, B. The invariance conditions in variable structure systems. *Automatica* 5, 3 (1969), 287–295.
- [8] DU, H., YU, M. C., AND LI, S. Chattering-free discrete-time sliding mode control. *Automatica* 68, 3 (2016), 87–91.
- [9] GAO, W., WANG, Y., AND HOMAIFA, A. Discrete-time variable structure control systems. *IEEE Transactions on Industrial Electronics* 42, 2 (1995), 117–122.
- [10] MA, H., WU, J., AND XIONG, Z. Discrete-time sliding-mode control with improved quasi-sliding-mode domain. *IEEE Transactions on Industrial Electronics* 63, 10 (2016), 6292–6304.
- [11] MILOSAVLJEVIĆ, Č. General conditions for the existence of a quasisliding mode on the switching hyperplane in discrete variable structure systems. *Automation and Remote Control* 46, 3 (1985), 307–314.
- [12] MILOSAVLJEVIĆ, Č., PERUNIČIĆ-DRAŽENOVIĆ, B., VESELIĆ, B., AND MITIĆ, D. Sampled data quasi-sliding mode control strategies. *IEEE International Conference on Industrial Technology* (2006), 2640–2645.
- [13] NIU, Y., HO, D.W.C., AND WANG, Z. Improved sliding mode control for discrete-time systems via reaching law. *IET Control Theory & Applications* 4, 11 (2010), 2245–2251.
- [14] UTKIN, V. Variable structure systems with sliding modes. *IEEE Transactions on Automatic Control* 22, 2 (1977), 212–222.
- [15] UTKIN, V., AND DRAKUNOV, S. V. On discrete-time sliding mode control. *IFAC Conference on Nonlinear Control* (1989), 484–489.

Paweł Latosiński, Ph.D.: Łódź University of Technology/Faculty of Electrical, Electronic, Computer and Control Engineering/Institute of Automatic Control, B. Stefanowskiego 18/22, 90-924 Łódź (pawel.latosinski@p.lodz.pl). The author gave a presentation of this paper during one of the conference sessions.

Andrzej Bartoszewicz, Prof.: Łódź University of Technology/Faculty of Electrical, Electronic, Computer and Control Engineering/Institute of Automatic Control, B. Stefanowskiego 18/22, 90-924 Łódź (andrzej.bartoszewicz@p.lodz.pl).

Kinematic analysis of the rolling locomotion of mobile robots based on tensegrity structures with spatially curved compressed components

Enrique Roberto Carrillo Li, Philipp Schorr, Tobias Kaufhold, Jorge Antonio Rodríguez Hernández, Lena Zentner, Klaus Zimmermann, Valter Böhm

Abstract: The use of mechanically compliant tensegrity structures in mobile robots is an attractive research topic, due to the possibility to adjust their mechanical properties reversibly during locomotion. In this paper rolling locomotion of mobile robots based on simple tensegrity structures, consisting of three compressed spatially curved members connected to a continuous net of prestressed tensional members, is discussed. Planar locomotion of these robots is induced by the movement of internal masses. The movement direction can be changed by changing the robot's shape between a cylinder and a truncated cone. The paper focuses on the description of the kinematics of these systems with respect to the shape change.

1. Introduction

The use of mechanically prestressed compliant structures in mobile robotics is a recently discussed topic. Tensegrity structures, consisting of a set of rigid disconnected compressed members connected to a continuous net of prestressed tensioned members build one specific class of these structures. Robots based on these structures are deployable, lightweight, have a simple system design, very high strength to weight ratio, and shock absorbing capabilities [1-3]. An overview of actual developments and development directions can be found in [4-8]. A recent development direction is the realization of rolling mobile robots based on these structures [9-11]. Known systems use conventional tensegrity structures, based on straight members. Rolling is realized by body deformation and tip-over movement sequences, due to periodically changing the length of selected tensioned or compressed members. The application of curved components in tensegrity structures indicates their potential ability for the use in rolling mobile robots. In our previous work ([12-14]) we have shown, that uniaxial rolling locomotion is possible by using structures with curved compressed members. In the present work we focus on the kinematic properties of a simple rolling mobile robot, based on a 3D non-conventional tensegrity structure with three spatially curved compressed members. In contrast to known works, planar rolling movement of this robot is possible without tip-over movement sequences. In section 2 the geometric properties of the structure of the robot are discussed. The system's kinematics is considered in section 3, partly with the help of a simple equivalent mechanical model in the cases uniaxial and planar locomotion. Finally, a brief summary and outlook are given in section 4.

2. Structural properties

The considered structure is based on the regular T3 tensegrity prism (called as Simplex), consisting of 3 compressed members which are indirectly connected pin-jointed by 9 tensioned members with each other. Due to the prestress, the structure is in stable equilibrium as depicted in Fig. 1 a,b. In case of identical mechanical parameters of the 6 tensioned members which build the upper and lower triangles of the prism (members D-E, D-F, E-F and members A-B, A-C, B-C), identical parameters of the diagonal tensioned members (A-E, B-F, C-D), and identical parameters of the compressed members (A-D, B-E, C-F), the structure is cyclic symmetric and the twist angle between the top and lower base triangles in planes parallel to each other is equal to $\pi/6$.

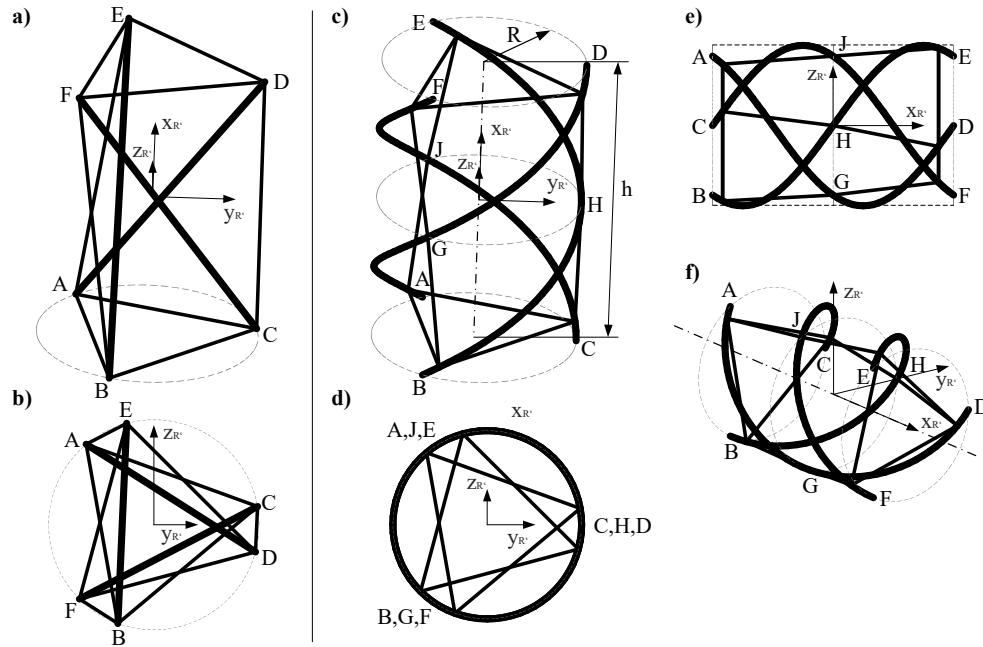


Figure 1. The regular T3 tensegrity prism (a) and b)) and the considered tensegrity structure with curved compressed members (c)–f), thick lines: compressed members, thin lines: tensioned members.

In the structure to be considered (see Fig. 1 c-f and Fig. 2) the straight compressed members ($i=1,2,3$) are replaced with right handed cylindrical helixes with constant radius R , slope $h/(R \cdot \varphi_{0,\max})$, and with arc lengths $L = \varphi_{0,\max} \cdot (R^2 + (h/\varphi_{0,\max})^2)^{0.5}$. With respect to the planned specific application, the helix turning angle is selected to $\varphi_{0,\max} = 4/3\pi$ (see also Section 3.1). The position of a point at φ_0

($\varphi_0=0 \dots \varphi_{0,\max}$) of compressed member i can be expressed with the position vector with respect to the Cartesian coordinate system $\{x_R, y_R, z_R\}$ with origin O' in the cylinder's center:

$$\vec{r}_i(\varphi_0) = \begin{pmatrix} h \cdot (\varphi_0 / \varphi_{0,\max} - 1/2) \\ R \cdot \cos(\varphi_0 + i \cdot 2\pi/3) \\ R \cdot \sin(\varphi_0 + i \cdot 2\pi/3) \end{pmatrix}; \quad i = 1, 2, 3, \quad (1)$$

The connectivity of the members is modified in a small manner with respect to the regular T3 tensegrity prism. To keep the tensegrity twist angle unchanged, the tensioned members corresponding to the lower and upper base triangles are attached to the curved compressed members at $\varphi_0=1/12\pi$ and $\varphi_0=(4/3-1/12)\pi$. In order to suppress possible rotatory motions of the curved compressed members inside the structure due to the pin-jointed connections, these members are connected also pin-jointed in their middle (points G, H, and J at $\varphi_0=\varphi_{0,\max}/2$) to the corresponding diagonal tensioned members.

As a result of the previous conventions, the outer hull of the resulting structure is assumed as a cylinder. In the resulting structure the tensegrity principle is still present, independent of the complex load situation in the compressed members. These members are only indirectly connected with each other.



Figure 2. Manufactured model of the considered tensegrity structure in different views.

The global shape of the cylindrical tensegrity structure can be influenced by asymmetric changing of their prestress. If an identical length or stiffness change of selected tensioned members is induced by means of actuators, the geometry of the structure changes from a cylinder to a truncated cone (conical frustum). The structure remains cyclic symmetric, if an equal stiffness change of all three tensioned members corresponding to the upper (members: D-E, D-F, E-F) or the lower base triangles (members: A-B, A-C, B-C) occurs. The intersection points of the three curved segments with planes perpendicular

to the $y_{R'}-z_{R'}$ plane lie on circles of variable radius, see Eq. 2. The global shape of the resulting structure can be characterized with the conicity parameter C_p ($-1 < C_p < +1$).

$$R(\varphi_0) = R \cdot (1 - C_p \cdot (1 - 2 \cdot \varphi_0 / \varphi_{0,\max})) \quad (2)$$

In this case, the coordinates of the points of the compressed members can be expressed following Eq. 1 with the position vectors with respect to the Cartesian coordinate system $\{x_{R'}, y_{R'}, z_{R'}\}$:

$$\vec{r}_i(\varphi_0) = \begin{pmatrix} h \cdot (\varphi_0 / \varphi_{0,\max} - 1/2) \\ R(\varphi_0) \cdot \cos(\varphi_0 + i \cdot 2\pi/3) \\ R(\varphi_0) \cdot \sin(\varphi_0 + i \cdot 2\pi/3) \end{pmatrix}; \quad i = 1, 2, 3 \quad (3)$$

The geometry of the structure is depicted exemplarily in Fig. 3 for two different values of C_p .

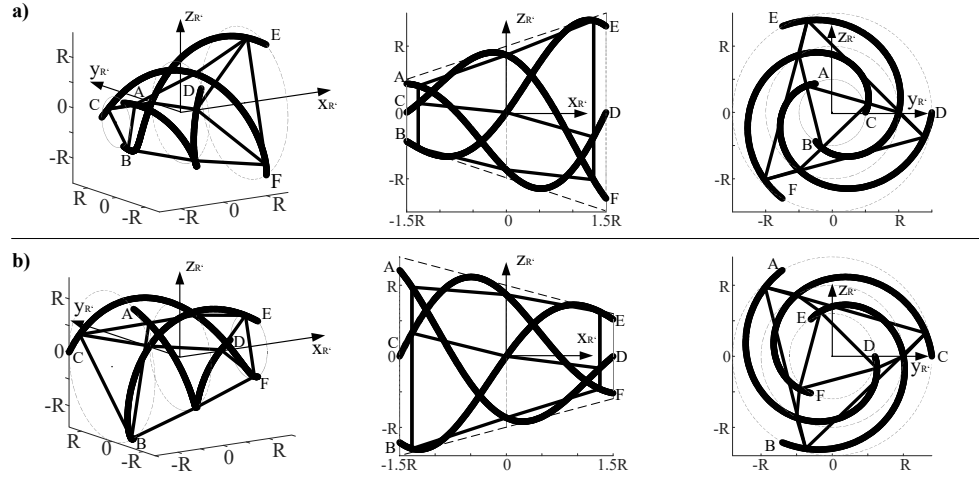


Figure 3. Geometry of the considered structure for the cases a): $C_p = +0.5$; b): $C_p = -0.4$, ($R/h = 1/3$; left/middle/right: isometric/side/front view).

3. Kinematics of the system

We consider rolling movement of the system on a plane surface without slipping. By assuming high prestress of the structure, elastic deformations will be neglected. During locomotion only the curved compressed members can touch the ground. The movement is induced by rotation of the structure about the longitudinal axis $x_{R'}$ (rotation angle: φ). In dependence of the conicity parameter C_p , movement on a straight line or movement on a curved path can be realized. By changing the conicity parameter during locomotion, planar movement of the system results.

3.1. Uniaxial movement

If $C_p=0$, uniaxial bidirectional locomotion can be realized corresponding to the cylindrical shape of the structure [15]. The center of the structure (O' , origin of the coordinate system $\{x_R, y_R, z_R\}$) moves along a straight line. In the case $x_R \parallel x_0$, the locomotion direction is the y_0 -direction (see Fig. 4). The position vector of O' can be expressed in the global Cartesian coordinate system $\{x_0, y_0, z_0\}$ by using the rolling condition ($O'(0,0,R)$ for $\varphi=0$): $\vec{r}_{O'}(\varphi)=(0, -R\varphi, R)^T$.

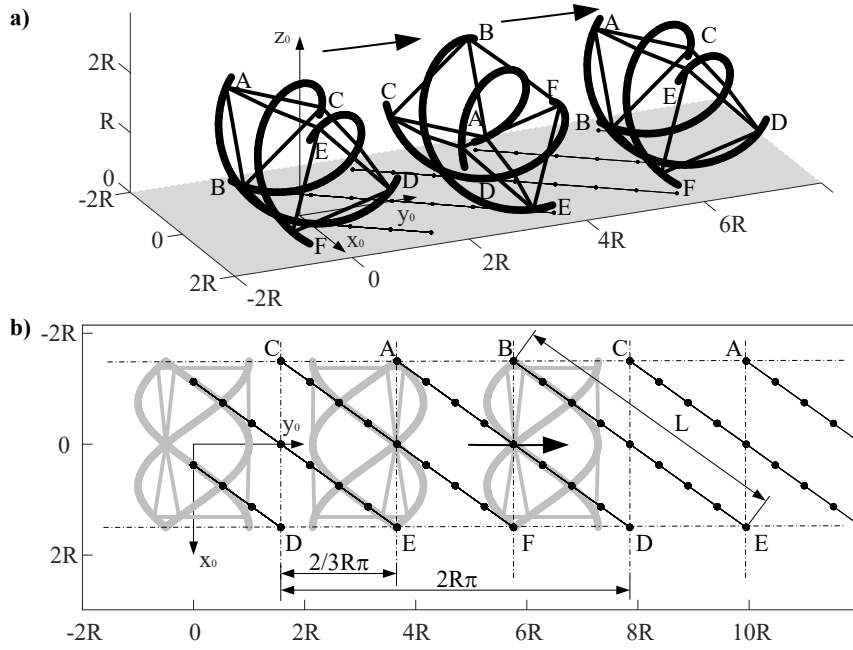


Figure 4. Uniaxial rolling of the considered structure (conicity parameter: $C_p=0$, $R/h=1/3$), a): isometric view, b): top view with paths of the contact points between structure and ground.

With the help of the transformation matrix $T_{xR}(\varphi)=[1,0,0; 0,\cos(\varphi),-\sin(\varphi); 0,\sin(\varphi),\cos(\varphi)]$ any points of the curved compressed members can be found in dependence of the rotation angle φ in $\{x_0, y_0, z_0\}$:

$$\vec{r}_i(\varphi, \varphi_0)^T = \vec{r}_i(\varphi_0)^T \cdot T_{xR}(\varphi) + \vec{r}_{O'}(\varphi); \quad i = 1, 2, 3. \quad (4)$$

Due to the specific geometry, the paths of the contact points on the ground correspond to straight-line segments (see Fig. 4). In general, there are two points of the structure in contact with the ground, due to the selected specific value of $\varphi_{0,\max}$ (see Fig. 4 b). These two points lie on two curved compressed components. During locomotion, these contact points change continuously on the curved compressed members. Furthermore, the contact points alternate on these members. As in the example in Fig. 4 is

shown, the contact points lie at the beginning of the movement on the curved compressed members $i=1$ (A-D) and $i=2$ (B-E), then on $i=2$ (B-E) and $i=3$ (C-F) and finally on $i=3$ (C-F) and $i=1$ (A-D). The orientation of the paths of the contact points can be characterized by the helix angle α_H , where $\tan(\alpha_H)=R \cdot \varphi_{0,\max}/h$. The length of a path built by the contact points corresponding to one compressed member equals to L .

The velocity vector of the center O' of the structure is given by $\dot{\vec{r}}_{O'}(\varphi(t))$. The angular velocity vector of the system has the orientation corresponding to the x_0 axis.

3.2. Movement on curved paths

If the conicity parameter equals to non-zero values ($C_P \neq 0$), the system moves along a curved path with constant radius R_P . To describe the system's kinematics for this second basic movement sequence, a substitute mechanical model, consisting of a rigid circular disc (radius R) and a rod (length $L_R=h/(2 \cdot C_P)$) is considered (Fig. 5).

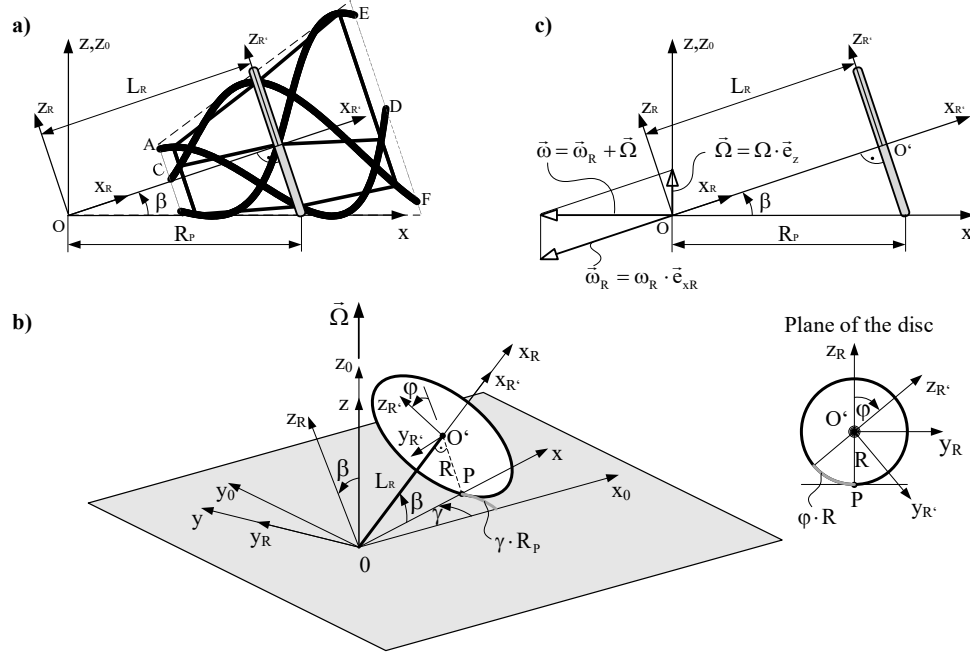


Figure 5. Geometrical parameters in case of movement on curved paths (a) and b)), c): direction of the angular velocity vector.

The rod (end points O, O') is connected to the centre point O' of the disc normal to the disc plane, without relative movement capability between disc and rod. The free end of the rod (point O) is rotatable supported in the origin of the inertial coordinate system $\{x_0, y_0, z_0\}$. With respect to the system to be

considered, in the simplified model the disc corresponds to the outer hull of the tensegrity structure in the x_R-y_R plane, and the rod to the line segment between the centre point O' of the tensegrity structure and the fixed point O , lying on their longitudinal axis. With respect to the specified parameters the path radius can be determined by using geometrical relationships (see Fig. 5): $R_p=R/\sin(\beta)$, with the conicity angle β , where $\tan\beta=C_p \cdot 2R/h$. The overall rotation of the structure about the z -axis during movement is described by the angle γ . The relationship between this angle and the rotation angle φ of the disc can be determined by considering the length of the path, build by the contact points between disc and the x_0-y_0 plane ($\gamma \cdot R_p$), and the corresponding arc length on the disc ($\varphi \cdot R$):

$$\gamma \cdot R_p = -\varphi \cdot R. \quad (5)$$

By using the above introduced geometrical relationships, Eq. (5) can be reformulated in dependence of the main geometrical parameters:

$$\gamma = -\varphi \cdot \sin(\tan^{-1}(C_p \cdot 2R/h)) = -\varphi \cdot K_p. \quad (6)$$

where K_p is a constant, representing the geometrical parameters of the structure. In Fig. 6, selected relationships between geometrical and movement parameters are depicted exemplarily.

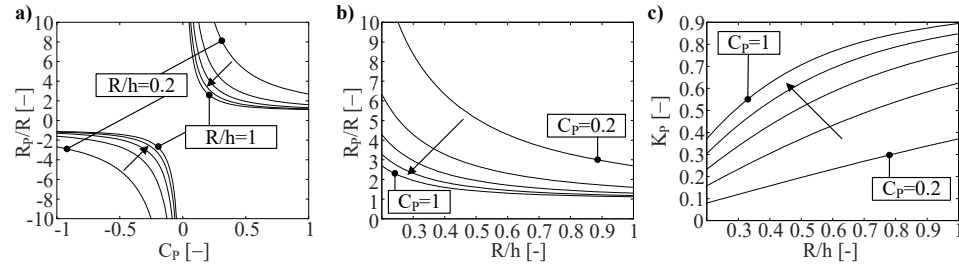


Figure 6. Movement parameters in dependence of geometrical parameters. a) and b): normalized path radius R_p/R in dependence of the conicity parameter C_p for different R/h values; c): K_p in dependence of the R/h ratio for different C_p values.

The position vector of O' can be expressed in the global Cartesian coordinate system $\{x_0, y_0, z_0\}$ by using the rolling condition ($O'(L_R \cdot \cos\beta, 0, R \cdot \cos\beta)$ for $\varphi=0$): $\vec{r}_{O'}(\varphi) = (L_R \cdot \cos\beta \cdot \cos\gamma, L_R \cdot \sin\gamma, R \cdot \cos\beta)^T$.

By using the transformation matrices $T_{xR}(\varphi)$, $T_{yR}(\beta) = [\cos(\beta), 0, \sin(\beta); 0, 1, 0; -\sin(\beta), 0, \cos(\beta)]$, and $T_\gamma(\varphi) = [\cos(\gamma), \sin(\gamma), 0; -\sin(\gamma), \cos(\gamma), 0; 0, 0, 1]$, any points of the curved compressed members can be found in dependence of the rotation angle φ in the $\{x_0, y_0, z_0\}$ reference system:

$$\vec{r}_i(\varphi, \varphi_0, \beta)^T = \vec{r}_i(\varphi_0)^T \cdot T_{xR}(\varphi) \cdot T_{yR}(\beta) \cdot T_\gamma(\varphi) + \vec{r}_{O'}(\varphi); \quad i = 1, 2, 3. \quad (7)$$

Due to the specific geometry, the paths of the contact points on the ground correspond to curved line segments with non-constant radii (see Fig. 7). As for $C_p=0$, in general there are two points of the structure in contact with the ground. These points lie on different curved compressed components. Similar to the uniaxial movement, these contact points change continuously on the curved compressed members during locomotion.

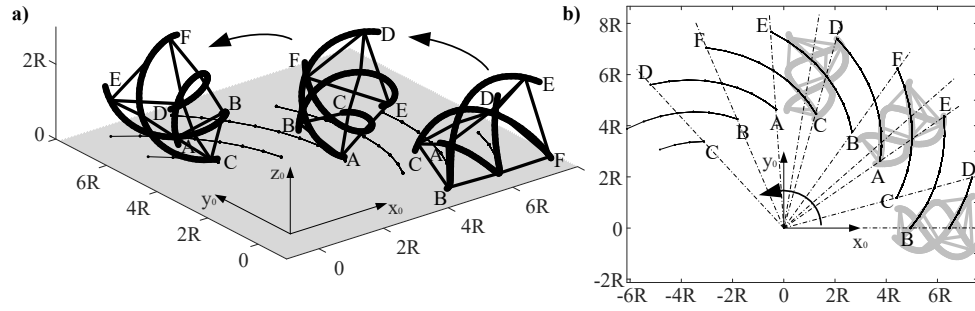


Figure 7. Movement of the system on a curved path (conicity parameter: $C_p=0.5$, $R/h=1/3$), a): isometric view, b): top view with paths of the contact points between structure and ground.

The velocity vector of the center O' of the structure is given by $\dot{\vec{r}}_{O'}(\varphi(t))$. The angular velocity of the structure with $d\varphi(t)/dt = \dot{\varphi} = \omega_R$ and $d\gamma(t)/dt = \dot{\gamma} = \Omega$ can be expressed with

$$\vec{\omega} = \vec{\omega}_R + \vec{\Omega} = \dot{\varphi} \cdot \cos(\beta) \cdot \vec{e}_x = \dot{\varphi} \cdot (\tan^{-1}(C_p \cdot 2R / h)) \cdot \vec{e}_x \quad (8)$$

where

$$\vec{\omega}_R = \omega_R \cdot \vec{e}_{xR} = \dot{\varphi} \cdot \vec{e}_{xR} = \dot{\varphi} \cdot (\cos(\beta) \cdot \vec{e}_x + \sin(\beta) \cdot \vec{e}_z), \quad (9)$$

$$\vec{\Omega} = \Omega \cdot (\sin(\beta) \cdot \vec{e}_{xR} + \cos(\beta) \cdot \vec{e}_{zR}) = \Omega \cdot \vec{e}_{z0} = \Omega \cdot \vec{e}_z = -\dot{\varphi} \cdot \sin(\beta) \cdot \vec{e}_z. \quad (10)$$

3.3. Movement in the plane

The introduced system needs two types of actuation, corresponding to the realization of rotation about its longitudinal axis (primary actuation), and corresponding to the needed shape change from cylindrical shape to conical shape (secondary actuation). As the above considerations show, this shape change is needed to change the locomotion direction. As an example, the primary actuation can be realized by moving of internal masses time-shifted along the three curved compressed members, as shown in [12-14]. Shape change of the system is realized preferably by change of lengths or stiffnesses of selected tensioned members, e.g. by replacing these members with shape memory alloy actuators or by using conventional additional length variable cables at these members.

Planar movement can be induced by purposeful variation of the conicity parameter C_p during locomotion. By a continuous change of C_p , the system moves on a path with continuous changing radius (Fig. 8).

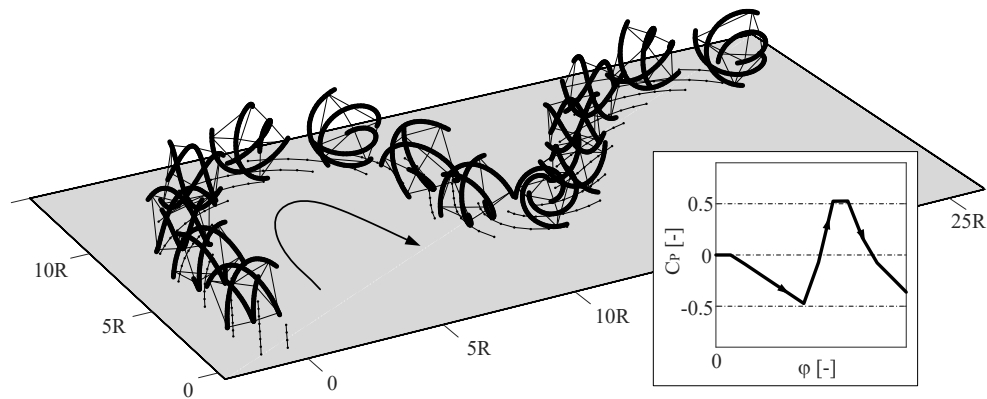


Figure 8. Example for the planar movement of the system ($R/h=1/3$).

4. Conclusions

In this paper the kinematics of a rolling mobile robot, based on a non-conventional tensegrity structure is considered. It was shown, that rolling locomotion can easily realized with tensegrity structures consisting of spatially curved compressed members. Movement in the plane is possible without tip-over movement sequences. The change of the movement direction is induced with global shape change of the robot. The influence of geometrical parameters on the movement behavior was discussed. Further investigations will focus on the description of the system's dynamics and on the realization and testing of a prototype.

Acknowledgments

This work is supported by the Deutsche Forschungsgemeinschaft (DFG project BO4114/2-2, and DFG projects ZE714/14-1, BO4114/3-1 within the Priority Programm SPP 2100).

References

- [1] Paul C., et al.: Gait production in a tensegrity based robot. Proc. of ICAR '05, 12th Int. Conf. on Advanced Robotics, Seattle, 2005, pp. 216–222.
- [2] Rieffel J.A., et al.: Morphological communication: exploiting coupled dynamics in a complex mechanical structure to achieve locomotion. *J. Roy. Soc. Interf.*, 7, 2010, pp. 613–621.
- [3] Koizumi Y., et al.: Rolling tensegrity driven by pneumatic soft actuators. Proc. of IEEE Int. Conf. on Robotics and Automation, Saint Paul, 2012, pp. 1988–1993.
- [4] Mirats Tur J.M., et al.: Tensegrity frameworks: Dynamic analysis review and open problems. *Int. Journal of Mechanism and Machine Theory*, 44(1), 2009, pp. 1–18.

- [5] Skelton R.E., et al.: *Tensegrity Systems*. Dordrecht, Springer, 2009.
- [6] Khazanov, M., et al.: Evolution of Locomotion on a Physical Tensegrity Robot. Proc. of the 14th Int. Conf. on the Synthesis and Simulation of Living Syst., New York, 2014, pp. 232-238.
- [7] Caluwaerts, K., et al.: Design and control of compliant tensegrity robots through simulation and hardware validation. *J. Roy. Soc. Interf.*, 11, 2014, 20140520.
- [8] Böhm, V., et al.: An approach to the dynamics and control of a planar tensegrity structure with application in locomotion systems. *Int. Journal of Dynamics and Control*, 3(1), 2015, pp. 41-49.
- [9] Vespignani, M. et al.: Design of SUPERball v2, a Compliant Tensegrity Robot for Absorbing Large Impacts. Proc. of IEEE/RSJ Int. Conf. on Intelligent Robots and Systems, Madrid, 2018, pp. 2865-2871.
- [10] Rieffel, J., et al.: Adaptive and Resilient Soft Tensegrity Robots. *J. Soft Robotics*, (5)3, 2018, pp. 318-329.
- [11] Zappetti, D., et al., A Soft Robot for Random Exploration of Terrestrial Environments. Proc. of IEEE Int. Conf. on Robotics and Automation, Brisbane, 2018, pp. 7492–7497.
- [12] Böhm, V., et al.: Dynamic analysis of a spherical mobile robot based on a tensegrity structure with two curved compressed members. *Archive of Applied Mechanics*, 87(5), 2017, pp. 853-864.
- [13] Böhm, V., et al.: Spherical mobile robot based on a tensegrity structure with curved compressed members. Proc. of IEEE Int. Conf. on Advanced Intelligent Mechatronics, Banff, 2016, pp. 1509-1514.
- [14] Kaufhold, T. et al.: Indoor locomotion experiments of a spherical mobile robot based on a tensegrity structure with curved compressed members. Proc. of IEEE Int. Conf. on Advanced Intelligent Mechatronics, München, 2017, pp. 523-528.
- [15] Carrillo Li, E.R.: A contribution to the investigation of the rolling movement of mobile robots based on tensegrity structures. Master's Thesis, Technische Universität Ilmenau, 2019.

Enrique Roberto Carrillo Li, M.Sc. (Ph.D. student): Pontificia Universidad Católica del Perú, Department of Engineering, Av. Universitaria N° 1801, San Miguel, Lima, Peru (ecarrillol@pucp.edu.pe).

Philipp Schorr, M.Sc. (Ph.D. student): Technische Universität Ilmenau, Technical Mechanics Group, Max-Planck-Ring 12, D-98693 Ilmenau, Germany (philipp.schorr@tu-ilmenau.de).

Tobias Kaufhold, Ph.D.: Technische Universität Ilmenau, Technical Mechanics Group, Max-Planck-Ring 12, D-98693 Ilmenau, Germany (tobias.kaufhold@tu-ilmenau.de).

Jorge Antonio Rodríguez Hernández, Professor: Pontificia Universidad Católica del Perú, Department of Engineering, Av. Universitaria N° 1801, San Miguel, Lima, Peru (crodrig@pucp.edu.pe).

Lena Zentner, Professor: Technische Universität Ilmenau, Compliant Systems Group, Max-Planck-Ring 12, D-98693 Ilmenau, Germany (lana.zentner@tu-ilmenau.de).

Klaus Zimmermann, Professor: Technische Universität Ilmenau, Technical Mechanics Group, Max-Planck-Ring 12, D-98693 Ilmenau, Germany (klaus.zimmermann@tu-ilmenau.de).

Valter Böhm, Professor: Ostbayerische Technische Hochschule Regensburg, Mechanics Group, Galgenbergstr. 30, D-93053 Regensburg, Germany (valter.boehm@oth-regensburg.de). The author gave a presentation of this paper during one of the conference sessions.

Fractional dynamics and power law behavior in soccer leagues

António M. Lopes, J. A. Tenreiro Machado

Abstract: This paper addresses the dynamics of soccer teams performance during a given league. The modeling perspective adopts the concepts of fractional calculus and power law. The proposed model embeds implicitly details such as the behavior of players and coaches, strategical and tactical maneuvers during the matches, errors of referees and a multitude of other effects. The scale of observation focuses on the teams behavior in the perspective of their classification along the league. Data characterizing 4 European soccer leagues are processed and discussed. The computational and mathematical modeling leads to the emergence of patterns that are analyzed and interpreted in the light of complex systems.

1. Introduction

Soccer is the most popular sport in Europe [2, 5]. The game is played by 2 teams of 11 players, on a rectangular field with a goal placed at each end. The objective of the game is to score by getting a spherical ball into the opposing goal. Each team includes 10 field players, that can maneuver the ball using any part of the body except hands and arms, and one goalkeeper, who is allowed to touch the ball with the whole body, as long as he/she stays in his/her penalty area. Otherwise, the rules of the field players apply. The match has 2 periods of 45 minutes each. The winning team is the one that scores more goals by the end of the match.

In most European countries, soccer competitions are organized hierarchically in leagues composed by groups of teams. At the end of each season, a promotion and relegation system decides which teams move up and down into the hierarchy. In a given league and season each pair of teams plays to matches, so that the visited and visitor interchange place. All teams start with zero points and, at every round, one {victory, draw, defeat} worths {3, 1, 0} points. By the end of the last round, the team that accumulated more points is the champion [1].

This paper studies the dynamical performance of soccer teams in a given league. The modeling perspective adopts the concepts of fractional calculus and power law [16, 15]. The proposed approach embeds implicitly details such as the behavior of players and coaches, strategical and tactical maneuvers during the matches, errors of referees and a multitude of

other effects. The scale of observation addresses the teams behavior in the perspective of their classification along the league. Data characterizing the year 2018-2019 and the 4 leagues Spanish ‘La Liga’, English ‘Premiership’, Italian ‘Serie A’ and French ‘Ligue 1’ are processed and discussed. The computational and mathematical modeling leads to the emergence of patterns that are analyzed and interpreted in the light of complex systems [11, 14, 3].

Bearing these ideas in mind, this paper is organized as follows. Section 2 models the behavior of the teams in 4 top European soccer leagues by means of power laws functions. Section 3 analyzes the leagues in the perspective of the entropy of the spatio-temporal patterns exhibited by distinct alternative models. Finally, Section 4 outlines the conclusions.

2. Power law behavior of the teams’ dynamics

Let us consider N teams competing in a league for one season. Therefore, the league has $R = 2(N - 1)$ rounds, and each team plays $R/2$ matches at home and $R/2$ matches away.

Let us denote by $x_i(k)$, $i = 1, \dots, N$, $0 \leq k \leq k_r$, the teams’ positions up to the round $k_r \in \{3, \dots, R\}$. The lower limit $k_r = 3$ is adopted to yield data-series with a minimum number of points for processing. Therefore, the signals $x_i(k)$ evolve in discrete time and 1-dimensional space, and can be seen as the output of a complex system.

We use the nonlinear least-squares [8, 4] to test the behavior of $x_i(k)$ for 6 hypotheses, namely power law (PL), Hoerl (Ho), shifted power (SP), quadratic (Qu), Hill (Hi) and vapor pressure (VP) models, given by:

$$PL : \hat{x}_i^{PL}(k) = a_i \cdot k^{b_i}, \quad (1a)$$

$$Ho : \hat{x}_i^{Ho}(k) = a_i \cdot b_i^k \cdot k^{c_i}, \quad (1b)$$

$$SP : \hat{x}_i^{SP}(k) = a_i \cdot |k - b_i|^{c_i}, \quad (1c)$$

$$Qu : \hat{x}_i^{Qu}(k) = a_i + b_i \cdot k + c_i \cdot k^2, \quad (1d)$$

$$Hi : \hat{x}_i^{Hi}(k) = \frac{a_i \cdot k^{b_i}}{c_i^{b_i} + k^{b_i}}, \quad (1e)$$

$$VP : \hat{x}_i^{VP}(k) = e^{\frac{a_i + b_i}{c_i \cdot \ln(k)}}, \quad (1f)$$

where \hat{x}_i denote the approximated values, k represents time and $\{a_i, b_i, c_i\} \in \mathbb{R}$ are the models’ parameters. Naturally, these parameters depend on k_r , that is, they vary with time.

We can adopt other fitting models, eventually with more parameters, that adjust better to some particular series $x_i(k)$. However, only simple analytical expressions, requiring a limited set of parameters, are considered [10], otherwise the interpretation of the parameters becomes unclear.

Fig. 1(a) depicts the time evolution of the FC Barcelona position, $x_1(k)$, and the fitting values, $\hat{x}_1(k)$, obtained with the models (1a)-(1f), up to the end of the 2018-2019 season, that is for $k_r = 38$. Fig. 1(b) represents the fitting error $x_1(k) - \hat{x}_1(k)$.

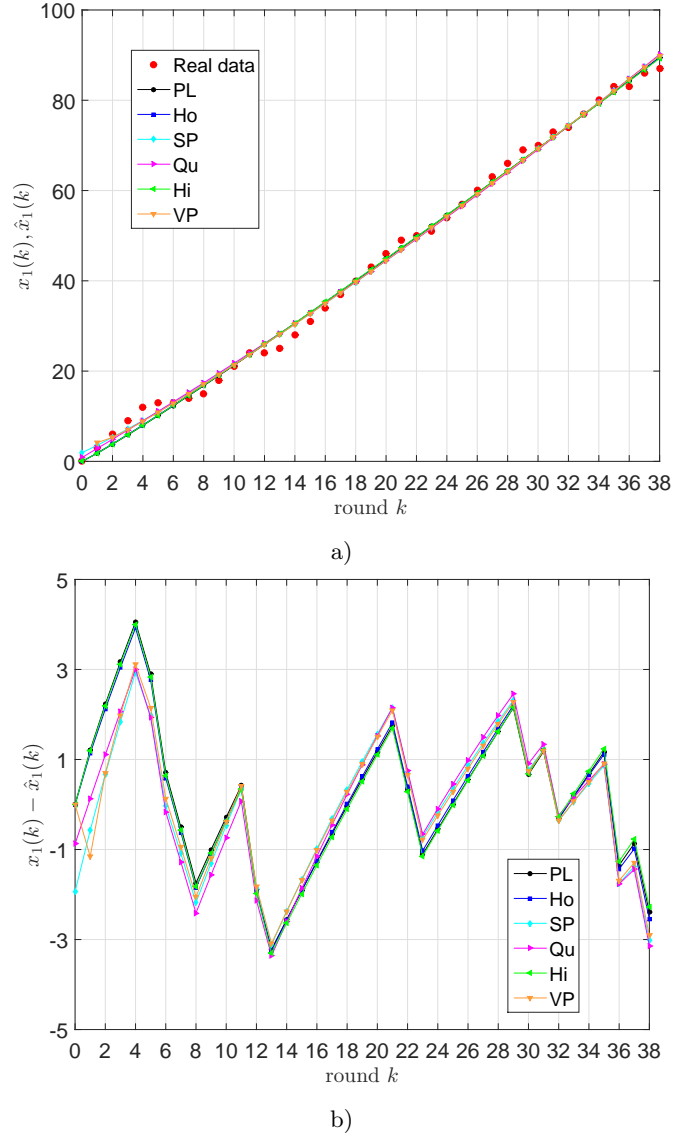


Figure 1. Time evolution of the FC Barcelona position up to the end of the 2018-2019 season ($k_r = 38$) and the approximate values obtained with the models (1a)-(1f) for: (a) position, $x_1(k)$, and fitting values, $\hat{x}_1(k)$; (b) fitting error $x_1(k) - \hat{x}_1(k)$.

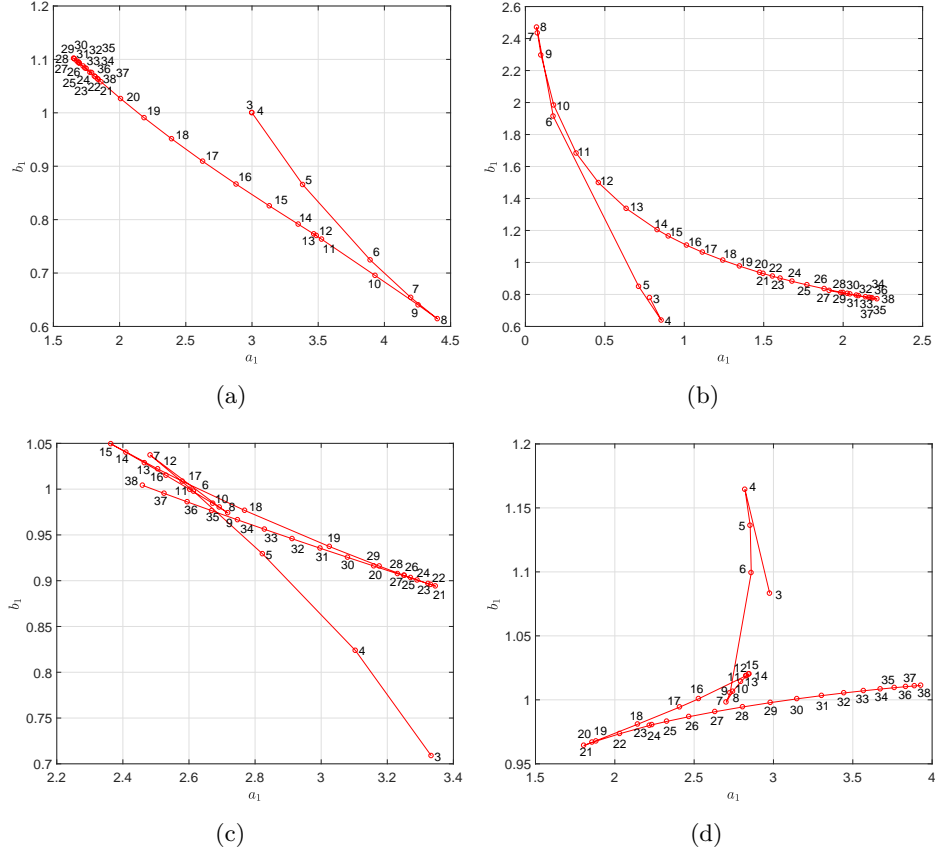


Figure 2. Locus of the the model parameters (a_1, b_1) for the 2018-2019 champions of ‘La Liga’ and ‘Premiership’: (a) PL model for FC Barcelona; (b) Ho model for FC Barcelona; (c) PL model for Manchester City; (d) Ho model for Manchester City. The point labels denote k_r .

Fig. 2 depicts the parameters (a_1, b_1) of the PL and Ho models for the 2018-2019 champions of ‘La Liga’ and “Premiership”, namely FC Barcelona and Manchester City, respectively. The point labels represent the value of k_r . For the Ho model the parameter c_i is omitted since it does not vary significantly. We verify that for the FC Barcelona we have two trends in the (a_1, b_1) locus. The first corresponds to the period $3 \leq k_r \leq 8$, where the (a_1, b_1) trajectory evolves influenced by a set of consecutive bad results between rounds 5 and 8. The second corresponds to the period $8 \leq k_r \leq 38$, where the (a_1, b_1) path changes direction driven by a consistent and positive team behavior towards the final victory at $k_r = 38$. For the Manchester City the (a_1, b_1) evolution is more complex. Initially, we

observe a route for the period $3 \leq k_r \leq 7$. Then, the locus has a slight change, due to a draw achieved by the team at round 8, but recovers fast its initial trend during for $9 \leq k_r \leq 15$. Again the locus (a_1, b_1) changes driven by the set of team negative results in rounds 16 - 19 and 24. From $k_r = 25$ onward, the (a_1, b_1) locus evolves positively influenced by the consecutive team victories until the end of the season at $k_r = 38$. For other teams we can draw similar conclusions, meaning that there exists a clear relationship between the models' parameters (a_i, b_i) and the teams' performance along the season. Moreover, we verify that, in general, abrupt changes in the (a_i, b_i) trend correspond to inconsistent results at early rounds, that is, small values of k_r . For larger k_r , eventual inconsistencies on the teams' behavior do not translate in significant modifications of the (a_i, b_i) patterns, since the fitting becomes less sensitive to the number of fitting points.

Fig. 3 depicts the 10, 50 and 90 percentiles of the root-mean-squared error (RMSE) of the PL and Ho fit to the data-series $x_i(k)$, for all teams, $i = 1, \dots, 20$, and rounds $0 \leq k \leq k_r$, for $k_r \in \{3, \dots, 38\}$, both for the 'La Liga' and the "Premiership" during the 2018-2019 season. The results demonstrate the adequacy of the fitting functions. For the other teams the fitting quality is similar, with the exception of the initial transient. Therefore, no specific model can be favored against the others. Nonetheless, the PL (1a) has the advantage of yielding a good fit while requiring only 2 parameters.

By approximating the output signals $x_i(k)$ through power law functions (1a) we are modeling the complex system as a fractional integrator [17, 6, 13, 12, 18] of order $b_i \in \mathbb{R}^+$ for a constant, step-like, input signal.

If a team obtains {victory, draw, defeat} in all matches, then $x_i(k)$ is a straight line with $a_i = \{3, 1, 0\}$ and $b_i = 1$. However, real-world teams have victories/draws/defeats and, thus, yield a fractal like response that follows a power law behavior. Therefore, fractional/unit values of b_i reflect variable/constant time evolution, while values of a_i close to 3/1/0 correspond to victory/draw/defeat results [15].

3. Entropy of the spatio-temporal patterns of the models' parameters

For each league we now compute the PL parameters (a_i, b_i) that fit the teams' positions $x_i(k)$, $i = 1, \dots, 20$, $0 \leq k \leq k_r$, up to the round $k_r \in \{3, \dots, 38\}$. Therefore, for every k_r we have an array of $20 \times (k_r - 2)$ points in a 2-dimensional space. We then determine the bi-dimensional histograms by binning the data of each array into $M \times M = 100 \times 100$ bins (α_j, β_k) , $j, k = 1, \dots, M$. Finally, we calculate the Shannon entropy [19, 7]:

$$S(k_r) = - \sum_{j=1}^M \sum_{k=1}^M P(\alpha_j, \beta_k) \log P(\alpha_j, \beta_k), \quad (2)$$

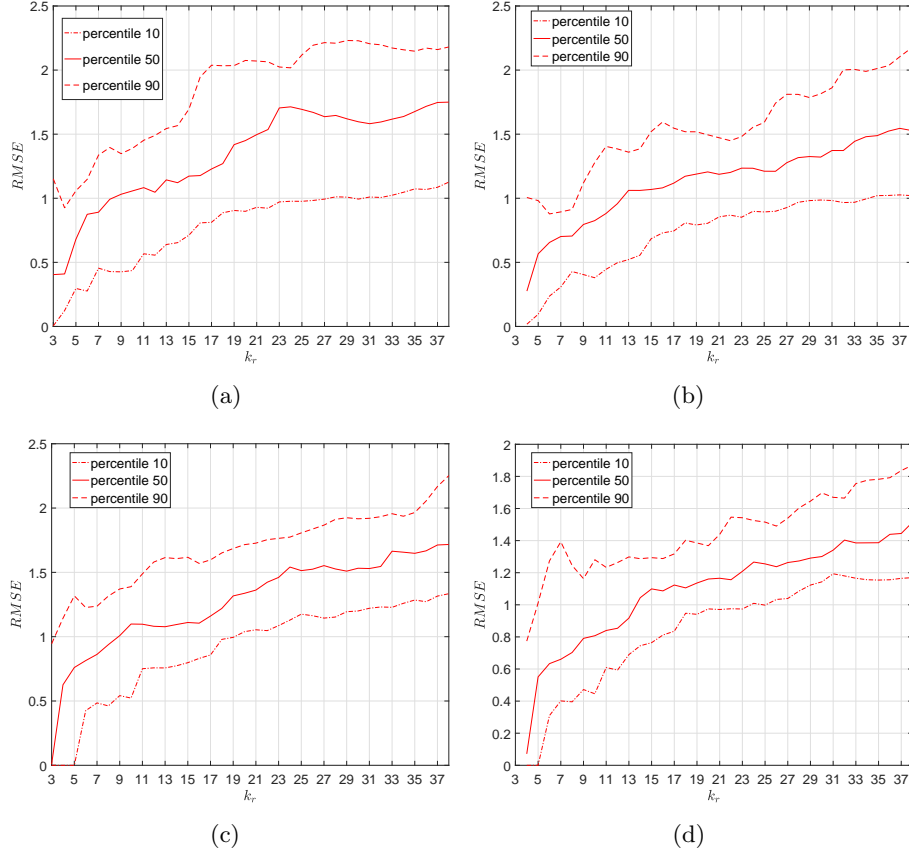


Figure 3. The RMSE of the PL and Ho model fit versus k_r : (a) PL for ‘La Liga’; (b) PL for ‘Premiership’; (c) Ho for ‘La Liga’; (d) Ho for ‘Premiership’.

where the probabilities $P(\alpha_j, \beta_k)$ are approximated by the data relative frequencies.

It should be mentioned that the entropy is a measure of regularity that has been successfully adopted in the study of complex systems [9, 14].

For example, Fig. 4 depicts the histograms of the 2018-2019 ‘La Liga’, ‘Premiership’, ‘Serie A’ and ‘Ligue 1’ for $k_r = 38$. We verify that the parameters (a_i, b_i) exhibit less dispersion for the pair $\mathcal{P}_1 = \{\text{‘La Liga’}, \text{‘Ligue 1’}\}$ than for the pair $\mathcal{P}_2 = \{\text{‘Premiership’}, \text{‘Serie A’}\}$, meaning that the results of the Spanish and French teams have lower time variability than the English and Italian ones.

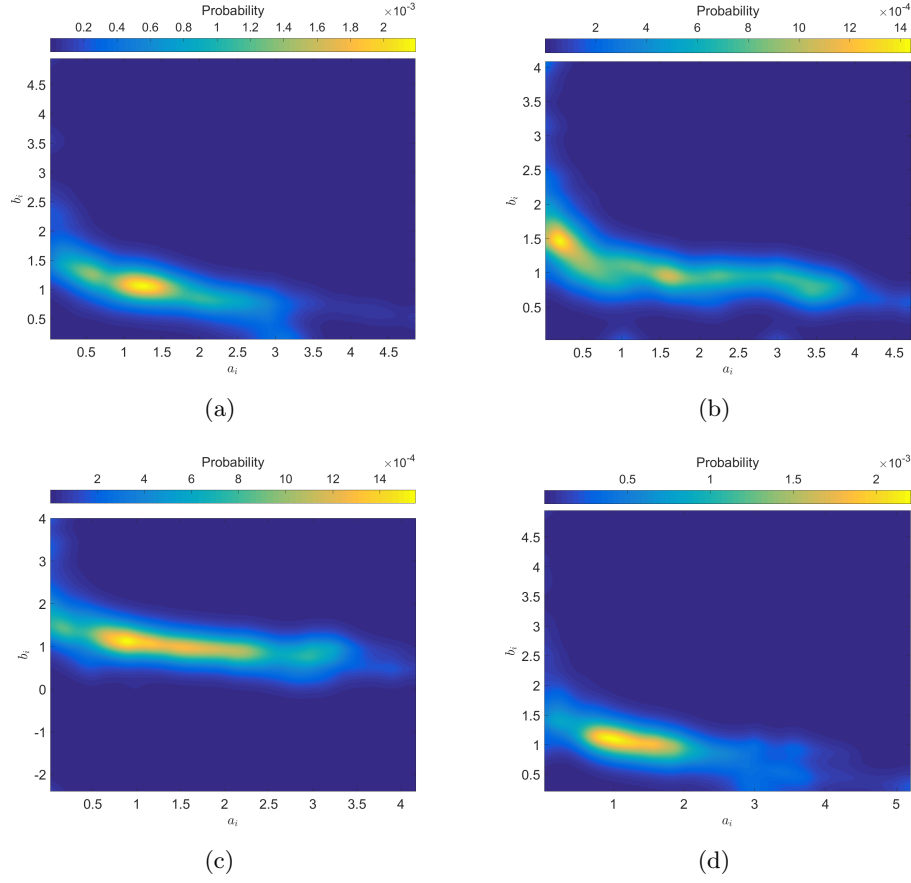


Figure 4. Histograms of the parameters (a_i, b_i) up to the end of the season 2018-2019 ($k_r = 38$) for 4 leagues: (a) ‘La Liga’; (b) ‘Premiership’; (c) ‘Serie A’; (d) ‘Ligue 1’.

Fig. 5 illustrates the evolution on the entropy, $S(k_r)$, up to each round $k_r \in \{3, \dots, 38\}$, of ‘La Liga’, ‘Premiership’, ‘Serie A’ and ‘Ligue 1’. Again, we verify that the pairs \mathcal{P}_1 and \mathcal{P}_2 reveal similar behavior. For the pair \mathcal{P}_1 the entropy increases faster with k_r than for the pair \mathcal{P}_2 . This means that, in the 2018-2019 season, the Spanish and French teams started more irregular than the English and Italian ones. Nevertheless, since for all leagues, $S(k_r)$ converges to a similar settling value, we conclude that by the end of the season the {victory, draw, defeat} global pattern exhibited by teams in different leagues is identical.

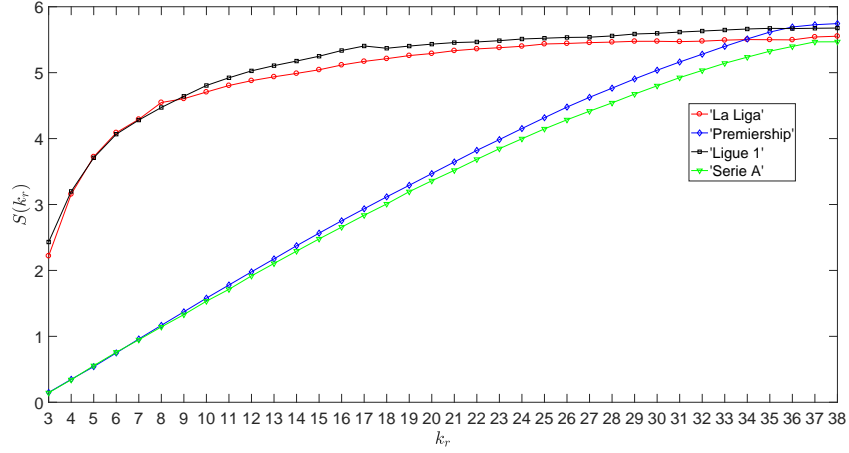


Figure 5. Evolution on the entropy $S(k_r)$ versus $k_r \in \{3, \dots, 38\}$, for the leagues ‘La Liga’, ‘Premiership’, ‘Serie A’ and ‘Ligue 1’.

4. Conclusions

We proposed a complex systems’ perspective for analyzing soccer teams competing within a league season. Firstly, we adopted 6 fitting models to describe the teams’ positions along one season and interpreted the loci of the models’ parameters as a signature of the system dynamics. Secondly, we studied the entropy of the models parameters’ spatio-temporal patterns for comparing different leagues. Both approaches represent valid tools to describe the complex behavior of such challenging systems.

Acknowledgments

The authors acknowledge the worldfootball.net organization (<http://www.worldfootball.net/>) for making data available.

References

- [1] BROCAS, I., AND CARRILLO, J. D. Do the “three-point victory” and “golden goal” rules make soccer more exciting? *Journal of Sports Economics* 5, 2 (2004), 169–185.
- [2] CARLING, C., WILLIAMS, A. M., AND REILLY, T. *Handbook of soccer match analysis: A systematic approach to improving performance*. Routledge, 2007.
- [3] COUCEIRO, M. S., CLEMENTE, F. M., MARTINS, F. M., AND MACHADO, J. A. T. Dynamical stability and predictability of football players: The study of one match. *Entropy* 16, 2 (2014), 645–674.

- [4] DRAPER, N. R., SMITH, H., AND POWNELL, E. *Applied regression analysis*, vol. 3. Wiley, New York, 1966.
- [5] GIULIANOTTI, R. Football. *The Wiley-Blackwell Encyclopedia of Globalization* (2012).
- [6] GORENFLO, R., AND MAINARDI, F. *Fractional calculus*. Springer, 1997.
- [7] JAYNES, E. Information theory and statistical mechanics. *Physical Review* 106 (1957), 620–630.
- [8] LAWSON, C. L., AND HANSON, R. J. *Solving least squares problems*, vol. 161. SIAM, 1974.
- [9] LOPES, A., AND TENREIRO MACHADO, J. Complexity analysis of global temperature time series. *Entropy* 20, 6 (2018), 437.
- [10] LOPES, A., TENREIRO MACHADO, J., AND GALHANO, A. Empirical laws and foreseeing the future of technological progress. *Entropy* 18, 6 (2016), 217.
- [11] LOPES, A. M., AND TENREIRO MACHADO, J. Entropy analysis of soccer dynamics. *Entropy* 21, 2 (2019), 187.
- [12] MACHADO, J., AND LOPES, A. M. Analysis of natural and artificial phenomena using signal processing and fractional calculus. *Fractional Calculus and Applied Analysis* 18, 2 (2015), 459–478.
- [13] MACHADO, J. T., AND LOPES, A. M. The persistence of memory. *Nonlinear Dynamics* 79, 1 (2015), 63–82.
- [14] MACHADO, J. T., AND LOPES, A. M. Multidimensional scaling analysis of soccer dynamics. *Applied Mathematical Modelling* 45 (2017), 642–652.
- [15] MACHADO, J. T., AND LOPES, A. M. On the mathematical modeling of soccer dynamics. *Communications in Nonlinear Science and Numerical Simulation* 53 (2017), 142–153.
- [16] MACHADO, J. T., PINTO, C. M., AND LOPES, A. M. A review on the characterization of signals and systems by power law distributions. *Signal Processing* 107 (2015), 246–253.
- [17] MILLER, K. S., AND ROSS, B. An introduction to the fractional calculus and fractional differential equations.
- [18] PINTO, C. M., LOPES, A. M., AND MACHADO, J. T. A review of power laws in real life phenomena. *Communications in Nonlinear Science and Numerical Simulation* 17, 9 (2012), 3558–3578.
- [19] SHANNON, C. A mathematical theory of communication. *The Bell System Technical Journal* 27 (July 1948), 379–423.

António M. Lopes, Ph.D.: UISPALAEITA/INEGI, Faculty of Engineering, University of Porto, Rua Dr. Roberto Frias, 4200 – 465 Porto, Portugal (*aml@fe.up.pt*).

J. A. Tenreiro Machado, Ph.D.: Institute of Engineering, Polytechnic of Porto, Dept. of Electrical Engineering, Rua Dr. António Bernardino de Almeida, 431, 4249 – 015 Porto, Portugal (*jtm@isep.ipp.pt*). The author gave a presentation of this paper during one of the conference sessions.

Nonlinear dynamics of the sensory element of the atomic force microscopy

Alexey Lukin, Popov Ivan, Udalov Pavel

In this paper, a microscope with a sensitive element in the form of a cantilever beam operating in the frequency contact mode. The problem of obtaining approximate analytical expressions describing the dynamics of the sensitive element in the case of forced oscillations, taking into account the pre-stressed state caused by static deformation and non-linear force of interaction with the sample. Asymptotic and variational methods of mathematical physics, a model is constructed and estimates are obtained, the result is compared with a numerical solution by the finite element method. The key focus in this work is the analysis of the nonlinear dynamics of the sensitive element of an atomic force microscope and the selection of the information signal from the nonlinear effects associated with the interaction of the indenter and the sample. It is interesting and practically important to conduct a qualitative analysis of the dynamics of a sensitive element using asymptotic methods of the nonlinear theory of oscillations, and to obtain final analytical expressions and curves that could serve as a basis for highlighting useful signal. Due to the generality of the method, the range of applicability of these results would not be limited to an atomic force microscope, and they would also prove useful in designing gyroscopic instruments.

1.1 Introduction

In this work, we will consider such a section of microscopy as scanning probe microscopy (SPM), which is one of the most powerful modern methods in studying the surfaces of objects.

In its turn, SPM is divided into two main layers, “modes” - scanning tunneling (STM) and atomic force microscopy (AFM), which allow studying the topography of both conductive and dielectric materials. Namely, a qualitative analysis of AFM devices, its operating modes, and a method for determining the surface will be made.

Before describing the AFM, it is necessary to say about its predecessor - a scanning tunneling microscope (STM). The main principle of its operation is that in the STM a metal needle is brought to the sample at a distance of 0.1 nm. Further, when a certain potential is applied, a tunnel current arises in this needle, which changes when interacting with electrons on the surface of the object under study. And just by this change you can judge the relief of the sample. In more detail, the principle of STM operation is considered in.

STM gives fairly accurate results of the surface of the sample, but since its principle of operation is associated with the tunneling current and its interaction with the electrons located on the sample, unfortunately, in some situations the STM will not be able to give correct and correct results.

There are extreme cases, for example, the presence of a sample in water, vacuum, the study of non-conductive, dielectric materials, in which the STM will not be able to give correct results, not to mention the fact that in some cases it cannot be used.

The next step in scanning probe microscopy was AFM, which can and works in almost any medium, not counting the one that can destroy it, for example, acid, etc. It is also possible to work with non-conductive and dielectric materials.

The sensitive element of the atomic force microscope is a beam of constant cross section with a tip at the end. A change in the distance between the tip and the surface of the test sample will give information about the topography of the sample. In contact mode, the AFM tip is subjected to repulsive forces due to the proximity of the electron shells of the tip and the sample. With this interaction, the beam is repelled to its equilibrium position, and then continues to pave near it. Further we will be based on the contact theory of Hertz, representing the contact between the infinite half-plane and the hemisphere (end of the tip).

For the most accurate operation of the AFM, phase modulation is used, in which the sample is subjected to a harmonic signal at the resonant frequency of the sensing element. And by changing this frequency from the resonance one can judge the topography of the object.

After that, we consider the case of subharmonic resonance, in which the sample will be excited at a frequency equal to the integer part of the resonance

1.2 Mathematical model

Next, we will consider the movement of the AFM during its operation in contact mode. When the probe is excited by an external harmonic signal, bending vibrations are observed, the movements of which occur in the vertical direction.

We choose a linear beam (Bernoulli – Euler beam) as a mechanical model of the AFM, to which a force is applied at its tip.

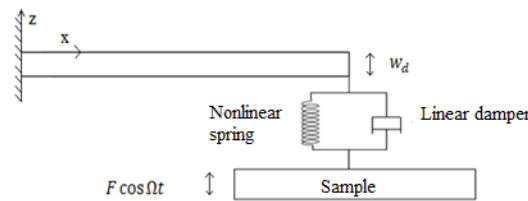


Figure. 1. Model of contact mode AFM.

Further, following the notation [4], we write the equation of bending vibrations and the corresponding boundary conditions:

$$\hat{w}^{IV} + \ddot{\hat{w}} = 0 \quad (1)$$

$$\hat{w}|_{\hat{x}=0}, \hat{w}'|_{\hat{x}=0} = 0 \quad (2)$$

$$\hat{w}''|_{\hat{x}=1} = 0 \quad (3)$$

$$(\hat{w}''' - \hat{\alpha}_1 \hat{w})|_{\hat{x}=1} = (\hat{\mu} \dot{\hat{w}} - \hat{\alpha}_2 \hat{w}^2 - \hat{\alpha}_3 \hat{w}^3 + \hat{F} \cos \hat{\Omega} \hat{t})|_{\hat{x}=1}, \quad (4)$$

where $(\cdot)^I, (\cdot)^{\dot{}}$ respectively denote the derivative with respect to the new dimensionless coordinate \hat{x} and dimensionless time \hat{t} . \hat{w} – dimensionless movement of the tip, $\hat{\mu}$ – dimensionless coefficient of friction, $\hat{\alpha}_1, \hat{\alpha}_2, \hat{\alpha}_3$ – Hertz dimensionless coefficients[4, 6], $\hat{F}, \hat{\Omega}$ – dimensionless amplitude and frequency of the exciting harmonic signal. Dimensionless quantities and the transition to dimensional are shown in [4].

1.3 Linear model of AFM motion

Next, we consider the mathematical model (1) - (4), discarding all nonlinear terms in it and find solution as:

$$\hat{w} = X_n(\hat{x}) \sin \hat{\omega}_n \hat{t}, \quad (5)$$

where $\hat{\omega}_n$ – dimensionless natural frequency of the AFM. Substitute (5) in (1)-(4) we get the expression for the natural frequencies of the AFM:

$$\hat{\alpha}_1 (ch b_n \sin b_n - sh b_n \cos b_n) + b_n^3 (1 + \cos b_n ch b_n) = 0 \quad (6)$$

where $\hat{\omega}_n^2 = b_n^4$.

And we get the expression of the mode shapes :

$$X_n(\hat{x}) = C \left(-\frac{sh(b_n) + \sin(b_n)}{ch(b_n) + \cos(b_n)} (ch(b_n \hat{x}) - \cos(b_n \hat{x})) + (\sin(b_n \hat{x}) - sh(b_n \hat{x})) \right) \quad (7)$$

where C – unknown constant that can be determined from the normalization condition.

1.4 Asymptotic formulation of the AFM motion problem

Next, we obtain an analytical expression for the cantilever deflection using the multi-scale method [].

Define the deflection of the beam \hat{w} in the form:

$$\hat{w} = \varepsilon \hat{w}_1(\hat{x}, \hat{T}_0, \hat{T}_1, \hat{T}_2) + \varepsilon^2 \hat{w}_2(\hat{x}, \hat{T}_0, \hat{T}_1, \hat{T}_2) + \varepsilon^3 \hat{w}_3(\hat{x}, \hat{T}_0, \hat{T}_1, \hat{T}_2) \quad (8)$$

where ε – small dimensionless parameter.

Further, by changing the variables with respect to time \hat{t} , we pass to the derivatives with respect to \hat{T}_n :

$$\frac{\partial}{\partial \hat{t}} = D_0^2 + \varepsilon D_1 + \varepsilon^2 D_2 \quad (9)$$

$$\frac{\partial^2}{\partial \hat{t}^2} = D_0^2 + 2\varepsilon D_0 D_1 + \varepsilon^2 (D_1^2 + 2D_0 D_2) + \dots \quad (10)$$

$$D_n = \frac{\partial}{\partial \hat{T}_n} \quad (11)$$

We renormalize the coefficient of linear friction and the amplitude of the exciting force, assuming that they have the corresponding second and third orders of smallness.

$$\hat{\mu} \rightarrow \varepsilon^2 \hat{\mu}, \hat{F} \rightarrow \varepsilon^3 \hat{F} \quad (12)$$

It is worth noting that it is at this moment that our liberty is present: namely, in the choice of the smallness of these values. But, as practice shows [3,5,6], it is precisely with the corresponding orders of smallness that the final expression for determining the topography of the surface of the studied sample, as will be shown below, will include all parameters of not only the AFM, but also the sample itself. Equating the expressions with the same powers of ε , we obtain the following problems:

ε :

$$\frac{\partial^4 \hat{w}_1}{\partial \hat{x}^4} = D_0^2 \hat{w}_1 \quad (13)$$

$$\hat{w}_1|_{\hat{x}=0} = 0 \quad (14)$$

$$\frac{\partial \hat{w}_1}{\partial \hat{x}}|_{\hat{x}=0} = 0 \quad (15)$$

$$\frac{\partial^2 \hat{w}_1}{\partial \hat{x}^2}|_{\hat{x}=1} = 0 \quad (16)$$

$$\frac{\partial^3 \hat{w}_1}{\partial \hat{x}^3} - \hat{\alpha}_1 \hat{w}_1|_{\hat{x}=1} = 0 \quad (17)$$

ε^2 :

$$\frac{\partial^4 \hat{w}_2}{\partial \hat{x}^4} + D_0^2 \hat{w}_2 = -2D_0 D_1 \hat{w}_1 \quad (18)$$

$$\hat{w}_2|_{\hat{x}=0} = 0 \quad (19)$$

$$\frac{\partial \hat{w}_2}{\partial \hat{x}}|_{\hat{x}=0} = 0 \quad (20)$$

$$\frac{\partial^2 \hat{w}_2}{\partial \hat{x}^2}|_{\hat{x}=1} = 0 \quad (21)$$

$$\frac{\partial^3 \hat{w}_2}{\partial \hat{x}^3} - \hat{\alpha}_1 \hat{w}_2|_{\hat{x}=1} = -\hat{\alpha}_2 \hat{w}_1^2|_{\hat{x}=1} \quad (22)$$

ε^3 :

$$\frac{\partial^4 \hat{w}_3}{\partial \hat{x}^4} + D_0^2 \hat{w}_3 = -[2D_0 D_1 \hat{w}_2 + (D_1^2 + 2D_0 D_2) \hat{w}_1] \quad (23)$$

$$\hat{w}_3|_{\hat{x}=0} = 0 \quad (24)$$

$$\frac{\partial \hat{w}_3}{\partial \hat{x}}|_{\hat{x}=0} = 0 \quad (25)$$

$$\frac{\partial^2 \hat{w}_3}{\partial \hat{x}^2} \Big|_{\hat{x}=1} = 0 \quad (26)$$

$$\left(\frac{\partial^3 \hat{w}_3}{\partial \hat{x}^3} - \hat{\alpha}_1 \hat{w}_3 \right) \Big|_{\hat{x}=1} = [\hat{\mu} D_0 \hat{w}_1 - 2\hat{\alpha}_2 \hat{w}_1 \hat{w}_2 - \hat{\alpha}_3 \hat{w}_1^3 + \hat{F} \cos \hat{\Omega} \hat{t}] \Big|_{\hat{x}=1} \quad (27)$$

The problem for ε (13)-(17) coincides with the linear problem (1) – (4).

After successively solving problems (18)-(22) and (23-27), determining the secular terms, we arrive at a system of differential equations for the amplitude c_r and phase c_i of the beam oscillations.

$$\frac{dc_r(\hat{T}_2)}{d\hat{T}_2} = -\frac{\hat{\mu} X_n(1)}{2\Delta} c_r - \frac{1}{2\omega_n \Delta} F \sin c_i \quad (28)$$

$$c_r \frac{dc_i(\hat{T}_2)}{d\hat{T}_2} = c_r \sigma + \frac{1}{\omega_n \Delta} \left[2\hat{\alpha}_2 \left(X_n(1) \tilde{X}_n(1) - 2B X_n(1) \right) + 3\hat{\alpha}_3 X_n^3(1) \right] \frac{c_r^3}{8} - \frac{1}{2\omega_n \Delta} F \cos c_i \quad (29)$$

where :

$$\Delta = \int_0^1 X_n^2(\hat{x}) d\hat{x} \text{ —norm of eigenfunction } X_n \quad (30)$$

σ -detuning parameter defined as:

$$\hat{\Omega} = \omega_n + \varepsilon^2 \sigma \quad (31)$$

$$B = -\frac{\hat{\alpha}_2 X_n^2(1)}{6 + 2\hat{\alpha}_1} \quad (32)$$

1.5 Periodic motions

Periodic motions correspond to the fixed points (c_{r0}, c_{i0}) of equations (28) and (29). Thus, letting

$\frac{dc_r(\hat{T}_2)}{d\hat{T}_2} = \frac{dc_i(\hat{T}_2)}{d\hat{T}_2} = 0$ in equations (28) and (29), we obtain the following frequency– response

equation:

$$\sigma = \frac{-2W c_{r0}^4 \pm \sqrt{4W^2 c_{r0}^8 - 4c_{r0}^2 (Z^2 c_{r0}^6 + W^2 c_{r0}^2 - Y^2)}}{2c_{r0}^2} \quad (33)$$

where:

$$Y = \frac{F}{2\omega_n \Delta} \quad (34)$$

$$Z = \frac{\hat{\mu} X_n(1)}{2\Delta} \quad (35)$$

$$W = \frac{1}{8\omega_n \Delta} \left[2\hat{\alpha}_2 \left(X_n(1) \tilde{X}_n(1) - 2B X_n(1) \right) + 3\hat{\alpha}_3 X_n^3(1) \right] \quad (36)$$

The maximum oscillation c_{r0} is reached when the radical expression disappears in equation (33), i.e., at maximum, the roots of this expression become multiple. Therefore, the value of the frequency detuning parameter, which corresponds to it, is known to us and is equal to $\sigma = \sigma_0$.

Thus we obtain the dependence of the frequency detuning parameter at which the maximum amplitude is observed on the cantilever's static deflection.

$$\sigma_0 = \frac{F}{8\hat{\mu}\Delta\omega_n^2} \left[-2\hat{\alpha}_2 \left(\tilde{X}_n(1) + \frac{\hat{\alpha}_2 X_n^2(1)}{3 + \hat{\alpha}_1} \right) - 3\hat{\alpha}_3 X_n^2(1) \right] \quad (37)$$

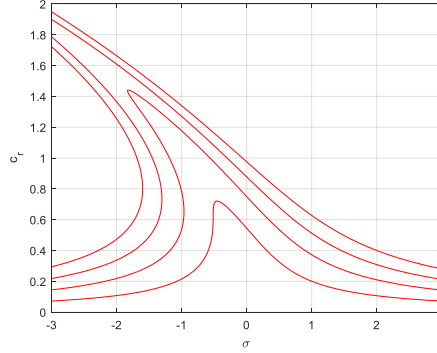


Figure 2. Graph of the frequency response of nonlinear oscillations in the case of $\hat{\alpha}_1 = 50$, $F = (1, 2, 3, 4)$, $\hat{\mu} = 0.12$, $\hat{\Omega} \approx \hat{\omega}_1$.

Figure 4 shows that up to two values of the amplitude of oscillations can correspond to a certain value of σ . And in order to establish whether we are really at the maximum amplitude, it is necessary to act in the following way: for example, first start to increase the frequency of external excitation, if the amplitude decreases, then, accordingly, the maximum is in the zone of lower frequencies. Then, it will be necessary to reduce the frequency - if the amplitude starts to increase and at some point decreases sharply, it means that we were at the maximum amplitude. If this is not observed, then we are not in the region of minimum amplitude. The main disadvantage of this operation - each measurement of the amplitude after changing the frequency, even waiting for a steady motion - takes time. It is the time taken to identify the amplitude of the oscillations that are one of the significant disadvantages of AFM in the case of resonant excitation.

AFM motion in the case of subharmonic resonance

Previously, AFM operation was considered when a sample was excited by a harmonic signal at one of the resonant frequencies. Next, we will consider the case in which the excitation frequency will be some part of the resonance, for example, half of natural frequency. Further construction will be based on [4]. Below are only the main points. We study the response of the probe to a subharmonic resonance at half the natural frequency.

We write the response of the system in the form of the sum of the forced and resonant component:

$$\hat{w}(\hat{x}, \hat{t}) = \hat{F}\hat{\Psi}(\hat{x}) \cos \hat{\Omega}\hat{t} + \hat{u}(\hat{x}, \hat{t}) \quad (38)$$

We write the periodic motions of the AFM in the case of subharmonic resonance in the Nayfe notation [4].

$$c_r' = -\hat{\mu}X_n^2(1)c_r + \frac{\Lambda}{2\hat{\omega}_n}c_r \sin \gamma \quad (39)$$

$$c_r\gamma' = -\sigma c_r + \frac{2a_e}{\hat{\omega}_n}c_r^3 + \frac{\Lambda}{\hat{\omega}_n}c_r \cos \gamma \quad (40)$$

where:

$$\hat{\Psi}(\hat{x}) = \frac{(\cos b_{\hat{\Omega}} + chb_{\hat{\Omega}})(shb_{\hat{\Omega}} - \sin b_{\hat{\Omega}}) + (\sin b_{\hat{\Omega}} \hat{x} + shb_{\hat{\Omega}}\hat{x})(\cos b_{\hat{\Omega}}\hat{x} - chb_{\hat{\Omega}}\hat{x})}{2[\hat{\alpha}_1(chb_{\hat{\Omega}} \sin b_{\hat{\Omega}} - shb_{\hat{\Omega}} \cos b_{\hat{\Omega}}) + b_{\hat{\Omega}}^3(1 + \cos b_{\hat{\Omega}}chb_{\hat{\Omega}})]} \quad (41)$$

where $b_{\hat{\Omega}}^2 = \hat{\Omega}$.

Such an approximation for the probe response is valid and exists for all frequencies $\hat{\Omega}$ far from the resonant ones. For $\hat{\Omega} = \hat{\omega}_n$, the denominator in (41) is zeroed.

$$\chi_0(\hat{x}) = \frac{\hat{x}^3 - 3\hat{x}^2}{6 + 2\hat{\alpha}_1} \quad (42)$$

$$\chi_2(\hat{x}) = \frac{(\cos b_{\lambda} + chb_{\lambda})(shb_{\lambda} - \sin b_{\lambda}) + (\sin b_{\lambda} \hat{x} + shb_{\lambda}\hat{x})(\cos b_{\lambda}\hat{x} - chb_{\lambda}\hat{x})}{2[\hat{\alpha}_1(chb_{\lambda} \sin b_{\lambda} - shb_{\lambda} \cos b_{\lambda}) + b_{\lambda}^3(1 + \cos b_{\lambda}chb_{\lambda})]} \quad (43)$$

where $b_{\lambda} = 2\hat{\omega}_n$

$$a_e = \frac{1}{8}X_n^4(1)\{2\hat{\alpha}_2^2[\chi_2(1) + 2\chi_0(1)] - 3\hat{\alpha}_3\} \quad (44)$$

$$\Lambda = -\hat{\alpha}_2\hat{F}X_n^2(1)\hat{\Psi}(1) \quad (45)$$

1.6 Periodic motions in the case of subharmonic resonance

Periodic motions correspond to the fixed points (c_{r0}, c_{i0}) of equations (28) and (229). Thus, letting

$c_r' = c_i' = 0$ in equations (39) and (40), we obtain the following frequency– response equation:

$$c_{r0}^2 \left[4\hat{\mu}^2 X_n^4(1) + \left(\sigma - \frac{2a_e c_{r0}^2}{\hat{\omega}_n} \right)^2 \right] = \frac{\Lambda^2}{\hat{\omega}_n^2} c_{r0}^2 \quad (46)$$

It is easy to see that two cases satisfy equation (46): $c_{r0} = 0, c_{r0} \neq 0$.

Second case give us:

$$c_{r0} = \sqrt{\frac{\hat{\omega}_n}{2a_e} \left[\sigma \pm \sqrt{\frac{\Lambda^2}{\hat{\omega}_n^2} - 4\hat{\mu}^2 X_n^4(1)} \right]} \quad (47)$$

The question of stability was fully considered in []. Let us write down only the values of the critical force, which will be enough to act on the system to deduce it from the trivial solution and the

critical parameter of the frequency detuning, which will determine the interval of the non-trivial solution for the beam oscillation amplitude.

$$\sigma_c = \pm \frac{\sqrt{\Lambda^2 - 4\hat{\mu}^2 X_n^4(1)}}{\hat{\omega}_n} \quad (48)$$

It determines the interval $[-\sigma_c, \sigma_c]$ of the forced frequency, within which the trivial solution is unstable.

On the other hand, with a fixed parameter σ , it is possible to act on the system with different levels of external force F .

The critical level of force that corresponds to the instability of the trivial solution:

$$F_c = \left| \hat{\omega}_n \frac{\sqrt{\sigma^2 + 4\hat{\mu}^2 X_n^4(1)}}{-\hat{\alpha}_2 X_n^2(1) \hat{\Psi}(1)} \right| \quad (49)$$

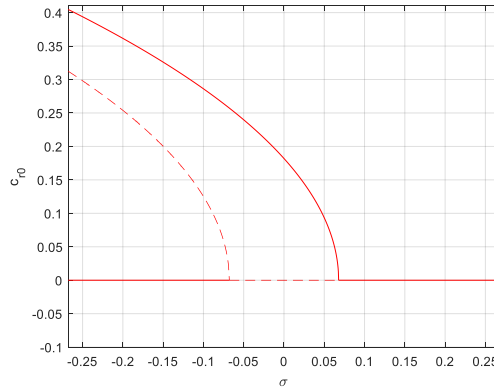


Figure 3. Solid lines show stable solutions, dashed lines indicate unstable solutions. In the experiment, only solutions on solid lines can be seen. A stable solution is stable for all values of the frequency detuning around $2\hat{\omega}_n$, except for the interval $[-\sigma_c, \sigma_c]$.

Stable and unstable branches of the solution are bent to the left, because the nonlinearity in this case is mitigating.

It can be seen from the foregoing that, generally speaking, the amplitude at subharmonic resonance can be zero, that is, in this case there will be no information signal for registering the surface of the sample. The interval of an unstable trivial amplitude value $[-\sigma_c, \sigma_c]$ was previously established, in which the zero position loses stability and switches to a solid branch. And it is precisely by the value of the amplitude on it that a conclusion will be made about the cantilever deflection.

The main difficulty associated with working in a subharmonic resonance is that it is necessary to select the parameters of the frequency detuning and the excitation force in such a way that the trivial solution loses its stability and switches to a nontrivial stable branch.

1.7 Asymptotic calculation of the first natural frequency

We turn to the transcendental equation to determine the natural frequencies of the beam (6).

Next, we represent trigonometric functions through interpolation polynomials describing their behavior on a half-wave period. We represent hyperbolic functions using the Padé approximation.

$$\sin(x) = -\frac{4}{\pi^2}(x^2 - \pi x) \quad (50)$$

$$\cos(x) = 1 - \frac{14}{3\pi^2}x^2 + \frac{8}{3\pi^4}x^4 \quad (51)$$

For example, we use the Padé approximation [0 1]. Substituting it and the representations (50) and (51) in (6). Next, using the direct decomposition method, we find the root at the zero degree of the small parameter.

The expression obtained for the first approximation of the root is obtained using symbolic calculations in Matlab. Only the value of the absolute error between the analytical expression for the natural frequency and asymptotic is given below.

Absolute error in the case of Padé approximation:

$$\delta_p = 4.07\% \quad (51)$$

Below is a graph illustrating the Padé table, those ratios of the numerator and denominator for which there is a minimum absolute error are highlighted in red. Errors of 99% are due to the fact that the approximant is trying to catch the zero frequency.

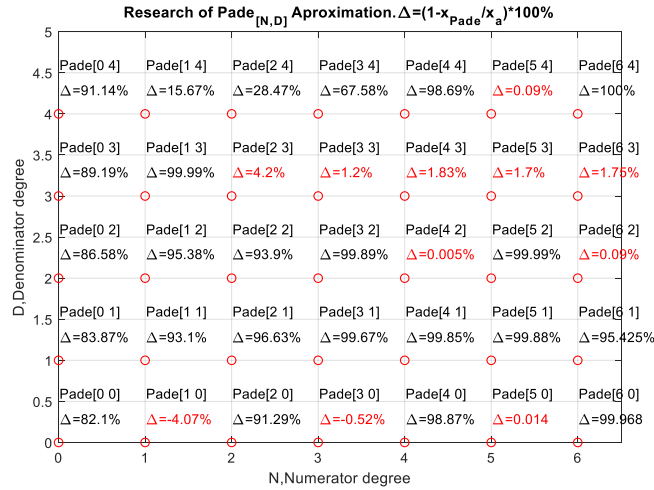


Figure 4. Padé's table

1.8 Conclusion

Summing up the above, I want to note that microscopy as a subject of scientific research is of great interest. Using AFM as an example, it was shown that special attention must be paid to modeling the force of interaction between the tip and tip, because for each operating mode this force is modeled individually.

The contact mode was selected as the main AFM mode. At first glance, the main problem was related to nonlinearity in the boundary conditions. Then we used the MMM, an asymptotic solution was constructed for the deflection function. As in all problems associated with MMM, in the end a nonlinear system of differential equations is obtained with respect to the amplitude and phase of the beam oscillations. Next, periodic motions were considered and the frequency response of nonlinear oscillations was constructed. A breakdown of the amplitude was revealed, which is characteristic of such problems.

Similar studies were conducted for subharmonic resonance. This is a resonance in which the sample is no longer excited at the resonant frequency, but, for example, at doubled. It was found that in this solution there is a trivial solution for the oscillation amplitude.

A qualitative study is carried out on the stability of trivial solutions and the boundaries of the frequency detuning parameter and the critical force for the instability of this trivial solution are established. Of course, each of these two methods for determining the surface of a sample has its pros and cons. In the case of resonant excitation, it is necessary to check whether we are at the maximum amplitude. In a subharmonic resonance, however, time is needed for the trivial solution to fall into the instability region.

References

1. Biderman V.L. Theory of mechanical vibrations. M.: "Higher School", 1980. 149 -160 p.
2. Voznesensky E.F., Sharifullin I.Sh., Abdullin I.Sh. Methods of structural studies of materials. Microscopy methods. Kazan. "Publishing house of KNITU", 2014. - 184 p.
3. Nayfeh A.Kh. Introduction to perturbation methods. M.: "World", 1984. -536 pp.
4. Abdel-Rahman E.M., Nayfeh A.H. - Contact force identification using the subharmonic resonance of a contact-mode atomic force microscopy. , Blacksburg IOP Publishing Ltd, 2005.199-207 p.
5. Garcia R., Perez R. Dynamic atomic force microscopy methods. , Elsevier Science B.V., 2002.-301 p.
6. Nayfeh A.H., Pai P.F. Linear and Nonlinear Structural Mechanics. Mörlenbach, WILEY - VCH Publ., 2004.-763p.
7. Mohammad I. Younis. MEMS Linear and Nonlinear Statics and Dynamics. New York, Springer Science + Business Media, 2011.-453 p.
8. Oliver Brand, Isabelle Dufour, Stephen M. Heinrich, Fabien Josse (Eds.). Resonant MEMS. Fundamental, Implementation and Application. Weinheim WILEY - VCH Publ., 2005. -483p
9. Roland Wiesendanger, Scanning Probe Microscopy and Spectroscopy. Methods and applications, Cambridge, Cambridge University Press, 1994, -626 p.
10. Timoshenko S, Goodier J N. Theory of Elasticity, New York, McGraw-Hill, 1951, -506p.

Size-dependent nonlinear vibrations of micro-plates subjected to in-plane magnetic field

Olga Mazur, Jan Awrejcewicz

Abstract: Nonlinear vibrations of the microplates subjected to the influence of a longitudinal magnetic field are considered. Size-dependent model based on a modified couple stress theory is employed. The governing equations for geometrically nonlinear vibrations use the von Karman plate theory. Effect of the magnetic field is taken into account due to the Lorentz force deriving from the Maxwell's equations. Developed approach is based on applying of the Bubnov-Galerkin method and reducing partial differential equations to an ordinary differential equation. Some calculations are performed to validate the proposed algorithm in comparison with the known from literature results. Influence of the magnetic field, material length scale-parameter, plate aspect ratio on the system behavior is studied.

It is clear that problems of micro and nano sized elements have been increasingly studied because of the widespread use of microplates, microbeams, microshells in high-tech industries. It is often the microelements are subjected to various loads which can significantly effects on its behavior. Investigation of plate under magnetic field in-plane influence is of great importance due to using as elements of NEMS, MEMS, resonators, sensors etc. The experimental and theoretical investigations allow to conclude that a size-dependent effect appears when thickness is in a micro or nano scale [1] and for accurate analysis classical elasticity theory can be not enough. Various theories have been applied to study of micro and nano structures, theory of micropolar elasticity by Cosserat and Cosserat [2], couple stress theory by Mindlin and Tiersten [3], Toupin [4], Koiter [5], the nonlocal elasticity theory by Eringen [6], strain gradient theory by Lam et al. [1]. In this paper we use modified couple stress theory (MCST) proposed by Yang et al [7], which contains only one additional material length scale parameter and a symmetric couple stress tensor.

Recently, MCST was used in linear vibrations, buckling and bending plate analysis [8-13], nonlinear vibrations of micro-plates [14,15], FG Mindlin microplates [16], viscoelastic plates [17], chaotic vibrations of nano-shells [18]. Influence of magnetic field on micro and nano plates is studied in [19-22] using nonlocal elasticity theory. Analysis of published results has shown that geometrically nonlinear vibrations of small-sized plates subjected to magnetic influence in framework MCST has not been investigated yet.

In the paper we present an analytical method for small-sized geometrically nonlinear vibrations of plates. The investigation is based on the modified couple stress theory, the von Karman plate theory,

Kirchhoff-Love hypotheses and Maxwell's relations. The governing PDEs is reduced to ODE by applying of the Bubnov-Galerkin method. The present results contain study of the magnetic field effect and material length scale parameter influence on the frequencies and backbone curves.

1.1. Formulation

Geometrically nonlinear vibrations of isotropic plate (see Fig.1) in magnetic field are considered. According to the modified couple strain theory [7] the strain energy unlike the classical elasticity theory depends on stress tensor and curvature tensor and it is presented as

$$U = \frac{1}{2} \int_V (\sigma_{ij} \varepsilon_{ij} + m_{ij} \chi_{ij}) dV \quad (1)$$

where $\sigma_{ij}, \varepsilon_{ij}, m_{ij} \chi_{ij}$ are components of stress tensor, strain tensor, diviatory part of the couple stress tensor, symmetric curvature tensor, that are defined as

$$\sigma_{ij} = \lambda \varepsilon_{kk} \delta_{ij} + 2\mu \varepsilon_{ij}, \quad \varepsilon_{ij} = \frac{1}{2} (u_{i,j} + u_{j,i} + u_{m,i} u_{m,j}), \quad (2)$$

$$m_{ij} = 2l^2 \mu \chi_{ij}, \quad \chi_{ij} = \frac{1}{2} (\theta_{i,j} + \theta_{j,i}), \quad (3)$$

where λ, μ are Lamé constants

$$\lambda = \frac{E\nu}{(1+\nu)(1-2\nu)}, \quad \mu = \frac{E}{2(1+\nu)}.$$

δ_{ij} is Kronecker delta, l is a material length scale parameter, ν is Poisson's ratio, E is Young's modulus, u_i are displacements, θ_i are components of rotation vector, which have form

$$\theta_i = \frac{1}{2} e_{ijk} u_{k,j}, \quad (4)$$

here e_{ijk} is permutation symbol.

The nonlinear dynamics of the plate is derived by the equations based on the von Karman theory. Mixed form of the governing equations in propagation of elastic waves in longitudinal equations are neglected is presented [18]

$$(D + D_L) \Delta^2 w = L(w, F) - \rho h \frac{\partial^2 w}{\partial t^2} + q_l, \quad (5)$$

$$\frac{1}{2} L(w, w) = -\frac{1}{Eh} \Delta^2 F, \quad (6)$$

$$L(w, w) = 2 \left(\frac{\partial^2 w}{\partial x^2} \frac{\partial^2 w}{\partial y^2} - \left(\frac{\partial^2 w}{\partial x \partial y} \right)^2 \right), \quad L(w, F) = \frac{\partial^2 w}{\partial x^2} \frac{\partial^2 F}{\partial y^2} + \frac{\partial^2 w}{\partial y^2} \frac{\partial^2 F}{\partial x^2} - 2 \frac{\partial^2 w}{\partial x \partial y} \frac{\partial^2 F}{\partial x \partial y}.$$

In (5), (6) F is the stress function [18,23], h is thickness of the plate, $D = \frac{Eh^3}{12(1-\nu^2)}$, $D_L = \frac{Elh^2}{2(1+\nu)}$, q is load.

System of equations (see Eq. 5, 6) is supplemented with the boundary conditions:

simply supported movable edges:

$$w = 0, \frac{\partial^2 w}{\partial x^2} + \nu \frac{\partial^2 w}{\partial y^2} = 0, \frac{\partial^2 F}{\partial x \partial y} = 0, \int_0^b \frac{\partial^2 F}{\partial y^2} = 0, x = 0, a, \quad (7)$$

$$w = 0, \frac{\partial^2 w}{\partial y^2} + \nu \frac{\partial^2 w}{\partial x^2} = 0, \frac{\partial^2 F}{\partial x \partial y} = 0, \int_0^a \frac{\partial^2 F}{\partial x^2} = 0, y = 0, b. \quad (8)$$

simply supported immovable edges:

$$w = 0, \frac{\partial^2 w}{\partial x^2} + \nu \frac{\partial^2 w}{\partial y^2} = 0, \frac{\partial^2 F}{\partial x \partial y} = 0, u = 0, x = 0, a, \quad (9)$$

$$w = 0, \frac{\partial^2 w}{\partial y^2} + \nu \frac{\partial^2 w}{\partial x^2} = 0, \frac{\partial^2 F}{\partial x \partial y} = 0, v = 0, y = 0, b. \quad (10)$$

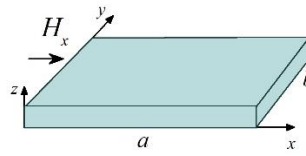


Figure 1. Microplate subjected to in-plane magnetic field

1.2. Influence of magnetic field

Changing the vibrational characteristics of the small-sized plates by an appropriate external influence can be effectively used in the structure design, vibration control etc. One of the significant effects is the use of a magnetic field. We consider the plate exposed to the uniaxial magnetic field [19,21,22], defined by the vector of magnetic field strength

$$\vec{H} = (H_x, 0, 0). \quad (11)$$

From Maxwell's relations distributing vector of the magnetic field \vec{h} has the form

$$\vec{h} = [\nabla, [\vec{U}, \vec{H}]], \quad (12)$$

where vector $\vec{U} = (u_x, u_y, u_z)$ is vector of displacements. After substitution (see Eq. 11) into (see Eq. 12) it can be obtained

$$\vec{h} = (-H_x \frac{\partial u_y}{\partial y} - H_x \frac{\partial u_z}{\partial z}, H_x \frac{\partial u_y}{\partial x}, H_x \frac{\partial u_z}{\partial z}). \quad (13)$$

Thus, current density \vec{J} is written as

$$\vec{J} = [\nabla, \vec{h}] = (H_x \frac{\partial^2 u_z}{\partial x \partial y} - H_x \frac{\partial^2 u_y}{\partial x \partial z}, -H_x \frac{\partial^2 u_z}{\partial x^2} - H_x \frac{\partial^2 u_y}{\partial y \partial z} - H_x \frac{\partial^2 u_z}{\partial z^2}, H_x \frac{\partial^2 u_y}{\partial x^2} + H_x \frac{\partial^2 u_y}{\partial y^2} + H_x \frac{\partial^2 u_z}{\partial y \partial z}). \quad (14)$$

The Lorentz force is defined as

$$f = (f_x, f_y, f_z) = \eta [\vec{J}, \vec{H}]. \quad (15)$$

In (see Eq. 15) η is the magnetic permeability.

It should be noted that the transverse vibrations are considered and only f_z is taken into account [22].

Formula (see Eq. 15) gives

$$f_z = \eta H_x^2 (\frac{\partial^2 u_z}{\partial x^2} + \frac{\partial^2 u_y}{\partial y \partial z} + \frac{\partial^2 u_z}{\partial z^2}). \quad (16)$$

For Kirchhoff-Love plate transverse component f_z takes form

$$f_z = \eta H_x^2 \left(\frac{\partial^2 w}{\partial x^2} - \frac{\partial^2 w}{\partial y^2} \right). \quad (17)$$

where w is mid-plane displacements of the plate along z directions. As a result, force produced by magnetic field can be presented as

$$q_l = \int_{-h/2}^{h/2} f_z dz = \eta h H_x^2 \left(\frac{\partial^2 w}{\partial x^2} - \frac{\partial^2 w}{\partial y^2} \right). \quad (18)$$

1.3. Linear vibrations of microplate in magnetic field

In the case of linear vibrations, system (see Eq. 5,6) is reduced and we have following equation

$$(D + D_L) \Delta^2 w = -\rho h \frac{\partial^2 w}{\partial t^2} + q_l. \quad (19)$$

Solution of such equation is taken as $w(x, y, t) = X(x, y) \cos \omega_{mn} t$, where $X = \sin \frac{m\pi}{a} \sin \frac{n\pi}{b}$ is shape function, that allows to obtain linear frequency of plate vibrations under in-plane magnetic field

$$\omega_{mn}^2 = \frac{(D + D_L) \left(\left(\frac{m\pi}{a} \right)^2 + \left(\frac{n\pi}{b} \right)^2 \right)^2 + \eta h H_x^2 \left(\left(\frac{m\pi}{a} \right)^2 - \left(\frac{n\pi}{b} \right)^2 \right)}{\rho h}. \quad (20)$$

For first mode (1,1) this formula is reduced to

$$\omega_{11}^2 = \frac{(D + D_L) \pi^4 \left(\frac{1}{a^2} + \frac{1}{b^2} \right)^2 + \eta h H_x^2 \pi^2 \left(\frac{1}{a^2} - \frac{1}{b^2} \right)}{\rho h}. \quad (21)$$

1.4. Nonlinear vibrations of microplate in magnetic field

Now let us consider system of equations (see Eq. 5,6). The deflection $w(x, y, t)$ is presented as

$$w(x, y, t) = w_0(t) \sin \frac{\pi x}{a} \sin \frac{\pi y}{b}. \quad (22)$$

Substitution (see Eq. 22) into the equation in (see Eq. 6) leads to

$$\frac{1}{Eh} \Delta^2 F = \frac{1}{2} w_0^2 \left(\frac{\pi}{a} \right)^2 \left(\frac{\pi}{b} \right)^2 \left(\cos \frac{2\pi x}{a} + \cos \frac{2\pi y}{b} \right). \quad (23)$$

The solution of the last equation (see Eq. 23) [23] is

$$F = \frac{Eh w_0^2}{32} \left(\frac{a^2}{b^2} \cos \frac{2\pi x}{a} + \frac{b^2}{a^2} \cos \frac{2\pi y}{b} \right) + p_1 x^2 + p_2 y^2. \quad (24)$$

Coefficients p_1 and p_2 can be found from boundary conditions, for case (see Eq. 9, 10) $p_1 = 0, p_2 = 0$, for case (see Eq. 7, 8)

$$p_1 = \frac{\pi^2 E h (a^2 + \mu b^2) w_0^2}{16(1 - \mu^2) a^2 b^2}, p_2 = \frac{\pi^2 E h (b^2 + \mu a^2) w_0^2}{16(1 - \mu^2) a^2 b^2}. \quad (25)$$

Next step is substitution expressions (see Eq. 22,24) into the first equation (see Eq. 5) of governing system and applying the Bubnov-Galerkin approach that leads to the following Duffing type equation

$$y'' + \omega_L^2 y + \alpha y^3 = 0, \quad (26)$$

where

$$\alpha = \frac{\pi^4 E h^2}{16 \rho} \left(\frac{1}{a^4} + \frac{1}{b^4} \right) + \frac{\pi^4 E h^2}{8(1-\nu^2) a^2 b^2} \left(\frac{b^2}{a^2} + \frac{a^2}{b^2} + 2\nu \right), \omega_L = \omega_{11}, y = \frac{w_0}{h}. \quad (27)$$

Equation (see Eq. 26) can be solved by the Bubnov-Galerkin approach, presenting the solution as $y(t) = A \cos \omega_N t$, where A, ω_N are amplitude and frequency of nonlinear vibrations. Thus, it can be obtained frequency ratio

$$\left(\frac{\omega_N}{\omega_L} \right)^2 = 1 + \frac{3}{4} \beta A^2, \beta = \frac{\alpha}{\omega_L^2}. \quad (28)$$

2. Validation

To verify presented method the results are compared with available ones, we considered size-dependent vibrations of rectangular simply supported plate without magnetic action. Dimensionless natural frequencies $\bar{\omega} = \omega_L \frac{a^2}{h} \sqrt{\frac{\rho}{E}}$ are presented in Table 1,2 for various values of l/h . The material properties for considered nanoplate are taken as $\rho = 1220 \text{ Kg/m}^3, E = 1.44 \text{ GPa}, \nu = 0.38$.

Table 1

Dimensionless natural frequencies $\bar{\omega}$ for isotropic simply supported square plate ($b/a=1$) depending on thickness ratio l/h

l/h	1/6	1/5	1/4	1/3	1/2	1
$b/a = 1$						
[17]	6.471	6.602	6.839	7.323	8.558	13.383
Present	6.471	6.603	6.839	7.323	8.558	13.383

Table 2

Dimensionless natural frequencies $\bar{\omega}$ for isotropic simply supported rectangular plate ($b/a=0.5$) depending on thickness ratio l/h

l/h	0.1	0.5	1
[17]	15.68	21.39	33.45
Present	15.685	21.396	33.459

In Table 3 nonlinear frequency ratios ω_N/ω_L for plate found by proposed method with $l = 0$ (classical theory) are presented. Material parameters are $\rho = 1220 \text{ Kg/m}^3, E = 1.44 \text{ GPa}, \nu = 0.3$. Boundary

conditions are supposed of type (see Eq. 9, 10). The results compared with ones obtained by another approaches [24-27].

Table 3

Nonlinear frequency ratio ω_N/ω_L for isotropic simply supported plate ($b/a = 1$)

$\frac{w}{h}$	[25]	[26]	[27]	[24]	Present
0.2	1.0195	1.0197	1.0195	1.0197	1.0195
0.4	1.0757	1.0768	1.0765	1.0767	1.0760
0.6	1.1625	1.1662	1.1658	1.1659	1.1641
0.8	1.2734	1.2813	1.2796	1.2813	1.2773
1	1.4024	1.4173	1.4163	1.4168	1.4095

Comparison of results allows to conclude about good agreement with the known ones in the literature.

3. Numerical results

To investigate the influence of magnetic field on vibration process dimensionless linear frequencies $\bar{\omega}$ for various values of magnetic parameter MP (here dimensionless magnetic parameter is introduced as $MP = \frac{\eta h H_x^2 a^2}{D}$) and thickness ratio l/h are calculated. It is assumed that plate has the following characteristics

$$\rho = 1220 \text{ Kg/m}^3, E = 1.44 \text{ GPa}, \nu = 0.38, a = 10 \text{ mm}, b/a = 1.5(a), b/a = 2(b), h/a = 0.01.$$

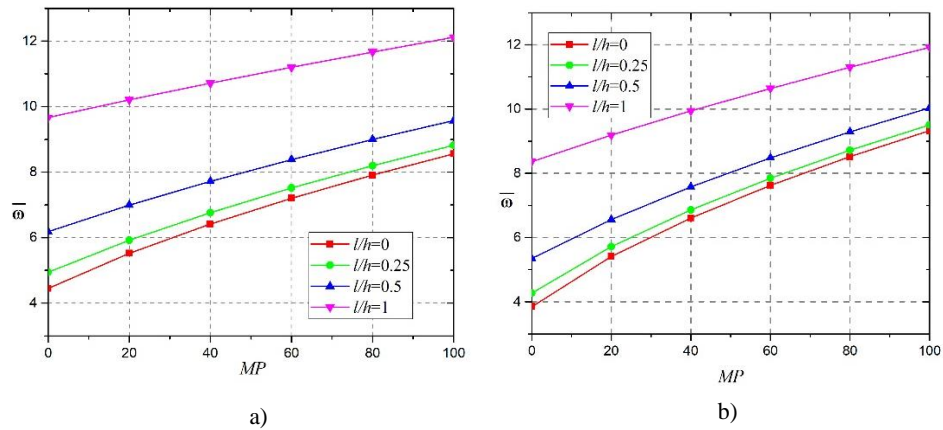


Figure 2. Dimensionless frequency for various values of material scale parameter, magnetic parameter, a) $b/a=1.5$, b) $b/a=2$.

Analyzing it can be seen that increasing of magnetic parameter leads to increasing of dimensionless frequency as well as it is observed the similar influence of length scale parameter on frequency in both cases of the plate aspect ratio. Also we can conclude that the aspect ratio has a small effect (especially when l/h is close to 1) on the frequency parameter at large values of the magnetic parameter.

Dimensionless frequency parameters $\bar{\omega}$ in terms of magnetic parameter and thickness ratio are calculated and presented on Figure 3. It can be found that frequency parameter generally increasing with increasing of magnetic parameter and material scale length parameter. Changing of magnetic parameter has smaller effect on vibration frequency when material length scale parameter is close to thickness of the plate. The minimum of dimensionless frequency achieves when MP and l vanish.

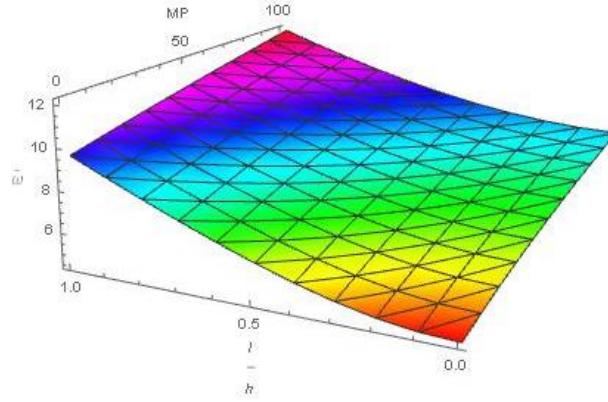


Figure 3. Dimensionless frequency parameter $\bar{\omega}$ in terms of MP and l/h

The effect of geometric nonlinearity is demonstrated on Figure 4, 5. The backbone curves (see Eq. 28) for rectangular plate specified by the aspect ratio $b/a=1.5$, thickness ratio $l/h=0$ and various MP are provided on Figure 4. According to obtained results frequency ratio decreases with increasing of magnetic parametric value MP . Further we fixed $MP=0$ to investigate the influence of material length scale parameter l on backbone curves, these results are presented on Figure 5. The size effect is more meaningful when $l/h>2.5$ and the difference in results obtained by classical theory and modified couple stress theory is insignificant when the thickness ratio l/h is small. Action of magnetic field as well as scale parameter is more significant in the case of immovable edges (see Eq. 9,10), in case of movable edges (see Eq.7,8) the backbone curves are closer each other (see Fig. 4, 5).

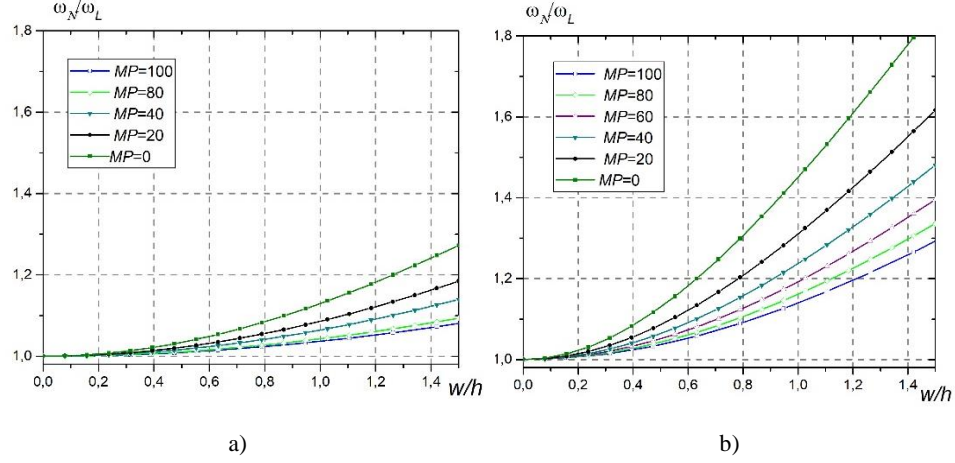


Figure 4. Frequency ratio (see Eq. 28) for two types of boundary conditions: a)-conditions (see Eq. 7,8), b) – conditions (see Eq. 9,10), $l/h=0$

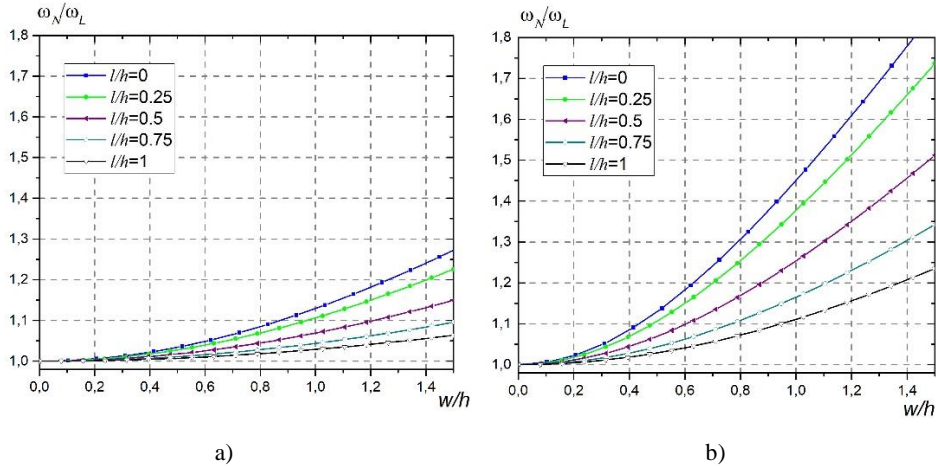


Figure 5. Frequency ratio (see Eq. 28) for two types of boundary conditions: a)-conditions (see Eq. 7,8), b) – conditions (see Eq. 9,10), $MP=0$

4. Conclusions.

The size-dependent nonlinear vibrations of microplates in magnetic field are studied. Governing PD equations are based on the modified couple stress theory, the Kirchhoff hypothesis, the von Karman theory. The influence of the material length scale parameter, the magnetic parameter, boundary conditions, aspect ratio on the linear frequency, nonlinear ratio is investigated. It has been shown that the linear frequency increases with increasing of length scale parameter and magnetic parameter unlike

the ratio of nonlinear frequency to linear frequency, which decreases. Also, the small-size effect and magnetic action are more significant for immovable simply supported plates.

References

- [1] Lam, D.C.C., Yang, F., Chong, A.C.M., Wang, J., Tong, P. Experiments and theory in strain gradient elasticity. *J Mech Phys Solids*, 51 (2003), pp. 1477–1508.
- [2] Cosserat, E, Cosserat, F. *Theory of deformable bodies*. In: Delphenich DH, editor. Scientific Library, 6. Paris: A. Herman and Sons., Sorbonne 6; 1909.
- [3] Mindlin, R.D., Tiersten, H.F. Effects of couple-stresses in linear elasticity. *Arch Ration Mech Anal*, 11 (1962), pp. 415–48.
- [4] Toupin, R.A. Elastic materials with couple stresses. *Arch Ration Mech Anal*, 11(1962), pp. 385–414.
- [5] Koiter, W.T. Couple stresses in the theory of elasticity, *I and II*. *Proc K Ned Akad Wet (B)*. 67 (1964), pp.17–44.
- [6] Eringen, A.C. On differential equations of nonlocal elasticity and solutions of screw dislocation and surface waves. *J Appl Phys*, 54 (1983), pp.4703–10.
- [7] Yang, F., Chong, A.C.M., Lam, D.C.C., Tong, P. Couple stress based strain gradient theory for elasticity. *Int J Solids Struct*, 39 (2002), pp.2731–43.
- [8] Tsiatas GC. A new Kirchhoff plate model based on a modified couple stress theory. *Int J Solids Struct*, 46 (2009), pp. 2757–64.
- [9] Yin L., Qian Q., Wang L., Xia W. Vibration analysis of microscale plates based on modified couple stress theory. *Acta Mech Solida Sin*, 23 (2010), pp.386–93.
- [10] Jomehzadeh, E., Noori, H.R., Saidi, A.R. The size-dependent vibration analysis of micro-plates based on a modified couple stress theory. *Physica E*, 43 (2011), pp.877–883.
- [11] Simsek, M., Aydın, M., Yurtcu, H. H., Reddy, J. N. Size-dependent vibration of a microplate under the action of a moving load based on the modified couple stress theory. *Acta Mech*, 226, (2015), pp. 3807–3822.
- [12] Akgöz, B., Civalek, Ö. Free vibration analysis for single-layered graphene sheets in an elastic matrix via modified couple stress theory. *Materials and Design*, 42 (2012), pp. 164–171.
- [13] Ziaee, S. Linear free vibration of micro-/nano-plates with cut-out in thermal environment via modified couple stress theory and Ritz method, *Ain Shams Engineering Journal*, 9 (2018), pp. 2373–2381.
- [14] Asghari, M. Geometrically nonlinear micro-plate formulation based on the modified couple stress theory. *International Journal of Engineering Science*, 51 (2012) 292–309.
- [15] Farokhi, H., Ghayesh, M.H. Nonlinear dynamical behaviour of geometrically imperfect microplates based on modified couple stress theory. *International Journal of Mechanical Sciences*, 90, (2015), pp. 133-144.
- [16] Ansari, R., Faghih Shojaei, M., Mohammadi, V., Gholami, R., Darabi, M.A. Nonlinear vibrations of functionally graded Mindlin microplates based on the modified couple stress theory *Composite Structures*, 114 (2014), pp. 124–134.

- [17] Ajri, M., Fakhrabadi, M. M. S. Nonlinear free vibration of viscoelastic nanoplates based on modified couple stress theory. *JCAMECH*, 49, No. 1, (2018), pp 44-53.
- [18] Krysko, V.A. , Awrejcewicz, J., Dobriyan, V., Papkova, I.V., Krysko, V.A. Size-dependent parameter cancels chaotic vibrations of flexible shallow nano-shells. *Journal of Sound and Vibration* 446 (2019), pp. 374-386.
- [19] Murmu, T., McCarthy, M.A., Adhikari, S. In-plane magnetic field affected transverse vibration of embedded single-layer graphene sheets using equivalent nonlocal elasticity approach. *Composite Structures*, 96 (2013) 57–63.
- [20] Ghorbanpour Arani, A.H., Maboudi, M.J., Ghorbanpour Arani, A., Amir, S. 2D-Magnetic Field and Biaxial In-Plane Pre-Load Effects on the Vibration of Double Bonded Orthotropic Graphene Sheets, *Journal of Solid Mechanics* ,Vol. 5, No. 2 (2013), pp. 193-205.
- [21] Kiani, K. Revisiting the free transverse vibration of embedded single-layer graphene sheets acted upon by an in-plane magnetic field. *Journal of Mechanical Science and Technology*, 28 (9) (2014), pp.3511-3516.
- [22] Atanasov, M.S., · Karlicic D., Kozic, P. Forced transverse vibrations of an elastically connected nonlocal orthotropic double-nanoplate system subjected to an in-plane magnetic field. *Acta Mech*, 228 (2017), pp.2165–2185.
- [23] Vol'mir, A. S. *Nonlinear Dynamics of Plates and Shells*, Nauka, Moscow, 1972
- [24] Singha, M.K., Rupesh Daripa. Nonlinear vibration and dynamic stability analysis of composite plates. *Journal of Sound and Vibration*, 328 (2009), pp. 541–554.
- [25] Chu, H.N., Herrmann, G. Influence of large amplitudes on free flexural vibrations of rectangular plates. *Journal of Applied Mechanics, Transactions of the ASME*, 23 (1956), pp. 532–540.
- [26] Sheikh, A.H., Mukhopadhyay, M., Large amplitude free flexural vibration of stiffened plates, *AIAA Journal*. 34 (1996), pp. 2377–2383.
- [27] Shi, Y., Lee, R.Y.Y., Mei, C. Finite element method for nonlinear free vibration of composite plates. *AIAA Journal*, 35 (1997), pp. 159–166.

Olga Mazur, Ph.D.: National Technical University “Kharkiv Polytechnic Institute”, Department of applied mathematics, 2, Kyrpychova str., 61002, Kharkiv, Ukraine (*mazuroly@gmail.com*). The author gave a presentation of this paper during one of the conference sessions.

Jan Awrejcewicz, Professor: Lodz University of Technology, Department of Automation, Biomechanics and Mechatronics, 1/15 Stefanowskiego Str., 90-924 Lodz, Poland (*jan.awrejcewicz@p.lodz.pl*).

Numerical and experimental investigations of dynamics of magnetic pendulum with an aerostatic bearing

Ewelina Ogińska, Krystian Polczyński, Dariusz Grzelczyk, Jan Awrejcewicz

Abstract: In this paper, both numerical and experimental results of the dynamics of a magnetic pendulum with an aerostatic bearing are presented. The experimental stand consists of the physical pendulum with a neodymium magnet at its end, whereas two electric coils are placed underneath. The pivot of the pendulum is supported by aerostatic bearing, therefore dry friction can be negligible, and it has only a viscous character. The electric current that flows through the coils is of a square waveform with a given frequency and duty cycle. Mathematical and physical models with the system parameters confirmed experimentally, are presented. The magnetic interaction is characterized as a moment of force as a function of the electric current and angular position of the pendulum. The results of the simulation and experiment showed the rich dynamics of the system, including various types of regular motion (multi-periodicity) and chaos.

1. Introduction

Pendulums are the objects of different studies in numerous scientific works due to their simplest construction and nonlinear character of motion. It is known that mechanical energy can be produced by an interaction between electric and magnetic fields with a high level of efficiency. This phenomenon is used, for example, in electric motors, which means that it is a developmental topic. In this paper we analyzed an original construction of a physical pendulum with magnetic interactions, and its axis of rotation coincides with the shaft's axis suspended in the pressured air generated by an aerostatic bearing. Electric coils, working as an excitation source, were introduced into the system, in order to repulse the neodymium magnet attached to the end of the pendulum. As a result, the considered case is a dynamical system in which electromagnetic forces affect the mechanical system. This system is coherent, so the pendulum's movement is closely dependent on the force generated by the electromagnetic field, but also on the distance from the coil. The presented dependency is the object of the study in this paper.

The investigations in which the pendulum behaviour depends on the electromagnetic field were carried out, for instance, by Kraftmakher [1,2]. In those papers, two magnets were placed on opposite sides of the pendulum's rod at different distances from the point of the rotation. The external magnetic field was driving the pendulum motion and could be used to modify the torque. Chaotic behaviour and nonlinear oscillations (forced and free) were detected and studied numerically. The Poincaré sections, phase plane graphs, histograms and Fourier's spectra were also presented.

In another paper Wojna et al. [3] analyzed numerically and experimentally the behaviour of a system containing a double physical pendulum with two permanent magnets forced by alternating magnetic field comes from the coils. They presented extended bifurcation diagrams for different frequencies of excitation signal as a control parameter, obtained both experimentally and numerically.

Berdahl and Lugt [4] investigated pendulum driven by rotating permanent magnet, using the power spectra, Poincaré maps and time-delay plots of the system. They observed that, depending on driving frequencies, some behaviour of Poincaré maps were periodic, and another chaotic. The time-lag plots for both periodic and chaotic motion were also presented in that study.

Polczyński et al. [5,6] described the behaviour of a two-degree-of-freedom system consists of two pendulums with magnets and elastic element coupling their pivots. Tests were conducted both numerically and experimentally. By using time histories, phase portraits, Poincaré sections and bifurcation graphs, they presented rich nonlinear dynamics of the considered system. Moreover, the results obtained experimentally were in good agreement with the simulation ones. The uniqueness of that work lies in the mechatronic system and the original way of the excitation source.

The modification of the Duffing equation of periodically driven iron pendulum in a magnetic field was analyzed by Donnagáin and Rasskazov [7]. Studies led to creating a special Poincaré section, time histories and phase portraits for the determined values of the parameters.

Kadjie and Wofo [8] presented a model of energy harvester consisting of an electromechanical pendulum subjected to nonlinear springs. The investigations showed that the suitable range of control parameters of the device vary led to the more efficient power generation than the case without springs. The transition from periodic to chaotic states were clearly noticed.

Concluding, in contrast to the above mentioned articles, this paper describes the periodic and chaotic behaviour of an asymmetrically forced physical pendulum system. One electric coil is mounted exactly under the pendulum, i.e. when the non-forced pendulum is in a stable position. The axis of rotation of the second electric coil is inclined at the angle of 45 degrees to the first one. Both coils generate an electromagnetic field, which defines the behavior of magnetic pendulum. An aerostatic bearing is the next new aspect, since it eliminates dry friction force and provides only viscous resistance.

2. Experimental rig and the electric excitation signal

The experimental setup of the considered physical pendulum system is presented in Fig. 1. The stand is equipped with the pendulum (1), which has a neodymium magnet (2) at the end of the rod. The axis of rotation has coincided with the shaft's axis suspended in the pressured air produced by an aerostatic bearing. Two electric coils (3) are mounted on the textolite board (4), whereas the angle between them is 45 degrees. The aluminium disk (5) with a diameter of 65 mm is attached to the shaft. Distance between the coils and the neodymium magnet during the experiment was equal to 2 mm. The test stand

is made of non-magnetic materials such as aluminium alloys, brass and polymer composites, due to diminishing the interaction with the magnetic elements of the investigated system.

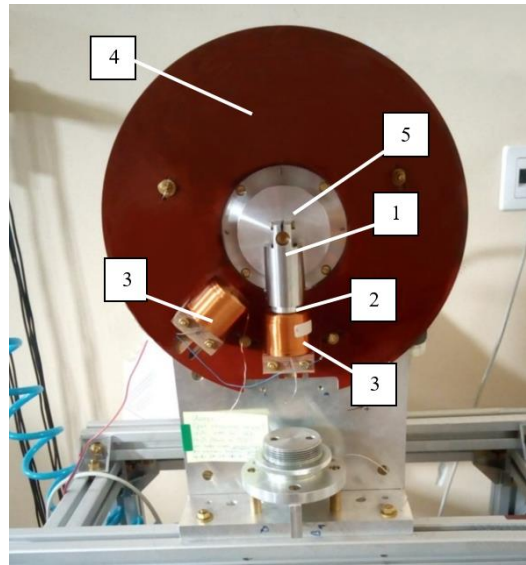


Figure 1. Experimental rig: 1 – physical pendulum, 2 – neodymium magnet, 3 – electric coils, 4 – textolite board, 5 – aluminium disk.

The shape of the electric current signal inside the electric coils is presented in Fig. 2 and flows through both coils at the same time. The parameters of the signal such as frequency and duty cycle can be controlled independently, whereas the amplitude i_a of the electric current was fixed to 0.5 A for the experimental tests.

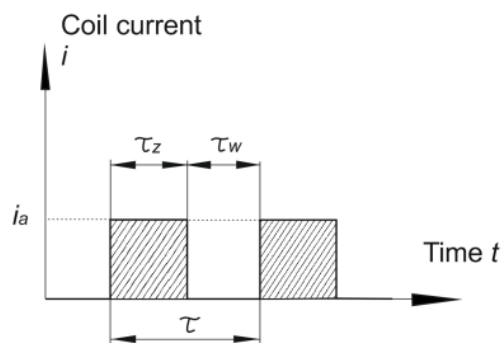


Figure 2. Excitation current signal: τ_z – switched on current; τ_w – switched off current; $\tau = \tau_z + \tau_w$ – the period of the signal; $w = \frac{\tau_z}{\tau} \cdot 100\%$ – duty cycle).

3. Mathematical model

In this section, the physical and mathematical models of the system are developed and presented. The physical model of the considered pendulum system is shown in Fig. 3.

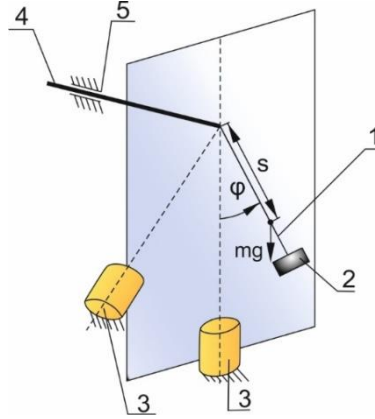


Figure 3. Physical model of the system: 1 – pendulum; 2 – neodymium magnet; 3 – electric coils; 4 – shaft; 5 – aerostatic bearing.

The mathematical model has been carried out according to classical mechanics laws. General equation of motion is as follow

$$I\ddot{\varphi} + c\dot{\varphi} + mgs \sin \varphi = M_{1mag}(\varphi, i) + M_{2mag}(\varphi, i), \quad (1)$$

where I stands for the moment of inertia of the pendulum, mg is the weight of the pendulum, s is the length between the pivot and centre of mass of the pendulum, and c stands for coefficient of viscous damping. The term $M_{1mag}(\varphi, i)$ describes the magnetic interaction between the magnet and coil placed under the pendulum, whereas $M_{2mag}(\varphi, i)$ concerns the inclined coil case. The argument i is the value of the current signal dependent on time.

4. Experiments versus numerical simulations

We started our studies from the identification of the system parameters. In order to reduce the number of the parameters which we had to find using numerical methods, some of them were identified experimentally. First of all, the value of the product of m and s parameters was obtained experimentally. While the electric coils were switched off (i.e. $M_{1mag}(\varphi, i) = M_{2mag}(\varphi, i) = 0$), the moment of gravity mgs

was balanced by the torque generated by force F . This torque was generated by tensometric beam connected with the aluminium disk with diameter D (attached to the shaft, see Fig. 1) by the string. This dependence could be written by using the equilibrium equation which yields

$$ms = \frac{FD}{2g \sin \varphi}. \quad (2)$$

Assuming values of the parameters $g = 9.81$ N/kg and $D = 0.065$ m, the values of the force F was measured for angles φ larger than zero. Taking into consideration Eq. (2) and measured values of force F , we received a constant value of $ms = 4.4 \cdot 10^{-3}$ kg·m.

In the next step, we identified the values of I and c based on time histories of the pendulum displacement obtained experimentally. The parameters I and c were obtained numerically, by fitting the Eq. (1) with neglected terms $M_{1mag}(\varphi, i)$ and $M_{2mag}(\varphi, i)$ to the experimental data of time histories of angular position of the pendulum during free oscillations. Figure 4 shows the time histories of angular position of the pendulum with the fitting process, where blue markers denote the experimental data and the red line is the fitted solution of Eq. (1). The fitting process was obtained by using *Mathematica* software. The best fit was obtained for $I = 0.21179 \cdot 10^{-3}$ kg·m² and $c = 9.28868 \cdot 10^{-6}$ N·m·s/rad.

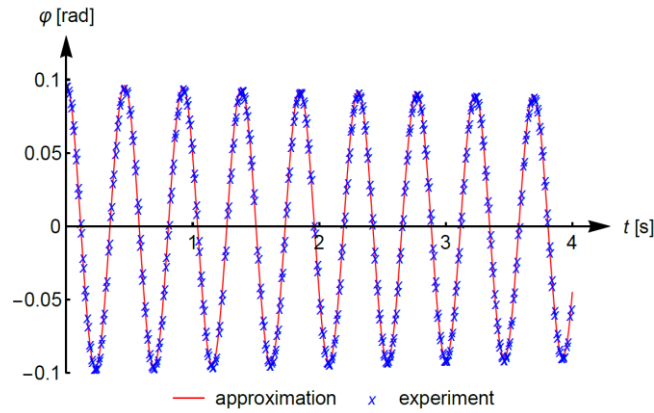


Figure 4. Time histories of free oscillations obtained experimentally (blue markers) and fitted numerical solution of Eq. (1) (red line).

In the last step, we modelled and identified the magnetic interaction between the magnet and coils based on the experimental data. For this purpose, to obtain experimental data, we used only the bottom coil of mentioned interaction and assume that the excitation of the second coil (located at an angle $\pi/4$ from the bottom coil) has the same nature as the first one. Therefore, we used modified

equation of motion in steady state by adding the magnetic interaction term $M_{1mag}(\varphi, i)$. For a fixed value of $i(t) = i_a = 0.5$ A the coil produces a steady torque $M_{1mag}(\varphi, i_a)$ for each φ . The torque $M_{1mag}(\varphi, i_a)$ can be computed by using the following formula

$$M_{1mag}(\varphi, i_a) = F \frac{D}{2} + mg \sin \varphi. \quad (3)$$

In further studies we have modelled magnetic torque $M_{1mag}(\varphi, i)$ as an analytical approximation of the obtained experimental data comes from Eq. (3). Moreover, the torque $M_{2mag}(\varphi, i)$ has been described by this same approximation formula, whereas the angle argument is shifted by the fixed angle $\pi/4$. Both formulas have the following forms

$$M_{1mag}(\varphi, i) = A i e^{-\lambda \varphi^2} \varphi, \quad (4)$$

$$M_{2mag}(\varphi, i) = A i e^{-\lambda \left(\varphi + \frac{\pi}{4}\right)^2} \left(\varphi + \frac{\pi}{4}\right), \quad (5)$$

where φ is limited to the range $[-\pi, \pi]$, A and λ are constants coefficients for a given pair of magnet and coil as well as a current signal. Figure 5 presents experimental data of torque $M_{1mag}(\varphi, i_a)$ calculated from Eq. (3) and analytical approximation described by Eq. (4). The fitting process conducted via *Mathematica* has given the following coefficients: $A = 0.943439$ N·m/(rad·A) and $\lambda = 14.6911$ 1/rad².

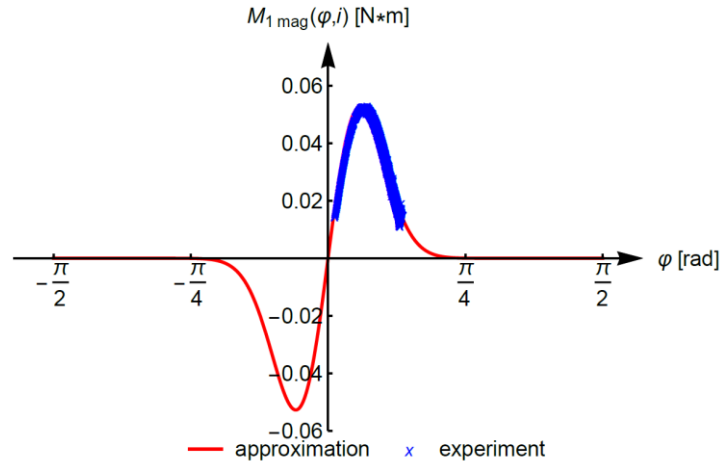


Figure 5. Comparison of experimental data (blue markers) and the torque $M_{1mag}(\varphi, i)$ obtained analytically from Eq. (4) (red line) for steady $i(t) = i_a = 0.5$ A.

Taking into account Eqs. (4) and (5), the total excitation torque acts on the pendulum can be expressed as the sum of both equations. The total value of magnetic interaction is presented in Fig. 6.

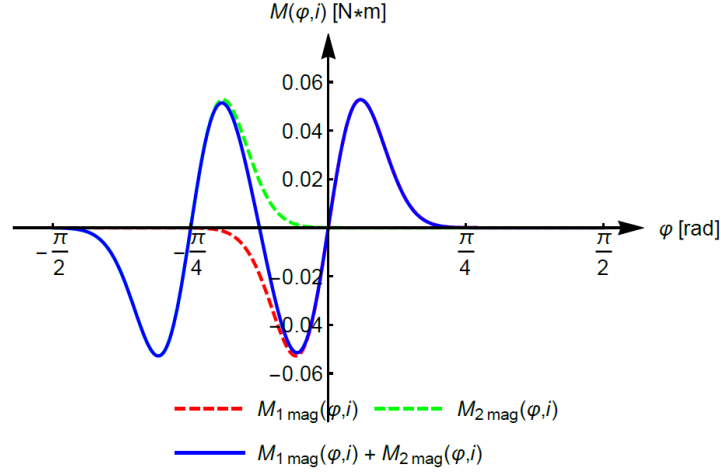


Figure 6. The total magnetic torque acting on the pendulum (blue line) as a sum of torques generated by both coils.

The developed mathematical model of the considered pendulum system subjected to the magnetic torque induces by two coils was verified experimentally. The angular position of the forced pendulum was recorded and confirmed with simulation. The current signal parameters during the experiment were fixed as follow: amplitude of current – $i_a = 0.5$ A, the frequency – $f = 2.2$ Hz, and the duty cycle – $w = 50\%$. Furthermore, the formula describes the rectangular waveform of the current signal reads [5]

$$(f, w, t) = i_a \frac{1}{2} \left[1 - \tanh \left(200 \sin(\pi f t) \sin \left(\pi f t - \frac{\pi w}{100} \right) \right) \right], \quad (6)$$

where f and w are frequency and duty cycle of the current signal, respectively, whereas t is time.

Fig. 7 shows time histories of angular position of the pendulum in different time intervals, obtained both experimentally and numerically.

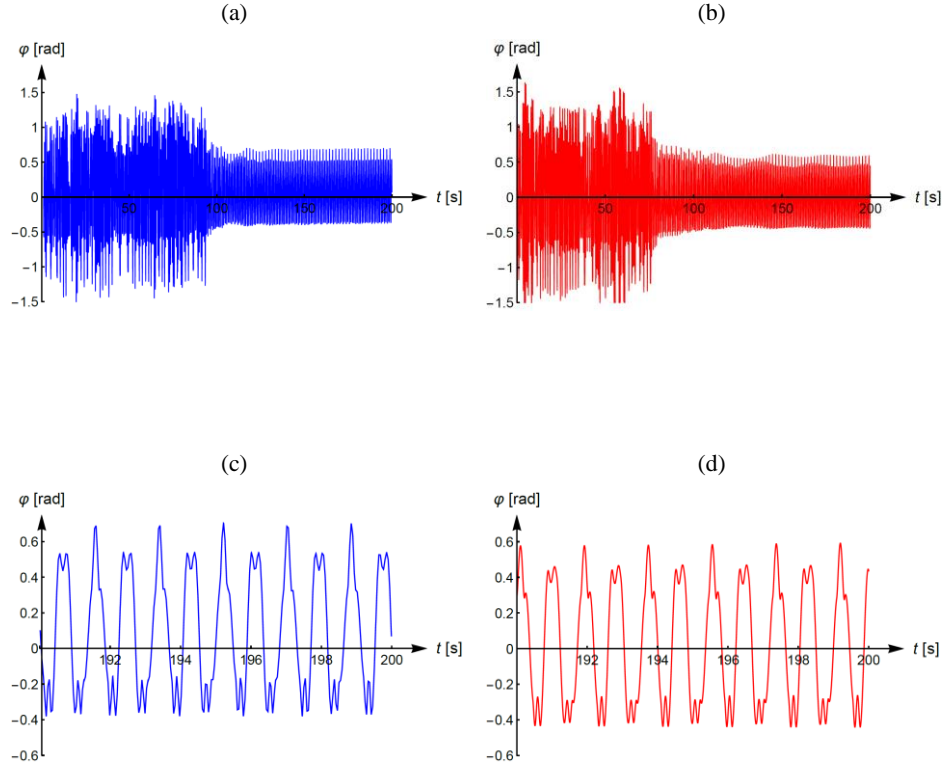


Figure 7. Comparison of experimental (a), (c) and numerical (b), (d) time histories of the angular positions of the pendulum for $f = 2.2$ Hz, $w = 50\%$ and $i_a = 0.5$ A.

As can be seen, the transient motion is clearly visible both in experimental and numerical investigations. Furthermore, the experimental transient behaviour is slightly longer than the simulation one. When the transient motion has vanished, the periodic oscillation has revealed for fixed parameters. The period and amplitude of the oscillation are in good agreement for both experimental and numerical analysis. In the considered case, the moment of impact of the pendulum on the magnetic barrier is clearly visible as a double amplitude peak, both in experimental and numerical results.

The bifurcation analysis has yielded a wider dynamical spectrum of the system motion. Figure 8 shows the numerical bifurcation diagrams with the frequency f as a control parameter, while the $w = 50\%$ and $i_a = 0.5$ A. Figure 8a displays the bifurcation for increasing value of frequency, and the windows of various multiperiodic motions as well as of chaotic motion can be recognized. In turn,

Fig. 8b displays the bifurcation diagram for decreasing frequency, and the coexisting attractors of periodic solution were exhibited.

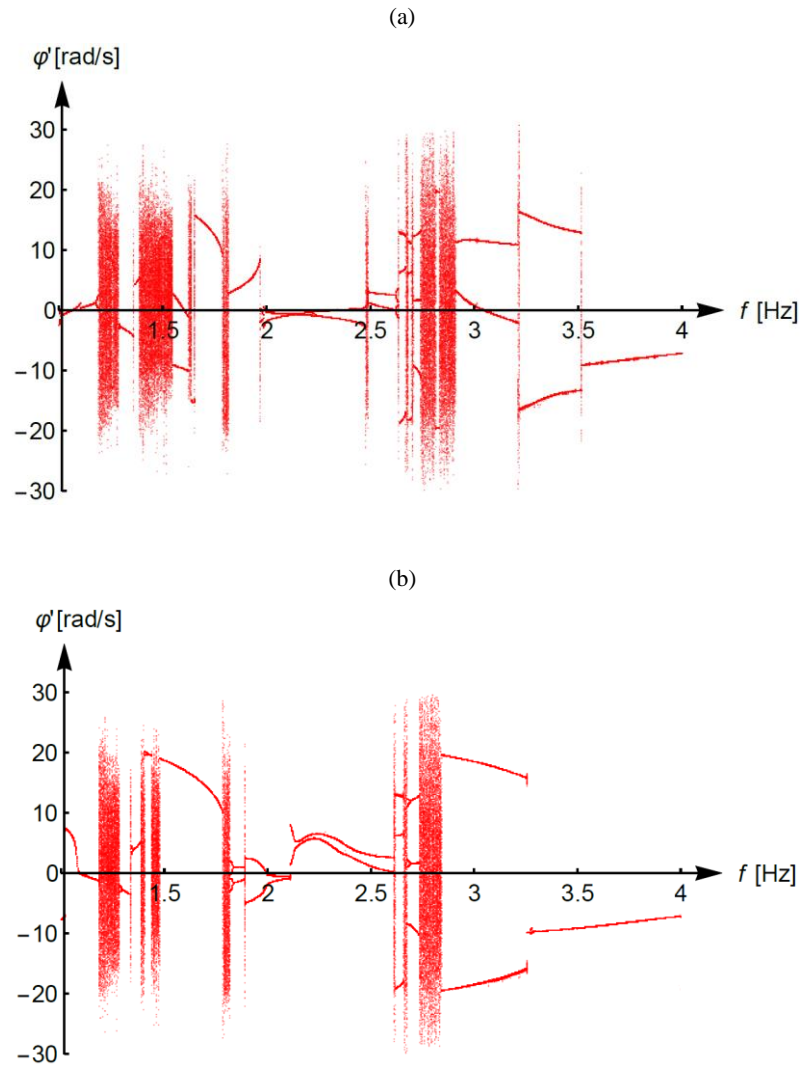
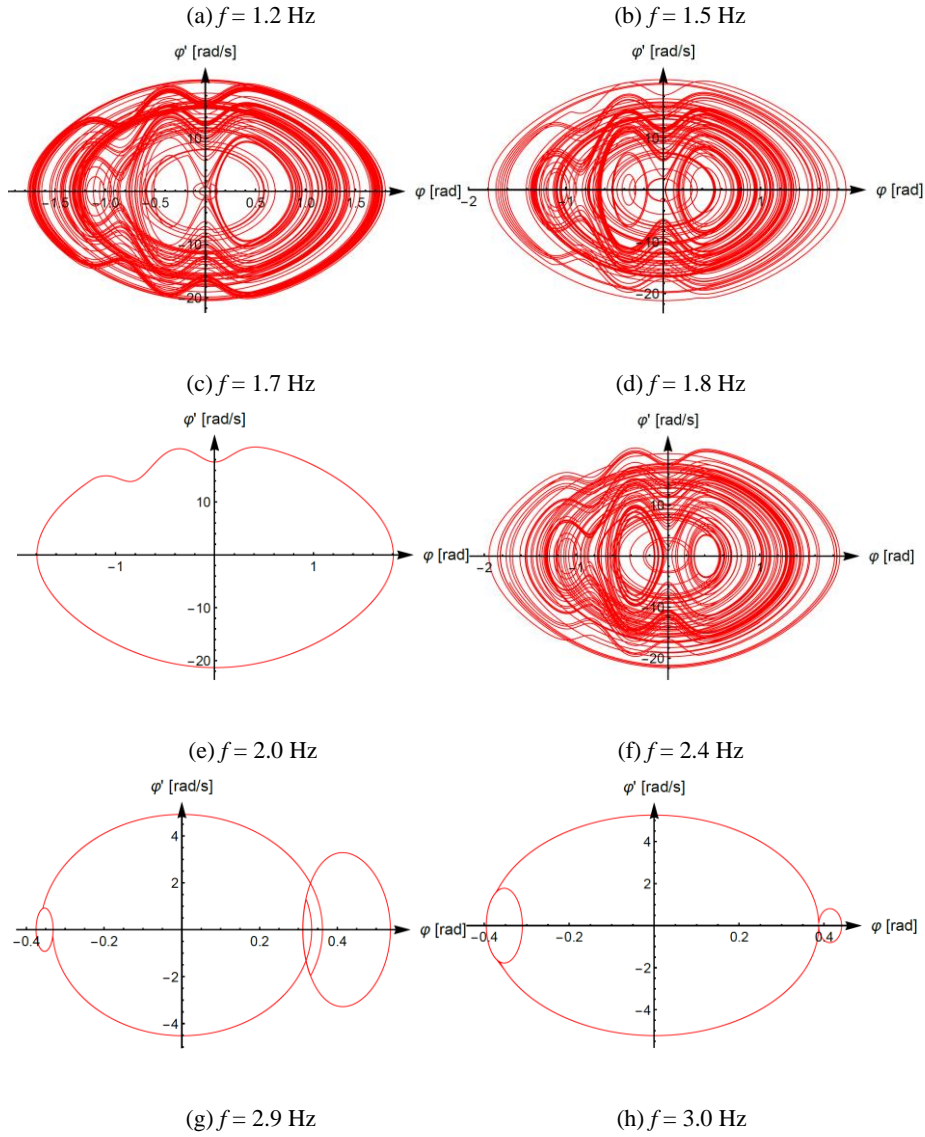


Figure 8. Comparison of bifurcation diagrams for increasing (a) and decreasing (b) value of frequency as a control parameter.

The phase plots for different regular and chaotic type of motion are presented in Fig. 9. The phase plots have been taken for a small increment of frequency to present the evolution of the trajectory. The rare trajectories of periodic motion are shown in Fig. 9c and 9i, the significant influence on the

form of the trajectories has the asymmetric nonlinear character of the magnetic interaction. The double amplitude peaks in the form of loops of the trajectory can be seen in Fig. 9e, 9f and 9i. Above the frequency 3.5 Hz, the one well-oscillation are exhibited by the system (see Fig. 9j).



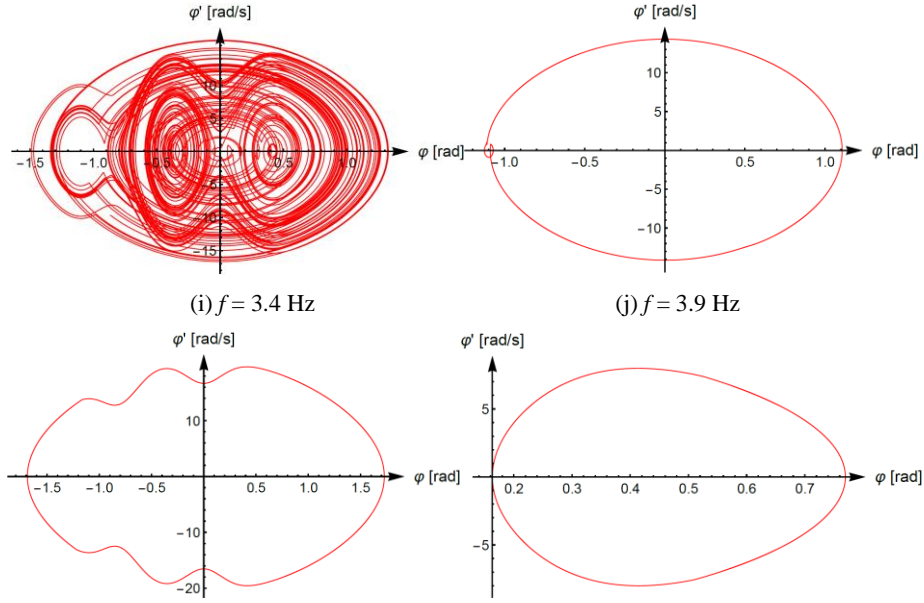


Figure 9. Regular (c, e, f, h, i, j) and chaotic (a, b, d, g) dynamics detected by phase portraits plotted in the range $t = 960$ - 1000 s for different values of frequency f .

5. Conclusions

In this paper the system of a magnetic pendulum supported by aerostatic bearing and subjected to an asymmetric repulsive magnetic field has been studied both experimentally and numerically. The magnetic field was alternating and induced by electric coils powered by a rectangular current signal. The current signal has controlled values of frequency, duty cycle and amplitude. The physical and mathematical models of the considered system have been developed, where magnetic interaction has been applied as an approximation function of experimental data. The numerical time histories plots of periodic motion have been shown and their good agreement with the experimental data. The bifurcation analysis has been presented for increasing and decreasing paths of frequency as a control parameter. The multiperiodic and chaotic ranges of oscillation as well as the coexisting attractors have been reported and discussed. Especially, evolution of the chaotic motion has been shown in a set of phase plots. The simplicity of the mathematical model is important for developing analytical solutions which can be experimentally validated. Therefore, the developed mathematical model and the constructed experimental stand are a valuable source for further investigations.

Acknowledgements

This work has been supported by the National Science Centre of Poland under the grant OPUS 14 No. 2017/27/B/ST8/01330. Special thanks to Grzegorz Wasilewski, PhD, (Department of Automation, Biomechanics and Mechatronics, Lodz University of Technology) for help with experimental investigations.

References

- [1] Y. Kraftmakher, Demonstrations with a magnetically controlled pendulum, *Am. J. Phys.* 78 (2009) 532–535. <https://doi.org/10.1119/1.3276412>.
- [2] Y. Kraftmakher, Experiments with a magnetically controlled pendulum, *Eur. J. Phys.* 28 (2007) 1007–1020. <https://doi.org/10.1088/0143-0807/28/5/023>.
- [3] M. Wojna, A. Wijata, G. Wasilewski, J. Awrejcewicz, Numerical and experimental study of a double physical pendulum with magnetic interaction, *J. Sound Vib.* 430 (2018) 214–230. <https://doi.org/10.1016/J.JSV.2018.05.032>.
- [4] J.P. Berdahl, K. Vander Lugt, Magnetically driven chaotic pendulum, *Am. J. Phys.* 69 (2001) 1016–1019. <https://doi.org/10.1119/1.1387041>.
- [5] K. Polczyński, A. Wijata, J. Awrejcewicz, G. Wasilewski, Numerical and experimental study of dynamics of two pendulums under a magnetic field, *Proc. Inst. Mech. Eng. Part I J. Syst. Control Eng.* 233 (2019) 441–453. <https://doi.org/10.1177/0959651819828878>.
- [6] K. Polczyński, A. Wijata, G. Wasilewski, G. Kudra, J. Awrejcewicz, Modelling and Analysis of Bifurcation Dynamics of Two Coupled Pendulums with a Magnetic Forcing, in: I. Kovacic, S. Lenci (Eds.), *IUTAM Symp. Exploit. Nonlinear Dyn. Eng. Syst.*, Springer International Publishing, Cham, 2020: pp. 213–223. https://doi.org/10.1007/978-3-030-23692-2_19.
- [7] M.Ó. Donnagáin, O. Rasskazov, Numerical modelling of an iron pendulum in a magnetic field, *Phys. B Condens. Matter.* 372 (2006) 37–39. <https://doi.org/10.1016/j.physb.2005.10.098>.
- [8] A.N. Kadje, P. Wofo, Effects of springs on a pendulum electromechanical energy harvester, *Theor. Appl. Mech. Lett.* 4 (2014) 063001. <https://doi.org/10.1063/2.1406301>.

Ewelina Ogińska, B.A. (M.Sc. student): Lodz University of Technology, Faculty of Mechanical Engineering, Department of Automation, Biomechanics and Mechatronics, Stefanowskiego 1/15, 90-924, Lodz, Poland (e.j.oginska@gmail.com). The author gave a presentation of this paper during one of the conference sessions.

Krystian Polczyński, M.Sc. (PhD student): Lodz University of Technology, Faculty of Mechanical Engineering, Department of Automation, Biomechanics and Mechatronics, Stefanowskiego 1/15, 90-924, Lodz, Poland (krystian.polczynski@edu.p.lodz.pl).

Dariusz Grzelczyk, PhD: Lodz University of Technology, Faculty of Mechanical Engineering, Department of Automation, Biomechanics and Mechatronics, Stefanowskiego 1/15, 90-924, Lodz, Poland (dariusz.grzelczyk@p.lodz.pl).

Jan Awrejcewicz, Professor: Lodz University of Technology, Faculty of Mechanical Engineering, Department of Automation, Biomechanics and Mechatronics, Stefanowskiego 1/15, 90-924, Lodz, Poland (jan.awrejcewicz@p.lodz.pl).

Analytical and numerical modelling of surface acoustic waves in rotating media

Alexey Papirovskiy, Alexey Lukin, Ivan Popov

Abstract: This paper presents results of analytical and numerical research of surface acoustic waves propagation process in rotating piezoelectric media. Various wave parameters such as frequency, phase velocity, wave mode are analyzed and their dependencies on angular velocity is investigated. The results obtained can be used to develop microelectromechanical devices in the field of navigation and signal processing. The relationship between phase velocity and rotation was determined without simplifying assumptions and was compared with previously obtained results from the literature. Based on the obtained analytical solutions, the numerical solution in COMSOL and ANSYS was verified. There is a great difficulty in solving such problems with rotating media by the finite element method, due to required numerical precision and necessity to solve eigenvalue boundary problem for non-self-adjoint linear operator. Equation-based COMSOL solver was used as a numerical method for such problems. The solution of the initial equations by the method of finite differences was also obtained.

1. Introduction

The use of various types of devices (micro-mechanical sensors, delay lines, particle manipulation systems in microchannels [1]) in various fields of instrumentation, the principle of which is based on the propagation of surface acoustic waves (SAWs) in solid media, promotes the development of analytical and numerical methods to study these processes.

All the above mentioned devices are MEMS devices. These devices combine micromechanical and microelectronic components. Wide use of MEMS in instrument-making is conditioned by the fact that such devices have many unique properties, namely: high resistance to external influences, lack of elastic inertial bonds in the construction of the device, low cost of manufacture, as well as a long service life relative to other known types of devices [2].

For the first time the method of generation of SAWs in piezoelectric media by means of a counterpointer transducer was proposed by White and Voltmer [3]. Wave propagation along the surface of piezoelectric materials is accompanied by modulation of the electric field for piezoelectrically active material directions, which makes it necessary to consider the connectivity of mechanical and electric fields in the construction of analytical and numerical models. Of particular interest for the study is the class of devices that operate in inertial reference systems, since it is

known that the phase velocity of the surfactant depends on the angular rotation speed of the half-space [4]. This effect can be used in the construction of inertial navigation systems [5]. For the first time, the problem of surface acoustic wave propagation in isotropic space, taking into account Coriolis forces and centrifugal forces, was presented by Schoenberg in 1973 [6], stimulating the study and construction of analytical models. Later, Lao [7] conducted a similar study in which he considered the dependence of the phase velocity of the surfactant on the angular velocity. The first micromechanical navigation devices based on surfactants were presented by such researchers as Kurosawa [8], Woods [9], Varadan [10]. At the moment, the need to build analytical models and develop numerical techniques remains in order to accurately study the dynamics of devices, finding the effective wave properties and characteristics of the process of surface acoustic waves propagation.

The subject of the study is the study of the process of surfactant propagation in a rotating half-space, as well as finding various wave parameters (frequency, phase velocity, wave modes, dispersion curves and their dependence on the angular velocity of the system).

The purpose of the work is to study in detail the analytical models and to build effective numerical schemes of finding the wave parameters.

2. The general formulation

Many MEMS devices have piezo-ceramic or piezoelectric materials as working elements. Wave generation is possible due to the piezo effect. This is the effect of mechanical deformation caused by an electric field. This is achieved by placing special systems of interdigital transducers (IDT) on the surface of piezoelectrics (Figure 1-2), which provide the generation of SAW.

If MEMS devices are also operated in non-inertial reference systems, mechanical distortions in the form of Coriolis forces and centrifugal forces begin to take effect on wave parameters [11].

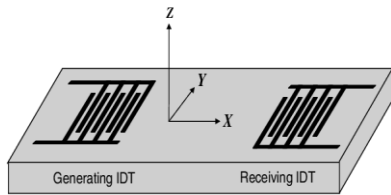


Figure 1. IDT

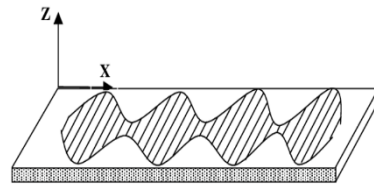


Figure 2. SAW motion

2.1 Surface acoustic waves in rotating half-space. Analytical solution

Consider the case of wave propagation for isotropic material in the system. To do this, introduce the Cartesian coordinate system $Ox_1x_2x_3$ and consider isotropic material that occupies the space ($x_3 \leq 0$) without mechanical loads on the surface ($x_3 = 0$). Around one of the x_i axes there is an angular

velocity vector component Ω_j . The elastokinetics equation and boundary conditions according to [12] will take the form:

$$\rho \frac{\partial^2 U_i}{\partial t^2} - C_{ijkl} \frac{\partial^2 U_i}{\partial x_j \partial x_k} + 2\rho \varepsilon_{ijk} \Omega_j \frac{\partial U_l}{\partial t} + \rho (\Omega_i \Omega_j U_j - \Omega_j^2 \Omega_i) = 0, i, j, k, l = 1, 2, 3, \quad (1)$$

$$T_{i3} = C_{i3kl} \frac{\partial U_k}{\partial x_l} = 0, x_3 = 0. \quad (2)$$

Where ρ – density; C_{ijkl} – tensor of elastic constants; ε_{ijk} – symbol of Levi-Civita; U_i – vector of movement; T_{i3} – stress.

We will search for a solution of the equation in the form of $U_i = a_i e^{ik(n_1 x_1 + n_2 x_2 + n_3 x_3 - Vt)}$, where V – phase velocity; n_i – directing cosines in the Cartesian axes x_i ; $k = \omega/V$ – wave number; ω – wave frequency. As is known, at $(\Omega \ll \omega)$ the contribution of centrifugal forces is much smaller than that of Coriolis. Therefore, at this stage we will not consider them in the solution.

Let the wave propagate along the x_1 axis, then the leading cosines will have the following values: $n_1 = 1, n_2 = 0, n_3 = n$. By substituting the type of solution into expression (1) we can write the equation in the following form:

$$\left(\Gamma_{ik} - \delta_{ik} \rho V^2 - 2i\rho \frac{V}{K} \varepsilon_{ikj} \Omega_j \right) a_k = 0. \quad (3)$$

Where $\Gamma_{ik} = C_{ijkl} n_j n_k$ – Christopheles' tensor; δ_{ik} – Kroneker delta.

The tensor of elastic constants C_{ijkl} for isotropic material depends only on two independent components. These components are expressed through the Lamé constants $\lambda (= c_{12})$, $\mu (= c_{44})$ and $c_{11} = \lambda + 2\mu$ [13]. Then we agree with the Einstein summation rule of Christopheles Γ_{ik} tensor can be presented in the following form:

$$\Gamma_{ik} = \begin{bmatrix} c_{11} + c_{44}n^2 & 0 & (c_{12} + c_{44})n \\ 0 & c_{44}(1 + n^2) & 0 \\ (c_{12} + c_{44})n & 0 & c_{11} + c_{44}n^2 \end{bmatrix}. \quad (4)$$

So, by substituting expressions for Γ_{ik} in (3), we can write (3) in algebraic form:

$$\begin{bmatrix} v_L^2 + v_T^2 n^2 & (v_L^2 - v_T^2)n - 2iV^2 \delta \\ (v_L^2 - v_T^2)n + 2iV^2 \delta & v_T^2 + v_L^2 n^2 \end{bmatrix} \begin{pmatrix} a_1 \\ a_3 \end{pmatrix} = V^2 \begin{pmatrix} a_1 \\ a_3 \end{pmatrix}. \quad (5)$$

Where $\delta = \Omega/\omega$ is the ratio of angular velocity to frequency. The phase velocities of the longitudinal and transverse waves will be $v_L = \sqrt{c_{11}/\rho}$ and $v_T = \sqrt{c_{44}/\rho}$.

The characteristic polynomial for the expression (5) will appear:

$$(v_L^2 + v_T^2 n^2 - V^2)(v_T^2 + v_L^2 n^2 - V^2) - (v_L^2 - v_T^2)^2 - 4\delta^2 V^4 = 0. \quad (6)$$

After finding the roots of the expression (6), corresponding to the SAW, it is necessary to find your own vectors a_i . Then the vector of movement is represented as a linear combination of two waves, longitudinal and transverse, and has the following form:

$$u = \sum_{j=1}^2 C_j a^{(j)} e^{ik(x_1 + n^{(j)}x_3 - vt)}. \quad (7)$$

Where C_j - an arbitrary coefficient, which is determined from the boundary conditions (2). To find it, it is necessary to allow the system:

$$\begin{bmatrix} a_3^{(1)} + n^{(1)}a_1^{(1)} & a_3^{(2)} + n^{(2)}a_1^{(2)} \\ c_{12}a_1^{(1)} + c_{11}n^{(1)}a_3^{(1)} & c_{12}a_1^{(2)} + c_{11}n^{(2)}a_3^{(2)} \end{bmatrix} \begin{pmatrix} C_1 \\ C_2 \end{pmatrix} = \begin{pmatrix} 0 \\ 0 \end{pmatrix}. \quad (8)$$

The resolution of the system (8) involves many mathematical difficulties. This is due to the fact that δ , which depends on the frequency of the wave and the phase velocity V is included in the roots and vectors of the system. These values are uncertain, and expression (8) is also complex. Therefore, it is necessary to construct an iterative procedure to resolve such a system. It is necessary to select such values of V , at which the system's determinant (8) will return to zero with a given accuracy [14]. In the process of iterative procedure it is necessary to turn to zero and the actual and imaginary parts of the determinant. It is not at all obvious that a value of V can always be found at which the equality of zero of one part of the determinant leads to the equality of zero of the other part. Numerical calculations and experimental data [15] confirm the existence of such values of phase velocities at which this requirement will always be met.

We will aim to derive the dependence of the phase velocity increment of the wave V on the value of the parameter δ as a solution. For this purpose, let us express the function $V=V(\delta)$. We will build the dependence of the species:

$$\frac{V-V_0}{V_0} = \delta. \quad (9)$$

Figure 3 shows the graph for expression (9) with a strict straightforward solution and for finding the roots (6) using numerical methods.

Now we will construct dispersion curves (see Fig. 4) as a function of the form $\omega = \omega(k)$ at different values of angular velocity Ω . As is known, surface acoustic waves do not have dispersion. By the phenomenon of dispersion we will understand the dependence of the phase velocity of the waves on their wavelength.

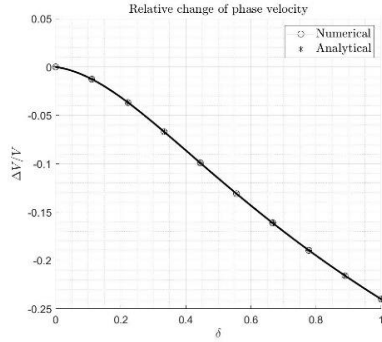


Figure 3. Phase velocity change V

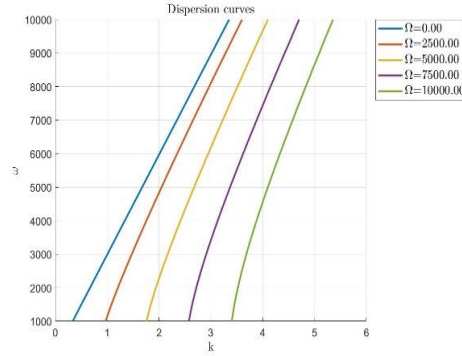


Figure 4. Dispersion curves

Now let us illustrate the change in the trajectory of the medium particle oscillations (see Fig. 5) at wave propagation depending on the value of the parameter δ . The particle's trajectory of motion has the form of an ellipse polarized horizontally, but taking into account the angular velocity, the particle's trajectory of motion begins to acquire vertical polarization.

We will bring to consideration centrifugal force. For this purpose, let's build a solution of the initial system (1) taking into account the summand $-\rho(\Omega_i \Omega_j U_j - \Omega_j^2 \Omega_i)$. We will also compare the solution of the initial system with the approximation of the initial solution [14]. Figure 6 shows a comparison of the direct analytical solution with and without centrifugal forces, as well as the approximation of the exact solution without centrifugal forces.

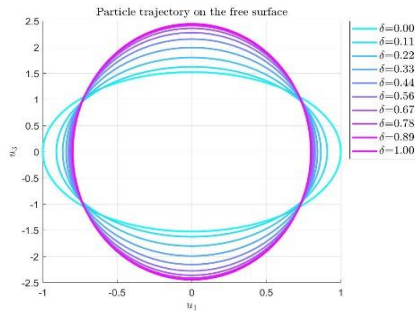


Figure 5. Particle oscillation trajectory

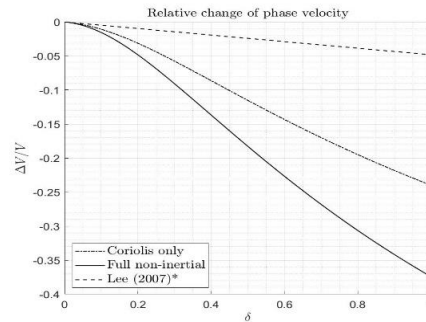


Figure 6. Comparison of the solutions

Analyzing the obtained solutions, we can say that the curve corresponding to the solution taking into account the centrifugal forces, clearly differs from the rest of the solution. On this basis, we can conclude that it is necessary to take into account the centrifugal forces for a qualitative assessment of the wave parameters depending on the rotation of the system.

3. Surface acoustic waves in a rotating half-space. Numerical solution

The chapter is devoted to the development and verification of numerical methods for solving the problem of surface acoustic wave propagation in isotropic rotating half-space.

3.1. Finite element solution

We will focus on solving the problem on our own values in a flat statement, limited geometrically to the region. The peculiarity of finding a solution for the process of propagation of surfactants of the Rayleigh type in rotating spaces is the asymmetry of its own operator, because of the presence in the system of rotation. This imposes significant difficulties on the choice of the numerical scheme of finding a solution to the original problem.

The numerical solution will be implemented in the Ansys software package [16]. Let's consider a cell of periodicity, the horizontal size of which is determined by the length of the surface wave, and the vertical one should provide its attenuation to the depth of the region. Figure 7 shows the finite element statement of the problem being solved with the illustration of boundary conditions.

At the lower boundary of the region, the displacement vector is set to zero. On the side edges of the region iteratively connect the pairs of nodes with the ratio for the components of the displacement vector. Thus, the periodicity of the structure is provided. The angle velocity vector is also applied in the region, and only the influence of Coriolis forces is considered for solution. The upper boundary of the region remains unloaded. The problem on eigenvalues is solved with the help of a special matrix method for asymmetric operators. Figure 8 shows the finite element model corresponding to the model of the surface acoustic wave of the Rayleigh type.

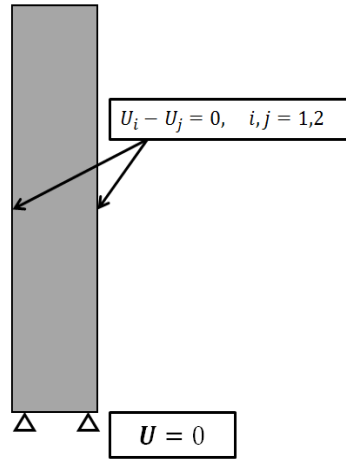


Figure 7. Boundary conditions

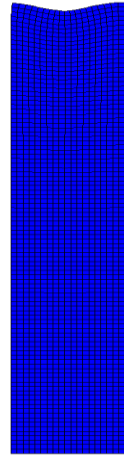


Figure 8. Finite element solution

As the second settlement complex we will choose system COMSOL Multiphysics [17]. Figure 9 shows the graphs of the phase velocities of SAWs depending on the parameter δ , as in the previous chapters, obtained in different design complexes. A comparison with the solution obtained analytically is also given.

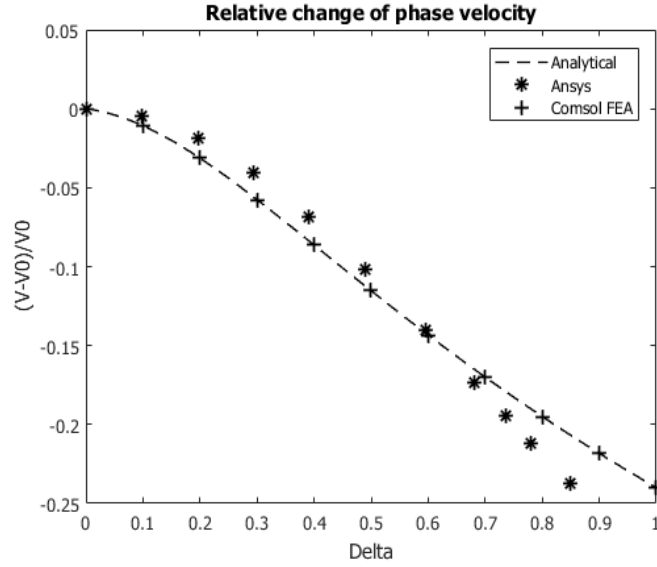


Figure 9. Comparison of the solutions

Analyzing the obtained decisions, it can be concluded that both decisions are characteristic of the analytical decision. But the results obtained in the COMSOL Multiphysics software suite are more accurate to the exact solution.

3.2. Finite difference solution

The positive aspects of applying the finite difference method are that it has no restrictions on the algebraic formulation of the problem, as in the case of using the finite element method, and allows to solve the original equation describing the process.

We will set a goal, solve the problem on our own values, as in the previous section. To implement the solution, we will use the COMSOL software package.

In the software complex for solving the problem by finite difference method, the general form of the differential equation for the problem by eigenvalues is as follows:

$$\lambda^2 e_a \mathbf{U} - \lambda d_a \mathbf{U} + \nabla \cdot \Gamma = f. \quad (10)$$

Where $\mathbf{U} = [u_1, u_2]^T$ - vector of movement; $\nabla = [\frac{\partial}{\partial x}, \frac{\partial}{\partial y}]$.

To solve the problem, it is necessary to determine the coefficients in equation (10): e_a , d_a , Γ , f . The value of f is assumed to be equal to zero, and the rest of the coefficients are assigned the following values:

$$\Gamma = \sigma = \begin{bmatrix} (\lambda + 2\mu) \frac{\partial u_1}{\partial x} + \lambda \frac{\partial u_2}{\partial y} & \mu (\frac{\partial u_1}{\partial y} + \frac{\partial u_2}{\partial x}) \\ \mu (\frac{\partial u_1}{\partial y} + \frac{\partial u_2}{\partial x}) & (\lambda + 2\mu) \frac{\partial u_2}{\partial y} + \lambda \frac{\partial u_1}{\partial x} \end{bmatrix}, \quad (11)$$

$$d_a = \begin{bmatrix} 0 & 2i\rho\Omega \\ -2i\rho\Omega & 0 \end{bmatrix}, \quad (12)$$

$$e_a = \begin{bmatrix} \rho & 0 \\ 0 & \rho \end{bmatrix}. \quad (13)$$

Where ρ - density, Ω - angular velocity, λ and μ - Lamé constants.

Figure 10 shows the geometric area and boundary conditions used to solve the problem.

The conditions on the side edges and on the lower boundary of the region are similar to the conditions of the previous problem. On the upper boundary there is a mathematical condition free from the surface load through the tensor σ , which is the stress tensor.

Figure 11 shows the obtained solution in the form of incremental phase velocity of the SAWs depending on the parameter δ and the analytical solution.

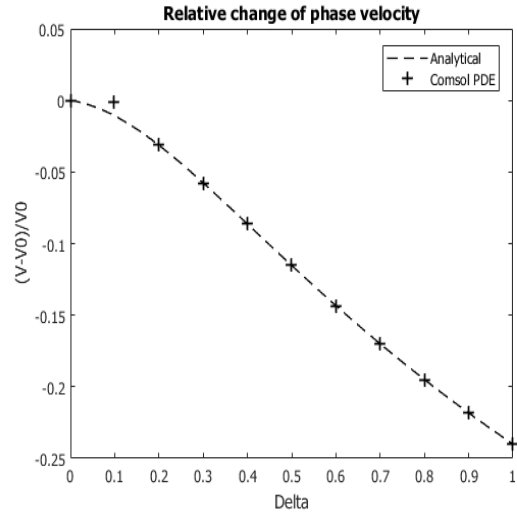
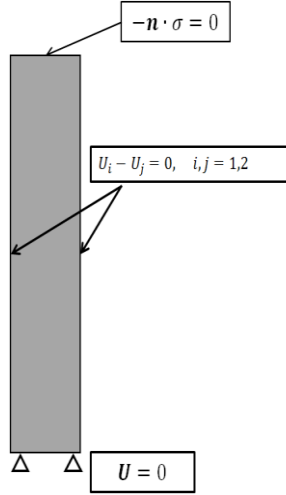


Figure 10. Boundary conditions

Figure 11. Comparison of the solutions

Analyzing the received decision it is possible to assert that the method of finite differences also corresponds to the analytical decision and therefore is applicable for practical calculations.

4. Conclusions

In summary, we will present the main results of the study.

1. The problem of propagation of surface acoustic waves of the Rayleigh type in isotropic elastic rotating half-space is set and solved. Wave parameters depending on the speed of rotation of the system are also found. The influence of centrifugal forces on the strict analytical solution of the system is taken into account.

2. Numerical methods for finding wave parameters depending on the system rotation have been developed and verified. By means of finite element method and finite difference method.

3. The developed methods further allow to study a number of phenomena influencing the process on already developed models, it is the account of electromechanical connection and anisotropic properties of piezoelectric media.

References

- [1] Johansson L.; Enlund J.; Johansson S.; Katardjiev I.; Yantchev V. Surface acoustic wave induced particle manipulation in a PDMS channel—principle concepts for continuous flow applications. *Biomed Microdevices*, November 2011
- [2] Lukyanov, D.P.; Filatov, Y.V.; Shevchenko, S.Y.; Shevelko, M.M.; Peregudov, A.N.; Kukaev, A.S.; Safronov, D.V. State of the art and prospects for the development of SAW-based solid-state gyros. *Gyroscopy Navig.* 2011, 4, 214–221.
- [3] White R. M., Voltmer F. W. Direct piezoelectric coupling to surface elastic waves // *Appl. Phys. Lett.* — 1965. — T. 7. — C. 314—316. — DOI:10.1063/1.1754276.
- [4] Guliaev, Yu.V.; Pleskiy, V.P. Surface acoustic wave propagation in periodic structures. *Successes of the physical sciences*. №1 (157). 1989. P. 85-127
- [5] Lukyanov DP, Filatov Yu.V. Current state and prospects for the development of solid microscopes on surface acoustic waves. *Gyroscopy and navigation*. №3 (74). 2011. P. 75-87.
- [6] Schoenberg M., Censor D. Elastic waves in rotating media // *Quart. Appl. Math.* – 1973. – V. 31. – P. 115-125.
- [7] Lao B.Y. Gyroscopic effect in surface acoustic waves // *IEEE Ultras. Symp.* – 1980. – P. 687–690.
- [8] Kurosawa M, Fukuda Y, Takasaki M and Higuchi T 1998 A Surface-acoustic-wave gyro sensor *Sensors Actuators A* 66 33–9
- [9] Woods C, Kalami H and Johnson B 2002 Evaluation of a novel surface acoustic wave gyroscope *IEEE Trans. Ultrason. Ferroelectr. Freq. Control* 49 136–41
- [10] Varadan V K, Suh W D, Xavier P B, Jose K A and Varadan V V 2000 Design and development of a MEMS-IDT gyroscope *Smart Mater. Struct.* 9 898–905
- [11] Biryukov, S.V.; Chmidt, H.; Weihnacht, M. Gyroscopic Effect for SAW in Common Piezoelectric Crystals. In *Proceedings of the 2009 IEEE International Ultrasonics Symposium (IUS)*, Rome, Italy, 20–23 September 2009; pp. 2133–2136.
- [12] Novatsky V., *Theory of elasticity*. Per. from Polish. B. E. Pobedri. - Moscow: Mir, 1975.

- [13] Sang Woo Lee et. al. A micro rate gyroscope based on the SAW gyroscopic effect. J. Micromech. Microeng. №17. 2007. P. 2272-2279
- [14] Krasilnikov V.A., Krylov V.V. Introduction to Physical Acoustics - Moscow: Mir, 1984.
- [15] Lothe J., Barnett D.M.-J., Appl. Phys., 1976
- [16] Ansys software - <https://www.ansys.com/>
- [17] COMSOL software - <https://www.comsol.com/>
- Alexei Papirovskiy, M.Sc. (Ph.D. student): Peter the Great St. Petersburg Polytechnic University, 195267, Russia (RU), (apapirovskiy@gmail.com).
- Alexei Lukin, Ph.D.: Peter the Great St. Petersburg Polytechnic University, 195251, Russia (RU), (lukin_av@spbstu.ru).
- Ivan Popov, Ph.D.: Peter the Great St. Petersburg Polytechnic University, 195251, Russia (RU), (popov_ia@spbstu.ru).

Dynamics of logistic train

Wojciech Paszkowiak, Tomasz Bartkowiak

Abstract: A rapid development in intralogistics is the argument for seeking new solutions in this field. An example of such a solution is a logistics train. An important problem in the application of intralogistics trains is the choice of adequate parameters of the kinematic system and the possibility to check before the commissioning whether the train is able to pass the given path without a collision with surrounding objects. In this paper, we present a dynamic model of a logistic train which was developed for the three most common steering systems: virtual clutch and drawbar, conventional clutch and drawbar as well as double Ackermann steering. In the paper, we consider a three-wheeled tractor towing passive wheeled trailers. The tractor consists of actuated steering wheel at front and a two passive rear wheels used for stable motion. Two types of trailers are considered. First one is connected to the tractor via a passive joint and it has two rear fixed wheels and two caster wheels in front. The latter has front wheels that follow Ackermann steering principle. The turn of front wheels is caused by rotation of drawbar. The rear wheels are synchronized with front ones but they rotate in the opposite direction. Dynamic model was created following Lagrange's theorem including the possibility of lateral slip. In order to calculate the side-slip angle we used relation between relative velocities for a given wheel. Then, the system of differential equations was numerically solved. The results obtained are presented in the form of animations presenting train run in various conditions.

1. Introduction

The objective of this paper is to develop a credible dynamic model of the multiple trailers on a tractor system for the production logistics application i.e. logistic train. This includes the most common steering: virtual clutch and drawbar system, conventional clutch and drawbar system as well as double Ackermann steering. This model should contribute to a better understanding of an impact of geometrical relations and friction on the trajectory of such systems in motion. This can facilitate the logistic train design for improved maneuverability in narrow corridors through choice of applicable number of trailers and selections of the best geometric parameters of the trolley. It can also help to estimate collision risk with nearby static objects.

1.1. Logistic train

Logistic trains are applied means of transport across all sectors of production supply [1]. A logistic train is usually called a milk-runner. The milk-run concept is derived from the method of delivering or receiving supplies in the dairy industry, where one tanker collects milk from many farmers. In the industry one train supplies multiple workstations.. The idea is to visit assigned locations by one supplier in a single run [2]. Milk-run system minimizes the total distance travelled, as a single vehicle is used instead of many [3], especially in case of repeatable flow of materials between the same locations. The specificity of the train is that it transports more goods than other intralogistics means of transport per each run [4].

The discussed train consists of a tractor and a certain number of trailers also called logistics trolleys. The tractor usually has an Ackermann steering system. The most common steering systems for trolleys are: conventional clutch with drawbar system, virtual clutch with drawbar system and Ackermann steering system. The classic solution for connecting the trolleys is drawbar at the front of the unit. This conventional connection could be potentially ineffective. It was shown that another two types of steering systems are better for ride in narrow corridors. Virtual clutch has drawbar at the back of the trolley. Rear wheels are fixed and front wheels are castor wheels. The most advanced steering system is double Ackermann. For this steering system, a number of degrees of freedom is higher than for other systems assuming the same number of trolleys. This is thanks to the rotary drawbar, which turns and determines the turn of front wheels of the trolley. Rear wheels rotate in the opposite direction than front, which direction of turning is consistent with drawbar. Comparison of kinematics of these steering systems was presented in [5].

1.2. Vehicle dynamics

Dynamic models of vehicles can be written based on Newton's second law or Lagrange's theorem [6]. These models are applicable in numerous fields including: mobile robots [7], autonomous vehicles [8], cars [9], trucks [10], agricultural vehicles [11], airplanes [12]. The most common models involve nonholonomic constraints [7]. The idea in those approaches is based on Chaplygin sleigh model, where lateral forces and lateral velocity are not considered for wheels [13]. This assumption causes the trajectory of vehicle movement to be known and dependent on kinematics, mass of vehicle and drive power. In those models it is assumed that the friction is not relevant. Nonholonomic constraints appear with the assumption of a non-slip condition. Center points of the wheels cannot move along the direction of the wheel own axis [14].

In order to take into account the slip effect, it requires to apply holonomic system of Lagrange formula or equations based on Newton's second law. This is also possible using the model for a non-holonomic system. In that case, forces acting on the system, as a result of lateral friction force, are

expressed as Lagrangian multipliers. The longitudinal contact forces are included in the input vector [15]. Many authors assume that the lateral force acting on a tire is proportional to the angle of slip. This assumption is valid for small slip angles. They must be smaller than the values of slip angle corresponding to the peak lateral force [16]. It allows determination of the slip angles without using trigonometric functions [17]. However, this assumption has some limitations. The model can represent a drive only in the smooth passing. It does not involve drifting or aggressive race [18]. The side-slip angles are determined by analyzing the constituents of wheel velocity vectors.

In this paper, the authors want to present a dynamic model of a multibody system, i.e. a tractor towing multiple trailers, which can allow visualization of its trajectory under different drive conditions. The additional goal is to provide animations when slip occurs. This can help to indicate the steering system which is the most and least susceptible to slipping. The aim is also to show an alternative way to determine the slip angle without analyzing the velocity vectors. This is possible by determining the velocities by calculating the derivative over time from the position of the wheel. This simplifies the determination of the slip angle.

2. Dynamic model

This section presents dynamic models of three types of logistic trains with various steering systems. Each system consists of a tractor with four trailers. Conventional and virtual clutch examples have the same kinematic model, which means that they also have the same dynamic model. We consider dynamic models with some simplifications. In this study, the air resistance, vertical or pitch motion are neglected as their impact on the system is potentially marginal. We assume that friction force is proportional to the side-slip angle in a full range including slipping. The main equation of motion for holonomic system by the Lagrange formula can be given as:

$$\mathbf{M}(\mathbf{q})\ddot{\mathbf{q}} + \mathbf{C}(\mathbf{q}, \dot{\mathbf{q}}) = \mathbf{Q}(\mathbf{q}). \quad (1)$$

$\mathbf{z}(\mathbf{q}, \dot{\mathbf{q}})$ is a vector representing the left side of the main equation (1) and it can also be expressed as:

$$\mathbf{z}(\mathbf{q}, \dot{\mathbf{q}}) = \frac{d}{dt} \left(\frac{\partial \mathcal{L}}{\partial \dot{\mathbf{q}}} \right) - \frac{\partial \mathcal{L}}{\partial \mathbf{q}}, \quad (2)$$

where \mathcal{L} is a Lagrangian of the system and it is the difference between kinetic energy T and potential energy U . For these systems potential energy is null. It causes that $\mathcal{L} = T$. System inertia matrix can be expressed as: $\mathbf{M}(\mathbf{q}) = \left[\frac{\partial \mathbf{z}(\mathbf{q}, \dot{\mathbf{q}})_k}{\partial \dot{\mathbf{q}}_j} \right]$, where k is a number of matrix row, j is a number of matrix column and they also indicate number of constituents of the vectors $\mathbf{z}(\mathbf{q}, \dot{\mathbf{q}})$, $\ddot{\mathbf{q}}$. The centripetal and Coriolis matrix can be denoted as: $\mathbf{C}(\mathbf{q}, \dot{\mathbf{q}}) = \mathbf{z}(\mathbf{q}, \dot{\mathbf{q}}) - \mathbf{M}(\mathbf{q})\ddot{\mathbf{q}}$.

2.1. Tractor

In our model, the tractor can be described using a tricycle model, where a single front wheel is powered [19]. The input parameters for this system are: drive torque τ and steering angle of the front wheel ψ_{f0} . Basic geometrical parameters are shown in Fig. 1a.

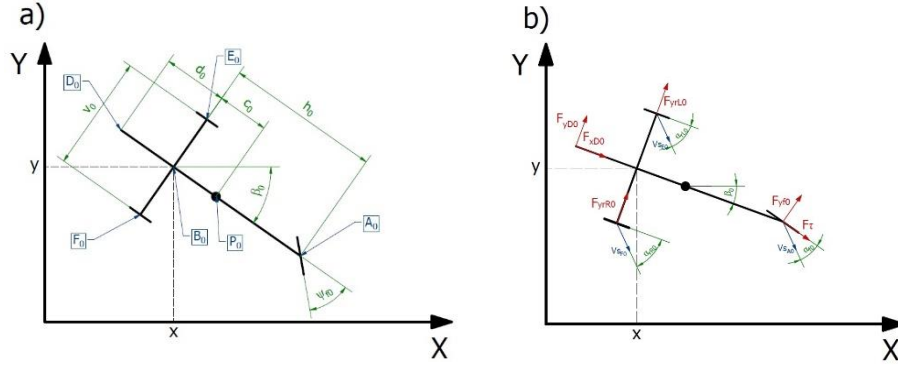


Figure 1. a) geometrical parameters, b) friction forces and slip-side angles for a tractor

P_0 is a point of center of mass. The configuration of the tractor can be expressed with generalized coordinate vector as $\mathbf{q} = [x \ y \ \beta_0]^T$. The kinetic energy of the tractor T_b can be denoted as:

$$T_b = \frac{1}{2} m_b (\dot{x}_{P0}^2 + \dot{y}_{P0}^2) + \frac{1}{2} I_b \dot{\beta}_0^2 + m_{w0} (\dot{x}^2 + \dot{y}^2) + \left(I_{w0} + m_{w0} \left(\frac{1}{2} v_0 \right)^2 \right) \dot{\beta}_0^2 + \frac{1}{2} m_{w0s} (\dot{x}_{A0}^2 + \dot{y}_{A0}^2) + I_{w0s} \dot{\beta}_0^2, \quad (3)$$

where: $x_{P0} = x + c_0 \cos(\beta_0)$, $y_{P0} = y - c_0 \sin(\beta_0)$, $x_{A0} = x + h_0 \cos(\beta_0)$, $y_{A0} = y - h_0 \sin(\beta_0)$. The side-slip angle is obtained for each wheel separately. It is the ratio of longitudinal and lateral velocity relative to the wheel. The idea of marking of the side slip angles is presented in Fig. 1b. The side-slip angles for a rear wheels α_{rL0} , α_{rP0} and the front wheel α_{f0} are expressed in the arctg function as: $\alpha_{rL0} = -\arctg\left(\frac{\dot{y}_{E0}}{\dot{x}_{E0}}\right) - \beta_0$, $\alpha_{rR0} = -\arctg\left(\frac{\dot{y}_{F0}}{\dot{x}_{F0}}\right) - \beta_0$, $\alpha_{f0} = -\arctg\left(\frac{\dot{y}_{A0}}{\dot{x}_{A0}}\right) - \beta_0 - \psi_{f0}$. They can be written as $x_{E0} = x + \frac{1}{2} v_0 \sin(\beta_0)$, $y_{E0} = x + \frac{1}{2} v_0 \cos(\beta_0)$, $x_{F0} = x - \frac{1}{2} v_0 \sin(\beta_0)$, $y_{F0} = x - \frac{1}{2} v_0 \cos(\beta_0)$. Forces acting to the tractor are presented in Fig. 3. These forces can be expressed as vector in a local coordinate system of the tractor:

$$\mathbf{F}_v = \begin{pmatrix} F_\tau \cos(\psi_{f0}) + F_{yf0} \sin(\psi_{f0}) + F_{xD0} \\ F_{yrR0} + F_{yrL0} - F_\tau \sin(\psi_{f0}) + F_{yf0} \cos(\psi_{f0}) + F_{yD0} \end{pmatrix}, \quad (7)$$

where: $F_\tau = \tau/r_{0f}$ is a driven force, F_{xD0} and F_{yD0} are elements of vector \mathbf{F}_{vD0} . For the tractor without trailers \mathbf{F}_{vD0} is a null vector, $F_{yf0} = C_{0f} \sin(\alpha_{f0})$, $F_{yrR0} = C_{0r} \sin(\alpha_{rR0})$, $F_{yrL0} = C_{0r} \sin(\alpha_{rL0})$.

$C_{0f} = \mu_{0f} F_{nf0}$ and $C_{0r} = \mu_{0r} F_{nr0}$ are friction forces derived from the stiffness of the tire. F_{nr0} and F_{nf0} are the normal forces acting on the wheels denoted as: $F_{nf0} = c_0 g m_b / h_0$, $F_{nr0} = (h_0 - c_0) g m_b / (2 h_0)$, where g is a gravity acceleration. In order to transformation forces to the global coordinate system \mathbf{F}_{vG} can be calculated using rotation matrix $\mathbf{R}(-\beta_0)$: $\mathbf{F}_{vG} = \mathbf{R}(-\beta_0) \cdot \mathbf{F}_v$. For the tractor, a vector of generalized force can be denoted as $\mathbf{Q}(\mathbf{q}) = [F_x \ F_y \ F_{\beta_0}]^T$, F_x is a first and F_y is a second element of vector \mathbf{F}_{vG} . F_{β_0} is a sum of momenta for generalized coordinate β_0 :

$$F_{\beta_0} = F_{yrr0}c_0 + F_{yrl0}c_0 + F_{\tau} \sin(\psi_{f0}) (h_0 - c_0) - F_{yf0} \cos(\psi_{f0}) (h_0 - c_0) + F_{yD0}(d_0 + c_0), \quad (11)$$

2.2. Conventional and virtual clutch with drawbar system

Conventional and virtual clutch with drawbar system follow the same kinematics. The only difference is the ratio of the length of the drawbar to the length of the hitch. For this reason, these two systems are presented in this one section. For this systems, we assume that front wheels has no effect on trajectory. Basic geometrical parameters for analyzed cases are presented in Fig. 2. The configuration of the system can be expressed with generalized coordinate vector as $\mathbf{q} = [x \ y \ \beta_0 \ \beta_1 \ \beta_2 \ \beta_3 \ \beta_4]^T$. The kinetic energy of the i -th trailer T_{ti} can be denoted as:

$$T_{ti} = \frac{1}{2} m_{ti} (\dot{x}_{Pi}^2 + \dot{y}_{Pi}^2) + \frac{1}{2} I_{ti} \dot{\beta}_i^2 + m_{wi} \left((\dot{x}_{Bi}^2 + \dot{y}_{Bi}^2) + (\dot{x}_{Ai}^2 + \dot{y}_{Ai}^2) \right) + 2 \left(I_{wi} + m_{wi} \left(\frac{1}{2} v_i \right)^2 \right) \dot{\beta}_i^2, \quad (12)$$

where i is a number of the trailer and $x_{Bi} = x - \sum_{j=0}^{i-1} d_j \cos(\beta_j) - \sum_{j=1}^i (h_j + d_{fj}) \cos(\beta_j)$, $y_{Bi} = y + \sum_{j=0}^{i-1} d_j \sin(\beta_j) + \sum_{j=1}^i (h_j + d_{fj}) \sin(\beta_j)$, $x_{Pi} = x_{Bi} + c_i \cos(\beta_i)$, $y_{Pi} = y_{Bi} - c_i \sin(\beta_i)$, $x_{Ai} = x_{Bi} + h_i \cos(\beta_i)$, $y_{Ai} = y_{Bi} - h_i \sin(\beta_i)$. Total energy of the system can be denoted as the sum of the energy of individual units: $T = T_b + \sum_1^4 T_{ti}$.

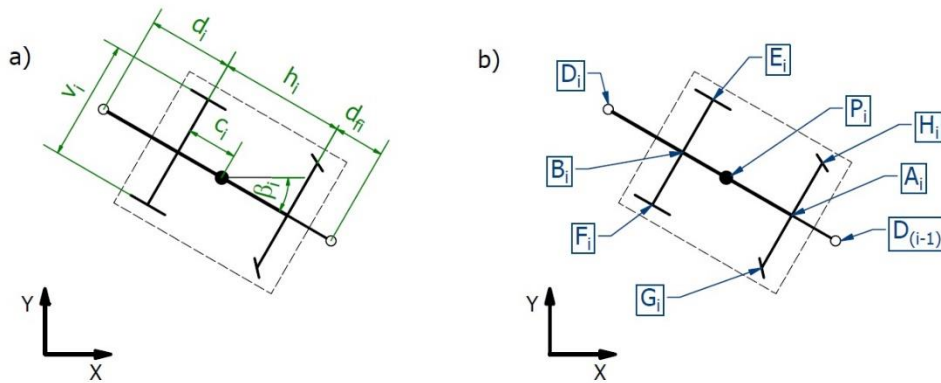


Figure 2. Drawbar system: a) basic geometrical parameters b) characteristic points

Side-slip angles and friction forces acting for this system are presented in figure 3.

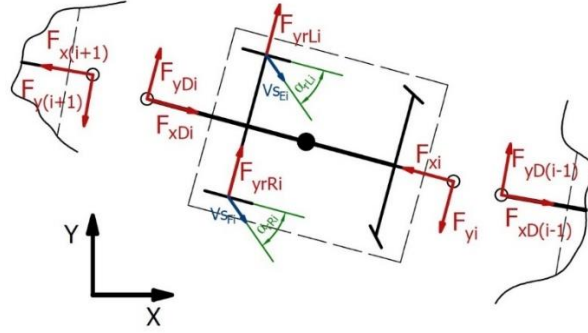


Figure 3. Friction forces and slip side angles

The side-slip angles for rear wheels of the i -th trailer can be expressed in the arctg function as: $\alpha_{rLi} = -\arctg(\dot{y}_{Ei}/\dot{x}_{Ei}) - \beta_i$, $\alpha_{rRi} = -\arctg(\dot{y}_{Fi}/\dot{x}_{Fi}) - \beta_i$, where coordinates can be written as: $x_{Ei} = x_{Bi} + \frac{1}{2}v_i \sin(\beta_i)$, $y_{Ei} = x_{Bi} + \frac{1}{2}v_i \cos(\beta_i)$, $x_{Fi} = x_{Bi} - \frac{1}{2}v_i \sin(\beta_i)$, $y_{Fi} = x_{Bi} - \frac{1}{2}v_i \cos(\beta_i)$. V_{Si} and V_{Fi} are the directions of velocity of the wheel for i -th trailer. The forces can be expressed as vector in a local coordinate system of i -th unit: $\mathbf{F}_i = [F_{xi} \ F_{yi}]^T$, where F_{xi} , F_{yi} is a sum of forces acting longitudinally (subscript x) and laterally (subscript y) relative to the unit. These sums can be saved as $F_{xi} = F_{xDi}$, and $F_{yi} = F_{yDi} + F_{yrRi} + F_{yrLi}$. For a last trailer F_{xDi} and F_{yDi} do not occur, so they are equal to zero. Forces F_{xi} , F_{yi} also are acting on front trailer ($i-1$), but they must be transformed to the local coordinate system of front trailer by rotation matrix $\mathbf{R}(\beta_{i-1} - \beta_i)$: $\mathbf{F}_{D(i-1)} = \mathbf{R}(\beta_{i-1} - \beta_i) \cdot \mathbf{F}_i$, where $\mathbf{F}_{D(i-1)} = [F_{xD(i-1)} \ F_{yD(i-1)}]^T$. The resulting vector contains forces acting on point D_{i-1} . For trailers, we note that $F_{yrRi} = C_{ir} \sin(\alpha_{rRi})$, $F_{yrLi} = C_{ir} \sin(\alpha_{rLi})$. $C_{ir} = \mu_{ir} F_{nri}$ are friction forces derived from the stiffness of the tire. F_{nri} is a normal force acting on the wheel denoted as: $F_{nri} = (h_i - c_i) g m_{ti} / (2 h_i)$. For this system generalized force vector can be denoted as $\mathbf{Q}(\mathbf{q}) = [F_x \ F_y \ F_{\beta_0} \ F_{\beta_1} \ F_{\beta_2} \ F_{\beta_3} \ F_{\beta_4}]^T$. F_{β_i} for trailers can be expressed as sum of moment for generalized coordinate β_i :

$$F_{\beta_i} = (F_{yrRi} + F_{yrLi})(h_i + d_{fi}) + F_{yDi}(d_i + h_i + d_{fi}), \quad (17)$$

where F_{yDi} does not occur for last trailer.

2.3. Double Ackermann steering system

A higher number of articulations (DOFs) causes a greater number of generalized coordinates for this system. Comparing with the previous systems, vector of generalized coordinates has been extended by angles defining the position of the drawbar β_{i2} . In this system angles defining the position of the trolley

are marked β_{i1} . Using the above assumptions, a vector of generalized coordinates can be obtained: $\mathbf{q} = [x \ y \ \beta_0 \ \beta_{11} \ \beta_{12} \ \beta_{21} \ \beta_{22} \ \beta_{31} \ \beta_{32} \ \beta_{41} \ \beta_{42}]^T$. The kinetic energy of the i -th trailer T_{ti} can be expressed as:

$$T_{ti} = \frac{1}{2} m_{dpi} (\dot{x}_{Pi1}^2 + \dot{y}_{Pi1}^2) + I_{dpi} \dot{\beta}_{i1}^2 + \frac{1}{2} m_{ti} (\dot{x}_{Pi2}^2 + \dot{y}_{Pi2}^2) + \frac{1}{2} I_{ti} \dot{\beta}_{i2}^2 + m_{wi} (\dot{x}_{Bi}^2 + \dot{y}_{Bi}^2) + (\dot{x}_{Ai}^2 + \dot{y}_{Ai}^2) + 2 \left(I_{wi} + m_{wi} \left(\frac{1}{2} v_i \right)^2 \right) \dot{\beta}_{i2}^2, \quad (18)$$

where $x_{Bi} = x - d_0 \cos(\beta_0) - \sum_{j=1}^{i-1} d_j \cos(\beta_{j2}) - \sum_{j=1}^i d_{pj} \cos(\beta_{j1}) - \sum_{j=1}^i h_j \cos(\beta_{j2})$, $y_{Bi} = y + d_0 \sin(\beta_0) + \sum_{j=1}^{i-1} d_j \sin(\beta_{j2}) + \sum_{j=1}^i d_{pj} \sin(\beta_{j1}) + \sum_{j=1}^i h_j \sin(\beta_{j2})$, $x_{Ai} = x_{Bi} + h_i \cos(\beta_{i2})$, $y_{Ai} = y_{Bi} - h_i \sin(\beta_{i2})$, $x_{Pi1} = x_{Ai} + c_{i1} \cos(\beta_{i1})$, $y_{Pi1} = y_{Ai} - c_{i1} \sin(\beta_{i1})$, $x_{Pi2} = x_{Bi} + c_{i2} \cos(\beta_{i2})$, $y_{Pi2} = y_{Bi} - c_{i2} \sin(\beta_{i2})$. Total energy of the system can be denoted as the sum of the energies of individual units: $T = T_b + \sum_1^4 T_{ti}$. Basic geometrical parameters for these systems are presented in Fig. 4.

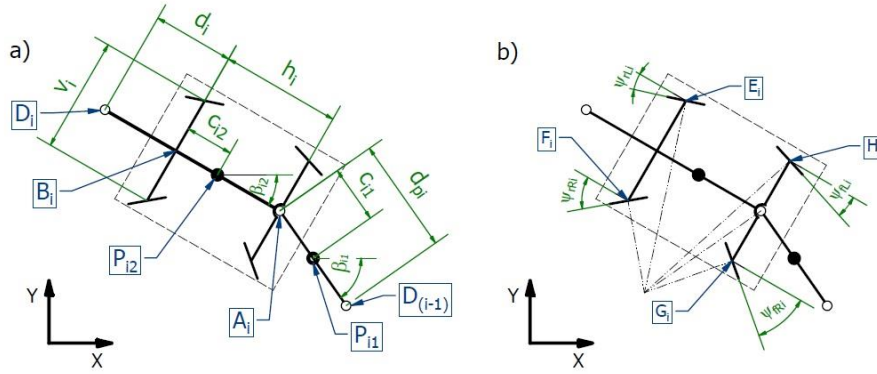


Figure 4. Double Ackermann steering system a) Basic geometrical parameters b) characteristic points

Side-slip angles and friction forces acting on the systems are presented in Fig. 5. The steering angle for double Ackermann steering system can be denoted as:

$$\psi_{fLi} = \arctg\left(\frac{h_i}{v_i + h_i \text{ctg}(\beta_{i1} - \beta_{i2})}\right) \text{ and } \psi_{fRi} = \arctg\left(\frac{h_i}{-v_i + h_i \text{ctg}(\beta_{i1} - \beta_{i2})}\right). \quad (20)$$

For rear wheels value of the steering angle is the same as in the front, but direction is opposite, so it can be expressed as $\psi_{rLi} = \psi_{fLi}$, $\psi_{rRi} = \psi_{fRi}$.

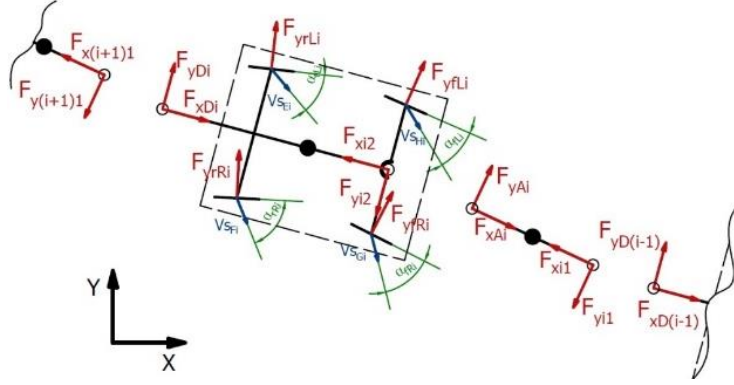


Figure 5. Forces and slip angles

The side slip angles for this system of the i -th trailer can be expressed as: for front wheels: $\alpha_{fLi} = -\arctg(\dot{y}_{Hi}/\dot{x}_{Hi}) - \beta_{i2} - \psi_{fLi}$, $\alpha_{fRi} = -\arctg(\dot{y}_{Gi}/\dot{x}_{Gi}) - \beta_{i2} - \psi_{fRi}$, for rear wheels: $\alpha_{rLi} = -\arctg(\dot{y}_{Ei}/\dot{x}_{Ei}) - \beta_{i2} + \psi_{rLi}$, $\alpha_{rRi} = -\arctg(\dot{y}_{Fi}/\dot{x}_{Fi}) - \beta_{i2} + \psi_{rRi}$, where: $x_{Ei} = x_{Bi} + \frac{1}{2}v_i \sin(\beta_{i2})$, $y_{Ei} = y_{Bi} + \frac{1}{2}v_i \cos(\beta_{i2})$, $x_{Fi} = x_{Bi} - \frac{1}{2}v_i \sin(\beta_{i2})$, $y_{Fi} = y_{Bi} - \frac{1}{2}v_i \cos(\beta_{i2})$, $x_{Gi} = x_{Ai} - \frac{1}{2}v_i \sin(\beta_{i2})$, $y_{Gi} = y_{Ai} - \frac{1}{2}v_i \cos(\beta_{i2})$, $x_{Hi} = x_{Ai} + \frac{1}{2}v_i \sin(\beta_{i2})$, $y_{Hi} = y_{Ai} + \frac{1}{2}v_i \cos(\beta_{i2})$. V_{sFi} , V_{sEi} , V_{sGi} , V_{sHi} are the directions of velocity of the wheel for i -th trailer. The forces can be expressed as vector in a local coordinate system of i -th unit: $\mathbf{F}_{vi2} = [F_{xi2} \ F_{yi2}]^T$, where F_{xi2} , F_{yi2} is a sum of forces acting longitudinally (subscript x) and laterally (subscript y) relative to the unit. These sums can be expressed as

$$F_{xi2} = F_{xDi} - F_{yRi} \sin(\psi_{rRi}) - F_{yLi} \sin(\psi_{rLi}) + F_{yRi} \sin(\psi_{fRi}) + F_{yLi} \sin(\psi_{fLi}), \quad (25)$$

$$F_{yi2} = F_{yDi} + F_{yRi} \cos(\psi_{rRi}) + F_{yLi} \cos(\psi_{rLi}) + F_{yRi} \cos(\psi_{fRi}) + F_{yLi} \cos(\psi_{fLi}). \quad (26)$$

For a last trailer F_{xDi} and F_{yDi} do not occur, so they are equal to zero. Forces F_{xi2} , F_{yi2} also are acting on front drawbar of the trailer, but they must be transformed to its local coordinate system by rotation matrix $\mathbf{R}(\beta_{i1} - \beta_{i2})$: $\mathbf{F}_{vAi} = \mathbf{R}(\beta_{i1} - \beta_{i2}) \cdot \mathbf{F}_{vi2}$, where $\mathbf{F}_{vAi} = [F_{xAi} \ F_{yAi}]^T$. $\mathbf{F}_{vi1} = \mathbf{F}_{vAi}$, where $\mathbf{F}_{vi1} = [F_{xi1} \ F_{yi1}]^T$. Forces F_{xi1} , F_{yi1} also act on front trailer ($i-1$), but they must be transformed to the local coordinate system of front trailer by rotation matrix $\mathbf{R}(\beta_{(i-1)2} - \beta_{i1})$: $\mathbf{F}_{vD(i-1)} = \mathbf{R}(\beta_{(i-1)2} - \beta_{i1}) \cdot \mathbf{F}_{vi1}$, where $\mathbf{F}_{vD(i-1)} = [F_{xD(i-1)} \ F_{yD(i-1)}]^T$. The resulting vector contains forces acting on point D_{i-1} . For trailers $F_{yRi} = C_{ir} \sin(\alpha_{rRi})$, $F_{yLi} = C_{ir} \sin(\alpha_{rLi})$, $F_{yRi} = C_{if} \sin(\alpha_{fRi})$, $F_{yLi} = C_{if} \sin(\alpha_{fLi})$. $C_{ir} = \mu_{ir} F_{nri}$, $C_{if} = \mu_{if} F_{nfi}$ are friction forces derived from the stiffness of the tire. F_{nfi} is normal force acting on the wheel denoted as: $F_{nfi} = (c_i g m_{ti})/h_i$ and $F_{nri} = (h_i - c_i)g m_{ti}/(2 h_i)$. For this system generalized force vector can be denoted as

$\mathbf{Q}(\mathbf{q}) = [F_x \ F_y \ F_{\beta 0} \ F_{\beta 11} \ F_{\beta 12} \ F_{\beta 21} \ F_{\beta 22} \ F_{\beta 31} \ F_{\beta 32} \ F_{\beta 41} \ F_{\beta 42}]^T \cdot F_{\beta_{i1}}$ for drawbar can be denoted as: $F_{\beta_{i1}} = F_{yAi} d_{pi}$. $F_{\beta_{i2}}$ for trailers can be expressed as sum of moment for generalized coordinate β_i :

$$F_{\beta_{i2}} = (F_{yRi} \cos(\psi_{rRi}) + F_{yLi} \cos(\psi_{rLi}))h_i + (F_{yRi} \sin(\psi_{rRi}) - F_{yLi} \sin(\psi_{rLi}) - F_{yfi} \sin(\psi_{fi}) + F_{yLi} \sin(\psi_{fi}))\frac{1}{2}v_i + F_{yDi}(d_i + h_i), \quad (32)$$

where F_{yDi} is not present for the last trailer.

3. Numerical experiments

In this section, we present results of numerical simulations, which were conducted for the all three systems discussed in this paper. In the simulations, coefficient of friction for the tractor wheels is constant: $\mu_{0f} = 30$ and $\mu_{0r} = 30$. Friction coefficient for trailer wheels for each of the systems were equal 20; 0.01; 0.0005; 0.0003. Initial conditions for all scenarios are the same as $q = q_0$ and $\dot{q} = \dot{q}_0$, where q_0, \dot{q}_0 are null vectors. The steering angle of the tractor front wheel ψ_{f0} is constant and equal $\pi/18$. Tractor drive torque τ is a function of time and its value was chosen so that the visualization most clearly showed the differences between rides. For $t < 200$ $\tau = 100 \text{ Nm}$ and otherwise $\tau = 40 \text{ Nm}$. Simulations have been conducted in *Wolfram Mathematica*. The results are obtained by solving a system of differential equations with the residual method [20]. The geometric parameters and mass properties of the system are given in Table 1. The results are presented in Fig. 6.

Table 1. Geometric parameters and mass properties

PARAMETERS		Conventional Clutch	Virtual Clutch	Double Ackermann
Mass [kg]	mb	1100	1100	1100
	m_{w0}, m_{w0s}	2	2	2
	m_{dpi}	-	-	5
	m_{ti}	500	500	500
	m_{wi}	1.5	1.5	1.5
Moment of inertia [kg m ²]	I_b	300	300	300
	I_{w0}, I_{w0s}, I_{wi}	0.02	0.02	0.02
	I_{dpi}	-	-	100
	I_{ti}	100	100	100
Dimensions [mm]	h_0	1000	1000	1000
	v_0	500	500	500
	$c_0, c_i/c_{i2}$	300	300	300
	r_{0f}	200	200	200
	r_{0r}	100	100	100
	d_0, d_i	200	800	300
	h_i	500	500	700
	d_{fi}/d_{pi}	800	200	400
	c_{i1}	-	-	200
	v_i	300	300	300
	r_{ir}	80	80	80

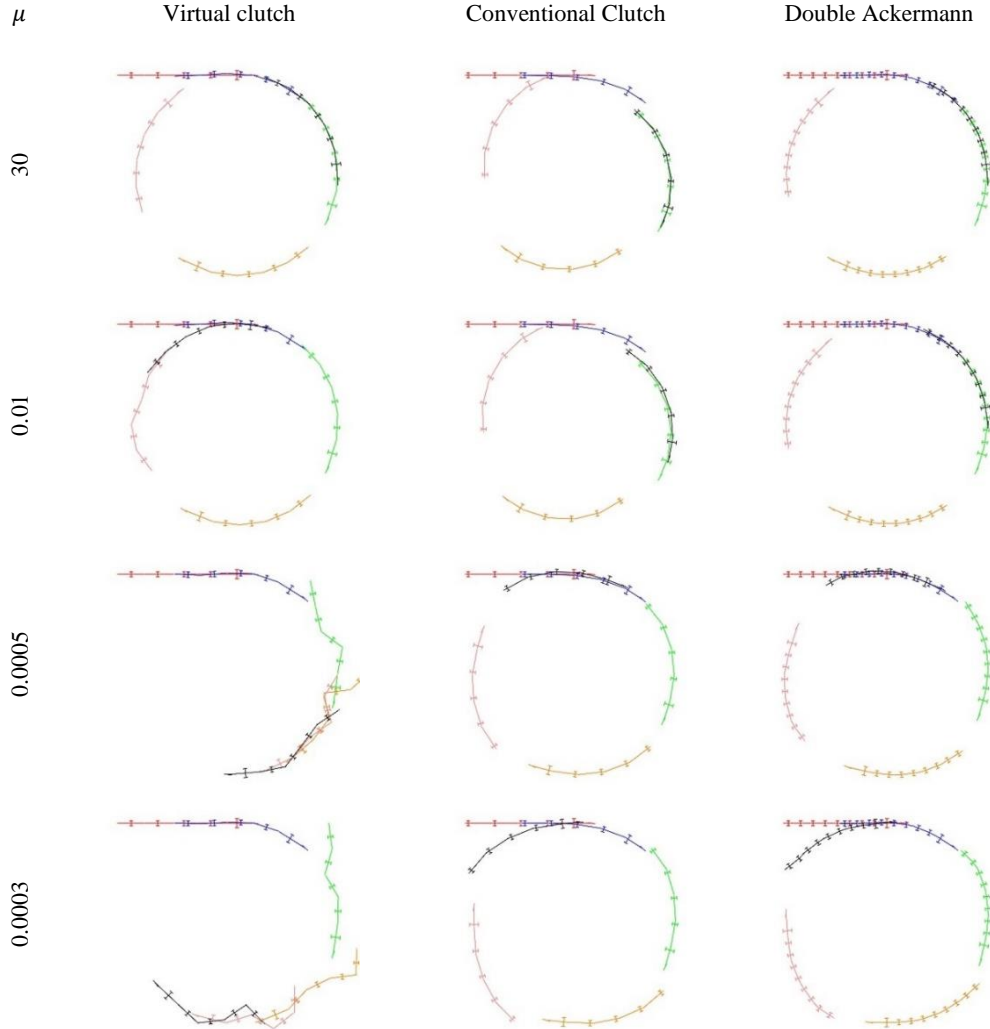


Figure 6. Train trajectories, where Red, Blue, Green, Orange, Pink and Black are for different time values in seconds: 0, 200, 400, 600, 800, 1000 respectively.

The obtained trajectories differ significantly in individual simulations. The high coefficient of friction (30) ensures no slip. A low coefficient of friction (0.0003 and 0.0005) causes slip effect for each system. It is most evident for the virtual clutch. In other systems, this effect is more subtle, but it still occurs. The slipping in the conventional clutch causes the trolleys to move away from the center of the circular trajectory due to centrifugal force. The double Ackermann steering system is less prone to the slip than the other systems. The reason for this is the influence of the front wheel and the possibility of their turning. In that case friction forces acting on the trolley both in longitudinal and lateral directions. In the others systems, only lateral friction forces act on the trailer.

Furthermore, the location of the tractor in time is different depending on the scenario for high values of coefficient of friction. This is due to the difference in kinetic energy. As the coefficient of friction decreases, the differences in the position of the tractor are greater, except for the virtual clutch system. This effect is the least visible for the double Ackermann system as friction forces decelerate the tractor. There is no this relationship for the virtual clutch with two the lowest friction coefficients. This is due to the velocities of the system at the beginning of the slip. Virtual clutch system is the most prone to the slipping. It means that the trolleys easily position themselves sideways to the direction of the motion. Then the friction forces are greatest because the slip angle is the highest, what causes deceleration.

4. Conclusions

In this paper, we showed the dynamic models of the three most popular steering systems for logistic trains. The obtained results allow comparison of their behavior in the presence of the slip effect. Kinematic analysis can help to choose the best system for non-slip rides. The slip effect affects the analyzed systems differently. Virtual clutch system is not very stable in contrast to the double Ackermann steering system. Factor favorable to the Ackermann steering system can be number of active wheels. This means that for virtual clutch system, only the weight acting on the rear axle of the trailer participated in the friction forces, as front castor wheels adapt their movement to the actual direction of motion.

Acknowledgments

This work was supported by the Polish Ministry of Science and Higher Education as part of subsidy - number 02/22/SBAD/1501.

References

- [1] Lieb, C., Prinz, T., Gunthner, W. and Fottner, J. (2019). Modeling and Simulation of Generic Handling Operations in In-Plant Milk-Run Systems. 2019 8th International Conference on Industrial Technology and Management (ICITM).
- [2] Kluska, K. and Pawlewski, P. (2018). The use of simulation in the design of Milk-Run intralogistics systems. IFAC-PapersOnLine, 51(11), pp.1428-1433.
- [3] Knez, M. and Gajsek B. (2015) Implementation of in-plant milkrun system for material supply in lean automotive parts manufacturing. The International Conference on Logistics & Sustainable Transport 2015.
- [4] Alnahhal, M., Ridwan, A. and Noche, B. (2014). In-plant milk run decision problems. 2014 International Conference on Logistics Operations Management.
- [5] Paszkowiak, W., Bartkowiak, T. and Pelic, M. (2019). Kinematic model of multiple trailers on a tractor system for production logistics applications. Archives of Mechanical Technology and Materials, 39(1), pp.16-25.

- [6] Ahmad Abu Hatab, R. (2013). Dynamic Modelling of Differential-Drive Mobile Robots using Lagrange and Newton-Euler Methodologies: A Unified Framework. *Advances in Robotics & Automation*, 02(02).
- [7] Keymasi Khalaji, A., Rahimi Bidgoli, M. and Moosavian, S. (2014). Non-model-based control for a wheeled mobile robot towing two trailers. *Proceedings of the Institution of Mechanical Engineers, Part K: Journal of Multi-body Dynamics*, 229(1), pp.97-108.
- [8] Kong, J., Pfeiffer, M., Schildbach, G. and Borrelli, F. (2015). Kinematic and dynamic vehicle models for autonomous driving control design. *2015 IEEE Intelligent Vehicles Symposium (IV)*.
- [9] Altche, F., Polack, P. and de La Fortelle, A. (2017). A simple dynamic model for aggressive, near-limits trajectory planning. *2017 IEEE Intelligent Vehicles Symposium (IV)*.
- [10] Iwona, A., Lukasz, D., Witold, G. and Stanislaw, W. (2019). Calibration of an Articulated Vehicle Model and Analysis of Friction Model in the Connection Between Two Vehicle Units. *Journal of Computational and Nonlinear Dynamics*, 14(5), p.051008.
- [11] Kayacan, E., Kayacan, E., Ramon, H. and Saeys, W. (2013). Modeling and identification of the yaw dynamics of an autonomous tractor. *2013 9th Asian Control Conference (ASCC)*.
- [12] Gao, J. and Jia, H. (2017). Control Research for a Small Fixed-Wing UAV During Ground Taxiing. *Journal of Harbin Institute of Technology (New Series)*, 24(2), pp.51-57.
- [13] Bloch, A., Krishnaprasad, P. and Murray, R. (2015). *Nonholonomic Mechanics and Control*. New York, NY: Springer New York, pp.26-30.
- [14] Bravo-Doddoli, A. and García-Naranjo, L. (2015). The dynamics of an articulated n-trailer vehicle. *Regular and Chaotic Dynamics*, 20(5), pp.497-517.
- [15] Lucet, E., Grand, C., Salle, D. and Bidaud, P. (2008). Stabilization Algorithm for a High Speed Car-Like Robot Achieving Steering Maneuver. *2008 IEEE International Conference on Robotics and Automation*.
- [16] Piyabongkarn, D., Rajamani, R., Grogg, J. and Lew, J. (2009). Development and Experimental Evaluation of a Slip Angle Estimator for Vehicle Stability Control. *IEEE Transactions on Control Systems Technology*, 17(1), pp.78-88.
- [17] Kayacan, E., Kayacan, E., Ramon, H. and Saeys, W. (2014). Nonlinear modeling and identification of an autonomous tractor-trailer system. *Computers and Electronics in Agriculture*, 106, pp.1-10.
- [18] Martinez, J., Avila, J. and Canudas de Wit, C. (2004). A New Bicycle Vehicle Model with Dynamic Contact Friction. *IFAC Proceedings Volumes*, 37(22), pp.625-630.
- [19] Yavin, Y. (2007). Modelling the motion of a trolley-like car: The case where the front wheel is constraint to roll on a given plane curve. *Mathematical and Computer Modelling*, 46(3-4), pp.307-315.
- [20] Chehab, J. and Laminie, J. (2005). Differential equations and solution of linear systems. *Numerical Algorithms*, 40(2), pp.103-124.

Wojciech Paszkowiak, M.Sc. (Ph.D. student): Poznan University of Technology, Institute of Mechanical Technology, Pl. M. Skłodowskiej-Curie, 60-965 Poznan, Poland (wojciech.z.paszkowiak@doctorate.put.poznan.pl). The author gave a presentation of this paper during one of the conference sessions.

Tomasz Bartkowiak, Ph.D: Poznan University of Technology, Institute of Mechanical Technology, Pl. M. Skłodowskiej-Curie, 60-965 Poznan, Poland (tomasz.bartkowiak@put.poznan.pl).

Experimental and simulation examination of the impact of the control model on the motion of a motorcar with a trailer in a critical situation

Leon Prochowski, Mateusz Ziubiński, Patryk Szwajkowski,
Tomasz Pusty, Mirosław Gidlewski

Abstract: The study covers an analysis of the selection of parameters and performance curves of one of the modules of the algorithm of controlling the movement of an autonomous motorcar with a trailer when an obstacle suddenly appearing in front of the vehicle is to be avoided. The algorithm is based on a “driving controller” model where the signals measured during motion of the car-trailer unit are processed with using fuzzy logic and the information received from the environment perception system is utilized by the model to identify the situation where a driver’s reaction is required. The resulting hazards arise from the complexity of the interactions taking place between the car, trailer, controller, and environment. The critical situations include trailer sway and jackknifing, specific to car-trailer units and caused by the trailer acting on the car and by the coupling between them. The issue in question covers an analysis of cooperation between several non-linear models (of the tractor, trailer, tyre-road interaction, and driving controller). Important areas of limiting the stability of functioning of such a combination of the models, especially when an obstacle suddenly appears in front of the vehicle moving with a high speed, have been identified. During experimental tests, attention was chiefly focused on validating the model representing the car-trailer unit and the behaviour of the car and the trailer during the obstacle avoidance manoeuvre. As an outcome of that research stage, the symptoms of critical situations resulting from the motion of the car-trailer unit were defined. Within the next step, the selection of the parameters and performance curves that may be decisive for the dynamics and stability of functioning of the models in the specific situation was analysed. The signals and indicators chosen for the analysis, describing the behaviour of the car-trailer unit, were treated as input data for the driver model. The values of the said signals and indicators rapidly increase with growing speed of the car-trailer unit and rising tow car’s steering wheel angle. The signals that are particularly sensitive in various road conditions have been indicated.

1. Introduction

Trailers are now universally used and this will not change in the next years. The adding of a trailer to a motorcar (used as a tow vehicle) offers a lot of benefits in passenger and cargo transport applications. However, difficulties in controlling car-trailer units when performing challenging road manoeuvres make a considerable drawback of such a vehicle combination.

The participation of autonomous motor vehicles in the road traffic is based on a few elementary driving models: following of the preceding vehicle; using of reference models; and using of lane-change models [2, 4]. The design of such models is based on results of the observation of road traffic and most frequent drivers' behaviours [3, 7]. This is of critical importance for the safe operation of autonomous vehicles in the environment and road traffic, where motor vehicles driven by human drivers will undoubtedly remain predominating for many years.

The autonomous vehicles move to follow the "preset trajectory", i.e. continually generated models of the vehicle trajectory immediately planned. This is also the case when the avoidance of an obstacle takes place. Two basic methods of generating (planning) the preset vehicle trajectory are used. In the first one, the vehicle trajectory is determined on the grounds of a vehicle drive pre-simulated by a simple reference model [4]. In the other one, curves are defined that describe the lateral displacement of the centre of vehicle mass in the form of algebraic equations, which may represent sequences of circular arcs, polynomial splines, clothoid splines, Bézier curves, etc. [8, 9, 10]. It is essential that the desired vehicle trajectory should be determined with considering the basic limitations dictated by the properties of real motor vehicles [16]. As an example, a method of generating the vehicle trajectory with taking into account the maximum acceptable values of the lateral (centripetal) acceleration of the motor vehicle under consideration has been presented in [11].

In most of the models examined hitherto, the controllers substituted for vehicle drivers minimize the distance between the current position of the centre of vehicle mass and the preset vehicle trajectory and minimize the difference between the angles of vehicle position and the position of the tangent to the preset vehicle trajectory. In this role, PID controllers and controllers based on fuzzy logic predominate. As an example: in [9], the control process is based on tracking the preset vehicle trajectory by a PID controller; the effective use of fuzzy logic in the controllers of mobile robots and motor vehicles has been shown in [3, 12]. A good result of controlling the drive of mobile platforms ([16]) was achieved by the use of two different control techniques. The controlling of a motor vehicle with a trailer in typical road situations has been analysed in [1], where the current obstacle position and the space limitations posed by the road infrastructure have been taken into account.

Most of the reported methods of generating the desired vehicle trajectory apply to typical manoeuvres often performed in road traffic. In the situation of an obstacle suddenly appearing in front of a vehicle, the on-board computer has a very short time for making the necessary calculations to determine the desired vehicle trajectory. There is a lack of vehicle and controller models applicable to critical situations with autonomous vehicles travelling with a high speed, where the vehicle and the obstacle move along collision paths in an environment that has been only partly defined.

In this study, a critical road situation will be analysed that may arise in result of e.g. other vehicle driver's failure to yield the right of way on a road intersection. This usually causes front-to-side

collisions of moving vehicles and the percentage of such collisions in the total number of road accidents in Poland shows an upward trend (amounting to 31 % at present) [15]. It should be added here that the safety at front-to-side vehicle collisions has been for many years within the main areas of scientific interest of the authors of this study (cf. [5]).

This work is aimed at determining the impact of some controller characteristics on the possibility of safe avoidance of a suddenly appearing obstacle that is moving along a collision path in relation to an autonomous car with a trailer (“car-trailer unit”) travelling with a high speed. The advantageous values of the input parameters for a fuzzy logic controller and the areas of acceptable control values for the road situation under analysis will be indicated. An assumption has been adopted that in a critical situation of this kind, the information sent by the environment perception system (i.e. the data recognition and interpretation) will cause the controller settings to be adjusted for the time of the obstacle avoidance process. Such settings will differ from those used to ensure stable vehicle motion before and after the obstacle avoidance manoeuvre.

The degree of difficulty of the controller operation in the case under analysis is very high. This is not only due to the short time available for the perception of a specific road situation but also because of the dilemmas arising from the situation where a non-collision solution does not exist.

2. Road situation under analysis

In the problem addressed here, a cargo trailer has been added to an autonomous car and the motion of such a car-trailer unit in analysed in a situation where an object moving along a collision path suddenly appears in front of the said vehicle and may be expected to block a part or the whole width of the lane used by this vehicle. Such a situation has been generally illustrated in Fig. 1.

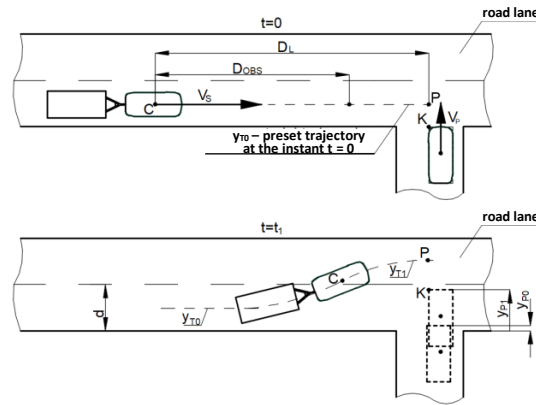


Fig. 1. Road situation under analysis: D_L – distance of environment recognition by the perception system; D_{obs} – distance over which the preset vehicle trajectory y_T is analysed by the controller; y_{T0} , y_{T1} – preset vehicle trajectory; y_{P0} , y_{P1} – obstacle position; K – foremost edge of the obstacle

At the instant when the car environment perception system (Fig. 2) finds out that such an obstacle begins to come out ($y_{P0} > 0$), distance x_0 between the car and the obstacle is shorter than the braking distance S_h of the car-trailer unit. Therefore, a safe solution may be a circumvention of the obstacle (with using the adjacent road lane) to avoid a collision.

The process of avoiding a suddenly appearing obstacle is usually based on the results of:

- analysis of the critical situation;
- determination of the forecasted position of the point of intersection of the trajectories of the objects under analysis (point P in Fig. 1);
- generation of the preset vehicle trajectory $y_T(x, t)$;
- immediate adjustment of the preset trajectory according to obstacle motion.

In the situation of sudden intrusion of an obstacle, as analysed in this study, the method with detection of the foremost obstacle edge K may be relatively effective. The determination of the current positions of edge K and point P (see Fig. 1) makes it possible to start the trajectory planning process, necessary for the controller to function.

3. Control system and model of dynamics of the vehicles

A schematic diagram of the control system has been shown in Fig. 2.

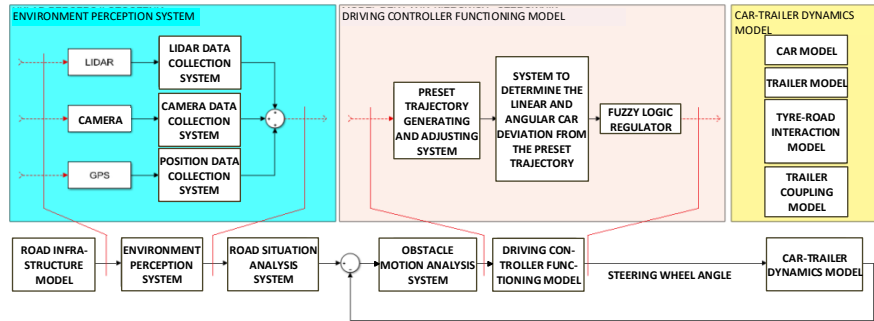


Fig. 2. Structure of the control system

In the next part of this study, particular attention has been paid to the models of the driving controller and the car-trailer unit. Important aspects of the controller operation have been described within the analysis of the critical situation. In turn, a model of the car-trailer unit has been presented in Fig. 3. In this model, the tow car body is treated as a rigid body with 6 degrees of freedom and each of the wheels has a degree of freedom related to its rotational motion. Hence, the car and trailer models have 10 degrees of freedom each.

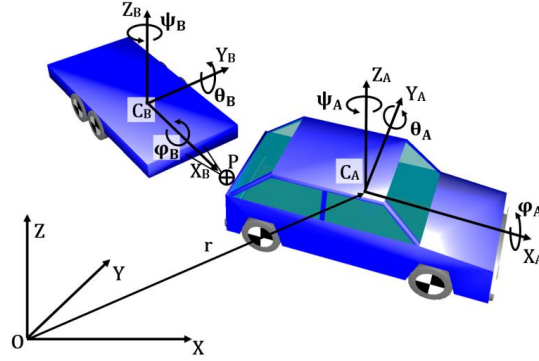


Fig. 3. Car-trailer unit with the global {O} and local {C} coordinate systems

The following generalized coordinates were used to describe the vehicle body motion:

$$\mathbf{q} = [x \ y \ z \ \varphi \ \theta \ \psi]^T \quad (1)$$

where:

x, y, z – global {O} coordinates of the origin of a local coordinate system {CA or CB};

φ, θ, ψ – quasi-Euler angles defining the orientation of system {C} relative to system {O}.

The equations of motion were expressed in the form of vectorial relations as follows:

$$m(\dot{\mathbf{v}} + \boldsymbol{\omega} \times \mathbf{v}) = \sum_{i=1}^n \mathbf{F}_i \quad (2)$$

$$\mathbf{T} \dot{\boldsymbol{\omega}} + \boldsymbol{\omega} \times \mathbf{T} \boldsymbol{\omega} = \sum_{j=1}^k \mathbf{M}_j \quad (3)$$

where:

m, \mathbf{T} – vehicle mass and tensor of inertia in relation to the centre of mass in {C};

$\mathbf{r}, \mathbf{v} = \dot{\mathbf{r}}, \dot{\mathbf{v}} = \ddot{\mathbf{r}}$ – vector extending from the origin of the global coordinate system to the centre of vehicle mass in {C} and vectors of the velocity and acceleration of the centre of mass in the global coordinate system {O};

\mathbf{F}_i and \mathbf{M}_j – external forces and moments, respectively, acting on the vehicle body in {C};

$\boldsymbol{\omega}$ – vector of the angular velocity of the vehicle body in {C}.

In the vehicle models, a few important non-linear characteristic curves plotted for the tyres and suspension systems were taken into account. The courses of these curves are essential as regards the analysed aspect of the vehicle motion at high values of vehicle body roll angle, steering angle, as well as tyre slip ratio and sideslip angle during the experimental and simulation tests, due to high vehicle speeds and curvatures of the vehicle trajectory during the obstacle avoidance process.

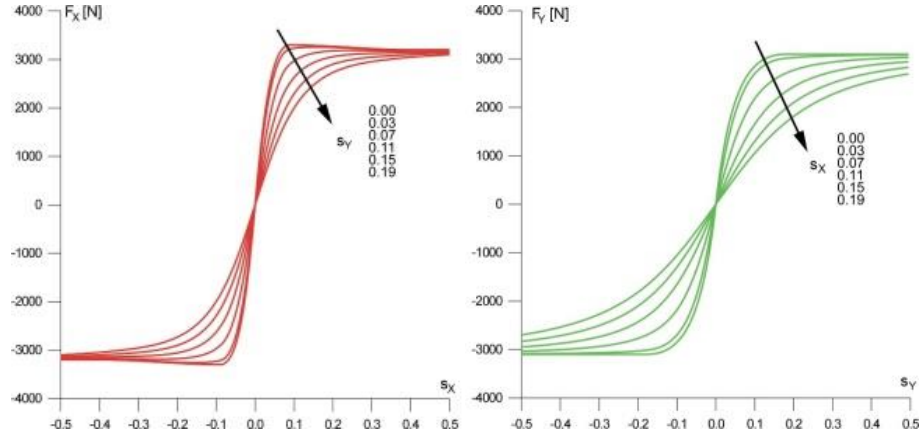


Fig. 4. Examples of non-linear characteristics of the tyre-road interaction in the motorcar and trailer models

Fig. 4 shows an example comparison of tangential force curves $F_X(s_X)$ and $F_Y(s_Y)$ for several tyre slip values s_X and s_Y . For the model, the course of these curves was determined with using a semi-empirical model TMeasy [6, 13], which enables the approximation of the actual forces and moments generated by the tyre (even at high tyre slip values) based on experimental tyre slip characteristics:

$$F_X(s_X) = \mu \cdot [\mu_x(s_X) \cdot F_Z] \quad F_Y(s_Y) = \mu \cdot [\mu_y(s_Y) \cdot F_Z] \quad (4)$$

where:

- F_Z – normal component of the force acting at the tyre-road contact point;
- F_X and F_Y – forces acting at the tyre-road contact point, limited by the tyre to road adhesion force F_μ ;
- $\mu(\mu_x, \mu_y)$ – tyre-road adhesion coefficient and unit tangential forces at the tyre-road contact point.

The model of dynamics of the car-trailer unit was validated in conditions corresponding to the avoidance of a suddenly appearing obstacle [14], with taking into account conformity between the results of experimental measurements and the results of simulation carried out with a model of avoidance of a suddenly appearing obstacle. The conformity was assessed by comparing the trajectory of the centre of vehicle mass, lateral accelerations at the centre of mass, vehicle body yaw and roll angles, and front and rear tyre sideslip angles. Fig. 5 shows photos of the experimental tests and comparisons of several curves, such as trajectory of the motorcar, lateral acceleration of the centre of mass of the car and the trailer, and trailer yaw angle ψ_B .

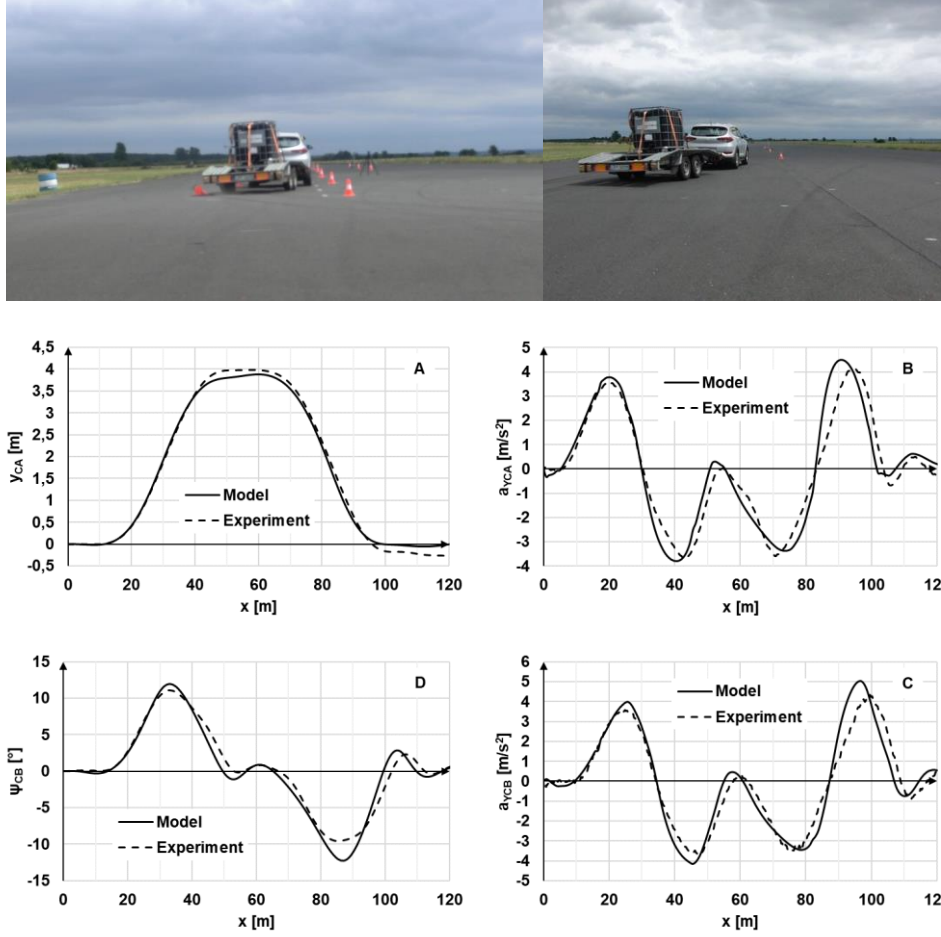


Fig. 5. Comparison of results of experimental and simulation tests with avoiding an obstacle suddenly appearing in front of the vehicle moving with a speed of $v = 60$ km/h

The validation confirmed good conformity between the results of experimental and model tests.

4. Analysis of the critical situation

The primary objective of the analysis is to determine the vehicle trajectory $y_T(t, x)$. It is assumed that the perception system is continuously monitoring the road situation and should detect the instant when the situation begins to be hazardous, i.e. when the y_{P0} value begins to be positive ($y_{P0} > 0$). Then, the process of analysis of the critical situation (see Fig. 2) should result in determining:

- y_{P0} and v_P , i.e. the position and velocity of the obstacle at the instant t_0 ;

- x_0 and v_S based on the state of motion of the car; x_0 is the distance from the car to the obstacle at the instant t_0 (when the obstacle just appears in front of the car);
 - whether $x_0 < S_h$; if yes, then the obstacle avoidance procedure should be started; S_h is the braking distance of the car-trailer unit in the current local road conditions;
 - next position of point K (at the instant t_l);
- and in calculating:

$$y_{P1} = v_P t_S \quad t_S = \frac{x_0}{v_S}, \text{ and} \quad (5)$$

- forecasted position of the target point (P in Figs 1 and 6)

$$y_P = y_{P1} + b_2 + y_W - 0.5d \quad (6)$$

where: b_2 – half of the width of the car-trailer unit; d – width of the road lane;
 y_W – clearance necessary for the safe avoidance of the obstacle (Figs 1 and 6).

When the position of point P is determined, it will be possible to generate the preset vehicle trajectory $y_T(t, x)$ as a continuation of the previous path ($y_{T0} \rightarrow y_{Tl}$; Figs 1 and 6), but with taking into account the critical situation detected. Additionally, it should be kept in mind that braking in the situation of $x_0 < S_h$ may be risky because it will cause the values of t_S and y_{P1} to increase; moreover, the braking will also “consume” a part of the tyre to road adhesion force F_μ available.

The preset vehicle trajectory $y_T(t, x)$ is designed in a two-dimensional space, based on the information obtained from the system of perception of the situation in front of the car. The working space thus described is told to be “partially defined”. To generate the vehicle trajectory y_T in such a space, the functions describing the necessary lateral displacement y (Fig. 6) of the centre of mass of the car-trailer unit during the transition from rectilinear to curvilinear motion were taken as the point of departure. The following functions were considered:

- a) cosine curve

$$y = y_P (1 - \cos\beta); \quad \beta = \frac{x}{x_0} 180^\circ; \quad x \in (0, x_0) \quad (7)$$

- b) composition of two circular arcs

$$\begin{aligned} \text{for } x \in [0, x_D], \quad y &= R - \sqrt{R^2 - x^2} \\ \text{for } x \in (x_D, x_0], \quad y &= y_P - R + \sqrt{R^2 - (x - x_0)^2} \\ x_D &= \frac{x_0}{2} \end{aligned} \quad (8)$$

- c) composition of two parabola segments

$$y = a_0 + a_1 x + a_2 x^2, \quad (9)$$

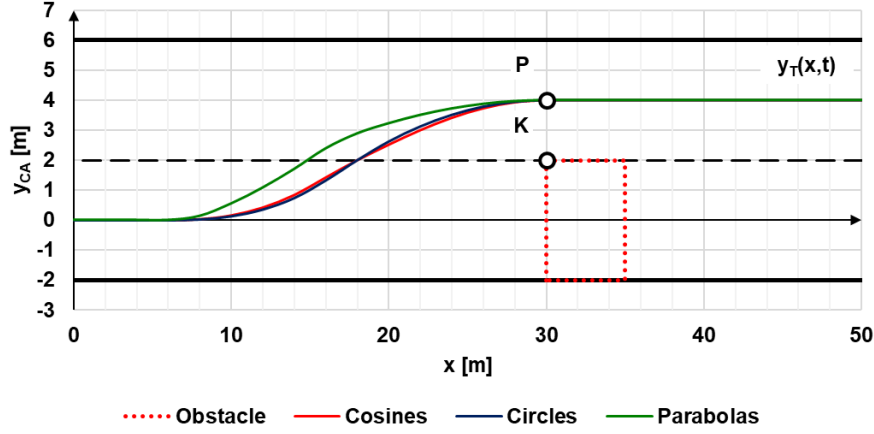


Fig. 6. Example preset vehicle trajectories during the obstacle avoidance process,

$$v = 60 \text{ km/h}, D_{obs} = 6 \text{ m}, y_w = 1 \text{ m}$$

The preset vehicle trajectory was calculated with taking into account the following limitations dictated by the properties of the specific car-trailer unit (examples calculated for the three functions mentioned above and the properties of the fuzzy logic model have been shown in Fig. 6):

$$\delta \leq \delta_{MAX} = 30 \dots 35^\circ \text{ (design confinement of the steering angle)} \quad (10)$$

$$v_S \leq v_{MAX} \quad (11)$$

$$R_{S \text{ MIN}} \geq \frac{L}{\tan \delta_{MAX}} \quad R_{P \text{ MIN}} \geq \sqrt{R_{S \text{ MIN}}^2 + l_h^2 - l_{hp}^2} \quad (12)$$

$$F_Q = m \frac{v_S^2}{R_S} \leq F_\mu = \mu g m \quad (13)$$

where:

$R_{S \text{ MIN}}, R_{P \text{ MIN}}$ – minimum radii of curvature of the car and trailer trajectories, respectively;

v_S – vehicle speed;

$a_{Y \text{ MAX}}$ – maximum acceptable lateral acceleration;

L – motorcar wheelbase.

$$\text{Hence: } R_{S \text{ MIN}} > \frac{v_S^2}{a_{Y \text{ MAX}}}; \quad a_{Y \text{ MAX}} < \mu g \quad (14)$$

The difference between the radii of curvature $R_P - R_S$ has an impact on the necessary clearance y_w between the vehicle and the obstacle in the curvilinear motion.

The results obtained hitherto from the experimental and simulation tests [14] provide grounds for identifying the following important criteria for the assessment of the quality and nature of the course of the obstacle avoidance process:

- effective avoidance of the obstacle;

- stable form of the vehicle trajectory;
- short time of “adjusting” the vehicle position (measured to 5 % of the deviation value) and limited value of the extreme overshoot in the trajectory;
- short time spent on the adjacent road lanes;
- as low as possible extreme values of the steering angle, steering wheel angle, tyre sideslip angles, lateral acceleration, roll angle, and drawbar turning angle.

The simulation test results were analysed with taking the above criteria into account.

5. Simulation test results

Extensive simulation research was carried out to determine the impact of the vehicle control model on the motion of the car-trailer unit when avoiding a suddenly appearing obstacle. In the tests, the PC-Crash program [13] was used and the calculations were made for the motion of the vehicle combination with speeds ranging from 40 km/h to 80 km/h. The following main assumptions were adopted for the simulations:

- The vehicle combination consisted of a motorcar with a mass of 1 800 kg and a centre-axle trailer with a mass of 1 800 kg as well.
- Before the critical situation occurred, the car-trailer unit moved rectilinearly with a constant speed in the middle of the right lane of a carriageway.
- The road had two lanes in each direction.
- The lane width was $d = 4$ m and the maximum width of the car-trailer unit was 2.4 m.

At the initial stage of the tests, the impact of the method of generating the preset vehicle trajectory and the reaction time or the D_{obs} distance (Fig. 1) on the functioning of the control system (Fig. 2) was determined. The assessment of this impact was based on results of the simulation of behaviour of the vehicle combination in the critical road situation. The following curves and values determined for the car and the trailer were assessed:

- trajectory of the centre of vehicle mass (Fig. 7);
- length of the distance $x(t)$ travelled by the vehicle before the lateral displacement y_{CA} and y_{CB} equal to 3 m is achieved and the y_{CA} and y_{CB} values actually achieved at the instance of passing-by the obstacle;
- extreme values of the steering wheel angle ($\delta_{HMAX}, \delta_{HMIN}$) and tyre sideslip angles ($\alpha_{MAX}, \alpha_{MIN}$) in the initial phase of the obstacle avoidance process.

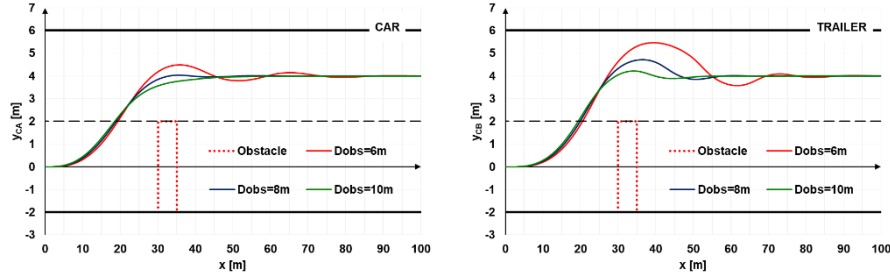


Fig. 7. Example trajectories of the car and trailer centres of mass during the obstacle avoidance process, $v = 60 \text{ km/h}$, $y_w = 1 \text{ m}$

Fig. 7 shows curves representing the trajectories of the vehicle centres of mass, obtained for three different D_{obs} values. The curves show that the selection of this value has an impact on the rate of growth in the lateral vehicle displacement and on the value of the first overshoot (y_{MAX}) during the obstacle avoidance process. Example curves representing the dependence of some characteristic values determined from the $x(y_{CA})$, $x(y_{CB})$ as well as $\alpha_A(x)$ and $\alpha_B(x)$ curves on the y_T generation method chosen and on the selection of the D_{obs} value have been juxtaposed in Fig. 8.

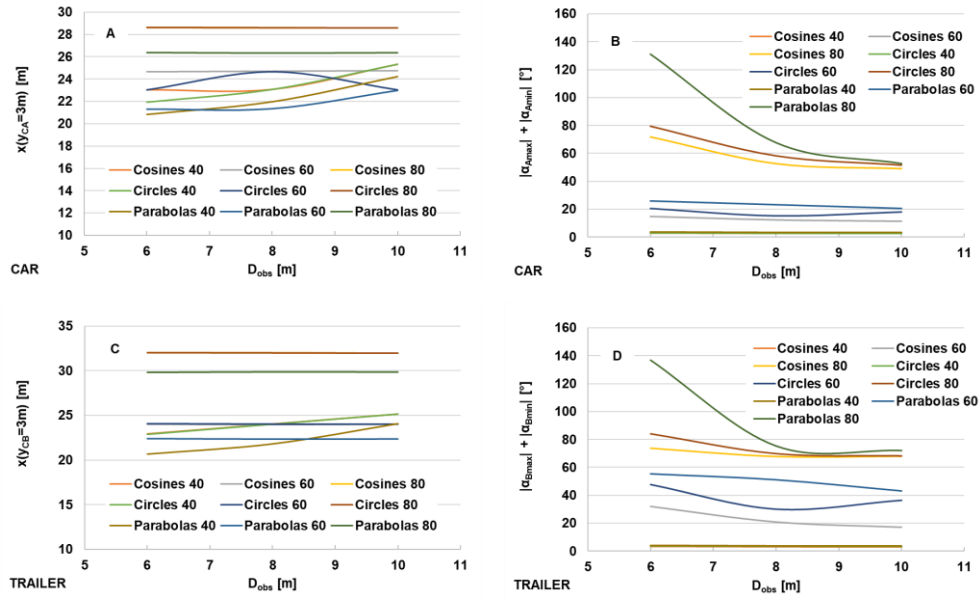


Fig. 8. Juxtaposition of some characteristic values to compare the simulation results for various methods of defining the preset vehicle trajectory y_T and selecting the D_{obs} distance; the calculations were carried out for $v = 40\text{-}80 \text{ km/h}$ and $y_w = 1 \text{ m}$

In Fig. 8, the course of the x_A and x_B curves (Figs 8A, 8C) below 30 m shows that the car and the trailer can avoid the obstacle that would appear at a distance of $x_0 = 30$ m. In Fig. 8C, there is one curve above 30 m indicating that the trailer moving with a speed of $v = 80$ km/h would hit the obstacle if the preset vehicle trajectory were designed as a composition of circular arcs. The curves in Figs 8B and 8D show that the collision would be accompanied by skidding of trailer wheels, with the skidding beginning to occur even at $v = 60$ km/h.

At the initial stage of the tests, the following could be determined:

- $y_T(t, x)$ generation method that would be advantageous in the critical road situation;
- minimum y_w value;
- D_{obs} length.

This in turn enabled passing to the second stage, at which the findings made at the initial stage were used and when the range of the acceptable δ_{HMAX} and δ_H^{PRM} values, such that a stable vehicle trajectory could be achieved during the obstacle avoidance process, was determined. The calculations revealed that the range of acceptable steering wheel angle values was very restricted (Fig. 9).

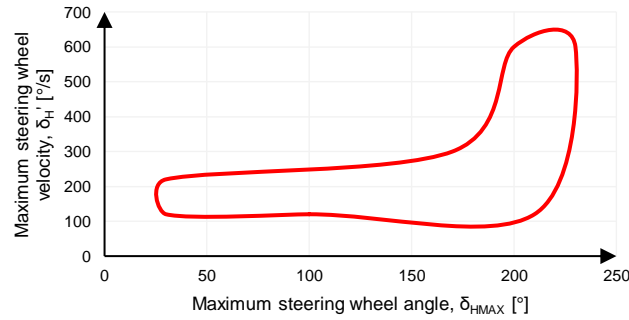


Fig. 9. Example of the restricted area of values of the δ_{HMAX} and δ_H^{PRM} settings of the control system under test at which a stable vehicle trajectory could be achieved during the obstacle avoidance process

6. Recapitulation and conclusions

In order to verify the possibility of safe avoidance of an obstacle moving along a collision path and, moreover, the adopted concept of functioning of the control system, extensive experimental and simulation research was carried out. During the experimental tests, some characteristic curves representing non-linear properties of vehicle tyres and suspension systems were determined and measurement results describing the car-trailer unit motion when avoiding a suddenly appearing obstacle were collected. This made it possible to validate the computer model used for testing the control system.

The simulation tests were carried out for a complex road situation; as early as at the initial stage, they revealed that the possibilities of controlling a motor car so that it could avoid an obstacle were very limited (cf. Figs 8 and 9). The conditions of vehicle motion and the controller settings were indicated at which the vehicle would hit the obstacle because the collision would be unavoidable. The findings made within the two stages of the tests include the following:

- To generate y_T in the critical situation under analysis, the use of a composition of parabola segments would be recommendable.
- The D_{obs} length should be 7-8 m.
- The y_w distance should exceed 1 m.

The acceptable areas of selection of the steering wheel angle values in the initial phase of the obstacle avoidance manoeuvre were also determined. The values indicated are applicable to the range of the necessary adjustment of controller parameters for the time of duration of the obstacle avoidance manoeuvre. Comprehensive fragments of the calculation results will be shown during the presentation of this paper.

7. References

- [1] Anderson Sterling J, Peters Steven C. *An optimal-control-based framework for trajectory planning, threat assessment, and semi-autonomous control of passenger vehicles in hazard avoidance scenarios*, Int. J. Vehicle Autonomous Systems, Vol. 8, Nos 2/3/4, 2010.
- [2] Balal Esmaeil, Cheu Ruey Long, Sarkodie-Gyan Thompson. *A binary decision model for discretionary lane changing move based on fuzzy inference system*, Transportation Research Part C: Emerging Technologies, Vol. 67, June 2016, <https://doi.org/10.1016/j.trc.2016.02.009>.
- [3] Chen G, Zhang WG, Zhang XN. (2013) *Fuzzy neural control for unmanned robot applied to automotive test*, Ind. Robot 40 (5), art. no. 17094477.
- [4] Gidlewski M, Żardecki D. *Influence of Nonlinearity Simplifications in a Reference Model of a Motor Vehicle on the Automatic Control of the Vehicle Steering System During a Lane-change Manoeuvre*, Proceedings of 13th International Conference Dynamical Systems – Theory and Applications DSTA2015, Lodz 2015, Poland, Dynamical Systems, Control and Stability.
- [5] Gidlewski M, Prochowski L, Jemioł L, Żardecki D. *The process of front-to-side collision of motor vehicles in terms of energy balance*, NONLINEAR DYNAMICS (2019) 97 (3), Springer Netherlands, <https://doi.org/10.1007/s11071-018-4688-x>.
- [6] Hirschberg W, Rill G, Weinfurter H. *User-appropriate tyre modelling for vehicle dynamics in standard and limit situation*, Vehicle System Dynamics 2002, 38(2).
- [7] Ivanov V. *A review of fuzzy methods in automotive engineering applications*, Germany, Eur. Transp. Res. Rev. (2015) 7: 29 DOI 10.1007/s12544-015.
- [8] Katrakazas Ch, Katrakazas M, Wen-Hua Ch, Lipika D. *Real-time motion planning methods for autonomous on-road driving: State-of-the-art and future research directions*, Transportation Research Part C: Emerging Technologies. 2005, Vol. 60.
- [9] Khalaji Ali Keymasi. *PID-based target tracking control of a car-trailer mobile robot* 14, Research Article 2019 <https://doi.org/10.1177/0954406219830438>

- [10] Korzeniowski D, Ślaski G. *Method of Planning Reference Trajectory of a Single Change Maneuver with Bezier curve*, IOP Conference Series: Materials Science and Engineering, 2016, Vol. 148. Paper No 012012.
- [11] Moshchuk Nikolai, Chen Shih-Ken, Zagorski Chad, Chatterjee Amy. *Path planning for collision avoidance maneuver*, Proceedings of the ASME 2013 International Mechanical Engineering Congress and Exposition, IMECE2013, November 2013, San Diego, USA.
- [12] Mercorelli P. *Fuzzy based control of a nonholonomic car-like robot for drive assistant systems*, 19th International Carpathian Control Conference, May 2018, Hungary – ieeexplore.ieee.org.
- [13] PC-Crash. *A simulation program for vehicle accidents. Manual Version 10.1*, Dr Steffan Datentechnik, Linz 2014.
- [14] Prochowski L, Pusty T, Gidlewski M, Jemioł L. *Experimental studies of the car-trailer system when passing by a suddenly appearing obstacle in the aspect of active safety of autonomous vehicles*, IOP Conference Series: Materials Science and Engineering, 421(3); Krakow, Poland, <https://doi.org/10.1088/1757-899X/421/3/032024>; Conference Date: SEP 2018.
- [15] *Road traffic accidents in Poland in 2018*, Polish Police Headquarters, Road Traffic Office, Warszawa 2019.
- [16] Yue Ming, Hou Xiaoqiang, Gao Renjing, Chen Jun, *Trajectory tracking control for tractor-trailer vehicles: a coordinated control approach*, Nonlinear Dynamics (2018) 91: 1061-1074 <https://doi.org/10.1007/s11071-017-3928-9>.

Leon Prochowski, Prof.: Military University of Technology (WAT), ul. gen. Sylwestra Kaliskiego 2, 01-476 Warszawa; ŁUKASIEWICZ Research Network – Automotive Industry Institute (ŁUKASIEWICZ – PIMOT), ul. Jagiellońska 55, 03-301 Warszawa, Poland (leon.prochowski@wat.edu.pl).

Mateusz Ziubiński, MSc. Eng.: Military University of Technology (WAT), ul. gen. Sylwestra Kaliskiego 2, 01-476 Warszawa, Poland (mateusz.ziubinski@wat.edu.pl).

Patryk Szwajkowski, MSc. Eng.: ŁUKASIEWICZ Research Network – Automotive Industry Institute (ŁUKASIEWICZ – PIMOT), ul. Jagiellońska 55, 03-301 Warszawa, Poland (p.szwajkowski@pimot.eu).

Tomasz Pusty, PhD. Eng.: ŁUKASIEWICZ Research Network – Automotive Industry Institute (ŁUKASIEWICZ – PIMOT), ul. Jagiellońska 55, 03-301 Warszawa, Poland (t.pusty@pimot.eu).

Mirosław Gidlewski, PhD. Eng.: ŁUKASIEWICZ Research Network – Automotive Industry Institute (ŁUKASIEWICZ – PIMOT), ul. Jagiellońska 55, 03-301 Warszawa, Poland (m.gidlewski@pimot.eu).

Study of the Duffing van der Pol system dynamics using *RQA* measures

Andrzej Rysak, Magdalena Gregorczyk

Abstract: This work presents a detailed study of the Duffing van der Pol system dynamics in different ranges of the driving force frequency. Bifurcation diagrams reveal the evolution of the system dynamics, from periodic and quasi-periodic to chaotic regimes. The specific dynamic states of the system are then distinguished by Lyapunov exponents and phase diagrams. In the current research, these methods are used as a reference to assess the system variability through the use of recurrence analysis. The application of recurrence analysis provides new variables confirming the changes observed in the system dynamics. It is shown that recurrence analysis can clearly distinguish between dynamic states singled out by Lyapunov exponents. In addition, the recurrence measures indicate some modifications in the system dynamics, which are not detectable by other well-established methods. In particular, interesting changes in system recurrences in periodic and quasi-periodic areas are analyzed in detail.

1. Introduction

The non-linear Duffing van der Pol (*DvP*) system [2, 6] is of great importance both in theoretical and practical studies due to its two coexisting dynamic properties: double-well potential and non-linear damping. Studies aimed at better understanding, control and detection of systems defined by the *DvP* equations usually make use of well-established analytical and numerical methods that yield easy-to-interpret results. Recurrence analysis is a method that achieves significant results in the study of dynamic systems; in spite of this fact, its interpretation basis is still being developed. The recurrence plot (*RP*) method as a tool for testing nonlinear systems was first proposed by Eckmann [3], and further developed by Webber and Zbilut [7], Casdagli [1], Marwan et al. [4] and others. From the very beginning, the study of transient dynamics in nonlinear systems was one of the important directions for the method's application [5]. In the present work, we aim to show the great inherent potential of this method by examining the *DvP* system and comparing the *RQA* results with those obtained by well-established numerical tools. Bifurcation diagrams and Lyapunov exponents were chosen as the reference methods. The numerical results show that the *RQA* measures change surprisingly clearly in the areas where the reference methods indicate unchanging dynamic characteristics.

2. Duffing van der Pol system

The *DvP* system was developed as a result of combining two nonlinear systems: the Duffing system with non-linear potential, and the van der Pol system characterized by non-linear damping. The DvP system with external excitation is determined by the following general non-linear equation:

$$\ddot{x} = -(\alpha + \beta x^2)\dot{x} + \gamma x - \delta x^3 + f \cos(\omega t), \quad (1)$$

where the coefficients α, β, γ and δ are real. Choosing $\beta = 0, \alpha > 0$ transforms this equation to the damped Duffing system with external excitation [2]

$$\ddot{x} = -\alpha \dot{x} + \gamma x - \delta x^3 + f \cos(\omega t), \quad (2)$$

whereas taking $\delta = 0$ leads to the van der Pol externally excited system [6]

$$\ddot{x} = -(\alpha + \beta x^2)\dot{x} + \gamma x + f \cos(\omega t), \quad (3)$$

In this work the Duffing - van der Pol equation is adopted in a form with reduced number of parameters:

$$\ddot{x} = \mu(1 - x^2)\dot{x} + ax - bx^3 + f \cos(\omega t) \quad (4)$$

and with constant coefficients: $\mu = 0.1, a = 0.5, b = 0.5$, and $f = 0.17$.

3. Numerical analysis

3.1. Simulation, bifurcation and Lyapunov exponents

This work analyzes the changes in the system dynamics caused by changes in the angular frequency ω of the excitation force. The main result under analysis was obtained by performing 960 simulations for the ω parameter, changing it from 0.475 to 0.535 with the step $\Delta\omega = 6.25 \cdot 10^{-5}$. The period T of the excitation force varies with the angular frequency, but the number of simulation steps per period nT is maintained constant at 24,000. Due to the high point density, it was checked that the simple Euler method is sufficient to integrate differential equations derived from (4). For every omega value, the settle time needed to fully develop the system dynamics $T_s = ST \cdot T$, where $ST = 3000$. The solutions collected in subsequent $NS = 300$ periods were used to determine Poincaré points and Lyapunov exponents. The bifurcation digram and results of Lyapunov exponents obtained for the full range of changes in the bifurcation parameter ω are compared in Fig. 1. The Lyapunov exponents clearly distinguish four main areas with different dynamics: *A* ($0.4750 < \omega < 0.4935$) with

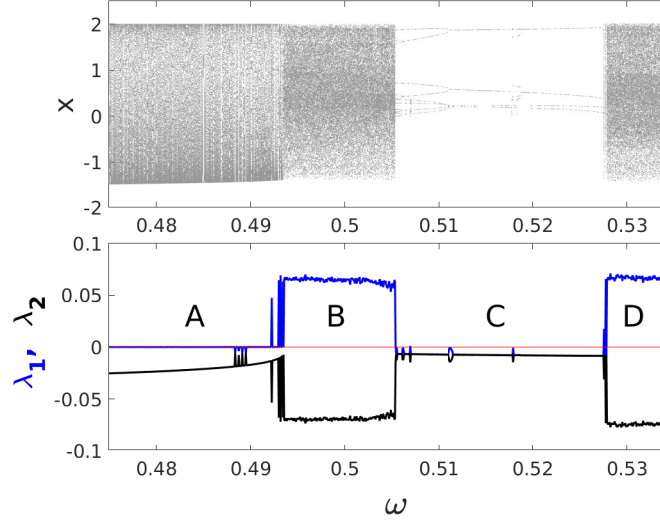


Figure 1. The Lyapunov exponents (λ_1, λ_2) are compared with the bifurcation diagram. The letters indicate four areas with different dynamics: quasi-periodic (A) , chaotic (B), periodic (C), and chaotic (D).

quasi-periodic variability, *B* for $(0.4935 < \omega < 0.5054)$ where the system is chaotic, *C* for $(0.5054 < \omega < 0.5278)$ -periodic and *D* for $(0.5278 < \omega < 0.5343)$ where the system returns to chaos. Phase diagrams for the results selected from these four ranges are shown in Fig. 2. With the change of ω , the trajectories of phase diagrams are continuously modified in individual ranges (A,B,C,D) which is not demonstrated either in the variability of the Lyapunov exponents or in the bifurcation diagrams.

3.2. Recurrence analysis

A *RP* is a graphic representation of the system's returns to its previous states. It is constructed by plotting the distance matrix $R_{i,j}^\varepsilon$ which determines the neighbors for each element of the vector time series \mathbf{v}_i . The recurrence matrix is defined as

$$R_{ij}^\varepsilon = \Theta(\varepsilon - \|\mathbf{v}_i - \mathbf{v}_j\|), \quad (5)$$

where ε is the threshold parameter. An example *RP* for a harmonically excited, chaotically vibrating non-linear system (Duffing), is shown in Fig. 3. The *RP* method does not require the use of many points. Therefore, prior the recurrence analysis, the number of points in the analyzed time series is reduced to 200 points per period ($ppT = 200$). The recurrence variables are determined on the basis of the recurrence plots built for a vectorial time series

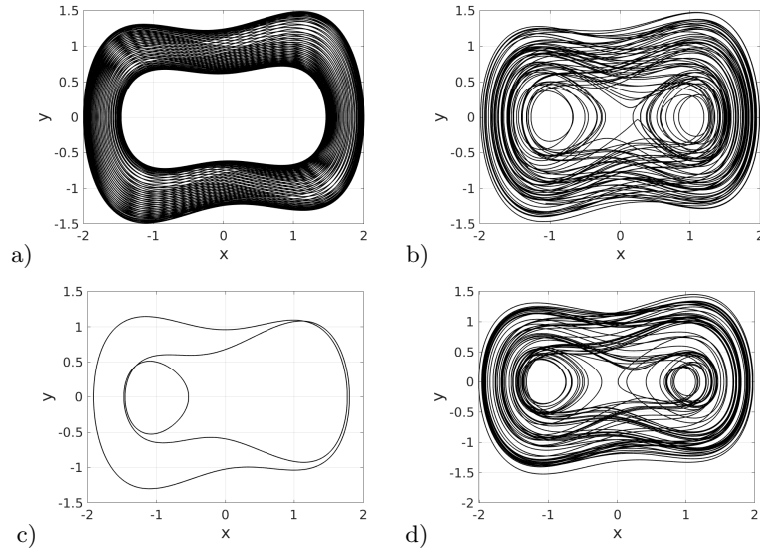


Figure 2. Phase diagrams for selected results obtained in individual ranges. a) quasi-periodicity, $\omega = 0.483$ (A); b) chaos, $\omega = 0.5$ (B); c) periodicity, $\omega = 0.5175$ (C); d) chaos $\omega = 0.535$ (D)

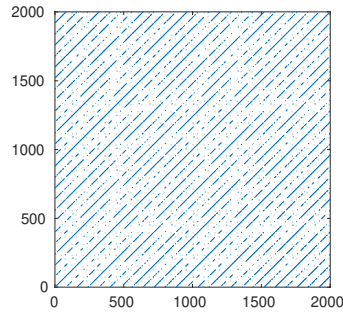


Figure 3. Sample *RP* of the Duffing system in chaotic mode

of 50 periods duration. This gives 10,000 points in the analyzed time series and 10^8 points in the *RP*. The four variables of recurrence quantification analysis (RQA): *RR* (recurrence rate), $\langle D \rangle$ (average length of diagonal lines), *LEnt* (laminar entropy), and *VEnt* (entropy of vertical lines) are chosen for studying the *DvP* system due to the fact that they show clear and interesting changes in the analyzed regions: A, B, C and D. These variables are defined

in the following way:

$$\begin{aligned}
RR(\epsilon, N) &= \frac{1}{N^2 - N} \sum_{\substack{i=j=1 \\ i \neq j}}^N R_{i,j}^\epsilon, & \langle D \rangle &= \frac{\sum_{l=2}^{N-1} l H_D(l)}{\sum_{l=2}^{N-1} H_D(l)}, \\
LEnt &= - \sum_{l=2}^{N-1} p_L(l) \log(p_L(l)), & p_L(l) &= \frac{H_D(l)}{\sum_{l=2}^{N-1} H_D(l)}, \\
VEnt &= - \sum_{v=2}^N p_V(v) \log(p_V(v)), & p_V(v) &= \frac{H_V(v)}{\sum_{v=2}^N H_V(v)}
\end{aligned} \tag{6}$$

where N is the number of points in time-series, l is the length of diagonal lines and v is the length of vertical lines. All measures are defined based on geometric statistics of the arrangement of colored points. $H_D(l)$, $H_V(v)$ are the histograms of diagonal and vertical lines, respectively. RR is the density of colored points in the RP . The meaning of other variables is described by their names. The entropy of diagonal and vertical lines are calculated according to the Shannon formula.

4. RQA variables vs. Lyapunov exponents and bifurcation diagrams

A comparison of the results obtained for the RQA variables with the Lyapunov exponents and bifurcation diagrams is presented in Fig. 4. Individual plots show the results of selected

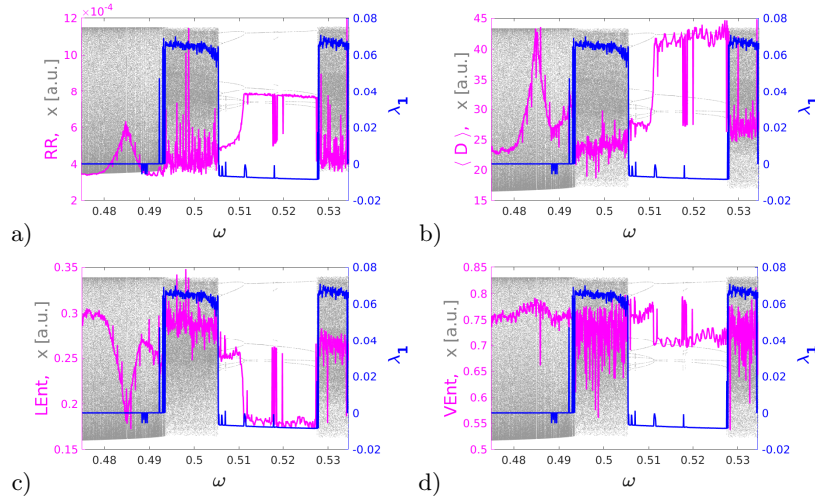


Figure 4. Plots comparing the results of RQA measures (magenta) with bifurcation diagrams (gray) and Lyapunov exponents (blue). a) $RR(\omega)$, b) $\langle D \rangle(\omega)$, c) $LEnt(\omega)$, d) $VEnt(\omega)$

RQA (magenta line) variables against the background of the bifurcation diagram (gray points) and the largest Lyapunov exponent (blue line).

5. Discussion

An analysis of the results reveals unique properties of the *RQA* variables enabling the detection of subtle changes in the dynamics of the system under study. Starting from the quasi-periodic area A, it can be observed that the Lyapunov exponents change only slightly with the ω parameter. In contrast, some *RQA* measures clearly change over a wide range of the A area. In addition, the sharp *RQA* peaks indicate in this area repeated changes in the system dynamics occurring in narrow ranges of the ω parameter (Fig. 5a). The *B* and

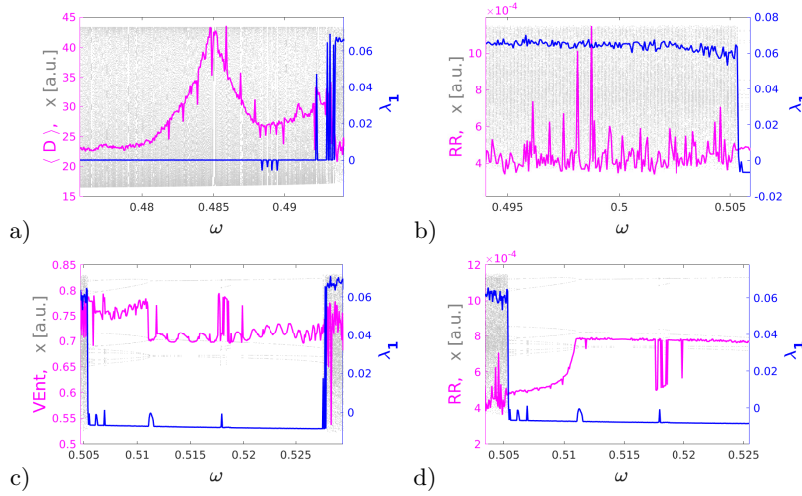


Figure 5. Selected exceptional results given by the *RQA* variables

D chaotic areas highlighted by the Lyapunov exponents are not clearly distinguished by the selected recurrence variables. They detect - as typical of chaos - rapid changes in dynamics that occur when the circular frequency of the excitation force changes. However, particularly pronounced peaks of the *RR* variable are visible in the *B* region (Fig. 5b). In the periodic area *C*, the bifurcation diagram shows two subareas with a basic period of $4T$ and $2T$, and with a bifurcation point for $\omega = 0.5112$. The *RQA* measures detect this point and distinguish both sub-areas. Some of them show specific variability along with the forcing frequency that occurs in the periodic region and leads to the transition $4T \rightarrow 2T$ (Fig. 5a). Changes in the Lyapunov exponents in this area are limited to a few small peaks. One of them indicates a bifurcation point. The narrow omega area ($0.5176 < \omega < 0.5199$) visible in the bifurcation diagram, in which the periodic solution switches between two orbits, is well identified by the *RQA* variables. Again, these changes are not visible in the Lyapunov exponents. In the periodic area *C*, the *LEnt* measure shows an intriguing value modulation reflecting slight modifications of the periodic orbit (Figs. 5c). Analyzing the results of *RQA* and Lyapunov

exponents in the area of transition of the system dynamics from the quasi-periodic area to chaos, one can notice a coincidence between both methods. Figure 6 shows this using the example of the $\langle D \rangle$ variable and the largest Lyapunov exponent λ_1 . As it can be seen in the

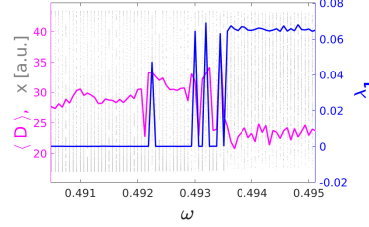


Figure 6. Coincidence between the Lyapunov exponents and the $\langle D \rangle$ measure near the boundary between quasi-periodicity (A) and chaos (B)

figure, the sharp peaks of the λ_1 exponent find their counterparts in the $\langle D \rangle$ measure. To distinguish the possibilities of the *RQA* method out, Fig. 7a presents the result obtained in the 3D *RQA* subspace selected from the multidimensional space of recurrence measures. The letters denote individual areas of the dynamics of the system dynamics that are clearly

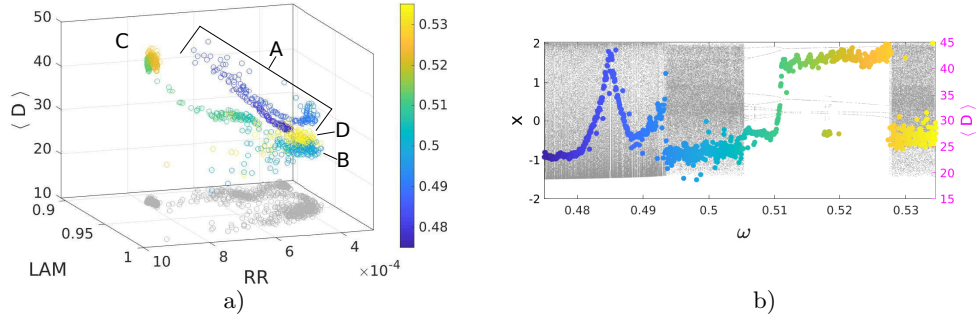


Figure 7. RQA variables in one of the possible 3D *RQA* subspaces

distinguished in this figure. The colors of the points in the *RQA* subspace are determined by the ω values in accordance with Fig. 7b.

6. Conclusions

The most important results obtained in the study of the *DvP* system can be summarized as follows. The bifurcation diagram indicated the presence of four areas with different dynamics. The Lyapunov exponents identified them as: quasi-periodicity (A), chaos (B), periodicity (C), and chaos (D). In these specified areas of dynamics, the *RQA* measures show

variability, while the observed changes in the Lyapunov exponents are relatively small. The *RQA* variables provide a particularly valuable information about the areas A and C. The dynamics of the *DvP* system did not change in these areas, but the changes in the frequency of excitation led to the modification of the trajectories in the phase space. Similar effects were not detected by the reference methods, which means that the recurrence analysis is particularly useful for studying and controlling nonlinear dynamic systems that vibrate in both stationary and transient modes.

Acknowledgments

The research was financed in the framework of the project Lublin University of Technology-Regional Excellence Initiative, funded by the Polish Ministry of Science and Higher Education (contract no. 030/RID/2018/19).

References

- [1] CASDAGLI, M. Recurrence plots revisited. *Phys. D*, 108 (1997), 12–44.
- [2] DUFFING, E. *Erzwungene Schwingungen bei Vernderlicher Eigenfrequenz*. F. Vieweg u. Sohn, Braunschweig, 1918.
- [3] ECKMANN, J. P., KAMPHORST, S. O., AND RUELLE, D. Recurrence plots of dynamical systems. *Europhys. Lett.* 4, 9 (1987), 973–977.
- [4] MARWAN, N., ROMARIO, M. C., THIEL, M., AND KURTHS, J. Recurrence plots for the analysis of complex systems. *Phys. Rep.*, 438 (1997), 237–329.
- [5] TRULLA, L., GIULIANI, A., ZBILUT, J., AND C.I. WEBBER, J. Recurrence quantification analysis of the logistic equation with transients. *Phys. Lett. A* 223 (1996), 225–260.
- [6] VAN DER POL, B., AND VAN DER MARK, J. Frequency demultiplication. *Nature*, 127 (1927), 363–364.
- [7] WEBBER, JR., C. L., AND ZBILUT, J. Dynamical assessment of physiological systems and states using recurrence plot strategies. *J. Appl. Physiology*, 76 (1994), 965–973.

Rysak Andrzej, Ph.D.: Lublin University of Technology, Faculty of Mechanical Engineering, Nadbystrzycka 36, 20-618 Lublin, Poland (*a.rysak@pollub.pl*).

Gregorczyk Magdalena, M.Sc.: Lublin University of Technology, Faculty of Mechanical Engineering, Nadbystrzycka 36, 20-618 Lublin, Poland (*m.gregorczyk@pollub.pl*). The author gave a presentation of this paper during one of the conference sessions.

Control of tremors of human's arm by a passive nonlinear absorber

Alireza Ture Savadkoohi, Claude-Henri Lamarque, Célien Goossaert

Abstract: The aim of this work is to develop a mechanical nonlinear absorber for cancellation of tremors of human's arm due to diseases such as Parkinson. Governing equations of the upper limb representing by a two-degrees-of-freedom pendulum are coupled to the equation of a nonlinear absorber. A time multiple scale method is exploited for detection of the responses of the system at different time scales, i.e. fast and slow scales. After revealing fast dynamics of the system, the characteristic points of the system are tracked. These points should correspond to comfortable amplitude variations of the arm. The analysis of the dynamics of the system provides tools for tuning parameters of the absorber.

1. Introduction

Since the last century, passive control of mechanical and structural systems is mainly carried out by linear absorbers, namely tuned mass dampers (TMD) [2]. These devices operate very well around the tuned linear frequency. However, they lose their efficiency if the targeted frequency of the main systems changes due to damage and nonlinearities of the system. It is shown that by using nonlinear properties of attachments, it is possible to increase the suppression band and so to increase the efficiency of the passive control process [9]. Since then, a lot of nonlinear passive controller devices are developed [6] from which we can mention the nonlinear energy sink (NES) [12] which is a pure nonlinear oscillator causing a one way vibratory energy channelling between main systems and the NES [3, 11]. Some of applications of such systems are structures [10, 13], acoustics [1], and aerospace [4]. For controlling the tremor at rest of human arm, there are some works which use the TMD [5]. The idea of this work is to use a nonlinear solution in general and the NES in detail for passive control of tremors of the arm. The paper is structured as it follows: The mathematical model of the system and its linearised form about an arbitrary postural position are provided in Sect. 2. Governing equations of the same model coupled to a nonlinear absorber is presented in Sect. 3 while its analytical treatments are shown in Sect. 4. An example of passive control of such a system which diverges mathematically is provided in Sect. 5. Finally, the paper is concluded in 6.

2. The mathematical model of the system without absorber: linearisation about a postural position

The mathematical model of locomotion of human's upper limb has been developed by Jackson et al. [7]. If we define the generated angles in arm and forearm as θ and ϕ , then following equations can be obtained [7]:

$$\begin{cases} \rho_{11}\ddot{\theta} + \rho_{12}\ddot{\phi} + \rho_{13} - T_I + V_I = H' \\ \rho_{21}\ddot{\theta} + \rho_{22}\ddot{\phi} + \rho_{23} - T_{II} + V_{II} = J' \end{cases} \quad (1)$$

where ρ_{sp} , $s = 1, 2$ and $p = 1, 2, 3$ are defined as:

$$\begin{cases} \rho_{11} = I + m_2(l_1^2 + l_2^2 + 2l_1l_2\cos(\phi)), \rho_{12} = m_2(l_2^2 + l_1l_2\cos(\phi)) \\ \rho_{13} = -m_2l_1l_2(2\dot{\theta} + \dot{\phi})\dot{\phi}\sin(\phi), \rho_{21} = m_2(l_2^2 + l_1l_2\cos(\phi)) \\ \rho_{22} = m_2l_2^2, \rho_{23} = -m_2l_1l_2\dot{\theta}\dot{\phi}\sin(\phi) \end{cases} \quad (2)$$

m_1 and l_1 are mass and length of the arm; m_2 and l_2 are equivalent mass and length of the forearm and hand and I is the moment of inertia of the upper arm with respect to the glenohumeral joint. H' and J' are applied torques about glenohumeral and elbow joints, respectively. If we linearise these equations about a postural positions as θ_0 and ϕ_0 , as $\theta_S = \theta - \theta_0$ and $\phi_S = \phi - \phi_0$ following system is obtained:

$$M \begin{pmatrix} \ddot{\theta}_S \\ \ddot{\phi}_S \end{pmatrix} + K \begin{pmatrix} \theta_S \\ \phi_S \end{pmatrix} = \begin{pmatrix} f_1 \sin(\omega t) \\ f_2 \sin(\omega t) \end{pmatrix} \quad (3)$$

Natural frequencies of the linear system of Eq. 3 can be traced as functions of postural positions which are depicted in Figs. 5 and 2. These figures show that the system frequencies change as functions of initial postural positions which means that the classical linear absorbers, i.e. different families of TMD, can not be efficient for passive control of the tremor. In the next section the original governing equations of human's upper limb are coupled to a NES and some preliminary results are presented.

3. The mathematical model of the system with coupled nonlinear absorber

Let us consider Fig. 3: a NES with the mass m_N , generalized displacement as u and with the distance of l_3 from the joint of forearm is coupled to the overall system. Equations of such system read:

$$\begin{cases} \rho_{11}\ddot{\theta} + \rho_{12}\ddot{\phi} + \rho_{13}\ddot{u} + \rho_{14} - T_1 + V_1 = H' \\ \rho_{21}\ddot{\theta} + \rho_{22}\ddot{\phi} + \rho_{23}\ddot{u} + \rho_{24} - T_2 + V_2 = J' \\ \rho_{31}\ddot{\theta} + \rho_{32}\ddot{\phi} + \rho_{33}\ddot{u} + \rho_{34} - T_3 + V_3 + c_N\dot{u} = 0 \end{cases} \quad (4)$$

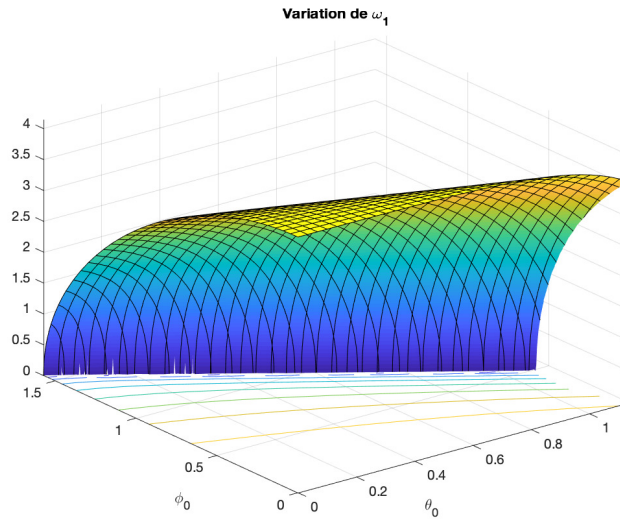


Figure 1. Variation of the first natural frequency of the system as function of initial posture (θ_0, ϕ_0) .

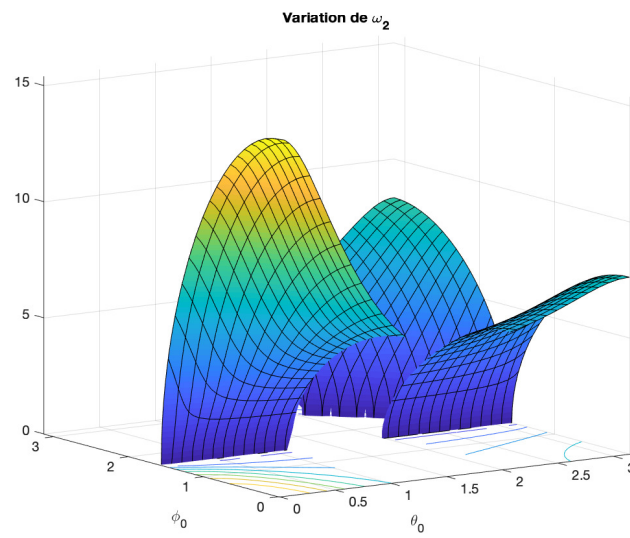


Figure 2. Variation of the second natural frequency of the system as function of initial posture (θ_0, ϕ_0) .

where ρ_{sp} , $s = 1, \dots, 3$, $p = 1, \dots, 4$ are functions of θ , ϕ , u and systems parameters. We can linearize the angles around a postural positions and after introducing a dimensionless small parameter $\epsilon = \frac{m_N}{m_2} \ll 1$, following compact form of system equations is obtained:

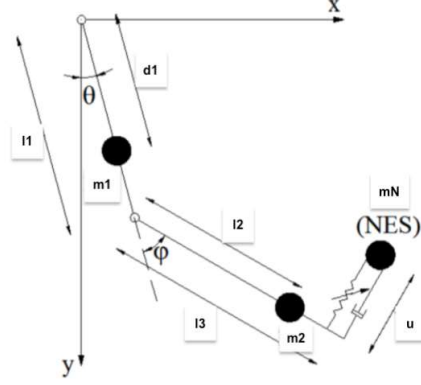


Figure 3. The human's upper limb model coupled to a NES

$$M' \begin{pmatrix} \ddot{\theta}_S \\ \ddot{\phi}_S \\ \ddot{u} \end{pmatrix} + K' \begin{pmatrix} \theta_S \\ \phi_S \\ u \end{pmatrix} + N' + A' + C' = \begin{pmatrix} F_1 \sin(\Omega t) \\ F_2 \sin(\Omega t) \\ 0 \end{pmatrix} \quad (5)$$

Moreover, we suppose that $p = \lfloor \frac{\omega_2(\theta_0, \phi_0)}{\omega_1(\theta_0, \phi_0)} \rfloor$, $p \in \mathbb{N}^*$, where $\lfloor \dots \rfloor$ stands for nearest integer function. We set:

$$\omega_1 = \Omega + \sigma_1 \epsilon, \quad \omega_2 = p\omega_1 + \widetilde{\sigma}_2 \epsilon = p\Omega + \sigma_2 \epsilon \quad (6)$$

Let us apply following change of variables in modal coordinates:

$$\begin{pmatrix} \theta_S \\ \phi_S \\ u \end{pmatrix} = P \begin{pmatrix} W_1 \\ W_2 \\ W_3 \end{pmatrix}, \text{ with } P = \begin{pmatrix} V_{11} & V_{12} & 0 \\ V_{21} & V_{22} & 0 \\ 0 & 0 & 1 \end{pmatrix} \quad (7)$$

where P is a matrix of eigenvectors of $M'^{-1}K'$. After introducing a damping matrix in the system, following set of equations can be obtained:

$$\begin{pmatrix} \ddot{W}_1 \\ \ddot{W}_2 \\ \ddot{W}_3 \end{pmatrix} + (D + \epsilon \Lambda) \begin{pmatrix} W_1 \\ W_2 \\ W_3 \end{pmatrix} + \epsilon C_D \begin{pmatrix} \dot{W}_1 \\ \dot{W}_2 \\ \dot{W}_3 \end{pmatrix} + \dot{W}_3(T + \epsilon U) + n_0(W_3)(X + \epsilon Y) + (A + \epsilon B) = \epsilon H \quad (8)$$

Where T, U, X, Y, A, B and H are vector while C_D is the diagonalised damping matrix.

4. Complexification of the system and its fast/slow dynamics

Let us introduce extended version of complex variables of Manevitch [8]:

$$\begin{cases} ib_1 + \Psi_1 \exp(i\Omega t) = \dot{W}_1 + i\Omega W_1 \\ ib_2 + \Psi_2 \exp(ip\Omega t) = \dot{W}_2 + ip\Omega W_2 \\ ib_3 + \Psi_3 \exp(i\Omega t) = \dot{W}_3 + i\Omega W_3 \end{cases} \quad (9)$$

We would like to keep just first harmonics of the system. This leads to:

$$\begin{pmatrix} \dot{\Psi}_1 + \frac{i(\omega_1 - \sigma_1 \epsilon)}{2} \Psi_1 \\ \dot{\Psi}_2 + \frac{i(\omega_2 - \sigma_2 \epsilon)}{2} \Psi_2 \\ \dot{\Psi}_3 + \frac{i(\omega_1 - \sigma_1 \epsilon)}{2} \Psi_3 \end{pmatrix} + (D + \epsilon \Lambda) \begin{pmatrix} -\frac{i}{2(\omega_1 - \sigma_1 \epsilon)} \Psi_1 \\ -\frac{i}{2(\omega_2 - \sigma_2 \epsilon)} \Psi_2 \\ -\frac{i}{2(\omega_1 - \sigma_1 \epsilon)} \Psi_3 \end{pmatrix} + \epsilon C_D \begin{pmatrix} \dot{\Psi}_1 \\ \dot{\Psi}_2 \\ \dot{\Psi}_3 \end{pmatrix} + \frac{\Psi_3}{2} (T + \epsilon U) + f_n(X + \epsilon Y) = \epsilon \mathbb{H} \quad (10)$$

Performing a time multiple scale leads to detection of Slow Invariant Manifold (SIM) at fast time scale and all characteristic points of the system at slow time scale. If we set $\Psi_j = N_j e^{i\delta_j}$, $j = 1, 2, 3$, then the SIM becomes a function of N_j and also $\delta = \delta_1 - \delta_2$. Some views of the SIM for some values of δ and some system parameters are illustrated in Fig. 4 and 5.

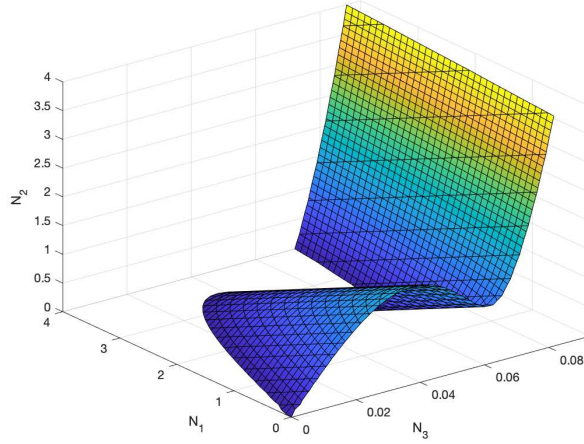


Figure 4. The SIM of the system for $\delta = 0$

5. An example for passive control

In this section, numerical results on the presented the model of the Sect. 2, i.e. the system without a coupled NES, are presented via creation of an exact resonance with the external

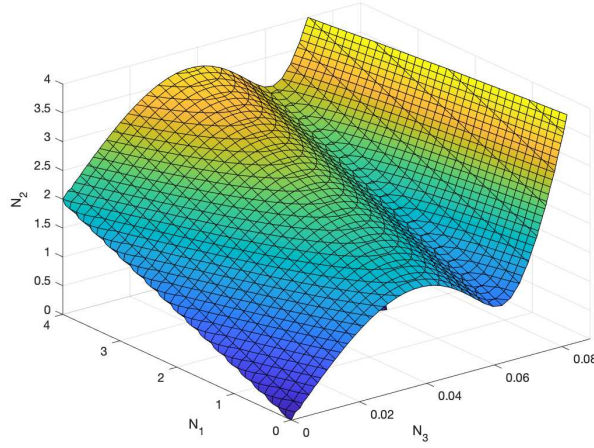


Figure 5. The SIM of the system for $\delta = \pi$

excitations. The same system is coupled to a NES. Figures 6 and 6 show that the coupling of the NES controls the diverging behaviours of the undaunted systems during the exact resonance.

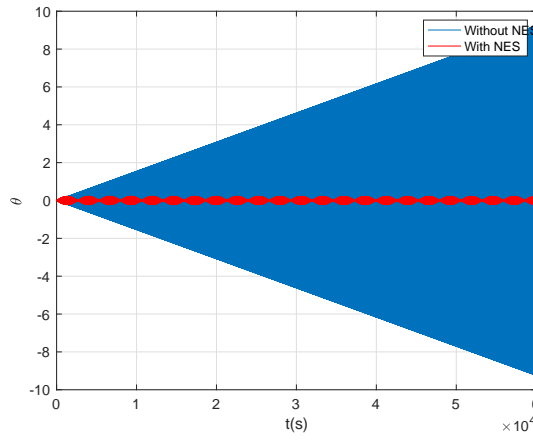


Figure 6. Time history of θ for the system without and with coupled NES.

6. Conclusions

The passive control of the tremor of human's arm by a nonlinear energy sink is presented. The linearisation of governing equations of the system about an arbitrary postural position

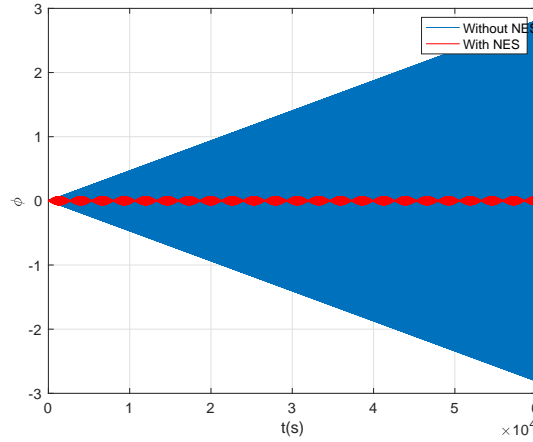


Figure 7. Time history of ϕ for the system without and with coupled NES.

revealed that the natural frequencies of the system change according to initial postural position. This means that using linear absorbers which are efficient at a tuned frequency will not be sufficient for tremor control. A nonlinear energy sink is coupled to the system and detection of fast/slow dynamics leads to tracing slow invariant manifold and characteristics points. An example of passive control for mathematically initially diverging system is presented showing that the nonlinear absorber can control the vibration of the main system in a considerable level.

References

- [1] BELLET, R., COCHELIN, B., HERZOG, P., AND MATTEI, P. Experimental study of targeted energy transfer from an acoustic system to a nonlinear membrane absorber. *Journal of Sound and Vibration* 329 (2010), 2768–2791.
- [2] FRAHM, H. Device for damping vibrations of bodies, Apr. 18 1911. US Patent 989,958.
- [3] GENDELMAN, O., MANEVITCH, L., VAKAKIS, A., AND M'CLOSKEY, R. Energy pumping in nonlinear mechanical oscillators: Part I-dynamics of the underlying hamiltonian systems. *Journal of Applied Mechanics-transactions of The Asme* 68 (01 2001), 34–41.
- [4] GENDELMAN, O. V., VAKAKIS, A. F., BERGMAN, L. A., AND MCFARLAND, D. M. Asymptotic analysis of passive nonlinear suppression of aeroelastic instabilities of a rigid wing in subsonic flow. *SIAM Journal on Applied Mathematics* 70 (2010), 1655–1677.
- [5] HASHEMI, S. M., GOLNARAGHI, M. F., AND PATLA, A. E. Tuned vibration absorber for suppression of rest tremor in parkinson's disease. *Medical and Biological Engineering and Computing* 42, 1 (2004), 61–70.

- [6] HOUSNER, G. W., BERGMAN, L. A., CAUGHEY, T. K., CHASSIAKOS, A. G., CLAUS, R. O., MASRI, S. F., SKELTON, R. E., SOONG, T. T., SPENCER, B. F., AND YAO, J. T. P. Structural control: past, present and future. *Journal of Engineering Mechanics* 123 (1997), 897–971.
- [7] JACKSON, K., JOSEPH, J. T., AND WYARD, S. A mathematical model of arm swing during human locomotion. *Journal of biomechanics* 11, 6-7 (1978), 277–289.
- [8] MANEVITCH, L. I. The description of localized normal modes in a chain of nonlinear coupled oscillators using complex variables. *Nonlinear Dynamics* 25 (2001), 95–109.
- [9] ROBERSON, R. E. Synthesis of a nonlinear dynamic vibration absorber. *Journal of Franklin Institute* 254 (1952), 205–220.
- [10] TURE SAVADKOOHI, A., VAURIGAUD, B., LAMARQUE, C.-H., AND PERNOT, S. Targeted energy transfer with parallel nonlinear energy sinks, part II: theory and experiments. *Nonlinear Dynamics* 67, 1 (2012), 37–46.
- [11] VAKAKIS, A., AND GENDELMAN, O. Energy pumping in nonlinear mechanical oscillators: Part II-resonance capture. *Journal of Applied Mechanics-transactions of The Asme* 68 (01 2001).
- [12] VAKAKIS, A., GENDELMAN, O., BERGMAN, L., MCFARLAND, D., KERSCHEN, G., AND LEE, Y. *Nonlinear Targeted Energy Transfer in Mechanical and Structural Systems, I & II*. Solid Mechanics and Its Applications. Springer Netherlands, 2008.
- [13] WEISS, M., VAURIGAUD, B., TURE SAVADKOOHI, A., AND LAMARQUE, C.-H. Control of vertical oscillations of a cable by a piecewise linear absorber. *Journal of Sound and Vibration* 435 (2018), 281 – 300.

Alireza Ture Savadkoohi, Ph.D.: Univ Lyon, ENTPE, LTDS UMR CNRS 5513, 3 rue Maurice Audin, 69518 Vaulx-en-Velin Cedex (alireza.turesavadkoohi@entpe.fr).

Claude-Henri Lamarque, Ph.D.: Univ Lyon, ENTPE, LTDS UMR CNRS 5513, 3 rue Maurice Audin, 69518 Vaulx-en-Velin Cedex (lamarque@entpe.fr). The author gave a presentation of this paper during one of the conference sessions.

Célien Goossaert, M.Sc.: Univ Lyon, ENTPE, LTDS UMR CNRS 5513, 3 rue Maurice Audin, 69518 Vaulx-en-Velin Cedex (celien.goossaert@entpe.fr).

Alternation of stability character in systems with positional non-conservative forces

Yury Selyutskiy

Abstract: The influence of non-conservative forces (both positional and velocity-dependent) upon stability of equilibrium positions of mechanical systems is discussed in many papers. In particular, it is well known that small dissipative forces can lead to instability. In the present work, the evolution of stability character of equilibrium is studied for the case when potential force corresponding to one generalized coordinate changes in presence of positional non-conservative forces. It is shown that, if parameters of the system satisfy certain conditions then the alternation of the stability character is observed (stability-instability-stability), as the stiffness in one of generalized coordinates increases. This effect is illustrated by the example of an aeroelastic system with two degrees of freedom.

1. Introduction

In the structure of equations of small oscillations of a mechanical system there are traditionally distinguished dissipative, gyroscopic, positional potential, and positional non-conservative (or circulatory) forces. A great number of works have been devoted to the study of various aspects of their influence on the stability of the trivial equilibrium (some results that have become classical are presented, in particular, in [3, 11]).

Currently, research in this area is actively ongoing. In particular, the problems of stability and stabilization of a general system in the case when the potential energy in equilibrium has a maximum are considered in [1]. In [12], the influence of the structure of matrices of the corresponding forces on the form of oscillations near the equilibrium position is analyzed.

One of the typical sources of instability is positional non-conservative forces (see, in particular, [9, 7]). On the other hand, it is known that these forces in certain situations are able to stabilize the equilibrium position, unstable in their absence.

Dissipative forces with full dissipation, as a rule, have a stabilizing effect on the system. Nevertheless, as the well-known Ziegler paradox shows, such forces can also lead to the loss of stability of the equilibrium. The effect of destabilization under the action of dissipative forces is discussed in detail, in particular, in [6]. It was shown in [4] that forces depending on velocities (dissipative and gyroscopic) can also have a destabilizing effect for systems with an infinite number of degrees of freedom.

The effect of small dissipative forces and dissipative forces with incomplete dissipation in systems with two degrees of freedom containing all types of forces is analyzed, e.g., in [5]. It is shown that such influence can be both stabilizing and destabilizing.

The presence of antidissipation in the system (i.e., negative eigenvalues of the matrix of dissipative forces) is also a source of instability (although, of course, stability is also possible in this situation).

In mechanical systems that describe technical objects, it is often difficult or impossible (due to technical reasons) to change parameters that determine the positional non-conservative forces. At the same time, parameters characterizing potential forces can often be changed relatively easily (for example, by changing the stiffness of structural elements). It seems interesting to describe the effect of such changes on the stability of the equilibrium in situations when the system contains positional non-conservative forces and / or dissipative forces without full dissipation.

Note that aerodynamic forces are a natural source of both positional non-conservative forces and dissipative forces with partial anti-dissipation. Accordingly, such an analysis can be useful, in particular, in the context of study of behavior of mechanical systems containing a rigid body moving in flow.

2. General considerations

Consider a mechanical system with two degrees of freedom. Denote the vector of generalized coordinates by $\mathbf{q} = (q_1 \ q_2)^T$. Assume that the system has a trivial equilibrium position. Then, as is well known, the equations of motion linearized near this equilibrium position can be written in the following structural form:

$$\mathbf{M}\ddot{\mathbf{q}} + \mathbf{B}\dot{\mathbf{q}} + \mathbf{C}\mathbf{q} = 0. \quad (1)$$

Here \mathbf{M} is the inertia matrix (positive definite), \mathbf{B} is the matrix of velocity-dependent forces, and \mathbf{C} is the matrix of positional forces.

Without the loss of generality, it is possible to assume that the equations are presented in dimensionless form.

We consider the influence of the change in stiffness in one of generalized coordinates (for definiteness, the first one) upon the stability.

To reduce the number of parameters and simplify the subsequent analysis, we perform a coordinate change such that a change in stiffness in the original partial system leads to a change in stiffness in only one of new generalized coordinates.

When stiffness in the first original generalized coordinate is added, Eq.(1) take the

following form:

$$\mathbf{M}\ddot{\mathbf{q}} + \mathbf{B}\dot{\mathbf{q}} + (\mathbf{C} + \tilde{\mathbf{K}}')\mathbf{q} = 0, \quad (2)$$

where

$$\tilde{\mathbf{K}}' = \begin{pmatrix} \tilde{\kappa} & 0 \\ 0 & 0 \end{pmatrix}.$$

Since the matrix \mathbf{M} is symmetric and positive definite, there exists a non-degenerate change of coordinates that reduces the matrix \mathbf{M} to identity and keep the matrix $\tilde{\mathbf{K}}'$ diagonal. The system obtained from (2) as a result of such transformation can be represented in the following form:

$$\ddot{\mathbf{x}} + (\mathbf{D} + \mathbf{G})\dot{\mathbf{x}} + (\mathbf{K} + \mathbf{K}' + \mathbf{N})\mathbf{x} = 0, \quad (3)$$

where $\mathbf{x} = (x_1 \ x_2)^T$ is the vector of new generalized coordinates, $\mathbf{D} = \mathbf{D}^T$ is the matrix of dissipative forces, $\mathbf{G} = \gamma\mathbf{Y}$ is the matrix of gyroscopic forces, $\mathbf{K} = \mathbf{K}^T$ is the matrix of conservative forces, $\mathbf{N} = \nu\mathbf{Y}$ is the matrix of positional non-conservative forces, and the matrices \mathbf{Y} and \mathbf{K}' have the following form:

$$\mathbf{Y} = \begin{pmatrix} 0 & 1 \\ -1 & 0 \end{pmatrix}, \quad \mathbf{K}' = \begin{pmatrix} \kappa & 0 \\ 0 & 0 \end{pmatrix}.$$

Thus, in the new coordinates, additional stiffness is also present only in one of the generalized coordinates.

We assume the coefficient κ non-negative.

The characteristic polynomial of our system looks as follows:

$$\lambda^4 + a_3\lambda^3 + (a_2 + \kappa)\lambda^2 + (a_1 + d_{22}\kappa)\lambda + a_0 + k_{22}\kappa, \quad (4)$$

where

$$\begin{aligned} a_3 &= d_{11} + d_{22}, & a_2 &= d_{11}d_{22} - d_{12}^2 + k_{11} + k_{22}, \\ a_1 &= d_{11}k_{22} + d_{22}k_{11} - 2k_{12}d_{12}, & a_0 &= k_{11}k_{22} - k_{12}^2 + \nu^2. \end{aligned}$$

As is well known, a sufficient condition for the asymptotic stability of the trivial equilibrium of a fourth order ODE system is the positivity of all coefficients of the characteristic polynomial and of the third principal minor of the Hurwitz matrix. In our case, these conditions are as follows:

$$\begin{aligned} a_0 + \kappa k_{22} &> 0, & a_1 + \kappa d_{22} &> 0, & a_2 + \kappa &> 0, & a_3 &> 0, \\ H_{3\kappa} &= (a_1 + \kappa b_1)(a_2 + \kappa)a_3 - a_3^2(a_0 + \kappa k_{22}) - (a_1 + \kappa d_{22})^2 > 0. \end{aligned} \quad (5)$$

Let us analyze how the introduction of additional stiffness into the first partial system will affect the fulfillment (or non-fulfillment) of these inequalities.

First, suppose that $d_{11}d_{22} < 0$, i.e. there is antidissipation in one of the generalized coordinates and dissipation in the other. In this situation, obviously, $H_{3\kappa} < 0$ if κ is large enough. Thus, even if in the original system the trivial equilibrium position is asymptotically stable, addition of a sufficiently large stiffness in one of the generalized coordinates will make it unstable. If this position in the original system is unstable, and the coefficient at κ in (5) is negative, then it is impossible to ensure stabilization by increasing stiffness in any generalized coordinate.

Interestingly, it doesn't matter if stiffness is added in the coordinate, for which damping takes place, or in the coordinate, for which anti-dissipation takes place.

Let us consider in more detail the case of $\kappa \gg 1$. Then the roots of the characteristic polynomial for a system with additional stiffness can be represented as follows:

$$\lambda_{1,2} = \pm i\sqrt{\kappa} - \frac{d_{11}}{2} + O(\kappa^{-1/2}), \quad \lambda_{3,4} = \frac{-d_{22} + \sqrt{d_{22}^2 - 4k_{22}}}{2} + o(1),$$

Note that $\lambda_{3,4}$ are the eigenvalues of the partial system corresponding to the second coordinate.

As should be expected, high-frequency oscillations are present in the system. If $d_{11} < 0$ and $d_{22} > 0$, then the amplitude of these oscillations, generally speaking, increases. If $d_{11} > 0$ and $d_{22} < 0$, then these oscillations are damped. However, the real part of at least one of $\lambda_{3,4}$ is positive. Thus, by increasing the stiffness in the partial system corresponding to the first coordinate, it is impossible to stabilize the second subsystem.

Now let $d_{11} > 0$ and $d_{22} > 0$, i.e. the oscillations of both partial systems are damped. Nevertheless, one of the eigenvalues of the matrix \mathbf{D} of system (3) can be negative (this means that the system does not have complete dissipation).

We first consider a situation where the trivial equilibrium of the original system is asymptotically stable, i.e. $a_i > 0$ ($i = 0 \dots 3$, see (4)) and $H_{30} > 0$.

If, in this case, expression for $H_{3\kappa}$ from (5), considered as a quadratic polynomial in κ , has no real roots or two real negative roots, then stability is preserved for any values of the additional stiffness. If both roots of this polynomial are positive, there is a range of values of κ , where the stability of the trivial equilibrium is lost.

In the general case, the expression for the discriminant of the mentioned quadratic trinomial is rather cumbersome. Therefore, we consider a special case.

Suppose that the system has a small parameter ε , and $H_{30} = \varepsilon \bar{H}_{30} > 0$. Then, under the condition

$$(d_{11} - d_{22})a_1 + (d_{22}k_{11} - d_{11}k_{22})a_3 + (d_{11}d_{22} - d_{12}^2 + \gamma^2)d_{22}a_3 < 0 \quad (6)$$

there is a range of values $0 < \kappa_1 < \kappa < \kappa_2$, where $H_{3\kappa} < 0$:

$$\begin{aligned}\kappa_1 &= -\frac{\varepsilon \bar{H}_{30}}{(d_{11} - d_{22}) a_1 + (d_{22} k_{11} - d_{11} k_{22}) a_3 + (d_{11} d_{22} - d_{12}^2 + \gamma^2) d_{22} a_3} + o(\varepsilon), \\ \kappa_2 &= -\frac{(d_{11} - d_{22}) a_1 + (d_{22} k_{11} - d_{11} k_{22}) a_3 + (d_{11} d_{22} - d_{12}^2 + \gamma^2) d_{22} a_3}{d_{11} d_{22}} + O(\varepsilon).\end{aligned}\quad (7)$$

Note that stability loss occurs already at small (of the order ε) values of added stiffness. Inequality (6) holds, in particular, if the following relations are satisfied:

$$d_{22} k_{11} / k_{22} < d_{11} < d_{22}, \quad \det(\mathbf{D} + \mathbf{G}) = d_{11} d_{22} - d_{12}^2 + \gamma^2 \leq 0.$$

Now suppose that the equilibrium position of the original system is unstable, and all the coefficients of the characteristic polynomial are positive, and $H_{30} < 0$. Then $H_{3\kappa}$, treated as a quadratic polynomial in κ , has one negative and one positive root. This means that a sufficiently large additional stiffness ensures stabilization of the equilibrium position.

3. Example: aeroelastic system with two translational degrees of freedom

As an example, consider an aeroelastic system consisting of bodies M_1 and M_2 connected with springs and able to move translationally along the axis OY (see Fig. 1). The body M_2 has a shape of rectangular cylinder.

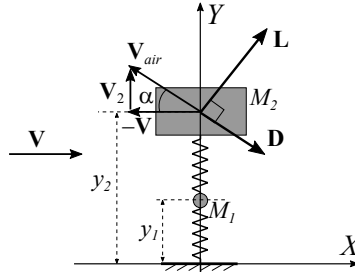


Figure 1. Aeroelastic system with two translational degrees of freedom.

This system is placed in the airflow; the air speed V is constant and perpendicular to the line of motion of bodies. We assume that the body M_2 interacts with the flow, while the aerodynamic load upon the body M_1 is negligible.

Systems of such kind (but containing only one body, i.e. with one degree of freedom) are widely studied. It is known that the so called galloping can arise in such systems, when the “natural” equilibrium becomes unstable if the flow speed gets large enough, and the bluff body starts oscillating. This effect is of great interest from the point of view of engineering,

on the one hand, because it can lead to the fatigue and break of structures, and on the other hand, because it can be used for power generation purposes.

Different aspects of the influence of various parameters on the galloping behavior was investigated numerically and experimentally, in particular, in [10, 8]. Questions of using this phenomenon for energy harvesting were discussed, in particular, in [2].

Here, we consider a modification of the conventional system, which comprises two bodies instead of one. Taking into account the above mentioned, the equations of motion can be written as follows:

$$\begin{aligned} m_1 \ddot{y}_1 + k_1 y_1 + h_1 \dot{y}_1 + k_2(y_1 - y_2) + h_2(\dot{y}_1 - \dot{y}_2) &= 0, \\ m_2 \ddot{y}_2 + k_2(y_2 - y_1) + h_2(\dot{y}_2 - \dot{y}_1) &= L \cos \alpha - D \sin \alpha = F_y. \end{aligned} \quad (8)$$

Here $y_{1,2}$ are deformations of springs; $k_{1,2}$ and $h_{1,2}$ are coefficients of stiffness and damping of springs; L , D are aerodynamic lift and drag forces acting upon the body M_2 , correspondingly. These forces can be represented in the following form:

$$\begin{aligned} L &= \frac{\rho S}{2} V_{air}^2 C_l(\alpha), \quad D = \frac{\rho S}{2} V_{air}^2 C_d(\alpha), \quad F_y = \frac{\rho S}{2} V_{air}^2 C_y(\alpha), \\ V_{air} &= \sqrt{V^2 + V_2^2} = \sqrt{V^2 + \dot{y}_2^2}, \quad \alpha = -\arctan \frac{\dot{y}_2}{V}, \end{aligned}$$

where ρ is the air density, S is the cross-section area of the body M_2 , V_{air} is the speed of this body with respect to the incoming flow, C_l , C_d , C_y are non-dimensional coefficients. We assume that they depend only upon the angle of attack α .

From symmetry considerations, it is clear that $C_y(0)=0$, and the system (8)) has the trivial equilibrium position: $y_1 = y_2 = 0$. However, it should be noted that for $k_1 = 0$ this equilibrium is not isolated.

Now we introduce characteristic length $L_c = b$ (width of the body M_2), characteristic time $T_c = b/V$, and characteristic mass $m_c = \mu \rho S b / 2$ (where μ is a non-dimensional coefficient characterizing the ratio of density of the body material to the air density). We then choose the units of measurement in such a way that these characteristic values would be equal to 1. This is equivalent to transition to non-dimensional variables.

Suppose, for simplicity sake, that $m_1 = m_2 = 1$. Then equations of motion linearized in the vicinity of the equilibrium position can be represented in the following form:

$$\mathbf{M} \ddot{\mathbf{y}} + \mathbf{D} \dot{\mathbf{y}} + \mathbf{K} \mathbf{y} = 0, \quad (9)$$

where

$$\mathbf{y} = \begin{pmatrix} y_1 \\ y_2 \end{pmatrix}, \quad \mathbf{M} = \begin{pmatrix} 1 & 0 \\ 0 & 1 \end{pmatrix}, \quad \mathbf{D} = \begin{pmatrix} h_1 + h_2 & -h_2 \\ -h_2 & h_2 + C_y^\alpha \end{pmatrix}, \quad \mathbf{K} = \begin{pmatrix} k_1 + k_2 & -k_2 \\ -k_2 & k_2 \end{pmatrix}.$$

Here $C_y^\alpha = \mu^{-1} dC_y(\alpha)/d\alpha|_{\alpha=0}$. From numerous experiments (e.g., [10]) it is known that $C_y^\alpha < 0$ for rectangular cylinders.

In this system, there are neither gyroscopic nor positional non-conservative (circulatory) forces. Besides, $\det \mathbf{K} = k_1 k_2 \geq 0$. Hence, if $\det \mathbf{D} > 0$ then the trivial equilibrium is asymptotically stable for any $k_{1,2} > 0$.

So, we consider the case when there is no full dissipation in the system, however, the damping in springs is large enough:

$$\det \mathbf{D} = h_1 h_2 + C_y^\alpha (h_1 + h_2) < 0, \quad C_y^\alpha + h_1 > 0, \quad C_y^\alpha + h_2 > 0. \quad (10)$$

The characteristic polynomial of (9) is as follows:

$$\begin{aligned} \lambda^4 + (C_y^\alpha + h_1 + 2h_2) \lambda^3 + (C_y^\alpha h_1 + C_y^\alpha h_2 + h_1 h_2 + 2k_2 + k_1) \lambda^2 \\ + ((C_y^\alpha + h_1)k_2 + (C_y^\alpha + h_2)k_1) \lambda + k_1 k_2. \end{aligned} \quad (11)$$

The third principal minor of the Hurwitz matrix is

$$\begin{aligned} H_3 = (h_1 + h_2)(C_y^\alpha + h_2)k_1^2 \\ + ((C_y^\alpha + h_1 + 2h_2)(C_y^\alpha (h_1 + h_2) + h_1 h_2)(C_y^\alpha + h_2) + 2h_2 k_2 (C_y^\alpha - h_1)) k_1 \\ + k_2 (C_y^\alpha + h_1)((C_y^\alpha (h_1 + h_2) + h_1 h_2 + 2k_2)(C_y^\alpha + h_1 + 2h_2) - k_2 (C_y^\alpha + h_1)) \end{aligned} \quad (12)$$

This is quadratic trinomial in k_1 . Note that, due to (10), the coefficient at k_1 in (12) is negative.

Obviously, if the stiffness of the second spring is small then the constant term in (12) is negative. This means that the trivial equilibrium is unstable for small k_1 . However, it becomes asymptotically stable for large enough k_1 .

Consider now the case when k_2 is large enough, so that $C_y^\alpha h_1 + C_y^\alpha h_2 + h_1 h_2 + 2k_2 > 0$. Then the constant term in (12) is positive. Suppose also that $C_y^\alpha + h_1 \ll 1$. This situation corresponds to one of the particular cases discussed above, and the equation $H_3 = 0$ has two positive roots κ_1 and κ_2 :

$$\begin{aligned} \kappa_1 &= \frac{k_2 (C_y^\alpha + h_1) (C_y^\alpha h_1 + 2k_2) (C_y^\alpha + h_1 + 2h_2)}{2h_2 ((C_y^\alpha (h_1 + h_2) + h_1 h_2) (C_y^\alpha + h_2) + k_2 (C_y^\alpha - h_1))} + o(C_y^\alpha + h_1), \\ \kappa_2 &= \frac{2h_2 ((C_y^\alpha (h_1 + h_2) + h_1 h_2) (C_y^\alpha + h_2) + k_2 (C_y^\alpha - h_1))}{(h_1 + h_2)(C_y^\alpha + h_2)} + O(C_y^\alpha + h_1). \end{aligned} \quad (13)$$

The trivial equilibrium is asymptotically stable for $k_1 \in (0, \kappa_1) \cup (\kappa_2, \infty)$, and unstable for $k_1 \in (\kappa_1, \kappa_2)$. This means that quite small stiffness of the first spring is sufficient to make the trivial equilibrium isolated and asymptotically stable. However, somewhat larger

stiffness results in stability loss. In order to make this system stable again, it is necessary to increase k_1 considerably.

In order to illustrate the dependence of the area of instability upon parameters of the system, we use numerical calculations. In Fig. 2, the domain of instability is shown in plane (k_1, k_2) for different values of damping coefficients (grey colored areas).

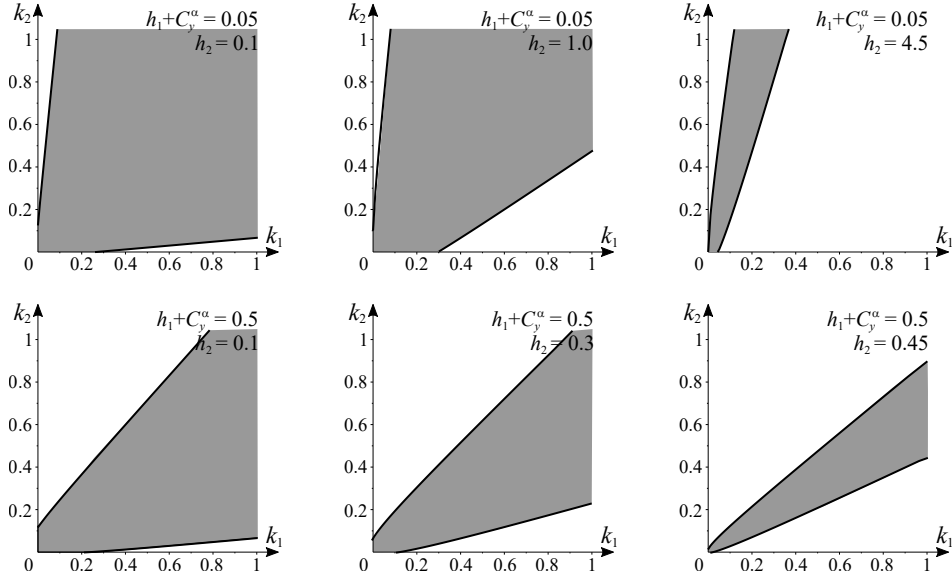


Figure 2. Domain of instability depending on parameters of the system.

These results demonstrate that the equilibrium is unstable, when both springs are “weak” (k_1 and k_2 are small enough), which is natural. However, for any sufficiently large value of k_2 there exists a range of values of k_1 , where the equilibrium is unstable. The same holds for the stiffness coefficient of the first spring: for any large enough k_1 there exists an interval of k_2 , where instability occurs.

It is interesting to note that making the system more “stiff” doesn’t necessarily make it stable. Moreover, in some situations it is sufficient to decrease stiffness coefficient of one spring to ensure the stabilization.

Such effect of change in stiffness looks somewhat unconventional.

The influence of structural damping upon stability is rather “normal”. One can readily see that increase in damping coefficient of the second and / or the first springs leads to shrinking of the area of instability, which could be expected. It is quite clear that if h_1 and h_2 are large enough, so that $\det \mathbf{D} > 0$, then the equilibrium is asymptotically stable for all positive values of stiffness coefficients of both springs.

4. Conclusions

The effect of change of stiffness in one of generalized coordinates on the stability of the trivial equilibrium is analyzed for linear mechanical systems with two degrees of freedom, where dissipative forces without full dissipation and/or positional non-conservative forces are present.

Conditions on parameters of the system are determined for existence of a range of values of the stiffness coefficient where the equilibrium is unstable. This means that, in some situations, increase in stiffness in one generalized coordinate can result in stability loss. Consideration of this rather unexpected effect can be useful for engineering applications.

As a mechanical example, oscillations of an aeroelastic system with two translational degrees of freedom (galloping) are considered. Areas of instability in the space of parameters of this system are constructed.

Acknowledgments

This work is supported by the Russian Foundation for Basic Research, project No. 18-01-00538.

References

- [1] AGAFONOV, S. The stability and stabilization of the motion of non-conservative mechanical systems. *J. Applied Mathematics and Mechanics* 74, 4 (2010), 401–405.
- [2] BARRERO-GIL, A., PINDADO, S., AND AVILA, S. Extracting energy from vortex-induced vibrations: A parametric study. *Applied Mathematical Modelling* 36, 7 (2012), 3153–3160.
- [3] CHETAEV, N. *The Stability of Motion*. Pergamon Press, Oxford, 1961.
- [4] HERRMANN, G., NEMAT-NASSER, S., AND PRASAD, S. Destabilizing effect of velocity-dependent forces in nonconservative continuous systems. *AIAA Journal* 4, 7 (1966), 1276–1280.
- [5] JEKEL, D., AND HAGEDORN, P. Stability of weakly damped mdgkn-systems: The role of velocity proportional terms. *Z. Angew. Math. Mech* 97, 9 (2017), 112811358.
- [6] KIRILLOV, O., AND VERHULST, F. Paradoxes of dissipation-induced destabilization or who opened whitney’s umbrella? *Z. Angew. Math. Mech* 90, 6 (2010), 462–488.
- [7] KRECHETNIKOV, R., AND MARSDEN, J. On destabilizing effects of two fundamental non-conservative forces. *Physica D* 214 (2006), 25–32.
- [8] LUO, S., CHEW, Y., AND NG, Y. Hysteresis phenomenon in the galloping oscillation of a square cylinder. *J. Fluids and Structures* 18, 1 (2003), 103–118.

- [9] MAILYBAEV, A., AND SEYRANIAN, A. The effect of nonconservative forces on the stability of systems with multiple frequencies and the nicolai paradox. *Doklady Physics* 56, 1 (2011), 32–38.
- [10] MASSAI, T., ZHAO, J., LO JACONO, D., BARTOLI, G., AND SHERIDAN, J. The effect of angle of attack on flow-induced vibration of low-side-ratio rectangular cylinders. *J. Fluids and Structures* 82 (2018), 375–393.
- [11] MERKIN, D. *Introduction to the Theory of Stability*. Springer-Verlag New York, New York, 1997.
- [12] ZHURAVLEV, V. Van der pols controlled 2d oscillator. *Rus. J. Nonlin. Dyn.* 12, 2 (2016), 211–222.

Yury Selyutskiy, Ph.D.: Lomonosov Moscow State University, Institute of Mechanics, 119192, Michurinsky prosp. 1, Moscow, Russia (*selyutski@imec.msu.ru*).

The influence of lateral swaying on the trajectory of articulated rigid body vehicles

Aleksander Skurjat

Abstract: The phenomenon of snaking of articulated vehicles is affected by many factors. One of them is lateral swaying of the vehicle caused by driving on uneven road, which can significantly affect the vehicle's steering angle and the trajectory of its motion. Typically, articulated vehicles are fitted with a rear driving tandem axle. The wheels that prevent the vehicle from tipping over are the front ones, which are attached directly to the vehicle frame. For this reason, the front wheels are loaded with lateral forces while swaying much more. Since the front wheels are distant from the steering joint, the resulting torque caused by the lateral forces tends to rotate the front body of the vehicle about the steering axle. This torque is counteracted (compensated) by the torque created by the steering system. Changes in the steering angle are proportional to the hydraulic steering system stiffness. Numerous experimental tests indicate that the relationship between stiffness and steering angle is not linear and might be approximated with an exponential function. The lateral (roll axis) oscillations are cyclical, an alternate angle change in the steering joint is observed. There is an alternate change in the steering angle due to changes in lateral forces acting on the front wheels. The article presents the results of the research on the impact of roll oscillations about the vehicle's lateral symmetry axis on the trajectory of vehicle motion.

1. Introduction

The phenomenon of vehicle snaking is present in almost all vehicles on the road. It is defined as a spontaneous sinusoidal deviation of the motion trajectory from the straight line direction assumed by the driver. Its frequency and amplitude depend on the design parameters of the vehicle. For cars, trajectory deviations caused by lateral forces, uneven ground are not a challenge for the driver, so the vehicle can move at high speeds. For articulated vehicles, e.g. heavy commercial vehicles, there are already maximum speed limits due to problems with driving and significant increase in braking distance. Driving problems are caused by the vehicle's design: high centres of gravity, significant changes in their position due to the type of load being carried. Placing heavy loads in a trailer at the rear, beyond the rear wheels' axles, can give rise to resonance phenomena that create oscillations between the tractor and trailer. Of course, this results in a change in the trajectory of the vehicle or in a serious traffic incident.

Both types of vehicles have front steering wheels, which enable precise compensation of the resulting trajectory deviations. In the case of vehicles with articulated steering and hydrostatic drives

(earth working machines), it is not possible to change the trajectory smoothly. The research conducted by the author showed that geometric parameters have a significant influence on the phenomenon of snaking, in particular: a) geometry of the steering system, b) distribution of the units' centres of gravity in relation to the steering joint, c) distance between the front and rear wheels in relation to the steering joint, d) width of the vehicle. The following can also be mentioned in the steering system: e) low bulk modulus of oil, f) volumetric expansion of hoses, g) leakage of valves and h) inability to compensate the oil volume quickly and precisely in steering cylinders. The drive type is also important: the rear one causes both frames to twist in relation to the steering joint (jackknife effect) and the front one straightens the vehicle while pulling.

Another important issue is to determine the influence of lateral swaying (at roll vehicle axle) of the whole vehicle on the changes in the steering angle and trajectory of motion. Lateral sway of the vehicle caused by unevenness can affect the steering angle of the vehicle. The rear rigid driving pendulum axle used in the earth working vehicles makes that only the front wheels prevent the vehicle from tipping over. This creates extra component of lateral forces on the front wheels, which are distant from the articulated axle by a considerable distance. Produced lateral force is of course greater on a wheel with higher normal tire-ground reaction. The resulting torque is applied to turn the front frame of the vehicle. The torque produced by the steering system (proportional to the stiffness) tries to compensate torque produced by the front wheels and make articulated joint to travel straight. Because of too small steering system stiffness and in a result in too small compensating torque produced steering angle will change. The steering angle changes alternately as a result of changes in the vertical forces on the front wheels. It should also be noted that the action of drive/braking forces also contributes to changes in the vertical loads on the wheels.

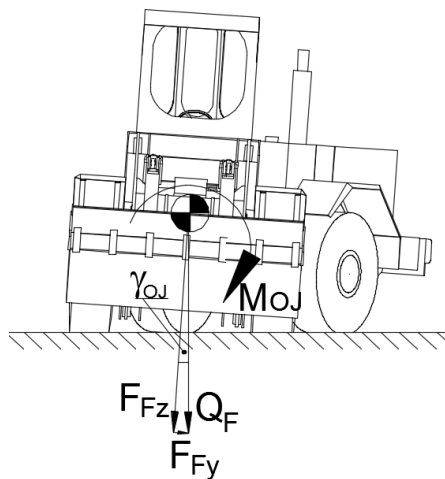
Snaking phenomenon depends strongly on a distance measured between steering joint and the center of gravity point position of both vehicles frames. Higher distance makes higher torques and amplitude in the joint of turn (γ) will increase. Velocity and moment of inertia plays an important role in vehicle course especially when asymmetry between front and rear part exist.

2. Basic vehicle parameters and mathematical model description

A mathematical model has been developed to investigate the effect of lateral swaying in the joint of oscillations of the rear rigid pendulum axle on oscillations in the joint of turn (γ). The model calculates the normal reactions on all wheels of the vehicle on the assumption that the normal reaction of the rear wheels reaches equal values. A sinusoidal waveform of the rear axle rotation angle is used as the force input function (generator). To calculate the reaction changes of the normal front wheels, the deflection of the front tires resulting from the rotation of the rear section was calculated, and on the basis of the known radial tires stiffness, the normal forces on all wheels were obtained. Changes in the reaction of

[illegible]

As a result of the forces that cause the vehicle to sway against the longitudinal axle of the vehicle, the situation shown in Fig. 2 occurs. The purpose of the test is to determine the relationship between the lateral tilts and the angular variations in the steering joint.



451

Oscillations in the steering system are induced by driving the vehicle in alternating lateral tilts with a specified frequency and amplitude and, at the same time, changes in the driving forces (braking and drive) also with a specified frequency and amplitude.

Adopted values are presented in Fig. 3.

Wheel track width of the vehicle W	1,0 [m]
Length of the vehicle $X_{wrj}+X_{wfj}$	1,66 [m]
Distance between front/rear axle and steering joint X_{wfj}/X_{wrj}	0,68/0,98 [m]
Distance of the centre of gravity of the front/rear section from the centre of symmetry X_{cgf}/X_{cgr}	0/0 [m]
Height of the centre of gravity of the front/rear section from the ground Z_{cgf}/Z_{cgr}	0,8/0,8 [m]
Weight of the front/rear section m_f/m_r	615/300 [kg]
Inertia moment of the front/rear section J_f/J_r	314/100 [kgm ²]

Figure 3. Model parameters adopted for tests

The following mathematical model has been prepared. The relationships were used to calculate the sum of reaction forces of front and rear wheels:

$$(X_{WRJ} + X_{WFJ}) + m_{RED}g = -F_v Z_{CGRED} \quad (1)$$

$$-F_F(X_{WRJ} + X_{WFJ}) = m_{RED}g X_{WRJ} + F_v Z_{CGRED} \quad (2)$$

$$F_R = m_{RED}g - F_F \quad (3)$$

To determine the static forces of normal front and rear wheels, the following were used:

$$F_{FLS}W = -F_{Fs} \left(\frac{W}{2} \right) \quad (4)$$

$$F_{FRS} = F_{Fs} - F_{FLS} \quad (5)$$

$$F_{RLS}W = -F_{Rs} \left(\frac{W}{2} \right) \quad (6)$$

$$F_{RRS} = F_{Rs} - F_{RLS} \quad (7)$$

The deflection of the front wheels is determined from the following relationship:

$$u_{FL} = W \sin(\gamma_{OJ}) \quad (8)$$

and the normal reaction from tyre deflection as:

$$F_{FLd} = u_{FL} k_{FL} \quad (9)$$

$$F_{FRd} = u_{FL} k_{FR} \quad (10)$$

which means the following is obtained:

$$F_{FL} = F_{FLs} + F_{FLd} \quad (11)$$

$$F_{FR} = F_{FRs} + F_{FRd} \quad (12)$$

$$F_{FL}^y = F_{FL} \sin(\gamma_{0j}) \quad (13)$$

$$F_{FR}^y = F_{FR} \sin(\gamma_{0j}) \quad (14)$$

$$M_\gamma = (F_{FL}^y + F_{FR}^y) * X_{wFj} \quad (15)$$

$$\gamma = \frac{M_\gamma}{k_\gamma} \quad (16)$$

3. Simulation testing of the anti- oscillation system in steering system

Vehicles with articulated steering system, such as wheel loaders, have rear wheels mounted on the rigid pendulum drive axle, which has the ability to rotate in the range of several degrees depending on the type of vehicle. This is a significant difference in relation to other wheeled vehicles in which the wheels are mounted (suspended) usually on flexible elements e.g. springs. Since the front wheels protect the vehicle against tipping over, additional forces are generated on them from front and rear inertia elements during tilting and lateral swaying (in relation to the longitudinal axle of the vehicle). The rear wheels are supported at the rear in the centre line of the vehicle and they only transmit the gravity forces generated by the resulting position of the centre of gravity of whole vehicle. The purpose of the test is to determine whether such a construction of the vehicle when engaged in lateral swaying affects the change in the steering angle of the front and rear parts of the vehicle in their axle of rotation, i.e. whether the snaking occurs. The tests are carried out for equal values enforcing lateral swaying of the vehicle and driving forces. However, they differ in the frequency of their occurrence. The obtained results are presented in Fig. 4.

Studies have shown that the oscillations of the drive forces F_{nap} and lateral swaying are interrelated. In the case when $f_{kol} = f_{nap} = 1$ Hz, the oscillations in the steering system $f_{skr} = 1$ Hz are also obtained. It can be noticed, however, that the slowing down of the lateral swaying ($f_{kol} \rightarrow 0$) also causes a decrease in the frequency of oscillations in the steering system (f_{skr}). This phenomenon can be observed e.g. in Fig. 4a.

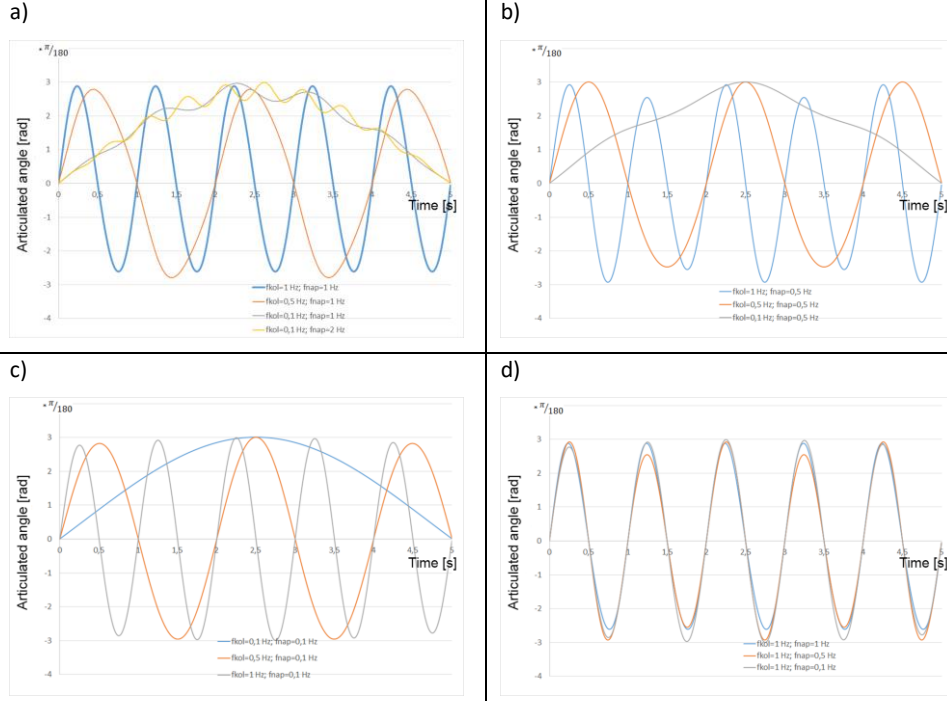


Figure 4. Study of the effect of the frequency of enforcing lateral swaying and drive forces on the oscillations of the vehicle's steering angle for different frequencies of enforcing lateral swaying f_{kol} and drive forces f_{nap}

In the case when $f_{kol}=0.1$ Hz and $f_{nap}=1$ Hz the visible oscillations of the steering angle (γ) are observed and are derived from the drive forces and imposed on a slow change in steering angle resulting from the vehicle's tilt. The amplitude increases with the vehicle's lateral tilt angle and then it decreases. If the drive torque frequency ($f_{kol}=0.1$ Hz and $f_{nap}=2$ Hz) increases, the steering angle frequency γ will of course increase too. This means that drive forces are particularly important when asymmetrical vertical forces occur on the front wheels.

The action of the drive system may cause the suppression of steering angle oscillations, as shown in Fig. 4b and the results $f_{kol}=1$ and $f_{nap}=0.5$ Hz. It may be noted that the values of the steering angle (γ) alternately reach the values of ± 3 and ± 2.5 degrees. This is due to the fact that the front wheels are relieved of load as a result of vehicle accelerating forces. The situation is different for the parameters $f_{kol}=0.5$ and $f_{nap}=0.5$ Hz (Fig4b). In this situation, the steering angles $\gamma = 3$ degrees and $\gamma = -2.5$ degrees are obtained. The steering system does not oscillate around the straight drive position and moves in a circle. The same phenomenon was also observed for $f_{kol}=1$ and $f_{nap}=1$ Hz (Fig4a), but it is less

noticeable. The above phenomena occur also for other parameters of $f_{kol}=1$ and f_{nap} simulations and are presented in Fig. 4c.

Fig. 4d. presents the results of the influence of changes in the frequency of f_{nap} drive forces on the oscillations γ with $f_{kol}=1=const$. Frequency changes between 0.1 and 1 Hz for the drive forces result in only minor changes to the steering angle, which confirms that the introduction of vehicle lateral swaying has a significant effect on the oscillations in the steering system and the trajectory of vehicle motion.

Conclusions

The paper presents a mathematical model used to check the mutual relations between the oscillations of drive force and lateral tilting in the vehicle on the changes in the steering angle. It has been specified for which group of vehicles the phenomenon of overlapping of lateral tilt oscillations and drive force occurs. It was shown that engaging a vehicle into lateral swaying with an amplitude of ± 14 degrees affects changes in steering angle γ in the range of ± 3 degrees. The action of drive/braking forces only makes a small contribution to changes in the steering angle γ . The mathematical analysis of the model shows that an increase in the distance between the front wheels and the steering joint increases the values of oscillation γ . Initial tests in the MBS environment also confirmed the correctness of the obtained results. Obtained mechanism of will be tested on a real machine in the near future.

References

- [1] Dudziński P., and Skurjat A., System for improving directional stability for articulated vehicles. W: Computational technologies in engineering (TKI'2018) Conference Proceedings, ISSN 0094-243X; vol. 2078 nr 1), 2019
- [2] Skurjat A., and Kosiara A., Directional stability control of body steer wheeled articulated vehicles. W: Dynamical Systems in Applications, Łódź, Poland, December 11-14, , Springer Proceedings in Mathematics & Statistics, ISSN 2194-1009; vol. 249 2017
- [3] Dudziński P., and Skurjat A., Research on the influence of geometric parameters on the phenomenon of snaking of articulated vehicles. Zeszyty Naukowe - Wyższa Szkoła Oficerska Wojsk Lądowych im. gen. T. Kościuszki, t. 186, vol. 49, nr 4, s. 294-301. 2017
- [4] Dudziński P., and Skurjat A., and Dacko P., Sposób aktywnej poprawy stateczności kierunkowej pojazdu z wieloczłonkowym układem podwoziowym, patent pending numer:421682. Published. 28.06.2019
- [5] Yin, YM (Yin, Yuming); Rakheja, S (Rakheja, Subhash); Yang, J (Yang, Jue); Boileau, PE (Boileau, Paul-Emile), Effect of articulated frame steering on the transient yaw responses of the vehicle, Proceedings Of The Institution Of Mechanical Engineers Part D-Journal Of Automobile Engineering Volume: 232 Issue: 3,2018.
- [6] Yin, YM (Yin, Yuming); Rakheja, S (Rakheja, Subhash); Yang, J (Yang, Jue); Boileau, PE (Boileau, Paul-Emile), Design optimization of an articulated frame steering system, Proceedings

Of The Institution Of Mechanical Engineers Part D-Journal Of Automobile Engineering Volume: 232 Issue: 10,2018.

- [7] Xuefei Li and Ya Wu and Wei Zhou, and Zongwei Yao, Study on Roll Instability Mechanism and Stability Index of Articulated Steering Vehicles, Hindawi Publishing Corporation, Mathematical Problems in Engineering, Article ID 7816503, Volume 2016,
- [8] Zongwei Yao and Guoqiang Wang and Xuefei Li and Junna Qu and Yuxin Zhang and Yonghai Yang, Dynamic simulation for the rollover stability performances of articulated vehicles, Proc IMechE Part D: J Automobile Engineering, Vol. 228(7), 2014
- [9] Yuming Yin and Subhash Rakheja and Jue Yang and Paul-Emile Boileau, Effect of articulated frame steering on the transient yaw responses of the vehicle, Proc IMechE Part D: J Automobile Engineering, 1–16, IMechE, 2017
- [10] Alireza Pazooki, Ride and directional dynamic analysis of articulated frame steer vehicles, A Thesis in The Department of Mechanical and Industrial Engineering, For the Degree of Doctor of Philosophy (Mechanical Engineering) at Concordia University Montreal, Quebec, Canada, 2012
- [11] Akira AOKI, Yoshitaka MARUMO and Ichiro KAGEYAMA, Directional Stability of Multi-Articulated Vehicles with Multiple Axles, Journal of Mechanical Systems for Transportation and Logistics, Vol. 4, No. 1, 2011
- [12] Yuming Yin, Enhancement of Ride and Directional Performances of Articulated Vehicles via Optimal Frame Steering and Hydro-Pneumatic Suspension, A Thesis in The Department of Mechanical, Industrial and Aerospace Engineering for the Degree of Doctor of Philosophy (Mechanical Engineering) at Concordia University Montreal, Quebec, Canada, 2017

Aleksander Skurjat, Ph.D.: Faculty of Mechanical Engineering, Department of Off-Road Machine and Vehicle Engineering, Wybrzeże Wyspiańskiego 27, 50-370, Wrocław, Poland (PL), (aleksander.skurjat@pwr.edu.pl)

Strong mode coupling in vibrations of single-walled carbon nanotubes

Valeri Smirnov, Leonid Manevitch

Abstract: Beam-like and shell-like nonlinear normal modes interaction of single-walled carbon nanotubes is considered in the framework of the thin shell theory. In order to reveal the mode interaction and the effects, which can arise as its results, we need in the transition to the nonlinear vibration theory. We consider the CNT oscillations in the framework of the nonlinear Sanders-Koiter theory and demonstrate that the effective reduction in the equations of motion in the combination with the asymptotic analysis allows us to study the nonlinear mode coupling and to reveal new stationary oscillations, which are absent in the linear approach, as well as to describe the non-stationary dynamics under condition of the 1:1 resonance.

1. Introduction

The vibrational properties of the carbon nanotubes (CNTs) are important from various viewpoints. If the CNTs are the part of some nano-devices (nano-electromechanical resonator, nanodetector, atomic force microscope, etc.) their oscillations determine the working regimes and capability of the devices [12, 11, 7, 6]. On the other hand, the deformability and transmissible characteristics of the nanotube reinforced composites depend on the CNTs' vibrational spectra [2, 4, 9]. Therefore, the oscillations of the CNTs have been repeatedly studied since their discovery at 1991 [3]. Because of the elementary cell of the CNT is complex enough, the vibrational spectrum consists of many branches, which correspond to different types of the oscillations [2]. The most low-frequency oscillations are represented by both the acoustical type ones (longitudinal tension, bending and twisting) and the optical-type circumferential flexure modes. The latter correspond to the shell-type oscillations when the CNT's cross section, which is normal to the nanotube's axis, undergoes periodic deformation. Their specific frequency is $\sim 30 \text{ cm}^{-1}$ for the (10,10) nanotubes. In spite of this mode is the optical type one, it may be under resonant conditions with acoustic-type modes at certain values of the longitudinal wave number k .

Taking into account the nonlinear character of the nanotube oscillations, we can expect the non-trivial effects resulting from their interactions. Really, the resonant interactions of the modes belonging to the same oscillation branch lead to the capture of the oscillation

energy in coherent domains in the case of the CNTs with finite length [17] or to the breather creation for the CNT of infinite length [16]. In the nanotubes of finite length the intensive energy exchange between some domains on the CNT's surface is changed by the energy localization, if the oscillation amplitude exceeds some threshold, the value of which is determined by the inverse aspect ratio (the ratio of CNT's radius to its length). Recently, it was shown that the resonant interaction of the nonlinear oscillations of different types is possible too [15], but the localization effect occurs in the finite range of the oscillation amplitude. The analytical model of the nonlinear interaction between bending and circumferential flexure modes has been developed in the framework of reduced Sanders-Koiter theory of thin elastic shells [1]. In order to reveal the mode interaction some additional assumptions have been made that allows us to study the nonlinear normal modes and their bifurcations. The analogous model has been used for the analysis of the circumferential flexure modes and it has been well verified in [5, 18].

2. Interaction of nonlinear normal modes

In this work we will consider the CNT as a thin elastic shell, which is specified by its radius R , length L and "thickness" of wall η (see fig. 2). The "material" of the shell is characterized by the Young modulus Y and the Poisson ratio ν . Such an approximation describes the behaviour of the CNT well, even if the nanotube deformation is large enough [20, 19, 8, 14, 13]. In the framework of the thin shell theory, the local deformation is expressed via the longitudinal (u), transversal (v), and radial (w) displacements of the middle surface of the equivalent shell (fig. 2).

Taking into account that undistorted CNT is circular, we can represent the displacement field as the Fourier series:

$$\{u, v, w\} = \sum_n \{U_n \cos n\theta, V_n \sin n\theta, W_n \cos n\theta\}, \quad (1)$$

where $n (= 0, 1, 2, \dots)$ is the circumferential wave number, θ is the azimuthal angle, and $\{U_n, V_n, W_n\}$ are the amplitudes of the longitudinal, transversal and radial displacements, respectively. The acoustic-type modes mentioned above correspond to $n = 0$ (longitudinal tension and twisting) and $n = 1$ (bending mode), while the circumferential flexure mode is associated with $n = 2$.

In this work we are interested in the dynamical processes, which result in the energy exchange and localization during the CNT oscillations. Therefore, we start from the oscillatory energy distribution, which is specific for the certain modes. As it will be shown below, the bending mode with the longitudinal wave number $k = 3$ (it corresponds to 3 half-waves on

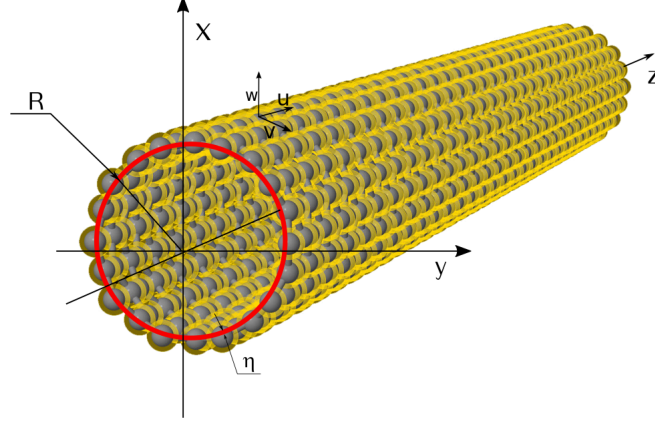


Figure 1. (Color online) The CNT geometry: red curve shows the middle surface, R and η are the radius and the effective thickness of CNT. The $\{u,v,w\}$ are the longitudinal, transversal and radial components of the displacement field, respectively.

the CNT's length) can be under resonant conditions with the circumferential flexure mode having the same longitudinal wave number. The energy distribution for the combination of these modes is exhibited in figures 4(a,b).

One can see that the combination of the bending and circumferential oscillations leads to some concentration of the energy along the generatrix at the azimuthal angle $\theta = \pi$.

There are two scenarios of the energy redistribution in the nonlinear systems [10]. The first one consists in that the localized energy domain migrates over the CNT surface from the initial position $\theta = \pi$ to new one at $\theta = 0$ with some period, which is determined by the modal frequency difference. Such a migration is similar to the beating in the system of two weakly couple identical oscillators, where the oscillatory energy migrates from one oscillator to another one and backwards. Another scenario implies that the domain of the energy localization is unmovable or can uninterruptedly move over the surface. The transition between these scenarios occurs when the amplitude of the oscillations overcomes some threshold, the value of which is determined by the certain condition.

In order to study the energy exchange and its localization we need in the dynamical equations, which describe the coupled bending and circumferential oscillations. Because the equations of the thin elastic theory are extremely difficult we should use some simplifying hypotheses. Both bending and circumferential flexure oscillations are specified by negligible

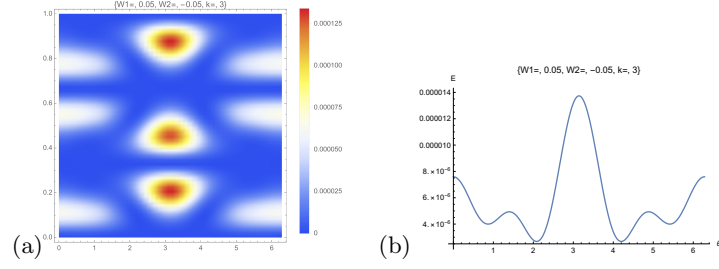


Figure 2. (Color online) (a) The elastic energy distribution over the CNT surface for the case of coupled bending and circumferential oscillations. (b) The energy distributions along the azimuthal coordinate.

changes of the contour length of the CNT cross section, which is normal to the nanotube axis. The shear deformations are also supposed to be infinitesimal. These two hypotheses allow us to find the relationships between amplitudes of the longitudinal, transversal and radial displacements both in linear and nonlinear approximations [16]. By such a manner, we obtain two coupled equations for the amplitudes of radial displacement for the bending (W_1) and circumferential flexure (W_2) oscillations (see details in [15]):

$$\begin{aligned}
& \frac{\partial^2 W_1}{\partial t^2} - \frac{\alpha^2}{2} \frac{\partial^4 W_1}{\partial t^2 \partial \xi^2} + \alpha^4 \frac{12 + \beta^2}{24} \frac{\partial^4 W_1}{\partial \xi^4} - \\
& \quad \frac{9\alpha^2}{16} \frac{\partial}{\partial \xi} \left(\frac{\partial W_1}{\partial \xi} \frac{\partial}{\partial t} \left(W_2 \frac{\partial W_2}{\partial t} \right) \right) = 0 \\
& \frac{\partial^2 W_2}{\partial t^2} + \frac{3\beta^2}{5} W_2 - \frac{\alpha^2 \beta^2 (3 + \nu)}{10} \frac{\partial^2 W_2}{\partial \xi^2} - \frac{\alpha^4}{20} \frac{\partial^4 W_2}{\partial \xi^2 \partial t^2} + \\
& \quad \frac{\alpha^4 (3 + 4\beta^2)}{60} \frac{\partial^4 W_2}{\partial \xi^4} + \frac{81}{40} W_2 \frac{\partial}{\partial t} \left(W_2 \frac{\partial W_2}{\partial t} \right) + \\
& \quad \frac{9\alpha^2}{40} \left[W_2 \left(\left(\frac{\partial^2 W_2}{\partial \xi \partial t} \right)^2 + 2 \frac{\partial^2}{\partial t^2} \left(\frac{\partial W_1}{\partial t} \right)^2 \right) - \right. \\
& \quad \left. \frac{\partial^2 W_2}{\partial t^2} \frac{\partial}{\partial \xi} \left(W_2 \frac{\partial W_2}{\partial \xi} \right) - \frac{\partial}{\partial \xi} \left(\frac{\partial W_2}{\partial \xi} \left(\frac{\partial W_2}{\partial t} \right)^2 \right) \right] = 0
\end{aligned} \tag{2}$$

The linear approximation of equations (2) leads to the dispersion relations under the boundary conditions, corresponding to the hinged CNT:

$$\begin{aligned}
\omega_1^2 &= \frac{(12 + \beta^2)}{12(2 + \alpha^2 \kappa^2)} \alpha^4 \kappa^4 \\
\omega_2^2 &= \frac{1}{20 + \alpha^2 \kappa^2} \left(12\beta^2 + 2\beta^2(3 + \nu) \alpha^2 \kappa^2 + \frac{(3 + 4\beta^2)}{3} \alpha^4 \kappa^4 \right),
\end{aligned} \tag{3}$$

where $\kappa = \pi k$ ($k = 0, 1, \dots$) is the longitudinal wave number. Figure 2 shows dispersion curves (3) in comparison with the exact ones, which were calculated by the solution of the full linearized system without the hypotheses mentioned above. One can observe that the resonant conditions at the bending (blue curve) and circumferential (red one) modes occur at the "wave number" $k = 3$.

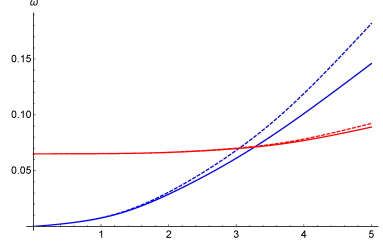


Figure 3. (Color online) Dispersion relations for BLOs and CFOs. Blue and red curves corresponds to the azimuthal wave numbers $n_1 = 1$ and $n_2 = 2$, respectively. Solid and dashed curves show the exact values and the values estimated by equations (3).

3. Asymptotic analysis

Equations (2) obtained in the previous section can not be solved directly in terms of functions W_1 and W_2 . In order to get the stationary solutions of equations (2) we use the asymptotic analysis with a small parameter ε whose value is determined by the resonance conditions for bending and circumferential modes. However, before performing the asymptotic expansion, it is useful to rewrite equations (2) in terms of the complex variables, which contain both the coordinate and the momentum:

$$\Psi_j(\xi, t) = \frac{1}{\sqrt{2}} \left(\sqrt{\omega} W_j(\xi, t) + \frac{i}{\sqrt{\omega}} \frac{\partial W_j(\xi, t)}{\partial t} \right), \quad j = 1, 2. \quad (4)$$

We assume that the parameter ω is stationary frequency, which is yet undefined. In order to obtain the stationary solutions one should extract the carrier frequency, i.e. we will find the nonlinear normal modes as follows:

$$\Psi_j(\xi, t) = \psi_j e^{-i(\omega t - \kappa \xi)}, \quad j = 1, 2 \quad (5)$$

assuming ψ_j do not depend on the time.

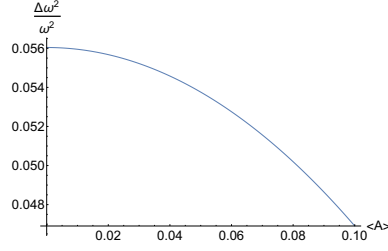


Figure 4. (Color online) The relative eigenfrequency difference versus the average amplitude of CFOs and BLOs for the CNT with $\alpha = 1/30$. The wave number $\kappa = 3\pi$.

Taking into account expressions (4, 5) with natural relation between modulus of function Ψ_j and oscillation amplitude A_j

$$|\Psi_j|^2 = X_j = \frac{\omega}{2} A_j^2. \quad (6)$$

we obtain the dispersion laws for the oscillation branches as follows:

$$\begin{aligned} \omega_1^2 &= \frac{4\alpha^4 (12 + \beta^2) \kappa^4}{96 + 48\alpha^2 \kappa^2 - 27\alpha^2 \kappa^2 A_2^2} \\ \omega_2^2 &= \frac{4(36\beta^2 + 6\alpha^2 \beta^2 (\nu + 3) \kappa^2 + \alpha^4 (4\beta^2 + 3) \kappa^4)}{3(4(20 + \alpha^2 \kappa^2) - 36\alpha^2 \kappa^2 A_1^2 + 9(9 - 2\alpha^2 \kappa^2) A_2^2)}. \end{aligned} \quad (7)$$

It is easy to see that the small-amplitude expansion of relations (7) coincides with linear dispersion law (3).

Figure 3 shows the dependences of the frequencies ω_1, ω_2 on the CFOs amplitude under the various BLOs amplitude at the "resonant" wave number $\kappa = 3\pi$. The relative difference $(\Delta\omega/\omega)$ between modes' frequencies in the vicinity of the resonance is depicted in figure 3.

To provide the processes of the energy migration in the extensive systems become perceptible on the background of modal oscillations, their duration should exceed the period of modes essentially. It means that we should separate the fast and slow processes in the system. The natural measures of the time scales are the natural frequencies (7) and their difference. The latter is shown in Fig. 3 as a function of the average amplitude $\langle A \rangle = (A_1 + A_2)/2$. Separating the system's motions with the different time scales, we suppose that the amplitudes ψ_1 and ψ_2 are the functions of the slow time $\tau \sim \Delta\omega t$. The respective evolution equations for amplitudes ψ_j have been developed in [15]:

$$\begin{aligned}
& i \left(1 + \frac{\alpha^2 \kappa^2}{2} \right) \frac{\partial \psi_1}{\partial \tau} - \left(-\frac{\omega}{2} + \alpha^2 \kappa^2 \omega - \alpha^4 \kappa^4 \frac{12 + \beta^2}{48\omega} \right) \psi_1 + \\
& \quad \frac{9\alpha^2 \kappa^2}{32} \psi_2^2 \psi_1^* = 0 \\
& i \left(1 + \frac{\alpha^2 \kappa^2}{20} \right) \frac{\partial \psi_2}{\partial \tau} - \left(\frac{5\omega^2 - 3\beta^2}{10\omega} + \alpha^2 \kappa^2 \frac{(\omega^2 - 2\beta^2(3 + \nu))}{40\omega} \right. \\
& \quad \left. - \alpha^4 \kappa^4 \frac{3 - 4\beta^2}{120\omega} \right) \psi_2 - \frac{9}{80} (9 - 2\alpha^2 \kappa^2) |\psi_2|^2 \psi_2 + \frac{9\alpha^2 \kappa^2}{20} \psi_1^2 \psi_2^* = 0
\end{aligned} \tag{8}$$

It is useful to rewrite equations (8) in terms of functions

$$\chi_1(\tau) = \psi_1(\tau); \quad \chi_2(\tau) = \frac{4\sqrt{2 + \alpha^2 \kappa^2}}{\sqrt{20 + \alpha^2 \kappa^2}} \psi_2(\tau), \tag{9}$$

which form the set of the canonical variables for the system with the Hamilton function

$$H = a_1 |\chi_1|^2 + a_2 |\chi_2|^2 + b_1 |\chi_2|^4 + b_2 (\chi_1^2 \chi_2^{*2} + \chi_1^{*2} \chi_2^2), \tag{10}$$

where

$$\begin{aligned}
a_1 &= \frac{-24\omega^2 - 12\alpha^2 \kappa^2 \omega^2 + \alpha^4 \kappa^4 (\beta^2 + 12)}{24\omega (2 + \alpha^2 \kappa^2)} \\
a_2 &= \frac{36\beta^2 - 60\omega^2 + 3\alpha^2 \kappa^2 (2\beta^2(\nu + 3) - \omega^2) + \alpha^4 \kappa^4 (4\beta^2 + 3)}{6\omega (20 + \alpha^2 \kappa^2)} \\
b_1 &= \frac{18 (-18 - 5\alpha^2 \kappa^2 + 2\alpha^4 \kappa^4)}{(20 + \alpha^2 \kappa^2)^2} \\
b_2 &= \frac{9\alpha^2 \kappa^2}{2 (20 + \alpha^2 \kappa^2)}
\end{aligned} \tag{11}$$

The equations of motion in terms of functions χ_j can be obtained as:

$$i \frac{\partial \chi_j}{\partial \tau} = - \frac{\partial H}{\partial \chi_j^*}. \tag{12}$$

An essential peculiarity of equations (12) is that they admit an additional integral besides the energy. It shows the level of the system excitation and is similar of the occupation number of the quantum mechanics. In our case it is expressed as follows:

$$X = |\chi_1|^2 + |\chi_2|^2. \tag{13}$$

It is known [10, 16] that the description of the energy redistribution resulted from the resonant interaction of the nonlinear normal modes needs in the introduction of the variables, which characterize the relative excitation of the different parts of the considered system. These variables are referred to as the "coherent domain" coordinates and expressed via the linear combination of the resonating normal modes:

$$\sigma_1 = \frac{1}{\sqrt{2}} (\chi_1 + \chi_2); \quad \sigma_2 = \frac{1}{\sqrt{2}} (\chi_1 - \chi_2). \quad (14)$$

It can be shown that the relations $\sigma_1 \gg \sigma_2$ or $\sigma_2 \ll \sigma_1$ correspond to the energy distributions, when the main part of the oscillation energy is concentrated at the azimuthal coordinate $\theta = \pi$ or $\theta = 0$. It is essential, that introduction of domain coordinates (14) preserves occupation number integral in the form (13). It allows us to introduce the polar representation for variables σ_1 and σ_2 :

$$\sigma_1 = \sqrt{X} \cos \theta e^{i\delta_1}; \quad \sigma_2 = \sqrt{X} \sin \theta e^{i\delta_2}. \quad (15)$$

Here the "angle" θ corresponds to the relative excitation of one and other domains and the difference $\Delta = \delta_1 - \delta_2$ shows the corresponding phase shift. The energy of the system turns out to be dependent on the difference of the phases $\Delta = \delta_1 - \delta_2$ and angle θ at the fixed value of the occupation number X .

$$H = \frac{1}{4}X \left(2(a_1 + a_2 - (a_1 - a_2) \sin 2\theta \cos \Delta) + \right. \\ \left. X(b_1(1 - \cos \Delta \sin 2\theta)^2 + b_2(4 \cos^2 \Delta + (2 - \cos^2 \Delta) \sin 4\theta)) \right) \quad (16)$$

The equations of motion in the terms θ and Δ result from the relations:

$$\sin 2\theta \frac{\partial \theta}{\partial \tau} = -\frac{\partial H}{\partial \Delta}; \quad \sin 2\theta \frac{\partial \Delta}{\partial \tau} = \frac{\partial H}{\partial \theta} \quad (17)$$

Due to existence of the occupation number integral X the phase space turns out to be two-dimensional and the dynamics of the system can be studied by the phase portrait method.

To start the analysis of the system dynamics at different excitation levels, one should remind that functions θ and Δ depend on the slow time τ only. Therefore, in the phase portrait (in terms of these variables) the stationary states corresponding to the nonlinear

normal modes, are represented as the points, but not as any trajectories. On the contrary, any dynamical processes, which describe the evolution of variables θ and Δ , appear as the trajectories surrounding the one of the stationary points. The trajectory divides the "domains of influence" of the stationary states and it is called the Limiting Phase Trajectory (LPT) (see Fig. 7(a) below). The detailed analysis of the transformations of the phase space with changing the occupation number X has been performed in [15]. Therefore, now we discuss only the bifurcations, which lead to the principal changing the phase space topology. The typical phase portrait at small occupation number X is shown in Fig. 7(a). One can see two stationary points at $\theta = \pi/4$ and $\Delta = 0$, and $\Delta = \pi$, which correspond to the nonlinear normal modes. The trajectories surrounding these points describe the slow energy exchange in the system. The LPT is the trajectory passing from $\theta = 0$ to $\theta = \pi/2$ with the phase shift $\Delta \approx \pi/2$. While the occupation number grows the new stationary points appear and if the value of X exceeds some threshold, the phase portrait transforms as it is shown in Fig. 7(b). The principal difference between Figs. 7(a) and (b) is that the latter does not contain any trajectories, which pass from $\theta = 0$ to $\theta = \pi/2$. It means that the energy initially concentrated in one domain can not flow to another one, i.e. we observe the capture of the oscillation energy in some part of the nanotube surface. It is not an analogy of the true localized excitations - breathers, because the latter can exist only outside of frequency spectrum. However, in the finite length systems the spectrum is discrete and a partial localization can exist in the gap between nonlinear normal modes. The threshold of energy capture is related with transformation of the LPT into the separatrix crossing the point $\{\theta = \pi/4; \Delta = \pi/2\}$ and can be written via the parameters of the Hamilton function:

$$X_{loc} = \frac{(a_1 - a_2) \left(b_1 - \sqrt{-b_1(b_1 + 2b_2)} \right)}{(b_1 + 2b_2)^2 + 4b_2^2} \quad (18)$$

At the given parameters of the nanotube ($\alpha = 1/30$, $\beta = 0.08$, $\nu = 0.19$) the threshold value of occupation number is $X_{loc} = 0.00187$.

However, while the occupation number grows, the phase portrait evolves and after next bifurcation it looks as it is shown in Fig. 7(c). The bifurcation value of the occupation number can be calculated as:

$$X = \frac{a_1 - a_2}{b_1} \quad (19)$$

($X = 0.00246$ at the chosen parameters of the CNT). The comparison of Figs 7(b) and (c) shows that their topology is the mirror image of one to another one. The further growth of parameter X leads to the phase portrait which is shown in Fig. 7(d), where the trajectories

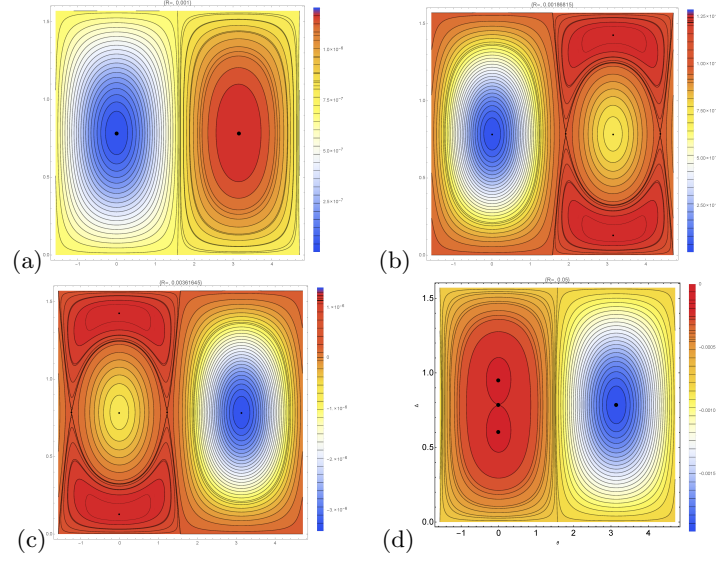


Figure 5. (Color online) Phase portraits in the variables (Δ, θ) at different values of occupation number X : (a) $X = 0.001$, (b) $X = 0.00186815$, (c) $X = 0.00361645$, (d) $X = 0.05$.

describing the full energy exchange appears again. It occurs if the occupation number exceeds the delocalization threshold

$$X_{deloc} = \frac{(a_1 - a_2) \left(b_1 + \sqrt{-b_1(b_1 + 2b_2)} \right)}{(b_1 + 2b_2)^2 + 4b_2^2}. \quad (20)$$

4. Conclusions

The nonlinear vibrations of the single-walled carbon nanotubes can be effectively studied in the framework of the nonlinear theory of the thin elastic shells. The strong coupling between nonlinear normal modes, even if they belong to different branches of the oscillation spectrum, leads to the long-time processes of the energy redistribution along the CNT's surface. The specific time of these processes multiple exceeds the oscillation period and it is controlled by the frequency difference of the interaction modes. The governing parameters turns out to be the oscillation amplitude, the value of that determines the resonant conditions. Under condition of the strong resonance the state with the localized oscillations has the infinite lifetime, but can be undergone some migration along the CNT's surface.

Acknowledgments

Authors are grateful to Russia Science Foundation (grant 16-13-10302) for the financial supporting of this work.

References

- [1] AMABILI, M. *Nonlinear vibrations and stability of shells and plates*. Cambridge University Press, Cambridge, 2008.
- [2] DRESSELHAUS, M. S., AND EKLUND, P. C. Phonons in carbon nanotubes. *Adv. in Phys.* 49 (2000), 705.
- [3] IIJIMA, S. Helical microtubules of graphitic carbon. *Nature* 354 (1991), 56–58.
- [4] KAHN, D., KIM, K. W., AND STROSCIO, M. A. Quantized vibrational modes of nanospheres and nanotubes in the elastic continuum model. *J. Appl. Phys.* 89 (2001), 5107.
- [5] KAPLUNOV, J., MANEVITCH, L. I., AND SMIRNOV, V. V. Vibrations of an elastic cylindrical shell near the lowest cut-off frequency. *Proceedings of the Royal Society of London A: Mathematical, Physical and Engineering Sciences* 472, 2189 (2016).
- [6] LÉONARD, F. *The physics of carbon nanotube devices*. William Andrew Inc., Norwich, NY, USA, 2008.
- [7] LI, C., AND CHOU, T.-W. Single-walled carbon nanotubes as ultrahigh frequency nanomechanical resonators. *Phys. Rev. B* 68 (2003), 073405.
- [8] LIEW, K. M., AND WANG, Q. Analysis of wave propagation in carbon nanotubes via elastic shell theories. *J. Eng. Sci.* 45 (2007), 227.
- [9] MAHDAVI, M., L.Y.JIANG, AND X.SUN. Nonlinear vibration of a double-walled carbon nanotube embedded in a polymer matrix. *Physica E* 43 (2011), 1813–1819.
- [10] MANEVITCH, L. I., AND SMIRNOV, V. V. Limiting phase trajectories and the origin of energy localization in nonlinear oscillatory chains. *Phys. Rev. E* 82 (2010), 036602.
- [11] PENG, H., CHANG, C. W., ALONI, S., YUZVINSKY, T. D., AND ZETTL, A. Ultrahigh frequency nanotube resonators. *Phys. Rev. Lett.* 97 (2006), 087203.
- [12] SAZONOVA, V., YAISH, Y., ÜSTÜNEL, H., ROUNDY, D., ARIAS, T. A., AND MCEUEN, P. L. A tunable carbon nanotube electromechanical oscillator. *Nature* 431 (2004), 284.
- [13] SILVESTRE, N. On the accuracy of shell models for torsional buckling of carbon nanotubes. *Eur. J. Mech. A* 32 (2012), 103.
- [14] SILVESTRE, N., WANG, C., ZHANG, Y., AND XIANG, Y. Sanders shell model for buckling of single-walled carbon nanotubes with small aspect ratio. *Composite Structures* 93 (2011), 1683.
- [15] SMIRNOV, V., AND MANEVITCH, L. Semi-inverse method in nonlinear mechanics: application to couple shell- and beam-type oscillations of single-walled carbon nanotubes. *Nonlinear Dynamics* 93 (2018), 205218.

- [16] SMIRNOV, V., MANEVITCH, L., STROZZI, M., AND PELLICANO, F. Nonlinear optical vibrations of single-walled carbon nanotubes. 1. energy exchange and localization of low-frequency oscillations. *Physica D: Nonlinear Phenomena* 325 (2016), 113 – 125.
- [17] SMIRNOV, V. V., SHEPELEV, D. S., AND MANEVITCH, L. I. Localization of low-frequency oscillations in single-walled carbon nanotubes. *Phys. Rev. Lett.* 113 (Sep 2014), 135502.
- [18] STROZZI, M., MANEVITCH, L. I., PELLICANO, F., SMIRNOV, V. V., AND S.SHEPELEV, D. Low-frequency linear vibrations of single-walled carbon nanotubes: Analytical and numerical models. *J. Sound and Vibration* 333 (2014), 2936–2957.
- [19] WANG, C. Y., RU, C. Q., AND MIODUCHOWSKI, A. Applicability and limitations of simplified elastic shell equations for carbon nanotubes. *J. Appl. Mech.* 71 (2004), 622.
- [20] YAKOBSON, B., BRABEC, C., AND BERNHOLC, J. Nanomechanics of carbon tubes: Instabilities beyond linear response. *Phys. Rev. Lett.* 76 (1996), 2511.

Smirnov Valeri, Ph.D.: Semenov Federal Research Center for Chemical Physics Russia Academy of Science, Department of Polymers and Composite Materials , 119991, 4 Kosygin str., Moscow, Russia (vvs@polymer.chph.ras.ru).

Manevitch Leonid, Professor: Semenov Federal Research Center for Chemical Physics Russia Academy of Science, Department of Polymers and Composite Materials , 119991, 4 Kosygin str., Moscow, Russia (manevitchleonid3@gmail.com). The author gave a presentation of this paper during one of the conference sessions.

Experimental assessment of the test station support structure rigidity by the vibration diagnostics method

Anna Šmeringaiová, Imrich Vojtko

Abstract: The paper presents the results of the impact test. The test has been done to assess the rigidity of the test station support frame. Test station was designed and constructed to test different types of gearing and belt transmissions. The test station allows to simulate different operating conditions. The procedure of the tests can be both short-term and long-term with different load levels. The basic support frame structure of the test station was evaluated as insufficient based on the results of measurement and processing of the measured low and high frequency vibration values in the verification series of experimental tests. The basic failure of the original design were the significant resonance actions that were the results of the dominant sources of vibration being near the natural frequencies of the vertical and horizontal beams of the test station base. A structural design of the test station supporting frame was designed and implemented. The impact tests were used to determine the values of the natural frequencies of the most stressed parts of the supporting structure - vertical and horizontal beams, before and after implementation of structural modifications. The comparability of the impact test results was determined by adherence to identical measurement conditions.

1. Testing station for dynamic testing of toothed and belt gear drives

When designing the gearbox, it is appropriate to know its dynamic characteristics. With improperly selected gearbox parameters, especially in transient states, there can be a high dynamic stress on their functional parts. There was designed and built a test station to realize the dynamic tests of gears at Department of Technical Systems Design and Monitoring, Faculty of Manufacturing Technologies of the Technical University of Košice with the seat in Prešov (see Fig. 1a). Designed test station allows to realize both, short and long-term comparative tests of various types of gearboxes. It is possible to test gearboxes with various design and technological modifications, to reduce their dynamic load in order to improve their parameters and increase their service life. The principle scheme and functional description of the test station is shown in [8].

1.1. Functional testing of the test station and verification of the proposed methodology for dynamic testing

The basic requirement for functional use of the test station was the achievability of objective and comparable results of the experiments. The main goal of the tests first stage was to verify the

functionality of the test station and of used measuring instruments and equipment. From this point of view, the selection of methods for measuring the wear of the functional parts of gears and diagnostic methods to assess their technical condition were also considered. Commonly manufactured Z80-J-010-P single-stage worm gear units were used as a test object. During the experimental operation, the technical conditions of the worm gear units were monitored in two different operating modes. The operating conditions have been deliberately designed to achieve a maximum of $70 \div 80$ % of the nominal transmission power guaranteed by the manufacturer and to stabilize the oil temperature below the limit. The following parameters (dynamic characteristics) were measured and evaluated for the tested worm gear units: load amplitude magnitudes and frequency, oil temperature, worm gear teeth wear. A detailed description of the preparation and course of a series of validation experimental measurements are described in [8, 9].

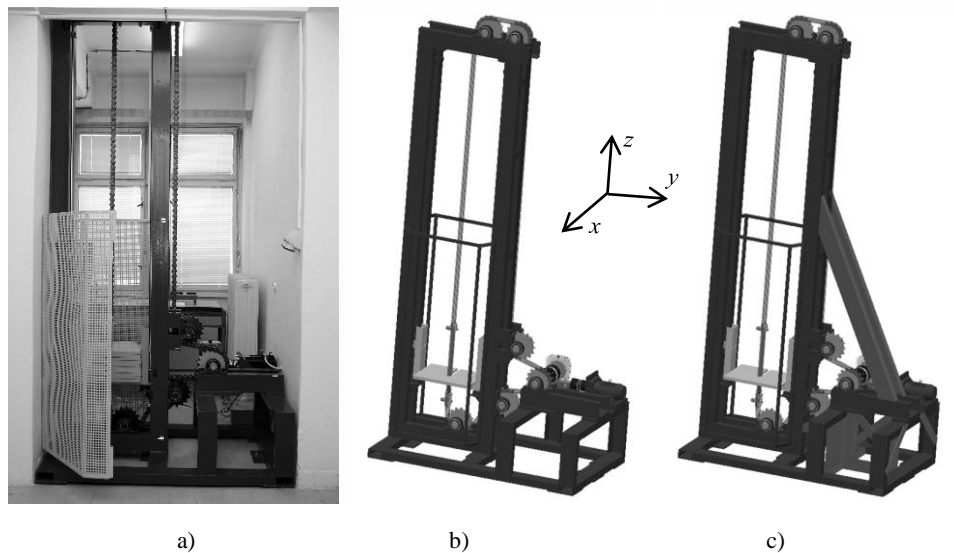


Figure 1. Dynamic Transmission Testing Station a), 3D stand model b) before and c) after the structural modification

1.2. Verification test results evaluation.

According to [9], results of measurements of dynamic quantities (temperature, vibration, ultrasound) were found:

- significant difference in measured parameters depending on transmission load,
- significant changes in the measured parameters during heating, the effect of thermal expansion on the clearance in the teeth of the worm gear, bearings and chain, until the temperature has stabilized.

- significant resonance events, high mechanical vibrations above the Alarm 2 recommended limit (hazard according to Vibration Severity Standard [2]) especially in area of the vertical beam and the horizontal frame under the sprocket, the transmission of these vibrations to the gearbox and a significant deterioration of the meshing conditions on the gears,
- unfavorable operating conditions when starting the engine (gearbox), mainly due to higher load, oscillation and insufficient chain guidance, and again transfer of vibrations to the gearbox.

The elementary structure of the test station was evaluated as unsatisfactory based on the results of measurement and processing of measured values of low-frequency and high-frequency vibrations in the verification series of experimental tests. The main drawback of the original design were significant resonance events, which were due to the fact that the dominant sources of vibration were close to the natural frequencies of the vertical and horizontal beam of the test station base structure.

In order to ensure acceptable measurement results of the tested gearboxes, it was necessary to prevent the occurrence of adverse resonance events and the occurrence of high mechanical vibrations inside the mechanical system (testing facility).

2. Solving adverse resonance events

In vibrodiagnostics and when performing rotating machine failures identification, in addition to common failures, we occasionally encounter a special error that is not actually a malfunction. It is a feature of a device that, in a given configuration, adversely affects the operation of the device. It is a resonance, resonance phenomenon or operation at critical speed. The problem arises with devices in which the excitation force frequency is identical to the intrinsic resonant frequency. For example, if the electric motor speed is the same as the natural resonant frequency of the mechanical system. In this case, even a small imbalance causes a high response in the system and high vibrations are generated. In order to eliminate this phenomenon, it is first of all necessary to identify it and to determine its intrinsic resonant frequencies. Usually, the natural frequencies are determined by the impact tests (Bump Test).

In general, there are two options how to solve resonant phenomena:

- a) changing the frequency of the driving force, (engine shaft revolutions),
- b) tuning the system, that means moving the resonant band to a frequency range where there is no excitation.

Generally for resonant frequency f_r :

$$f_r = \frac{1}{2\pi} \sqrt{\frac{k}{m}}, \quad (1)$$

where k is force constant (rigidity) and m is weight. From the equation (1) it follows that as the rigidity (k) increases, the resonance frequency increases and with the increase in mass (m) the resonance frequency decreases.

In this case, the option b) - optimization of the structure of the supporting frame was chosen for the solution of resonance phenomena. The aim is to increase the rigidity of the test station base structure. Frame reinforcement and other measures, such as chain guiding and adequate fastening of weights, should have a positive effect on eliminating vibrations and shifting the resonant band of the base structure beyond the frequency range of the driving forces. The design of the supporting frame of the testing station was developed and implemented. The 3D model of the test station with the designed structural modification is shown in Fig. 1c. By measuring and comparing the natural frequencies of the basic design of the test station before and after the design changes, the control of the fulfillment of the expected target was performed.

3. Impact test (Bump test)

The intrinsic frequencies of the mechanical system were determined by the bump test in the resting state of the mechanical system:

- a) Before design of the test station, after completion of the functional tests described in [9].
- b) After modification of the test station frame support design.

The natural frequencies of the most stressed parts of the supporting structure (vertical and horizontal beam) and of the tested worm gearbox before and after the design modifications were determined. The comparability of the bump test results was conditioned by observing identical measurement conditions.

3.1. Description of the bump test conditions

Used measuring instruments and aids:

- measurement system OKTALON, graphical programming software LabVIEW with measurement algorithms – recording and processing of the measured signal,
- vibration acceleration sensor - ACC-100 mV/g, fixing - flat magnet,
- impact hammer.

Measurement procedure:

- Calculation of expected excitation force frequencies (operating frequencies values) – Table 1.
- Preparation of measuring system and vibration measuring aids.
- Choice of united coordinate system - Fig. 1.
- Determination of measuring points, location of sensors, direction and sense of impact – Fig. 2a, 5a, 7a and Fig. 9a.

- Measurement at selected measurement locations: vibration acceleration sensor mounting, bump hammer strike near the sensor, vibration acceleration dumping time recording.
- Signal processing: vibration velocity waveform as a result of vibration acceleration time wave integration, FFT vibration velocity time waveform analysis, graphical and tabular processing of dominant frequencies.
- Comparison of bump test results before and after design – Table 2.

3.2. Bump test - Measurements Results

At figures 2a, 5a, 7a and Fig. 9a the location and course of the bump test at selected locations are shown. The direction of sensing the vibration signal and the direction of the modal hammer bump are indicated. After bumping in the indicated direction, the vibrations generated were recorded by a vibration acceleration sensor.

Measurement 1 – Measurement of the natural frequency in vertical direction.

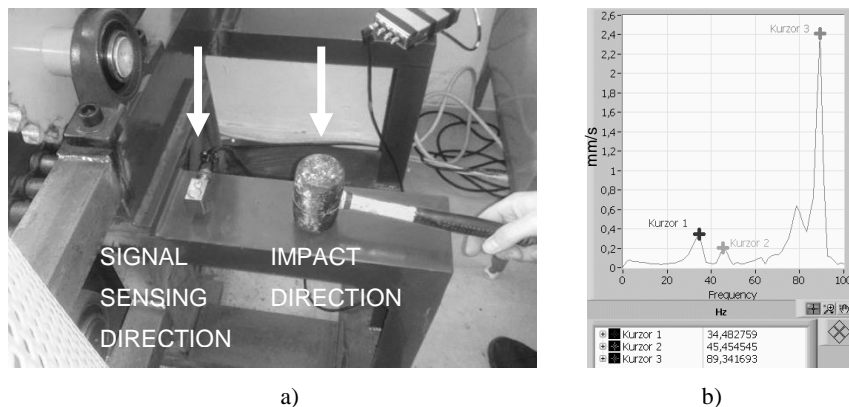


Figure 2. Measurement 1 – Measurement of the natural frequency in vertical direction. a) measurement execution b) frequency spectre before the design change

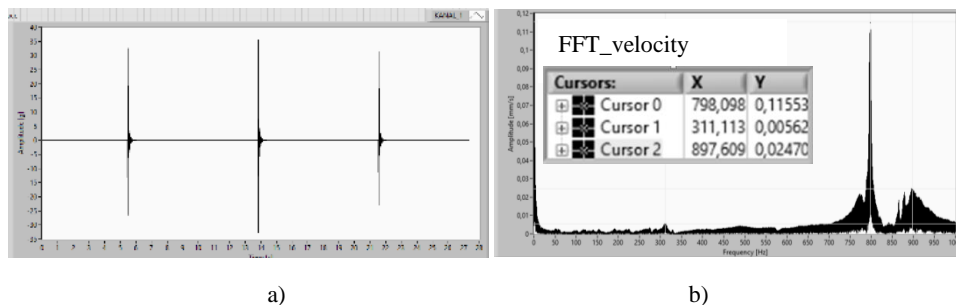


Figure 3. Measurement 1 a) time course of vibration acceleration b) FFT- velocity after design change

Figures 2b, 5b, 7b and Fig. 9b are shown details of frequency analysis of the shock damping time course with the indication of the dominant frequencies obtained from the measurement before test station redesign and at figures 3, 4, 6, 8 and 10 are shown the results of a frequency analysis time course of the shock damping after design changes have been made.

Regarding the determination of natural frequencies, it does not matter whether the spectrum is calculated from the ACCELERATION or VELOCITY time course. The frequencies in the spectrum are in the same positions on the "x" axis. The only difference is that VELOCITY is calculated from acceleration by integration. This proportionally amplifies the lower frequencies and suppresses the higher frequencies.

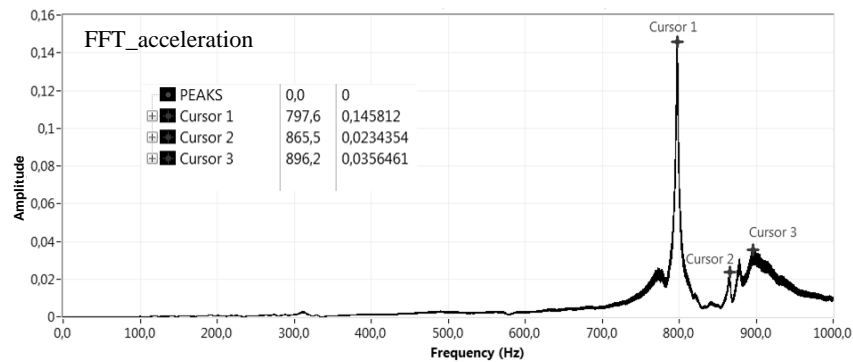


Figure 4. Measurement 1 – frequency spectre after design modification

Measurement 2 – Measurement of natural frequency of the table with drive mechanism in horizontal direction

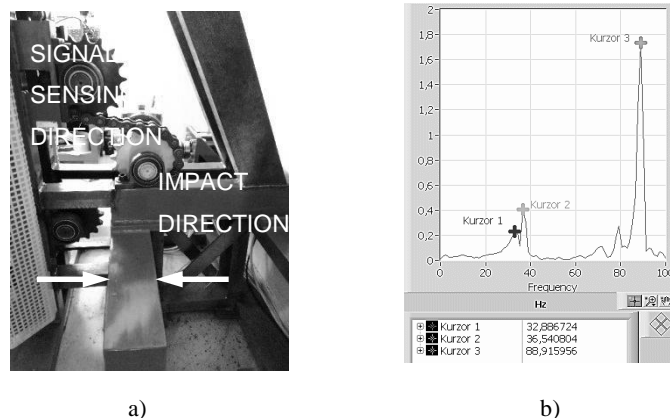


Figure 5. Measurement 2 – Measurement of natural frequency of the table in horizontal direction, a) measurement execution, b) frequency spectre before the design

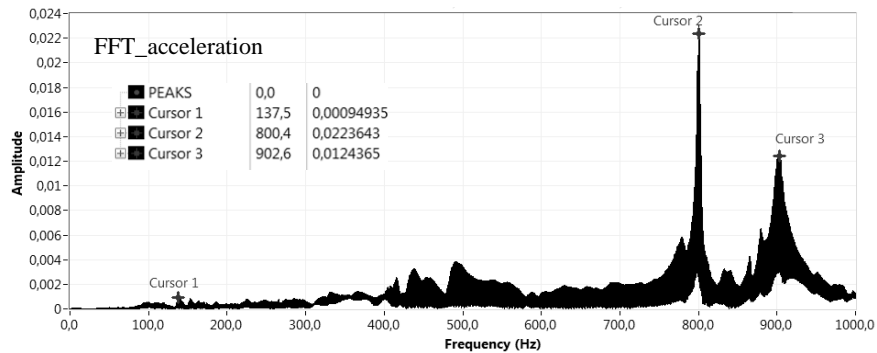


Figure 6. Measurement 2 – dominant frequencies identified after the design change

Measurement 3 – Measurement of natural frequency of vertical frame

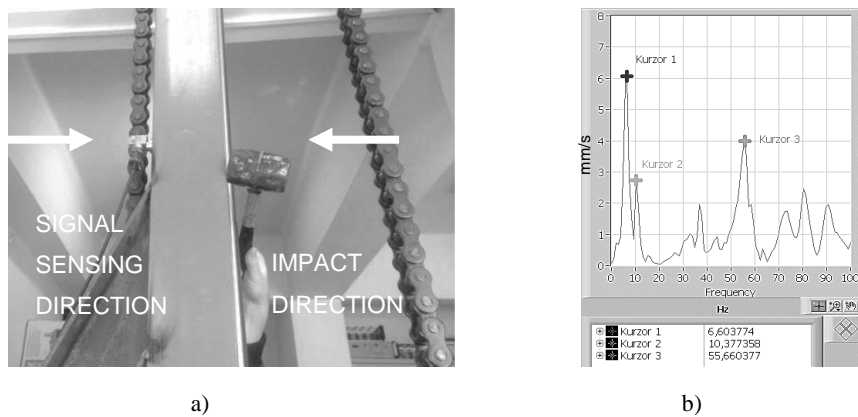


Figure 7. Measurement 3 – Measurement of natural frequency of the vertical frame, a) measurement execution, b) frequency spectre before the design modification

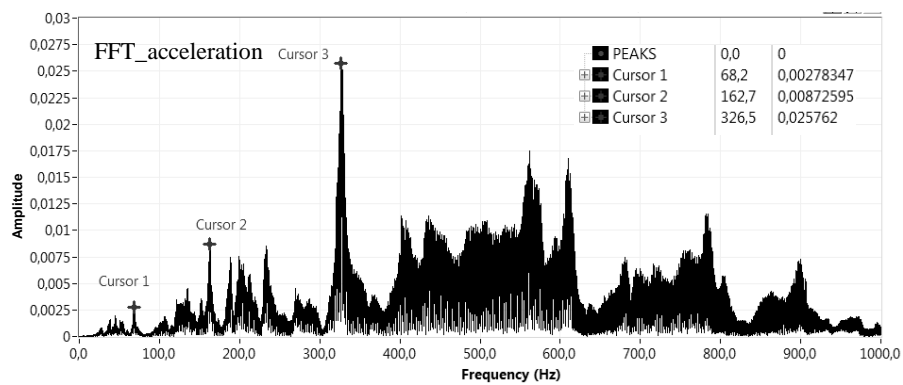


Figure 8. Measurement 3 - Measurement of natural frequency of the vertical frame

Measurement 4 – Measurement of the natural frequency of worm gear – horizontally in worm gear axis direction

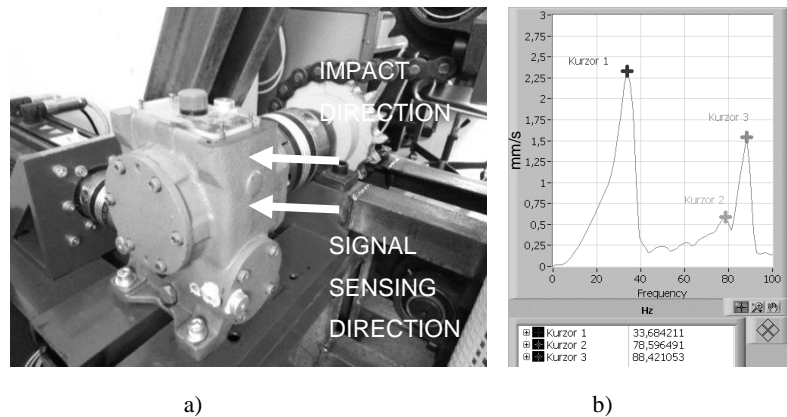


Figure 9. Measurement 4 – Measurement of the natural frequency of the worm gearbox, a) measurement execution, b) frequency spectre before the design change of the frame

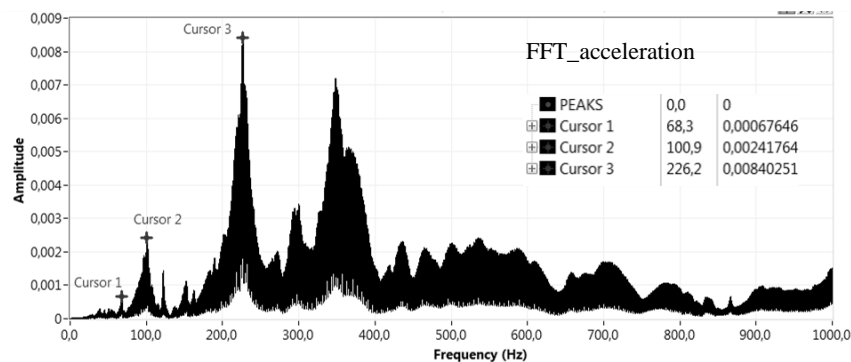


Figure 10. Measurement of gearbox natural frequency in worm gear axis direction

4. Evaluation of natural frequency measurement results

To suppress possible resonance events in the process of experimental operation of the tested gearboxes, we chose to tune the system by changing the rigidity of the base frame of the test station. Based on the analysis of the results of the above described functional tests of the worm gears and results of the bump test, there were found high mechanical vibrations of mainly vertical "lift" beams and horizontal table beam under the sprocket were found. The transmission of these vibrations to the gearbox during operation in the short term significantly worsened the meshing conditions in the worm gear. The aim of the design modifications was to increase the stiffness of the basic structure, especially the vertical frame and table base on which the machine drive mechanism is mounted.

A repeated bump test revealed a significant shift of the natural frequencies of both vertical and horizontal beams in the frequency spectrum (see Table 2). After the frame has been reinforced, there has been a significant decrease in the vibration velocity amplitude and a shift of the dominant frequencies far beyond the operating values of the excitation forces frequencies. This occurrence had happened in both the vertical and horizontal directions. For example, in the case of a horizontal table beam, the dominant frequencies have shifted from the range from 30 Hz to 90 Hz to near 800 Hz. This is a prerequisite for obtaining objective results of planned experimental measurements also for other transmissions and other operating conditions.

The natural frequencies of the worm gear housing were also measured repeatedly. The drift of dominant frequency values with significant amplitude peaks can be explained as a result of gearbox disassembly and reattachment on a reinforced table.

Table 1 Expected frequency - basic calculation

Structural Node	Frequency	
	Cycles / min	Hz
Engine, input into gearbox, Clutch, Worm	1400	23,3
Output of the Gearbox, Sprocket	45,16	0,753
Transmission chain, frequency of chain links	768	12,80

Table 2. Frequencies with dominant vibration values before and after design

	Frequency [Hz]			
	Measurement 1	Measurement 2	Measurement 3	Measurement 4
Condition before design change	34,5	32,9	6,6	33,7
	45,5	36,5	10,4	78,6
	89,3	88,9	55,7	88,4
Condition after design change	797,6	137,5	68,2	68,3
	865,5	800,4	162,7	100,9
	896,2	902,6	326,59	226,2

5. Conclusions

Vibration diagnostics belongs to modern methods of non-destructive technical diagnostics, by means of which it is possible to determine the current technical state of various production machines and equipment directly in the process of operation. The aim of the design modifications of the testing station for dynamic testing of toothed and belt drives was to eliminate the danger of resonance and increase the stiffness of the basic stand structure. A bump test performed under the same conditions before and after frame reinforcement confirmed that by the structural modification of the testing

facility was achieved a higher rigidity of the base frame. Shifting the natural frequencies, especially of the vertical and horizontal beam, outside the operating frequencies of the tested transmissions is a necessary condition for achieving objective results of the planned experiments.

Acknowledgments

Authors thank for supporting this research by grant VEGA 1/0910/17 of Agency of Ministry of Education, Science, Research and Sport of the Slovak Republic.

References

- [1] Biloš, J. and Bilošová, A., *Aplikovaný mechanik jako součást týmu konstruktérů a vývojářů: část Vibrační diagnostika*, VŠB TU Ostrava, 2012.
- [2] ISO 10816-3:2009 Mechanical vibration. Evaluation of machine vibration by measurements on non-rotating parts - part 3
- [3] Krenický, T., Ružbarský, J. and Panda, A., Operation and Diagnostics of Machines and Production Systems Operational States 3. *Key Engineering Materials* Vol. 669, Pfaffikon: Trans Tech Publications (2016), p. 596.
- [4] Maščeník, J. and Vojtko, I., Experimental monitoring and diagnostics of belt gears in testing device. In: *MM Science Journal*. Vol. 2016, no. September (2016), p. 964-968.
- [5] Murčinková, Z., Murčinko, J. and Adamčík, P., The multi-parameter on-line monitoring system applied for rotating machinery. In: *Review of Industrial Engineering Letters*. Vol. 3, no. 2 (2016), p. 19-28.
- [6] Pavlenko, S., Maščeník, J. and Krenický, T., *Worm gears: general information, calculations, dynamics and reliability*. Lüdenscheid: RAM-Verlag, 2018.
- [7] STN ISO 2041 Vibration and shock. Vocabulary
- [8] Šmeringaiová, A., Vojtko, I., and Monková, K. Experimentelle Analyse der Dynamik von Zahnradgetrieben – Teil 1. *tm-Technisches Messen* 82, 2 (2015), p. 57-64.
- [9] Šmeringaiová, A., Vojtko, I., and Monková, K. Experimentelle Analyse der Dynamik von Zahnradgetrieben – Teil 2. *tm-Technisches Messen* 82, 4 (2015), p. 224-232.
- [10] Žiaran, S., *Nizkofrekvenčný hluk a kmitanie*. Bratislava: STU, 2016. 316 s.

Anna Šmeringaiová, Ph.D.: Faculty of Manufacturing Technologies of the Technical University of Košice with a seat in Prešov, Bayerova 1, 080 01 Prešov, Slovakia (anna.smeringaiova@tuke.sk).

Imrich Vojtko, M.Sc.: Faculty of Manufacturing Technologies of the Technical University of Kosice with a seat in Prešov, Bayerova 1, 080 01 Prešov, Slovak Republic (imrich.vojtko@tuke.sk).

Parameters estimation by harmonic probing of hysteresis models of bolted jointed

Rafael Teloli, Samuel da Silva, Gaël Chevallier

Abstract: This paper proposes parameters estimation of hysteresis effect by fitting an approximation of the higher-order frequency response functions (FRFs) described using the Bouc-Wen model. The higher-order FRFs are obtained handling the harmonic probing of a previous smoothing of this Bouc-Wen model. The approach is tested using the nonlinear vibrations time-series measured in an assembled structure of a bolted joint. The estimated model reproduces the hysteretic damping and the hysteresis restoring force for a broader level of bolt preload torque adequately.

1. Introduction

Hysteresis effect appears in all the engineering fields, such as wind turbines, bit-rock interaction in drill strings, damper devices, aerospace structures, among others. In particular, jointed structures by bolted are stimulating an international research effort which intends to advance alternative forms of dealing with features concerning frictional contact, variations in the stiffness and damping with the micro-slip regime or even softening effects [6].

One traditional approach to represent such systems is through numerical models [2]. In this context, these models must be capable of capturing the nonlinear features of jointed structures, including the presence of the hysteresis effect. There are some simplified models in the literature to achieve this task, such as the LuGre model, the classical Iwan model, the Bouc-Wen model, or even models with amplitude-dependent restoring force. Despite the applicability of the Bouc-Wen model to represent many engineering systems, such as magnetorheological dampers, piezoelectric actuators, and energy dissipation systems, its use for capturing the dynamic behavior in jointed structures is still modest [3]. Recently, Teloli and da Silva (2019) [1] introduced a new approach for harmonic probing of hysteretic systems through a nonlinear smooth operator. The authors predicted, using closed-form solutions, the output of a Bouc-Wen oscillator after rewriting the loading and unloading regimes of the hysteresis loop through smooth operators, which are based on the Taylor series procedure.

The multidimensional Fourier transform of the Volterra kernels, so-called higher-order frequency response functions (FRFs) and obtained through the classic harmonic probing method in Teloli and da Silva (2019), is an attractive framework for white-box modeling,

aiming into an alternative tool for model updating purposes. Toward this background, this paper proposes a parameter estimation using these higher-order FRFs the of a simplified hysteresis model of Bouc-Wen for a cantilever aluminum beam that carries a bolted connection at its middle.

The paper is organized as follows. First of all, an overview of the higher-order FRFs for hysteretic systems by using harmonic probing. Next point discussed is the estimation of the parameters of the Bouc-Wen model for the bolted joint of the assembled structure. Finally, the conclusion pointed out the benefits of the proposed procedure.

2. Overview of the higher-order FRFs for hysteretic systems

This section compiles the main results reached in Teloli and da Silva (2019) [1], beginning with the smoothing procedure employed for the Bouc-Wen model, and then performing the framework for determining the analytical expressions of the higher-order FRFs.

2.1. On the smoothing of the Bouc-Wen model

The single-degree-of-freedom Bouc-Wen model is given by:

$$\ddot{y}(t) + 2\zeta\omega_n\dot{y}(t) + ky(t) + \mathcal{Z}(y, \dot{y}) = \tilde{u}(t) \quad (1)$$

$$\dot{\mathcal{Z}}(y, \dot{y}) = \alpha\dot{y}(t) - \gamma|\dot{y}(t)| |\mathcal{Z}(y, \dot{y})|^{\nu-1} \mathcal{Z}(y, \dot{y}) - \delta\dot{y}(t) |\mathcal{Z}(y, \dot{y})|^\nu \quad (2)$$

where ω_n is the natural frequency, ζ is the damping ratio, k is a normalized stiffness coefficient and $\ddot{y}(t)$, $\dot{y}(t)$ and $y(t)$ are the acceleration, velocity and displacement, respectively, of the hysteretic oscillator when subjected to an input $\tilde{u}(t)$, whereas $\mathcal{Z}(y, \dot{y})$ is the hysteretic restoring force that obeys the differential term $\dot{\mathcal{Z}}(y, \dot{y})$. α , γ , δ and ν are the Bouc-Wen parameters. For this paper, it set $\nu = 1$.

The hysteretic restoring force of the Bouc-Wen model allows its division into four different paths. Moreover, since the hysteresis force is weak, each of these paths can be smoothed by a functional expansion through the Taylor series approach:

- path (i): $\dot{y} \leq 0, \mathcal{Z} \geq 0$

$$\mathcal{Z}_1 \approx \frac{\alpha}{(\delta - \gamma)} \left(1 - \left[\sum_{n=0}^{\infty} \frac{[-(\delta - \gamma)]^n (y - y_0)^n}{n!} \right] \right) \quad (3)$$

- path (ii): $\dot{y} \leq 0, \mathcal{Z} \leq 0$

$$\mathcal{Z}_2 \approx -\frac{\alpha}{(\delta + \gamma)} \left(1 - \left[\sum_{n=0}^{\infty} \frac{[(\delta + \gamma)]^n (y - y_0)^n}{n!} \right] \right) \quad (4)$$

- path (iii): $\dot{y} \geq 0, \mathcal{Z} \leq 0$

$$\mathcal{Z}_3 \approx -\frac{\alpha}{(\delta - \gamma)} \left(1 - \left[\sum_{n=0}^{\infty} \frac{[(\delta - \gamma)]^n (y + y_0)^n}{n!} \right] \right) \quad (5)$$

- path (iv): $\dot{y} \geq 0, \mathcal{Z} \geq 0$

$$\mathcal{Z}_4 \approx \frac{\alpha}{(\delta + \gamma)} \left(1 - \left[\sum_{n=0}^{\infty} \frac{[-(\delta + \gamma)]^n (y + y_0)^n}{n!} \right] \right) \quad (6)$$

Moreover, when a BIBO hysteretic system is subjected to a harmonic excitation force $u(t) = A \cos(\omega t)$, its hysteresis loop is described by loading and unloading paths, bounded in the displacement interval of $[y_{\min}, y_{\max}]$. Thus, since that any bounded function into a determined interval admits a polynomial approximation, Teloli and da Silva (2019) suggested the following bounding functions according to the order used in the Taylor series approach:

$$\mathcal{F}^\uparrow[y(t)] = \lambda_0 + \lambda_1 y(t) - \lambda_2 y^2(t) + \lambda_3 y^3(t) \quad \text{for} \quad \text{sign}[\dot{u}(t)] \geq 0 \quad (7)$$

$$\mathcal{F}^\downarrow[y(t)] = -\lambda_0 + \lambda_1 y(t) + \lambda_2 y^2(t) + \lambda_3 y^3(t) \quad \text{for} \quad \text{sign}[\dot{u}(t)] \leq 0 \quad (8)$$

where λ_0 [N], λ_1 [N/m], λ_2 [N/m²] and λ_3 [N/m³] are their coefficients. The coefficients of the polynomial form are expressed as a function of the Bouc-Wen parameters by minimizing an error function described by:

$$E(\lambda_0, \lambda_1, \lambda_2, \lambda_3) = \int_{-Y}^{y_0} \left\{ \mathcal{Z}_2 - \mathcal{F}^\downarrow[y(t)] \right\}^2 dy + \int_{y_0}^Y \left\{ \mathcal{Z}_1 - \mathcal{F}^\uparrow[y(t)] \right\}^2 dy \quad (9)$$

subjected to $\frac{\partial E}{\partial \lambda_i} = 0$, for $i = 0, 1, 2, 3$. This results in the following expressions:

$$\lambda_0 = \frac{\alpha y_0}{16} (3\delta Y + 8\gamma y_0 - 16) \quad (10)$$

$$\lambda_1 = \alpha \quad (11)$$

$$\lambda_2 = \frac{\alpha}{16Y} (8\delta^2 Y y_0 + 8\gamma^2 Y y_0 + 15\delta\gamma y_0^2 - 8\gamma Y - 15\delta y_0) \quad (12)$$

$$\lambda_3 = \frac{\alpha}{96Y^5} \left(16\delta^2 Y^5 + 70\delta\gamma Y^4 y_0 - 70\delta\gamma Y^2 y_0^3 - 35\delta Y^4 + 105\delta Y^2 y_0^2 - 105\delta y_0^4 \right) \quad (13)$$

where $Y = |y_{\min}| = |y_{\max}|$ and y_0 is a threshold displacement. These equations are valid only for harmonic excitations that ensure a weak hysteretic force and when the force \times displacement plane draws a single loop.

The Bouc-Wen model holds the rate-independent property. Due to this alongside with the symmetry of the hysteresis loop, the bounding functions present an equivalent structure. Further, it is worthy of note that the switch between bounding functions occurs according to $\text{sign}[\dot{u}(t)]$. Thus, it is proposed an equivalent system with hysteresis:

$$\ddot{y}(t) + 2\zeta\omega_n\dot{y}(t) + ky(t) + \underbrace{u_0(t) + \lambda_1 y(t) + \varrho y^2(t) + \lambda_3 y^3(t)}_{=\mathcal{F}[y(t)]} = \tilde{u}(t) \quad (14)$$

where $\mathcal{F}[y(t)]$ is the nonlinear operator responsible for encoding the hysteretic characteristics smoothly, and ϱ is defined as $\varrho = \lambda_2$ ($\varrho = -\lambda_2$ for $\text{sign}[\dot{u}(t)] < 0$ ($\text{sign}[\dot{u}(t)] > 0$)). Additionally, the term $u_0(t) = \lambda_0\Phi[\dot{u}(t)]$, which is considered as an additional input applied to the equivalent system, is given by:

$$u_0(t) = \frac{j2\lambda_0}{\pi} \underbrace{\sum_{k=1}^2 \left(\frac{e^{-j[1+2(k-1)]\omega t} - e^{j[1+2(k-1)]\omega t}}{1 + 2(k-1)} \right)}_{=\Phi[\dot{u}(t)]} \quad (15)$$

where $\Phi[\dot{u}(t)]$ is the complex exponential Fourier series up to the second term.

2.2. Higher-order FRFs

For multi-input and single-output (MISO) systems, the functional of the Volterra series in continuous time domain is given by [5]:

$$\begin{aligned} y(t) &= \sum_{\eta=1}^{\infty} y_{\eta}(t) = \sum_{p=1}^j \sum_{k=1}^j \cdots \sum_{n=1}^j \int_{\mathbb{R}^{\eta}} h_{\eta}^{(u_p, u_k, \dots, u_n)}(\tau_1, \tau_2, \dots, \tau_{\eta}) \\ &\times \prod_{i=1}^{\eta} u_p(t - \tau_1) u_k(t - \tau_2) \dots u_n(t - \tau_{\eta}) d\tau_1 d\tau_2 \dots d\tau_{\eta} \end{aligned} \quad (16)$$

where $y_{\eta}(t)$ is each contribution of the total output $y(t)$, and the term $h_{\eta}^{(u_p, u_k, \dots, u_n)}(\tau_1, \tau_2, \dots, \tau_{\eta})$ is called Volterra kernel related to the j^{th} input. The multi-dimensional Fourier transform of the Volterra kernels for multi-inputs can be calculated by [7]:

$$\begin{aligned} \mathcal{H}_{\eta}^{(u_p, u_k, \dots, u_n)}(\omega_1, \omega_2, \dots, \omega_{\eta}) &= \int_{\mathbb{R}^{\eta}} h_{\eta}^{(u_p, u_k, \dots, u_n)}(\tau_1, \tau_2, \dots, \tau_{\eta}) \times \\ &\prod_{i=1}^{\eta} e^{-j\omega_i \tau_i} d\tau_1 d\tau_2 \dots d\tau_{\eta} \end{aligned} \quad (17)$$

where $\mathcal{H}_\eta^{(u_p, u_k, \dots, u_n)}(\omega_1, \omega_2, \dots, \omega_\eta)$ are the higher-order frequency response functions, which can be used to describe the system output for any input with a well-known mathematical expression. Additionally, the computation of the analytical expressions for each higher-order FRFs is carried out through the harmonic probing method. In this work, the harmonic probing method is applied considering the equation (14), resulting in higher-order FRFs expressions which take into account the Bouc-Wen parameters.

3. Identification procedure based on higher-order FRFs

Figure 1 presents the jointed structure investigated. The test rig is formed of two aluminum beams, each one with dimensions of $270 \times 25.4 \times 6.35$ mm and assembled by a bolted joint with a tightening torque of 5 Nm. The excitation of the structure was conducted by Modal Shop 2400E shaker located at 85 mm from the clamped end of the cantilever beam. Due to observability purposes for modeling the first vibrating mode of the structure, the system output was measured at the free end of the beam, using a laser vibrometer Polytec®OFV-525/5000S. The data acquisition system is the LMS SCADAS. This paper regards the voltage supplied by the shaker amplifier as the excitation signal.

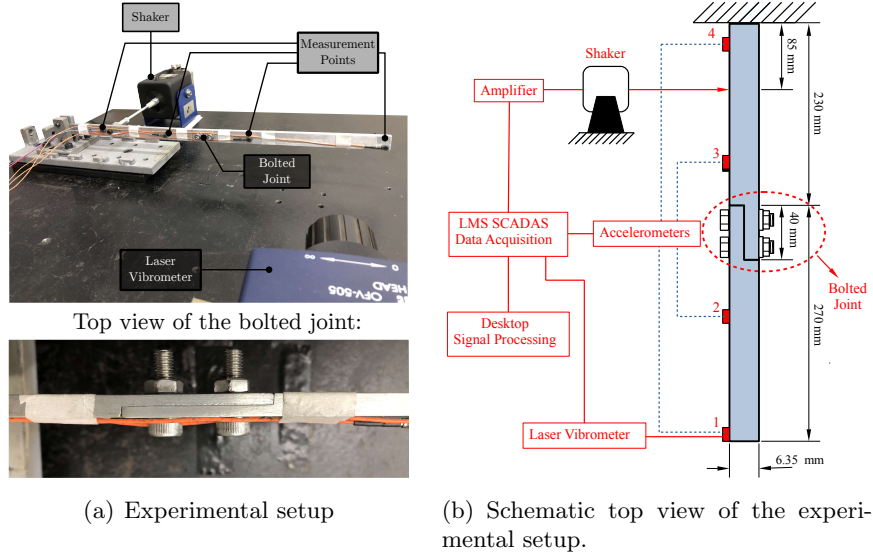


Figure 1. Experimental setup and the schematic representation illustrating the cantilever beam which carries a bolted joint connection.

Figure 2(a) illustrates the receptance calculated during a sweep sine test from 0 to 40 Hz (around the first mode) regarding different input levels supplied in the shaker amplifier,

0.05 (low force level), 0.10 (medium force level) and 0.20 V (high force level). On the receptance, it is worthy of remark that the FRF begins to exhibit distortions and shifts in the resonant peak as the input force level increases. Further, Figure 2(b) depicts the frequency response curve for a stepped sine test from 3 up to 23 Hz, which indicates that the resonant frequency decreases when the forcing amplitude increases, revealing the bolted joint softening operation.

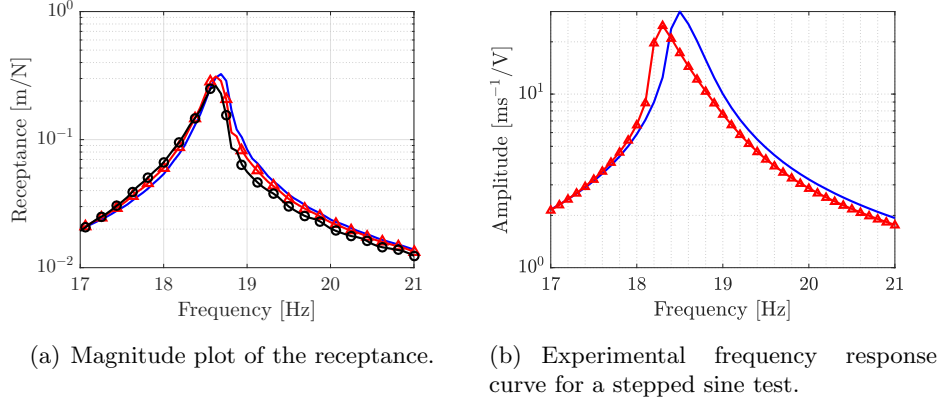


Figure 2. Frequency response plots for different excitation amplitudes: — for low amplitude level (0.05 V), \triangle for medium amplitude level (0.10 V), and \circ for high amplitude level (0.20 V).

Figure 3 shows the identification procedure proposed here. The initial action consists in identifying, during the linear regime of motion, the first-order Volterra kernel, which is given as:

$$\mathcal{H}_1(\omega) = \frac{1}{-\omega^2 + j2\omega\zeta\omega_n + \omega_n^2} \quad (18)$$

where $\omega_n = \sqrt{k + \alpha}$. The identification of this kernel is performed using the line-fit method [4] procedure on the experimental FRF, which is calculated when the system is subjected to a random noise input with low excitation level.

The second step is based on exciting the structure harmonically around one-third of the linear resonant frequency, i. e. $\frac{\omega_n}{3}$, and determining experimentally the third-order Volterra kernel, which is given by:

$$\hat{\mathcal{H}}_3(\omega, \omega, \omega) = \frac{4Y(3\omega)}{\hat{A}^3} \quad (19)$$

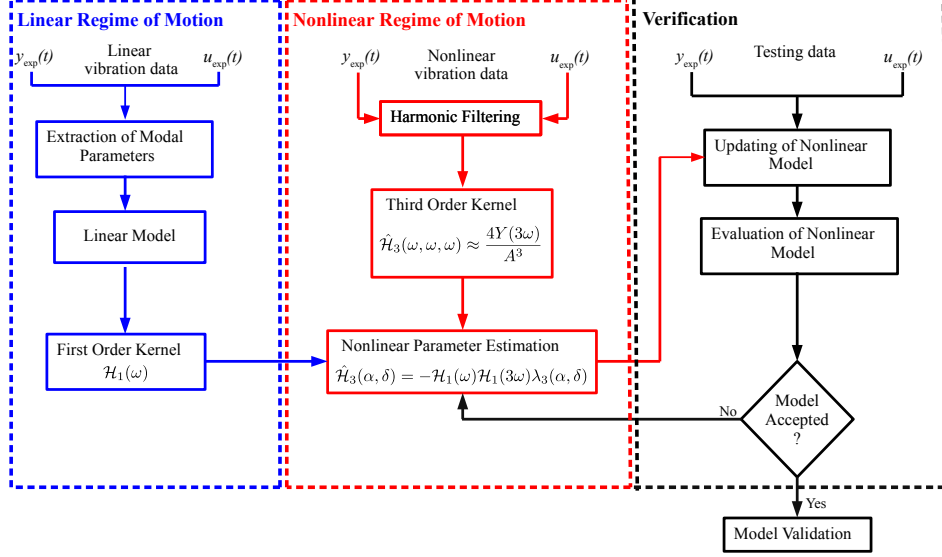


Figure 3. Description of parameters estimation procedure based on the higher-order FRFs.

where A is the input amplitude and $Y(3\omega)$ is the third-order harmonic amplitude response obtained through Fourier filtering of the output $y(t)$. When the system is harmonically excited around $\frac{\omega_n}{3}$, the hysteresis loop is almost closed ($y_0 = 0$) and the metric for nonlinear parameters estimation into the third-order Volterra kernel is given by:

$$\min J(\Theta_1) = \frac{\|\hat{\mathcal{H}}_3 - \mathcal{H}_3(\Theta_1)\|}{\|\hat{\mathcal{H}}_3\|} \quad (20)$$

subject to:

$$\begin{aligned} 0 < \alpha \leq \omega_n^2 \text{ and } \alpha + k &= \omega_n^2 \\ 0 < \delta &\leq 500 \end{aligned} \quad (21)$$

where $\Theta_1 = [\alpha \ \delta]$ is a vector which contains the Bouc-Wen parameters for updating, and $\mathcal{H}_3(\Theta)$ is the analytical kernel given by:

$$\mathcal{H}_3(\Theta_1) = -\mathcal{H}_1(\omega)\mathcal{H}_1(3\omega)\lambda_3(\Theta_1) \quad (22)$$

This work considers the sequential quadratic programming (SQP) algorithm as optimization procedure to identify the unknown parameters, and the initial conditions were chosen as $\alpha_{(ini)} = \frac{\omega_n^2}{2}$ and $\delta_{(ini)} = 250$.

Further, it is essential to point out that these parameters derived when the hysteresis loop is almost closed are held for the shape of the hysteretic cycle and, by this reason, this step is vital in the identification procedure. Thus, the next step of the proposed strategy aims to identify the last parameter γ , which controls the opening of the hysteresis loop when the jointed structure operates under a nonlinear regime of motion. The vector parameter Θ_1 to be identified into the Bouc-Wen model are presented in equations (1) and (2). The objective function to find the optimal parameters $\Theta_2 = [\gamma]$ is based on the normalized mean square error (NMSE) between the experimental output \hat{y} and the integrated numerical output of the Bouc-Wen model:

$$\min J(\Theta_2) = \frac{\|\hat{y} - y(\Theta_2)\|}{\|\hat{y} - \text{mean}(\hat{y})\|} \quad (23)$$

subject to:

$$0 < \gamma \leq \delta \quad (24)$$

where $[y(\Theta_2) \ \dot{y}(\Theta_2) \ \ddot{y}(\Theta_2)]^T$ are obtained through a numerical integration scheme with the 4th order Runge-Kutta method with variable time-step. The initial value for γ is selected as $\gamma_{(ini)} = \frac{\delta}{2}$ and, in addition, the collected testing data for this step is based on a sweep sine test applied for the first vibrating mode with high excitation amplitude. After that, to ensure that the Bouc-Wen model is able to capture accurately the nonlinear physical behavior of the experimental setup, the updated nonlinear model is evaluated and then validated.

4. Results and discussion

Figure 4(a) represents a correlation between the FRF obtained experimentally and the fitted first-order Volterra kernel from equation (18). The jointed structure was excited with a random excitation with an amplitude of 0.05 V to estimate the experimental FRF. Under this operating condition, the system behaves linearly and the identified parameters were $\omega_n = 2\pi \times 18.80$ rad/s and $\zeta = 0.44\%$. The first-order kernel is then used for feeding the analytical third-order kernel.

The structure was harmonically excited at the frequencies of [5, 5.5, 6, 6.5, 6.75] Hz with an amplitude level of 0.15 V to determine the third-order harmonic amplitude to identify

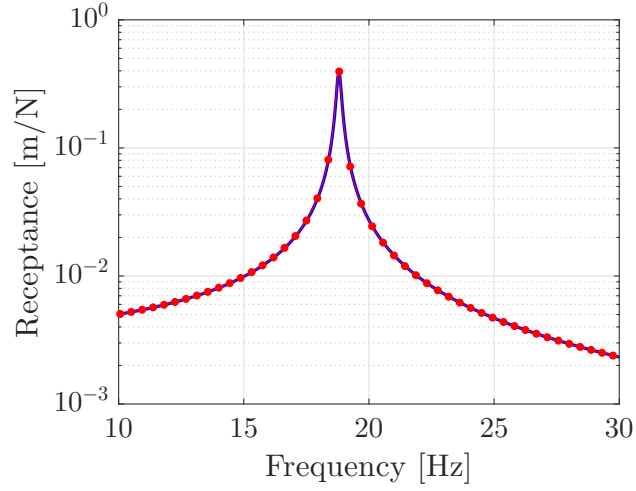


Figure 4. Estimated FRF with random input regarding an amplitude provides to the shaker of 0.05 V. — is the first-order Volterra kernel, whereas • is the experimental FRF.

the kernel $\hat{\mathcal{H}}_3$. After minimizing Eq. (19), the parameters α and δ were estimated with approximated values of 500 [N/(mkg)] and 351.42, respectively. Since that $\omega_n = \sqrt{k + \alpha}$, the value of k is close to 1345 [N/(mkg)]. Figure 4(b) shows the identified third-order Volterra kernel with a valid agreement comparing with the experimental amplitudes.

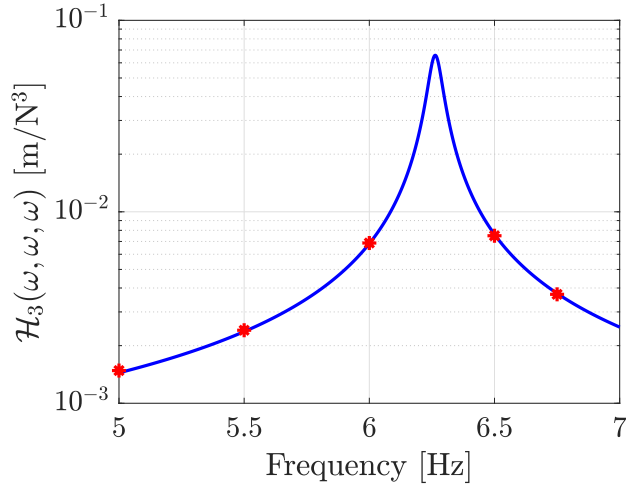


Figure 5. Diagonal of the third-order Volterra kernel estimated with an excitation amplitude of 0.15 V: — identified Volterra kernel versus • experimental.

For minimizing the objective function in equation (23) using the SQP algorithm, the

experimental output \hat{y} was measured for a sweeping sine test from 0 to 40 Hz with the amplitude level of 0.20 V. The structure behaves non-linearly under this regime of motion caused by the hysteretic damping, as shown in Figure 2. After identifying the parameter $\gamma = 12.57$, new data were measured for different excitation amplitudes intending the validation of the identified model. Figure 6 illustrates the predicted response comparing the validation data for a sweeping sine test with high excitation amplitude. This plot evidences that the Bouc-Wen model can accommodate enough accuracy of experimental setup.

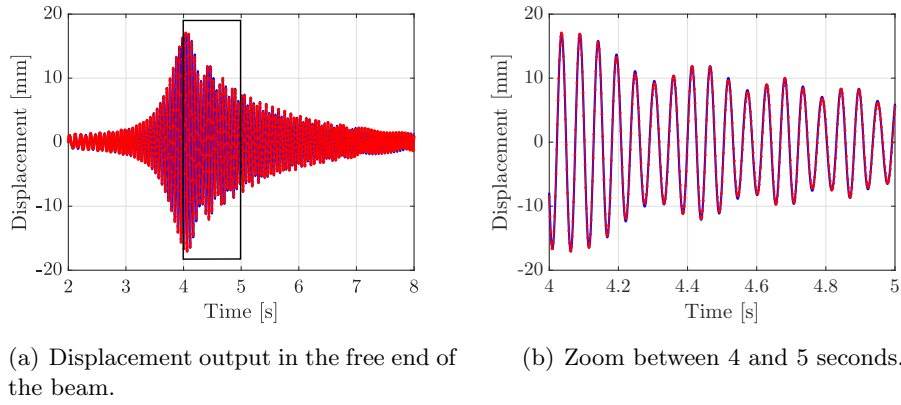


Figure 6. —identified Bouc-Wen model versus • experimental for a sweeping sine excitation with an amplitude of 0.20 V.

Another way to evaluate the performance of the identified Bouc-Wen model is by examining its hysteresis loop. Figure 7 exhibits the measured and the predicted hysteresis loops for different amplitudes applied in the shaker. In all cases, both hysteretic cycles enclose substantially the same area on the restoring force \times displacement plane.

5. Final remarks

This paper proposes an identification procedure of hysteresis parameters for structures with bolted joints based on the harmonic probing method and the higher-order FRFs framework. A white-box Bouc-Wen modeling strategy established a three-step algorithm. The effectiveness of the higher-order FRFs allows us to analyze inherent properties of the hysteretic system, for instance, the first-order Volterra kernel encoding the linear dynamics of the jointed structure, and also the third-order Volterra kernel in identifying parameters related to the shape of the hysteretic loop. Additionally, the method is based on traditional vibration data using random and sinusoidal tests. This paper attests that it is possible to use

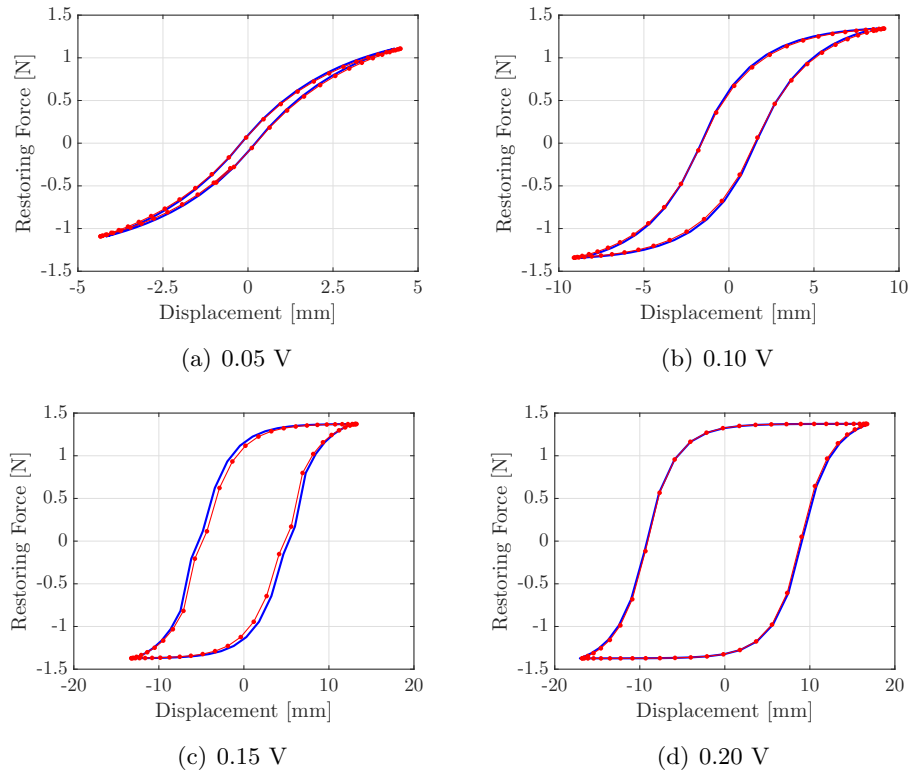


Figure 7. — hysteresis loop by the the identified Bouc-Wen model versus • experimental assuming different forcing amplitudes provides to the shaker.

Volterra series and its higher-order FRFs for a complex application involving weak hysteresis force, despite the criticism in the literature regarding dealing with industrial cases.

Acknowledgements

The authors are thankful for the financial support provided by São Paulo Research Foundation (FAPESP) Grant numbers 2016/21973 – 5, 2017/15512 – 8 and 2019/06540 – 3 and the Brazilian National Council for Scientific and Technological Development (CNPq) grant number 307520/2016-1.

References

- [1] DE O. TELOLI, R., AND DA SILVA, S. A new way for harmonic probing of hysteretic systems through nonlinear smooth operators. *Mechanical Systems and Signal Processing* 121 (2019), 856 – 875.

- [2] FESTJENS, H., CHEVALLIER, G., AND DION, J. Nonlinear model order reduction of jointed structures for dynamic analysis. *Journal of Sound and Vibration* 333, 7 (2014), 2100 – 2113.
- [3] ISMAIL, M., IKHOUANE, F., AND RODELLAR, J. The hysteresis Bouc-Wen model, a survey. *Archives of Computational Methods in Engineering* 16, 2 (Jun 2009), 161–188.
- [4] MAIA, N. M. M., AND E SILVA, J. M. M. *Theoretical and experimental modal analysis*. Research Studies Press, 1997.
- [5] SCHETZEN, M. *The Volterra and Wiener Theories of Nonlinear Systems*. John Wiley and Sons, 1980.
- [6] SEGALMAN, D. J., GREGORY, D. L., STARR, M. J., RESOR, B. R., JEW, M. D., LAUFFER, J. P., AND AMES, N. M. Handbook on dynamics of jointed structures. *Sandia National Laboratories, Albuquerque, NM 871852009* (2009).
- [7] WORDEN, K., MANSON, G., AND TOMLINSON, G. A hamonic probing algorithm for the multi-input Volterra series. *Journal of Sound and Vibration* 201, 1 (1997), 67 – 84.

de Oliveira Teloli, Rafael, Ph.D. student: UNESP - Universidade Estadual Paulista, Departamento de Engenharia Mecânica, Av. Brasil, 56, 15385-000, Ilha Solteira, SP, Brasil (rafael.teloli@unesp.br). The author gave a presentation of this paper during one of the conference sessions.

da Silva, Samuel, Associate Professor: UNESP - Universidade Estadual Paulista, Departamento de Engenharia Mecânica, Av. Brasil, 56, 15385-000, Ilha Solteira, SP, Brasil (samuel.silva13@unesp.br).

Chevallier, Gaël, Full Professor: Université de Bourgogne Franche-Comté, Département Mécanique Appliquée, 24 rue de l'Epitaphe, 25000, Besançon, France (gael.chevallier@univ-fcomte.fr).

Dynamics of non-linear processes in a backward-wave tubes chain: Chaos and strange attractors

Valentin B. Ternovsky, Alexander V. Glushkov, Eugeny V. Ternovsky and
Andrey Tsudik

Abstract: The paper is devoted to development of the effective mathematical and computational approach to studying and forecasting the complex nonlinear processes in the backward-wave tube and the backward-wave tubes chain. The general approach is based on the combining the backward-wave tube nonstationary theory equations solutions, non-linear analysis and chaos theory methods (chaos-geometric formalism). The chaos-geometric formalism includes a group of non-linear analysis and chaos theory methods such as the integral-differential equations solutions qualitative analysis, the correlation integral and average mutual information algorithms, the Lyapunov's exponents and Kolmogorov entropy analysis, nonlinear prediction models etc. As illustration we present the results of the numerical studying scenarios of generating chaos in a chain of the relativistic backward-wave tubes and computing the characteristics of chaotic dynamics for different modes of operation. The numerical data on the topological and dynamical invariants, namely, the correlation, embedding, Kaplan-Yorke dimensions, the Lyapunov's exponents, Kolmogorov entropy are listed too.

1. Introduction

As it is well known, an actual problem of relativistic microwave electronics includes, first of all, the quantitative study of the mechanisms of energy conversion of high-intensity (accelerated to relativistic velocities) electron fluxes into powerful coherent electromagnetic radiation and, of course, their use in different applications. One could remind about a great interest and importance of studying the generators of chaotic oscillations in a microwave range for plasmas heating in fusion devices, modern systems of information transmission using dynamic chaos and other applications. Among the most studied of vacuum electronic devices with complex dynamics are backward-wave tubes (BWT), for which the possibility of generating chaotic oscillations has been theoretically and experimentally found [1-12]. The BWT is an electronic device for generating electromagnetic vibrations of the super high frequencies range. Authors [3] formally considered the possible chaos scenario in a single relativistic BWT. Authors [4,5] have studied dynamics of a non-relativistic BWT, in particular, phase portraits, statistical quantifiers for a weak chaos arising via period-doubling cascade of self-modulation and the same characteristics of two non-relativistic backward-wave tubes. The authors of

[4,5] have solved the equations of nonstationary nonlinear theory for the O-type BWT without account of the spatial charge, relativistic effects, energy losses etc. It has been shown that the finite-dimension strange attractor is responsible for chaotic regimes in the BWT. The multiple studies [1-8], increasing the beam current in the system implemented complex pattern of alternation of regular and chaotic regimes of generation, completes the transition to a highly irregular wideband chaotic oscillations with sufficiently uniform continuous spectrum.

In this paper we present the results of studying dynamical characteristics of non-linear processes in the chain of relativistic BWT and analysis and modeling the parameters for of the corresponding chaotic time series, which are the solutions of the BWT integral-differential dynamical equations. The computational chaos-geometric approach includes a combined set of non-linear analysis and chaos theory methods such as an autocorrelation function method, correlation integral approach, average mutual information, surrogate data, false nearest neighbours algorithms, the Lyapunov's exponents and Kolmogorov entropy analysis, spectral methods and nonlinear prediction (predicted trajectories, neural network etc) algorithms (in versions [8-23]). The chaotic dynamics data for the chain of the relativistic BWTs are firstly obtained. All computing is performed with using "Geomath" and "Quantum Chaos" computational codes [8-12,23-31].

2. Dynamics of relativistic backward-wave tube and chain of tubes

As it is known (c.g., [3-8]), a nonlinear dynamics of the BWT system is described by means of the non-stationary nonlinear theory equations for an amplitude of an electromagnetic field and a motion of the beam:

$$\partial^2 \theta / \partial \xi^2 = -(1 + \nu \partial \theta / \partial \xi)^{3/2} \text{Re} \{ 1/2 L [\delta(\xi) + \delta(\xi - L) F e^{i\theta}] \} \quad (1a)$$

$$\partial F / \partial \tau - \partial F / \partial \xi = - \left[1/\pi \int_0^{2\pi} e^{-i\theta} d\theta_0 \right] 1/2 L [\delta(\xi) + \delta(\xi - L)] \quad (1b)$$

with boundary conditions:

$$\begin{aligned} \theta(0, \tau) &= \theta_0, \\ \partial \theta(0, \tau) / \partial \xi &= 0, \\ F(L + 0, \tau) &= 0. \end{aligned} \quad (2)$$

Here $\theta(\xi, \tau, \theta_0)$ is a phase of the electron, which runs in a space of interaction with the phase θ_0 in a field, $F(\xi, \tau)$ is a dimensionless complex amplitude of the wave $E(x, t) = \text{Re}[E_0(x, t) \exp(i\omega_0 t - i\beta_0 x)]$, $\xi = \beta_0 C x$ is the dimensionless coordinate, parameter $L = \beta_0 l C = 2\pi C N$ is the dimensionless length of the interaction space, l is a length of the system, N is a number of slow waves, covering over the length of system,

$C = \sqrt[3]{I_0 K_0 / (4U)}$ is the known Pierce parameter, I_0 is a current of beam, U is an accelerated voltage, K_0 is a resistance of link of the slowing system, $\tau = \omega_0 C (t - x/v_0) (1 + v_0/v_{rp})^{-1}$ (i.e. $\tau \sim \tau - \xi/v_0$) is the dimensionless "retarded" time, $\nu = 2C(\gamma_0^2 - 1)$ is the known relativistic parameter, C - modified gain parameter, γ_0 - the ratio of the electron energy to the rest energy on entering into the interaction space.

As the solutions of the system (1) give the field distributions $F(\xi, \tau)$ for any $\tau > \tau'$, within chaos-geometric approach and dynamical systems theory, a set of the possible functions F can be treated as a phase space, where every point corresponds to the definite state. When a state changes in time according to solutions of the system (1), the corresponding point moves in a space of functions along some phase trajectory. The control (governing) parameter is provided by the normalized length L . As a rule, this parameter is usually varied by changing the current of the electron beam I_0 through variation of voltage on the governing electrode in an electron gun ($L \sim I_0^{1/3}$). It is known that for a single relativistic backward-wave TUBE the stable state is realized for the little values of L . At the same time for $L=L_{st}=1.97327$ there is a bifurcation of loss of the unmoved point stability [3,4]. In order to reduce the threshold of the transition to the development of chaos, in this paper we propose to use a chain of two relativistic BWTs. The master system of evolution equation for the system is as follows:

$$\partial^2 \theta_{1,2} / \partial \xi^2 = -(1 + \nu \partial \theta / \partial \xi)^{3/2} \text{Re} \{ 1/2 L_{1,2} [\delta(\xi) + \delta(\xi - L) F_{1,2} e^{i\theta_{1,2}}] \}, \quad (3a)$$

$$\partial F_{1,2} / \partial \tau - \partial F_{1,2} / \partial \xi = - \left[1/\pi \int_0^{2\pi} e^{-i\theta_{1,2}} d\theta_0 \right] 1/2 L_{1,2} [\delta(\xi) + \delta(\xi - L_{1,2})]. \quad (3b)$$

where $\theta_{1,2}$ are the phases of electron relative to the wave, θ_0 - the initial phase, $F_{1,2}$ are the dimensionless slowly varying amplitudes of the fields, ξ and τ are the dimensionless coordinate and time, respectively. The equation (3a) represent equation of motion of electrons in the field of the electromagnetic wave and equation (3b) is the non-stationary equations of excitation of a decelerating structure by a current of the slowly varying amplitude. The subscripts indicate the item number of the chain. The dynamics of the partial generator depends on a single bifurcation parameter $L = 2\pi CN$. When the first oscillator acts on the second one, then the boundary conditions for equations (3a) and (3b) can be written as follows:

$$\theta_{1,2} \Big|_{\xi=0} = \theta_0 \in [0; 2\pi], \quad (4a)$$

$$\frac{\partial \theta_{1,2}}{\partial \xi} \Big|_{\xi=0} = 0, \quad (4b)$$

$$F_1(\xi = 1) = 0, F_2(\xi = 1) = RF_1(\xi = 0)., \quad (4c)$$

where R is a coupling parameter, which can be assumed real without the loss of generality.

3. Analysis of nonlinear dynamics of the relativistic backward-wave tube chain:

Results and conclusions

Below we present the results of studying nonlinear dynamics of the single relativistic BWT and a chain of BWT using an analysis and simulation of the model (1) solutions and the chaos-geometric approach. The approach includes nonlinear analysis and prediction technique [1-3], namely, the wavelet analysis, multi-fractal formalism, mutual information approach, correlation integral analysis, false nearest neighbours algorithm, the Lyapunov's exponents and Kolmogorov entropy analysis, surrogate data method, different prediction models etc (see details in Refs. [4,5,13-31]).

As usually, one should consider a set of measurement (or calculational) data $s(n) = s(t_0 + n\Delta t) = s(n)$, where t_0 is the start time, Δt is the time step, and is n the number of the measurements. The next step is to reconstruct phase space using as well as possible information contained in the $s(n)$. Such a reconstruction results in a certain set of d -dimensional vectors $\mathbf{y}(n)$ replacing the scalar measurements. Usually one should use the Packard et al method of the time-delay coordinates (c.g. [14-16]). There one should determine the embedding dimension d_E in order to reconstruct a Euclidean space R^d . In accordance with the embedding theorem, the embedding dimension, d_E , must be greater, or at least equal, than a dimension of the corresponding attractor, d_A , i.e. $d_E > d_A$. There are several standard approaches to reconstruct the attractor dimension (see, e.g., [14-18]), but in our technique we use two methods: the correlation integral one (or algorithm of Grassberger and Procaccia [17]) and method of the false neighbours. The multifractal spectral calculations can be performed with using the algorithm, which is presented in [9].

The prediction block includes computing the Lyapunov's exponents which are the dynamical invariants of the studied nonlinear system.

As example, in Figure 1 we present the numerical temporal dependence of the output signal amplitude of the relativistic BWT for $L=4.1$ (a) and $L=6.1$ (b). We carried out the numerical realization of the prediction model for the relativistic BWT in the chaos (I) and hyperchaos regimes (II).

In Table 1 we present our data on the correlation dimension d_2 , the embedding dimension determined based on the algorithm of false nearest neighboring points (d_N) with percentage of false neighbors (%) calculated for different values of time lag τ . In Table 2 we list the results of computing the Lyapunov's exponents, the, Kolmogorov entropy K_{entr} . For the studied series there are positive and negative values of the Lyapunov's exponents.

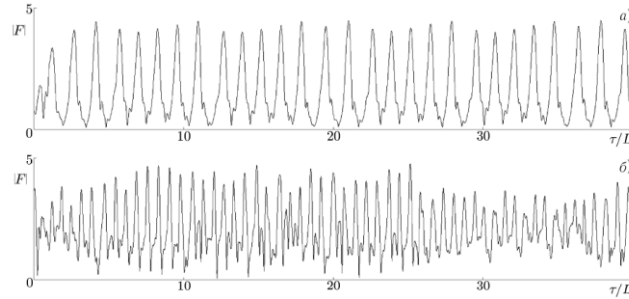


Figure 1. Numerical temporal dependence of the output signal amplitude of the relativistic BWT for $L=4.2$ (a) and $L=6.1$ (b).

Table 1. Correlation dimension d_2 , the dimension of the attachment determined based on the algorithm of false nearest neighboring points (d_N) with percentage of false neighbors (%) calculated for different values of time lag τ

Chaos (I)			Hyperchaos (II)		
τ	d_2	d_N	τ	d_2	d_N
60	3.6	5 (5.5)	67	7.2	10 (12)
6	3.1	4 (1.1)	10	6.4	8 (2.1)
8	3.1	4 (1.1)	12	6.4	8 (2.1)

Table 2. Numerical values of the parameters of chaotic self-oscillations in the backward-wave tube: λ_1 – λ_4 are the Lyapunov exponents in descending order, K is the Kolmogorov entropy

Regime	λ_1	λ_2	λ_3	λ_4	K
Chaos ($L=4.2$)	0.261	0.0001	–0.0004	–0.528	0.26
Hyperchaos ($L=6.1$)	0.514	0.228	0.0000	–0.0002	0.74

Further let us consider two results on studying dynamics of the chain of the backward-wave tubes. In the first modeling we accept that the BWTs are operating in regime of the periodical automodulation (in full analogy with the non-relativistic case [5]). The values of the L parameter are as follows: $L_1=4.05$, $L_2=4.55$; The analysis shows that with growth of R the oscillations become chaotic and scenario of destroying quasi-periodic motion is main. Note that the similar picture is principally observed in the non-relativistic case except some quantitative differences including additional peaks. In Figure 2 we present data on the temporal dependence of the output amplitude and signals spectrum for two different sets of the parameter values: (In) - input BWT and (Out) -

Output BWT for $R=0.050$. In the first case one deals with the Feigenbaum type scenario. In the second case there is the transition “chaos-order” through intermittency.

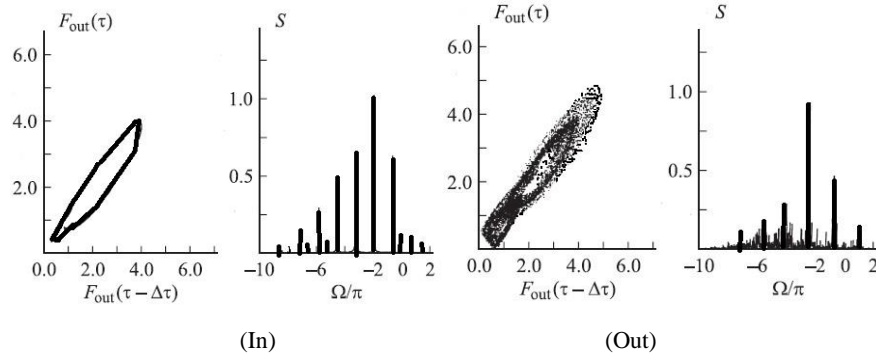


Figure 2. The temporal dependence of the output amplitude and the signals spectrum: (In) - input BWT; (Out) -Output BWT $R=0.050$;

In conclusion we note that quantitative modeling chaotic dynamics of nonlinear processes in relativistic BWTs (single one and chain) is carried out using the same uniform chaos-geometric and multi-system approach. It is important to note that the chaos generation features in dynamics of a chain of the relativistic tubes are firstly found.

Acknowledgments

The authors would like to thank Prof. Jan Awrejcewicz and colleagues for invitation to make contributions to DSTA-2019 (Łódź, Poland). The useful comments of the anonymous referees are very much acknowledged too.

References

- [1] Wiggins S. *Introduction to applied nonlinear dynamical systems and chaos*. Springer, N.Y., 1997.
- [2] Glushkov, A.V. *Methods of a chaos theory*. Astroprint, Odessa, 2012.
- [3] Kuznetsov, A.P., Shirokov, A.P. Discrete model of relativistic backward-wave tube. *Russian Journ.of Phys.: Ser. PND*. 5(1997), 76-83.
- [4] Kuznetsov, S.P., Trubetskov, D.I. Chaos and hyperchaos in backward-wave tube. *Russian Journ.of Phys.: Ser. Radiophys*. XLVII,5 (2004), 1-8.
- [5] Ryskin, N.M., Titov V.N. The transition to the development of chaos in a chain of two unidirectionally-coupled backward-wave tubes. *Journ. Techn. Phys.* 73 (2003), 90-94.
- [6] Prepelitsa, G.P., Buyadzhi, V.V., Ternovsky, V.B. Non-linear analysis of chaotic self-oscillations in backward-wave tube. *Photoelectronics* 22, (2013), 103-107.

- [7] Glushkov, A.V., Kuzakon, V.M., Ternovsky, V.B., and Buyadzhi, V.V. Dynamics of laser systems with absorbing cell and backward-wave tubes with elements of a chaos. *Dynamical Systems Theory*, eds. J. Awrejcewicz, M. Kazmierczak, P. Olejnik, J. Mrozowski. Lodz Univ., Łódź. T1 (2013), 461-466.
- [8] Glushkov, A.V., Khetselius, O.Yu., Kuzakon, V.M., Prepelitsa, G.P., Solyanikova, E.P., Svinarenko, A.A. Modeling of interaction of the non-linear vibrational systems on the basis of temporal series analyses (application to semiconductor quantum generators). *Dynamical Systems - Theory and Applications*, Lodz Univ. (2011), BIF110.
- [9] Glushkov, A.V., Prepelitsa, G.P., Svinarenko, A.A., Zaichko, P.A. Studying interaction dynamics of the non-linear vibrational systems within non-linear prediction method (application to quantum autogenerators). *Dynamical Systems Theory*, eds. J. Awrejcewicz, M. Kazmierczak, P. Olejnik, J. Mrozowski. Lodz Univ., Łódź. T1 (2013), 467-477.
- [10] Buyadzhi, V., Glushkov, A., Gurskaya, M., Khetselius, O., Ternovsky, E., Mashkantsev, A., Kirianov, S. A novel combined chaos-geometric and vibration blind source monitoring approach to damage analysis and detection of engineering structures (nuclear reactors) under varying environmental, operational conditions and emergency accidents. *Sens. Electr. and Microsyst. Techn.* 14, 4 (2017), 60-72.
- [11] Glushkov, A.V., Ternovsky, V.B., Buyadzhi, V.V., Prepelitsa, G.P. Geometry of a Relativistic Quantum Chaos: New approach to dynamics of quantum systems in electromagnetic field and uniformity and charm of a chaos. *Proc. Intern. Geom. Center.* 7, 4 (2014), 60-71.
- [12] Glushkov, A.V., Buyadzhi, V.V., Kvasikova, A.S., Ignatenko, A.V., Kuznetsova, A.A., Prepelitsa, G.P., and Ternovsky, V.B. Nonlinear chaotic dynamics of Quantum systems: Molecules in an electromagnetic field and laser systems. *Quantum Systems in Physics, Chemistry, and Biology. Series: Progress in Theoretical Chemistry and Physics*, ed. A.Tadger, R.Pavlov, J.Marvani, E.Brändas, G.Delgado-Barrio. Springer, Cham. 30 (2017), 169-180.
- [13] Glushkov, A.V., Khetselius, O.Yu., Svinarenko, A.A., Buyadzhi, V.V., *Methods of computational mathematics and mathematical physics. P.I.* TES, Odessa, 2015.
- [14] Packard, N.H., Crutchfield, J.P., Farmer, J.D., Shaw, R.S. Geometry from a time series. *Phys. Rev. Lett.* 45 (1980), 712-716.
- [15] Kennel, M.B., Brown, R., and Abarbanel, H. Determining embedding dimension for phase-space reconstruction using a geometrical construction. *Phys. Rev. A* 45 (1992) 3403-3411.
- [16] Abarbanel, H.D.I., Brown, R., Sidorowich, J.J., and Tsimring, L.Sh. The analysis of observed chaotic data in physical systems. *Rev. Mod. Phys.* 65 (1993), 1331-1392.
- [17] Grassberger, P., and Procaccia, I. Measuring the strangeness of strange attractors. *Physica D*. 9 (1983), 189-208.
- [18] Glushkov, A.V., Khetselius, O.Y., Bunyakova, Yu.Ya., Prepelitsa, G.P., Solyanikova, E.P., Serga E.N. Non-linear prediction method in short-range forecast of atmospheric pollutants: low-dimensional chaos. *Dynamical Systems - Theory and Applications*, Lodz. (2011), LIF111.
- [19] Glushkov, A.V., Khetselius, O.Y., Brusentseva, S.V., Zaichko, P.A., Ternovsky, V.B. Studying interaction dynamics of chaotic systems within a non-linear prediction method: application to neurophysiology. *Advances in Neural Networks, Fuzzy Systems and Artificial Intelligence, Series: Recent Advances in Computer Engineering*, Ed. J.Balicki. WSEAS Pub., Gdansk. 21 (2014), 69-75.
- [20] Glushkov, A.V., Svinarenko, A.A., Buyadzhi, V.V., Zaichko, P.A., Ternovsky, V.B. Chaos-geometric attractor and quantum neural networks approach to simulation chaotic evolutionary dynamics during perception process. *Advances in Neural Networks, Fuzzy Systems and Artificial*

Intelligence, Series: Recent Advances in Computer Engineering, Ed. J.Balicki. WSEAS Pub., Gdansk. 21 (2014), 143-150.

[21] Khetselius, O.Yu. Forecasting evolutionary dynamics of chaotic systems using advanced non-linear prediction method. *Dynamical Systems Applications*, ed. J. Awrejcewicz, M. Kazmierczak, P. Olejnik, J. Mrozowski. Lodz Univ., Łódź. T2 (2013), 145-152.

[22] Glushkov, A.V., Safranov, T.A., Khetselius, O.Yu., Ignatenko, A.V., Buyadzhi, V.V., Svinarenko A.A. Analysis and forecast of the environmental radioactivity dynamics based on methods of chaos theory: General conceptions. *Environmental Problems*. 1, 2 (2016), 115-120.

[23] Khetselius, O.Yu., Brusentseva, S.V., Tkach, T.B. Studying interaction dynamics of chaotic systems within non-linear prediction method: Application to neurophysiology. *Dynamical Systems Applications*, ed. J. Awrejcewicz, M. Kazmierczak, P. Olejnik, J. Mrozowski. Lodz Univ., Łódź. T2 (2013), 251-259.

[24] Glushkov, A.V. *Relativistic quantum theory. Quantum mechanics of atomic systems*. Astroprint, Odessa, 2008.

[25] Glushkov, A.V., Gurskaya, M.Yu., Ignatenko, A.V., Smirnov, A.V., Serga, I.N., Svinarenko, A.A., Ternovsky, E.V. Computational code in atomic and nuclear quantum optics: Advanced computing multiphoton resonance parameters for atoms in a strong laser field. *J. Phys: Conf. Ser.* 905, 1 (2017), 012004.

[26] Bunyakova, Yu.Ya., Glushkov, A.V. *Analysis and forecast of the impact of anthropogenic factors on air basein of an industrial city*. Ecology, Odessa, 2010.

[27] Bunyakova, Yu.Ya., and Khetselius, O.Yu. Non-linear prediction statistical method in forecast of atmospheric pollutants. *Proc. of 8th Intern. Carbon Dioxide Conference (Germany)*. T2-098 (2009).

[28] Buyadzhi, V.V., Glushkov, A.V., Mansarliysky, V.F., Ignatenko, A.V., Svinarenko A.A. Spectroscopy of atoms in a strong laser field: New method to sensing AC Stark effect, multiphoton resonances parameters and ionization cross-sections. *Sensor Electr. and Microsyst. Techn.* 12, 4 (2015), 27-36.

[29] Glushkov, A.V., Mansarliysky, V.F., Khetselius, O.Yu., Ignatenko, A.V., Smirnov, A.V., Prepelitsa, G.P. Collisional shift of hyperfine line for thallium in an atmosphere of the buffer inert gas. *J. Phys.: Conf. Ser.* 810 (2017), 012034.

[30] Glushkov, A.; Khetselius, O.; Svinarenko, A.; Buyadzhi, V. *Spectroscopy of autoionization states of heavy atoms and multiply charged ions*. TEC, Odessa, 2015.

[31] Glushkov, A., Khetselius, O., Svinarenko, A., Serbov, N., The sea and ocean 3D acoustic waveguide: rays dynamics and chaos phenomena. *J. Acoust. Soc. America*. 123, 5 (2008), 3625.

Valentin B. Ternovsky, Assoc.-Professor: Odessa State Environmental University, Pure and Applied Mathematics Department, L'vovskaya str. 15, 65009 Odessa, Ukraine (ternovskyvb@gmail.com). The author gave a presentation of this paper during one of the conference sessions.

Alexander V. Glushkov, Professor: Odessa State Environmental University, Pure and Applied Mathematics Department, L'vovskaya str. 15, 65009 Odessa, Ukraine (glushkovav@gmail.com).

Eugeny V. Ternovsky, Senior Sci. Worker: Odessa State Environmental University, Pure and Applied Mathematics Department, L'vovskaya str. 15, 65009 Odessa, Ukraine (ternovskyev@gmail.com).

Andrey Tsudik, M.Sc. (Ph.D. student): Odessa State Environmental University, Pure and Applied Mathematics Department, L'vovskaya str. 15, 65009 Odessa, Ukraine.

Bifurcations and transitions in railway vehicle dynamics

Hans True

Abstract: The Railway Vehicle Dynamical problems are multibody problems with from 7 to 80+ degrees of freedom. The mathematical models are nonlinear and non-smooth and most often with tabulated constraints. Only autonomous problems are considered in this paper. The dynamics depend on the speed V as a control parameter and the vehicle can run steady, oscillate symmetric or asymmetric periodically, multi-periodically, quasi-periodically or chaotic, possibly with multiple attractors. Several kinds of bifurcations and transitions exist. The theoretical dynamical models are investigated numerically. Some interesting bifurcations will be shown.

1. Introduction, the object

We investigate the dynamics of moving railway vehicles. The main objective is the investigation of critical values of the speed, especially ‘the critical speed’ V_C , which is the lowest speed where self-oscillating motions occur. A typical railway vehicle is shown on figure 1.

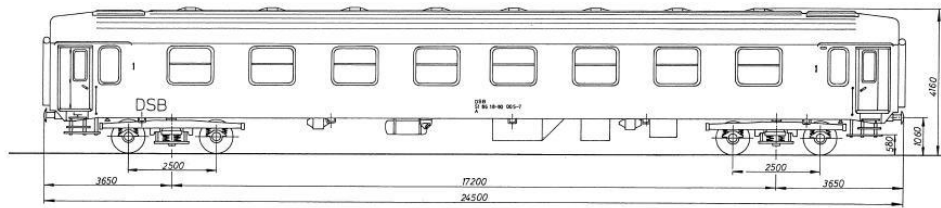


Figure 1. A four-axle bogie railway passenger car.

The car body is supported on the frames of two two-axle small carriages – called bogies (bo^ugies) – through the *secondary suspension*. The bogie frames are supported on two wheel sets that run on the rails by the *primary suspension*. The suspension elements have in general nonlinear characteristics but in many cases, they can be assumed linear. Due to the deformation of both the wheels and the rails under the load of the vehicle a contact surface develops between them in which tangential strains develop with components in the tangential plane called *creep* and a normal rotation component called *spin creep*. The creeps normalized by the forward speed V_0 are called *creepages*. Due to the dry friction, resultant *longitudinal and lateral creep forces* and a *spin creep torque* are created. The creep

forces are handled as forces and a torque that attack in one point in the contact surface, but with realistic rail/wheel contact geometries there may be multi point contact (see Fig. 2). The creep forces depend nonlinearly and non-smoothly on the creepages (see Fig. 3). When the slope of the contact surface, *the conicity*, is small, which on a straight track most often is the case, then the spin creep can be neglected.

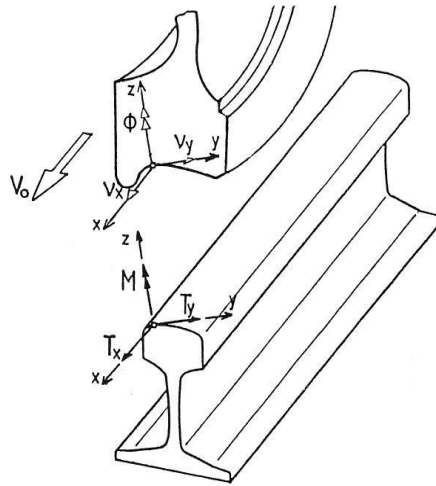


Figure 2. The wheel/rail creepages v_x , v_y and ϕ and the creep forces T_x , T_y and M

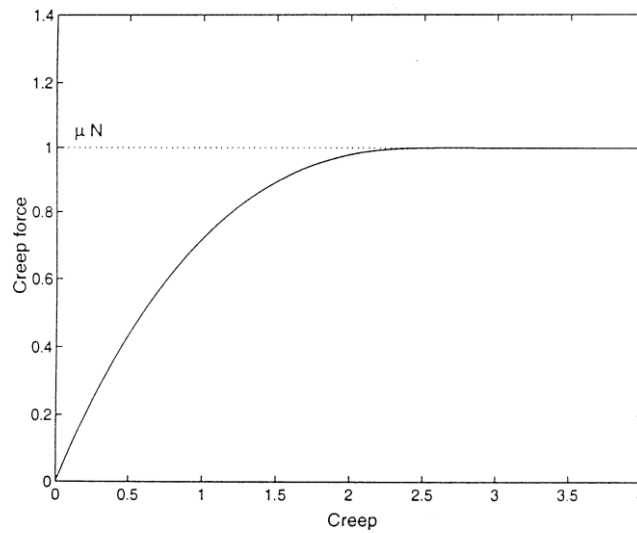


Figure 3. The general form of the dependence of the normalized creep force on the creep. N is the normal force in the contact point and μ is the coefficient of adhesion

The mathematical dynamical models are all formulated in a Cartesian coordinate system that is centered in the track and moving with the speed, V , of the vehicle. Since all the interesting phenomena that govern the nonlinear behavior depend on the bogie design and the wheel/rail contact, we shall concentrate on the dynamics related to them. First, we have investigated the so-called Cooperrider bogie with linear suspension elements in detail (see Fig. 4).

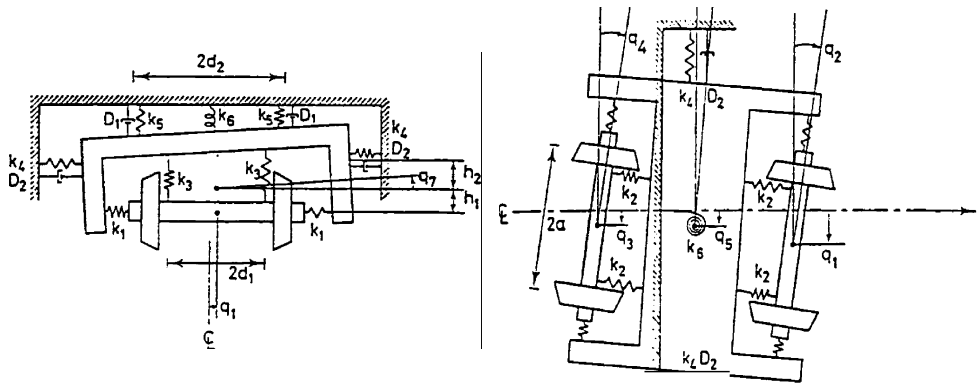


Figure 4. A diagram of the Cooperrider bogie

2. Some bifurcations and transitions

2.1. The non-smooth bifurcation in $V = 0$

Christian Kaas Petersen [1] calculated the bifurcation diagram (see Fig. 5) for the Cooperrider bogie. He assumed that the conical wheels has a constant conicity and run on rails with a circular profile. The wheel flanges were approximated by very stiff linear springs with a clearance. The diagram was calculated numerically using CKP's program 'PATH' [2] that could follow stable as well as unstable steady and periodic motions. A is a bifurcation point from where an unstable periodic solution bifurcates subcritically to the critical speed V_c in a tangent bifurcation in point B where flange contact occurs. The periodic motion above the critical speed is called *hunting*.

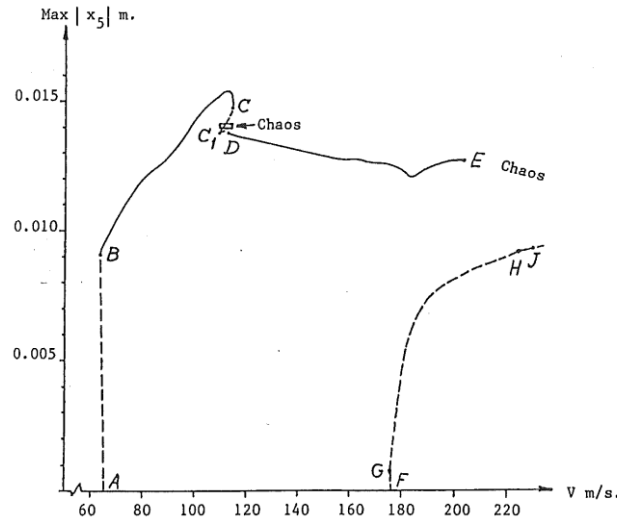


Figure 5. The Cooperrider bifurcation diagram. The full lines indicate asymptotically stable solutions, and the dotted lines indicate unstable solutions

CKP observed that when $V \rightarrow 0$, then the positive real part of a large number of the eigenvalues of the linearized problem converge towards zero, indicating that $V = 0$ is a bifurcation point. It is indeed! When the bogie rolls at a low speed, then there exists one asymptotically and globally stable motion, an equilibrium point. When the bogie stands still under the normal load, there exists a bounded domain of a quadruple infinite number of neutrally stable combinations of the lateral and yaw positions of the two wheel sets on the rail. They are all equilibrium points. This is a *non-smooth bifurcation from one equilibrium point into a bounded quadruple infinity of equilibrium points*.

2.2 The Slivsgaard bifurcation

In her master's thesis, Eva Slivsgaard [3] investigated the dynamics of a single-axle bogie that is virtually the half of a Cooperrider bogie without the dampers. The first bifurcation point into a periodic solution is at a much lower speed than in the Cooperrider bogie, and it is a supercritical bifurcation. Slivsgaard made an enlarged figure of the solutions in the neighborhood of the bifurcation point (see Fig. 6) and found that the amplitude of the bifurcating periodic solution initially grows linearly with growing speed in contrast to the expected square root growth of the expected Hopf bifurcation. We first thought it might be a numerical fluke, but the author succeeded in formulating a kind of normal form for this bifurcation [4] and thereby to demonstrate that the

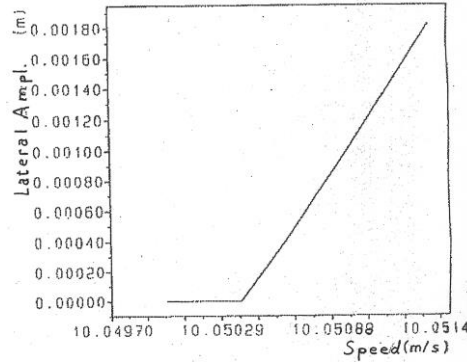


Figure 6. The Slivsgaard bifurcation

bifurcation is a new non-smooth type of bifurcation. It is now fashionable to name bifurcations after the person, who first found it, so this bifurcation therefore should be named a *Slivsgaard bifurcation*. The non-smoothness is connected with the analytic expression of the creep/creep force curve in figure 3. It must represent an odd function in order to hold also for negative values of the creep, and the correct formulation is therefore:

$$\begin{aligned} F/\mu N &= c - c|c|/3 + c^3/27 & |c| \leq 3 \\ F &= \mu N & |c| > 3 \end{aligned}$$

Now the non-smoothness is obvious.

$$\frac{d^2}{dc^2}(F/\mu N) = \begin{cases} -2/3 + 2c/9 & c > 0 \\ 2/3 + 2c/9 & c < 0 \end{cases}$$

The second derivative of F jumps in $c = 0$, so Hopf's basic assumption of a continuous second derivative in the bifurcation point is violated.

Joos Kalker [5] told me that the non-smoothness in $c = 0$ is physically realistic. In rolling contact with friction, Hertz [6] found that the contact surface between the wheel and the rail is divided into two domains, one with stick and one with slip between the wheel and the rail. The slip zone grows from 0 to the entire contact zone when the creep grows from 0 to 3 (see Fig. 3) and it lies in the rear end of the contact zone relative to the direction of travel of the wheel. When the creep (and the direction of travel) changes direction, the slip zone jumps when the creep changes sign, see Fig. 7.



Figure 7. The domain of pure sliding in the contact surface (shaded) jumps when c changes sign

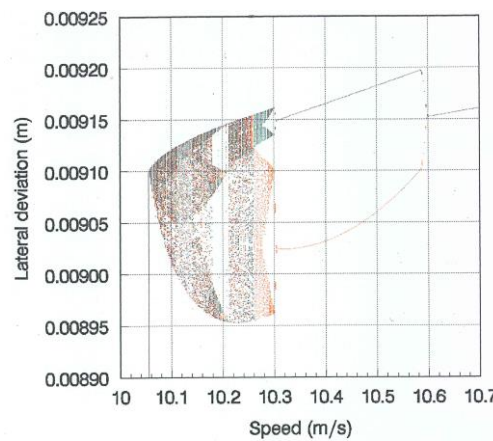


Figure 8. The total bifurcation diagram showing the bifurcations from a trivial solution into an asymptotically stable symmetric periodic solution

Slivsgaard [3] calculated numerically the bifurcation diagram in Fig. 8. After the supercritical bifurcation at $V = 10.050$ m/s the amplitude of the periodic solution grows fast and reaches flange contact at $V = 10.0555$ m/s with an amplitude of 9.1 mm. The contact is modeled by a very stiff linear spring. The change into chaos starts with a symmetry breaking pitchfork bifurcation that creates two asymmetric limit cycles. The two solutions are reflections of each other in the centre line of the track. Each of these undergoes a complete periodic doubling cascade into chaos. The details cannot be seen in Fig. 8 but Slivsgaard [3] describes them. It is interesting to notice the split of the chaotic attractor into two asymmetric chaotic attractors at $V \sim 10.26$ m/s. Each of them splits into two-band chaos when the speed grows through 10.28 m/s. The four bands narrow down to two asymmetric periodic solutions, which undergo a reverse period doubling bifurcation at $V = 10.303$ m/s. As the speed is increased further, the symmetry is restored at $V = 10.596$ m/s. The amplitude of the symmetric limit cycle then grows monotonically with the speed.

The examples presented were investigated numerically using Kaas-Petersen's path following routine PATH [2] with the LSODA solver [7]. The time integration across the non-smoothnesses was

performed either by the routine itself or by a smoothing function. They gave the same dynamical results.

3. On the dynamics of a European two-axle freight wagon

In the next example, events were introduced in all encounters with the non-smoothnesses. When a non-smoothness was detected, the time step integration was stopped, and the position of the point of non-smoothness was found with a Newton iteration. Then the time integration was re-started from the point of non-smoothness using the mathematical model of the non-smoothness as the initial value. The path following was done by ramping using an implicit Runge-Kutta solver with error control as the solver, see Hoffmann [8].

Hoffmann investigated in his Ph.D. thesis [8] the dynamics of a European two-axle freight wagon. The wheel/rail contact was modeled realistically using the UIC S1002 profile for the wheel profile and the UIC60 profile for the rail profile. The position of the contact points in dependence on the lateral displacement of the wheel set relative to the track was calculated with the RSGEO routine [9] and tabulated. The contact angle and the lateral position of the contact point on the wheel have several points of non-smoothness as a function of the lateral displacement of the wheel set on the track. Multiple points of contact occur, and in those cases the creep forces were calculated using the approximation by Pascal and Sauvage [10] [11]. In European two-axle freight wagons the most used suspension is the UIC standard suspension see Fig. 9. The car body is supported by a leaf spring and hangs in links with dry friction contact surfaces that deliver the damping forces. The dry friction introduces stick/slip in the dynamics between the elements of the construction as well in the spring as in the links. Furthermore, there is a lateral as well as a longitudinal clearance between the axle box and the guidances see Fig. 10. They introduce non-smoothness in the dynamical system. The rails have a cant towards the center of the track. In Europe, the cant is $1/20$, $1/30$ or $1/40$. Hoffmann [8] calculated the bifurcation diagrams on Fig. 11 for all the three values. The maximum lateral displacements of the leading wheel set and the car body are shown in dependence on the speed. They all have in common that the position of the wheel set in the steady motion for low speed is undetermined (the shaded domain). In all the diagrams a stable *periodic flange-to-flange attractor*, *the hunting*, develops in a tangent bifurcation at $V = 40$ m/s. In the diagram denoted 5.1 the unstable periodic solution stems from a subcritical bifurcation into an unstable periodic motion at $V = 52$ m/s. In the two other diagrams, the development of *the flange-to-flange attractor* is more complicated and may be read on the diagrams.

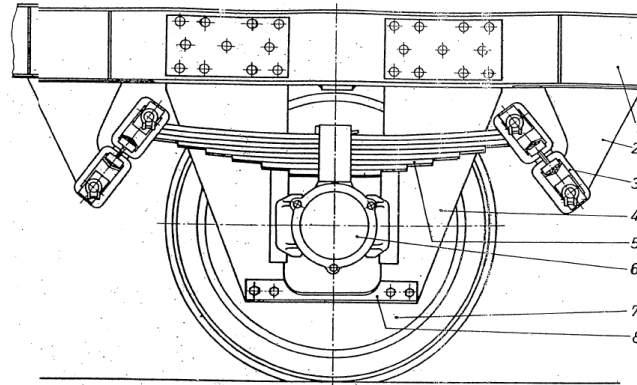


Figure 9. The UIC suspension

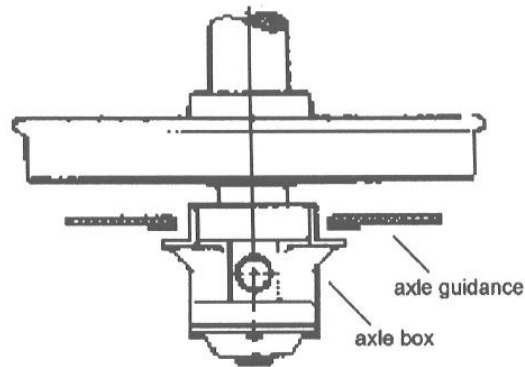


Figure 10. The clearances between the axle box and the guidances

In the two lower diagrams there exist also a *periodic medium amplitude attractor* with an increasing amplitude for decreasing speed. The sudden increase is the consequence of a resonance motion of the wagon that was suggested by Stichel [12]. He suggested that a resonance between the lateral excitation frequency of the wheel sets and the yaw eigenfrequency of the carbody might occur. Hoffmann [8] made realistic estimates of the frequencies see Fig. 12, and it is seen that the excitation frequency, the so-called Klingel frequency, which grows linearly with the speed, coincides with the yaw eigenfrequency of the carbody at $V = 12$ m/s, 18 m/s and 49 m/s respectively. The peaks of the medium amplitude attractor in the 1/30 and the 1/40 case are due to this resonance. There is no medium amplitude attractor in the 1/20 case, however, the resonance still occurs at 49 m/s as predicted, but it is in the speed interval for which the wheel sets are on the flange-to-flange attractor. The car body oscillates violently in that case.

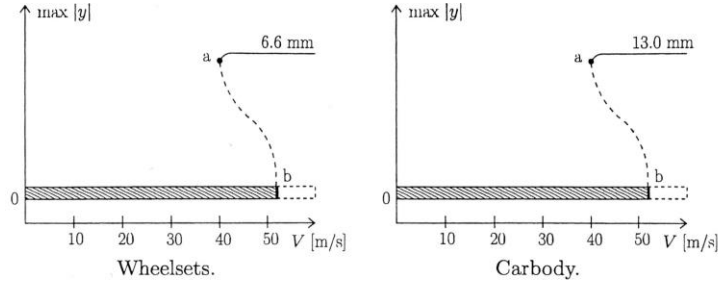


Figure 5.1: Attractors, 1/20 rail inclination.

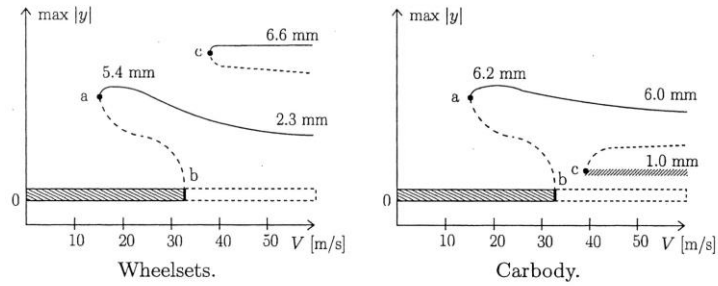


Figure 5.2: Attractors, 1/30 rail inclination.

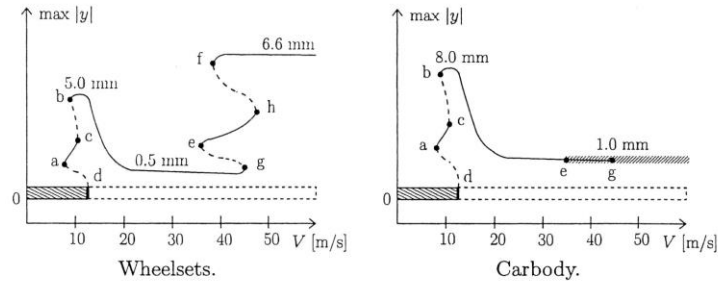


Figure 5.3: Attractors, 1/40 rail inclination.

Fig. 11. The bifurcation diagrams. A full line indicates an asymptotically stable motion, and a dotted line indicates the existence somewhere in between of an unstable motion.

On the flange-to-flange attractor in the cases with 1/30 and 1/40 cants the lateral excitation frequency of the wheel sets is far beyond the yaw eigenfrequency of the car body, hence no resonance occurs and the result is a weak car body response.

The shaded domains on the oscillating branches for the car body indicate varying amplitudes. The kind of motion has not been determined, but a spectral analysis of the frequency of the wheel set

oscillations in that domain shows that their oscillations are aperiodic with an almost constant amplitude.

It should be noted that several features on the bifurcation diagrams that Hoffmann calculated have been found in real life with real railway wagons

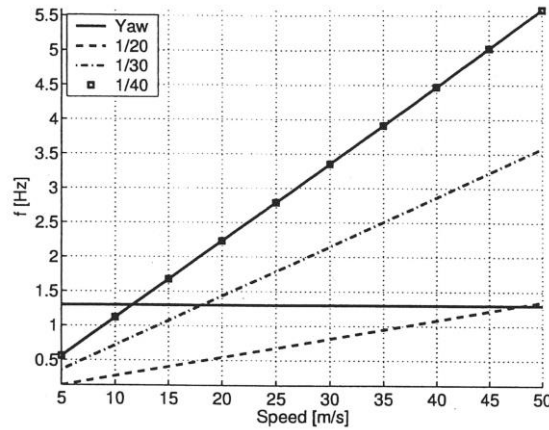


Figure 12. The horizontal line shows the estimated yaw eigenfrequency of the car body, and the inclined lines show the estimated Klingel frequencies for the three different cants of the rails.

4. Conclusions

In this article, we have shown some of the many different kinds of bifurcations and transitions that may occur in railway vehicle dynamics. Several are related to the non-smoothness in the mathematical dynamical model. One bifurcation, (section 2.1), although known for some time, has not been described earlier.

In most cases, the railway vehicles will not be allowed to run with speeds above the critical speed. The reader may wonder that the world speed record for a conventional train set is 574.8 km/h set by a French TGV train set in 2007, but the critical speeds in this article are significantly smaller. It is possible to achieve a high critical speed by the use of special designs of the suspension, but they are expensive. They are therefore only used in passenger trains that are especially designed for high-speed travel, and they do not contain dry friction elements in the suspension. Dry friction elements are cheap and simple in manufacture, and they are therefore extensively applied in freight wagons, where the price of the vehicle is a very important factor. An example is the freight wagon presented in section 3.

The American three-piece-freight truck is the most widespread bogie in the world due to its low price, simplicity and durability. It has dry friction wedge shaped damping elements called ‘snubbers’. The critical speed of a wagon with the original design of the bogie is around 74 km/h, but the wagons run with higher speeds around the world. They run supercritically. Xia [13] investigated the dynamics of a wagon with three-piece-freight trucks in detail. A supercritical bifurcation leads to an asymptotically stable periodic solution, which soon after loses stability, and a jump to a large-amplitude stable chaotic motion takes place. Tests have confirmed Xia’s results. Today many three-piece-freight trucks have been modified so the critical speed is higher, but they still run supercritically and chaotic.

Chaos seems to be the usual supercritical behavior, when dry friction with stick/slip enters the design. True and Asmund 2002 [14], True and Trzepacz 2002 [15] and True and Briec [16] analyzed simpler models that all oscillate chaotically.

Finally, it should be noticed that Isaksen and True [17] treat the ultimate transition to chaos in the dynamics of the Cooperrider bogie in section 2 in detail. The transition takes place in a narrow speed range $203 \text{ m/s} < V < 204 \text{ m/s}$. There are series of bifurcations and different transitions involving symmetry breaking, quasi-periodicity and periodic windows with multiperiodicity, where an asymmetric period 11 solution plays an important role. We calculated the highest Lyapunov exponents to verify the results of the numerical calculations, and the highest Lyapunov dimension found is 3.03.

References

- [1] True, H., and Kaas-Petersen, C. A Bifurcation Analysis of Nonlinear Oscillations in Railway Vehicles. *Proc. 8th IAVSD-IUTAM Symposium on Vehicle System Dynamics, The Dynamics of Vehicles on Roads and Tracks* (1984) 655-665.
- [2] Kaas-Petersen, C. *PATH – User’s Guide*. Department of Applied Mathematical Studies and Centre for Nonlinear Studies, University of Leeds, 1989.
- [3] Slivsgaard, E, and True, H. Chaos in Railway Vehicle Dynamics. *Nonlinearity and Chaos in Engineering Dynamics*, 183-192, John Wiley & Sons, Chichester, 1994.
- [4] True, H. On a new Phenomenon in Bifurcations of Periodic Orbits. *Dynamics, Bifurcations and Symmetry, New Trends and New Tools*, 327-331. Kluwer Academic Publishers, Dordrecht, The Netherlands, 1994.
- [5] Conversation between Joos Kalker and the Author, 1993.
- [6] Hertz, H. Über die Berührung zweier feste elastischer Körper. *Journal für die reine und angewandte Mathematik* 92 (1882), 156-171.
- [7] LSODA (2005): <http://www.oecd-neo.org/tools/abstract/detail/uscd1227>
- [8] Hoffmann, M. *Dynamics of European two-axle Freight Wagons*. Ph.D. thesis, The Technical University of Denmark, 2006, H.True.
http://www2.imm.dtu.dk/pubdb/views/publication_details.php?id=4853

- [9] Kik, W. RSGEO. <http://www.argecare.de/produkte.htm>, 2001.
- [10] Sauvage, G., and Pascal, J.P. Solution of the multiple wheel and rail contact dynamic problem. *Vehicle System Dynamics* 19 (1990), 257-272.
- [11] Pascal, J.P., and Sauvage, G. New method for reducing the multicontact wheel/rail problem to one equivalent contact patch. *Proc. of the 12th IAVSD Symposium*, 1991, 475–489.
- [12] Stichel, S., How to improve the running behaviour of freight wagons with UIC–link suspension. *Vehicle System Dynamics Supplement*, 33 (1999), 394–405.
- [13] Xia, F., The Dynamics of The Three-Piece-Freight Truck, Ph.D. Thesis, IMM, The Technical University of Denmark, 2002, H. True.
<http://www2.imm.dtu.dk/pubdb/public/search.php?searchstr=Fujie+Xia&n=5&searchtype=strict>
- [14] True, H., and Asmund, R. The Dynamics of a Railway Freight Wagon Wheelset with Dry Friction Damping. *Vehicle System Dynamics*, 38, 2 (2002), 149-163.
- [15] True, H., and Trzepacz, L. The Dynamics of a Railway Freight Wagon Wheelset with Dry Friction Damping in the Suspension, *Proc. 18th IAVSD Symposium on Vehicle System Dynamics, The Dynamics of Vehicles on Roads and Tracks* (2004), 587—596.
- [16] True, H., and Briec, G. The Dynamics of a Railway Wagon Wheel-set with Dry Friction Damping. *Proc. 11th Miniconf. on Vehicle System Dynamics, Identification and Anomalies* Budapest, Nov. 10-12, 2008, Budapest University of Technology and Economics, 203-210.
- [17] Isaksen, P., and True, H. On the Ultimate Transition to Chaos in the Dynamics of Cooperrider's Bogie, *Chaos, Solitons and Fractals*, 8, 4 (1997), 559—581.

Hans True, Retired Professor: The Technical University of Denmark, DTU Compute, Richard Petersens Plads 324, DK-2800 Kgs.Lyngby, Denmark (htru@dtu.dk)

The author gave a presentation of this paper during one of the conference sessions.

Systems with fast limit cycles and slow interaction

Ferdinand Verhulst

Abstract: We will review the theory of slow-fast systems that started with papers by Tykhonov, Pontryagin, Levinson, Anosov, Fenichel and other scientists. After this review we focus on systems with limit cycles. The Pontryagin-Rodygin theorem for slow-fast systems has an ingenious proof; also it has as advantage that it can be applied if the slow manifolds of the slow-fast system are all unstable. A serious disadvantage is that for application we have to know the fast solutions explicitly with the slow part in the form of parameters. Another disadvantage is the relatively short timescale where the results are valid. In practice there are very few cases where the theorem applies. However, the Pontryagin-Rodygin idea can be used again on assuming that the fast limit cycle arises in higher order approximation; this allows an approximation approach to study the slow motion. At this point we have still a restricted timescale but extension is then possible by looking for continuation on stable, in particular slow manifolds. We will demonstrate this extension of the theory by studying various types of self-excited, coupled slow and fast Van der Pol oscillators.

1. Introduction

We will be concerned with slow-fast systems of the form:

$$\varepsilon \frac{dy}{dt} = f(t, x, y) + \varepsilon R_1, \quad \frac{dx}{dt} = g(t, x, y) + \varepsilon R_2. \quad (1)$$

$x \in \mathbb{R}^n, y \in \mathbb{R}^m, \varepsilon$ is a small, positive parameter.

With excuses to people left out we mention the following founding scientists:

1. Tikhonov (1952)
2. Flatto and Levinson (1955)
3. Anosov (1960)
4. Pontryagin - Rodygin (1960)
5. Tikhonov expansions, Vasil'eva (1963), O'Malley (1968)
6. Fenichel (1971 - 1979)

7. Jones and Kopell (1994)

The early developments in the period 1952-1970 were concerned with asymptotic approximations and periodic solutions. In the second period new developments were stimulated by invariant manifold theory and new dynamics results.

2. Early results

We start with an example of (1): a prey-predator system with unequal interaction.

The population N preyed upon is abundant with respect to the predators P ; the prey-population grows fast (we will return to the example later on):

$$\varepsilon \dot{N} = r(t)N \left(1 - \frac{N}{K(t)}\right) - \varepsilon NP, \quad \dot{P} = cNP - dP - P^2. \quad (2)$$

The growth rate $r(t)$ and carrying capacity $K(t)$ are positive for $t \geq 0$ and T -periodic, c and d are positive constants; we have $N, P \geq 0$. Think for $r(t), K(t)$ of seasonal variations.

Tikhonov [13] studied system (1) by putting $\varepsilon = 0$ and supposing that $y = \phi(t, x)$ is an isolated, asymptotically stable root of the equation $f(t, x, y) = 0$ (with t, x as parameters). He proved then that $y(t)$ jumps fast to the 'slow' solution of the equation:

$$\frac{dx}{dt} = g(x, \phi(t, x)). \quad (3)$$

The resulting approximation is valid on a time-interval $O(1)$ for the slow motion of x . Examples show that without further assumptions this result is optimal. Vasil'eva [14] and O'Malley [10] improved Tikhonov's theorem in a practical way by assuming in addition that the stability of the root $y = \phi(t, x)$ is exponential:

$$\text{ReSp} \frac{\partial f(t, x, y)}{\partial y} \Big|_{(y = \phi(t, x))} < 0. \quad (4)$$

With this assumption the jumps take time $O(\varepsilon)$ and we can obtain asymptotic expansions in ε valid on time intervals $O(1)$. Vasil'eva [14] uses matched asymptotic expansions, O'Malley [10] introduces multiple timescale expansions for this singular perturbation problem.

Qualitative results regarding the existence of periodic solutions of system (1) were obtained by Flatto and Levinson [8] and by Anosov [1]. Suppose that the slow equation (3) contains an isolated T_0 -periodic solution, with only one multiplier 1, then the original system contains a T_ε -periodic solution with $T_\varepsilon \rightarrow T_0$ as $\varepsilon \rightarrow 0$. The theorems in [8, 1] show minor differences in formulation, the important step is that they involve structural stability of the asymptotic phenomena, they anticipate in a sense Fenichel's results.

An interesting quantitative result was produced by Pontryagin and Rodygin [11]. Consider again the slow-fast system (1) in autonomous form and assume:

1. For x fixed the fast equation for y contains an exponentially stable limit cycle of the form $y^*(\tau, x)$ with period $T(x)$ (x a parameter, $\tau = t/\varepsilon$).
2. For fixed positive T_1, T_2 we have $T_1 \leq T(x) \leq T_2$.
3. Replace t by $\varepsilon\tau$ and average $g(x, y)$ over the limit cycle.

Then with corresponding initial values we have with $\bar{x}(\tau)$ from the averaged equation:

$$y(\tau, \varepsilon) - y^*(\tau, \bar{x}) = O(\varepsilon), x(\tau, \varepsilon) - \bar{x}(\tau) = O(\varepsilon), \delta(\varepsilon) \leq \tau \leq L/\varepsilon. \quad (5)$$

For the Pontryagin-Rodygin theorem, weak and strong points are:

- The timescale of validity is restricted to $O(1/\varepsilon)$ in τ , so $O(1)$ in t .
- To apply the theorem we have to know $x^*(\tau, y)$ with period $T(y)$ explicitly; this will be rarely the case.
- Strong point: the result is also useful if the system contains an unstable slow manifold.

So in practice the Pontryagin-Rodygin theorem is useless but, as we shall see, it can be an inspiration for a related approach. First an example to show the weak points:

$$\begin{cases} \varepsilon \dot{x}_1 &= x_2 + y(x_1 - \frac{1}{3}x_1^3), \\ \varepsilon \dot{x}_2 &= -x_1 - yx_1^2, \\ \dot{y} &= 1 - y, 0 \leq y \leq 1. \end{cases} \quad (6)$$

There are two roots of the fast equation, called slow manifolds, both are unstable. Differentiation of the 1st equation with $x_1 = x$ produces:

$$\frac{d^2x}{d\tau^2} + x + yx^2 = yx'(1 - x^2) + \varepsilon(1 - y)(x - \frac{1}{3}x^3). \quad (7)$$

Doelman and F.V. [3] showed that at parameter value $y = 1/\sqrt{7}$ the limit cycle vanishes; see for an illustration fig. 1.

3. Modern results

Fenichel [4, 5, 6, 7] formulated geometric singular perturbation theory with many consequences for the existence of slow manifolds leading to a reformulation of quantitative results. The theory was introduced for autonomous systems where the geometric interpretation is easier, but it can be generalised to systems with periodic coefficients in time. Consider system (1) with the vector fields time-independent. Put $\varepsilon = 0$ and suppose as in Tykhonov's

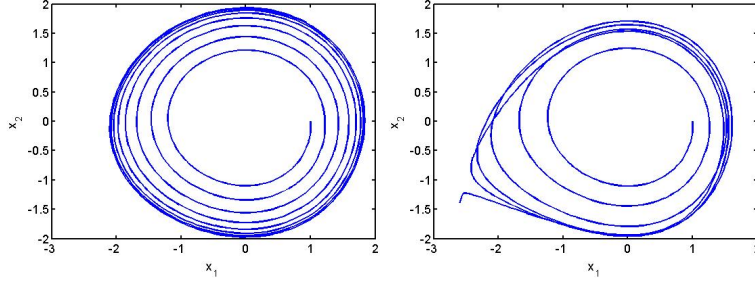


Figure 1. Left eq. (7) if y is constant, right varying y .

theorem that $y = \phi(x)$ is an isolated root of the (fast) y -equation with x as parameter.

Fenichel: If $y = \phi(x)$ defines a compact manifold M_0 and

$$Re Sp \frac{\partial f(x, y)}{\partial y} |_{(y = \phi(x))} \neq 0$$

then system (1) contains an invariant manifold M_ε ε -close to M_0 .

The dynamics on the slow manifold M_ε is approximated by the flow of the slow equation $dx/dt = g(x, y(x))$.

The theorem does not require asymptotic stability of the root, it has to be structurally stable and so be stable or unstable. Note that the existence and approximation of periodic solutions in a slow manifold is much easier than in the theorems of Flatto-Levinson and Anosov as we “got rid of” the fast dynamics and can restrict our attention to the slow manifold equation. One drawback is that the overall condition of compactness and the spectral assumption is sometimes not met in applications.

For an example of obtaining existence and approximation of a periodic solution we return to the time-periodic case of system (2), a prey-predator system with unequal growth of prey N . The growth rate $r(t)$ and carrying capacity $K(t)$ are T -periodic. The slow manifolds SM_1, SM_2 are described by: $SM_1 : N = 0$, $SM_2 : N = K(t)$. SM_1 is unstable, SM_2 is stable. $N = K(t)$ is a first order periodic approximation of the prey population in SM_2 . We will find co-existence of prey and predator from the next approximation (omitted here).

Discussion of the Tikhonov theorem versus Fenichel.

The Tikhonov theorem can describe transient motion. Consider the Van der Pol equation with $\mu \gg 1$:

$$\ddot{x} + x = \mu(1 - x^2)\dot{x}, \tag{8}$$

with Liénard transformation producing:

$$\frac{1}{\mu}\dot{x} = z + x - \frac{1}{3}x^3, \quad \dot{z} = -\frac{1}{\mu}x. \quad (9)$$

With $1/\mu = \varepsilon$ we identify root $z = -x + \frac{1}{3}x^3$. Along the stable parts of the cubic curve

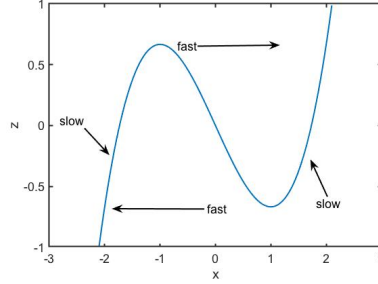


Figure 2. Slow manifolds and fast motion for Van der Pol relaxation.

we have slow motion, during a cycle 2 fast jumps take place. We obtain the well-known relaxation oscillation with slow motions periodically followed by fast transitions from one stable manifold to the other one; $\mu = 20$. The jumps are described by Tikhonov's theorem, choosing compact parts of the stable cubic curves we can apply Fenichel; the complete picture arises by patching parts together using singular perturbation theory.

4. Slow-fast limit cycles at higher order

Consider again the system of ODEs (1). Assume that leaving out the $\varepsilon R_1, R_2$ and $O(\varepsilon^2)$ terms, the system does not contain a limit cycle but suppose that, adding these perturbations, one or more limit cycles emerge by a bifurcation. A well-known example is the Hopf bifurcation arising in the Van der Pol-equation. Suppose we can solve the system when omitting the perturbation terms to construct the so-called variational equations in $\tau = t/\varepsilon$:

$$\begin{cases} r'_f = \varepsilon F_1(r_f, \phi_f, r_s, \phi_s) + O(\varepsilon^2), & r'_s = \varepsilon^2 G_1(r_f, \phi_f, r_s, \phi_s) + O(\varepsilon^3), \\ \phi'_f = \Omega_1 + \varepsilon F_2(r_f, \phi_f, r_s, \phi_s) + O(\varepsilon^2), & \phi'_s = \varepsilon \Omega_2 + \varepsilon^2 G_2(r_f, \phi_f, r_s, \phi_s) + O(\varepsilon^3), \end{cases} \quad (10)$$

where ' represents differentiation with respect to τ , the index f indicates a fast variable, s indicates slow. The dimensions of r_f, ϕ_f, r_s, ϕ_s depend on system (1). In this way we have reduced the system to a quasi-periodic system where averaging over angles is possible, see [12] ch. 5. If the limit cycle of the fast equation is asymptotically stable it is natural to average over the fast limit cycle which means averaging over ϕ_f . Averaging over angles

involves the analysis of resonance manifolds. This theory has many aspects that are difficult to capture in one theorem. We summarize the procedure as it runs in general.

1. Average over the fast angles ϕ_f with attention to the possible presence of resonance manifolds. We obtain a system without angle ϕ_f .
2. Consider the resonance manifolds separately, see [12] ch. 5.
3. We can rescale $\tau \rightarrow t$ or alternatively use the slow angles ϕ_s as a timelike variable. The resulting slow-fast system may contain a slow manifold M .
4. Consider the dynamics in the slow manifold M by eliminating r_f . We can average over the slow angle ϕ_s in the slow manifold. Critical points will correspond with periodic solutions or tori producing interesting phenomena in the original slow-fast system (10).
5. This procedure enables us to extend the description of the dynamics to 3 timescales: $t/\varepsilon, t$ and εt , expressed in the corresponding angles. Some aspects of this analysis corresponds with the treatment of slow-fast systems in [2].

In actual applications we will meet problems of normal hyperbolicity of slow manifolds and certain degeneracies. This is not uncommon in applications as in practice symmetries and specific parameter values may destroy aspects of the general mathematical theory.

Example 1

Interaction of slow-fast Van der Pol limit cycles.

We assume $(x_1, x_2) \in \Gamma_1, (y_1, y_2) \in \Gamma_2$ with $\Gamma_1, \Gamma_2 \subset \mathbb{R}^2$, compact subsets containing the origin. This produces a relatively simple interaction problem as we have only one fast angle (or time). Consider the system with parameters a_1, a_2 , positive frequency ω , parameter $\mu > 0$:

$$\begin{cases} x'_1 &= x_2 + \varepsilon(x_1 - \frac{1}{3}x_1^3), x'_2 = -x_1 - \varepsilon a_1 y_1^2 x'_1, \\ \dot{y}_1 &= y_2 + \mu(y_1 - \frac{1}{3}y_1^3), \dot{y}_2 = -\omega^2 y_1 - \mu a_2 x_1^2 \dot{y}_1. \end{cases} \quad (11)$$

Differentiation is respectively with respect to $\tau = t/\varepsilon$ and t . The slow manifold of system (11) is given by the plane $x_1 = x_2 = 0$. If $\varepsilon = 0$ the slow manifold is Lyapunov (neutrally) stable. It contains an asymptotically stable slow limit cycle corresponding with the Van der Pol-oscillator in (y_1, y_2) coordinates. Another invariant manifold is given by the plane $y_1 = y_2 = 0$ where a fast Van der Pol-oscillator is found in (x_1, x_2) coordinates. The question of interest is the interaction of the two oscillators outside the 2 coordinate planes.

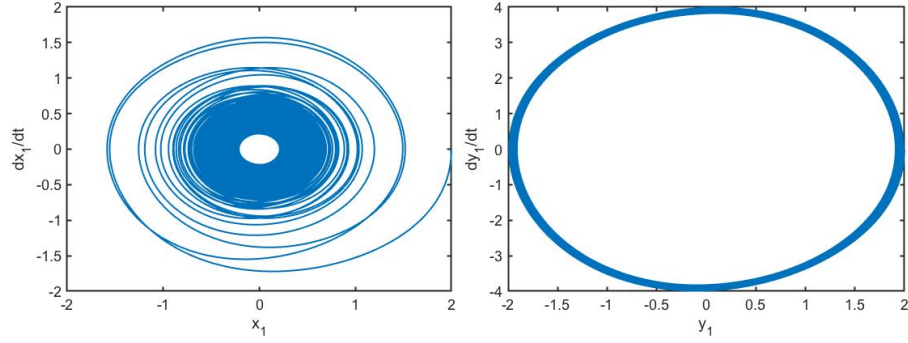


Figure 3. Numerical approximation of a stable torus of system (12). Left the projection of $x_1(t), \dot{x}_1(t)$ (fast), right the projection of $y_1(t), \dot{y}_1(t)$ (slow) with $x_1(0) = 2, \dot{x}_1(0) = 0, y_1(0) = 2, \dot{y}_1(0) = 0, \varepsilon = \mu = 0.1, a_1 = 0.5, a_2 = 0.3, \omega = 2$. The choice of parameters corresponds with the analysis of the slow manifold (16) leading to a stable torus.

The more familiar (equivalent) scalar equations in respectively τ and t are:

$$\begin{cases} \frac{d^2 x_1}{d\tau^2} + x_1 &= \varepsilon(1 - x_1^2 - a_1 y_1^2) \frac{dx_1}{d\tau}, \\ \frac{d^2 y_1}{dt^2} + \omega^2 y_1 &= \mu(1 - y_1^2 - a_2 x_1^2) \frac{dy_1}{dt}. \end{cases} \quad (12)$$

We transform to amplitude-angle variables: $x_1 = r_1 \sin \phi_1, x_1' = r_1 \cos \phi_1, y_1 = r_2 \sin \phi_2, \dot{y}_1 = r_2 \omega \cos \phi_2$. The equations from system (12) produce with differentiation with respect to τ :

$$\begin{cases} r_1' &= \varepsilon \cos^2 \phi_1 [1 - r_1^2 \sin^2 \phi_1 - a_1 r_2^2 \sin^2 \phi_2], \\ \phi_1' &= 1 + \varepsilon \sin \phi_1 \cos \phi_1 [1 - r_1^2 \sin^2 \phi_1 - a_1 r_2^2 \sin^2 \phi_2], \\ r_2' &= \varepsilon \mu r_2 \cos^2 \phi_2 [1 - r_2^2 \sin^2 \phi_2 - a_2 r_1^2 \sin^2 \phi_1], \\ \phi_2' &= \varepsilon \omega - \varepsilon \mu \sin \phi_2 \cos \phi_2 [1 - r_2^2 \sin^2 \phi_2 - a_2 r_1^2 \sin^2 \phi_1]. \end{cases} \quad (13)$$

We can average over the fast angle ϕ_1 to obtain the approximating system:

$$\begin{cases} \tilde{r}_1' &= \frac{1}{2} \varepsilon [1 - \frac{1}{4} \tilde{r}_1^2 - a_1 \tilde{r}_2^2 \sin^2 \tilde{\phi}_2], \\ \tilde{r}_2' &= \varepsilon \mu \tilde{r}_2 \cos^2 \tilde{\phi}_2 [1 - \tilde{r}_2^2 \sin^2 \tilde{\phi}_2 - \frac{a_2}{2} \tilde{r}_1^2], \\ \tilde{\phi}_2' &= \varepsilon \omega - \varepsilon \mu \sin \phi_2 \cos \phi_2 [1 - r_2^2 \sin^2 \phi_2 - \frac{a_2}{2} \tilde{r}_1^2]. \end{cases} \quad (14)$$

Starting at the same initial values as r_1, r_2, ϕ_2 , the approximations $\tilde{r}_1, \tilde{r}_2, \tilde{\phi}_2$ have validity $O(\varepsilon)$ on the timescale $1/\varepsilon$ in τ (as in the Pontryagin-Rodygin theorem). We conclude from system (14) that the only possibility to quench the fast oscillator *completely* is if $a_1 > 0$.

We will consider the case $\mu = O(\varepsilon)$.

Put $\mu = \varepsilon\mu_0$ with μ_0 a positive constant independent of ε . In this case $\tilde{\phi}_2$ is timelike with respect to \tilde{r}_2 and we can reformulate system (14) as:

$$\begin{cases} \frac{d\tilde{r}_1}{d\tilde{\phi}_2} = \frac{1}{2\omega}[1 - \frac{1}{4}\tilde{r}_1^2 - a_1\tilde{r}_2^2 \sin^2 \tilde{\phi}_2] + O(\varepsilon), \\ \frac{d\tilde{r}_2}{d\tilde{\phi}_2} = \varepsilon \frac{\mu_0}{\omega} \tilde{r}_2 \cos^2 \tilde{\phi}_2 [1 - \tilde{r}_2^2 \sin^2 \tilde{\phi}_2 - \frac{a_2}{2}\tilde{r}_1^2] + O(\varepsilon^2). \end{cases} \quad (15)$$

System (15) has a slow manifold given by

$$1 - \frac{1}{4}\tilde{r}_1^2 - a_1\tilde{r}_2^2 \sin^2 \tilde{\phi}_2 = 0. \quad (16)$$

The slow manifold is stable if we find a positive solution for \tilde{r}_1 . Eliminating \tilde{r}_1 with (16) we find for the dynamics in the slow manifold:

$$\frac{d\tilde{r}_2}{d\tilde{\phi}_2} = \varepsilon \frac{\mu_0}{\omega} \tilde{r}_2 \cos^2 \tilde{\phi}_2 [1 - 2a_2 - \tilde{r}_2^2(1 - 4a_1a_2) \sin^2 \tilde{\phi}_2] + O(\varepsilon^2). \quad (17)$$

There is no obstruction to average again, this time over $\tilde{\phi}_2$. We find in the slow manifold the equation:

$$\frac{d\tilde{r}_2}{d\tilde{\phi}_2} = \varepsilon \frac{\mu_0}{2\omega} \tilde{r}_2 [1 - 2a_2 - \frac{1}{4}(1 - 4a_1a_2)\tilde{r}_2^2]. \quad (18)$$

The solutions of eq. (18) are valid to $O(\varepsilon)$ on an $1/\varepsilon$ timescale in $\tilde{\phi}_2$, which means a long timescale in t . A periodic solution in $\tilde{\phi}_2$ arises if

$$\tilde{r}_2^2 = 4 \frac{1 - 2a_2}{1 - 4a_1a_2} \quad (19)$$

with positive righthand side. If in addition both $1 - 2a_2$ and $1 - 4a_1a_2$ are positive, the periodic solution $\tilde{r}_2(\tilde{\phi}_2)$ is stable. A corresponding approximation in the slow manifold for \tilde{r}_1 can be found from eq. (16). The approximations for r_1 and r_2 represent a torus in 4-space; a finite-dimensional torus will contain quasi-periodic solutions. See fig. 3 for an illustration.

The analysis of coupled slow-fast Van der Pol-oscillators is more complicated if we have more than 2 oscillators. To avoid discussing too many cases we reduce the number of free parameters.

Example 2

The case of one fast and two slow Van der Pol-oscillators.

We will present an abbreviated account with an illustration. Consider the system of 3 scalar equations with parameters $a, b > 0$:

$$\begin{cases} x'' + x &= \varepsilon(1 - x^2 - by^2 - bz^2)x', \\ \ddot{y} + y &= \varepsilon(1 - ax^2 - y^2 - z^2)\dot{y}, \\ \ddot{z} + z &= \varepsilon(1 - ax^2 - y^2 - z^2)\dot{z}, \end{cases} \quad (20)$$

where again a prime indicates differentiation with respect to $\tau = t/\varepsilon$, a dot indicates differentiation with respect to time t . The coordinate planes correspond with invariant manifolds, we consider the dynamics outside the coordinate planes.

Using amplitude-angle variables and fast time τ also for the 2 slow equations we have the equivalent system:

$$\begin{cases} r_1' &= \varepsilon r_1 \cos^2 \phi_1 (1 - r_1^2 \sin^2 \phi_1 - br_2^2 \sin^2 \phi_2 - br_3^2 \sin^2 \phi_3), \\ \phi_1' &= 1 - \frac{\varepsilon}{2} \sin 2\phi_1 (1 - r_1^2 \sin^2 \phi_1 - br_2^2 \sin^2 \phi_2 - br_3^2 \sin^2 \phi_3), \\ r_2' &= \varepsilon^2 r_2 \cos^2 \phi_2 (1 - ar_1^2 \sin^2 \phi_1 - r_2^2 \sin^2 \phi_2 - r_3^2 \sin^2 \phi_3), \\ \phi_2' &= \varepsilon - \frac{\varepsilon^2}{2} \sin 2\phi_2 (1 - ar_1^2 \sin^2 \phi_1 - r_2^2 \sin^2 \phi_2 - r_3^2 \sin^2 \phi_3), \\ r_3' &= \varepsilon^2 r_3 \cos^2 \phi_3 (1 - ar_1^2 \sin^2 \phi_1 - r_2^2 \sin^2 \phi_2 - r_3^2 \sin^2 \phi_3), \\ \phi_3' &= \varepsilon - \frac{\varepsilon^2}{2} \sin 2\phi_3 (1 - ar_1^2 \sin^2 \phi_1 - r_2^2 \sin^2 \phi_2 - r_3^2 \sin^2 \phi_3). \end{cases} \quad (21)$$

As before we can average over the fast angle ϕ_1 to find:

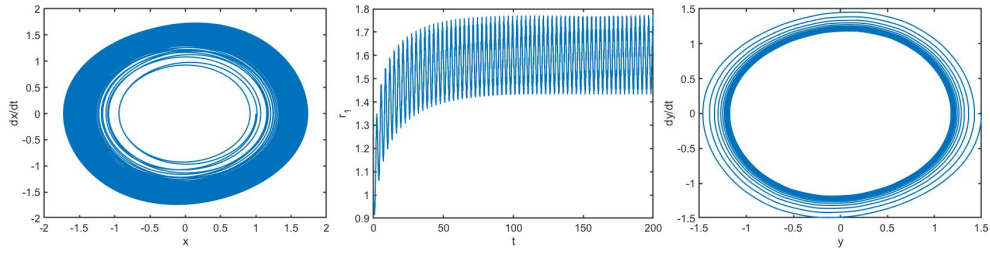


Figure 4. Numerical approximation of a stable torus of system (20). Left the projection of the phaseplane $x_1(t), \dot{x}_1(t)$ (fast), middle $r_1(t) = \sqrt{x_1^2(t) + \dot{x}_1^2(t)}$, right the projection of the phaseplane $y_1(t), \dot{y}_1(t)$ (slow) with $x_1(0) = 1, \dot{x}_1(0) = 0, y_1(0) = 1.5, \dot{y}_1(0) = 0, z(0) = 1.3, \dot{z}(0) = 0, \varepsilon = 0.1, a = b = 0.3$. The choice of parameters corresponds with the analysis of the slow manifold (27) leading to a stable torus.

$$\begin{cases} \tilde{r}_1' &= \frac{\varepsilon}{2} \tilde{r}_1 (1 - \frac{1}{4} \tilde{r}_1^2 - 2b\tilde{r}_2^2 \sin^2 \tilde{\phi}_2 - 2b\tilde{r}_3^2 \sin^2 \tilde{\phi}_3), \\ \tilde{r}_2' &= \varepsilon^2 \tilde{r}_2 \cos^2 \tilde{\phi}_2 (1 - \frac{a}{2} \tilde{r}_1^2 - \tilde{r}_2^2 \sin^2 \tilde{\phi}_2 - \tilde{r}_3^2 \sin^2 \tilde{\phi}_3), \\ \tilde{\phi}_2' &= \varepsilon - O(\varepsilon^2), \\ \tilde{r}_3' &= \varepsilon^2 \tilde{r}_3 \cos^2 \tilde{\phi}_3 (1 - \frac{a}{2} \tilde{r}_1^2 - \tilde{r}_2^2 \sin^2 \tilde{\phi}_2 - \tilde{r}_3^2 \sin^2 \tilde{\phi}_3), \\ \tilde{\phi}_3' &= \varepsilon - O(\varepsilon^2). \end{cases} \quad (22)$$

System (22) has in τ a relatively fast amplitude r_1 , fast angles ϕ_2, ϕ_3 and slow amplitudes r_2, r_3 . We will average over the fast angles outside the resonance domain determined by $\tilde{\phi}'_2 = \tilde{\phi}'_3$. We find for the slow amplitudes:

$$\begin{cases} \tilde{r}'_2 &= \frac{\epsilon^2}{2} \tilde{r}_2 (1 - \frac{a}{2} \tilde{r}_1^2 - \frac{1}{4} \tilde{r}_2^2 - \frac{1}{2} \tilde{r}_3^2), \\ \tilde{r}'_3 &= \frac{\epsilon^2}{2} \tilde{r}_3 (1 - \frac{a}{2} \tilde{r}_1^2 - \frac{1}{2} \tilde{r}_2^2 - \frac{1}{4} \tilde{r}_3^2). \end{cases} \quad (23)$$

Interesting dynamics may happen if the following 2 ellipsoids intersect:

$$\frac{a}{2} \tilde{r}_1^2 + \frac{1}{4} \tilde{r}_2^2 + \frac{1}{2} \tilde{r}_3^2 = 1, \quad \frac{a}{2} \tilde{r}_1^2 + \frac{1}{2} \tilde{r}_2^2 + \frac{1}{4} \tilde{r}_3^2 = 1.$$

This leads to

$$\tilde{r}_2 = \tilde{r}_3, \quad \frac{a}{2} \tilde{r}_1^2 = 1 - \frac{3}{4} \tilde{r}_2^2. \quad (24)$$

In this case the dynamics of system (20) reduces to the case of 1 fast and 1 slow oscillator which we discussed before. Looking for solutions in system (20) of the form $y^2 = z^2$ gives a shortcut to the problem.

The resonance cases $\phi_2 - \phi_3 = 0, \pi$ lead to a first integral:

$$r_2 = \frac{r_2(0)}{r_3(0)} r_3. \quad (25)$$

Replacing ϕ_3 or $\phi_3 + \pi$ by ϕ_2 we can average over ϕ_2 to obtain in the 2 resonance cases:

$$\begin{cases} \tilde{\tilde{r}}'_2 &= \frac{\epsilon^2}{2} \tilde{\tilde{r}}_2 (1 - \frac{a}{2} \tilde{\tilde{r}}_1^2 - \frac{1}{4} \tilde{\tilde{r}}_2^2 - \frac{1}{4} \tilde{\tilde{r}}_3^2), \\ \tilde{\tilde{r}}'_3 &= \frac{\epsilon^2}{2} \tilde{\tilde{r}}_3 (1 - \frac{a}{2} \tilde{\tilde{r}}_1^2 - \frac{1}{4} \tilde{\tilde{r}}_2^2 - \frac{1}{4} \tilde{\tilde{r}}_3^2). \end{cases} \quad (26)$$

Another approach is to consider first the slow manifold obtained from system (22) for \tilde{r}_1 . We find (leaving out the tildes)

$$r_1^2 = 4 - 8b(r_2^2 \sin^2 \phi_2 + r_3^2 \sin^2 \phi_3). \quad (27)$$

Eliminating \tilde{r}_1 from the equations for \tilde{r}_2, \tilde{r}_3 in system (22) we have after averaging over the angles for the dynamics in the slow manifold:

$$\begin{cases} \tilde{\tilde{r}}'_2 &= \frac{\epsilon^2}{2} \tilde{\tilde{r}}_2 [1 - 2a - (\frac{1}{4} - ab) \tilde{\tilde{r}}_2^2 - 2(\frac{1}{4} - ab) \tilde{\tilde{r}}_3^2], \\ \tilde{\tilde{r}}'_3 &= \frac{\epsilon^2}{2} \tilde{\tilde{r}}_3 [1 - 2a - 2(\frac{1}{4} - ab) \tilde{\tilde{r}}_2^2 - (\frac{1}{4} - ab) \tilde{\tilde{r}}_3^2]. \end{cases} \quad (28)$$

We can draw several conclusions from system (28). An important one is that we find in the slow manifold of system (22) a stable torus if

$$0 < a < \frac{1}{2}, \quad 0 < ab < \frac{1}{4}. \quad (29)$$

See fig. 4. We leave out the figures for other cases suggested by conditions (29); for instance changing in the data of fig. 4 b to $b = 1$, the slow solutions y, z tend to a stable periodic solution (if the y, z frequencies would be different we would obtain a stable 2-dimensional torus), the fast oscillator is quenched and tends to the x, \dot{x} coordinate plane. Reversing the role of the parameters by putting $a = 1, b = 0.3$ the slow solutions y, z are quenched and tend to the 2 coordinate planes, the fast solution tends to a limit cycle in the x, \dot{x} phaseplane.

The examples of slow-fast oscillators with Van der Pol self-excitation that we discussed have common features like averaging first over a fast angle, averaging after that over slow angles, the presence of slow manifolds and the possibility of local resonance manifolds. To facilitate the demonstrations we have in the examples only a few parameters. A consequence of this is more symmetry producing sometimes non-generic reductions in the analysis. It would be of interest to repeat studying the examples with more parameters. Many more bifurcations are to be expected.

5. Conclusions

1. Slow-fast systems arise naturally in applications involving interactions and quenching.
2. Limit cycles obtained in a perturbation framework can be used to study long time slow-fast interactions described by 3 timescales: $t/\varepsilon, t$ and εt .

Acknowledgement

The author declares that he has no conflict of interest.

References

- [1] Anosov, D.V. *On limit cycles in systems of differential equations with a small parameter in the highest derivatives*, Mat Sb (1960) 50, pp. 299-334; transl. AMS Trans. Ser. 2, vol. 33, pp. 233-276.
- [2] Blekhman, I.I. *Vibrational Mechanics-nonlinear dynamics effects, general approach, application*, (2000) Singapore, World Scientific.
- [3] Doelman, A. and Verhulst, F. *Bifurcations of strongly non-linear self-excited oscillations*, (1994) Math. Methods Appl. Sciences 17, pp. 189-207.
- [4] Fenichel, N. *Persistence and smoothness of invariant manifolds for flows*, (1971) Indiana Univ. Math. J. 21, pp. 193-225.
- [5] Fenichel, N. *Asymptotic stability with rate conditions*, (1974) Indiana Univ. Math. J. 23, pp. 1109-1137.

- [6] Fenichel, N. *Asymptotic stability with rate conditions, II*, (1977) Indiana Univ. Math. J. 26, pp. 81–93.
- [7] Fenichel, N. *Geometric singular perturbations theory for ordinary differential equations*, (1979) J. Diff. Eq. 31, pp. 53–98.
- [8] Flatto L. and Levinson, N. *Periodic solutions of singularly perturbed systems*, (1955) J. Rat. Mech. Analysis 4, pp. 943–950.
- [9] Jones, C.K.R.T. *Geometric singular perturbation theory*, in *Dynamical Systems*, Montecatini Terme (1994) (Johnson, R., ed.) Lecture Notes in Mathematics 1609, pp. 44–118, Springer.
- [10] O’Malley, Jr., R.E., *Topics in singular perturbations*, (1968) Adv. Math. 2, pp. 365–470.
- [11] Pontryagin L.S. and Rodygin, L.V. *Approximate solution of a system of ordinary differential equations involving a small parameter in the derivatives*, (1960) Soviet Math. Doklady 1, pp. 237–240 (1960), orig. Russian: Dokl. Ak. Nauk SSSR 131, pp. 255–258.
- [12] Sanders, J.A. Verhulst, F. and Murdock, J. *Averaging methods in nonlinear dynamical systems* 2nd ed., (2007) Appl. Math. Sciences 59, Springer, New York etc..
- [13] Tikhonov, A.N. *Systems of differential equations containing a small parameter multiplying the derivative*, (1952) Mat. Sb. 31, pp. 575–586.
- [14] Vasil’eva, A.B., *Asymptotic behaviour of solutions to certain problems involving nonlinear differential equations containing a small parameter multiplying the highest derivatives*, (1963) Russ. Math. Surv. 18, pp. 13–84.

Ferdinand Verhulst, PhD: University of Utrecht, Mathematisch Instituut, PO Box 80.010, 3508 TA Utrecht, The Netherlands (f.verhulst@uu.nl).

The author gave a presentation of this paper during one of the conference sessions.

Multibody models for gait analysis

Wiktoria Wojnicz, Bartłomiej Zagrodny, Michał Ludwicki,
Jerzy Mrozowski, Jan Awrejcewicz, Edmund Wittbrodt

Abstract: The aim of this study was to create multibody biomechanical models to analyze a normal gait of the human. Proposed models can be used to identify joint moments of the lower limbs during normal gait in the single and double support phases. Applying Newton-Euler formulation, following planar models were developed: 1) a mathematical 6DOF model describing a gait in the sagittal plane of the body for single support phase and double support phase; 2) a mathematical 7DOF model describing a gait in the sagittal plane of the body for single support phase and double support phase; 3) a mathematical 7DOF model describing a gait in the frontal plane of the body for single support phase and double support phase. Proposed mathematical models can be applied to solve a forward dynamic task or inverse dynamic task. A validation of these models had been performed by comparing results measured over examination of normal human gait and results calculated by solving an inverse dynamic task.

1. Introduction

From the mechanical point of view a gait of the human is considered as periodical movements of lower limbs that alternately generate stable and unstable states. Over each phase of the gait a body weight is propelled by maintaining a stable posture due to functioning of posture-stabilizing mechanisms controlled by the human nervous system. A normal gait occurs when the right and left parts of the human body perform similar motions with respect to the anatomical planes of the body. This gait can be analyzed by deriving planar dynamic models describing motions occurring in a sagittal and frontal plane of the body. A pathological gait occurs when the right and left parts of the human body perform asymmetrical motions in space. To analyze this gait the spatial dynamic models should be derived.

A human body is treated as a musculoskeletal system composed of segments having defined number of degrees of freedom (DOFs). Net joint moments, net joint intersegmental forces and net joint powers generated in this system during gait can be estimated by using an inverse dynamics approach [11]. To solve an inverse dynamic task, the following data should be assessed: 1) biomechanical data of the subject (segment masses and dimensions; segment radii of gyration; segment moments of inertia); 2) kinematic data of human segments (joint centers, proximal and distal points of segments that are used to calculate angular displacement, angular velocity and angular acceleration of body parts); 3) kinetic data (reaction forces of interaction with the ground that can be measured by using a force plate); 4) EMG data (to estimate activity of muscles producing motion and muscle excitation timing).

A gait is composed of single and double support phases. During each double support phase a system becomes a closed system. This demands to solve an indeterminacy problem referring to estimation of external force/moment distribution.

The aim of this study was to create multibody biomechanical models to analyze a normal gait of the human and to identify joint moments of the lower limbs during all gait phases. The scope of the study was to derive dynamic models to analyze: 1) single support phase (open sagittal 6DOF model, open sagittal 7DOF model and open frontal 7DOF model); 2) double support phase, which occurs due to interaction between the sole of the swinging leg and a ground (closed sagittal 6DOF model, closed sagittal 7DOF model and closed frontal 7DOF model)..

2. Materials and Methods

A human body was treated as a multibody system composed of two ankle joints, two knee joints and one hip joint (sagittal models) or two hip joints (frontal models). An influence of the upper part of the body (the pelvis, torso, head, neck and upper limbs) was modelled by using two approaches. The first one implies that the upper part of the body is modelled as one concentrated force applied at the center of gravity of the upper body part. An influence of this force is modelled as a load (force and its moment) transmitted through the hip joint to the stance leg (single support phase) or both legs (double support phase). This approach was adapted to create a sagittal 6DOF model and a frontal 7DOF model. The second approach treats the upper part of the body as one additional segment, which is connected to the hip joint. This approach was adapted to create a sagittal 7DOF model.

To simulate behavior over single and double support phases (Fig.1) there were proposed two different type of models: open sagittal 6DOF model and closed sagittal 6DOF model; open sagittal 7DOF model and closed sagittal 7DOF model; open frontal 7DOF model and closed frontal 7DOF model. It should be mentioned that the Fig.1 illustrates behavior of the 6DOF model (behavior of each 7DOF model is similar).

Biomechanical multibody models presented in this paper were derived by applying Newton-Euler formulation [1,4]. Proposed biomechanical model can be applied to analyze forward or inverse dynamics problems. It is worth noticing that proposed models are more complex ones with respect to the models presented in [5-6, 12].

It should be mentioned that real biomechanical system is composed of joints that are linking neighboring segments through passive tissues (bursa, ligaments, tendons) and active tissues (muscles). An influence of both tissues can be considered by inputting rheological models composed of viscoelastic elements. These elements are also implemented in the joints of proposed biomechanical models.

An approach to solve a problem with interaction, which occurs when the heel of the swing leg strikes the ground (initiation of the double support phase), is described in the below subsection referring to the interaction modelling. Considering a homogeneous mass distribution, the segmentation (i.e. body partitioning) was performed according to Zatsiorsky's method [2-3]. Proposed biomechanical models were implemented in MATLAB software by creating author programs.

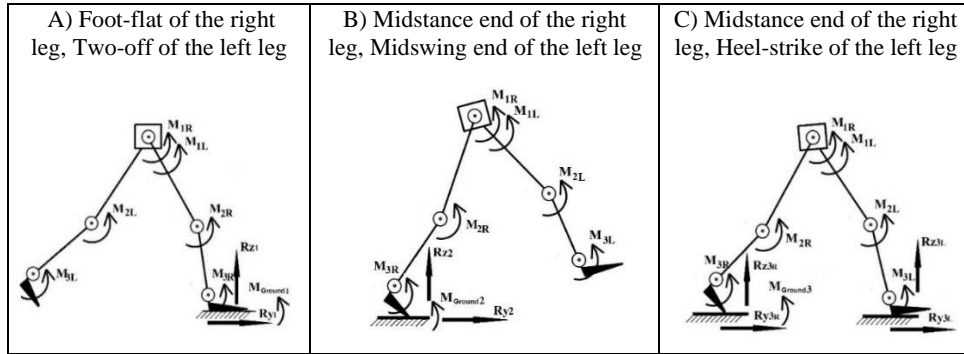


Figure 1. Structural 6DOF model in the single support phase (A, B) and double support phase (C): $M_{Ground1}$ – the ground moment during the single support phase (A), $M_{Ground2}$ – the ground moment during the single support phase (B), $M_{Ground3}$ – the ground moment during the double support phase (C); R_{yj} – the y-th component of the leg reaction force (anterior-posterior component) during the j-th single support phase ($j = 1, 2$); R_{zj} – the z-th component of the leg reaction force (vertical component) during the j-th single support phase ($j = 1, 2$); R_{z3R} and R_{z3L} – the z-th components of the reaction force of the right and left leg during the double support phase; R_{y3R} and R_{y3L} – the y-th components of the reaction force of the right and left leg during the double support phase; M_{iL} – i-th moment acts at the i-th joint of the left leg; M_{iR} – i-th moment acts at the i-th joint of the right leg

Sagittal 6DOF model

Considering the body as a structure composed of six segments serially linked through the hinge joints in a sagittal plane, there were created two models (Fig. 2): 1) open sagittal 6DOF model, which can be applied to model a single support phase (in this case both y-th (F_y) and z-th (F_z) components of reaction force of the swing leg are equal to zero); 2) closed sagittal 6DOF model, which can be used to describe a double support phase. Both models can be applied to analyze kinematics and dynamics of normal gait in a sagittal plane over specific phases. An influence of the upper part of the body was modelled as one concentrate force G_7 (it is a gravity force of upper part of the body) and the moment of this force M_{G7} . It was assumed that this force and its moment influence the stance leg. The hinge joint O models the metatarsophalangeal joint of the stance feet by assuming that it does not cause any dissipation phenomenon. A complete mathematical models of the open sagittal 6DOF model and closed sagittal 6DOF model are described in [8-9].

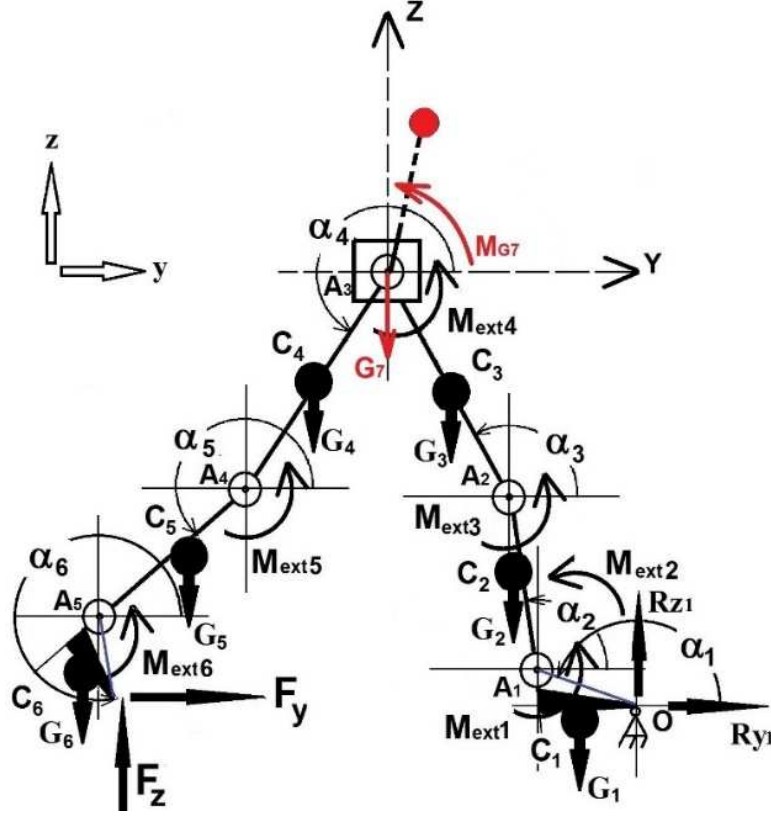


Figure 2. The sagittal 6DOF model (O – the point between the support foot and the ground (the metatarsophalangeal joint); A_1 – the ankle joint of stance leg; A_2 – the knee joint of stance leg; A_3 – the hip joint; A_4 – the knee joint of swing leg; A_5 – the ankle joint of swing leg; α_i – the angle of the i -th segment (each angle is measured as an absolute coordinate); G_i – the gravity force of the i -th segment that acts at its center of gravity C_i ; M_{ij} – the net joint moment between the i -th segment and j -th segment ($M_{ij} = M_{ji}$); M_{exti} – the external moment loading the i -th segment; R_{y1} – the y -th component of stance leg reaction force (anterior-posterior component); R_{z1} – the z -th component of the stance leg reaction force (vertical component); F_y and F_z – the y -th and z -th component of reaction force of the swing leg during double supporting phase; y – the sagittal axis; z – the vertical axis) [9]

Sagittal 7DOF model

Considering the body as a dendritic structure composed of seven segments in a sagittal plane, there were created (Fig. 3): 1) the open sagittal 7DOF model, which can be applied to model a single support phase (in this case both the y -th (F_y) and z -th (F_z) components of reaction force of the swing leg are equal to zero); 2) the closed sagittal 7DOF model, which can be applied to model a double support

phase. These models can be applied to model kinematics and dynamics of normal gait in a sagittal plane over specific phases. An influence of the upper part of the body was modelled as the seventh segment, which gravity force acts at the center of mass placed at the point C_7 . Mathematical models of the open sagittal 7DOF model and closed sagittal 7DOF model are described in detail in [9]

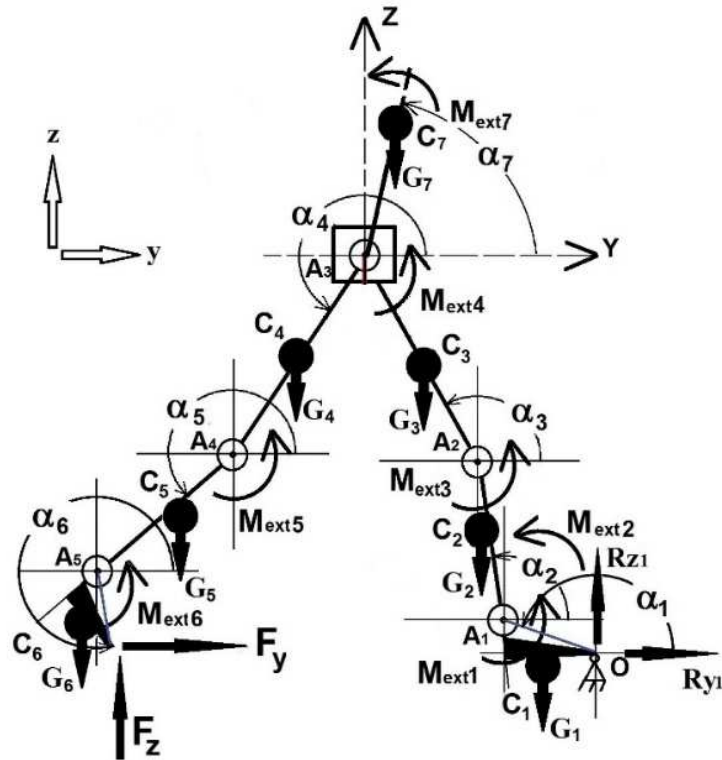


Figure 3. The sagittal 7DOF model (symbols are described in the Figure 2) [9]

Frontal 7DOF model

Considering a frontal plane and treating a body as a structure composed of seven segments serially linked through the hinge joints, there were created (Fig. 4): 1) the open frontal 7DOF model, which can be applied to model a single support phase (in this case both the x -th component of reaction force (R_{x2}^F) and the z -th component of reaction force (R_{z2}^F) are equal to zero); 2) the closed frontal 7DOF model, which can be used to describe a double support phase. Both models can be applied to analyze kinematics and dynamics of normal gait in a frontal plane during specific phases. An influence of the upper part of

the body was modelled as one concentrate force G_7 (it is a gravity force of upper part of the body) and its moment $M(b)$.

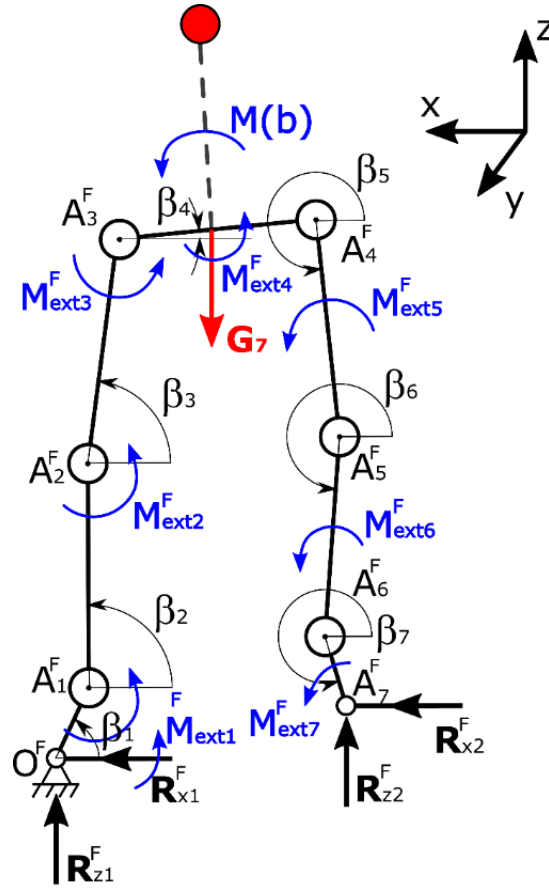


Figure 4. The frontal 7DOF model: (O^F – the point between the support foot and the ground; A^F_1 – the ankle joint of stance leg; A^F_2 – the knee joint of stance leg; A^F_3 – the stance leg hip joint; A^F_4 – the swing leg hip joint; A^F_5 – the knee joint of swing leg; A^F_6 – the ankle joint of swing leg; β_i – the angle of the i -th segment in the frontal plane (each angle is measured as an absolute coordinate); G – gravity force of the upper part of the body; M_{exti}^F – the external moment influenced the i -th segment in the frontal space; R_{x1}^F – the x -th component of stance leg reaction force (medio-lateral component); R_{z1}^F – the z -th component of the stance leg reaction force (vertical component); R_{x2}^F – the x -th component of reaction force during double support phase; R_{z2}^F – the z -th component of reaction force during double support phase; x – the transverse axis; y – the sagittal axis; z – the vertical axis)

A general mathematical description of the open frontal 7DOF model is a non-linear system of seven differential equations:

$$\begin{aligned}
& B_{11} \cdot \ddot{\beta}_1 + B_{12}(\beta_1, \beta_2) \cdot \ddot{\beta}_2 + B_{13}(\beta_1, \beta_3) \cdot \ddot{\beta}_3 + B_{14}(\beta_1, \beta_4) \cdot \ddot{\beta}_4 + B_{15}(\beta_1, \beta_5) \cdot \ddot{\beta}_5 + \\
& \quad + B_{16}(\beta_1, \beta_6) \cdot \ddot{\beta}_6 + B_{17}(\beta_1, \beta_7) \cdot \ddot{\beta}_7 = M_{1F} \\
& B_{21}(\beta_1, \beta_2) \cdot \ddot{\beta}_1 + B_{22} \cdot \ddot{\beta}_2 + B_{23}(\beta_2, \beta_3) \cdot \ddot{\beta}_3 + B_{24}(\beta_2, \beta_4) \cdot \ddot{\beta}_4 + B_{25}(\beta_2, \beta_5) \cdot \ddot{\beta}_5 + \\
& \quad + B_{26}(\beta_2, \beta_6) \cdot \ddot{\beta}_6 + B_{27}(\beta_2, \beta_7) \cdot \ddot{\beta}_7 = M_{2F} \\
& B_{31}(\beta_1, \beta_3) \cdot \ddot{\beta}_1 + B_{32}(\beta_2, \beta_3) \cdot \ddot{\beta}_2 + B_{33} \cdot \ddot{\beta}_3 + B_{34}(\beta_3, \beta_4) \cdot \ddot{\beta}_4 + B_{35}(\beta_3, \beta_5) \cdot \ddot{\beta}_5 + \\
& \quad + B_{36}(\beta_3, \beta_6) \cdot \ddot{\beta}_6 + B_{37}(\beta_3, \beta_7) \cdot \ddot{\beta}_7 = M_{3F} \\
& B_{41}(\beta_1, \beta_4) \cdot \ddot{\beta}_1 + B_{42}(\beta_2, \beta_4) \cdot \ddot{\beta}_2 + B_{43}(\beta_3, \beta_4) \cdot \ddot{\beta}_3 + B_{44} \cdot \ddot{\beta}_4 + B_{45}(\beta_4, \beta_5) \cdot \ddot{\beta}_5 + \\
& \quad + B_{46}(\beta_4, \beta_6) \cdot \ddot{\beta}_6 + B_{47}(\beta_4, \beta_7) \cdot \ddot{\beta}_7 = M_{4F} \\
& B_{51}(\beta_1, \beta_5) \cdot \ddot{\beta}_1 + B_{52}(\beta_2, \beta_5) \cdot \ddot{\beta}_2 + B_{53}(\beta_3, \beta_5) \cdot \ddot{\beta}_3 + B_{54}(\beta_4, \beta_5) \cdot \ddot{\beta}_4 + B_{55} \cdot \ddot{\beta}_5 + \\
& \quad + B_{56}(\beta_5, \beta_6) \cdot \ddot{\beta}_6 + B_{57}(\beta_5, \beta_7) \cdot \ddot{\beta}_7 = M_{5F} \\
& B_{61}(\beta_1, \beta_6) \cdot \ddot{\beta}_1 + B_{62}(\beta_2, \beta_6) \cdot \ddot{\beta}_2 + B_{63}(\beta_3, \beta_6) \cdot \ddot{\beta}_3 + B_{64}(\beta_4, \beta_6) \cdot \ddot{\beta}_4 + \\
& \quad + B_{65}(\beta_5, \beta_6) \cdot \ddot{\beta}_5 + B_{66} \cdot \ddot{\beta}_6 + B_{67}(\beta_6, \beta_7) \cdot \ddot{\beta}_7 = M_{6F} \\
& B_{71}(\beta_1, \beta_7) \cdot \ddot{\beta}_1 + B_{72}(\beta_2, \beta_7) \cdot \ddot{\beta}_2 + B_{73}(\beta_3, \beta_7) \cdot \ddot{\beta}_3 + B_{74}(\beta_4, \beta_7) \cdot \ddot{\beta}_4 + \\
& \quad + B_{75}(\beta_5, \beta_7) \cdot \ddot{\beta}_5 + B_{76}(\beta_6, \beta_7) \cdot \ddot{\beta}_6 + B_{77} \cdot \ddot{\beta}_7 = M_{7F}
\end{aligned} \tag{1}$$

where β_i – the i -th angular displacement of the i -th segment (the i -th joint angle) in the frontal plane; $\dot{\beta}_i$ – the i -th angular velocity of the i -th segment in the frontal plane; $\ddot{\beta}_i$ – the i -th angular acceleration of the i -th segment in the frontal plane, $B_{ij}(\beta_i, \beta_j)$ – the ij -th coefficient depending on the mechanical characteristics.

A general mathematical description of the closed sagittal 7DOF model, which is an overactuated system, is a non-linear system of seven differential equations:

$$\begin{aligned}
& B_{11} \cdot \ddot{\beta}_1 + B_{12}(\beta_1, \beta_2) \cdot \ddot{\beta}_2 + B_{13}(\beta_1, \beta_3) \cdot \ddot{\beta}_3 + B_{14}(\beta_1, \beta_4) \cdot \ddot{\beta}_4 + B_{15}(\beta_1, \beta_5) \cdot \ddot{\beta}_5 + \\
& \quad + B_{16}(\beta_1, \beta_6) \cdot \ddot{\beta}_6 + B_{17}(\beta_1, \beta_7) \cdot \ddot{\beta}_7 = M_{1F} - L_1 \cdot \sin(\beta_1) \cdot R^F_{x2} + L_1 \cdot \cos(\beta_1) \cdot R^F_{z2} \\
& B_{21}(\beta_1, \beta_2) \cdot \ddot{\beta}_1 + B_{22} \cdot \ddot{\beta}_2 + B_{23}(\beta_2, \beta_3) \cdot \ddot{\beta}_3 + B_{24}(\beta_2, \beta_4) \cdot \ddot{\beta}_4 + B_{25}(\beta_2, \beta_5) \cdot \ddot{\beta}_5 + \\
& \quad + B_{26}(\beta_2, \beta_6) \cdot \ddot{\beta}_6 + B_{27}(\beta_2, \beta_7) \cdot \ddot{\beta}_7 = M_{2F} - L_2 \cdot \sin(\beta_2) \cdot R^F_{x2} + L_2 \cdot \cos(\beta_2) \cdot R^F_{z2} \\
& B_{31}(\beta_1, \beta_3) \cdot \ddot{\beta}_1 + B_{32}(\beta_2, \beta_3) \cdot \ddot{\beta}_2 + B_{33} \cdot \ddot{\beta}_3 + B_{34}(\beta_3, \beta_4) \cdot \ddot{\beta}_4 + B_{35}(\beta_3, \beta_5) \cdot \ddot{\beta}_5 + \\
& \quad + B_{36}(\beta_3, \beta_6) \cdot \ddot{\beta}_6 + B_{37}(\beta_3, \beta_7) \cdot \ddot{\beta}_7 = M_{3F} - L_3 \cdot \sin(\beta_3) \cdot R^F_{x2} + L_3 \cdot \cos(\beta_3) \cdot R^F_{z2} \\
& B_{41}(\beta_1, \beta_4) \cdot \ddot{\beta}_1 + B_{42}(\beta_2, \beta_4) \cdot \ddot{\beta}_2 + B_{43}(\beta_3, \beta_4) \cdot \ddot{\beta}_3 + B_{44} \cdot \ddot{\beta}_4 + B_{45}(\beta_4, \beta_5) \cdot \ddot{\beta}_5 + \\
& \quad + B_{46}(\beta_4, \beta_6) \cdot \ddot{\beta}_6 + B_{47}(\beta_4, \beta_7) \cdot \ddot{\beta}_7 = M_{4F} - L_4 \cdot \sin(\beta_4) \cdot R^F_{x2} + L_4 \cdot \cos(\beta_4) \cdot R^F_{z2} \\
& B_{51}(\beta_1, \beta_5) \cdot \ddot{\beta}_1 + B_{52}(\beta_2, \beta_5) \cdot \ddot{\beta}_2 + B_{53}(\beta_3, \beta_5) \cdot \ddot{\beta}_3 + B_{54}(\beta_4, \beta_5) \cdot \ddot{\beta}_4 + B_{55} \cdot \ddot{\beta}_5 + \\
& \quad + B_{56}(\beta_5, \beta_6) \cdot \ddot{\beta}_6 + B_{57}(\beta_5, \beta_7) \cdot \ddot{\beta}_7 = M_{5F} - L_5 \cdot \sin(\beta_5) \cdot R^F_{x2} + L_5 \cdot \cos(\beta_5) \cdot R^F_{z2} \\
& B_{61}(\beta_1, \beta_6) \cdot \ddot{\beta}_1 + B_{62}(\beta_2, \beta_6) \cdot \ddot{\beta}_2 + B_{63}(\beta_3, \beta_6) \cdot \ddot{\beta}_3 + B_{64}(\beta_4, \beta_6) \cdot \ddot{\beta}_4 + \\
& \quad + B_{65}(\beta_5, \beta_6) \cdot \ddot{\beta}_5 + B_{66} \cdot \ddot{\beta}_6 + B_{67}(\beta_6, \beta_7) \cdot \ddot{\beta}_7 = M_{6F} - L_6 \cdot \sin(\beta_6) \cdot R^F_{x2} + L_6 \cdot \cos(\beta_6) \cdot R^F_{z2} \\
& B_{71}(\beta_1, \beta_7) \cdot \ddot{\beta}_1 + B_{72}(\beta_2, \beta_7) \cdot \ddot{\beta}_2 + B_{73}(\beta_3, \beta_7) \cdot \ddot{\beta}_3 + B_{74}(\beta_4, \beta_7) \cdot \ddot{\beta}_4 + \\
& \quad + B_{75}(\beta_5, \beta_7) \cdot \ddot{\beta}_5 + B_{76}(\beta_6, \beta_7) \cdot \ddot{\beta}_6 + B_{77} \cdot \ddot{\beta}_7 = M_{7F} - M(R^F_{x2}) + M(R^F_{z2})
\end{aligned} \tag{2}$$

where $M(R_{x2}^F)$ and $M(R_{z2}^F)$ – moments originating from the components of interaction reaction that influence the seventh segment $A^F_6A^F_7$ (Fig. 4); L_i – length of the i -th segment that is placed under the i -th angle β_i .

Approaches for interaction modelling

In order to study an influence of interaction one could apply two approaches: the first one for inverse dynamic problem solution; the second one for forward dynamic task solution. According to the first approach, measured ground force values (the y -th component (F_y) and z -th component (F_z) in each sagittal model; the x -th component (R_{x2}^F) and z -th component (R_{z2}^F) in the frontal model) influenced by an interaction with the ground can be inputted into the chosen model. These values can be measured by using a second force plate. According to the second approach, an interaction with a ground can be modelled by applying an additional analytical model that estimates the value of external load needed to stay a strike foot in the narrow range of the ground level [9].

3. Results

A validation of proposed biomechanical models had been performed by solving an inverse dynamic task without using any optimization approach. To compare measured data with calculated ones the experimental researches had conducted on the group of health males. In this paper there are presented results of validation for one random chosen male person (body mass 72.2 kg and body height 177.5 cm) (Fig.5A). To obtain kinematic data there was used a marker setting (Rizzoli protocol) of OPTITRACK system composed of six cameras working with 120 Hz frequency and dedicated software (Fig.5B-5C). To measure kinetic data (interaction forces) the Steinbichler force plate was applied. A subject was given an oral instruction. This subject did five successful trials (each trial contained three full steps) by walking barefoot in preferred speed with open eyes. Specific gait phases were defined on the base of the analysis of the posture reproduced by the motion capture system (Fig. 6).

Applying Zatsiorsky's segmentation method and principles of mechanics, centers of gravity of all segments (right and left foot, right and left calf, right and left thigh, upper body part) were calculated for each frame recorded by the motion capture system. It was also assumed that the subject examined was in a homogenous gravity field (gravity acceleration equals to $g = 9.8 \text{ m/s}^2$).

On the base of markers' displacements there were calculated angular displacements of all segments of the body: a) in a sagittal plane (in Fig. 7 relative angular displacements are given as $Hip = \alpha_3 - \alpha_7$, $Knee = \alpha_3 - \alpha_2$ and $Ankle = \alpha_1 - \alpha_2 - \pi/2$ [7]); b) in a frontal plane (Fig. 8). To estimate segment angular velocities and segment angular acceleration, the kinematic data were processed by applying: 1) filtering (the Butterworth filter of the fourth order with 5Hz cut-off frequency was applied); 2) cubic spline interpolation; 3) differentiation by applying three-point difference method.

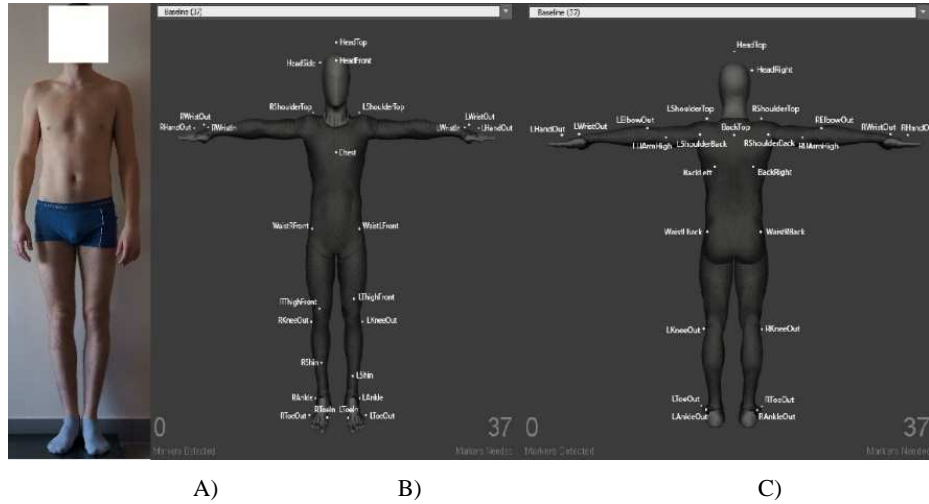


Figure 5. A) a subject examined; B) marker setting (anterior); C) marker setting (posterior)

A validation was performed by comparing a vertical component of interaction measured during single phase with a vertical component of interaction calculated by applying a sagittal 6DOF model (Fig. 9), sagittal 7DOF model (Fig. 10) and frontal 7DOF model (Fig. 11). Moreover, there were also compared data referring to a horizontal component of interaction measured during this phase and a horizontal component of interaction calculated by applying a sagittal 6DOF model (Fig. 12), sagittal 7DOF model (Fig. 13) and frontal 7DOF model (Fig. 14). Due to the fact that only one force plate was available in practice, we limited a validation of our models only to the single phase of the gait.

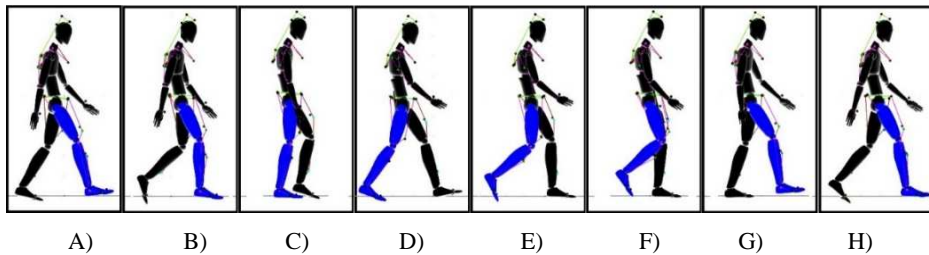


Figure 6. Posture setting during the one full step of the gait: A) Double support phase; B) Single support phase (foot-flat of right leg and toe-off of left leg); C) Single support phase (stance of right leg and deceleration of swing left leg); D) Double support phase; E) Single support phase (foot-flat of left leg and toe-off of right leg); F) Single support phase (stance of left leg and swing right leg); G) Single support phase (stance of left leg and deceleration of swing right leg); H) Double support phase [8-9]

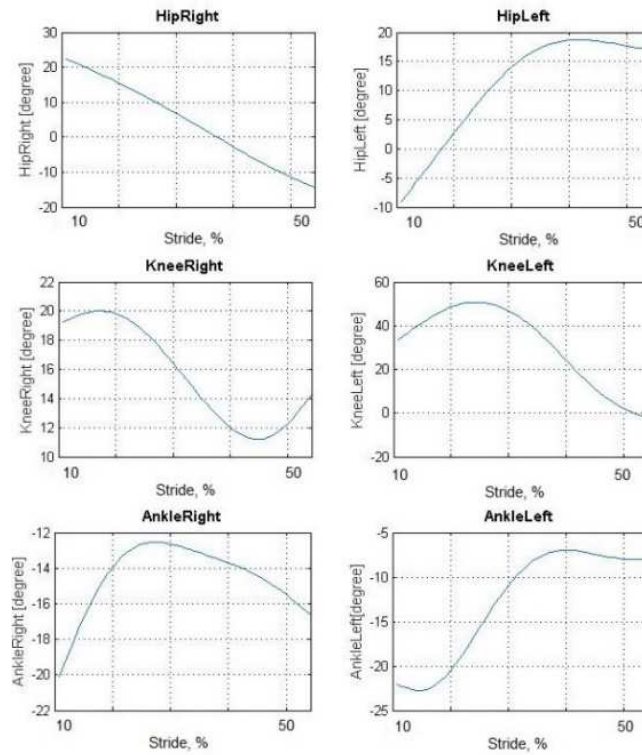


Figure 7. Kinematic data (sagittal plane)

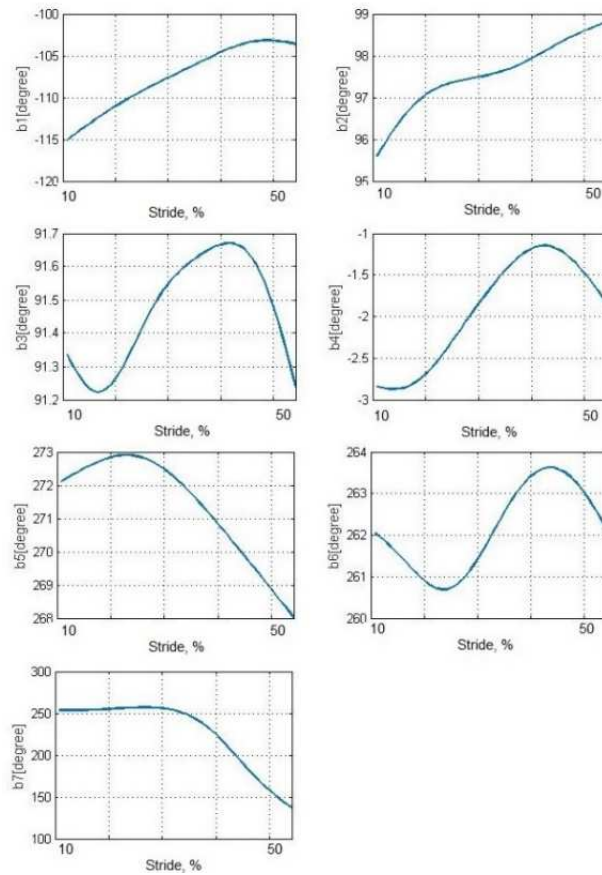


Figure 8. Kinematic data (frontal plane)

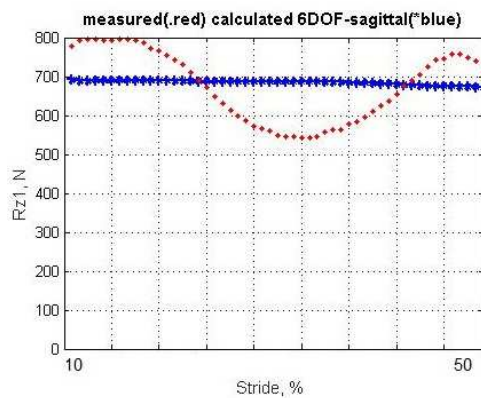


Figure 9. Vertical component of interaction: measured component and calculated component for sagittal 6DOF model

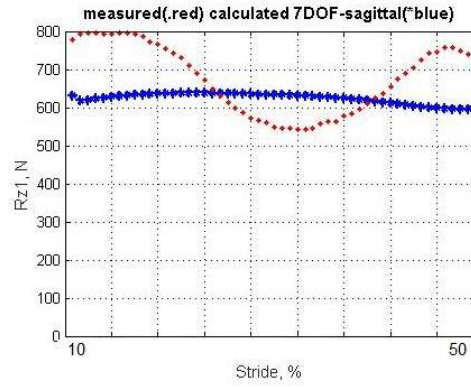


Figure 10. Vertical component of interaction: measured component and calculated component for sagittal 7DOF model

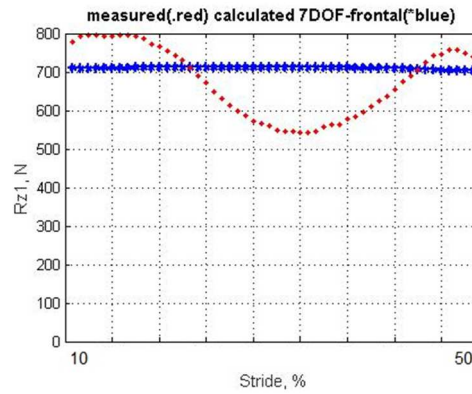


Figure 11. Vertical component of interaction: measured component and calculated component for frontal 7DOF model

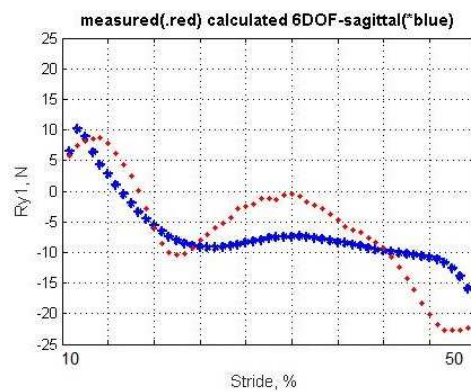


Figure 12. Horizontal component of interaction: measured component (towards sagittal axis) and calculated component for sagittal 6DOF model

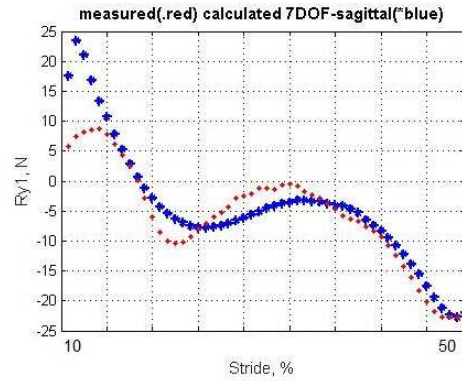


Figure 13. Horizontal component of interaction: measured component (towards sagittal axis) and calculated component for sagittal 7DOF model

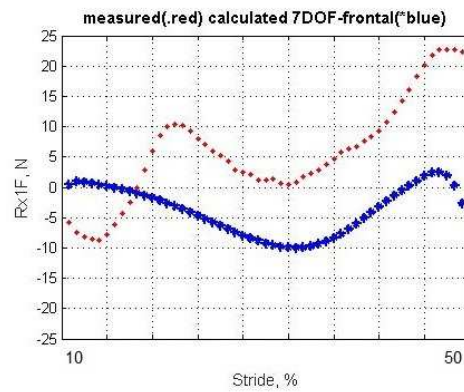


Figure 14. Horizontal component of interaction: measured component (towards transverse axis) and calculated component for frontal 7DOF model

4. Discussion

On the base of the obtained data (measured and calculated) given in the section 3, we concluded that over single support phase:

- all three vertical components of interaction calculated by using a sagittal 6DOF model (Fig. 9), sagittal 7DOF model (Fig. 10) and frontal 7DOF model (Fig. 11) have very similar shapes and values that are approximate to the measured one. Values of absolute relative error of calculated component with respect to the measured one are following: 26.7% (sagittal 6DOF model (Fig. 9)), 22.2% (sagittal 7DOF model (Fig. 10)) and 31.4% (frontal 7DOF model (Fig. 11));
- the horizontal component calculated by the sagittal 6DOF model (Fig. 12) and sagittal 7DOF model (Fig. 13) is closely approximated to the measured horizontal one;

- the horizontal component calculated by the frontal 7DOF model (Fig. 14) has only slightly similar shape with respect to the measured horizontal one. This discrepancy is observed in the small range of force value.

It is worth emphasizing that calculated components were obtained without applying any optimization approach that could be used to fit the calculated data with the calculated ones. Considering presented results of validation, one should keep in mind that following factors are very crucial and have a big impact on the calculated results:

- 1) a method of segmentation used to calculate segment masses, segment lengths, segment radii of gyration (in the study it was applied Zatsiorsky's method, which assumes that each segment is a homogenous cylinder);
- 2) segment moments of inertia that influence dynamics of system considered (in this study a Zatsiorsky's method was used to calculate segment moments of inertia);
- 3) methods applied for kinematic data processing that are used to calculate segment angular velocities and segment angular accelerations (data processing should constrain non-physiological jerks);
- 4) data that describe the upper body part influence in each planar model (location of mass of upper body with respect to the hip joints of each model);
- 5) data that describe the seventh segment of the sagittal 7DOF model (mass m_7 , length L_7 , radius of gyration S_7 and moment of inertia J_7).

5. Conclusions

The aim of this study was to create multibody biomechanical models that can be used to analyze a normal gait of the human and to identify joint moments of the lower limbs during normal gait in the single and the double support phase. Applying Newton-Euler formulation, six planar biomechanical models were developed: 1) a mathematical 6DOF model describing gait in the sagittal plane of the body for single support phase (open sagittal 6DOF model); 2) a mathematical 6DOF model describing a gait in the sagittal plane of the body for double support phase (closed sagittal 6DOF model); 3) a mathematical 7DOF model describing a gait in the sagittal plane of the body for single support phase (open sagittal 7DOF model); 4) a mathematical 7DOF model describing a gait in the sagittal plane of the body for double support phase (closed sagittal 7DOF model); 5) a mathematical 7DOF model describing a gait in the frontal plane of the body for single support phase (open frontal 7DOF model); 6) a mathematical 7DOF model describing a gait in the frontal plane of the body for double support phase (closed frontal 7DOF model). Proposed mathematical models can be applied to solve a forward dynamic task or an inverse dynamic task. A validation of these models had been performed by comparing results measured over examination of normal human gait with calculated ones obtained by

solving an inverse dynamic task. Applying a sagittal 7DOF model, the influence of the moment of inertia of the upper body is taken into account, whereas the sagittal 6DOF model and the frontal 7DOF model only consider an influence of upper body load. Due to the fact that proposed biomechanical models only describe planar motions, they should be applied with caution to analyze an asymmetrical gait.

Applying models presented in this paper, one can assess joint moments and joint intersegmental forces that origin due to influence of elements linking neighboring segments. These elements model an influence of soft tissues that are bending each joint (ligaments, bursa, muscles with tendons) and also affecting acceleration or deceleration of segments, especially at the end of the range of motion. Moreover, joint moments and joint intersegmental forces are produced due to interaction (contact) between the components of musculoskeletal system. On the base of calculated kinematic and kinetic data one can assess power produced by the chosen segments and joint powers produced by the chosen joints of the lower limb. However, one should take in mind that application of an inverse dynamic approach does not allow to consider influence of multi-joint muscles and to detect a co-contraction phenomenon that is very important to maintain a stable posture [9]. Proposed biomechanical models can be used to obtain data to design a mechanical construction of the exoskeleton used to enhance performance of the lower limbs. Also, these models can be used to design a control system of this exoskeleton to enhance the given motion performance by keeping the chosen range of the human locomotive stability. Moreover, considering motions of the human, one should keep in mind that all motions are performed in some range of variability [10].

It is worth remembering that planar models presented in this paper cannot model phenomena occurring due to rotations in the transverse plane, since presented models only describe phenomena occurring towards a medio-lateral axis of rotation (in the sagittal plane of the body) and anterior-posterior axis of rotation (in the frontal plane of the body).

Acknowledgments

The work has been supported by the Polish National Science Centre under the grant OPUS 9 No. 2015/17/B/ST8/01700 for years 2016-2018. Calculations were carried out at the Academic Computer Centre in Gdansk, Poland.

References

- [1] Awrejcewicz J.: Classical Mechanics. Dynamics. Springer Berlin (2012).
- [2] De Leva P. Adjustments to Zatsiorsky-Seluyanov's segment inertia parameters. *Journal of Biomechanics* 29 (9), 1996, 1223–1230 (1996)

- [3] De Leva P.: Joint center longitudinal positions computed from a selected subset of Chandlers' data. *J Biomech* 29 (9), 1231–1233 (1996)
- [4] Grzelczyk D., Awrejcewicz J.: Modeling and control of an eight-legged walking robot driven by different gait generators. *International Journal of Structural Stability and Dynamics* (in press). doi: 10.1142/S0219455419410098
- [5] Onyshko S., Winter D.A.: A mathematical model for the dynamics of human locomotion. *J Biomechanics* 13, 361–368 (1980)
- [6] Troy J.J.: Dynamic balance and walking control of biped mechanisms. *Retrospective Theses and Dissertations*, 11095, Iowa State University (1995)
- [7] Winter D.A.: Overall principle of lower limb support during stance phase of gait. *J Biomech* 13, 923–927 (1980)
- [8] Wojnicz W., Zagrodny B., Ludwicki M., Syczewska M., J. Mrozowski, Awrejcewicz J.: Approach for determination of functioning of lower limb muscles. *Dynamical Systems in Applications* (ed. J. Awrejcewicz). *Springer Proceedings in Mathematics & Statistics*, Vol. 249, 423–38 (2018)
- [9] Wojnicz W.: *Biomechaniczne modele układu mięśniowo-szkieletowego człowieka* (Biomechanical models of the human musculoskeletal system). Wydawnictwo Politechniki Gdańskiej, Gdańsk, Poland, 1-209, ISBN 978-83-7348-727-7 (2018)
- [10] Zagrodny B., Ludwicki M., Wojnicz W., Mrozowski J., Awrejcewicz J.: Cooperation of mono- and bi-articular muscles: human lower limb. *Journal of Musculoskeletal and Neuronal Interactions*, 1–7 (2018)
- [11] Zajac F.E., Neptune R.R., Kautz S.A.: Biomechanics and muscle coordination of human walking. Part I: Introduction to concepts, power transfer, dynamics and simulations. *Gait Posture* 16, 215–232 (2002)
- [12] Yamaguchi G.T., Zajac F.E.: Restoring Unassisted natural gait to paraplegics via functional neuromuscular stimulation: a computer simulation study. *IEEE Transactions on biomedical engineering* 37 (9), 886–902 (1990)

Wiktoria Wojnicz, Ph.D. DSc, Associate Professor: Gdansk University of Technology, str. G. Narutowicza 11/12, 80-233 Gdansk, POLAND (wiktoria.wojnicz@pg.edu.pl). The author gave a presentation of this paper during one of the conference sessions.

Bartłomiej Zagrodny, Ph.D.: Lodz University of Technology, str. Stefanowskiego 1/15, 90-924 Lodz, POLAND (bartlomiej.zagrodny@p.lodz.pl).

Michał Ludwicki, Ph.D.: Lodz University of Technology, str. Stefanowskiego 1/15, 90-924 Lodz, POLAND (michal.ludwicki@p.lodz.pl).

Jerzy Mrozowski, Ph.D., DSc, Associate Professor: Lodz University of Technology, str. Stefanowskiego 1/15, 90-924 Lodz, POLAND (jerzy.mrozowski@p.lodz.pl).

Jan Awrejcewicz, Professor: Lodz University of Technology, str. Stefanowskiego 1/15, 90-924 Lodz, POLAND (jan.awrejcewicz@p.lodz.pl).

Edmund Wittbrodt, Professor.: Gdansk University of Technology, str. G. Narutowicza 11/12, 80-233 Gdansk, POLAND (Edmund.wittbrodt@pg.edu.pl).

Nonlinear stability of a spring-supported pipe conveying fluid

Kiyotaka Yamashita, Naoto Nishiyama, Kohsuke Katsura, Hiroshi Yabuno

Abstract: Instabilities of pipes conveying fluid have been investigated for a long time. The dynamics of the lateral displacement in pipe system is described by non-self-adjoint partial differential governing equation and the eigen-functions in this problem do not belong to the system of orthogonal functions. In addition to that, it has been well known that the system shows many complex nonlinear motions. Therefore, nonlinear dynamics of pipes conveying fluid has been regarded as an essential model of the self-excited vibration in the continuous system from the view points of the non-conservative elastic problems and the flow-induced vibrations. In this study, a spring-supported pipe conveying fluid is considered. We take up the problem of double degeneracy point associated with a pitchfork and a Hopf bifurcation. In the theoretical analysis, we use the adjoint eigen-functions to project system nonlinearity to the unstable eigenspaces. In particular, the experiments are conducted with the silicon rubber pipe and the lateral displacements of the pipe are measured by the image processing system. In a certain range of the flow velocity, we confirm that there are three steady-state solutions (1) two stable buckled states (2) a self-excited vibration around the straight position of the pipe.

1. Introduction

The pipe system is well known as a non-conservative system subjected to the circulatory force. The dynamics of a pipe conveying fluid is described by non-self-adjoint partial differential governing equation and the eigen-functions in this problem do not belong to the system of orthogonal functions. The effects of the added mass and the spring support on the linear stability have been investigated from the view point of non-conservative elastic theory [3]. In addition to that, the system shows many complex nonlinear motions. Therefore, nonlinear dynamics of pipes conveying fluid has been regarded as an essential model of the self-excited vibration in the continuous non-conservative system. Jin and Zou[2] theoretically focused on the doubly degenerate point, where coupled flutter and divergence bifurcation become a problem. Ghayesh et al.[1] theoretically and experimentally investigated the 3-D nonlinear dynamics of a cantilevered pipe fitted with an end-mass and additionally supported by an intra-span spring array.

In this study, a spring-supported pipe conveying fluid is considered. We take up the problem of double degeneracy point associated with a pitchfork and a Hopf bifurcation. In

the theoretical analysis, we use the adjoint eigen-functions to project system nonlinearity to the unstable eigen-spaces. In particular, we conduct the experiments to verify the theoretical results. The experiments are conducted with the silicon rubber pipe and the lateral displacements of the pipe are measured by the image processing system. The image processing system enables us to conduct non-contact three dimensional measurements with 200 frames per second. In a certain flow velocity region, we confirm that there are three steady-state solutions (1) two stable buckled states (2) a self-excited vibration around the straight position of the pipe.

2. Analytical model and basic equations

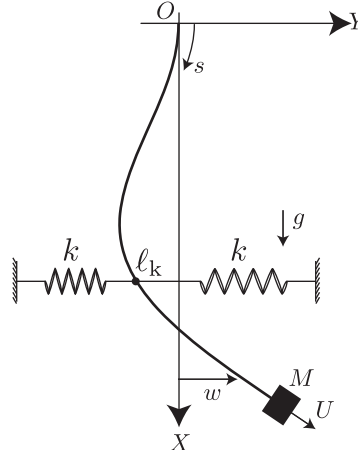


Figure 1. Analytical model of the pipe with a spring support

Figure 1 shows the analytical model of the pipe with a spring support. We briefly give some basic definitions and assumptions to derive the nonlinear governing equations presented in Yoshizawa [4]. Pipe is hung vertically under the influence of gravity g . s is the curvilinear coordinate along the pipe axis. The lateral displacement w can be described by s and time t . Let ℓ , EI , ρ and S be the overall length of the pipe, flexural rigidity, density of the fluid and pipe and bore area of the pipe. The pipe is long enough as compared to its diameter and is regarded as a beam. The pipe is supported by two linear spring at $s = \ell_k$. The spring constant is k . The flow velocity relative to the pipe motion is U . It is assumed that U is constant and the flow is one dimensional parallel to the pipe axis.

Non-dimensionalization is achieved using the overall length of the pipe ℓ and the characteristic time $\sqrt{(m + \rho S)\ell^4/EI}$. The equation of pipe vibration in the $X - Y$ plane can be

written with terms up to the third order of w^* in non-dimensional form:

$$\begin{aligned}
\ddot{w} + 2\sqrt{\beta}V\dot{w}' + V^2w'' - \gamma\{(1-s)w'\}' + w'''' + 2\kappa\delta(s-\eta) = \\
-w' \int_0^s \dot{w}'^2 ds - w' \int_0^s w' \ddot{w}' ds + w'' \int_s^1 \int_0^s \dot{w}'^2 ds ds + \frac{1}{2}\ddot{w}w'^2 - w'' \int_s^1 \ddot{w}w' ds \\
+ w'' \int_s^1 \int_0^s w' \ddot{w}' ds ds - \sqrt{\beta}Vw'^2\dot{w}' - \frac{1}{2}V^2w'^2w'' + \frac{1}{2}\gamma(1-s)w'^2w'' \\
- \frac{1}{2}\gamma w'' \int_s^1 w'^2 ds - \frac{3}{2}w''^3 + \frac{1}{2}w''w_1'^2 - 3w'w''w''' - \frac{1}{2}w'^2w'''' \\
+ \kappa w w' \delta(s-\eta),
\end{aligned} \tag{1}$$

where $(\dot{})$ and $()'$ denote the derivatives with respect to t and s , respectively. The subscript expression w_1 indicates w at $s = 1$. The boundary conditions for the pipe vibration in the $X - Y$ plane are also expressed as follows:

$$\begin{aligned}
s = 0 : \quad w = 0, \quad w' = 0, \\
s = 1 : \quad w'' = 0, \\
w''' = -\frac{1}{2}w''''w'^2 - w''^2w'
\end{aligned} \tag{2}$$

Six dimensionless parameters are involved in Eqs. (1) and (2):

$$\begin{aligned}
V = \sqrt{\frac{\rho S l^2}{EI}}U, \quad \alpha = \frac{M}{(m + \rho S)l}, \quad \beta = \frac{\rho S}{m + \rho S}, \quad \gamma = \frac{(m + \rho S)gl^3}{EI}, \\
\eta = \frac{\ell_k}{\ell}, \quad \kappa = \frac{k\ell^3}{EI}.
\end{aligned} \tag{3}$$

In order to systematically derive the amplitude equations, Eqs. (1) and (2) can be converted to a vector form by defining $\mathbf{w} = (w \ \dot{w} + 2\sqrt{\beta}Vw')^t$. The governing equation of \mathbf{w} and boundary conditions associated with \mathbf{w} are expressed as follows:

$$\dot{\mathbf{w}} = L\mathbf{w} + \mathbf{N}, \tag{4}$$

where

$$\begin{aligned}
L = \begin{pmatrix} -2\sqrt{\beta}V(\cdot)' & 1 \\ L_{21} & 0 \end{pmatrix}, \quad \mathbf{N} = \begin{pmatrix} 0 \\ n \end{pmatrix}, \\
L_{21} = -(\cdot)'''' + \gamma\{(1-s)(\cdot)'\}' - V^2(\cdot)''.
\end{aligned} \tag{5}$$

$$s = 0 : B_1\mathbf{w} = 0, \quad s = 1 : B_2\mathbf{w} = \mathbf{N}_b, \tag{6}$$

where

$$B_1 = \begin{pmatrix} 1 & 0 \\ (\cdot)' & 0 \end{pmatrix}, \quad B_2 = \begin{pmatrix} (\cdot)'' & 0 \\ (\cdot)''' & 0 \end{pmatrix}, \quad N_b = \begin{pmatrix} 0 \\ b \end{pmatrix}, \quad (7)$$

and n and b in Eqs. (5) and (7) are nonlinear terms, which are described in Eqs. (1) and (2).

3. Linear stability analysis

To investigate the linear stability of the system, we ignore the nonlinear terms in Eqs. (4) and (6). Letting $\mathbf{w} = \mathbf{q}_n e^{\lambda_n t}$ and $\mathbf{q}_n(s) = (\Phi_{n1} \ \Phi_{n2})$, we construct the eigenvalue problems. λ_n is equal to $-\omega_{ni} + i\omega_{nr}$, where ω_{nr} is the n th natural frequency and ω_{ni} is the damping ratio of the n th mode.

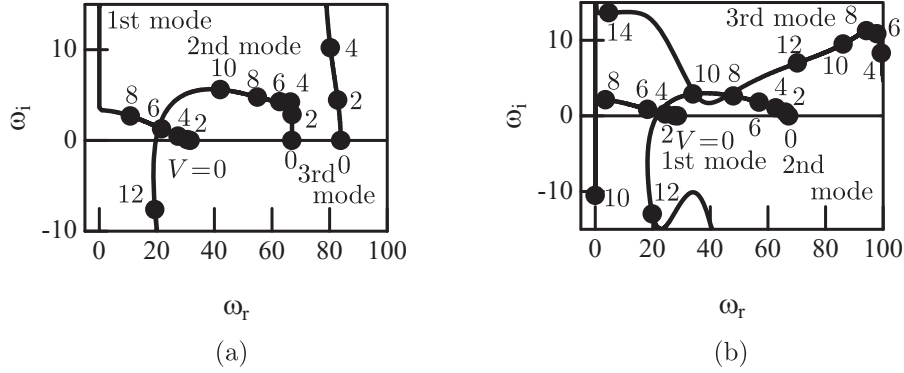


Figure 2. Variation of the eigenvalues of the lowest three modes as a function of V . (a) $\beta=0.27$, $\gamma=120$, $\kappa=500$, $\eta=0.9$, (b) $\beta=0.27$, $\gamma=120$, $\kappa=500$, $\eta=0.95$

In the case of $\beta = 0.27$, $\gamma = 120$ and $\kappa = 500$, we calculate ω_{nr} and ω_{ni} ($n = 1, 2, 3$) are shown as a function of V . In the case of $\eta = 0.9$, variations of ω_{nr} and ω_{ni} ($n = 1, 2, 3$) are shown in Fig. 4(a). The first mode and the third mode are stable because $\omega_{1i} > 0$ and $\omega_{3i} > 0$. When V increases, ω_{2i} becomes negative at $V = 11.65$, and the system becomes unstable by Hopf bifurcation. In the case of $\eta = 0.95$, the variation of λ_1 shows the static instabilities for $8.1 < V < 11.0$. ω_{2i} becomes also negative over $V = 10.9$, and the second mode becomes unstable by Hopf bifurcation.

4. Amplitude equations

We can express the solution space \mathbf{Z} as $\mathbf{Z} = \mathbf{X} \oplus \mathbf{M}$. Then, \mathbf{X} is spanned by two unstable eigenvectors \mathbf{q}_1 and \mathbf{q}_2 , and \mathbf{M} is the complementary sub-space of \mathbf{X} . Therefore, \mathbf{w} is

expressed as $\mathbf{w} = C_1 \mathbf{q}_1 + C_2 \mathbf{q}_2 + \mathbf{y} + \text{c.c.}$, where \mathbf{y} is the element of \mathcal{M} . Using the adjoint functions, we can project the nonlinear governing equation on the eigenspaces spanned by \mathbf{q}_1 and \mathbf{q}_2 and obtain the following evolutionary amplitude equations .

$$\dot{A} = -\omega_{1i}A + \xi_1 A^3 + \xi_2 A B \bar{B}, \quad (8)$$

$$\dot{B} = -\omega_{2i}B + \xi_3 B^2 \bar{B} + \xi_4 A^2 B, \quad (9)$$

where $C_1 = A$ and $C_2 = B e^{i\omega_{2r}t}$. Letting $A = a$ and $B = b \exp(i\psi)/2$ in Eqs. (8) and (9), we obtain following two evolutionary equations.

$$\dot{a} = \left(-\omega_{1i} + \frac{\xi_1}{4}a^2 + \frac{\xi_2}{4}b^2 \right) a, \quad (10)$$

$$\dot{b} = \left(-\omega_{2i} + \frac{\xi_3}{4}b^2 + \frac{\xi_4}{4}a^2 \right) b. \quad (11)$$

5. Experiment

5.1. Experimental apparatus and procedures

Experiment was conducted with the silicone rubber pipe. The pipe was silicone rubber with an external diameter of 13 mm and an internal diameter of 7 mm and an overall length ℓ of 590 mm. We use two coiled springs to support the pipe at $s = \eta$ and the pipe motion was not restricted by any constraints. The flowing fluid was water and its velocity was maintained constant by letting the water flow through a large accumulator tank. The upper end of the pipe was clamped and the other end was free end.

Figure 3 shows the experimental apparatus and measurement system. Figure 3 (a) is a schematic diagram of the experimental apparatus and measurement system and (b) is a photograph of the experimental system. The experimental apparatus consists of a water circulation system, a flexible pipe and a measurement system. The pressure at the bottom of the accumulator tank was measured by a Bourdon tube pressure gauge and the volume of flowing water was measured by the Colioris flow sensor. Image processing system consists of a computer and two video cameras which take in 200 high speed images per second continuously for about 8 second. Then, the system estimates the pipe displacements at $s^* = 0.5$ in 3D space.

5.2. Experimental results

The pipe is supported by two springs with identical stiffness k at a distance $s = \eta$ from the upper clamped end. k , η and the flow velocity U are used as the control parameters in experiment.

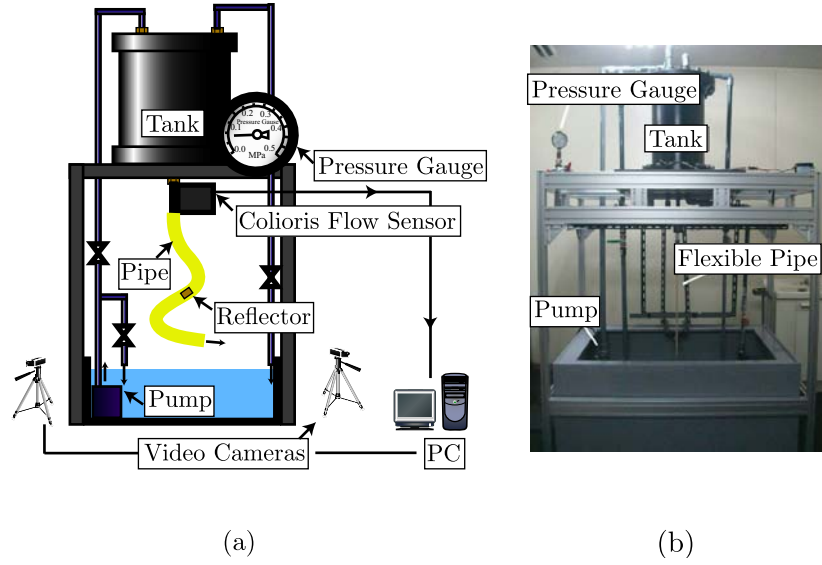


Figure 3. Experimental apparatus and measurement system: (a) a schematic diagram of the experimental apparatus, (b) photograph of the experimental system.

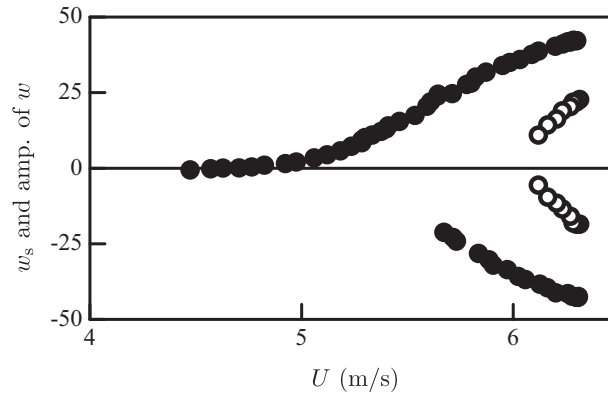


Figure 4. Bifurcation diagram of the stable static equilibrium w_s and amplitude of self-excited vibration: ● amplitude of buckling, ○ amplitude of self-excited vibration.

Figure 4 shows the bifurcation diagram of the spring supported pipe. The ● and ○ denote the stable static equilibrium w_s and the stable amplitude of self-excited vibration. The mean flow velocity was increased slowly from $U = 4.5$ m/s. The straight original static equilibrium position was stable below $U = 5.0$ m/s. When the flow velocity increased above $U = 5.0$ m/s, the pipe buckled. As shown in Fig. 4, it can be seen that the system loses its stability by

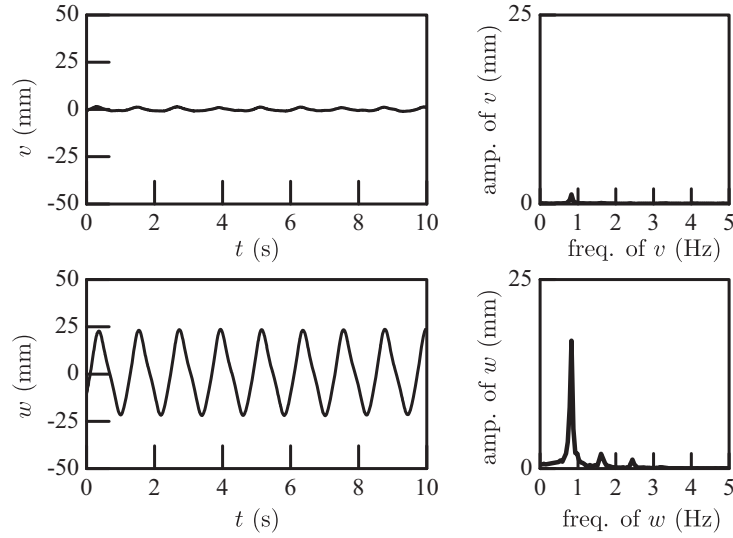


Figure 5. Time histories of lateral deflections v and w and their spectrum analyses. v is the lateral deflection in the direction perpendicular to $X - Y$ plane. The self-excited pipe vibration is periodic and occurred in $X - Y$ plane.

a perturbed pitchfork bifurcation at $U = 5.0$ m/s. From $U = 5.0$ m/s to $U = 5.7$ m/s, there is only one stable non-trivial static solution. From $U = 5.7$ m/s to $U = 6.1$ m/s, there are two asymmetric stable non-trivial static solutions corresponding to the buckling of the pipe to either side of the straight original position. These two amplitudes of buckling increased as U increased.

When the flow velocity increased further, the self-excited pipe vibration was observed as shown in Fig. 5. In Fig. 5, v is the lateral deflection in the Z direction perpendicular to the Y direction. The pipe vibration is nearly planar vibration and the self-excited pipe vibration occurred in $X - Y$ plane. The amplitude of self-excited vibrations increased as U was increased. For $6.1 < U$, there are three steady-states depending on the initial condition : (a) two non-trivial static equilibriums and (b) self-excited vibration.

6. Conclusions

We have studied the nonlinear stabilities of the spring supported pipe conveying fluid. Non-linear analyses are conducted to clarify the nonlinear interactions between unstable first and second modes.

We first derive the complex amplitude equations from a nonlinear nonself-adjoint partial differential equation and its boundary conditions. In particular, we conduct the experiments

to verify the theoretical results. The experiments are conducted with the silicon rubber pipe and the lateral displacements of the pipe are measured by the image processing system. In a certain flow velocity region, we confirm that there are three steady-state solutions (1) two stable buckled states (2) a self-excited vibration around the straight position of the pipe.

Acknowledgments

The authors thank Professor Emeritus M. Yoshizawa for the useful discussions.

References

- [1] GHAYESH, M., AND PAÏDOUSSIS, M. Three-dimensional dynamics of a cantilevered pipe conveying fluid, additionally supported by an intermediate spring array. *International Journal of Non-Linear Mechanics* 45 (2010), 507–524.
- [2] JIN, J., AND ZOU, G. Bifurcations and chaotic motions in the autonomous system of a restrained pipe conveying fluid. *Journal of Sound and Vibration* 260 (2003), 783–805.
- [3] PAÏDOUSSIS, M. *Fluid-structure Interactions: Slender Structures and Axial Flow. Vol. 1.* Academic Press, 1998.
- [4] YOSHIZAWA, M., SUZUKI, T., AND HASHIMOTO, K. Nonlinear lateral vibration of a vertical fluid-conveying pipe with end mass. *JSME International Journal Series C* 41 (1998), 652–661.

Kiyotaka Yamashita, Professor: Department of Mechanical Engineering, Fukui University of Technology, 3-6-1 Gakuen, Fukui-shi, Fukui, Japan (*yamashita@fukui-ut.ac.jp*). The author gave a presentation of this paper during one of the conference sessions.

Naoto Nishiyama, Ph.D. student: Graduate Schoool of Engineering, Fukui University of Technology, 3-6-1 Gakuen, Fukui-shi, Fukui, Japan (*nishiyama@fukui-ut.ac.jp*).

Kohsuke Katsura, M.Sc.: Graduate Schoool of Engineering, Fukui University of Technology, 3-6-1 Gakuen, Fukui-shi, Fukui, Japan (*kosuke.katsura@gmail.com*).

Hiroshi Yabuno, Professor: Graduate School of Systems and Information Engineering, University of Tsukuba, 1-1-1 Ten-no-dai, Tsukuba Science, Ibaraki, Japan (*yabuno@esys.tsukuba.ac.jp*).

On the dynamics of blood through the circular tube along with magnetic properties

Azhar Ali Zafar, Jan Awrejcewicz

Abstract: In this article, we will investigate a blood flow model with suspended magnetic particles. The fluid is influenced by an external magnetic field and an oscillating pressure gradient. Exact solutions for the velocity of fluid and velocity of magnetic particles will be obtained by means of integral transforms. Obtained results will be expressed in terms of post transient and transient parts. Moreover, to study the influence of the material parameters, numerical simulations and graphical illustrations will be used and useful consequences will be summarized.

1. Introduction

Basically, blood consists of multiple components, a mixture of various cells in plasma which behaves like an incompressible Newtonian fluid [1]. Moreover, plasma in a capillary flow behaves like Newtonian fluid [2]. It is more likely a bio-magnetic fluid, so its flow is effected by the magnetic field [3]. Furthermore, blood magnetic property is significantly influenced by the state of oxygenation [4]. The use of magnetic field for streamlining the flow of blood in the body could be utilized to control poor circulation of blood and the risk of heart attack to a person [3]. In [5] Haik et al. developed a bio fluid dynamics model closely resembling to the ferro-hydrodynamics. Further Varshney et al. [6] numerically investigated the effect of magnetic field on the blood flow in artery having multiple stenosis, Bourhan and Magableh [7] studied the effects of magnetic field on heat transfer and fluid flow characteristics of blood flow in multi-stenosis arteries. In 2015, Sharma et al. [4] have numerically investigated the fluid flow parameters of blood together with magnetic particles in a cylindrical tube.

Our aim is to investigate the dynamics of proposed blood flow model with magnetic particles through a cylindrical tube under the influence of magnetic field and oscillatory pressure gradient in the axial direction [4]. However, we look for the exact solutions for the dimensionless form of the fluid velocity and magnetic particles velocity and express the obtained results in terms of steady state and transient parts. Furthermore, influence of the external magnetic field, particles concentration parameter and particles mass parameters on the dynamics of fluid and particles is investigated via numerical simulations and graphical illustrations.

2. Description of the problem

The artificial blood (75% water and 25% Glycerol) along with magnetic particles (iron oxide) is assumed to be flowing in a cylindrical glass tube under the influence of axial pressure gradient. The magnetic particles are supposed to be uniformly distributed throughout the blood. The blood is flowing in the axial direction and a uniform transverse magnetic field is applied. We assume that:

- No-slip condition at the wall of tube is applied that the blood and magnetic particles have zero velocities at the wall of the tube.
- The magnetic Reynolds number is very small; hence the induced magnetic field effect is neglected [7].

2.1. Proposed geometry of the model

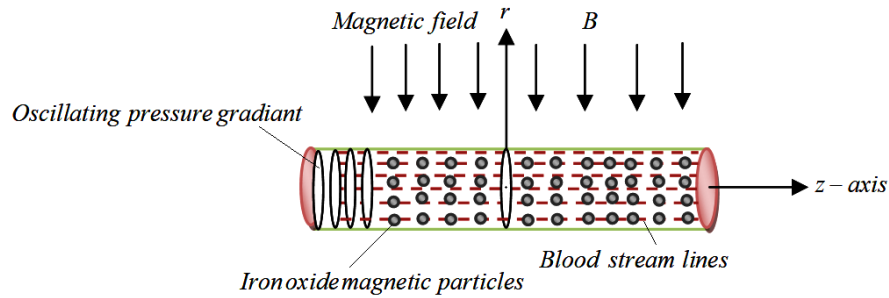


Figure 1. Proposed geometry of the model

Nomenclature

\vec{J}	Current density
σ	Electrical conductivity
\vec{E}	Electric field intensity
\vec{V}	Velocity vector
\vec{B}	Magnetic flux intensity
μ_0	Magnetic permeability
ρ	Density of the fluid
μ	Dynamic viscosity of the fluid
ν	Kinematic viscosity of the fluid
N	Number of magnetic particles per unit volume
S	Stokes constant

Ha Hartmann number

C Particles concentration

M Particles mass parameter

2.2. Mathematical model

Based on the fact that, when a magnetic field is applied on an electrically conducting fluid, an electromagnetic force is generated due to the interaction of current with magnetic field. In our model, iron oxide (magnetic particles) are suspended in blood (bio-magnetic fluid) which makes the blood more conducting and a strong electromagnetic force is experienced (due to the interaction of current with magnetic field). The strength of this electromotive force also depends on the speed of motion of the magnetic particles as well as magnetic flux intensity [8]. The governing equations of our problem involves both Navier-Stokes equations describing the fluid flow and Maxwell's relations for magnetic field interactions. Now, from

$$\text{(Ohm's law)} \quad \vec{J} = \sigma(\vec{E} + \vec{V} \times \vec{B}), \quad (1)$$

$$\text{(Maxwell's equations)} \quad \nabla \cdot \vec{B} = 0, \quad \nabla \times \vec{B} = \mu_0 \vec{J}, \quad \nabla \times \vec{E} = -\frac{\partial \vec{B}}{\partial t}. \quad (2)$$

(Electromagnetic force included

$$\text{in the momentum equation)} \quad \vec{F}_m = \vec{J} \times \vec{B} = \sigma(\vec{E} + \vec{V} \times \vec{B}) \times \vec{B} = -\sigma B^2 u'_b \hat{e}_z, \quad (3)$$

where $u'_b(r, t)$ is the axial velocity of the blood.

Consider blood is flowing in an axi-symmetric cylindrical tube of radius “ a ” with axis of the cylinder along z' - axis, subject to the pressure gradient $\frac{\partial p'}{\partial z'}$ and transverse magnetic field of strength B . The governing momentum equation for fluid flow in cylindrical polar coordinates is given by [4], [5]

$$\frac{\partial u'_b}{\partial t'} = -\frac{1}{\rho} \frac{\partial p'}{\partial z'} + \nu \left(\frac{\partial^2 u'_b}{\partial r'^2} + \frac{1}{r'} \frac{\partial u'_b}{\partial r'} \right) + \frac{SN}{\rho} (u'_p - u'_b) - \frac{\sigma B^2 u'_b}{\rho}, \quad (4)$$

where $u'_p(r', t')$ is the velocity of the particles. For small Reynolds number of the relative velocity the force between blood and magnetic particle is proportional to the relative velocity.

Moreover, motion of the magnetic particles is governed by

$$m_{av} \frac{\partial u'_b}{\partial t'} = S(u'_b - u'_p), \quad (5)$$

where m_{av} is the average mass of the magnetic particles.

Like in [9], pressure gradient is considered as

$$-\frac{\partial p'}{\partial z'} = \psi_0 + \psi_1 \cos(\omega' t'), \quad (6)$$

where ψ_0 is the constant amplitude of the pressure gradient and ψ_1 is the amplitude of the pulsatile component giving rise to systolic and diastolic pressure. In experiments this kind of pressure gradient is maintained by peristaltic pump.

The initial and boundary conditions on the velocity field are given by [4]

$$u'_b(r', 0) = u'_p(r', 0) = 0 \text{ for } r' \in (0, a), \quad (7)$$

$$\left. \frac{\partial u'_b(r', t')}{\partial r'} \right|_{r'=0} = 0 \text{ for } t' > 0, \quad (8)$$

$$u'_b(a, t') = u'_p(a, t') = 0 \text{ for } t' > 0, \quad (9)$$

By introducing the following dimensionless variables and parameters [4] in to Eqs. (4) – (9)

$$r^* = \frac{r'}{a}, \quad u_b^* = \frac{au'_b}{v}, \quad u_p^* = \frac{u'_p a}{v}, \quad t^* = \frac{vt'}{a^2}, \quad p^* = \frac{a^2 p'}{\rho v^2}, \quad (10)$$

and dropping star notation, we have the following dimensionless initial-boundary problem

$$\frac{\partial u_b(r, t)}{\partial t} = \psi_0 + \psi_1 \cos(\omega t) + \left(\frac{\partial^2 u_b(r, t)}{\partial r^2} + \frac{1}{r} \frac{\partial u_b(r, t)}{\partial r} \right) + C[u_p(r, t) - u_b(r, t)] - Ha^2 u_b(r, t), \quad (11)$$

$$M \frac{\partial u_b(r, t)}{\partial t} = u_b(r, t) - u_p(r, t), \quad (12)$$

$$u_b(r, 0) = u_p(r, 0) = 0, \quad r \in [0, 1], \quad (13)$$

$$\left. \frac{\partial u_b(r, t)}{\partial r} \right|_{r=0} = 0, \quad (14)$$

$$u_b(1, t) = u_p(1, t) = 0 \quad t > 0, \quad (15)$$

where $Ha = Ba\sqrt{\frac{\sigma}{\mu}}$, $C = \frac{SNa^2}{\mu}$ and $M = \frac{m\mu}{\rho a^2 S}$.

3. Solution of the problem

Applying Laplace transform to Eqs. (11), (12) and (15) and using initial conditions (13), we get

$$q\bar{u}_b(r, q) = \frac{\psi_0}{q} + \psi_1 \frac{q}{q^2 + \omega^2} + \left(\frac{\partial^2 \bar{u}_b(r, q)}{\partial r^2} + \frac{1}{r} \frac{\partial \bar{u}_b(r, q)}{\partial r} \right) + C\bar{u}_p(r, q) - (C + Ha^2)\bar{u}_b(r, q), \quad (16)$$

$$\bar{u}_p(r, q) = \frac{\bar{u}_b(r, q)}{Mq + 1}, \quad (17)$$

$$\bar{u}_b(1, q) = 0, \quad \bar{u}_p(1, q) = 0. \quad (18)$$

Using Eq. (17) into Eq. (16), we obtain

$$q\bar{u}_b(r, q) = \frac{\psi_0}{q} + \psi_1 \frac{q}{q^2 + \omega^2} + \left(\frac{\partial^2 \bar{u}_b(r, q)}{\partial r^2} + \frac{1}{r} \frac{\partial \bar{u}_b(r, q)}{\partial r} \right) + C \frac{\bar{u}_b(r, q)}{Mq + 1} - (C + Ha^2) \bar{u}_b(r, q). \quad (19)$$

Eq. (19) can be written in an equivalent form

$$\left(\frac{\partial^2}{\partial r^2} + \frac{1}{r} \frac{\partial}{\partial r} \right) \bar{u}_b(r, q) = \frac{Mq^2 + (1 + M(C + Ha^2)q + Ha^2)}{Mq + 1} \bar{u}_b(r, q) - \left(\frac{\psi_0}{q} + \psi_1 \frac{q}{q^2 + \omega^2} \right). \quad (20)$$

Applying finite Hankel transform [10] of order zero and using the boundary conditions, we get

$$\bar{u}_{bH}(r_n, q) = G(q) \frac{J_1(r_n)}{r_n} \cdot \frac{Mq + 1}{Mq^2 + (1 + M(C + H_a^2 + r_n^2)q + (H_a^2 + r_n^2))}, \quad (21)$$

where $G(q) = \frac{\psi_0}{q} + \psi_1 \frac{q}{q^2 + \omega^2}$.

Now, Eq. (21) can be rewritten as

$$\begin{aligned} \bar{u}_{bH}(r_n, q) &= \frac{J_1(r_n)}{r_n} G(q) \frac{Mq + 1}{Mq^2 + \alpha_n q + \beta_n} \\ &= \frac{J_1(r_n)}{r_n} \frac{1}{M} \left[\chi_{1n} \frac{1}{q + a_{1n}} + \chi_{2n} \frac{1}{q + a_{2n}} + \frac{\psi_0 M}{q \beta_n} + \chi_{3n} \frac{q}{q^2 + \omega^2} + \frac{\chi_{4n}}{\omega} \frac{\omega}{q^2 + \omega^2} \right], \end{aligned} \quad (22)$$

where $\alpha_n = 1 + M(C + H_a^2 + r_n^2)$, $\beta_n = H_a^2 + r_n^2$, $a_{1n} = \frac{1}{2M}(\alpha_n - \sqrt{\alpha_n^2 - 4M\beta_n})$,

$$a_{2n} = \frac{1}{2M}(\alpha_n + \sqrt{\alpha_n^2 - 4M\beta_n}), \quad b_{1n} = a_{2n}M(\omega^2 M - \beta_n) + \alpha_n \beta_n, \quad b_{2n} = a_{1n}M(\omega^2 M - \beta_n) + \alpha_n \beta_n,$$

$$b_{3n} = \frac{M}{\beta_n} [\psi_0 \omega^2 M(M\beta_n - \alpha_n) - M\beta_n^2(\psi_0 + \psi_1)], \quad c_{1n} = M(\omega^2 M - \beta_n) - \alpha_n(a_{2n}M - \alpha_n),$$

$$c_{2n} = M(\omega^2 M - \beta_n) - \alpha_n(a_{1n}M - \alpha_n), \quad c_{3n} = \frac{M^2}{\beta_n} [\beta_n(1 - \alpha_n)(\psi_0 + \psi_1) - \psi_0 M \omega^2],$$

$$\chi_{1n} = \frac{b_{3n}c_{2n} - b_{2n}c_{3n}}{b_{1n}c_{2n} - b_{2n}c_{1n}}, \quad \chi_{2n} = \frac{b_{1n}c_{3n} - b_{3n}c_{1n}}{b_{1n}c_{2n} - b_{2n}c_{1n}}, \quad \chi_{3n} = -\left(\frac{\psi_0 M}{\beta_n} + \chi_{1n} + \chi_{2n} \right),$$

$$\chi_{4n} = M(\psi_0 + \psi_1) - \frac{a_{2n}M - \alpha_n}{M} \chi_{1n} - \frac{a_{1n}M - \alpha_n}{M} \chi_{2n}.$$

Taking the inverse Laplace transform, we obtain

$$u_{bH}(r_n, t) = \frac{J_1(r_n)}{r_n} \left[\frac{\chi_{1n}}{M} e^{-a_{1n}t} + \frac{\chi_{2n}}{M} e^{-a_{2n}t} + \frac{\psi_0}{\beta_n} + \frac{\chi_{3n}}{M} \cos(\omega t) + \frac{\chi_{4n}}{M\omega} \sin(\omega t) \right]. \quad (23)$$

Taking the inverse Hankel transform [11], we obtain

$$u_b(r,t) = 2 \sum_{n=1}^{\infty} \frac{J_0(rr_n)}{r_n J_1(r_n)} \left[\frac{\psi_o}{\beta_n} + \frac{\chi_{3n}}{M} \cos(\omega t) + \frac{\chi_{4n}}{M\omega} \sin(\omega t) \right] + \frac{2}{M} \sum_{n=1}^{\infty} \frac{J_0(rr_n)}{r_n J_1(r_n)} \left[\chi_{1n} e^{-a_{1n}t} + \chi_{2n} e^{-a_{2n}t} \right] \quad (24)$$

or as the sum of steady-state part $u_{st}(r,t)$ and transient part $u_t(r,t)$ can be written

$$u_b(r,t) = u_{bst}(r,t) + u_{bt}(r,t), \quad (25)$$

where

$$u_{bst}(r,t) = 2 \sum_{n=1}^{\infty} \frac{J_0(rr_n)}{r_n J_1(r_n)} \left[\frac{\psi_o}{\beta_n} + \frac{\chi_{3n}}{M} \cos(\omega t) + \frac{\chi_{4n}}{M\omega} \sin(\omega t) \right] \quad (26)$$

and

$$u_{bt}(r,t) = \frac{2}{M} \sum_{n=1}^{\infty} \frac{J_0(rr_n)}{r_n J_1(r_n)} \left[\chi_{1n} e^{-a_{1n}t} + \chi_{2n} e^{-a_{2n}t} \right]. \quad (27)$$

The particles velocity $u_p(r,t)$ can be obtained introducing Eq. (24) into (12) and using Eq. (18), we get

$$u_p(r,t) = \frac{1}{M} \int_0^t u_b(r,s) \exp\left(-\frac{t-s}{M}\right) ds. \quad (28)$$

or

$$\begin{aligned} u_p(r,t) = & 2 \sum_{n=1}^{\infty} \frac{J_o(rr_n)}{r_n J_1(r_n)} \left[\frac{\psi_o}{H_a^2 + r_n^2} + \frac{\psi_1}{(a_{1n}^2 + \omega^2)(a_{2n}^2 + \omega^2)} \times \right. \\ & \times \left((a_{1n}a_{2n} + \omega^2(Mc_n - 1)) \cos(\omega t) + \omega(a_{1n} + a_{2n} + M(\omega^2 - a_{1n}a_{2n})) \sin(\omega t) \right) + \\ & \left. + \frac{1 - Ma_{1n}}{a_{1n} - a_{2n}} \left(\frac{\psi_o}{Ma_{1n}} + \frac{a_{1n}\psi_1}{a_{1n}^2 + \omega^2} \right) e^{-a_{1n}t} - \frac{1 - Ma_{2n}}{a_{1n} - a_{2n}} \left(\frac{\psi_o}{Ma_{2n}} + \frac{a_{2n}\psi_1}{a_{2n}^2 + \omega^2} \right) e^{-a_{2n}t} \right]. \end{aligned} \quad (29)$$

Moreover, in more elegant form we can write

$$u_p(r,t) = u_{pst}(r,t) + u_{pt}(r,t), \quad (30)$$

where

$$u_{pst}(r,t) = 2 \sum_{n=1}^{\infty} \frac{J_o(rr_n)}{r_n J_1(r_n)} \left[\frac{\psi_o}{H_a^2 + r_n^2} + \frac{\psi_1}{(a_{1n}^2 + \omega^2)(a_{2n}^2 + \omega^2)} \right. \\ \left. \left((a_{1n}a_{2n} + \omega^2(Mc_n - 1)) \cos(\omega t) + \omega(a_{1n} + a_{2n} + M(\omega^2 - a_{1n}a_{2n})) \sin(\omega t) \right) \right], \quad (31)$$

$$u_{pt}(r,t) = 2 \sum_{n=1}^{\infty} \frac{J_o(rr_n)}{r_n J_1(r_n)} \left[\frac{1 - Ma_{1n}}{a_{1n} - a_{2n}} \left(\frac{\psi_o}{Ma_{1n}} + \frac{a_{1n}\psi_1}{a_{1n}^2 + \omega^2} \right) e^{-a_{1n}t} - \frac{1 - Ma_{2n}}{a_{1n} - a_{2n}} \left(\frac{\psi_o}{Ma_{2n}} + \frac{a_{2n}\psi_1}{a_{2n}^2 + \omega^2} \right) e^{-a_{2n}t} \right] \quad (32)$$

the steady-state and transient components of the particles velocity.

4. Numerical results and discussion

In this section our interest is to analyze the influence of the system parameters i.e. Hartmann number, particles concentration parameter and particles mass parameter on the velocity of the fluid as well as the flow velocity of the magnetic particles. In order to evaluate numerical values of the velocities, we need the positive roots of the Bessel function J_0 . These roots are generated by a numerical subroutine using MATHCAD 15.

The profiles of velocities versus r are plotted as shown in the Fig. 2 in order to discuss the influence of the Hartmann number on the flow of fluid and particles at different values of dimensionless times t . Here we have considered $Ha \in \{1, 2, 3, 4, 5\}$ and $M = 0.5, C = 2$. As expected it is noticed that both fluid velocity $u_b(r, t)$ and particles velocity $u_p(r, t)$ decreases with the increasing values of Hartmann number. Because, Lorentz force (that appears when transverse magnetic field is applied to a moving electrically conducting fluid) resists the flow of fluid and magnetic particles. From the Fig. 2, it is reported that the effect of Hartmann number on $u_b(r, t)$ and $u_p(r, t)$ is quite significant about the axis of the cylinder and both the velocities decreases from maximum value to zero as $r \rightarrow 1$. In comparison the fluid flows faster than the particles flow. Moreover, as the time progresses both the velocities increases.

The diagrams of Fig. 3 are plotted in order to discuss the influence of the particle concentration parameter C on both the velocities $u_b(r, t)$ and $u_p(r, t)$. In this case we take $C \in \{2, 4, 6, 8, 12\}$ and we have used the other parameters $M = 1, Ha = 3$. A similar trend is observed like the case of Ha . Because, due to the increase of concentration, collision of the particles results in the displacement from their initial positions and leave the fluid stream lines. This deviation from their dynamic equilibrium state will induce relative velocity between the particles and the fluid, resulting in an additional energy dissipation and gives rise to an increase in effective viscosity. Moreover, from the profiles it is also noticed that $u_p(r, t) > u_b(r, t)$ and the influence of C on $u_b(r, t)$ is significant but less significant on $u_p(r, t)$ and diminishes with time. Here also influence of C is significant near the axis of cylinder and both the velocities approaches to zero as $r \rightarrow 1$.

From the profiles of velocities versus r for different values of particles mass parameter M and at different values of dimensionless times, as noticed from Fig. 4 that velocity of particle $u_p(r, t)$

increases with the increasing values of parameter M , but the parameter M has no significant influence on the fluid velocity and this influence diminishes with time. Here, we take $M \in \{0.6, 0.7, 0.8, 0.9, 1.2\}$ and $C = 4$, $Ha = 3$.

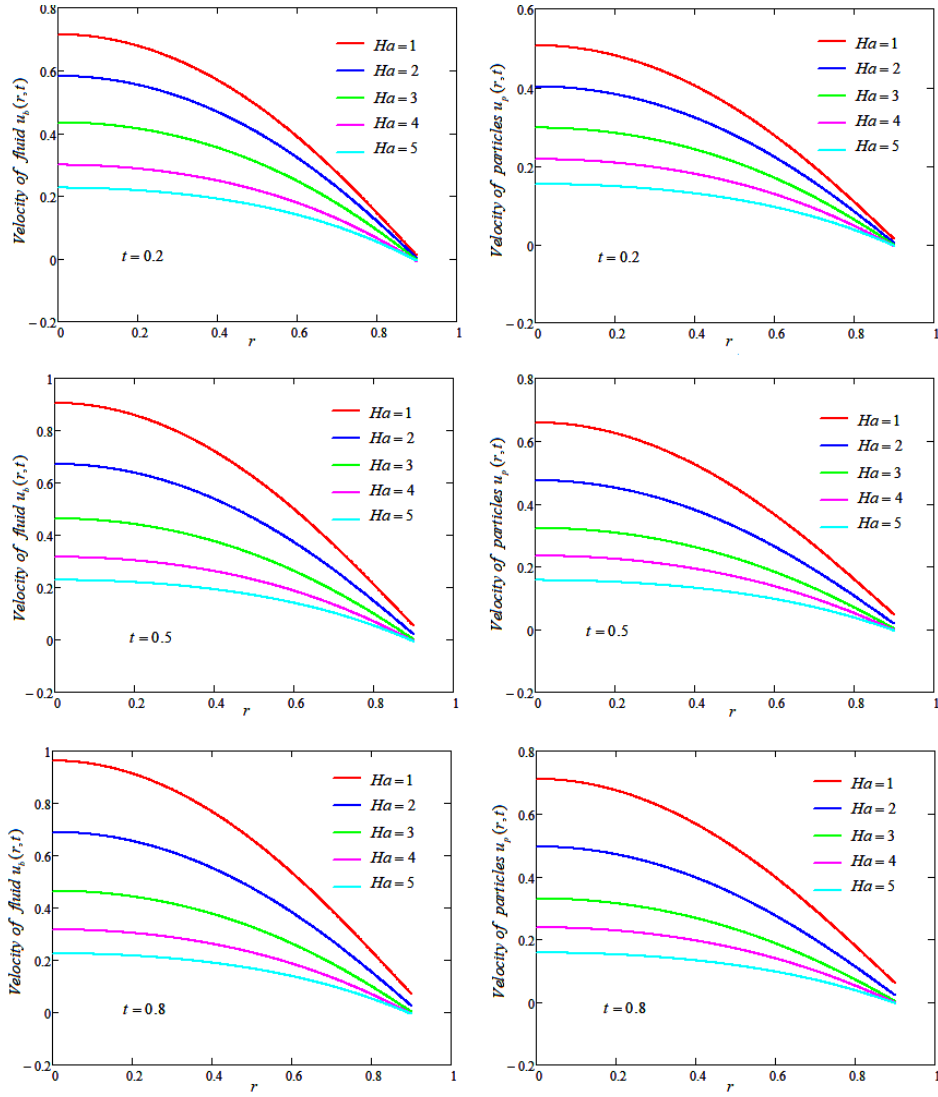


Figure 2. Profiles of velocities for different values of Hartmann number and times.

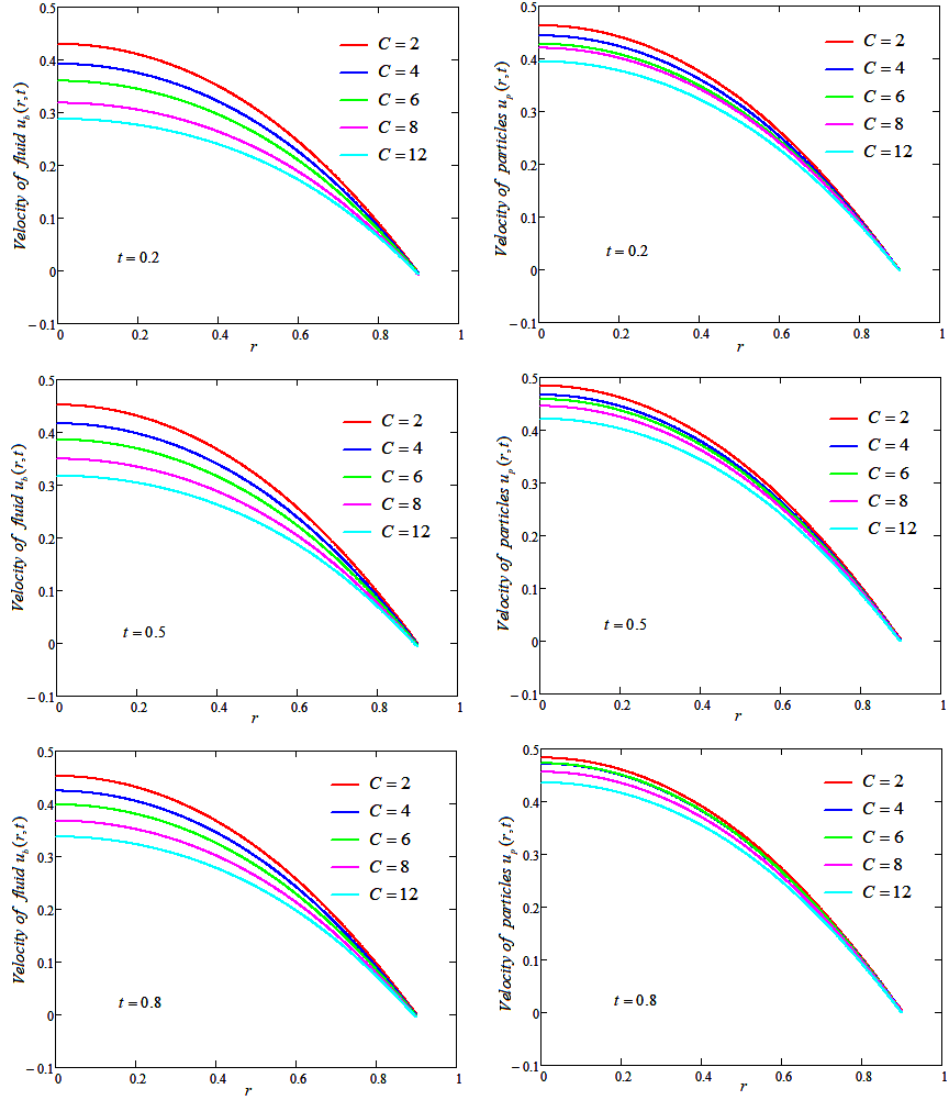


Figure 3. Profiles of velocities for different values of particles concentration parameter and times.

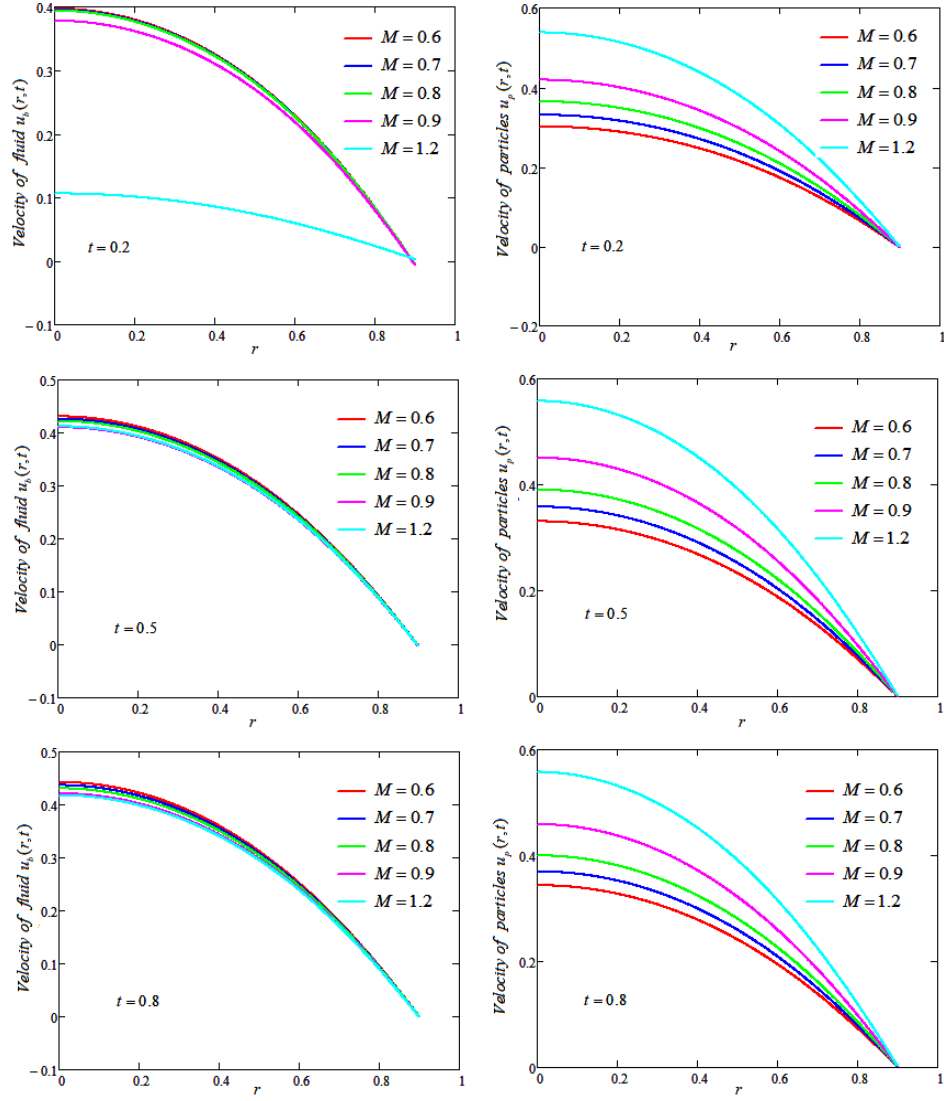


Figure 4. Profiles of velocities for different values of particles mass parameter and times.

In all the diagrams we have chosen the values of the parameters ψ_0 , ψ_1 and ω to be 1, 0.8 and $\frac{\pi}{6}$ respectively.

5. Conclusions

The purpose of this investigation was to study the dynamics of proposed blood model with suspended magnetic particles flowing through a cylindrical tube under the influence of magnetic field and oscillatory pressure gradient. The exact solutions for the dimensionless form of the fluid velocity and magnetic particles velocity are obtained and expressed in terms of steady state and transient parts. Furthermore, influence of the external magnetic field, particles concentration and mass parameters on the dynamics of fluid and particles is investigated via numerical simulations and graphical illustrations

The noteworthy conclusions of the investigation are as under:

- Strength of Hartmann number Ha , retarded the flow of fluid as well as particles.
- The velocities of fluid as well as of particles are decreasing functions of particles concentration parameter.
- Influence of concentration parameter is significant on fluid velocity as compare to particles velocity.
- The particles mass parameter influence inversely on particles velocity, while its effect on the fluid velocity is insignificant.

Acknowledgments

This work has been supported by the Polish National Science Centre under the grant OPUS 14 No. 2017/27/B/ST8/01330.

References

- [1] J.C.F. Chow, Blood flow: Theory, effective viscosity and effects of particle distribution, Bull. Math. Bio. (37) (1975) 471–488.
- [2] E.W. Merrill, A.M. Benis, E.R. Gilliland, T.k. Sherwood, E.W. Salzman, Pressure flow relations of human blood in hollow fibres at low flow rates, J. Appl. Physiology, 20 (50) (1965) 954–967.
- [3] P. Charles, E. Postow, Handbook of biological effects of electromagnetic fields, CRC press (1996) ISBN: 0-8493-0641-8.
- [4] S. Sharma, U. Singh, V. K. Katiyar, Magnetic field effect on flow parameters of blood along with magnetic particles in a cylindrical tube, J. Magn. Magn. Mater. 377 (2015) 395–401.
- [5] Y. Haik, V. Pai, C. J. Chen, Biomagnetic Fluid Dynamics at Interfaces, Cambridge University Press, Cambridge, 1999 439–452.
- [6] V. K. G. Varshney, S. K. Kumar, Effect of magnetic field on the blood flow in artery having multiple stenosis: a numerical study, Int. J. Eng. Sci. Technol. 2 (2010) 67–82.
- [7] A. Bourhan, T. Magableh, Magnetic field effect on heat transfer and fluid flow characteristics of blood flow in multi-stenosis arteries, Heat Mass Transf. 44 (2008) 297–304.

- [8] G. W. Sutton, A. Sherman, Engineering Magnetohydrodynamics, McGraw-Hill, New York, 1965.
- [9] P. K. Mandal, An unsteady analysis of non-Newtonian blood flow through tapered arteries with stenosis, Int. J. Nonlinear Mech. 40 (2005) 151–164.
- [10] I. N. Sneddon, Fourier transforms, McGraw-Hill Book Company, Inc., New York, Toronto, London (1951).
- [11] B. Davies, Integral transforms and their applications, Springer Science & Business Media, 2002.

Azhar Ali Zafar, Post-Doctoral Fellow: Lodz University of Technology, Department of Automation, Biomechanics and Mechatronics, 1/15 Stefanowski St. 90-924 Lodz, Poland (azhar.zafar@p.lodz.pl). The author gave a presentation of this paper during one of the conference sessions.

Jan Awrejcewicz, Professor: Lodz University of Technology, Department of Automation, Biomechanics and Mechatronics, 1/15 Stefanowski St. 90-924 Lodz, Poland (jan.awrejcewicz@p.lodz.pl).

Mathematical model and a prototype of a linear motor controlled by a periodic magnetic field

Klaus Zimmermann, Igor Zeidis, Victor Lysenko, Simon Gast,
Lars Günther, Florian Schale, Michel Rohn

Abstract: A mathematical model and a prototype of a linear motor in which the slider moves progressively are presented. The motion of the slider occurs due to the periodic motion of two slide-blocks (cylinders) with integrated coils and the interaction between the slider and a magnetorheological fluid (MRF), filled in the space between the slider and the cylinders. The periodic motion of the cylinders is caused by an external oscillator. The net displacement of the cylinders for a period is equal to zero. The viscosity of the MRF (and, hence, the friction force acting on the slider) at constant temperature depends on the magnitude of the magnetic field and the concentration of the particles. The controllable magnetic field provides an asymmetry of the friction for forward and backward motions, which enables the net displacement of the slider for a period. A mathematical model of such a motion is presented. An expression for the average velocity of the motion of the slider is obtained for the case where the force of friction is assumed to be small in comparison with the driving force of the slide-blocks. The value of the average velocity is studied as a function of the excitation parameters and the properties of the MRF. On the basis of the theoretical principles outlined above, a prototype of the linear motor was created.

1. Introduction

State-of-the-art are drive systems which use vibrations to generate a linear or rotary motion. For example, these drives use magnetostrictive, piezoelectric, electrostatic or magnetic transducers to excite an oscillator [4][5][6]. A rotor is driven by the periodic interaction with this oscillator and realizes a strictly monotonous motion. For generating a translational or rotational motion with constant direction based on a vibrating oscillator, anisotropic friction properties can also be used. Active elements for the realization of such an anisotropy are, for example, flakes, bristles and inclined hairs, which produce a positive fit with a rough surface [7][9].

This article deals with a linear drive in which anisotropic friction is induced by a magnetic field that influences a magnetorheological fluid (MRF) [10]. In contrast to other MRF-based drive solutions [3][8], the smart material is not only used for transmission (e.g. as a coupling) but also for motion generation itself. The working principle is shown in Figure 1. Two

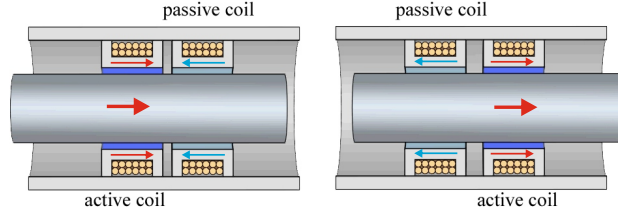


Figure 1. Basic elements and working principle of the MRF-based drive.

drive elements with coils and MRF filling (slide-blocks), positioned on a slider, are excited to oscillate with the help of an external energy supply. The magnetic field acting on the MRF is controlled by active (energized) and passive (de-energized) coils in a phase-shifted manner. When the current is switched on in a slide-block, the built-up magnetic field leads to an increased viscous friction force between the drive element and the slider, as a result of which the drive's active element moves.

2. Modelbased theoretical investigations

Consider a mechanical system consisting of two hollow cylinders (slide-blocks)(1) that perform periodic motion. A rod (slider) (2) capable of moving progressively is placed inside the cylinders. Between the slider and the slide-blocks there is an MRF (3), see Figure 2.

2.1. Mechanical model and equation of motion

The two cylinders, moving along the axis OX (Fig. 2) are subjected to a kinematic constraint that specifies the periodic time history $2l(t)$ between the bodies with a period T and zero average.

Let $x_1(t)$ and $x_2(t)$ denote the coordinates of the cylinders. Both cylinders move with the same velocity in opposite directions relative to the point O . Thus

$$x_2(t) - x_1(t) = 2l(t), \quad x_2(t) + x_1(t) = 0, \quad l(t+T) = l(t), \quad \int_0^T l(t)dt = 0. \quad (1)$$

Since the stock moves progressively, to describe the motion, it suffices to take an arbitrary point with the coordinate x . The slider is acted upon by the viscous friction forces depending on the relative slider velocity $F_i(\dot{x} - \dot{x}_i)$ ($i = 1, 2$). The motion of the slider is described by the differential equation

$$m\ddot{x}(t) = F_1(\dot{x} - \dot{x}_1) + F_2(\dot{x} - \dot{x}_2), \quad (2)$$

where m is the mass of the slider.

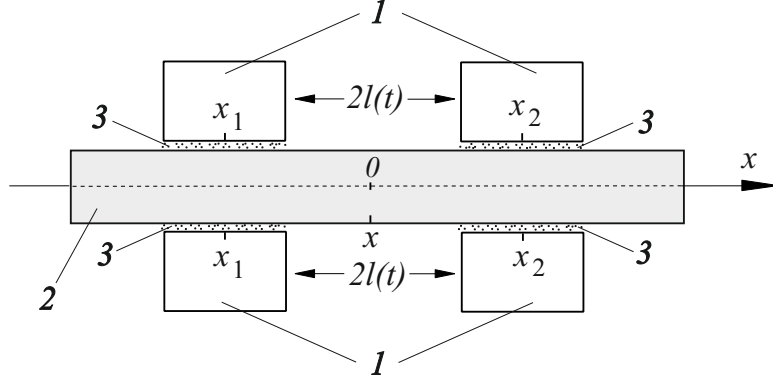


Figure 2. Mechanical model of the linear drive.

Based on the equations (1) we obtain

$$x_1 = -l(t), \quad x_2 = l(t), \quad v = \dot{x}, \quad v_1 = \dot{x}_1 = -\dot{l}(t), \quad v_2 = \dot{x}_2 = \dot{l}(t). \quad (3)$$

We assume that the force of viscous friction F_i is proportional to the relative velocity of the rod $v - v_i$, and the coefficient of proportionality k_i depends on the velocity of the sliders (bodies) v_i , i.e.,

$$F_i = -k_i(v_i)(v - v_i), \quad i = 1, 2. \quad (4)$$

Hence, the equation of motion (2) takes the form

$$m\dot{v}(t) = -k_1(v_1)(v(t) - v_1) - k_2(v_2)(v(t) - v_2). \quad (5)$$

The distance $l(t)$ is assumed to be harmonic, i.e.

$$l(t) = a \sin \omega t, \quad \dot{l}(t) = a\omega \cos \omega t, \quad v_1 = -a\omega \cos \omega t, \quad v_2 = a\omega \cos \omega t, \quad (6)$$

where a is the amplitude of the oscillations of the cylinders, and ω is the circular frequency.

In the following, the so-called asymmetric viscous friction is considered, where the coefficient of viscous friction k_i depends on the direction of motion of the slide-blocks

$$k_1(v_1) = \begin{cases} k_-, & v_1 \leq 0, \\ k_+, & v_1 > 0, \end{cases} \quad k_2(v_2) = \begin{cases} k_-, & v_2 \leq 0, \\ k_+, & v_2 > 0. \end{cases} \quad (7)$$

Taking into account expressions (6), we rewrite expression (7) in the form:

$$k_1(v_1) = \begin{cases} k_+, & \cos \omega t < 0, \\ k_-, & \cos \omega t \geq 0, \end{cases} \quad k_2(v_2) = \begin{cases} k_-, & \cos \omega t \leq 0, \\ k_+, & \cos \omega t > 0. \end{cases} \quad (8)$$

The dimensionless (asterisked) variables can be introduced as follows:

$$v^* = \frac{v}{2a\omega}, \quad v_1^* = \frac{v_1}{2a\omega}, \quad v_2^* = \frac{v_2}{2a\omega}, \quad t^* = t\omega, \quad k_1^* = \frac{k_1}{k_+}, \quad k_2^* = \frac{k_2}{k_+}, \quad (9)$$

with

$$k_1^*(v_1^*) = \begin{cases} 1, & \cos t^* < 0, \\ \kappa, & \cos t^* \geq 0, \end{cases} \quad k_2^*(v_2^*) = \begin{cases} \kappa, & \cos t^* \leq 0, \\ 1, & \cos t^* > 0, \end{cases} \quad (10)$$

$$\kappa = \frac{k_-}{k_+}, \quad 0 \leq \kappa \leq 1.$$

Using (9) and (10) the equation of motion (5) in dimensionless variables takes the form

$$\dot{v}^*(t^*) = -\varepsilon \left(k_1^* \left(v^*(t^*) + \frac{1}{2} \cos t^* \right) + k_2^* \left(v^*(t^*) - \frac{1}{2} \cos t^* \right) \right), \quad \varepsilon = \frac{k_+}{m\omega}. \quad (11)$$

2.2. Method of averaging

The equation of motion (11) can be written as (the asterisks are omitted)

$$\dot{v} = -\varepsilon \left(k_1 \left(v + \frac{1}{2} \cos t \right) + k_2 \left(v - \frac{1}{2} \cos t \right) \right). \quad (12)$$

The right-hand side of equation (12) is 2π -periodic in t . If the parameter ε is small ($\varepsilon \ll 1$) the method of averaging [2] can be applied to this equation.

Consider the equation

$$\dot{V} = -\frac{\varepsilon}{2\pi} \int_0^{2\pi} \left(k_1 \left(V + \frac{1}{2} \cos t \right) + k_2 \left(V - \frac{1}{2} \cos t \right) \right) dt. \quad (13)$$

Let $v(t)$ and $V(t)$ be the solutions of the equations (12) and (13), respectively, with the initial conditions $v(0) = V(0)$. Then

$$|v(t) - V(t)| = O(\varepsilon), \quad t \in [0, \xi], \quad \xi \sim 1/\varepsilon. \quad (14)$$

After averaging, the following result is obtained

$$\dot{V} = -\frac{\varepsilon}{\pi} (\pi(1 + \kappa)V - (1 - \kappa)). \quad (15)$$

The average velocity of the periodic motion of the system governed by equation (12) is approximated by the steady-state solutions of equation (15). The steady-state solution V_{st} is defined as a root of the function on the right-hand side of (15)

$$V_{st} = \frac{1}{\pi} \cdot \frac{1 - \kappa}{1 + \kappa}, \quad 0 \leq \kappa \leq 1. \quad (16)$$

Therefore,

$$0 \leq V_{st} \leq \frac{1}{\pi}, \quad (V_{st})_{max} = \frac{1}{\pi}. \quad (17)$$

The dimensional steady-state velocity is

$$V_{st} = \frac{2a\omega}{\pi} \cdot \frac{1 - \kappa}{1 + \kappa} = 4a\nu \frac{1 - \kappa}{1 + \kappa}, \quad \nu = \frac{\omega}{2\pi}. \quad (18)$$

Accordingly, the dimensional maximum steady-state velocity yields

$$(V_{st})_{max} = \frac{2a\omega}{\pi} = 4a\nu. \quad (19)$$

Figure 3 presents the numerical solution to equation (12) for the initial conditions $v(0) = 0$ with $\varepsilon = 0.02$ and $\kappa = 0.5$. For comparison, the dimensionless steady-state velocity found from the equation (16) is $V_{st} = 0.106$.

3. Experimental evaluation on a prototype

A prototype of the linear motor was developed for the experimental evaluation of the results from the previous section, see Figure 4. For the developed prototype the hydrocarbon-based magnetorheological fluid LORD MRF-140CG with the following parameters was used [1]: viscosity $\eta = 0.28 \text{ Pa} \cdot \text{s}$, density $\rho = 3.6 \cdot 10^3 \text{ kg/m}^3$, particle weight concentration is 0.85, distance $2a = 1.25 \text{ cm}$, frequency $\nu = 5 \text{ Hz}$.

For the design of the mechanical and electrical components, a FEM simulation (ANSYS® 19.1 Workbench) of the cylinders with coils and fluid was performed. Figure 5 shows the magnetic flux density for the volumes comprising the slide-blocks. It should be noted that the system is considered to be a magnetostatic one. The flux density is given in a vector representation and the color of the vector arrows corresponds to the magnitude of the flux density. It is highest in the area between the slider and the slide-blocks, because of the material's small cross-section of the material in this area. The maximum value is below 1 T and is therefore still away from the saturation flux density. The experiment was carried out with the technical parameters mentioned above in the text and the captions. For these specific parameters the dimensional value of the steady-state velocity found by equation (18) is 4.25 cm/s (in dimensionless form the value is 0.106), see Figure 3. The measured average

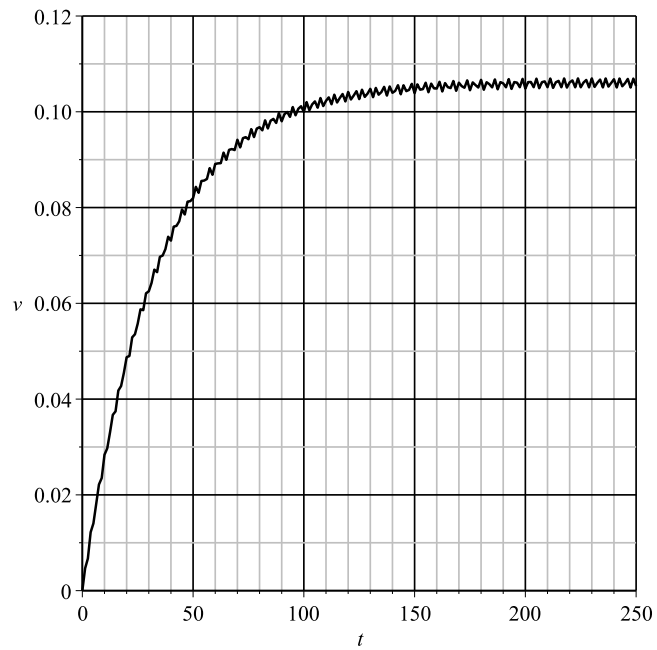


Figure 3. Time history stationary velocity of the rod.

velocity in the experiment is 2.6 cm/s. The difference between the calculated and measured velocities is mainly due to friction in the bearings and the change in the rheological properties of the MRF under the influence of the applied magnetic field.

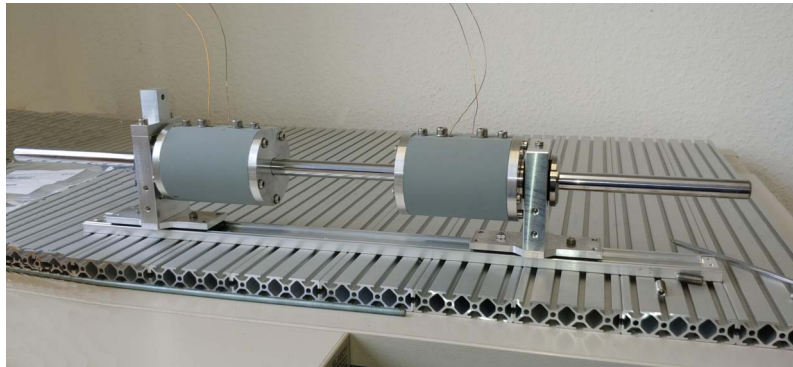


Figure 4. The prototype of the linear motor based on vibrations of the slide-blocks and the controlled viscosity of a MRF

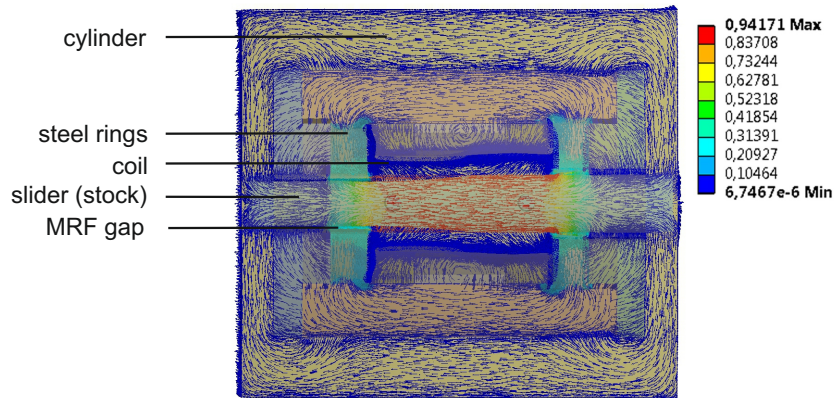


Figure 5. The magnetic flux density of a cylinder with one coil (125 windings, 0.4 A current strength).

4. Conclusions and outlook

A mathematical model and a prototype of a linear motor based on vibrations of two slide-blocks and the controlled viscosity of a MRF was considered. A controllable magnetic field provides an asymmetry of the friction for forward and backward motions, which enables the net displacement of the slider for one period. Based on NEWTONs second law the motion equations for the system are obtained. Using the method of averaging the expression for the stationary velocity of the motion of the slider is formulated in an analytical form. This formula is valid if the force of friction is small compared to the driving force of the slide-blocks. On the basis of the theoretical principles outlined above, a prototype of the linear motor was created. The results of the theoretical calculations agree qualitatively with the experiments. In order to improve the quantitative agreement of the results, dry friction as well as viscous friction will be considered in an extended model. This friction occurs among other effects at the sealing elements and bearings and influences the velocity of the slider as well.

The principle of motion, which was presented in the article, can also be transferred to a rotary drive. The development of such a motor is planned as the next experimental step.

Acknowledgments

The authors would like to thank the Deutsche Forschungsgemeinschaft (DFG) for financial support within SPP1681 research program under the project ZI 540-17/3.

References

- [1] Lord Technical Data MRF-140CG. LORD Corp. OD DS 7012 (Rev.1 7/08). *www.lord.com*, 2 p.
- [2] BOGOLIUBOV, N., AND MITROPOLSKY, Y. *Asymptotic methods in the theory of non-linear oscillations*. Gordon and Breach Science, New York, 1961.
- [3] HAJALILOU, A., MAZLAN, S., LAVVAFI, H., AND SHAMELI, K. *Field Responsive Fluids as Smart Materials*. Springer Nature, Singapore, 2016.
- [4] JANOCHA, H. *Actuators-Basics and Applications*. Springer-Verlag, Berlin, 2004.
- [5] JANOCHA, H. *Unkonventionelle Aktoren: Eine Einführung*. Oldenbourg, München, 2013. 2. Aufl.
- [6] KARPELSON, M., WEI, G., AND WOOD, R. Driving high voltage piezoelectric actuators in microrobotic applications. *Sensors and Actuators A: Physical* 176 (2012), 78–89.
- [7] MIZZI, J. Actuators, motors and wheelless autonomous robots using vibratory transducer drivers, patent US 5.770.913, 1998.
- [8] RÖSLER, U. Drehmomentenbegrenztes Kupplungselement sowie Verfahren zum drehmomentbegrenzten Kuppeln, Patent DE 10 2009 034 055.6, 2009.
- [9] SASHIDA, T. Supersonic vibration driven device, patent US 4.548.090, 1984.
- [10] ZIMMERMANN, K., LYSENKO, V., GÜNTHER, L., AND BECKER, F. Vorrichtung, System und Verfahren zur Erzeugung einer überwiegend gleichgerichteten translatorischen oder rotatorischen Bewegung, Patent DE 10 2018 121 831 A1, 2018.

Klaus Zimmermann, Ph.D.: Technische Universitaet Ilmenau, PF 100565 D-98684 Ilmenau, Germany (DE) (*klaus.zimmermann@tu-ilmenau.de*). The author gave a presentation of this paper during one of the conference sessions.

Igor Zeidis, Ph.D.: Technische Universitaet Ilmenau, PF 100565 D-98684 Ilmenau, Germany (DE) (*igor.zeidis@tu-ilmenau.de*).

Victor Lysenko, Ph.D.: Belarusian National Technical University, Belarus, 220013, Minsk, Nezavisimosty Ave., 65, Belarus (BY) (*victor_lysenko@mail.ru*).

Simon Gast, M.Sc. (Ph.D. student): Technische Universitaet Ilmenau, PF 100565 D-98684 Ilmenau, Germany (DE) (*simon.gast@tu-ilmenau.de*).

Lars Günther, M.Sc.: Technische Universitaet Ilmenau, PF 100565 D-98684 Ilmenau, Germany (DE) (*lars.guenther@tu-ilmenau.de*).

Florian Schale, Ph.D.: Technische Universitaet Ilmenau, PF 100565 D-98684 Ilmenau, Germany (DE) (*florian.schale@tu-ilmenau.de*).

Michel Rohn, B.A. (M.Sc. student): Technische Universitaet Ilmenau, PF 100565 D-98684 Ilmenau, Germany (DE) (*michel.rohn@tu-ilmenau.de*).

Energy spectrum of inhomogeneous rods with elastic and viscous boundary conditions

Ádám Zsiros, János Lelkes, Tamás Kalmár-Nagy

Abstract: In this work, we search for the energy spectrum of a continuous longitudinal vibration of an inhomogeneous rod model. This rod model is a continuous limit of a chain oscillator with a spring and a damper between a fixed wall and one end of the chain oscillator. The model describing the system is a wave equation with viscous and elastic boundary conditions. In order to determine the eigenvalues and mode shapes of the rod, separation of variables (space and time) was applied. This method results in a Sturm-Liouville problem for the spatial part, which is solved by using series solution. The distributions of the kinetic and the potential energy are calculated and the energy spectrum of the rod is determined for constant and exponentially varying stiffness.

1. Introduction

Energy transfer occurs in many natural and engineering process along an especially wide range. Some of the most frequent engineering applications are the vibration reduction systems for machines and buildings [2, 3, 4, 5, 6, 7, 9, 12, 16].

A typical example of a process with multi-scale energy transfer is turbulent flow. The energy cascade model of Richardson [13] describes turbulence. The largest whirls break up into smaller eddies, and the energy dissipation of turbulence happens at the smallest scales through viscosity. This process transfers the turbulent kinetic energy of the flow towards the smallest scales. This phenomenon is phenomenologically described by the mechanistic turbulence model via a binary tree (Fig. 1) of Kalmár-Nagy and Bak [10].

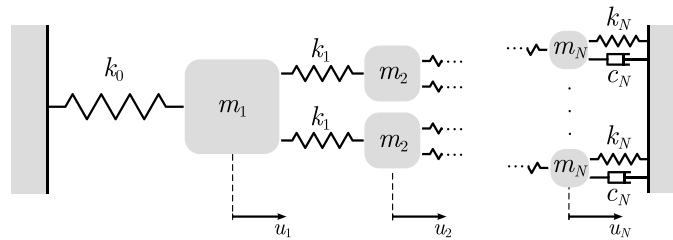


Figure 1. The n -level binary tree model

The energy spectrum \hat{E} describes how the energy is exactly distributed in the different scales of the whirls. It can be defined as a distribution function along the κ wave number:

$$E = \int \hat{E}(\kappa) d\kappa. \quad (1)$$

This definition was applied by Kalmár-Nagy and Bak (2019) [10] and the wavenumber was defined as an inversely proportional quantity to the length-scale of a whirl: $\kappa \sim 1/L$. In case of the binary tree model the wavenumber can be defined as an analogy of the length-scales of the whirls: $\kappa_l = 1/m_l$ (the wavenumber of a certain level is inversely proportional to the mass scale of the level). The different parameters of the mechanistic binary tree model were chosen by Kalmár-Nagy and Bak [10] so as to obtain an energy spectrum similar to the Kolmogorov spectrum [11]:

- A certain level contains only masses of the same size and the sum of the masses on a certain level equals to 1.
- The stiffnesses of the springs are described by a power law as a function of the level.

The binary tree model can be ‘renormalized’ to the N -mass chain oscillator model shown in Fig. 2 [10].

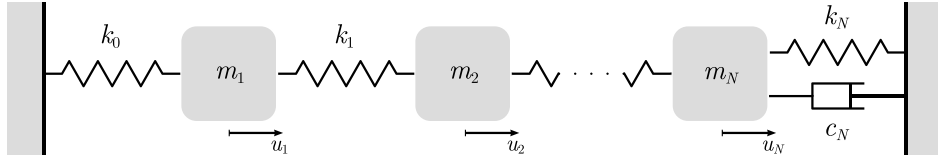


Figure 2. The N -level chain-oscillator model

The parameters of the damped chain oscillator model are the following: m_i is the weight of the i th mass, k_i is the stiffness of the i th spring for $i = 1, 2, \dots, N$ and c_N is the damping. Let the position of the masses in Figure 2 be $u_i = u_i(t)$ for $i = 1, 2, \dots, N$; additionally, the $i = 0$ and $i = N + 1$ cases represent the positions of the fixed ends ($u_0 = 0, u_{N+1} = 0$). The parameter distribution that has the least error compared to the Kolmogorov-spectrum has been investigated for a discrete chain oscillator model for 20 levels ($N = 20$) by Kalmár-Nagy and Bak (2019) [10]. The aim of this study is to create a continuous model of the chain oscillator ($N \rightarrow \infty$) and investigate the spectrum in case of different parameter distributions.

2. Derivation of the continuous model

In this section we derive the equations of motion of a continuous (rod) model (Figure 3), which is the limit of the chain oscillator regarding the number of masses ($N \rightarrow \infty$). These

equations contain time and spatial derivatives. The notation for the time derivative is $\dot{\square} = \frac{\partial}{\partial t}\square$ and for the spatial derivative is $\square' = \frac{\partial}{\partial x}\square$. The equations of motion for the system are:

$$m_i \ddot{u}_i = f(\delta_{i+1}, k_{i+1}) - f(\delta_i, k_i), \quad \text{for } i = 1, 2, \dots, N, \quad (2)$$

where f [N] is the force ($f > 0$ when the spring is under tension):

$$f(k, \delta) = k\delta, \quad (3)$$

δ [m] is the contraction of the spring (compared to its tensionless length):

$$\delta_i = u_i - u_{i-1} \quad (4)$$

and k [N/m] is the stiffness of the spring.

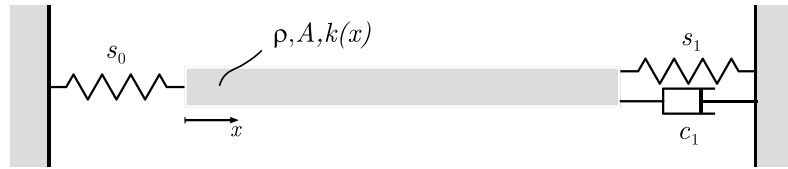


Figure 3. The continuous rod-model of the discrete chain-oscillator

In order to reduce the number of parameters, it is worth introducing dimensionless quantities:

$$\hat{u} = \frac{u}{U}, \quad \hat{f} = \frac{f}{F}, \quad \hat{k} = \frac{k}{K}, \quad \hat{\delta} = \frac{\delta}{\Delta}, \quad \hat{t} = \frac{t}{T}, \quad (5)$$

where u (position), f (force), k (stiffness), δ (displacement), t (time) are dimensional quantities, $\hat{u}, \hat{f}, \hat{k}, \hat{\delta}, \hat{t}$ are their dimensionless representations. These dimensionless quantities are defined by using the following scales: U (position), F (force), K (stiffness), Δ (displacement), T (time) are the *scales* that create connection between the dimensional and non-dimensional quantities. The governing equations of the system are the following:

$$m_i \frac{d^2 u_i}{dt^2} = m_i \frac{d^2 (U \hat{u}_i)}{d(T \hat{t})^2} = K \Delta \left(\hat{f}(\hat{\delta}_{i+1}, \hat{k}_{i+1}) - \hat{f}(\hat{\delta}_i, \hat{k}_i) \right), \quad \text{for } i = 1, 2, \dots, N, \quad (6)$$

which can be written in the following form:

$$\frac{d^2 \hat{u}_i}{d\hat{t}^2} = \frac{T^2 K \Delta}{U m_i} \left(\hat{f}(\hat{\delta}_{i+1}, \hat{k}_{i+1}) - \hat{f}(\hat{\delta}_i, \hat{k}_i) \right). \quad (7)$$

For simplicity a new notation is introduced: the dimensionless parameters (with hat on themselves) will be written without hat, since all of the quantities are dimensionless along the remaining part of the paper. In order to minimize the number of parameters the following combination of the dimensionless quantities are used:

$$\frac{\Delta}{U} = N, \quad \frac{T^2 K}{m_i} = 1. \quad (8)$$

Based on Rosales (2001) [14], the model can be made continuous on the $x \in [0, 1]$ interval. Discrete quantities with index i are changed to continuous quantities $\hat{u}(x), \hat{\delta}(\hat{u}(x))$. The equations of motion for a rod with $k(x)$ stiffness distribution can be written as

$$\ddot{u}(x, t) = \frac{\partial}{\partial x} [k(x)u'(x, t)], \quad (9)$$

with boundary conditions

$$k(0)u'(0, t) = s_0 u(0, t), \quad (10)$$

$$k(1)u'(1, t) = -s_1 u(1, t) - c_1 \dot{u}(1, t), \quad (11)$$

considering the force equilibrium at the ends of the rod. Because of the continuity of the stiffness distribution we have

$$s_0 = \lim_{x \rightarrow 0} k(x), \quad s_1 = \lim_{x \rightarrow 1} k(x). \quad (12)$$

The 2 initial conditions are specified

$$u(x, 0) = \varphi(x), \quad (13)$$

$$u'(x, 0) \equiv 0. \quad (14)$$

The shape $\varphi(x)$ will be determined later in Section 3.

3. Solving the model equations

The boundary value problem (9)–(11) can also be formulated as the Sturm-Liouville problem:

$$\ddot{u}(x, t) = \frac{\partial}{\partial x} [k(x)u'(x, t)], \quad (15)$$

$$k(0)u'(0, t) = s_0 u(0, t), \quad (16)$$

$$k(1)u'(1, t) = -s_1 u(1, t) - c_1 \dot{u}(1, t). \quad (17)$$

To determine the eigenvalues and eigenfunctions of the system the separation of variables method is applied (Hull, 1994) [8]:

$$u(x, t) = U(x)T(t). \quad (18)$$

Equation (18) is substituted into Equation (15):

$$\frac{\ddot{T}(t)}{T(t)} = \left(\frac{U''(x)}{U(x)}k(x) - \frac{U'(x)}{U(x)}k'(x) \right) = \lambda^2, \quad (19)$$

from which

$$T(t) = \tau e^{\lambda t}, \quad (20)$$

$$\frac{\partial}{\partial x} [k(x)U'(x)] + \lambda^2 U(x) = 0. \quad (21)$$

At this point, we consider two special cases, where $k(x)$ is a constant function and where $k(x)$ is an exponentially varying function.

3.1. The $k(x) = \text{const.}$ case

The simplest case of the system is $k(x) = k = \text{const.}$ case. The eigenvalues and the eigenfunctions (mode-shapes) of the rod can be determined in this case in a simple manner. Substituting the constant $k(x)$ into Equation (21) yields

$$kU''(x) + \lambda^2 U(x) = 0, \quad (22)$$

which has the solution

$$U(x) = C_1 e^{\frac{\lambda}{\sqrt{k}}x} + C_2 e^{-\frac{\lambda}{\sqrt{k}}x}, \quad (23)$$

where C_1 and C_2 are constants, which can be determined using the boundary conditions:

$$U'(0) = U(0), \quad (24)$$

$$U'(1) = U(1) - \frac{c_1}{k} \lambda U(1). \quad (25)$$

The following matrix equation results from Equations (23)–(25):

$$\begin{pmatrix} 1 - \frac{\lambda}{\sqrt{k}} & 1 + \frac{\lambda}{\sqrt{k}} \\ e^{\frac{\lambda}{\sqrt{k}}} \left(k + (c_1 + \sqrt{k})\lambda \right) & e^{-\frac{\lambda}{\sqrt{k}}} \left(k + (c_1 - \sqrt{k})\lambda \right) \end{pmatrix} \begin{pmatrix} C_1 \\ C_2 \end{pmatrix} = \begin{pmatrix} 0 \\ 0 \end{pmatrix}. \quad (26)$$

Assuming $C_1, C_2 \neq 0$, the determinant of the matrix should be equal to 0:

$$\frac{c_1 \lambda^2 + 2\lambda}{1 + \lambda c_1 + \lambda^2} + \tanh(\lambda) = 0. \quad (27)$$

Equation (27) is the characteristic equation of the system. For a certain k and c_1 values the eigenvalue pairs can be calculated. Notice, that the characteristic equation (27) has infinitely many eigenvalues. Using these eigenvalues, eigenfunction pairs can be determined from Equation (23). In order to calculate the solution function, it is worth applying the series solution method used by Hull (1994) [8]. A suitable initial condition is the sum of the mode-shapes:

$$\varphi(x) = \sum_{n=-\infty}^{\infty} U_n(x), \quad (28)$$

from which the solution function is

$$u(x, t) = \sum_{n=-\infty}^{\infty} U_n(x) T_n(t). \quad (29)$$

Figure 4a illustrates the first 2 dominant eigenvalue pairs of the system for constant $k = 1$ and varying c_1 (root locus plot). Figure 4b illustrates the first 2 mode-shapes of the system.

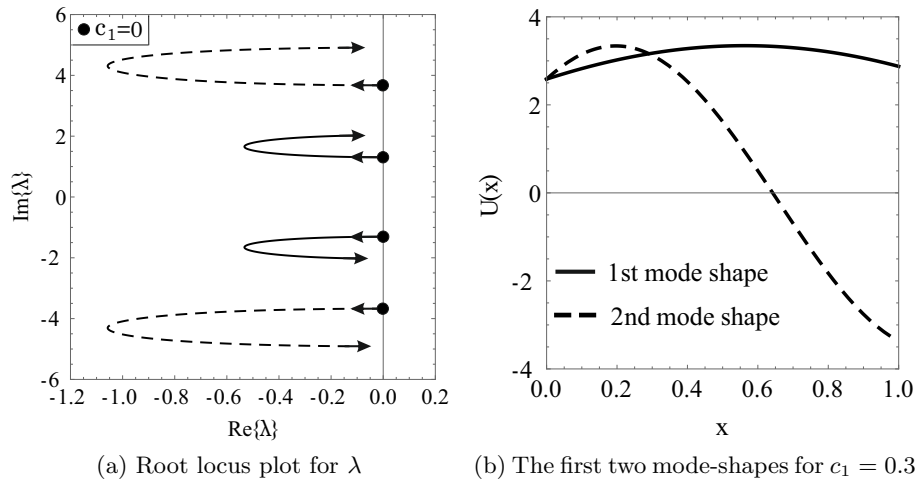


Figure 4. The characteristic roots and the mode-shape for $k = 1$

Following the steps of Hull (1994) [8], the function $u(x, t) = U_{-1}(x)T_{-1}(t) + U_1(x)T_1(t)$ provides a real solution.

3.2. The exponentially changing case

In order to create an analogue model to the binary tree of Kalmár-Nagy and Bak (2019) [10], an exponential term can be used for the stiffness of the rod:

$$k(x) = e^{-2\sigma x}, \quad \sigma \neq 0 \text{ and } x \in [0, 1]. \quad (30)$$

Based on the work of Arfken and Weber (1985) [1, pp. 497-538], the solution of Equation (21) for this case is

$$U(x) = e^{\sigma x} \left[C_1 i I_1 \left(\frac{\lambda e^{\sigma x}}{\sigma} \right) + 2C_2 K_1 \left(\frac{\lambda e^{\sigma x}}{\sigma} \right) \right], \quad (31)$$

where $I_1(z)$ is the first modified Bessel function of the first kind and $K_1(x)$ is the first modified Bessel function of the second kind. The C_1 and C_2 constants can be determined from the boundary conditions (Equations (16)–(17)). The calculation results characteristic equation as in Equation (26)–(27) and real solutions can be determined via series solution method (Equation (29)) as in Section 3.1.

4. Energy spectrum of the rod

In case of the chain oscillator, the energy spectrum is a discrete distribution due to the discrete number of masses, while it is a continuous distribution in the case of the rod model. It is worth collecting the required properties of the ‘wavenumber function’:

- at $x = 0$, the wavenumber is 1
- at $x = 1$ ($N \rightarrow \infty$), the wavenumber is ∞ .

One possible choice is

$$\kappa(x) = 2^{\frac{x}{1-x}}. \quad (32)$$

4.1. Formulation of the energy spectrum

Based on the work of Wohlever and Bernhard (1992) [15], the energy at a point x of the rod can be calculated as

$$E(x, t) = \underbrace{\frac{1}{2} k(x) \left(\frac{du(x, t)}{dx} \right)^2}_{\text{potential energy}} + \underbrace{\frac{1}{2} \left(\frac{du(x, t)}{dt} \right)^2}_{\text{kinetic energy}}. \quad (33)$$

The total energy of the rod is

$$E_{\text{total}}(t) = \underbrace{\frac{1}{2} \int_0^1 k(x) \left(\frac{du(x, t)}{dx} \right)^2 + \left(\frac{du(x, t)}{dt} \right)^2 dx}_{\text{energy of the rod}} + \underbrace{\frac{1}{2} s_0 u^2(0, t) + \frac{1}{2} s_1 u^2(1, t)}_{\text{energy of the springs}}. \quad (34)$$

Substituting back the function of the series solution for the separation of variables method applied from Hull (1994) [8] in Equation (29), Equations (33)–(34) results the energy values. The introduced quantities in Equations (33)–(34) are time-varying quantities, on the

contrary, for calculating the energy spectrum, discrete values are needed at x . In order to define a discrete value at x , it is useful to define a mean energy in the asymptotic limit (Kalmár-Nagy and Bak, 2019) [10]:

$$\bar{E}(x) = \frac{\omega}{\pi} \int_{\tau}^{\tau+\pi/\omega} E(x, t) dt, \quad \tau \rightarrow \infty, \quad (35)$$

$$\bar{E}_{\text{total}} = \frac{\omega}{\pi} \int_{\tau}^{\tau+\pi/\omega} E_{\text{total}}(t) dt, \quad \tau \rightarrow \infty, \quad (36)$$

where ω is the eigenfrequency corresponding to the dominant eigenvalue of the system ($\omega = \text{Im}\{\lambda_1\}$). The same mean energy can be calculated for the total energy, as well; and the fraction of these two mean energies gives the energy spectrum:

$$\hat{E}(x) = \frac{\bar{E}(x)}{\bar{E}_{\text{total}}}, \quad (37)$$

where $\hat{E}(x)$ is the energy spectrum in the range of x (along the rod), $\bar{E}(x)$ is the energy of the rod at x and \bar{E}_{total} is the total energy of the rod. Figure 5. presents the energy spectrum of the rod model in case of constant stiffness ($k = 1$), and plots can be compared for two different damping values. It can be seen, by increasing the damping, the energy spectrum shifts downwards. There is no significant change in the characteristics of the distribution. The spectrum of the kinetic and potential energy are equal to each other.

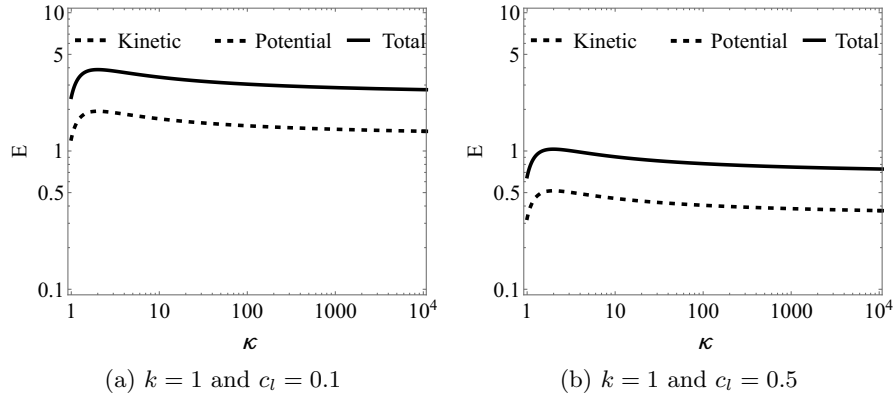


Figure 5. The energy spectrum of the model with constant stiffness for different values

It is worth checking the case where the end-springs have different stiffness, than they were decided on in Equation (12). Figure 6 represents these cases for $k = 1$, $c_1 = 0.5$ and $s_0 s_1 = 1$.

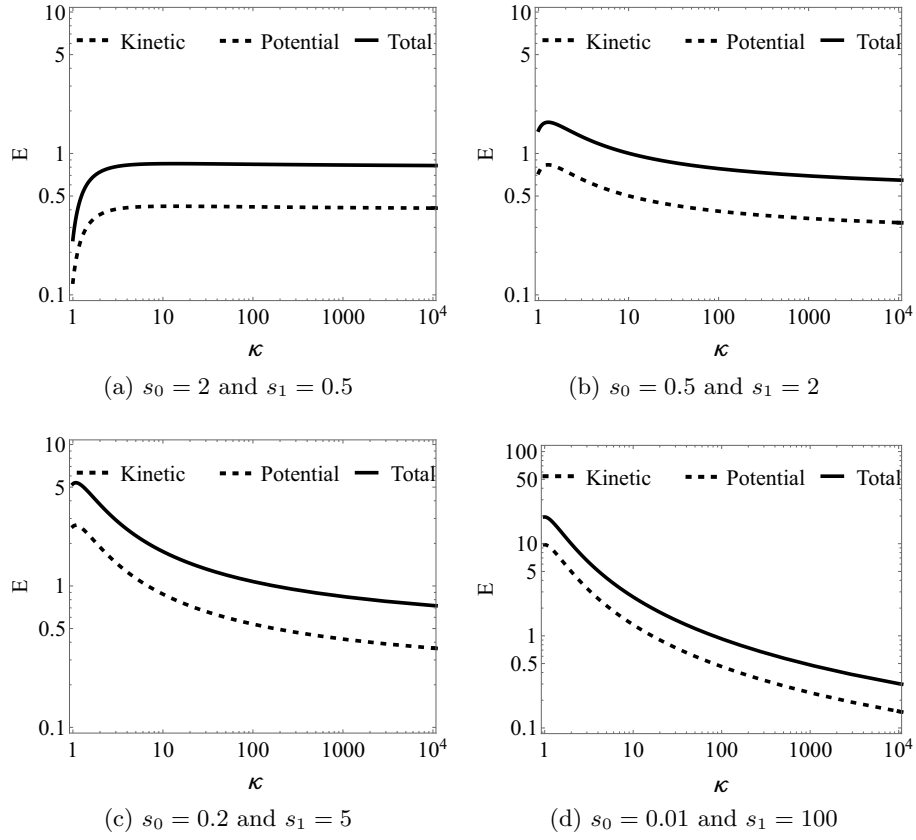


Figure 6. The energy spectrum of the model with constant stiffness for $k = 1$ and $c_1 = 0.5$ and different stiffness values for the end-springs

Figure 6 shows, that increasing s_1 results in a decreasing slope in the energy spectrum. In this case the constant part of the energy spectrum occurs for larger κ values. This constant value is decreasing by increasing s_1 . It can be seen, that decreasing the value of s_0 , the energy value at $\kappa = 1$ is larger.

Figure 7 presents the energy spectra for exponentially varying $k(x)$ in the case of $c_1 = 0.5$ and 4 different σ values. It can be seen, that for $\sigma < 0$, the dominant part of the total energy is the potential energy and for $\sigma > 0$, the dominant part of the total energy is the kinetic energy.

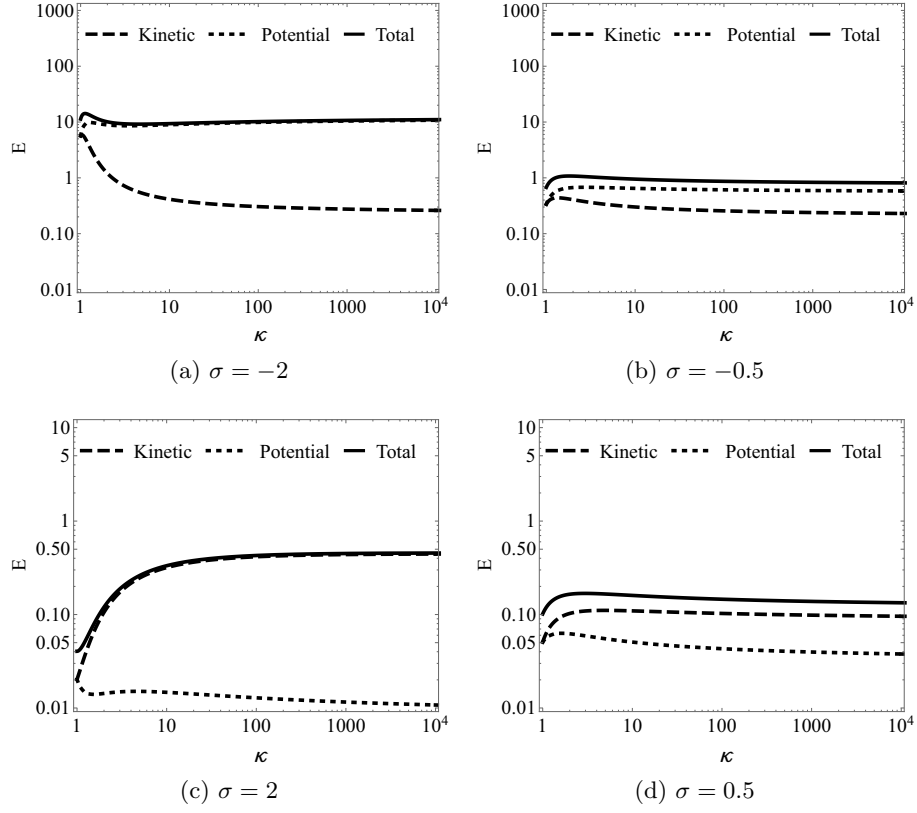


Figure 7. The energy spectrum of the model with exponentially varying stiffness for $c_1 = 0.5$ and different σ values

5. Summary

The chain oscillator model of Kalmár-Nagy and Bak (2019) [10] was extended regarding the number of masses (levels). The new model is continuous, since the number of masses (levels) tends to infinity ($N \rightarrow \infty$). The key parameters of the model is the stiffness distribution and the damping of the system. The eigenvalues and eigenfunctions of the system were determined and the expression for the energy of the rod was derived. The eigenvalues have complex parts, so the system is oscillating. So as to get a discrete value for the energy at a certain wavenumber, it is worth averaging the oscillating energy over its period. Considering a properly long time: after the most of the oscillations are decayed, the energy oscillation can be averaged over an oscillation period connected to the most significant characteristic root. The energy spectrum can be determined for certain $k(x)$ functions, different $c_1 = \text{const.}$ values and different s_0, s_1 stiffness values.

Acknowledgements

The publication of the work reported herein has been supported by the ÚNKP-19-2-I and ÚNKP-19-3-I New National Excellence Program of the Ministry for Innovation and Technology. The publication of the work reported herein has been supported by ETDB at BME. The research reported in this paper was supported by the Higher Education Excellence Program of the Ministry of Human Capacities in the frame of the Water sciences & Disaster Prevention research area of BME (BME FIKP-VÍZ). The research reported in this paper has been supported by the National Research, Development and Innovation Fund (TUDFO/51757/2019-ITM, Thematic Excellence Program).

References

- [1] ARFKEN, G. B., AND WEBER, H. J. *Sturm-Liouville Theory–Orthogonal Functions*, 3rd ed. Orlando, FL: Academic Press, 1985, ch. 9.
- [2] BRILLOUIN, L. *Wave propagation in periodic structures: electric filters and crystal lattices*. Courier Corporation, 2003.
- [3] FRAHM, H. Device for damping vibrations of bodies, 1911.
- [4] GIURDANELLA, S., AND SPARAVIGNA, A. C. Self frequency-locking of a chain of oscillators.
- [5] GÜRGÖZE, M. On various eigenvalue problem formulations for viscously damped linear mechanical systems. *International Journal of Mechanical Engineering Education* 33, 3 (2005), 235–243.
- [6] GÜRGÖZE, M., AND ÖZER, A. On the slightly damped uniform n-mass oscillator. *Computers & Structures* 59, 5 (1996), 797–803.
- [7] HERMANRUD, O. C. Active and passive damping systems for vibration control of metal machining equipment. Master’s thesis, 2017.
- [8] HULL, A. J. A closed form solution of a longitudinal bar with a viscous boundary condition. *Journal of Sound and Vibration* 169, 1 (1994), 19–28.
- [9] ISIĆ, S., MEHREMIĆ, S., KARABEGOVIĆ, I., AND HUSAK, E. Systems for passive and active vibration damping. 96–104.
- [10] KALMÁR-NAGY, T., AND BAK, B. D. An intriguing analogy of Kolmogorov’s scaling law in a hierarchical mass–spring–damper model. *Nonlinear Dynamics* (2019).
- [11] KOLMOGOROV, A. N. The local structure of turbulence in incompressible viscous fluid for very large reynolds numbers. *Cr Acad. Sci. URSS* 30 (1941), 301–305.
- [12] MCNAMARA, R. J. Tuned mass dampers for buildings. *Journal of the Structural Division* 103, 9 (1977), 1785–1798.

- [13] RICHARDSON, L. F. The supply of energy from and to atmospheric eddies. *Proc. R. Soc. Lond. A* 97, 686 (1920), 354–373.
- [14] ROSALES, R. R. Discrete to continuum modeling, 2001.
- [15] WOHLEVER, J. C., AND BERNHARD, R. J. Mechanical energy flow models of rods and beams. *Journal of Sound and Vibration* 153, 1 (1992), 1–19.
- [16] ZHENG, Z., FENG, X., AO, B., AND C. CROSS, M. Synchronization of groups of coupled oscillators with sparse connections. *EPL (Europhysics Letters)* 87 (09 2009).

Ádám Zsiros, B.Sc. (M.Sc. student): Budapest University of Technology and Economics, Faculty of Mechanical Engineering, Department of Fluid Mechanics, H-1111 BUDAPEST, Bertalan Lajos Street 4-6. (*adam.zsiros@live.com*). The author gave a presentation of this paper during one of the conference sessions.

János Lelkes, M.Sc. (Ph.D. student): Budapest University of Technology and Economics, Faculty of Mechanical Engineering, Department of Fluid Mechanics, H-1111 BUDAPEST, Bertalan Lajos Street 4-6. (*lelkes@ara.bme.hu*).

Tamás Kalmár-Nagy, Ph.D. (associate professor): Budapest University of Technology and Economics, Faculty of Mechanical Engineering, Department of Fluid Mechanics, H-1111 BUDAPEST, Bertalan Lajos Street 4-6. (*kalmarnagy@ara.bme.hu*).

INDEX OF AUTHORS

Albanbay Nurtay	11
Alzarooni Tariq	25
AL-Shudeifat Mohammad	25
Arabi Sadaf	171
Augustynek Krzysztof	215
Awrejcewicz Jan	37, 47, 55, 65, 183, 227, 277, 289, 301, 365, 375, 523, 547
Bartkowiak Tomasz	397
Bartoszewicz Andrzej	323
Bielski Włodzimierz	75
Bilichenko Dmytro	37
Bizyaev Ivan	87
Borisov Alexey	87
Böhm Valter	335
Bunyakova Yuliya	259
Buyadzhi Anna	99, 267
Buyadzhi Vasily	99
Carrillo Li Enrique Roberto	335
Cheib Akram Khalil	37
Chernyshev Alexey	99
Chevallier Gaël	479
Chruściel Jarosław	107
Chwastek Stefan	117
Da Silva Samuel	479
Dulf Eva-H.	129
Fiebig Wiesław	139
Fonseca Gustavo de Freitas	151
Frątczak Anna	107
Galewski Marek	249
Gast Simon	559
Gidlewski Mirosław	163, 409
Glushkov Alexander	259, 491
Goossaert Célien	431
Gregorczyk Magdalena	423
Grolet Aurélien	171

Grzelczyk Dariusz	183, 227, 375
Gunn Ben	193
Günther Lars	559
Herisanu Nicolae	205
Ignatenko Anna	267
Jarzębowska Elżbieta	215
Jarzyna Olga	227
Jayaprakash Kalkunte R.	237
Jemioł Leszek	163
Kaliński Krzysztof	249
Kalmár-Nagy Tamás	567
Kaufhold Tobias	335
Katsura Kohsuke	539
Khetselius Olga	259, 267
Kilin Alexander	87
Kir'yanov Sergey	99
Koruba Zbigniew	313
Krylova Ekaterina	301
Krysko Anton	47, 277
Krysko Vadim	47, 65, 277, 289
Krysko-jr Vadim	289, 301
Krzysztofik Izabela	313
Kutepov Ilya	277
Lamarque Claude-Henri	431
Latosiński Paweł	323
Lelkes János	567
Lopes António	345
Losyeva Nataliya	37
Ludwicki Michał	523
Lukin Alexey	355, 387
Lysenko Victor	559
Machado J.A. Tenreiro	345
Mamaev Ivan	87
Manevitch Leonid	457

Marinca Vasile	205
Mazur Michał	249
Mazur Olga	365
Medetov Bekbolat	11
Morawska Natalia	249
Mrozowski Jerzy	523
Muresan Cristina-I.	129
Nabarrete Airton	151
Nataraj C.	25
Nishiyama Naoto	539
Ogińska Ewelina	375
Papirovskiy Alexey	387
Papkova Irina	301
Paskowski Wojciech	397
Pavlov Eugeny	99
Pavlov Sergey	65
Pivovarova Elena	87
Plisetskaya Evgeniya	99
Polczyński Krystian	375
Popov Ivan	355, 387
Prochowski Leon	409
Puchalska Angelika	107
Pusty Tomasz	409
Puzyrov Volodymyr	37
Rodríguez Hernández Jorge Antonio.....	335
Rohn Michel	559
Rothberg Steve	193
Rysak Andrzej	423
Saltykova Olga	47
Savadkoohi Alireza Ture	431
Schale Florian	559
Schorr Philipp	335
Selyutskiy Yury	439
Shami Zein	171

Shiryayev Oleg	25
Skurjat Aleksander	449
Smirnov Valeri	457
Starosta Roman	55
Starosvetsky Yuli	237
Streibl Siam	107
Svinarenko Andrey	259, 267
Sypniewska-Kamińska Grażyna	55
Szwajkowski Patryk	409
Šmeringaiová Anna	469
Theodossiades Stephanos	193
Teloli Rafael	479
Ternovsky Eugeny	491
Ternovsky Valentin	491
Timis Daniel D.	129
True Hans	499
Tsudik Andrey	491
Udalov Pavel	355
Urbaś Andrzej	215
Verhulst Ferdinand	511
Vojtko Imrich	469
Wittbrodt Edmund	523
Wojnar Ryszard	75
Wojnicz Wiktoria	523
Yabuno Hiroshi	539
Yamashita Kiyotaka	539
Zafar Azhar Ali	547
Zagrodny Bartłomiej	107, 523
Zaks Michael	11
Zeidis Igor	559
Zentner Lena	335
Zhigalov Maxim	65, 289
Zimmermann Klaus	559, 335
Ziubiński Mateusz	409

Zsiros Ádám	567
Žardecki Dariusz	163

